

Energy Systems in Electrical Engineering

M. K. Jayaraj
Aldrin Antony
P. P. Subha *Editors*

Energy Harvesting and Storage

Fundamentals and Materials



Springer

Energy Systems in Electrical Engineering

Series Editor

Muhammad H. Rashid, Florida Polytechnic University, Lakeland, USA

Energy Systems in Electrical Engineering is a unique series that aims to capture advances in electrical energy technology as well as advances electronic devices and systems used to control and capture other sources of energy. Electric power generated from alternate energy sources is getting increasing attention and supports for new initiatives and developments in order to meet the increased energy demands around the world. The availability of computer-based advanced control techniques along with the advancement in the high-power processing capabilities is opening new doors of opportunity for the development, applications and management of energy and electric power. This series aims to serve as a conduit for dissemination of knowledge based on advances in theory, techniques, and applications in electric energy systems. The Series accepts research monographs, introductory and advanced textbooks, professional books, reference works, and select conference proceedings. Areas of interest include, electrical and electronic aspects, applications, and needs of the following key areas:

- Biomass and Wastes Energy
- Carbon Management
- Costs and Marketing
- Diagnostics and Protections
- Distributed Energy Systems
- Distribution System Control and Communication
- Electric Vehicles and Tractions Applications
- Electromechanical Energy Conversion
- Energy Conversion Systems
- Energy Costs and Monitoring
- Energy Economics
- Energy Efficiency
- Energy and Environment
- Energy Management, and Monitoring
- Energy Policy
- Energy Security
- Energy Storage and Transportation
- Energy Sustainability
- Fuel Cells
- Geothermal Energy
- Hydrogen, Methanol and Ethanol Energy
- Hydropower and Technology
- Intelligent Control of Power and Energy Systems
- Nuclear Energy and Technology
- Ocean Energy
- Power and Energy Conversions and Processing
- Power Electronics and Power Systems
- Renewable Energy Technologies
- Simulation and Modeling for Energy Systems
- Superconducting for Energy Applications
- Tidal Energy
- Transport Energy

M. K. Jayaraj · Aldrin Antony · P. P. Subha
Editors

Energy Harvesting and Storage

Fundamentals and Materials

 Springer

Editors

M. K. Jayaraj
Department of Physics
Cochin University of Science
and Technology
Kochi, Kerala, India

Aldrin Antony
Department of Physics
Cochin University of Science
and Technology
Kochi, Kerala, India

P. P. Subha
Department of Physics
Cochin University of Science
and Technology
Kochi, Kerala, India

ISSN 2199-8582

ISSN 2199-8590 (electronic)

Energy Systems in Electrical Engineering

ISBN 978-981-19-4525-0

ISBN 978-981-19-4526-7 (eBook)

<https://doi.org/10.1007/978-981-19-4526-7>

© The Editor(s) (if applicable) and The Author(s), under exclusive license to Springer Nature Singapore Pte Ltd. 2022

This work is subject to copyright. All rights are solely and exclusively licensed by the Publisher, whether the whole or part of the material is concerned, specifically the rights of translation, reprinting, reuse of illustrations, recitation, broadcasting, reproduction on microfilms or in any other physical way, and transmission or information storage and retrieval, electronic adaptation, computer software, or by similar or dissimilar methodology now known or hereafter developed.

The use of general descriptive names, registered names, trademarks, service marks, etc. in this publication does not imply, even in the absence of a specific statement, that such names are exempt from the relevant protective laws and regulations and therefore free for general use.

The publisher, the authors, and the editors are safe to assume that the advice and information in this book are believed to be true and accurate at the date of publication. Neither the publisher nor the authors or the editors give a warranty, expressed or implied, with respect to the material contained herein or for any errors or omissions that may have been made. The publisher remains neutral with regard to jurisdictional claims in published maps and institutional affiliations.

This Springer imprint is published by the registered company Springer Nature Singapore Pte Ltd.

The registered company address is: 152 Beach Road, #21-01/04 Gateway East, Singapore 189721, Singapore

Preface

This book “Energy Harvesting and Storage: Fundamentals and Materials” is written primarily for Researchers and Masters students in photovoltaics and energy storage. This will also be of interest to practising engineers and scientists who would like to update their knowledge in this domain. The book could be a gateway to the fascinating realm of solar cells, lithium-ion batteries, and supercapacitors; presenting detailed information on the basics and the latest research developments in the field. The development of efficient renewable energy harvesting and energy storage techniques is one of the major challenges that humanity is facing nowadays. Over the past decades, spectacular improvements in energy harvesting and energy storage technologies call for potential future progress. This book on “Energy harvesting and energy storage: fundamentals and materials” discusses the fundamentals, principles, mechanisms, possible materials for fabricating efficient devices, etc. Chapter “[Solar Cell Technologies: An Overview](#)” gives an overview of solar cell technologies in which silicon technology is explored in detail. Chapter “[Physics and Technology of Carrier Selective Contact Based Heterojunction Silicon Solar Cells](#)” redefines silicon-based solar cells by introducing the concept of charge-carrier selective contacts. Chapter “[Perovskite Solar Cells: Concepts and Prospects](#)” offers information on the structural, optical, and electrical properties of organic-inorganic halide perovskite materials. The evolution of perovskite-based solar cells is explained in detail, including their fabrication process and working principles. The radiation hardness, a new characterization technique and bistability regarding Methylammonium containing Perovskite solar cells, is discussed in Chapter “[Radiation Hardness, a New Characterization Technique and Bistability Regarding Methylammonium Containing Perovskite Solar Cells](#)”. Chapter “[Tackling the Challenges in High Capacity Silicon Anodes for Li-Ion Cells](#)” is devoted to a detailed discussion of different strategies that can be effectively implemented to address the challenges associated with high-capacity anode materials and arrive at suitable solutions to identify ideal anode materials for developing high energy density Li-ion cells for applications in next generation energy storage systems. The state-of-the-art research activities related to high capacity cathode materials, including their structural and electrochemical features, challenges, and strategies that have been adopted to improve their performance are discussed in

Chapter “[The Renaissance of High-Capacity Cathode Materials for Lithium Ion Cells](#)”. Chapter “[Lithium-Ion Pouch Cells: An Overview](#)” provides a brief overview of the different aspects of lithium ion pouch cells and the various strategies introduced in upgrading the performance of this thin design. Chapter “[An Overview of Polymer Based Electrolytes for Li-Ion Battery Applications](#)” gives an overview of the various polymer-based electrolytes that are currently under research and development for use in LIBs. Prior to explaining the polymer-based electrolytes, the general properties of electrolytes are outlined with some of the conventionally used liquid electrolyte systems and their characteristics. In Chapter “[Carbon Based Composites for Supercapacitor Applications](#)”, the focus is on the different types of supercapacitors such as electric double-layer capacitor (EDLC), pseudo-capacitor, and hybrid capacitors, their analytical techniques, and potential nanostructured electrode materials such as carbon nanomaterials and carbon-based composite materials for high-performance supercapacitors. Chapter “[Wearable Supercapacitors](#)” focuses on the various flexible substrates used in supercapacitors from one-dimensional to three-dimensional and different electrode deposition processes to make flexible and thin electrode layers. At the end of the chapter, a brief discussion on the assembling and packaging of the supercapacitor for various wearable applications is also given. In short, the book will be an asset for academicians and researchers in the field of photovoltaics and energy storage.

Kochi, India

M. K. Jayaraj
Aldrin Antony
P. P. Subha

Acknowledgements

It is very exciting to finally publish this book on “Energy harvesting and storage: fundamentals and materials”. Under the firm grip of the Covid-19 pandemic, there had been a slowdown in academics and research activities. As a group, the researchers of Nanophotonic and Optoelectronics Device Laboratory (NPOED), Cochin University of Science and Technology, were faced with the challenge of how to keep the researchers safe at the workplace and to plan the future. The researchers of NPOED came up with the idea of compiling the research activities of the laboratory in the form of a book during the lockdown and quarantine period. Together with the researchers of NPOED, our collaborators from India and abroad also contributed to the book. This book is written primarily for Masters and Research students in photovoltaics and energy storage. This will also be of interest to practising engineers and scientists who would like to update their knowledge in this domain.

The book contains 10 chapters with a content variety that includes fundamentals and novel materials for energy harvesting and storage. There are many people to whom we are grateful for their valuable contributions. We extend our sincere thanks to Dr. Kurias K. Markose, Ms. Mary Vijila C. V., Ms. Merin K. Wilson, Mr. Abhilash A., Ms. Soumya Ravi, and Dr. Jasna M., researchers, Nanophotonic and Optoelectronic Devices Laboratory, Department of Physics, Cochin University of Science and Technology. They have contributed their research results meticulously for each chapter of this book. We also take this opportunity to thank with due regard Dr. Joaquim Puidollers, Dr. Cristobal Voz, and Mr. Eloi Ros, Universitat Politècnica de Catalunya, Spain, Dr. Heinrich Christoph Neitzert, Department of Industrial Engineering (DIIN), University of Salerno, Italy, Dr. G. Landi, Institute for Polymers, Composites and Biomaterials, CNR, Portici, Italy, Dr. F. Lang, Dr. J. Bundesmann, Dr. S. Albrecht, and Dr. N. Nickel, Helmholtz Zentrum Berlin für Materialien und Energie GmbH (HZB), Germany, A. Denker, Department of Physics, Beuth Hochschule Berlin, Germany, P. C. Ramamurthy, Department of Materials Engineering, Indian Institute of Science, Bangalore, India, A. Sambandam, Department of Chemistry, National Institute of Technology, Tiruchirappalli, India. Dr. Bibin John, Akhilash M., Dr. Salini P. S., Mercy T.D., Sumol V. Gopinadh, Anoopkumar V., Jamal Nawaz Ansari, Deepak Srivastava, Arjun Raj M., Aiswarya

Samridh, Vijayakumar P. S., Energy Systems Division, PCM Entity, Vikram Sarabhai Space Centre, Thiruvananthapuram, India. Dr. Manoj M., Department of Applied Physics, University of Eastern Finland, Finland, Dr. Jayan Thomas, Mr. Kowsik Sambath Kumar, Mr. Deepak Pandey, and R. Rajkumar Gurjar, Department of Materials Science and Engineering, NanoScience Technology, CREOL, College of Optics and Photonics, University of Central Florida, United States, for their contributions.

It was a pleasant experience to work with the Springer Nature Editorial team, which enabled the timely publication of this book.

M. K. Jayaraj
Aldrin Antony
P. P. Subha

Contents

Solar Cell Technologies: An Overview	1
Kurias K. Markose, Aldrin Antony, and M. K. Jayaraj	
Physics and Technology of Carrier Selective Contact Based Heterojunction Silicon Solar Cells	61
Joaquim Puigdollers, Cristobal Voz, and Eloi Ros	
Perovskite Solar Cells: Concepts and Prospects	97
C. V. Mary Vijila, Aldrin Antony, and M. K. Jayaraj	
Radiation Hardness, a New Characterization Technique and Bistability Regarding Methylammonium Containing Perovskite Solar Cells	135
H. C. Neitzert, G. Landi, F. Lang, J. Bundesmann, A. Denker, S. Albrecht, N. Nickel, P. C. Ramamurthy, and A. Sambandam	
Tackling the Challenges in High Capacity Silicon Anodes for Li-Ion Cells	149
Merin K. Wilson, A. Abhilash, S. Jayalekshmi, and M. K. Jayaraj	
The Renaissance of High-Capacity Cathode Materials for Lithium Ion Cells	181
M. Akhilash, P. S. Salini, Bibin John, and T. D. Mercy	
Lithium-Ion Pouch Cells: An Overview	209
Sumol V. Gopinadh, V. Anoopkumar, Md. Jamal Nawaz Ansari, Deepak Srivastava, Arjun Raj M., Bibin John, Aiswarya Samridh, P. S. Vijayakumar, and T. D. Mercy	
An Overview of Polymer Based Electrolytes for Li-Ion Battery Applications	225
Soumya Ravi and M. K. Jayaraj	

Carbon Based Composites for Supercapacitor Applications 259
Mannayil Jasna, Muraleedharan Pillai Manoj,
and Madambi Kunjukutan Ezhuthachan Jayaraj

Wearable Supercapacitors 285
Kowsik Sambath Kumar, Deepak Pandey, Rajkumar Gurjar,
and Jayan Thomas

Solar Cell Technologies: An Overview



Kurias K. Markose, Aldrin Antony, and M. K. Jayaraj

1 Global Energy Demands

Energy is an irreplaceable need for human endurance. The advancement of society is inextricably linked to the availability of energy. Access to safe, dependable, and affordable energy is a critical enabler of higher living standards, including the ability to live a longer and healthier life. Global energy demand is expected to dramatically increase double fold by 2050 due to growing population, urbanization and developing economies (India Energy Outlook 2021). For many years, growth in electricity demand has outpaced growth in final energy demand. Presently, most of the total energy requirement is met from fossil-derived fuels, including oil, coal and gases (IEA 2019). Unfortunately, fossil fuel reserves will be depleted in the coming century, with the reserve for oil and natural gas lasting 40–60 years and coal lasting fewer than roughly 115 years (Ritchie 2017; Statistical Review of World Energy 2016). The continuous use of fossil fuels is therefore not viable due to its limited accessibility and outflow of greenhouse gases and air toxins, including carbon monoxide (CO), carbon dioxide (CO₂) and sulphur dioxide (SO₂) (Schneidmesser et al. 2015), (Lamb et al 2021), (Montzka et al. 2011).

K. K. Markose (✉) · A. Antony
Department of Physics, Cochin University of Science and Technology, Cochin 682022, Kerala, India
e-mail: kurias@cusat.ac.in

A. Antony
Centre of Excellence in Advanced Materials, Cochin University of Science and Technology, Cochin 682022, Kerala, India

Inter University Centre for Nanomaterials and Devices, Cochin University of Science and Technology, Cochin 682022, Kerala, India

M. K. Jayaraj
University of Calicut, Thenihpalam, Malappuram 673635, Kerala, India

Furthermore, fossil fuels are not equally available to all; oil reserves are primarily found in the Middle East (Miller and Sorrell 2014; Olejarnik and IEA 2009). As most countries depend on other countries, this inconsistency in its availability has many serious consequences, leading to resource-driven tensions and crises. The sudden fluctuations in oil prices caused by policy decisions, natural disasters, and production cost significantly impact the day-to-day lives of ordinary people (Sek et al. 2015; Lim and Sek 2017). There is an immense urge for sustainable, carbon-neutral and environment-friendly alternative energy sources to complement the fossil fuels for future generations; in this way, one of our society's most overwhelming challenges. Renewable energy (RE) sources (e.g., wind, hydroelectricity, solar, and geothermal energies) have the potential to replace the non-RE energy resources and supplement in the long run (Global Energy Review 2020). Figure 1a shows the global energy mix from various energy sources over the years. It is apparent that, as a result of the increased demand, energy production has been continuously increasing over the year (Our World in Data 2020). Fossil fuels dominate with around 80% share (Enerdata 2020). However, renewable energy sources have registered a steady uptrend in recent years, leading to higher contributions in the coming years (World Adds Record New Renewable Energy Capacity 2021).

Another serious issue confronting humankind is the unprecedented climatic changes and the calamities that follow (Ekwurzel et al. 2017). According to the Paris agreement of the "United Nations Framework Convention on Climate Change (2015), each country should strengthen the global response to climate change by taking measures to reduce the usage of fuel energy to limit the global temperature rise well below 2 °C above the pre-industry level by 2050" (The Paris Agreement 2015). Figure 1b depicts annual worldwide CO₂ emissions from 1900 to 2019, clearly demonstrating the upsurge in the CO₂ emissions. In the inset of Fig. 1b, the contribution of each sector to CO₂ emissions is shown. About 2/3 of the total greenhouse emissions come from energy production and usage, which include electricity

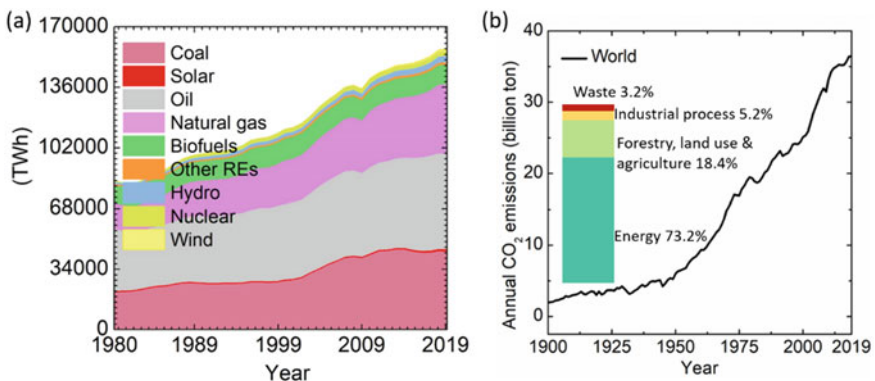


Fig. 1 a Share of various energy sources to the world's energy production from 1980 to 2019. b Annual CO₂ emission of the world over the year (inset: sector-wise contribution to CO₂ emission) [source our world in data]

generation and transportation. Therefore, switching to renewable energy sources in these sectors is important to ensure a 90% reduction in CO₂ emissions by the year 2050. Figure 2 shows an action plan to reduce CO₂ emissions, thereby decreasing the threats due to climate changes and other catastrophes caused by increased CO₂ releases. Solar photovoltaics (PV) and wind energy are currently the mainstream options in this expedition as alternative clean energy resources. The photovoltaic module instalment has boomed in the last few years, contributing to 2.4% of global electricity production. According to the 2020 report by Fraunhofer ISE, crystalline silicon (c-Si) solar cells (including monocrystalline and polycrystalline) are dominating the world PV market with a market share greater than 95% (Fraunhofer 2020). The rest is hydrogenated amorphous silicon (a-Si:H), cadmium telluride (CdTe), and copper-indium-gallium-diselenide (CIGS) thin film solar cells. The cost of Si-based solar cells has been reduced by a great extent in recent times. The learning curve of PV predicts a 20% dip in the price of the solar cell modules for every doubling of the cumulative shipped volume. It can be seen that high conversion efficiencies will be the central point for further reduction in solar electricity costs. In addition to reducing CO₂ emissions by providing an alternative to fossil-based electricity generation, the deployment of PV technology can likewise function as an impetus for different advances with the possibility to handle environmental changes. PV is presently the most economical power source in some market portions. The accessibility to this modest power is beginning to permit a forward leap in green fuels (Detollenaere 2020).

Unexpectedly, in 2020, the global energy demands were severely disrupted due to the pandemic COVID-19 and the resultant lockdown. Even though the emission of carbon dioxide has fallen, the crisis does not change the trends in the energy sector that have endured for quite a long time. Alternatively, the bounce in the CO₂

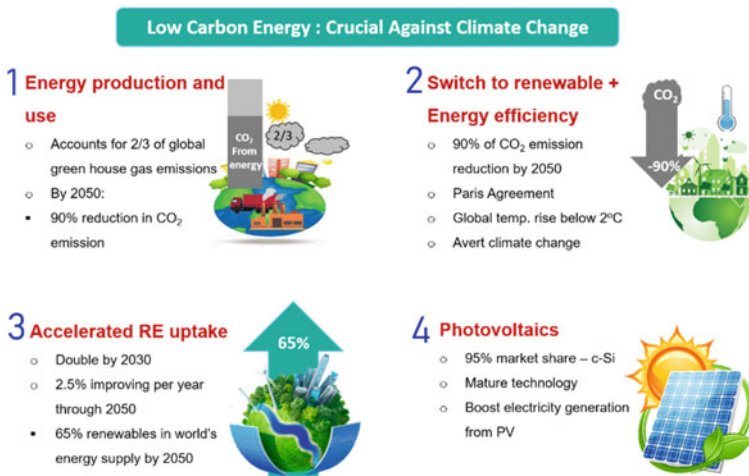


Fig. 2 Action plan to reduce CO₂ emissions and prevent climate changes

emission may be bigger than the decay unless the rush of ventures to restart the economy is devoted to cleaner and more robust RE infrastructure (Global Energy Review 2020). In their 2020 reports, International Energy Agency (IEA) pointed out that “RE sources show resilience to the Covid-19 crisis” as it is set to meet a kind of development regardless of the final state of the economic recovery (Stevens 2020; IEA 2020).

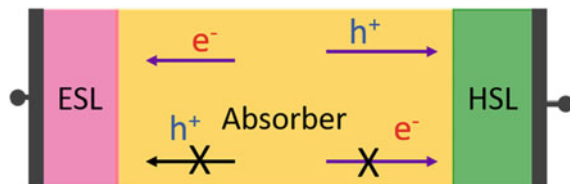
We have seen the importance of photovoltaics in the present energy demand scenarios. Now we will briefly discuss the working of a solar cell emphasizing various metrics to improve the performance of the device.

2 General Picture of a Solar Cell

In order to understand and improve the performance of any solar cell, the underlying physics of a solar cell, especially how charge carriers are generated, separated and transported, needs to be understood. The following discussions begin with the broader picture of a solar cell to not possibly miss any prospects (*pn*-junction, heterojunctions, organic solar cells). Let us consider the general picture of a solar cell in the thermodynamic framework to include all possibilities to build an ideal solar cell (Würfel 2005). Essentially, a solar cell consists of an absorber material that absorbs the incoming light radiations and generates electron–hole pairs. To obtain a net current, there must be some physical mechanism that isolates and extracts electrons and holes at positive and negative terminals, respectively. This process of charge carrier selectivity implies an ‘asymmetric internal flow of charge carriers towards the contact region’ (reprinted from Allen et al. (2019), copyright @ 2019, springer nature limited). In other words, there must be ‘semi-permeable membranes’ at both ends of the absorber material such that electrons and holes must only be collected at the opposite end of the absorber respectively, to generate a flowing charge current (Fig. 3). The membrane which allows only electrons and blocks holes are called the electron selective layer (ESL).

Similarly, the hole selective layer (HSL) must allow holes and block electrons. A combination of a selective membrane and the metal contact (sometimes TCOs) are collectively specified as a ‘carrier selective contact’. In practice, the electron selective contact that blocks holes should have large conductivity for electrons and very low conductivity for holes and the hole selective contact should behave vice versa. It is well known that an *n*-type semiconductor offers low conductivity towards

Fig. 3 Sketch of a solar cell with the absorber sandwiched between two selective layers



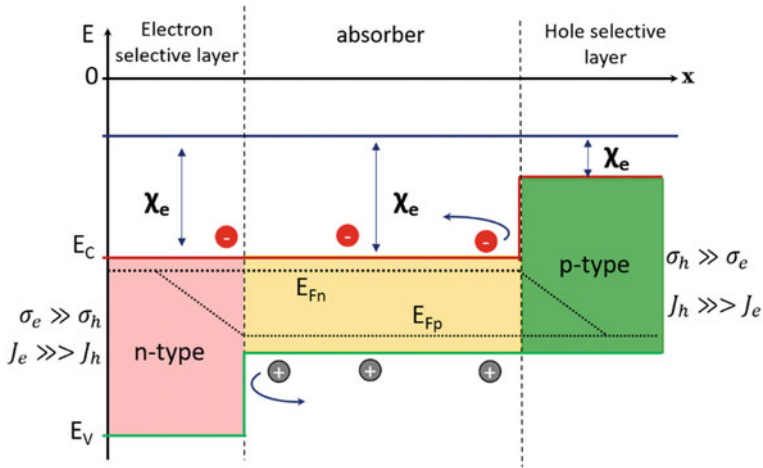


Fig. 4 General schematic of the band structure of a solar cell with the absorber layer with *n*- and *p*-type selective layers

holes and large conductivity for electrons. Similarly, *p*-type semiconductor offers low conductivity to electrons. Therefore, *n*- and *p*-type semiconductors can act as ESL and HSL, respectively. Figure 4 shows a typical band structure satisfying these requirements, where the *n*-type material will block the injection of holes due to the large valance band offset.

In contrast, *p*-type material will block the injection of electrons due to the energy barrier in the conduction band, which enables the collection of electrons and holes at opposite contacts. Considering the large bandgap of the *n*- and *p*-type materials, all the photons are absorbed by the absorber material. Therefore, within the absorber materials, where many electrons and holes are present, the quasi-Fermi levels for electrons (E_{Fn}) and holes (E_{Fp}) are treated as totally straight, as shown in Fig. 4. In the case of ESL, electrons are the majority carriers, and holes are the minority carriers. Within the ESL, the E_{Fn} is almost straight due to the high concentration of electrons throughout ESL. That means the electron transport/crossing is almost lossless. Moreover, the E_{Fn} and E_{Fp} meets at metal contact since Fermi level splitting is not possible within metal due to the lack of bandgap in metals. It can also be observed that the E_{Fp} bends towards E_{Fn} , since the hole concentration is much lower in this region than in the rest of the solar cell. However, in case of interface defects present, Fermi level pinning (FLP) happens and the E_{Fn} will encounter some gradient within the ESL and results in some loss (reflected as loss in V_{oc}). Also, the gradient of the E_{Fp} across the ESL could drive holes to the contact resulting in minority recombination and, therefore, unavoidable. One practical approach to minimise this minority recombination is to make the hole concentration minimum at ESL. In reality, this is achieved by reducing the hole conductivity (σ_h) as much as possible. So, for an ideal electron selective contact, the electron conductivity (σ_e) should be very larger

than hole conductivity (σ_h), i.e. $\sigma_e \gg \sigma_h$. For the hole selective contact, the discussion is the same, with holes as the majority and electrons as the minority carriers.

The key principles that determine the transport of carriers in a solar cell can be established through the Equations,

$$J_e = n\mu_e \nabla E_{Fn} \quad (1)$$

$$J_h = p\mu_h \nabla E_{Fp} \quad (2)$$

where J_e is the electron current density, J_h is the hole current density, n is the electron density, p is the hole density, μ_e and μ_h are the mobility of electrons and holes, ∇E_{Fn} and ∇E_{Fp} are the quasi-Fermi level gradients for electrons and holes. It has to be noted that the terms $n\mu_e$ and $p\mu_h$ are proportional to the electron conductivity (σ_e) and hole conductivity (σ_h) respectively. Looking at Eqs. 1 and 2, the main criteria for charge separation in a solar cell is that one type of carrier should move freely. At the same time, the other one is blocked—i.e. the asymmetry in the conductivity for electrons and holes. Therefore, in other words, the driving force behind the charge separation is the chemical potential differences of the contacts (Fermi-level gradient) (Cheng et al. 2016). Hence, in any solar cell, a pn -junction, band bending or a built-in potential are neither necessary nor sufficient conditions for charge separation (Wurfel et al. 2015). Conductivities (σ_e and σ_h) in the above Eqs. (1) and (2) are independent variables that drive the quasi-Fermi level gradients and the current densities. However, from the solar cell engineering point of view, only the carrier density can be easily controlled. Material properties like electron affinity (χ), work function (Φ), bandgap (E_g) and density of states (DOS) are varied to manipulate the carrier concentration.

2.1 Crystalline Silicon Solar Cell

A good but not ideal architecture, which fulfils the requirements mentioned above, is the conventional c-Si p - n homojunction. It is one of the most well-studied and simple photovoltaic systems that can be easily extended to other kinds of solar cells. During the p - n junction formation, due to the difference in the hole and electron concentration, diffusion of charges (electrons) from n -side to p -side and (holes) from p -side to n -side occurs. This leaves the region near the junction depleted of mobile charges and gradually gives rise to the space charge region (depleted region) with fixed charged ions of opposite polarities (ionised impurity donor or acceptor atom). Furthermore, it gives rise to an electric field that originates from the n -side to the p -side. The presence of the internal electric field induces the built-in potential or the junction voltage (V_{bi}) as given by the equation,

$$V_{bi} = \frac{kT}{q} \ln\left(\frac{N_A N_D}{n_i^2}\right) \quad (3)$$

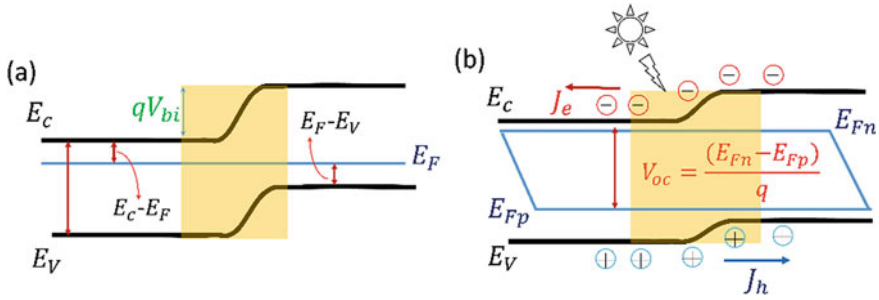


Fig. 5 Energy band diagram of a p–n junction under **a** thermal equilibrium (dark) and **b** under illumination (open circuit condition)

where N_A and N_D are the doping densities and n_i is the intrinsic carrier concentration. Figure 5a shows the equilibrium energy band diagram of a *pn*-junction under dark conditions. Within the space charge region, the valance band and conduction band are bent.

However, the position of the Fermi level in the quasi-neutral region and the isolated p- and n-type region does not change and remains equal to an equilibrium value E_F . When a *pn*-junction is under illumination, excess electrons and holes are generated, thereby increasing the minority carrier concentrations in n- and p-regions. The excess photogenerated minority carriers begin to cross the quasi-neutral regions; i.e. holes move from n-side to p-side, and electrons move from p-side to n-side. This flow of photogenerated current to the preferential direction results in the so-called photogenerated current (J_{ph}), which comprises of electron (J_e) and hole current (J_h). When the *pn*-junction is not connected to an external circuit (open circuit condition), the recombination current (J_0) should balance the photo- and the thermally-generated carriers. The J_0 is increased by lowering the electrostatic barrier across the *pn*-junction, as shown in Fig. 5b. The amount by which the electrostatic barrier is lowered is referred to as the open-circuit voltage. The upper limit set to the V_{oc} is determined by the difference in the contact potential or chemical potential (Qi and Wang 2012; Caprioglio et al. 2019);

$$V_{oc_max} = \left(\frac{E_{Fn} - E_{Fp}}{q} \right) \tag{4}$$

In order to comprehend the electrical behaviour of a c-Si *pn*-junction solar cell device, it is convenient to make an electrically equivalent model, and the behaviour of the discrete component is well known. Figure 6a shows the two-diode model of a solar cell. The solar cell is modelled by the parallel combination of a constant current source (photogenerated carriers) with diodes; D1 and D2 (D1—ideal diode (diffusion) and D2—junction recombination). Also, the resistance losses in solar cells are accommodated into the model through the series and shunt resistances (Enebish et al. 1993), (Hovinen 1994), (Humada et al. 2016). Equation of the double diode in the dark is given by,

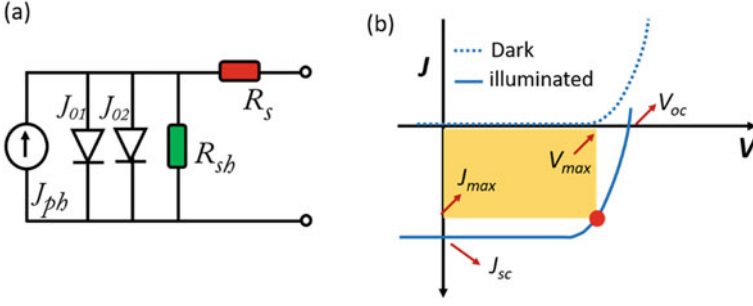


Fig. 6 **a** Equivalent circuit of a *pn*-junction solar cell and **b** typical I–V characteristics of solar cell under dark and illumination

$$J(V) = J_{ph} - J_{01} \left(e^{\left(\frac{qV + R_s J}{n_1 k T} \right)} - 1 \right) - J_{02} \left(e^{\left(\frac{qV + R_s J}{n_2 k T} \right)} - 1 \right) - \frac{V + R_s J}{R_{sh}} \quad (5)$$

where J_{01} is the saturation current density corresponding to the diffusion-limited—diode (D1) and J_{02} is the saturation current density corresponding to the recombination-limited-diode (D2). The n_1 and n_2 are the ideality factors of the diodes D1 and D2, where generally n_1 and n_2 is assumed to be 1 and 2, respectively. However, in general, a more compact equation with the two diodes replaced by a single diode is given by,

$$J(V) = J_{ph} - J_0 \left(e^{\left(\frac{qV + R_s J}{nkT} \right)} - 1 \right) - \frac{V + R_s J}{R_{sh}} \quad (6)$$

where, J_0 is the effective recombination current density. The voltage across the output terminal when the solar cell is not connected to an electrical circuit is called the open-circuit voltage (V_{oc}),

$$V_{oc} \approx \frac{nkT}{q} \ln \left(\frac{J_{ph}}{J_0} + 1 \right) \approx \frac{nkT}{q} \ln \left(\frac{J_{ph}}{J_0} \right) \quad (7)$$

for $J_{ph} \gg J_0$. When the terminals are connected in a short circuit, i.e. $V = 0$, the current density through the terminals is called short circuit current density (J_{sc}). In the case of an ideal solar cell with very low R_s , low J_0 and high R_{sh} , then,

$$J_{sc} \approx J_{ph} \quad (8)$$

Figure 6b shows the typical IV curve of the solar cell, where the different parameters are marked. It can be seen that the power generated at the open-circuit voltage and short circuit current density operating points is zero. Another important parameter is the fill factor, generally represented as FF that is defined as,

$$FF = \frac{P_{max}}{J_{sc} V_{oc}} = \frac{J_{max} V_{max}}{J_{sc} V_{oc}} \quad (9)$$

The photo-conversion efficiency (PCE or η) of a photovoltaic device is defined as,

$$PCE = \eta = \frac{P_{max}}{P_{in}} = \frac{J_{sc} V_{oc} FF}{P_{in}} \quad (10)$$

where P_{in} is the input power (100 mW/cm² for standard test conditions).

2.2 Design Rule of a Solar Cell

As mentioned earlier, photo-conversion efficiency is a function of J_{sc} , V_{oc} , and FF . Each of these parameters should be considered and maximised to achieve higher efficiency. The short circuit density can be expressed as,

$$J_{sc} = qG(L_n + W + L_p) \quad (11)$$

where G is the generation rate, L_n and L_p are the minority carrier diffusion lengths for electrons and holes, respectively and W is the transition region width. Therefore, the generation of the $e-h$ pairs should be maximum to obtain a high J_{sc} . That means most of the incoming radiation should be absorbed within the absorber material irrespective of various optical losses like reflection losses, sub-bandgap photon losses (transmission losses) and reflection from the metallic grid on the front contact (Fig. 7a). The reflection losses are generally minimised by using anti-reflection coatings (ARC) and surface texturing (Fig. 7b). ARCs are dielectric layers with a large bandgap coated over the c-Si surface. ARC reduces the reflection losses by destructive interference, given that n_1 is the refractive index of the ARC, then the optimum thickness (d) of ARC is, $d = \lambda_o/4n_1$, where λ_o is the wavelength of the radiation. Texturing the c-Si surface is another method to minimise the reflection loss. The front and rear surfaces are textured to random pyramids to meet the total internal reflection condition and thereby enhance the optical path length of the light. A randomly textured rear surface is called a *Lambertian* reflector that results in a $4n^2$ factor enhancement in optical path length (n : refractive index of the semiconductor) (Yablonoivitch and Cody 1982). Spectral modification approaches are also used in solar cells to improve the light absorption in solar cells by exploiting the ultraviolet and infra-red region in the solar spectrum, which otherwise is lost. In order to deal with sub-bandgap photons, upconversion phosphors (UCP) are demonstrated in solar cells, where these materials absorb the transmitted long-wavelength light and emit short-wavelength light which is reabsorbed by the solar cell (Markose et al. 2020a), (Markose et al. 2016), (Fischer et al. 2018), (Cheng et al. 2016), (Markose et al. 2018). Down conversion phosphors

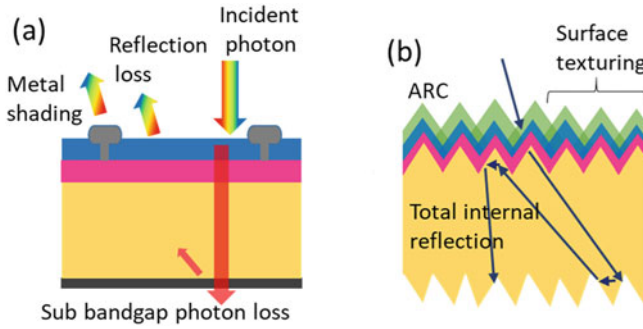


Fig. 7 **a** Various optical losses in a planar solar cell. **b** ARC and surface texturing light trapping method to reduce reflection losses

are also utilised in solar cells to make use of the high-energy light (ultraviolet light) that is often dissipated as thermalization loss (Mora et al. 2017; Jia et al. 2019).

Apart from enhancing light absorption, the resistive losses in the solar cell should be minimum to obtain high efficiency. The fill factor of the solar cell is affected by the series (R_s) and shunt (R_{sh}) resistance in the device. The series resistance of a solar cell is a combination of all ohmic losses, the resistance of the metal contacts at the front and rear (R_M), the resistance of the absorber material, resistance from TCOs, and the resistance from the metal–semiconductor interface or contact resistance (R_c). The R_{sh} is the resistance offered for leakage current through shunt paths. For high-efficiency solar cells, R_s is generally reported $<0.2 \Omega \text{ cm}^2$ (should be low) and R_{sh} is $>1 \text{ k}\Omega \text{ cm}^2$ (should be high).

The V_{oc} of a solar cell is primarily affected by the recombination process in the solar cell, both bulk and surface recombinations. As per Eq. 7, for obtaining a higher V_{oc} , the recombination current density, J_0 should be minimum. The lowest value for J_0 is obtained when the recombination and thermal recombination rates are equal. Thus in practice, the J_0 can be kept low by reducing the minority carrier injection and the recombination in the solar cell by providing passivation. Minority carrier injection can be minimised by reducing the minority concentration at equilibrium; the selective contact approach can reduce the concentration of minority carriers. Carrier selectivity and passivation are, therefore, important to achieving high-efficiency solar cells.

2.2.1 Carrier Selectivity

Carrier selectivity is the term used to mention the ability of a particular contact to allow only one type of carrier while blocking the other. The carriers must be transported selectively to their respective contacts and extracted with a minimum voltage drop into the metal contacts. Earlier, J_0 was used to quantify the effectiveness of carrier selective contact where low J_0 means excellent carrier selectivity. However,

J_0 alone does not represent the carrier selection ability of contact since the asymmetry between the hole and the electron conductance is also crucial for the selective extraction of holes or electrons. Based on the theoretical framework by Brendel et al., the electron conductance (ρ_n) and hole conductance (ρ_p) are given as,

$$\rho_n = \left(\frac{\partial dJ_p}{\partial dV} \right)^{-1} = \frac{v_{th}}{f_c J_0} \quad (12)$$

$$\rho_p = \left(\frac{dJ_p}{dV} \right)^{-1} = \frac{\rho_c}{f_c} \quad (13)$$

where v_{th} is the thermal voltage, f_c is the contact fraction and J_0 is the minority carrier combination current (Brendel et al. 2016). The contact selectivity (S_{10}) is defined as the ratio between electron to hole conductance:

$$S_{10} = \log_{10} \left(\frac{\rho_n}{\rho_p} \right) = \log_{10} \left(\frac{v_{th}}{J_0 \rho_c} \right) \quad (14)$$

S_{10} is an excellent figure of merit to quantify the potential of a particular electron or hole contact and is useful in solar cell designing. The two requirements for a good carrier selective contact is, therefore, low J_0 and low ρ_c . There are many advanced strategies used to achieve the desired contact selectivity.

The most common strategy is to use heavy doping (p^+ or n^+) in c-Si, for example, the aluminium back surface field (Al-BSF) solar cell. Figure 8a shows an electron selective layer formed by n^+ doping in c-Si(n). The heavy doping decreases the concentration and mobility of the minority carriers at the n^+/c -Si contact, which enables to achieve low J_0 even when the c-Si/metal interface defect density is high. Simultaneously, at the n^+/c -Si(n) contact, the conductivity of the majority carriers increases due to the high concentration of majority carriers leading to low ρ_c . Another way to modulate carrier concentration at the surface is by using dielectric layers with fixed charges. Dielectric materials like Al_2O_3 and HfO_3 with a positive or negative charge will result in the accumulation of electrons or holes, thereby providing carrier selectivity (Fig. 8b). Alternatively, this can be achieved using a heterojunction of c-Si and wide bandgap material having desired conductivity (n or p) with suitable Fermi level alignment and conduction band or valance band offset ΔE_C or ΔE_V . The most well-known carrier selective heterojunction structure is the c-Si/a-Si:H. Figure 8c represents an ideal case in which the ΔE_C is negligible; therefore, electrons can easily cross over the junction. Due to high ΔE_V , the minority carrier holes are blocked, and carrier selectivity is achieved. In the c-Si/a-Si:H, the a-Si:H is either doped p - or n -type to manipulate the conductivity of the carriers. Therefore, the combination of doping and band offset together provides the selectivity (Melskens et al. 2018).

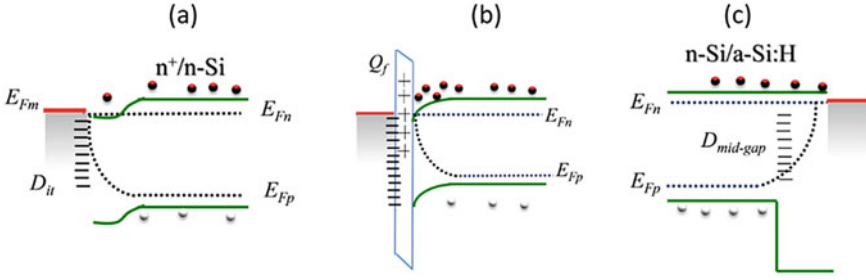


Fig. 8 Various carrier selective approaches using **a** heavy doping, **b** dielectric layer with fixed charges and **c** heterojunction in solar cells

2.2.2 Passivation Properties

The performance of any solar cell is affected by the recombination process in the materials. The photogenerated electron–hole pair concentration decays once the illumination is removed. How fast the decay happens depends on the various recombination process dominating in the material, here c-Si. The recombination is characterised by the effective lifetime (τ_{eff}) of the carrier (mainly minority carrier), which is a resultant of the bulk lifetime (τ_b) and surface lifetime (τ_s). The various bulk and surface recombination processes observed in c-Si solar cells are summarised in Fig. 9a–d. Figure 9a shows radiative recombination, where the electrons and holes recombine directly by emitting a photon. Shockley–Read–Hall (SRH) recombination is a type of recombination that is aided by trap levels or impurities in the bandgap (Fig. 9b). The traps or defects arise from crystallographic defects or atomic impurities in the bulk. However, SRH recombination is insignificant in high-quality c-Si. Auger recombination is observed at a high level of carrier concentration ($>10^{17} \text{ cm}^{-3}$), and it involves an additional electron. The energy released during the electron–hole recombination is utilised to excite a second electron onto a higher energy level, from which it de-excites by releasing energy as phonons, as shown in Fig. 9c. Auger and radiative recombination are intrinsic to a material; however, SRH recombinations can be minimised using a high-quality c-Si wafer. Therefore, the performance of high-efficiency solar cells is mainly limited by the surface recombinations (Fig. 9d). The presence of dangling bonds at the c-Si surface act as trap states within the bandgap. In order to overcome this issue, the interface of the c-Si must be passivated. Thin layers of SiO_x , SiN_x , a-Si:H(i) or Al_2O_3 are used to passivate the c-Si surface. Post-annealing and hydrogen plasma treatment are also demonstrated to improve the passivation at the a-Si/c-Si interface (Soman and Antony 2021). The passivation property is characterised by surface recombination velocity (S). By combining all possible recombination processes in a solar cell, the effective lifetime (τ_{eff}) is given by,

$$\frac{1}{\tau_{eff}} = \frac{1}{\tau_b} + \frac{1}{\tau_s} \quad (15)$$

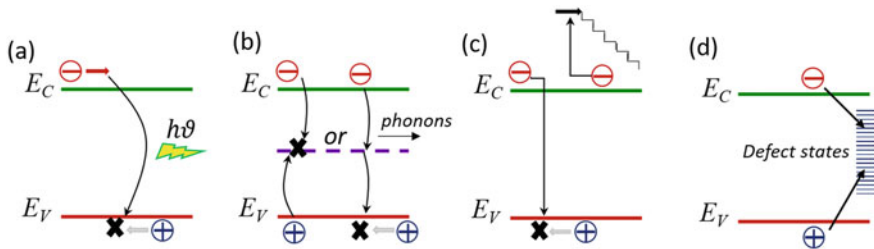


Fig. 9 Various recombination processes in a solar cell: **a** radiative recombination, **b** SRH recombination, **c** Auger recombination, and **d** surface recombination

$$\frac{1}{\tau_{eff}} = \left(\frac{1}{\tau_{Rad}} + \frac{1}{\tau_{SRH}} + \frac{1}{\tau_{Auger}} \right)_{bulk} + \frac{S_{front}}{W} + \frac{S_{back}}{W} \quad (16)$$

where, τ_{Rad} , τ_{SRH} , and τ_{Auger} are lifetimes associated with radiative, SRH and Auger recombination. S_{front} is the surface recombination velocity at front and S_{back} is the surface recombination velocity at the back surface. Most of the carrier selective and passivation approaches discussed above are based on Si doping, i.e., either by heavy doping of c-Si (n^+ or p^+) or by using a-Si:H(n) or a-Si:H(p) to extract the carriers selectively. Heavy doping increases the Auger recombination. The high thermal budget involved in doping c-Si, use of toxic gases like silane, phosphine and diborane, the complexity of fabrication (PECVD) and parasitic absorption (E_g of a-Si:H is 1.7 eV) promoted, exploration of alternative materials as carrier selective contacts.

In conclusion, we have seen that the main architectural elements required for any solar cells are the absorber material which absorbs the incoming radiation and generates photo excited charge carriers (E.g. Si, Ge and CdTe), membrane—generally, a pn -junction which inhibits the recombination of generated carrier and contacts—where the carriers are collected. Many schemes and architectural advancements have been developed to improve the performance of Si solar cells over the year to utilize their full potential. In the following session, different high-efficiency Si solar cells, their designs and advantages are briefly discussed.

3 Evolution of Silicon Solar Cells

The first report on silicon solar cells came in 1941 by Ohl et al. with a melt grown pn -junction and a conversion efficiency of $< 1\%$ (Ohl et al. 1941). The schematic of the device is shown in Fig. 10a. The device performance was limited mainly by the poor quality silicon material and lack of control over the junction formation (Raval and Madugula Reddy 2020). It was in 1954 that a silicon solar cell with a reasonable

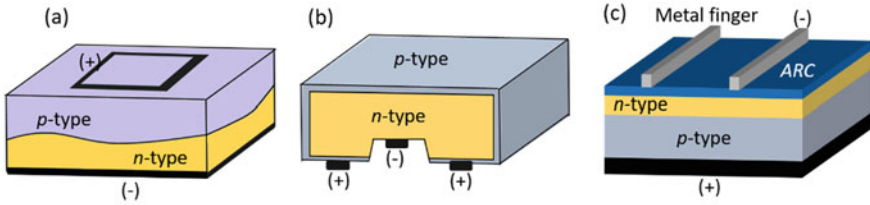


Fig. 10 Schematic of solar cells reported by **a** Ohl et al. in (1941), **b** Daryl Chapin, Calvin Fuller and Gerald Pearson in 1954 and **c** the evolved silicon solar cell design of the early 1960s

conversion efficiency of 6% was demonstrated at the Bell Laboratories in the U.S. by Daryl Chapin, Calvin Fuller and Gerald Pearson (Chapin et al. 1954).

The schematic of the device is shown in Fig. 10b, which had a ‘wrap-up’ around architecture with *n*-type silicon (arsenic doped) and boron-doped emitter. Even though the electrical contacts at the rear side reduced the shading loss, but led to a high resistive loss. In the early 1960s, solar cells were only used in space applications; thus, the cell design evolved to meet the needs of space applications, particularly to ensure maximum radiation resistance (Wenham and Green 1996). During that period, the solar cell design evolved using metal grids at the front surface, as shown in Fig. 10c. Also, high resistivity ($10 \Omega \text{ cm}$) *p*-type silicon was used since space irradiation hardness was reported to be less harmful to solar panels with *p*-type bases along with silicon monoxide ARC at the front side to reduce the reflection losses (Wolf 1963; Glunz et al. 2012). By 1963 commercialisation of solar cells began and, they were available to the general public.

Further advancement comes in the form of the Al back surface field (Al-BSF) in the early 1970s. Sintering of aluminium over a *p*-type Si wafer at high temperatures resulted in forming a highly doped p^+ region beneath the metal contact at the silicon/metal interface known as Al-BSF. These heavily diffused layers reduced the extent of recombination at the metal contacts by suppressing the minority carrier concentration and enhancing the open-circuit voltage. Implementing finer and closely spaced fingers for top metallization contact through photolithography, the requirement of heavy phosphorous doping along the top surface was reduced, and the surface dead layer was eliminated, further improving the shorter wavelength response. As ARC, a titanium dioxide (TiO_2) layer was used, and its thickness was optimized to improve the shorter wavelength response, giving it the characteristic violet colour, and the cell was called a ‘violet cell’ with superior performance (Fig. 11a (Wenham and Green 1996)). Employing a textured front surface by anisotropic etching in these solar cells reduced the reflection losses and improved the light trapping. These solar cells with the upright pyramid textured front surface with the antireflection coating appeared ‘black velvet’ due to low reflection and hence their title black cells (Fig. 11b). Thus, with substantial development, including the Al-BSF, refined front grid metal contacts and ARC coating with texturization, the efficiencies of terrestrial solar cells reached 17% in the late 1970s.

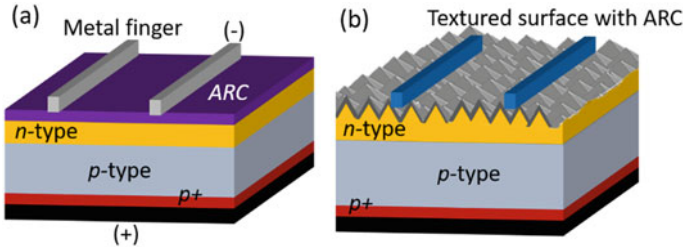


Fig. 11 Sketch of **a** the ‘violet cell’ with Al-BSF and fine metal grids and **b** the ‘black cell’ with a chemically textured front surface and Al BSF

3.1 Industrial Al-BSF Solar Cell

Al-BSF solar cells have been used for decades and were the leading PV technology until 2020, accounting for roughly 80% of the PV market share. We have already seen the evolution of solar cells and the features of the Al-BSF solar cells. Even though many improvements happened within the Al-BSF solar cells, the salient features of industrial Al-BSF solar cells can be summarized as follows.

The manufacturing process flow of conventional Al-BSF solar cells is depicted in Fig. 12. Typical solar cell architecture consists of a p -type c-Si wafer ($1\text{--}5\ \Omega\ \text{cm}$) with n^+ diffusion forming the pn -junction. The p -type Si substrate is cleaned following the standard procedures and random texturization forming upright pyramids, which reduces the reflection loss. The front emitter layer is then formed by phosphorous doping with typical N_D of $10^{20}\ \text{cm}^{-3}$ at the surface, which gradually decreases to values below the N_A in a depth of less than $1\ \mu\text{m}$ forming the pn -junction which separates the excited carriers. In order to avoid the shunt paths through the edges, the n^+ region around the edges is removed using the edge isolation process by UV laser ablation. An amorphous hydrogenated SiN_x layer (thickness $\approx 75\ \text{nm}$) is then deposited on the front surface that serves as the anti-reflection coating. In addition to reducing the reflection loss, these layers provide passivation to the front n^+ surface, leading to improved open-circuit voltage. The front Ag metal grids are generally deposited by screen printing followed by contact firing. After screen printing the front and back metal contacts, the solar cells are passed through a high temperature ($600\ \text{°C}\text{--}800\ \text{°C}$) furnace. At the front contact, the Ag crystallites penetrate through the SiN_x layer into Si at approximately $100\ \text{nm}$ depth and form an alloy with Si resulting in a low resistive ohmic contact. The rear side is fully covered with screen-printed aluminium paste. Al diffuses into Si during contact firing, which serves as an acceptor type impurity in Si and dopes the wafer p^+ near the contact, forming the BSF. These kinds of solar cells with monocrystalline and multi-crystalline Si wafers achieved efficiencies of 18.5% and 19.8%, respectively (Zhang et al. 2016; Liu et al. 2018).

The silicon solar cell technology has shown a remarkable steady uptrend, and many superior performance cells have been reported in the last two decades (Yu et al.

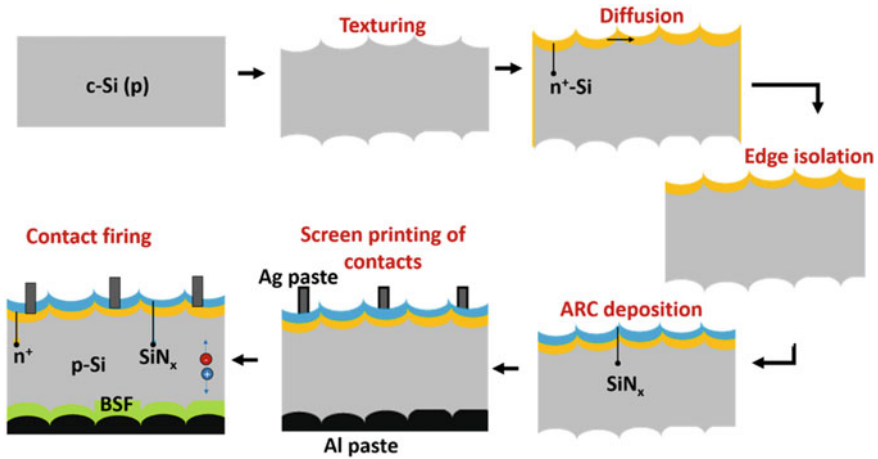


Fig. 12 Process flow of conventional Al-BSF solar cell

2018). Most of the high-efficiency c-Si solar cells technology features a novel device architecture, excellent light trapping mechanism, efficient collection of electrons and holes, low contact resistance and reduced recombination at the metal contacts. As we have seen, by the 1970s itself, texturing, ARC and BSF featured solar cells obtained high short circuit current density.

Further attempts to push the efficiency limits of the solar cell were focused on minimizing the bulk and surface recombination losses where the bulk recombination resides on the material quality. In the next session, we will discuss some of the reported high-efficiency solar cells and their features. Although these solar cells have high efficiencies, they are not widely commercialized due to the difficulty in fabrication steps and the costs involved.

3.2 Passivated Emitter Solar Cells (PESC) and Laser Grooved Buried Contact (LGBC) Solar Cells

The PESC was the first silicon solar cell to achieve efficiencies over 20%. Figure 13a shows the typical structure of a PESC solar cell. The main features of the PESC solar cells are as follows. In PESC solar cell, a shallow *n*-emitter is used to form the *pn*-junction. This reduces the recombination within the emitter. In order to passivate the surface recombination at the *n*-emitter, a thin high-quality thermal oxide is grown (~6 nm). Closely spaced front metal contact is deposited by vacuum evaporation of Ti/Ag, facilitating the smooth collection of carriers without many resistive losses. For the contact deposition, tiny openings are made in the thermal oxide using a photolithographic technique reducing the metal–semiconductor contact area. At the rear side, full area Al contact is deposited, which forms the BSF on sintering. From

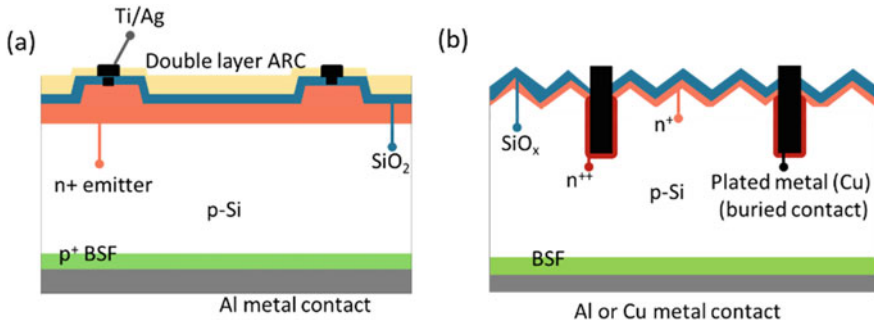


Fig. 13 Schematic diagram of **a** PESC and **b** LGBC solar cell

the optical aspect, instead of texturing, micro grooving is implemented to reduce the reflection losses along with a double layer ARC of ZnS and MgF₂. With an improved top surface by reducing the front side recombination and enhanced light management technique, efficiencies greater than 20% was achieved in PESC architecture (Saitoh et al. 1987; Blakers and Green 1986). However, the expensive photolithographic process involved limits the PESC space application.

LGBC solar cells were first developed in the early 1980s at UNSW. A typical schematic of an LGBC solar cell is shown in Fig. 13b. The major difference between LGBC and PESC is the use of laser grooving instead of photolithography for metal contact deposition and the plated metal contacts inside the grooves. After the front side *n*-diffusion and the thick thermal oxide growth step, a laser (infra-red) is used to scribe grooves in the wafer. Another diffusion step is employed, making the exposed regions in the grooves heavily doped—*n*⁺⁺; fortunately, the thermal oxide prevents the diffusion to other areas. The thick oxide layer acts as a passivation layer and metal plating mask. SiN_x layers, which can also act as an ARC, can be used instead of thermal oxide. It is then followed by Ni/Cu (Cu has low resistivity than screen-printed metal paste) electroplating inside the groove, forming the buried contact with a high height to width aspect ratio (Chong et al. 1988), (Jordan and Nagle 1994), (Raval and Solanki 2013). The Cu metal can be diffused into the Si through the SiO_x layer, forming deep trap levels that serve as the recombination centres and reduce carrier lifetime.

Nevertheless, the Ni as a seed layer acts as a diffusion barrier preventing the Cu diffusion into Si and improving the adhesion between the Si and Cu (Rehman and Lee 2014). Compared to conventional screen-printed contacts, Ni/Cu plated contacts have many advantages, which includes low contact resistance and a high aspect ratio (Lee et al. 2019; ur Rehman et al. 2016). However, background plating or parasitic plating due to impurities on the surface results in the undesirable performance of the solar cell and the process complexities are its challenges (Braun et al. 2011). Optimizing the groove depth and the metal finger pitch could reduce the resistance of the cells (Vivar et al. 2010). As a result of the high aspect ratio of the buried contacts, fine, closely packed fingers can be used, which reduces the shading losses to <3% and enhances

the longer wavelength response. Due to the large contact area with the Si, the buried contacts offer low parasitic resistance, especially low emitter resistance and thereby improve the fill factor of the device. The front side n^+ beneath the buried contacts acts as a front side surface field, similar to the Al-BSF and reduces the recombination at the contacts enhancing the open-circuit voltages. However, for commercial applications, multiple diffusion steps involving high temperature and expensive equipment requirements limit its wide production. LGBC solar cells with efficiencies greater than 20% were reported at the laboratory level, while commercial cells were reported to have efficiencies of $\sim 17\%$ (Wenham et al. 1994; Tous, et al. 2011).

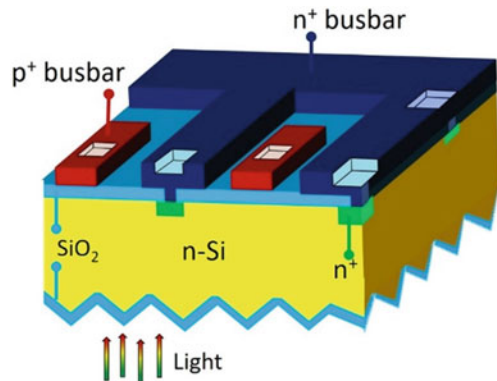
3.3 Point Contact Solar Cells

Further enhancement in the solar cell performance was achieved by point-contact solar cells. The main feature of the point-contact solar cell is that the metal–semiconductor contact is limited to the array of small holes at the rear side, as shown in Fig. 14.

Point contact solar cells of efficiency $\sim 22\%$ were demonstrated in 1988 (Swanson 1986). The high efficiency of point-contact solar cells is attributed to improved light management—i.e., textured front and reflective back surfaces, an increased lifetime and high resistivity thin Si base, and entire surface passivation between the contacts (see Fig. 14). Since there are no diffused regions in the lighted front surface, the surface recombination velocity is expected to be low, enabling a strong blue response. Because the free carriers are created in a lightly doped base, expect extended diffusion lengths (Swanson 1986).

Point contact design at the rear side demands high quality of bulk silicon and passivation since the photogenerated carriers at the front surface must reach the respective contacts at the rear side before recombining. Similarly, top surface recombination must be extremely low. As a result, the method is unsuitable for space cells,

Fig. 14 Schematic of a typical point-contact solar cell



where radiation damage quickly degrades the top surface. This structure, however, is better suited for concentrated solar cells. A thermal oxide layer passivates both the front and rear side surface. The local contacts are deposited by local diffusion employing photolithographic technique followed by metallization. Since the contacts are situated at the rear side, the shading loss in this architecture is zero.

3.4 *Passivated Emitter and Rear Contact (PERC) Solar Cell Family*

In the PESC architecture, we have seen that front side passivation significantly reduces the recombination and improves the device performance. On the other hand, the rear side full area Al-BSF only provided moderate passivation. Only 70% of the long-wavelength region is reflected back into the solar cell by the rear Al contacts, reducing the light absorption.

It is well known that rear side passivation can reduce recombination and push the open-circuit voltage higher, which is necessary for further efficiency enhancement. With the distinctive rear side features, the PERC design circumvented the rear side optical and recombination losses. Reduced rear surface recombination (typically, S ranges 60–200 cm^{-1}) was achieved as a result of the synergistic combination of surface passivation by dielectric layers and a smaller metal/semiconductor contact area. Also, improved rear surface reflection was achieved by using a dielectrically displaced back metal reflector (Green 2015). Blakers et al. first reported PERC solar cells at the University of New South Wales (UNSW) in 1988 with a conversion efficiency of 22.8% on p -type wafers (Blakers et al. 1989). This concept enabled UNSW to achieve a record efficiency of ~25% for solar cells multiple times (NREL 2020).

The salient features of the PERC architecture consist of a thermally grown passivating oxide dielectric layer at the rear side. The dielectrically displaced Al electrode was evaporated onto the rear side through small holes opened by photolithography, forming point contacts covering about 1% of the rear surface with 1 mm spacing. Recombination and resistance losses are balanced by the rear contact fraction and spacing (Blakers 2019). The insertion of a low refractive index dielectric layer between the Si and metal significantly increases the reflection at the rear side, from 89% for the direct Al contact to 98% for the dielectric displaced Al contact (Green 2015). The front side resembles the PESC design with random texturization, a passivation layer, an anti-reflection layer and a selective phosphorous emitter underneath the metal contacts, as shown in Fig. 15a. It is often considered as a cost-effective architecture to achieve efficiency above 20%. It has currently become the preferred manufacturing technology in the industry. Al_2O_3 and SiO_x dielectric layers showed better passivation properties due to low defect levels at the interface. Stacks of $\text{Al}_2\text{O}_3/\text{SiN}_x$ or $\text{SiO}_2/\text{SiN}_x$ are implemented at the rear side of high-efficiency PERC solar cells. The introduction of passivation layers and point contact at the rear

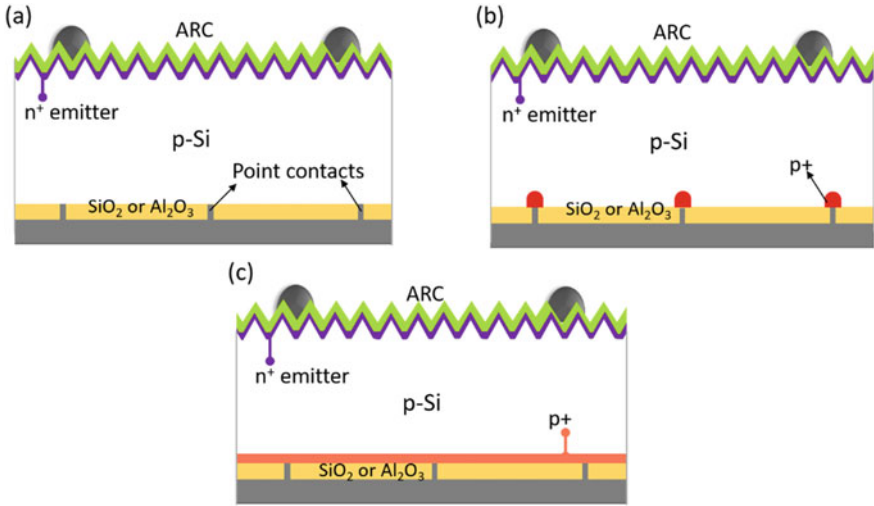


Fig. 15 Schematic diagram of **a** PERC, **b** PERL and **c** PERT solar cells

side reduced the recombination and obtained an open-circuit voltage above 700 mV. Earlier, PERC cells did not have the back side p^+ layer generated by Al alloying. Rather direct Al contact worked well, providing low resistive contact with p -Si wafers at contact fractions ranging from 0.1 to 10%. In some cases aluminium alloying was used; however, the results were not improved due to void formation and dielectric layer damage caused by high-temperature annealing, increasing recombination and contact resistances (Horbelt et al. 2016), (Urrejola et al. 2011a), (Meemongkolkiat et al. 2006). On the commercial scale, screen printing or physical vapour deposition is used to deposit Al (Rauer et al. 2011), (Urrejola et al. 2011b), (Blakers et al. 1989).

Later in 1990, Zhao et al. demonstrated the passivated emitter, rear locally diffused (PERL) cell with 24.5% record efficiency (Zhao et al. 1990). To reduce recombination at the rear contact even further, a boron diffusion is used to form local p^+ regions (local back surface field), as depicted in Fig. 15b, perhaps at the expense of increasing device complexities. It acts as a minority carrier reflector at the contact region, reducing recombination and contact resistance. Even though PERL cells showed excellent optical properties, the heavy doping at the local metal contacts resulted in recombination losses due to inadequate passivation (Allen et al. 2019). Later, a passivated emitter rear floating (PERF) cell with very high V_{oc} of 720 mV was demonstrated (Altermatt et al. 1996). After the passivation layer deposition, Al is deposited by evaporation or screen printing, and finally, a laser is used to form a local contact (Schneiderlöchner et al. 2002; Choi et al. 2019; Kumar et al. 2014). The rear side contact formation is influenced by factors like the method used for dielectric opening, the firing process, contact geometry and Al used (Balaji et al. 2020).

Besides, in 1988s rear side boron diffusion covering the entire back surface was explored, called the passivated emitter, rear totally diffused (PERT) solar cells as

shown in Fig. 15c. Although there have been a few attempts to fabricate PERC cells using n -wafer, the PV industry prefers to rely on p -wafer due to the ease of using well understood phosphorous diffusion in p -wafer versus boron diffusion in n -wafer. All these high-efficiency homojunction designs have an effective light trapping feature. The complete metal blanket at the rear side, separated by a thin oxide layer from the substrate, gives the advantage of a rear-side reflector. The weakly absorbed light of longer wavelengths gets reflected from the rear side and enhances the absorption (Blakers 2019).

3.5 Tunnel Oxide Passivated Contacts (TOPCon)

The local contact opening in the PERC or PERL design required additional patterning steps and suffered from additional shunt paths. Fraunhofer ISE developed a new technology named tunnel oxide passivated contact (TOPCon) in 2013, based on full area passivating and carrier selective contact, thus minimizing the manufacturing complexities in PERL design.

TOPCon technology is widely regarded as the next big thing after PERC as it offers low J_o and ρ_c values with high FF . Furthermore, because of its high thermal stability, this technology is compatible with the conventional fabrication processes of solar cells like laser-firing or diffusion of dopants (Ingenito et al. 2018; Feldmann et al. 2018). The schematic of the TOPCon solar cell is depicted in Fig. 16a, where an n -type wafer is used as the substrate. The architecture consists of a thin SiO_x layer of a few nanometers (~ 2 nm) at the rear side silicon surface, and it passivates the entire silicon surface since it is fully coated (Moldovan et al. 2015; Feldmann et al. 2014). The thickness of the SiO_x layer is optimized such that the carriers can tunnel through it while providing passivation (Steinkemper et al. 2015). Lowering the thickness of SiO_x reduces the passivation, while thicker SiO_x hinders the charge transport through tunnelling. The tunnel oxide is generally deposited by wet chemical methods, UV/O_3 treatment, or thermal oxidation. In addition, a phosphorous doped Si layer is deposited (using low-pressure chemical vapour deposition) over the entire SiO_x and annealed at high temperature to form a doped n -type polysilicon layer. It is followed by complete rear side metallization. Rear side texturing is not needed in this architecture. The n -type polysilicon layer provides the BSF. Boron doped emitter with an $\text{Al}_2\text{O}_3/\text{SiN}_x$ passivation stack is used at the front side. A record conversion efficiency of 25.7% with V_{OC} of 725 mV was achieved by Fraunhofer ISE in 2017 using TOPCon technology (Richter et al. 2017).

Figure 16b shows the rear side band diagram of a typical TOPCon solar cell with n -Si/ SiO_x /poly-Si(n) interfaces. At the n -Si/ SiO_x interface, the band bends, resulting in the accumulation of majority carriers at the interface. Moreover, at the interface, the carrier tunnelling will be asymmetric depending on the type of carries. Due to the large valance band offset (ΔE_V) at the interface, holes encounter larger barriers compared to electrons. Additionally, when the doping density of the poly-Si increases (up to an optimum value), the interface band shifts, limiting the transport

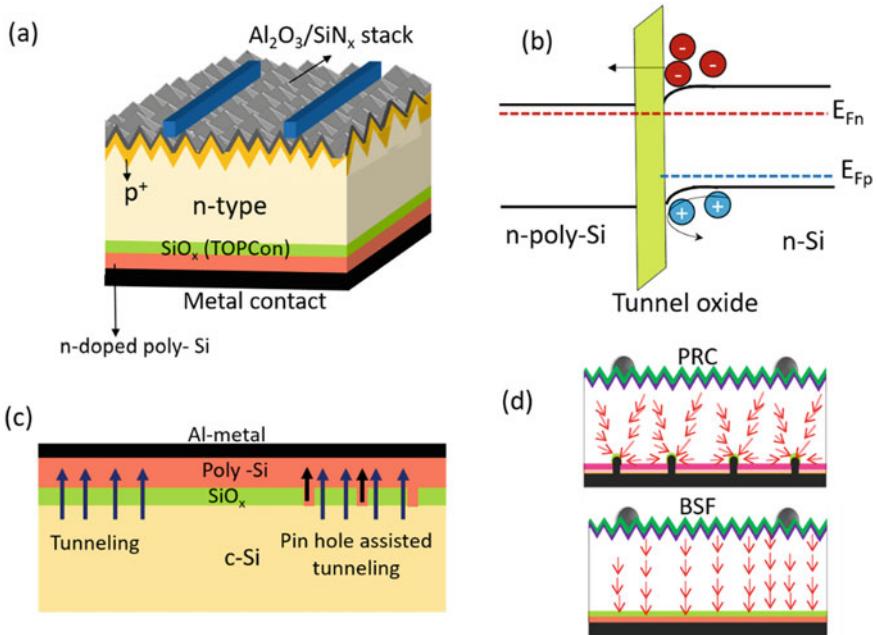


Fig. 16 Schematic of **a** typical TOPCon solar cell, **b** the band structure at the poly-Si/n-Si with tunnel oxide, **c** the charge transport in TOPCon solar cells, and **d** the majority current flow in passivated rear contact (PRC) and BSF cell designs

of the minority carriers, thereby enhancing the V_{oc} by minimizing the recombination and improving carrier selectivity (Mitra et al. 2019). The carrier transport through the thin interfacial oxide, in particular, has been the topic of much debate, and various physical models exist (Mitra et al. 2019), (Zeng et al. 2017), (Graaff and Groot 1979), (Nicolai et al. 2018). Figure 16c depicts the two limiting cases: the solar cell with a thin SiO_x homogenous layer without rupture and the cell with a thicker oxide layer with pinholes (Padi et al. 2021). The tunnelling will be the prominent transport mechanism in the first case, where the device has a homogenous oxide layer without any pinholes. For the latter case, pinhole-assisted tunnelling will be dominant. The TOPCon solar cells treated at a high temperature ($\sim 800^\circ\text{C}$) yielded improved surface passivation and reduced ρ_c . However higher temperature ($\geq 900^\circ\text{C}$) treatment resulted in lower passivation due to the rupturing of the interfacial oxide. The JV measurements of these devices, annealed at 800°C and 900°C , showed nonlinear and linear characteristics confirming the quantum mechanical tunnelling and ohmic behaviour (due to pinholes), respectively (Feldmann et al. 2018). The high electrical performance of the TOPCon solar cells is also attributed to the full area BSF at the rear side with the one-directional current flow of electrons (Richter et al. 2021). The sketch of the current flow in a passivated rear contact (PRC) and TOPCon structure is shown in Fig. 16d for comparison (Glunz et al. 2015). Since the TOPCon

offers carrier selectivity, the base resistance of the Si wafer has no significance in the device performance, contrary to the case of PERC solar cell, where optimized base resistance is inevitable to obtain high efficiency (Richter et al. 2017). TOPCon architecture ensures high efficiency while simplifying device manufacturing by a simple rear contact approach with two additional steps in the fabrication process and is soon expected to dominate the industry.

3.6 Interdigitated Back Contact (IBC) Solar Cell

Interdigitated back contact (IBC) solar cell structure is a promising route to realize high-efficiency c-Si solar cells for large-scale industrial production. In this device structure, the charge collecting contacts for p - and n -type are placed interdigitated at the rear side of the cell, thereby reducing the reflection losses as presented in Fig. 17a and b. As a result, this device architecture ensures better light absorption since there are no metallic contacts at the front side and a higher short circuit current. The main advantages of the IBC structure can be pointed out as (a) the contact resistance problems can be elevated by using wider grids without shading loss, (b) better possibility of addressing front side passivation and (c) module integration becomes simple and fine-looking.

One of the interesting advantages of the TOPCon and IBC concept is that they can be fabricated using n -type wafers, which are devoid of light-induced degradation. On the other hand, the light-induced degradation in p -type wafers results from the complex formation between boron and oxygen. These complexes will serve as defect centres, lowering device performance. In addition, the purification of n -wafers is cost-effective compared to p -wafers. Thus using n -wafers can reduce solar cell fabrication costs to achieve high-efficiency cells. The front side surface recombination is critical in IBC design since the pn -junction is located at the rear side (Liu et al. 2018). The passivation of the front side greatly affects the performance of an IBC solar cell.

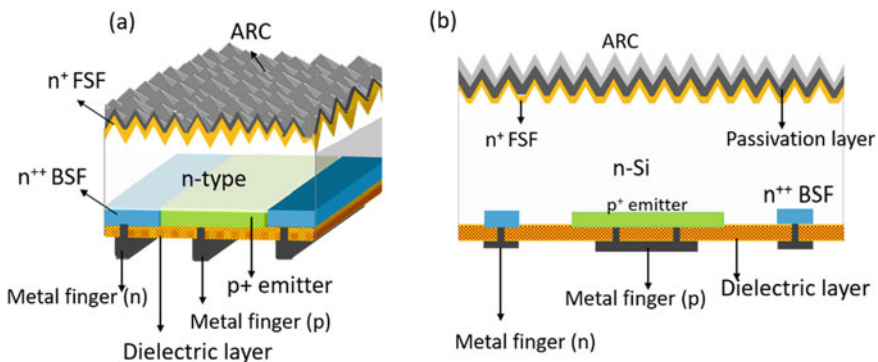


Fig. 17 Device structures of **a** IBC solar cells. **b** The cross-sectional image of IBC architecture

Sun Power Corporation is the leading manufacturer of IBC solar cells and achieved a record efficiency of 25.2%, with a V_{OC} of 737 mV, J_{SC} of 41.33 mA/cm² and FF of 82.7% on an n -type CZ silicon in the year 2016 (Smith et al. 2016).

3.7 Silicon Heterojunction Solar Cells

A more exquisite arrangement comprises utilizing passivating hetero-contacts, which simultaneously satisfy both passivation and contact roles are known as silicon heterojunction (SHJ) solar cells (de Wolf et al. 2012). The salient feature of SHJ is the displacement of the contacts (recombination active) from c -Si by introducing a thin passivating layer of wide bandgap (Yablonovitch et al. 1985).

In order to achieve full device potential, interface defect density at the hetero-interface should be low (Allen et al. 2019). Reducing the recombination with an optimized passivation layer will significantly improve the FF and V_{oc} (>750 mV) of the SHJ solar cell (Adachi et al. 2015; Herasimenka et al. 2013). Among various materials, hydrogenated amorphous silicon (a -Si:H) thin layers are the best candidates for fabricating SHJ solar cells. The first successful heterojunction between a -Si:H and c -Si was introduced by SANYO (currently Panasonic) in 1992 called heterojunction with intrinsic thin-layer (HIT) cell (Fig. 18a). The HIT-SHJ solar cell comprises a thin c -Si, covered with an intrinsic a -Si:H of a few nanometers (5–8 nm) on either side, which provide a high degree of passivation. Doped amorphous silicon on the either side of the solar cell— a -Si:H(n) and a -Si:H(p)—is deposited to extract electrons and holes selectively. The main advantage of this device architecture is that the various layers can be deposited at low temperatures (<200 °C) (Mikolášek 2017). Transparent conducting oxides provide the necessary lateral conductivity and act as an anti-reflection layer. HIT cells have been the focus of much research since their introduction. In 2017, Yoshikawa et al. (Kaneka corporation) achieved a record efficiency of 26.3%, with V_{OC} of 744 mV, J_{SC} of 42.3 mA/cm² and FF of 83.8% for an IBC-HIT cell (Fig. 18b), approaching the theoretical efficiency limit of 29.43% for c -Si single junction solar cells (Yoshikawa et al. 2017; Richter et al. 2013). Later a record efficiency of 26.6% on the CZ wafer was obtained with improved contact resistivity (Yoshikawa et al. 2017). Since the fabrication of these impressive efficiency solar cells necessitates various etching and patterning processes, they are not favourable for the cost-efficient, highly productive manufacturing of solar cells at an industrial scale (Nakamura et al. 2014; Tomasi et al. 2017). A considerably more simplified back contacted SHJ, based on the surface-dependent growth (PECVD) features of Si thin layers with simplified patterning and alignment procedures, yielded an η of 22.5%. The carrier transport in these solar cells involves interband tunnelling, hence called tunnel-IBC solar cells (Tomasi et al. 2017; Esaki 1958).

Other than a -Si:H, large bandgap materials like nanocrystalline silicon oxide (nc -SiO_x:H) (Kirner 2015), microcrystalline silicon oxide (μc -SiO_x:H) (Mazzarella et al. 2015a) and amorphous silicon carbide (a -SiC:H) (Cleef et al. 1998) are also utilized to fabricate SHJ solar cells. Compared with a -Si:H, solar cells with these materials

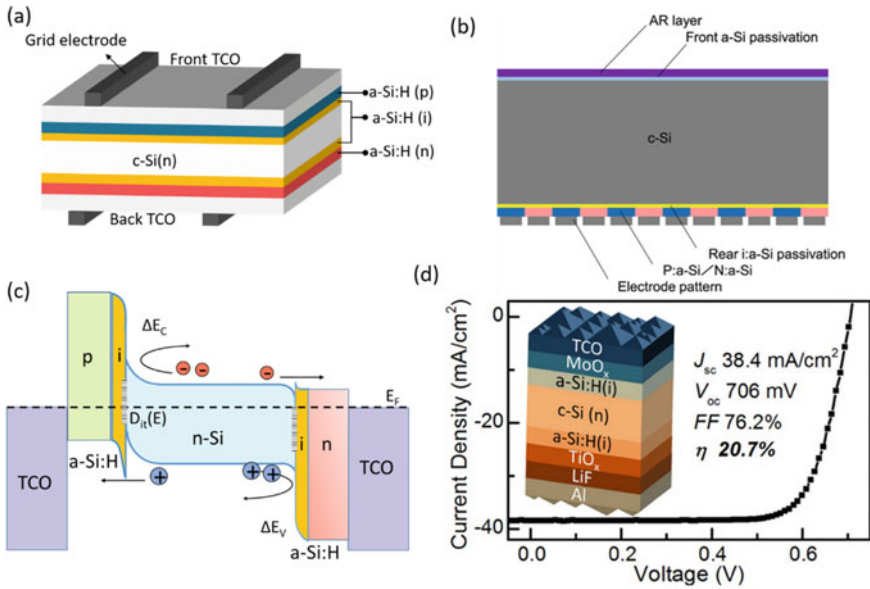


Fig. 18 Device structure of **a** silicon heterojunction (HIT-SHJ) solar cell and **b** IBC-HIT record efficiency solar cell (Reprinted with permission from Yoshikawa et al. (2017), Copyright (2017) *JVBullock et al. (2018)* © Elsevier). **c** The band diagram of HIT SHJ solar cell and **d** schematic of HIT solar cell with metal oxide selective contacts and the illuminated characteristics (Reprinted with permission from, Copyright (2018) © American Chemical Society)

gain a slight increase in the J_{sc} value ~ 1 mA/cm² due to reduced parasitic absorption (Mazzarella et al. 2015b; Zhong et al. 2014). Also, HIT architecture with impressive efficiencies $>22\%$ could be realized with thin c-Si wafers (<100 nm) made them economically attractive (Herasimenka et al. 2013; Inoue et al. 2009). Despite using a-Si:H, no significant light-induced degradation is observed in SHJ, as observed in thin-film a-Si solar cells (Wright et al. 2020). Moreover, few studies showed light-induced efficiency gain ($\sim 0.3\%$ absolute) in SHJ due to the reduced density of recombination centres (Kobayashi et al. 2016).

The front and rear side passivation by a-Si:H and the reduced emitter current are the main factors that lead to the enhanced performance of HIT solar cells (Ghannam et al. 2015). The typical band diagram of a HIT SHJ solar cell is shown in Fig. 18c. Valence band and conduction band discontinuities (ΔE_V and ΔE_C) are formed when a-Si:H (E_g 1.7 eV) and c-Si (E_g 1.12 eV) with different band gaps and electrical characteristics form junction (Ghosh et al. 2012). Thus the performance enhancement in an SHJ is accomplished by reducing (a) the density of active recombination sites and (b) the carrier concentration of either electron or hole (depending on the type of contact) at the interface via field effect (Olibet et al. 2007).

The deposition of a-Si layers requires the use of hazardous gases (such as silane, borane, and phosphine). Nonetheless, because these layers have a bandgap around

1.7 eV, they contribute significantly to parasitic absorption loss, limiting further efficiency improvements to achieve the theoretical limit. Recently, alternative materials based on metal oxides or organic materials have been implemented as passivating and selective contacts in SHJ devices. They provide the advantage of having a larger bandgap, and most of these metal oxides can be easily deposited by spin coating, thermal evaporation and sputtering techniques at room temperature. Materials like MoO_x , WO_x , V_xO_x , Cu_2O , NiO_x and organic materials like PEDOT:PSS were used as passivating hole selective contacts (Kurias et al. 2019), (Bhatia et al. 2019), (Kumar et al. 2019), (Markose et al. 2020b, c), (Bivour et al. 2017), (Nayak et al. 2019), (Islam et al. 2015). Alkali metals and metal fluorides like LiF_x , MgF_x and KF_x and low work function metal oxides like ZnO and TiO_2 were used as electron selective contact (Bhatia et al. 2020), (Wan et al. 2016), (Ding et al. 2018). They are generally called as carrier selective contact (CSC) solar cells and have approached efficiencies near 20% (Bullock et al. 2018; Geissbühler et al. 2015; Gao et al. 2018). More details of these novel selective contacts are discussed in the next chapter.

3.8 Polycrystalline Silicon on Oxide (POLO) Solar Cells

Even though the a-Si/c-Si heterojunction offers a good degree of passivation, but due to temperature limitations, normal processes like metallization and interconnection, which are typically carried out at a high temperature, must be carried out at a low temperature in these solar cells.

Also, the fabrication of IBC-SHJ necessitates a complex patterning process to form interdigitated contacts. These limitations are addressed in the POLO solar cells developed by Institute for Solar Energy Research in Hamelin (ISFH). Figure 19 shows the schematic diagram of a typical POLO solar cell. The POLO architecture comprises an interfacial oxide layer beneath a doped poly-Si layer, on which metal contacts are formed. The n^+ -poly-Si and p^+ -poly-Si provide electron and hole selectivity (Hollemann et al. 2020). Even though poly-Si has a high defect density, the poly-Si PN junction in the POLO solar cells shows reduced recombination (Rienäcker et al. 2016). The current transport mechanism across these contacts is dominated by charge flow through pinholes rather than tunnelling (Gan and Swanson 1990; Peibst et al. 2014). One of the main advantages of the POLO device is its high thermal stability. The electrical studies on the poly-Si/c-Si junction with a thin oxide layer showed lower contact resistance, carrier selectivity, and lower saturation current density than the a-Si/c-Si junction (Rienäcker et al. 2016). Figure 20 shows the short circuit current density loss in a-Si:H and poly-Si layer due to parasitic absorption. These losses are more than twofold as large for the same thickness of a-Si:H layers as for the same thickness of poly-Si layers. The larger losses in J_{SC} as the doping level increases are attributed to the increased free carrier absorption (Reiter et al. 2016). Various groups have obtained promising results with enhanced voltage and fill factor

implementing POLO structure (Romer et al. 2015), (Yan et al. 2015), (Young et al. 2016), (Yang et al. 2016), (Rienacker et al. 2017). IFSH obtained a record efficiency of 26.1%, adapting the POLO-IBC structure using laser openings with a *p*-type wafer base (Haase et al. 2018).

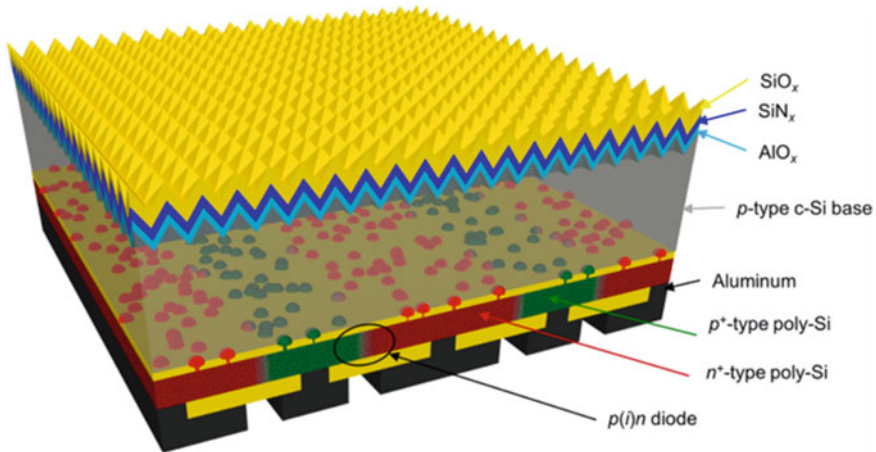


Fig. 19 Schematic of a typical high-efficiency POLO-IBC solar cell [Reprinted with permission from Hollemann et al. (2020), copyright (2020) © Springer Nature]

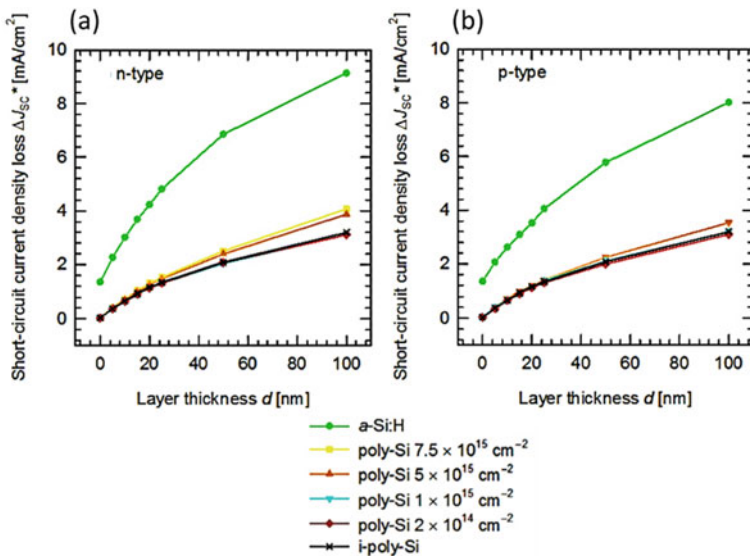


Fig. 20 Short circuit current density loss due to parasitic absorption of **a** *n*-type and **b** *p*-type poly-Si compared with a-Si:H. The doping concentration of poly-Si is also varied [Reprinted with permission from Reiter et al. (2016), copyright (2016) © Elsevier]

3.9 Bifacial Solar Cells

The bifacial solar architecture allows light to enter from both sides, mainly aimed at building integrated photovoltaic applications (BIPV). The first report on such a device came in 1966 by M. Hiroshi (Hiroshi 1966). In principle, every solar cell is bifacial as long as the rear side is not prevented from entering light. Bifacial solar panels are more efficient than mono facial panels resulting in higher total production efficiency (Fertig et al. 2016a), (Appelbaum 2016), (Chieng and Green 1993), (Fertig et al. 2016b). This unique structure delivers 5–30% more power output and a 2–6% reduced levelized cost of energy (LCOE) due to its ability to absorb sunlight from both sides (Patel et al. 2019). Bifacial solar cells typically feature a front surface design comparable to screen-printed industrial solar cells (Yang et al. 2011). The main variation is the structure of the rear surface contact. Figure 21a shows the schematic of a typical bifacial TOPCon solar cell. Rather than entirely covering the rear surface with Al reflective contact, a ‘finger’ grid contact is deposited, allowing sunlight to enter through the back side as well. Because the photogenerated carriers at the rear side of the cell must reach the emitter, bifacial solar cells use high-quality silicon. As encapsulating materials, transparent glass or organic coatings are used on both sides of the modules for light to pass through.

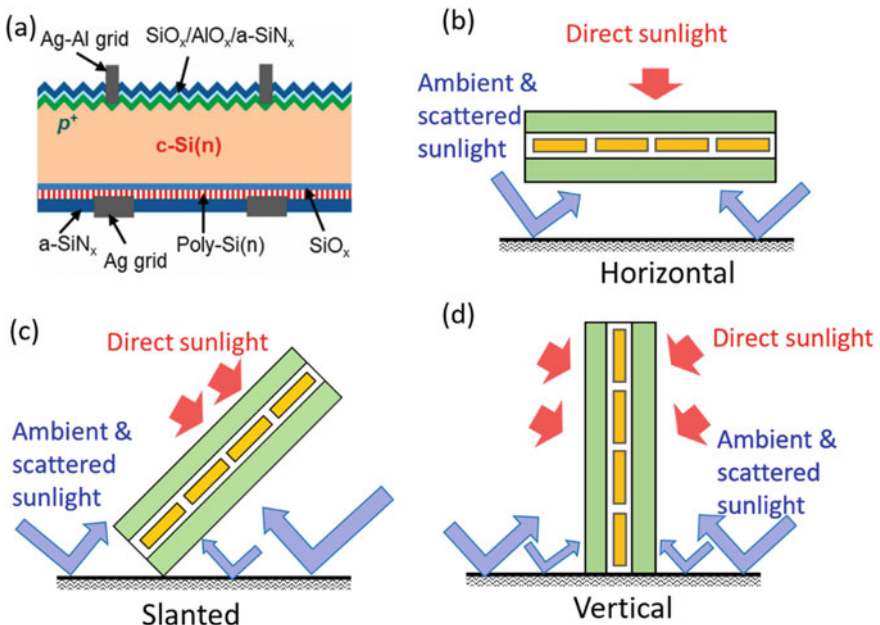


Fig. 21 Schematic of **a** bifacial TOPCon solar cell and **b** implementation options for bifacial modules [Reprinted with permission from Kafle et al. (2021), copyright (2021) © Elsevier]

The development of solar cells based on n-Si favoured bifaciality since the metalization grid can be easily used at the rear side instead of full area Al-metal contacts. Bifacial PERC family, HIT, and IBC solar cells are commercially available (Fellmeth et al. 2018; Baliozian et al. 2018). Bifacial solar cells are deployed vertically or at an angle to admit light from both sides. Figure 21b–d depicts the various positioning options for the module in order to use double-sided illumination. The performance of bifacial photovoltaics depends on factors like sun position, shading, ground albedo, tilt angle, orientation, diffuse coefficient and soiling (Van Aken and Carr 2014; Gu et al. 2020). Modules with an inclination (slanted) typically mounted on rooftops and ground result in high energy production and low LCOE. Horizontal modules also yield high energy efficiency depending on the installation geography and albedo of the underlying surface.

On the other hand, vertically mounted bifacial arrays open many intriguing applications. Compared to horizontally mounted arrays, vertically mounted bifacial arrays take up less space and have low dust accumulation (Khan et al. 2017). They have been utilized as light and sound barriers on highways (Vallati et al. 2015; Bellini 2019). Bifacial solar cell efficiency is usually determined by employing the independent efficiencies of front and rear sides under one sun. In industry, the bifacial solar cells are characterized by the bifaciality factor (BF). It is defined as the ratio between the rear side to front side efficiency of the bifacial cell under standard test conditions.

$$BF = \frac{\eta_{rear}}{\eta_{front}} \quad (17)$$

The BF of a front junction bifacial solar cell is determined by the rear side metal shading, diffusion profile and base resistivity. Numerical simulations show that the rear side illuminated bifacial solar cell with front-junction having low base resistivity yielded low J_{sc} due to increased recombination in the BSF (Van Aken et al. 2017). Optimizing various parameters is therefore important to maximize the bifacial solar cell performance.

4 Thin Film Solar Cells

Thin film solar cells are second-generation photovoltaics, consisting of multiple layers of thin films, typically a thickness range of a few microns. Even though silicon solar cells presently dominate the PV market, wafer-based PV technology has many disadvantages. Silicon solar cells are comparably expensive, where the high-quality silicon material accounts for the larger part of the silicon solar cell cost. As mentioned earlier, the ideal bandgap desired for a solar cell absorber layer is ~ 1.5 eV with a high absorption coefficient greater than 10^5 cm^{-1} . Being an indirect band gap material of ~ 1.12 eV, silicon is not an ideal solar cell material. To have a reasonable absorption of light, about $50 \mu\text{m}$ thick Si is required along with light trapping methods.

The complexities in the c-Si solar cell fabrication, the requirement of sophisticated equipment, and high thermal budget, prevent further cost reduction for c-Si modules. Furthermore, the use of thick Si wafers inhibits the development of flexible applications, which are in high demand right now. Thin film solar cell technology has the potential to lower module costs due to the advantages in materials and fabrication procedures. A thin film is formed by the “random nucleation and growth of condensing or reacting atomic, ionic, or molecular species on a substrate” (reprinted from Chopra et al. (2004), copyright @ 2017, Elsevier). A wide range of carefully regulated deposition parameters, as well as thickness influence the physical and optoelectronic properties of thin films. Thin films come in a wide range of thicknesses from a few nanometers to micrometres, so ideally, they are defined in terms of growth process rather than thickness. That is, using techniques like ablation, slurry spray and others, one can make a bulk material thin material, but not a thin film. Depending on the growth conditions, the microstructure of thin film materials can range from extremely amorphous to highly oriented epitaxial growth (Chopra et al. 2004).

The scientists at the Institute of Energy Conversion at the University of Delaware in the USA pioneered thin film solar cell research back in the 1970s. Calculators powered by amorphous silicon solar cell strips were available on the market by the late 1970s. In the following years, the demand for thin film solar cells increased as they can be easily installed on curved surfaces or buildings due to their flexibility. Other potential thin film solar cells are cadmium telluride (CdTe) and CIGS solar cells. Organic and sensitized solar cells are also considered thin film devices, but we will discuss them later as emerging technologies for the convenience of the discussion. Table 1 compares various optoelectronic properties of prominent thin film solar cell materials—a-Si, CdTe and CIGS. These direct band gap materials with high absorption coefficients ensure a low thickness requirement for solar cell application.

The basic architecture of a thin film solar cell consists of a sunlight-absorbing layer sandwiched between two contact layers. One or more layers may be required to passivate the interfaces between the layers; otherwise, these interfaces may operate

Table 1 Comparison of various parameters of thin film solar cell materials (Reprinted with permission from Lee and Ebong (2017) Copyright © 2021 Elsevier)

Parameters	a-Si	CdTe	CIGS
Absorption coefficient (cm^{-1})	1.74×10^6	1.1×10^6	1×10^5
Bandgap (eV)	Direct 1.75	Direct 1.44	Direct 1–1.6
Thickness requirement (μm)	1	3–5	1–2
Temperature coefficient ($\%/^\circ\text{C}$)	–0.3	–0.25	–0.26
Remarks		Cadmium toxicity	

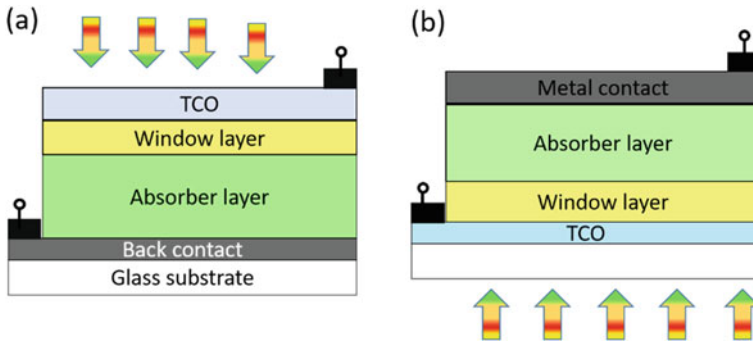


Fig. 22 Schematic of thin film solar cell in **a** substrate and **b** superstrate structure

as recombination centres, reducing the quantity of generated electrons and lowering the conversion efficiency. The thin films solar cells take two possible configurations depicted in Fig. 22a, b. In the first case, Fig. 22a, the sunlight enters through the transparent conducting oxide layer called the substrate configuration. Front contact layers provide the necessary electrical contact and possess light trapping and antireflection properties. In the superstrate configuration, the light enters through the glass substrate (Fig. 22b). Instead of glass substrate polymer films, plastics substrates and metal foils are also used to deposit thin film solar cells. Thus the features of thin film solar cells are the ease of fabrication, cost-effective, lightweight and flexible PVs, low light application, heat resistance and also the carbon emission during its production is very low compared to the conventional Si solar cells. However, thin film solar cells face degradation induced by light and often showing a lesser lifetime than c-Si solar cells.

In the following session, we briefly discuss thin film solar cells, including a-Si:H, CdTe and CIGS, emphasizing their main features and potentials.

4.1 Amorphous Silicon Solar Cells

Amorphous silicon (a-Si) layers were first reported in 1965, deposited in a radio frequency glow discharge from silane (SiH_3) (Sterling and Swann 1965). In 1975, Spear and LeCombor reported that the conductivity of the a-Si layer could be easily modified by adding phosphine (PH_3) or diborane (B_2H_6) to SiH_3 for making *n*- and *p*-type, respectively (Spear and Comber 1975). This was a huge breakthrough because amorphous silicon had previously been assumed to be impossible to be doped. Unlike the c-Si atomic arrangement, the a-Si atomic arrangement is in short order, with atoms forming a random network, as seen in Fig. 23a. Additionally, these atoms may not all be fourfold coordinated, resulting in dangling bonds, which act as defects. a-Si layers often have a large number of defects $\sim 10^{20} \text{ cm}^{-3}$, resulting in a high recombination rate and anomalous electrical properties. Later it was discovered that alloying with

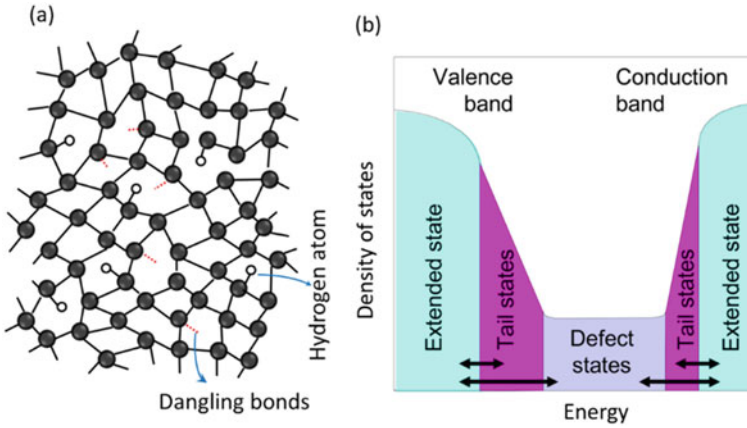


Fig. 23 Schematic representation of **a** amorphous silicon and **b** band diagram of a-Si:H

hydrogen (~ 10 at% H_2) greatly reduces the defect density ($< 10^{16} \text{ cm}^{-3}$), therefore called hydrogenated amorphous silicon, denoted as a-Si:H. The hydrogen atoms bond with the dangling bonds and passivate them. In reality, a-Si doped *n*- or *p*-type is an alloy of silicon and hydrogen designated as a-Si:H(n) or a-Si:H(p) correspondingly.

Compared to c-Si, a-Si:H has many advantages in material properties and deposition techniques used. a-Si:H can be deposited at very low temperatures over a large area using easy and inexpensive methods. a-Si:H layers can be easily deposited onto plastic and polymer flexible substrates. The a-Si:H has a direct band gap of ~ 1.7 eV. With a high optical absorption coefficient of 10^{16} cm^{-1} , even a $1 \mu\text{m}$ thick a-Si:H layer is sufficient to absorb 90% of the solar radiation available (Table 1). On the other hand, the dangling bonds in the a-Si:H result in energy states in the band gap, where the energy states are divided into three regions called (a) the extended state (mobility edge) below and above the conduction band, (b) the tail states and (c) the localized defects states in the bandgap as illustrated in Fig. 23b. The bandgap of the a-Si:H is defined as the lowest energy gap (mobility gap) between the extended conduction band and valance bands, with a typical value ranging from 1.7 eV to 1.8 eV. The band gap of a-Si:H is found to become wider as the amount of hydrogen in the a-Si:H film increases, caused by the changes in the hydrogen microstructure in the film. Alloying the a-Si:H with elements like C, Ge, N and O can be used to deposit a-Si alloying having a wide range of bandgap. For instance, alloying with C (a-SiC:H) and Ge (a-SiGe:H) results in the increase (2 eV) and decrease (1.2 eV) of the band gap, respectively. However, the defect states in the band gap result in recombination and poor mobility of the a-Si:H thin films.

The a-Si:H solar cells makes use of the drift-based carrier transport rather than the diffusion-based due to the low life of the photoexcited free carriers in different a-Si:H layers resulting from the high defect level concentration associated with doping. As a result, instead of a *pn*-junction, an a-Si:H solar cell has a *p-i-n* architecture. That is, an undoped layer (a-Si:H(i)) with a low defect density is introduced between the *p*-

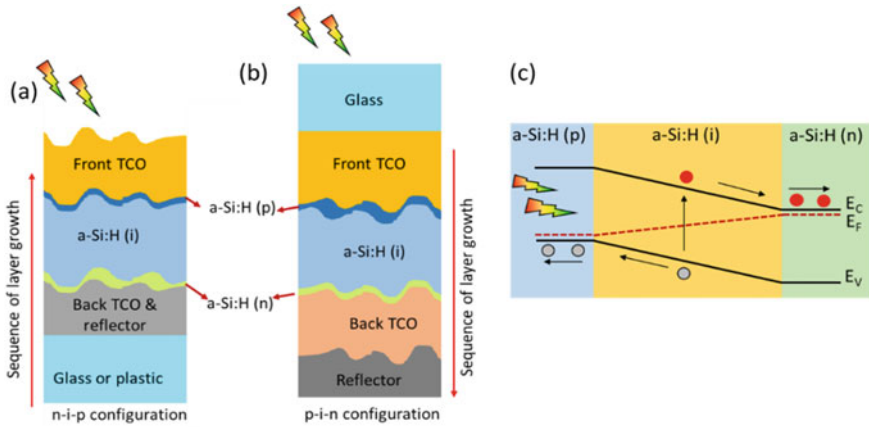


Fig. 24 Schematic of **a** n-i-p and **b** p-i-n configuration a-Si solar cells. **c** The band diagram of a-Si:H solar cell

and n-type layers such that the mean free path of the slowest carriers (holes) is long enough to spatially isolate and extract them from photogenerated electrons in this region (Carlson and Wronski 1976). Depending on the deposition sequence, a-Si:H solar cells have two device configurations, the substrate architecture known as *n-i-p* configuration (Fig. 24a) and the superstrate architecture known as *p-i-n* configuration (Fig. 24b). In *n-i-p* configuration, the *n*-layer is deposited onto the conductive back contacts (TCO/metal) coated over substrates like glass, PET, PI or PEN. The *i*-layer comes next, followed by the deposition of the *p*-layer and the front TCOs.

On the other hand, in the *p-i-n* configuration, the *p*-layer is first deposited onto TCO-coated substrates like glass, polyethylene naphthalene etc., followed by the *n*-layer and the back contact TCO/metal. The *n-i-p* and *p-i-n* structures offer a wide range of applications. The superstrate design (*p-i-n*) is appropriate for building-integrated PV applications, where the glass substrate could be utilized as an architectural component. The substrate design (*n-i-p*) is suitable for flexible solar cell applications, where the a-Si:H layers are deposited on flexible substrates like stainless steel or polymeric substrates. In a-Si:H solar cell, the Fermi energies of the p-type and n-type materials are substantially different. These Fermi energies must be equalized to achieve the thermal equilibrium when *p-i-n* or *n-i-p* junction is formed. While electrons are transferred from the n-layer to the p-layer, creating a built-in electric field. The electric field present rapidly separates the photogenerated electron–hole pairs in the a-Si:H(i) region. As illustrated in Fig. 24c, electrons and holes drift in the electric field towards the *n*- and *p*-layers, respectively, and are collected at the contacts.

In a-Si:H solar cells, light trapping is achieved using textured TCO substrates creating random reflections/diffractions of light, resulting in internal reflections. After a few hundred hours of illumination, amorphous silicon solar cells encounter a significant deterioration in efficiency called the Staebler–Wronski effect. Because

the a-Si:H bonds are weaker and less stable, they break and generate new defect levels if sufficient energy is obtained from heating or light, resulting in a drop in performance. However, Staebler–Wronski effect can be cured, and the initial performance can be restored by high temperature (160 °C) annealing for a few minutes. Various deposition techniques have been used for a-Si:H layers. Plasma-enhanced chemical vapour deposition (PECVD) is the most common method used to deposit a-Si:H layers having the advantage of high-quality uniform film deposition; however, the deposition rate is slow. The hot wire CVD technique offers fast film deposition, but the uniformity of the deposited film is an issue. Deposition parameters like gas mixing ratios, substrate temperature and the working pressure are controlled to obtain device quality films. a-Si:H solar cells combined with microcrystalline silicon thin film solar cells in tandem architecture (micromorph cells) were introduced to gain higher efficiency of ~12%.

4.2 Cadmium Telluride (CdTe) Solar Cells

The CdTe solar cell technique is one of the most successful thin film solar cell technologies. Since the first CdTe/CdS heterojunction solar cell was published in 1972 by Bonnet and Rabenhorst (η ~6%), enormous progress has been made, with efficiency reaching 22.1%. CdTe is a *p*-type (V_{cd}) semiconductor material belonging to the II–IV group with a direct bandgap of 1.45 eV (polycrystalline) and an absorption coefficient of $>10^{14} \text{ cm}^{-1}$. CdTe films deposited via closed space sublimation (CSS) had reported a carrier concentration $>10^{14} \text{ cm}^{-3}$ sufficient for junction formation with its *n*-type counterpart (Bai et al. 2011). Even with a 1 μm thick CdTe, the majority of the incoming solar radiation may be absorbed. With the band gap near to optimum value (1.5 eV) according to SQ limits, CdTe solar cells can reach efficiencies greater than 30% with open-circuit voltage and short circuit current density greater than 1 V and 30 mA/cm², respectively. CdTe has a high bond energy of 5.7 eV, making it chemically and thermally stable, enabling it radiation-resistant and suitable for space applications. From the solar cell device point of view, polycrystalline CdTe of grain size ~1 μm is widely accepted as device quality film. Since the thickness requirement of CdTe is about 1 μm , the low minority carrier lifetime is acceptable and high purity thin films are not imperative for solar cell fabrication. Another advantage is that the grain boundary of CdTe is electrically inactive, hence does not contribute to the recombination of the photogenerated carriers. As this happens naturally, grain boundary passivation is not essential in CdTe films. The size of the CdTe grains changes with the substrate temperature.

Since CdTe is the sole stable compound in the Cd–Te phase diagram, it is impossible to modify its bandgap by alloying it with other elements. Further, the CdTe films grown under a Cd-rich environment forms *n*-type conductivity where the Fermi-level is pinned near the mid gap by the compensating donor effect Cd_i^{2+} . Moreover, the CdTe films grown in Te-rich conditions behave as *p*-type semiconductors where the

Fermi levels lie near the valance band maximum. Besides, doping with group III and IV elements could be used to tailor the bandgap of CdTe films.

Like several other thin film PV devices, CdTe solar cells can be manufactured in both substrate and superstrate architecture. However, the superstrate arrangement (Fig. 25a) is the most efficient since this structure provides for the essential post-deposition treatment (Romeo and Artegianni 2021). Homo junction of *p*-CdTe/*n*-CdTe solar cell device performance is limited due to the low minority diffusion length of carriers. Therefore, heterojunction between CdTe and CdS is preferred where the *p*-type CdTe is generally deposited on an *n*-type CdS thin film. Having a direct bandgap of 2.4 eV, CdS does not contribute to the absorption of the solar radiation, and it is often called a buffer/window layer. Generally, thin layers of CdS film grown by chemical bath deposition (CBD) are used as the buffer layer, minimising the interface mismatch between CdTe and TCO. The CdS layer used as a buffer usually is high-quality stoichiometric films with high resistivity to minimise the interface trap density. Likewise, if used as a window or active layer, the resistivity should be small to form an ohmic contact with TCO and form a strong electric field at the CdTe-CdS junction. In solar cells, thin layers of CdS are used to ensure high transmission and have high conductivity with a carrier concentration of $\sim 10^{16} \text{ cm}^{-3}$. The performance of a CdTe solar cell is highly dependent on the CdTe/CdS interface properties. From the band structure point of view, type I heterojunction with small ΔE_C ($0.1 \text{ eV} \leq \Delta E_C \leq 0.3 \text{ eV}$) is acceptable to provide good efficiency solar cells. However, the CdTe/CdS band structure (Fig. 25b) analysis shows a cliff ($\Delta E_C < 0 \text{ eV}$) like interface results in high hole concentration near the interface, which leads to recombination and reduce the V_{OC} of the device (Song et al. 2016). Another material, $\text{Mg}_x\text{Zn}_{1-x}\text{O}$ (MZO) and CdSe are promising higher bandgap alternative window layer materials that can be used instead of CdS. CdTe solar cells with MZO windows layer have achieved efficiencies greater than 18%.

Glass, stainless steel, molybdenum and polyamide are the common substrate materials used for CdTe solar cell fabrications. TCOs like FTO, AZO, CTO and ITO are widely used as the front contact in CdTe/CdS solar cells. TCOs are first deposited on

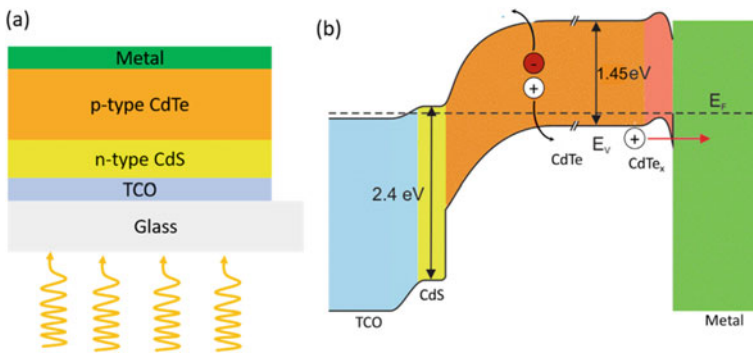


Fig. 25 a Schematic of CdTe solar cell and b the band diagram

the substrate glass, and they can affect the structural properties of the following layers CdTe and CdS. Also, the impurity diffusion from the TCO to the active junction can affect the performance of the device. Metals such as Au, Al, Mo, Ag, Cu, and others are commonly used as electrode contacts. Passivation treatments are important to obtain high-efficiency CdTe solar cells, of which CdCl₂ treatment is found to be extremely important where large efficiency gains are obtained. CdCl₂ post-treatment on CdTe enhances grain growth, increases the carrier concentration, provides passivation at grain boundaries, decreases the defect density, and reduces the pinholes in the CdTe films. Typically wet chemical methods and vacuum treatment are used to treat with CdCl₂. Figure 26a shows the PL spectra of the as-deposited and CdCl₂ treated film. The as-deposited CdTe film has many sub-bandgap features due to defects as observed. After the 1st and 2nd CdCl₂ treatment, the sub-bandgap features reduced significantly (Dharmadasa et al. 2015). Figure 26b shows the schematic of band structure illustrates the reduction of defect states after the CdCl₂ treatment. The CdCl₂ treated polycrystalline CdTe films show better functionality because of passivation and defect compensation. The main challenge the CdTe solar cells address is the toxicity issues related to cadmium. Also, tellurium is a scarce element, further limiting its production, and it is necessary to use a thin layer of CdTe to extend the supply of Te. Another issue is the impurity diffusion from various layers towards the device junction, which reduces the device performance.

4.3 CIGS Solar Cell

The Cu(In, Ga) (S, Se)₂ (CIGS) is another promising thin film solar cell technology for higher efficiency potential (including CuGaSe₂, CuLnSe₂, CuGaS) (Powalla et al. 2013). CIGS semiconductor has a chalcopyrite crystal structure with a bandgap in the range of 1–1.6 eV.

Of the various chalcopyrite materials, CuInSe₂ shows better performance; however, it has a bandgap of 1 eV. It is often alloyed with Ga (Cu(In, Ga)Se₂) to increase its bandgap, obtaining 1.15 eV. CIGS is direct bandgap material with p-type conductivity that arises due to the indium vacancies and the Cu atoms on In sites. This enables control of the conductivity of the material by adjusting the In to Cu ratio during its deposition. Therefore, it needs not necessary to have a uniform band gap throughout the material. In fact, by changing the composition, the desired bandgap at the front and the rear of the material can be achieved.

The typical structure of a CIGS solar cell is shown in Fig. 27a. Like CdTe solar cells, CIGS also solar cell is fabricated in heterojunction design with CdS as the window layer. The photogenerated carriers separate due to the built-in field, and the electrons move to the CdS while the hole moves to the CIGS and is collected at the respective electrodes (Fig. 27b). CIGS solar cell is often deposited in substrate configuration—on flexible polymer substrates and rigid soda-lime glass (SLG) substrates. However, using SLG has its advantage. The Na in the SLG diffuses into CIGS during its growth, influencing the morphology and improving p-type conductivity

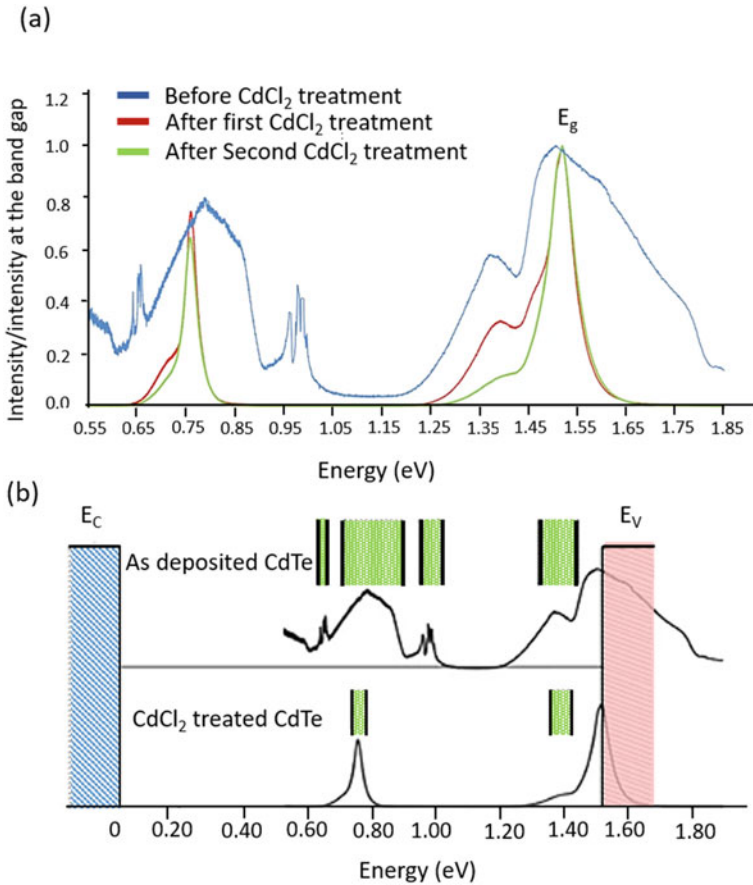


Fig. 26 **a** The PL spectra of as-deposited and CdCl_2 treated CdTe. **b** Schematic of the band structure of CdTe before and after CdCl_2 treatment (Reprinted with permission from Dharmadasa et al. (2015), copyright (2015) © Springer Nature)

(Rudmann et al. 2004). CIGS is often deposited in a two-step process. Initially, Cu, In, and Ga precursors are deposited on the substrate by co-evaporation or sputtering. The precursor film is annealed in the selenium atmosphere in the second step to obtain CIGS.

Sputtered Mo is mostly used as the back contact since it is stable in the corrosive Se/S atmosphere where CIGS is deposited. A thin layer of MoSe_2 is formed at the interface during the deposition, improving the adhesion and contact properties (Fig. 27b). On the front side, TCO is used to extract the electrons. Typically, a bilayer structure of intrinsic ZnO (*i*-ZnO) and Al-doped ZnO (AZO) is used. The *i*-ZnO acts as a buffer layer protecting from the sputtering damage and prevents the shunt paths through the pinholes. In order to further passivate the interface, dielectric layers like Al_2O_x have been used and obtained promising results. Structures of

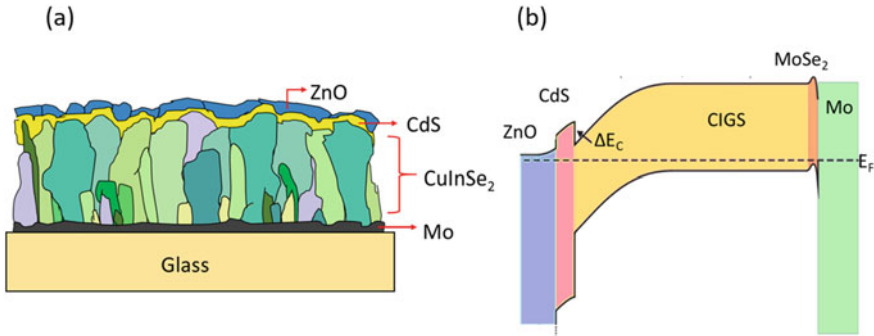


Fig. 27 a Schematic of CIGS solar cell and b its band diagram

patterned (point contact) Al₂O_x and tunnel oxide Al₂O_x have been reported to have excellent passivating properties. However, the presence of toxic Cd in the solar cell in the form of CdS is the main challenge faced by CIGS. Material like MZO and Zn(O, S) also have been attempted as buffer layer CIGS.

5 Emerging Photovoltaics

The last few decades have witnessed the emergence of several new thin film solar cell technologies with high potential and offer many advantages for low – cost low – temperature flexible solar cell applications. Dye-sensitized solar cells (DSSC), quantum dot solar cells (QDSC), Organic solar cells, and perovskite solar cells are a few. In the next session, we will briefly discuss the emerging solar cells concepts.

5.1 Organic Solar Cells

Organic semiconductors that can be easily processable are among the best candidates for large area-low-cost flexible solar cells. Compared to inorganic solar cells, the active materials in organic solar cells only have a thickness of 100 nm, providing low material consumption. Organic materials are easily deposited at room temperature by the solution-based process.

When photons of sufficient energy are absorbed by the organic semiconductor, the carriers are excited, and electrons move to the lowest unoccupied molecular orbital (LUMO) and leave a hole in the highest occupied molecular orbital (HOMO). However, these electrons and holes are not free; rather, they are in a bound state by Coulombic attraction, and the electron–hole pair is called an exciton. The exciton can return to its ground state by releasing energy or being separated into respective contacts. The exciton binding energy of organic semiconductors is of the order

~ 0.5 eV making it impossible to separate the carriers at room temperature (~ 26 meV) and result in recombination. Therefore, the exciton separation required a large internal field to get split. Organic solar cells are made up of donor (D) and acceptor (A) moieties that come into close contact with one another. Donor and acceptor organic molecules have different electron affinities and provide the driving force to dissociate the exciton into electron and hole through the channel I (electron transfer from donor to acceptor) and channel II (hole transfer from acceptor to the donor) charge transfer as seen in Fig. 28a. Efficient charge transfer or dissociation at the interface can occur if the following requirement is met (i.e., the energy level difference of donor and acceptor LUMO should be greater than the binding energy of exciton):

$$E_A^A - E_A^D > U_D \quad (18)$$

where U_D is the binding energy of exciton in the donor, E_A^A and E_A^D are the electron affinity of acceptor and donor molecules, respectively (Abdulrazzaq et al. 2013). The potential energy difference of the LUMO layer of A and D is crucial in the charge transfer process; the higher the difference, the higher the dissociation. D and A with large energy offset results in high V_{bi} and leads to large V_{OC} . Furthermore, because the exciton diffusion length of most conjugated polymers is ~ 10 nm, the active polymer domain size must be compatible with the exciton diffusion length for effective exciton diffusion to the D–A interface and eventually charge separation

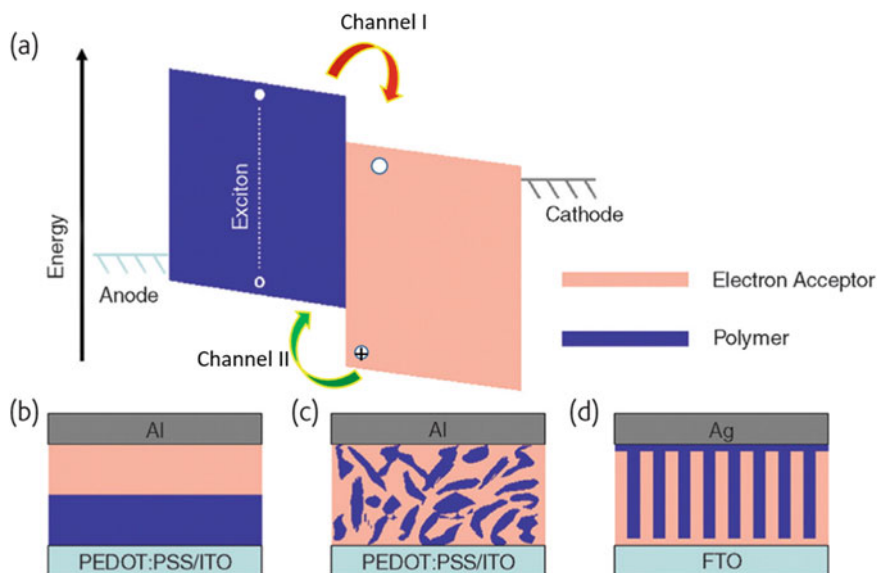


Fig. 28 a Energy band structure of organic heterojunction solar cell. Various organic solar cells based on junction formation b bilayer heterojunction, c bulk heterojunction and c ordered heterojunction (reprinted from Mayer et al. (2007), Copyright (2021) © Elsevier)

(Lee et al. 2019). Besides, the motilities of electrons and holes are many orders of magnitude lower than inorganic material. Several device architectures are considered to alleviate these issues to increase the D–A interface. Generally, organic solar cells consist of D–A layers sandwiched between cathode and anode contacts. Between the anode and D layer, HTL layers are used to suppress recombination by blocking electrons. ETL layers are used between the anode and acceptor layer to block holes and facilitate electron conduction. Figure 28b–d shows various organic solar cell architectures with different D–A interfaces. The first one (Fig. 28b) is called bilayer heterojunction, or planar heterojunction comprises subsequent layers of D and A. It is then sandwiched between the cathode (transparent high work function material; near donor) and anode (low work function material; near acceptor). In this architecture, the diffusion of the exciton to the interface is low; the only exciton generated at the interface can get separated.

However, the bulk heterojunction architecture (Fig. 28c) provides a larger area D–A interface. Here, the donor and acceptor blend is deposited to form a thin film with the donor and acceptor separation is only a few nanometers. This expedites an increased probability of exciton diffusion to the interface and gets split (Zhang et al. 2011). Figure 28d shows the ordered bulk heterojunction, an ideal architecture for organic solar cells. In this architecture, the inorganic semiconductor acceptors are deposited onto nanowire, nanorod, and nanotube morphology grew on the conducting substrate. The active layer infiltrates the nonporous structures providing a direct charge transport pathway. This architecture is also achieved by active layers with ordered morphology attained by using nanowires or nanoimprint lithography, forming an interdigitated junction between the donor and acceptor (Yang et al. 2012), (Hu et al. 2012), (He et al. 2011), (Ding et al. 2015), (Guo 2007).

Materials such as polymers and small molecules are used to fabricate organic solar cells. The donor or the active material should possess strong absorption and an ideal HOMO–LUMO energy gap to absorb the solar spectrum and high hole mobility. The acceptor molecules should have an increased ability to accept electrons and high electron mobility. Also, they should have a higher electron affinity than the donor molecule to provide an energetically favourable band structure. Inorganic materials such as TiO_2 , ZnO , and others are also used as acceptors (Bonasera et al. 2020). Various novel device architectures and materials are being used to enhance the efficiency of organic solar cells. Employing quaternary active blends and the double cascading energy level alignment, a record efficiency of 18.07% in single-layered active material organic solar cells has been demonstrated recently (Zhang et al. 2021). One of the main challenges amidst many advantages is the low efficiency of the organic solar cell compared to its conventional inorganic counterparts. Another issue is the degradation and durability of organic solar cells, where strong encapsulation is required to retain the performance of organic solar cells.

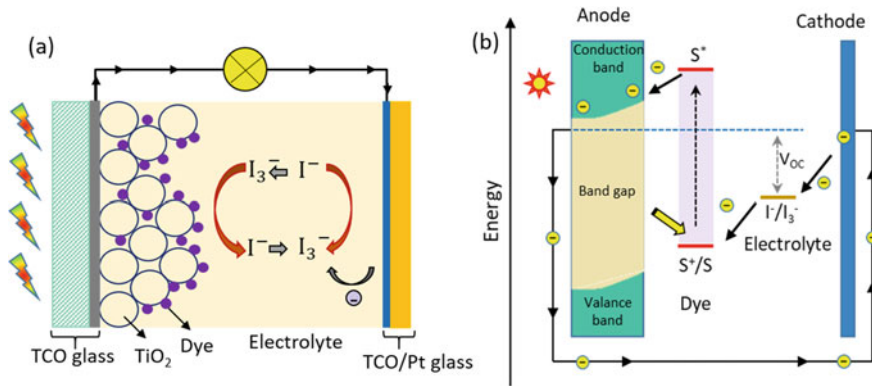


Fig. 29 Schematic of a typical DSSC and b the energy band diagram

5.1.1 DSSC and QD Solar Cell

Grätzel et al. pioneered and first reported dye-sensitised solar cell research in 1991, and these cells are commonly referred to as Grätzel cells (O’Regan and Grätzel 1991). In DSSC, dye molecules adsorbed on the surface of wide bandgap semiconductors, typically TiO₂, serve as absorbers. The primary benefit of DSSC solar cells is their low-cost fabrication, which generally involves environmentally friendly materials, and a reasonable efficiency of ~14% is achieved (Kakiage et al. 2015). Because dye molecules have a specific absorption range, coloured solar cells can be made by selecting the appropriate dye molecule, which improves the aesthetics of solar cells. DSSC has been employed for indoor applications due to its high response to low-intensity light (Devadiga et al. 2021; Biswas and Kim 2020). A typical structure of DSSC is depicted in Fig. 29a.

DSSC consist of a glass substrate with conducting TCO (ITO or FTO) layer onto which ETL is coated. Wide semiconducting materials, typically porous TiO₂, are commonly used as ETL, where the porosity ensures a high surface area. The dye molecule that serves as the absorber is then coated or adsorbed onto the TiO₂ layers. Ruthenium-based metal–organic complexes or natural dyes are used in DSSC. Organic solvents with the iodide/tri-iodide redox system are used as electrolytes. Another TCO coated with platinum or graphite is used as the cathode.

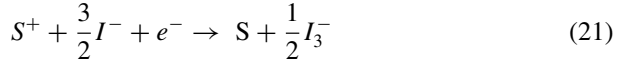
When sufficient energy photons is absorbed by the dye molecule, it gets excited into a higher energy state (S^*) from the ground state (S) given by,

$$S + h\nu \rightarrow S^* \tag{19}$$

The excited dye molecule now has a higher energy content and can cross the semiconductor bandgap. Within a time range of femtoseconds, the dye molecule in the excited state (S^*) get oxidized and inject an electron into the conduction band of the wide bandgap semiconductor, TiO₂.



The electron is then collected at the working electrode, typically TCO. At the time, the oxidized dye molecule (S^+) gets reduced by receiving an electron from the iodine in the electrolyte solution by reducing the iodide ion to tri iodide (I_3^-).



Later the tri iodide diffused to the counter electrode and regenerated by accepting the free electrons there, thus completing the cycle.



The HOMO–LUMO levels of DSSC, the Fermi level of the TiO_2 electrode, and the redox potential of the mediator (I^-/I_3^-) in the electrolyte are deterministic in the performance of DSSC. However, due to the poor optical absorption of sensitizer dyes, DSSC has a low conversion efficiency. Besides, the degradation of dye due to radiation, water, variation in temperature and chemicals reduces its life cycle. Many novel dyes and electrolytes are suggested to improve the performance of DSSCs.

Due to their exceptional optical properties, quantum dot sensitized solar cells are considered a potential alternative for DSSC, an area of great interest in recent decades and called quantum dot sensitized solar cells (QDSSC). Generally, PbS, CdS, CdTe and PbSe are used as the active layer in QDSSC. Due to the quantum confinement effect, by adjusting the size of the QDs, the bandgap and other optical properties can be tuned. QDs have the advantage of multiple exciton generation, an increased surface-to-volume ratio and broad optical absorption with a tunable bandgap. Also, stable QDSSC can be easily fabricated at room temperature. Theoretical efficiency calculation predicts ~42% efficiency for QDSSC. However, the mid-gap states present in the QDs leads to a reduction of the open-circuit voltage of QDSSC. QDSSC is expected to open novel low-cost solar cells with efficiency and stability improvements.

5.2 Perovskite Solar Cells

Perovskite materials have many exceptional optoelectronic and physical properties, with the chemical formula ABX_3 , where A and B are organic cation and inorganic cation, respectively, and X is a halide (Sahoo et al. 2018). The bandgap of perovskite materials changes with the halide ranging from 1.6 eV to 3.2 eV for I and Cl, respectively. They have a long carrier diffusion length, low recombination losses, and low material cost. Within the few years of its inception, perovskite solar cells have achieved high efficiencies of ~20%.

However, instability, sensitivity to moisture, and toxic lead as a constituent challenge its commercial application. Current research is focused on using perovskite as the top cell in perovskite/Si tandem solar cells. Details of the perovskite solar cell are discussed in Chap. 3.

6 Solar Cell Applications

Although Si PV technologies dominate the industry, new technologies have their own market niches and potentials (Heinrich et al. 2020). Incorporating different solar cell technologies for various applications like solar farms, building integrating PVs, consumer products, space applications, and electronic gadgets needs to meet certain design and performance requirements. The major concerns are efficiency, production cost, stability, lifetime, temperature tolerance and low light performance. From the design point of view, flexibility, size variability, aesthetics, and material toxicity are of serious concern.

For building integrated photovoltaic (BIPV) applications, rigid and flexible solar cells have been used depending on the needs. Generally, wafer-based Si PVs and thin film solar cells are widely used in BIPV applications. Being high-efficiency solar cells, c-Si modules require a lesser area than thin film solar cells for similar output power. However, for flexible BIPV, organic and DSSC technologies are preferred, along with a-Si:H, CIGS and CdTe solar cells deposited on flexible substrates. Further, DSSC, organic and perovskite solar cells have the intrinsic potential for colour and offer aesthetics to the building (Yeop Myong and Won Jeon 2015). There are few attempts to give colour to the conventional Si solar cells. Nanophotonic coating called Selectively Modulated Aesthetic Reflector Technology (SMART) coatings have been demonstrated to provide colours to any mature BIPVs, as seen in Fig. 30a, b (Soman and Antony 2019).

However, this coating reduces the efficiency of the modules due to selective reflection of certain wavelengths but provides a pleasant look to the buildings. Therefore, these coatings are better to work for c-Si PV, which has the highest efficiencies. Si solar cells with different shapes and appropriate metal bus bars are also reported recently (Fig. 30c–e). Another issue with conventional solar cells is that they are not transparent. Therefore they cannot be applied to the window panes of the skyscrapers, which contributes to the large surface area. Transparent thin film solar cells or DSSC will likely be used in window panes. By adjusting the dye, the windows can have different colours. Recently, “neutral coloured transparent silicon solar cells” have been reported with photoconversion efficiency reaching 12%, the highest to date for a transparent solar cell (Fig. 31a–c). In order to make transparent Si solar cells, micro-hole light transmission windows invisible to the naked eye are put on a 200 μm silicon wafer as seen in Fig. 31.

Today, the Internet of Things (IoT) connects various wearable microelectronic sensors for health and activity monitoring, where they usually work in indoor conditions. For these devices with microwave power requirements, a self-sustaining power

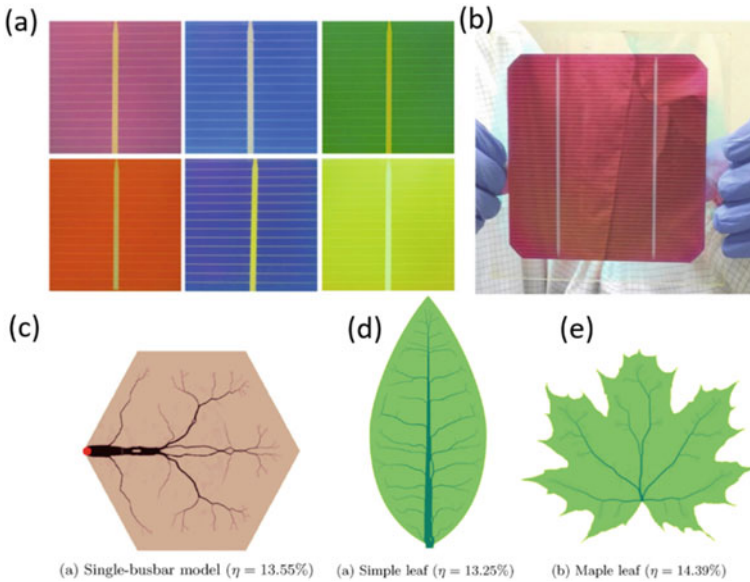


Fig. 30 **a** SMART coating on c-Si solar cells. **b** The front bus bar demonstrates the transparency of the SMART coating on the glass [Reprinted with permission from Soman and Antony (2019), copyright (2019) © Elsevier]. Various metallization patterns for free form solar cells—**c** hexagonal **d** simple leaf and **e** maple leaf designs (Gupta et al. 2016)

source that harvests indoor light is better suited (Biswas and Kim 2020). Generally, low-cost, stable, and efficient PV cells with size tunability and high performance in low-intensity or diffused light are used for indoor applications. Organic solar cells, a-Si, DSSCs and perovskite solar cells, for example, have obvious advantages for interior applications owing to their ‘light-weight, spectral matching with indoor light sources (LED, CFL, etc.), mechanical flexibility, high V_{OC} and PCE’. (Chen et al. 2017), (Xu et al. 2021), (Arai et al. 2019), (Teran et al. 2016), (Jahandar et al. 2021; He et al. 2021; Biswas and Kim 2020). Figure 32 shows the emission spectra of various indoor light sources compared with the solar spectrum. The solar spectrum is broader, extending to the infra-red region, while indoor lights have a narrow emission band around 600 nm. Therefore, a solar cell active layer with a bandgap of ~ 1.9 eV is ideal for indoor applications. For consumer product applications, a-Si solar cells are used due to their high efficiency and life cycle. They are easily deposited to large and small areas on flexible substrates.

The demand for space solar cells has increased as the space industry has expanded rapidly, with exploration continuing throughout outer space and the energy need of telecommunication satellites. The space environment is not the same as terrestrial conditions. Strong radiations and alternating temperatures are the main characteristics of the space environment (Thirsk et al. 2009). The early satellites had silicon solar cells to power them (Bouisset et al. 1992). Later GaAs solar cells have been used for their superior characteristics, including higher efficiency, direct bandgap, and

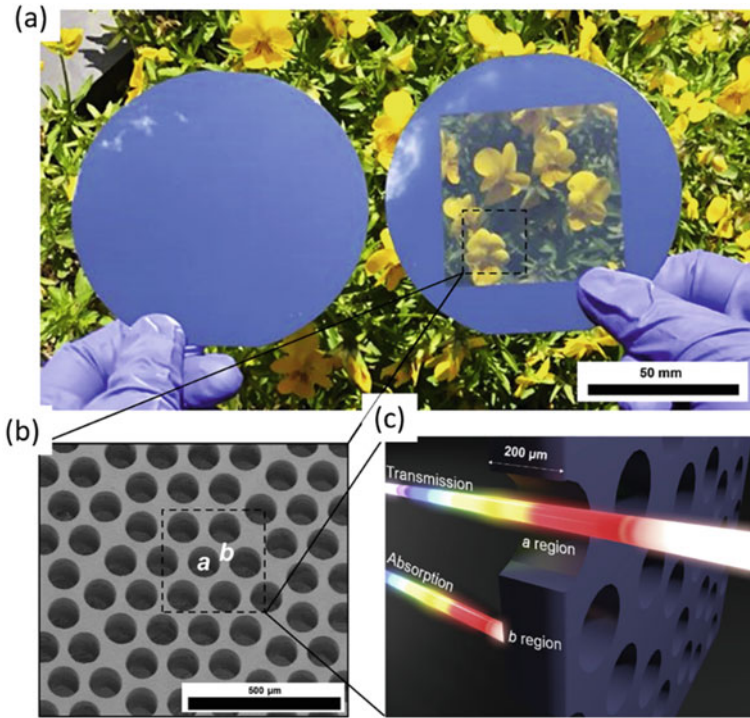
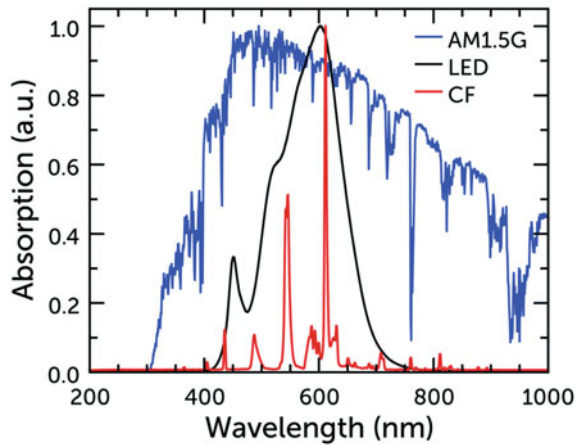


Fig. 31 **a** Photo of conventional and neutral-colour transparent silicon. **b** SEM image of the Si wafer showing “a” light-transmitting and “b” light-absorbing windows. **c** Graphic of the neutral-coloured transparent Si wafer [Reprinted with permission from Lee et al. (2020), copyright (2020), © Elsevier]

Fig. 32 Normalized emission spectra of warm white CF and LED bulbs and the AM1.5G standard spectrum (Reprinted with permission from Michaels et al. (2021), copyright (2021) © Royal Society of Chemistry)



radiation resistance. Space solar cells should generally have high efficiency, high radiation resistance, higher specific power, and long-term stability (Reddy 2003; Yamaguchi 2001). Higher efficiency solar cells allow the solar arrays to be smaller and lighter; as a result, the payload of the satellite is increased while the overall expense of the satellite power system is reduced (Li 2021). In order to screen solar cells from radiations (photons, cosmic and gamma), a protective layer of special glass is used, thereby adding to the weight of the solar array. Therefore, the solar cell must possess high specific power. Si solar cells have a specific power of 1 W/g, while GaInP/GaAs/GaInAs III–V triple-junction solar cells have specific power above 3 W/g. Even though polymer or perovskite solar cells fabricated on flexible, lightweight substrates like polymer sheets or thin foils offer high specific power, the long-term stability and radiation resistance research are in the infancy and need more improvement as the lifetime of the solar arrays determine the life of the satellite too (Tu et al. 2021). Presently, multi-junction (MJ) III–V solar cells with solar concentrators are widely used. They also perform better in elevated temperatures than conventional Si solar cells. Recently, a six junction solar cell using alloys of III–V semiconductors yielding photoconversion efficiency of 47.1% under concentrated illumination was demonstrated (Geisz et al. 2020).

7 Photovoltaics: Industrial Status

As we said initially, the PV markets are expected to be driven by a transition to renewable energy sources due to the rising demand for clean, sustainable, and environmentally friendly energy sources and higher electricity consumption in the coming years. In the next years, new market opportunities will emerge as a result of different government policies and inducements and the demand for renewable energy supplies to minimize environmental impact (Solar PV Panels Market Size Share Report 2020). PV business is rapidly expanding with a figure of USD 87.2 billion in 2020 and is expected to surpass USD 251.4 billion in 2030 at a compound annual growth (CAGR) of 10.1% (nextmsc 2021). Geographically, the PV market is dominated by the Asia–Pacific regions due to expanding urbanization, industrialization, growing populations and rising power needs in nations like China, Thailand and India. With a 35% share of worldwide solar energy generation in 2019, China is anticipated to dominate the PV industry as both manufacturer and a consumer. Based on application, the PV market is broadly segmented as residential, commercial and industrial. Si PVs, both mono and polycrystalline solar cells, are in great demand in the residential segment. Si PV holds 95% of the world PV module market share. The remaining 5% is divided among CdTe, CIGS, and a-Si:H technologies, with low-cost modules and increased efficiency being the key drivers. On the other hand, the comparably low-efficiency thin film panels necessitate extra land requirements, undermining the cost-effectiveness of the pannels.

Figure 33a shows the market shares of various Si solar cell technologies over the year. Out of a range of technologies, Al-BSF solar cell panels have dominated the

Si PV industry in past years, with an average module efficiency of 20%. However, the demand for this mono-facial Al-BSF has waned in recent years. The market is presently highly interested in PERC technology, with an average module efficiency of 21.1%, and its market share increased to 65% in 2019 (Shaw 2021). The bifacial PERC technology is likely to dominate the Si PV industry for the next five years. However, the potential for further increasing the efficiency of PERC solar cells is nearly exhausted, with a theoretical maximum limit of efficiency of about 24.5% (Zhang et al. 2021; Wilson 2020). Figure 33b depicts the further improvement potential of various Si PV technologies. In addition to efficiency, many aspects must be considered when comparing different solar cell technologies. The rate of deterioration, temperature coefficient, the lifetime of modules and LCOE must all be taken into account. When comparing p-type and n-type wafers, the light-induced deterioration is greater in *p*-type wafers. Furthermore, the temperature coefficient of solar cells made using *n*-type wafers is 0.3%/°C, whereas the temperature coefficient of solar cells manufactured using *p*-type wafers is 0.43%/°C, implying that *n*-type based technology delivers a superior yield to *p*-type technology (Wang and Barnett 2019). Consequently, after the *p*-type wafer-based Al-BSF and PERC technologies, the next generation PV module technology will be based on *n*-type Si wafers (Svarc 2021), (Derek 2021), (Future industrial solar PV technologies: Champion cell announcements versus industrial reality 2021). The passivating contact technologies, TOPCon and HIT—IBC solar cells, are now being discussed as next-generation cell technologies to replace PERC with theoretical limits of 28.7% and 27.5%, respectively (Shaw 2021). Recently, n-type TOPCon solar cells achieved efficiencies >25% and race for record efficiencies continues (Stoker 2021; Scully 2021). Some big players in c-Si PV markets are Trina Solar, Sun Power, First Solar, Jinko Solar, Canadian Solar, LONGi Solar, JA Solar, Risen, LG, REC etc.

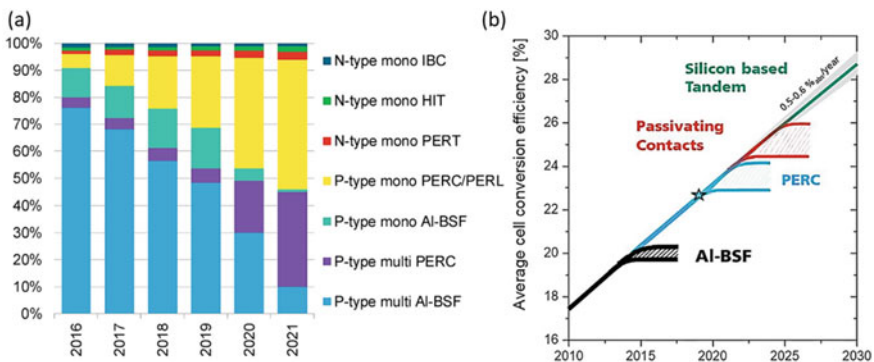


Fig. 33 a Market share of various Si PV technologies over the year (Wang and Barnett 2019). b The potential for various Si-based PV technologies to enhance their efficiency (Reprinted with permission from Hermle et al. (2020), copyright (2020) © AIP)

However, the market expansion is being hampered by issues like low-efficiency modules, land requirements, installation costs, reliability, and energy storage. Nowadays, PV manufacturers give a warranty of 25 years for most of the modules with a degradation rate between 0.5% to 0.8% per year (Jordan and Kurtz 2013). Most solar cell technologies assure a yield of ~80% at the end of the warrantied 25th year. For residential applications, solar cells are deployed mostly on rooftops. However, land requirements for non-residential applications are a concern. High-efficiency bifacial solar cells could solve this challenge to a considerable extent. Solar cells based on tandem technology are projected to hit the market in 2023, with an efficiency greater than 40% (Vos 1980). Some of the tandem architectures under intense investigation are perovskites on c-Si, perovskite on perovskite, group III–V on c-Si, and CIGS on c-Si (Essig et al. 2017), (Leijtens et al. 2018), (Oberbeck et al. 2020). Along with the expansion of the PV sector, the advancement of the energy storage industry is also critical, and the two should work together. Batteries/inverters with a long-life cycle, storage capacity, and less cost are in demand.

Another aspect that has to be addressed soon or later is the end-of-life management of PV modules. PV modules are categorized as e-waste at the end of their life (Farrell et al. 2020; Kumar et al. 2017). Worldwide, PV waste is expected to reach and account for 10% of the total e-waste. PV modules based on Cd and perovskites (especially Pb) pose serious environmental threats unless disposed of properly (Seo et al. 2021). Materials like Ag, Al, Si, copper, and glass in PV modules can be reclaimed and recycled by mechanical, thermal and chemical (Latanussa et al. 2016; Padoan et al. 2019). Proper and preventative measures must be taken to manage and recycle PV wastes in order to prevent hazardous substances from entering the environment. For effective disposal of PV wastes, government laws and regulations for PV waste management, collection, and recycling must be enacted.

8 Summary

We have briefly discussed the various aspects of a solar cell. The stepping stone to achieving high-efficiency solar cells is to minimize the optical and electrical losses in solar cells by using light trapping methods, reducing the contact resistance and recombination losses. High-efficiency solar cells like PERC, TOPCon, SHJ, and POLO solar cells all have in common an excellent light trapping method with reduced recombination at the interface using passivation layers.

Thin films and emerging solar cells have their unique potential and place in the market. Since its introduction, a-Si solar cells have been widely used in many consumer products. Unfortunately, the cost of electricity generation using a-Si solar cells is higher than other thin film-based and c-Si solar cells. As a result, the commercialisation of a-Si solar cells registered a depreciation in recent years. The CIGS technologies have greater potential once the material availability and recombination issues are addressed. DSSC and organic solar cells will continue to be the favourites for indoor applications. QD solar cells are the preferred candidate for

developing multijunction solar cells. The ease of fabrication and material stability make them promising candidates in future. Thin film solar cells will continue to prosper in the coming decades due to increased applications in harsh environments, diffuse light conditions, and high temperatures. Shortly, the primary focus of research will be on developing technologies with high efficiency, decreased manufacturing complexities, and reduced material utilisation. Policies on how to dispose of or reuse solar cell materials after their life should also be thoroughly considered.

References

- Abdulrazzaq OA, Saini V, Bourdo S, Dervishi E, Biris AS (2013) Organic solar cells: a review of materials, limitations, and possibilities for improvement. *Part Sci Technol* 31(5):427–442. <https://doi.org/10.1080/02726351.2013.769470>
- Adachi D, Hernández JL, Yamamoto K (2015) Impact of carrier recombination on fill factor for large area heterojunction crystalline silicon solar cell with 25.1% efficiency. *Appl Phys Lett* 107(23):233506. <https://doi.org/10.1063/1.4937224>
- Allen TG, Bullock J, Yang X, Javey A, de Wolf S (2019) Passivating contacts for crystalline silicon solar cells. *Nat Energy* 4(11):914–928. <https://doi.org/10.1038/s41560-019-0463-6>
- Altermatt PP et al (1996) Rear surface passivation of high-efficiency silicon solar cells by a floating junction. *J Appl Phys* 80(6):3574–3586. <https://doi.org/10.1063/1.363231>
- Appelbaum J (2016) Bifacial photovoltaic panels field. *Renewable Energy* 85:338–343. <https://doi.org/10.1016/j.renene.2015.06.050>
- Arai R, Furukawa S, Hidaka Y, Komiyama H, Yasuda T (2019) High-performance organic energy-harvesting devices and modules for self-sustainable power generation under ambient indoor lighting environments. *ACS Appl Mater Interfaces* 11(9):9259–9264. <https://doi.org/10.1021/acami.9b00018>
- Bai Z, Yang J, Wang D (2011) Thin film CdTe solar cells with an absorber layer thickness in micro- and sub-micrometer scale. *Appl Phys Lett* 99(14):143502. <https://doi.org/10.1063/1.3644160>
- Balaji N, Raval MC, Saravanan S (2020) Review on metallization in crystalline silicon solar cells. *Solar cells*. IntechOpen. <https://doi.org/10.5772/intechopen.84820>
- Baliozian P, Lohmüller E, Fellmeth T, Wöhrle N, Krieg A, Preu R (2018) Bifacial p-type silicon shingle solar cells—the ‘pSPEER’ concept. *Solar RRL* 2(3):1700171. <https://doi.org/10.1002/solr.201700171>
- Bellini E (2019) Bifacial modules ridin’ down the highway. *pv magazine*. Photovoltaics markets and technology
- Brendel R, Peibst R (2016) Contact selectivity and efficiency in crystalline silicon photovoltaics. *IEEE J Photovoltaics* 6(6):1413–1420 7565514 <https://doi.org/10.1109/JPHOTOV.2016.2598267>
- Bhatia S, Khorakiwala IM, Markose KK, Nair PR, Antony A (2019) MoO₃ as hole-selective contact for diffusion-free solar cells, pp 329–333. https://doi.org/10.1007/978-3-319-97604-4_50
- Bhatia S, Khorakiwala IM, Markose KK, Raorane N, Nair PR, Antony A (2020) Optimization of TiO₂ for low-temperature dopant-free crystalline silicon solar cells BT. *Adv Energy Res* 1: 183–189
- Biswas S, Kim H (2020) Solar cells for indoor applications: progress and development. *Polymers* 12(6):1338. <https://doi.org/10.3390/polym12061338>
- Bivour M, Zähringer F, Ndione P, Hermle M (2017) Sputter-deposited WO_x and MoO_x for hole selective contacts. *Energy Procedia* 124:400–405. <https://doi.org/10.1016/j.egypro.2017.09.259>
- Blakers A (2019) Development of the PERC solar cell. *IEEE J PhotovoltS* 9(3):629–635. <https://doi.org/10.1109/JPHOTOV.2019.2899460>

- Blakers AW, Green MA (1986) 20% efficiency silicon solar cells. *Appl Phys Lett* 48(3):215–217. <https://doi.org/10.1063/1.96799>
- Blakers AW, Wang A, Milne AM, Zhao J, Green MA (1989) 22.8% efficient silicon solar cell. *Appl Phys Lett* 55(13):1363–1365. <https://doi.org/10.1063/1.101596>
- Bonasera A, Giuliano G, Arrabito G, Pignataro B (2020) Tackling performance challenges in organic photovoltaics: an overview about compatibilizers. *Molecules* 25(9):1–39. <https://doi.org/10.3390/molecules25092200>
- Bouisset P et al (1992) Quality factor and dose equivalent investigations aboard the Soviet space station MIR. *Adv Space Res* 12(2–3):363–367. [https://doi.org/10.1016/0273-1177\(92\)90130-P](https://doi.org/10.1016/0273-1177(92)90130-P)
- Braun S, Zuschlag A, Raabe B, Hahn G (2011) The origin of background plating. *Energy Procedia* 8:565–570. <https://doi.org/10.1016/j.egypro.2011.06.183>
- Bullock J et al (2018) Stable dopant-free asymmetric heterocontact silicon solar cells with efficiencies above 20%. *ACS Energy Lett* 3(3):508–513. <https://doi.org/10.1021/acsenerylett.7b01279>
- Caprioglio P et al (2019) On the relation between the open-circuit voltage and quasi-Fermi level splitting in efficient perovskite solar cells. *Adv Energy Mater* 9(33):1901631. <https://doi.org/10.1002/aenm.201901631>
- Carlson DE, Wronski CR (1976) Amorphous silicon solar cell. *Appl Phys Lett* 28(11):671–673. <https://doi.org/10.1063/1.88617>
- Chapin DM, Fuller CS, Pearson GL (1954) A new silicon p-n junction photocell for converting solar radiation into electrical power. *J Appl Phys* 25(5):676–677. <https://doi.org/10.1063/1.1721711>
- Chen C-Y et al (2017) Performance characterization of dye-sensitized photovoltaics under indoor lighting. *J Phys Chem Lett* 8(8):1824–1830. <https://doi.org/10.1021/acs.jpcclett.7b00515>
- Cheng YY et al (2016) Increased upconversion performance for thin film solar cells: a trimolecular composition. *Chem Sci* 7(1):559–568. <https://doi.org/10.1039/C5SC03215F>
- Chiang YK, Green MA (1993) Computer simulation of enhanced output from bifacial photovoltaic modules. *Prog Photovoltaics Res Appl* 1(4):293–299. <https://doi.org/10.1002/pip.4670010406>
- Choi JM et al (2019) Modified laser-fired contact process for efficient PERC solar cells. *Prog Photovoltaics Res Appl* 27(12):1092–1103. <https://doi.org/10.1002/pip.3187>
- Chong CM, Wenham SR, Green MA (1988) High-efficiency, laser grooved, buried contact silicon solar cells. *Appl Phys Lett* 52(5):407–409. <https://doi.org/10.1063/1.99453>
- Chopra KL, Paulson PD, Dutta V (2004) Thin-film solar cells: an overview. *Prog Photovoltaics Res Appl* 12(23):69–92. <https://doi.org/10.1002/pip.541>
- de Graaff HC, de Groot JG (1979) The SIS tunnel emitter: a theory for emitters with thin interface layers. *IEEE Trans Electron Devices* 26(11):1771–1776. <https://doi.org/10.1109/T-ED.1979.19684>
- de la Mora MB, Amelines-Sarria O, Monroy BM, Hernández-Pérez CD, Lugo JE (2017) Materials for downconversion in solar cells: Perspectives and challenges. *Sol Energy Mater Sol Cells* 165:59–71. <https://doi.org/10.1016/j.solmat.2017.02.016>
- De Vos A (1980) Detailed balance limit of the efficiency of tandem solar cells. *J Phys D Appl Phys* 13(5):839–846. <https://doi.org/10.1088/0022-3727/13/5/018>
- de Wolf S et al (2012) High-efficiency silicon heterojunction solar cells: a review. *Green* 2(2015):7–24. <https://doi.org/10.1515/green-2011-0039>
- Derek Z (2021) High efficiency n-type cell technology: development and prospects. *InfoLink*. <https://www.infolink-group.com/en/solar/analysis-trends/n-type-high-efficiency-cell-technology-development-and-prospect>
- Detollenaere A, Van Wetter J, Masson G, Kaizuka I, Jäger-Waldau A, Donoso J (2020) Snapshot of global PV markets 2020 PVPS task 1 strategic PV analysis and outreach <https://doi.org/10.13140/RG.2.2.24096.74248>
- Devadiga D, Selvakumar M, Shetty P, Santosh MS (2021) Dye-sensitized solar cell for indoor applications: a mini-review. *J Electron Mater* 50(6):3187–3206. <https://doi.org/10.1007/s11664-021-08854-3>

- Dharmadasa IM et al (2015) Effects of CdCl₂ treatment on deep levels in CdTe and their implications on thin film solar cells: a comprehensive photoluminescence study. *J Mater Sci: Mater Electron* 26(7):4571–4583. <https://doi.org/10.1007/s10854-015-3090-4>
- Ding G, Jin Q, Chen Q, Hu Z, Liu J (2015) The fabrication of ordered bulk heterojunction solar cell by nanoimprinting lithography method using patterned silk fibroin mold at room temperature. *Nanoscale Res Lett* 10(1):491. <https://doi.org/10.1186/s11671-015-1194-7>
- Ding J, Zhou Y, Dong G, Liu M, Yu D, Liu F (2018) Solution-processed ZnO as the efficient passivation and electron selective layer of silicon solar cells. *Prog Photovoltaics Res Appl* 26(12):974–980. <https://doi.org/10.1002/pip.3044>
- Ekwurzel B et al (2017) The rise in global atmospheric CO₂, surface temperature, and sea level from emissions traced to major carbon producers. *Clim Change* 144(4):579–590. <https://doi.org/10.1007/s10584-017-1978-0>
- Enebish N, Agchbayar D, Dorjkhand S, Baatar D, Ylemj I (1993) Numerical analysis of solar cell current-voltage characteristics. *Sol Energy Mater Sol Cells* 29(3):201–208. [https://doi.org/10.1016/0927-0248\(93\)90035-2](https://doi.org/10.1016/0927-0248(93)90035-2)
- Enerdata (2020) Global energy statistical year book. Enerdata. <https://yearbook.enerdata.net/renewables/wind-solar-share-electricity-production.html>
- Esaki L (1958) New phenomenon in narrow germanium p–n junctions. *Phys Rev* 109(2):603–604. <https://doi.org/10.1103/PhysRev.109.603>
- Essig S et al (2017) Raising the one-sun conversion efficiency of III–V/Si solar cells to 32.8% for two junctions and 35.9% for three junctions. *Nat Energy* 2(9):17144. <https://doi.org/10.1038/nenergy.2017.144>
- Farrell CC et al (2020) Technical challenges and opportunities in realising a circular economy for waste photovoltaic modules. *Renew Sustain Energy Rev* 128:109911. <https://doi.org/10.1016/j.rser.2020.109911>
- Feldmann F, Bivour M, Reichel C, Steinkemper H, Hermle M, Glunz SW (2014) Tunnel oxide passivated contacts as an alternative to partial rear contacts. *Sol Energy Mater Sol Cells* 131:46–50. <https://doi.org/10.1016/j.solmat.2014.06.015>
- Feldmann F et al (2018) A study on the charge carrier transport of passivating contacts. *IEEE J PhotovoltS* 8(6):1503–1509. <https://doi.org/10.1109/JPHOTOV.2018.2870735>
- Fellmeth T et al (2018) Industry related approaches for bifacial p-type PERC solar cells. *Jpn J Appl Phys* 57(8S3):08RB18. <https://doi.org/10.7567/JJAP.57.08RB18>
- Fertig F et al (2016a) Bifacial potential of single- and double-sided collecting silicon solar cells. *Prog Photovoltaics Res Appl* 24(6):818–829. <https://doi.org/10.1002/pip.2732>
- Fertig F et al (2016b) Economic feasibility of bifacial silicon solar cells. *Prog Photovoltaics Res Appl* 24(6):800–817. <https://doi.org/10.1002/pip.2730>
- Fischer S et al (2018) Upconversion solar cell measurements under real sunlight. *Opt Mater* 84:389–395. <https://doi.org/10.1016/j.optmat.2018.05.072>
- Fraunhofer ISE (2020) Fraunhofer ISE annual report 2019/2020
- Future industrial solar PV technologies: champion cell announcements versus industrial reality. *PV Tech*. <https://www.pv-tech.org/future-industrial-solar-pv-technologies-champion-cell-announcements-versus-industrial-reality/> (accessed Oct. 23, 2021)
- Gan JY, Swanson RM (1990) Polysilicon emitters for silicon concentrator solar cells. In: 21st IEEE photovoltaic specialists conference 1:245–250
- Gao P et al (2018) Dopant-free and carrier-selective heterocontacts for silicon solar cells: recent advances and perspectives. *Adv Sci* 5(3):1700547. <https://doi.org/10.1002/advs.201700547>
- Geissbühler J et al (2015) 22.5% efficient silicon heterojunction solar cell with molybdenum oxide hole collector. *Appl Phys Lett* 107(8):081601. <https://doi.org/10.1063/1.4928747>
- Geisz JF et al (2020) Six-junction III–V solar cells with 47.1% conversion efficiency under 143 Suns concentration. *Nat Energy* 5(4):326–335. <https://doi.org/10.1038/s41560-020-0598-5>

- Ghannam M, Shehadah G, Abdurraheem Y, Poortmans J (2015) On the possible role of the interfacial inversion layer in the improvement of the performance of hydrogenated amorphous silicon/crystalline silicon heterojunction solar cells [HIT]. *Sol Energy Mater Sol Cells* 132:320–328. <https://doi.org/10.1016/j.solmat.2014.09.008>
- Ghosh K, Tracy C, Goodnick S, Bowden S (2012) Effect of band bending and band offset in the transport of minority carriers across the ordered/disordered interface of a-Si/c-Si heterojunction solar cell. In: 2012 38th IEEE photovoltaic specialists conference, pp 000221–000226. <https://doi.org/10.1109/PVSC.2012.6317605>
- Global Direct Primary Energy Consumption (2020) Our world in data. <https://ourworldindata.org/grapher/global-primary-energy?time=2000..2019>
- Global Energy Review 2020 (2020) Global energy review 2020. <https://doi.org/10.1787/a60abbf2-en>
- Glunz SW, Preu R, Biro D (2012) Crystalline silicon solar cells. In: Comprehensive renewable energy. Elsevier, pp 353–387. <https://doi.org/10.1016/B978-0-08-087872-0.00117-7>
- Glunz SW et al (2015) The irresistible charm of a simple current flow pattern—25% with a solar cell featuring a full-area back contact. In: Proceedings of the 31st European photovoltaic solar energy conference and exhibition, pp 259–263. <https://doi.org/10.4229/EUPVSEC20152015-2BP.1.1>
- Green MA (2015) The passivated emitter and rear cell (PERC): from conception to mass production. *Sol Energy Mater Sol Cells* 143:190–197. <https://doi.org/10.1016/j.solmat.2015.06.055>
- Gu W, Ma T, Ahmed S, Zhang Y, Peng J (2020) A comprehensive review and outlook of bifacial photovoltaic (bPV) technology. *Energy Convers Manag* 223: 113283. <https://doi.org/10.1016/j.enconman.2020.113283>
- Guo LJ (2007) Nanoimprint lithography: methods and material requirements. *Adv Mater* 19(4):495–513. <https://doi.org/10.1002/adma.200600882>
- Gupta DK, Langelaar M, Barink M, van Keulen F (2016) Optimizing front metallization patterns: efficiency with aesthetics in free-form solar cells. *Renewable Energy* 86:1332–1339. <https://doi.org/10.1016/j.renene.2015.09.071>
- Haase F et al (2018) Laser contact openings for local poly-Si-metal contacts enabling 26.1%-efficient POLO-IBC solar cells. *Sol Energy Mater Sol Cells* 186(March):184–193. <https://doi.org/10.1016/j.solmat.2018.06.020>
- He X et al (2011) Formation of well-ordered heterojunctions in polymer:PCBM photovoltaic devices. *Adv Func Mater* 21(1):139–146. <https://doi.org/10.1002/adfm.201000573>
- He X et al (2021) 40.1% record low-light solar-cell efficiency by holistic trap-passivation using micrometer-thick perovskite film. *Adv Mater* 33(27):2100770. <https://doi.org/10.1002/adma.202100770>
- Heinrich M et al (2020) A comparison of different solar cell technologies for integrated. In: 37th European photovoltaic solar energy conference (EUPVSEC), pp 7–11
- Herasimenka SY, Dauksher WJ, Bowden SG (2013) >750 mV open circuit voltage measured on 50 μm thick silicon heterojunction solar cell. *Appl Phys Lett* 103(5):053511. <https://doi.org/10.1063/1.4817723>
- Hermle M, Feldmann F, Bivour M, Goldschmidt JC, Glunz SW (2020) Passivating contacts and tandem concepts: approaches for the highest silicon-based solar cell efficiencies. *Appl Phys Rev* 7(2):021305. <https://doi.org/10.1063/1.5139202>
- Hiroshi M (1966) Radiation energy transducing device. US Patent 3278811A
- Hollemann C et al (2020) Separating the two polarities of the POLO contacts of an 26.1%-efficient IBC solar cell. *Sci Rep* 10(1):658. <https://doi.org/10.1038/s41598-019-57310-0>
- Horbelt R, Ebert S, Ulbikaite V, Hahn G, Job R, Terheiden B (2016) Al-density variation as one driving force for void formation in PERC solar cells. *Phys. Status Solidi (RRL)—Rapid Res Lett* 10(7):515–519. <https://doi.org/10.1002/pssr.201600078>
- Hovinen A (1994) Fitting of the solar cell IV—curve to the two diode model. *Phys Scr T54*:175–176. <https://doi.org/10.1088/0031-8949/1994/T54/043>

- Hu J, Shirai Y, Han L, Wakayama Y (2012) Template method for fabricating interdigitate p-n heterojunction for organic solar cell. *Nanoscale Res Lett* 7(1):469. <https://doi.org/10.1186/1556-276X-7-469>
- Humada AM, Hojabri M, Mekhilef S, Hamada HM (2016) Solar cell parameters extraction based on single and double-diode models: a review. *Renew Sustain Energy Rev* 56:494–509. <https://doi.org/10.1016/j.rser.2015.11.051>
- IEA (2019) World energy outlook 2019. <https://www.iea.org/reports/world-energy-outlook-2019>
- IEA (2020) Renewables 2020, IEA, Paris. <https://www.iea.org/reports/renewables-2020>
- India energy outlook 2021 (2021) OECD. <https://doi.org/10.1787/ec2fd78d-en>
- Ingenito A et al (2018) A passivating contact for silicon solar cells formed during a single firing thermal annealing. *Nat Energy* 3(9):800–808. <https://doi.org/10.1038/s41560-018-0239-4>
- Inoue H et al (2009) Improving the conversion efficiency and decreasing the thickness of the HIT solar cell. *MRS Proceedings* 1210:1210-Q07–01. <https://doi.org/10.1557/PROC-1210-Q07-01>
- Islam R, Ramesh P, Hyung Nam J, Saraswat KC (2015) Nickel oxide carrier selective contacts for silicon solar cells. In: 2015 IEEE 42nd photovoltaic specialist conference (PVSC), pp 1–4. <https://doi.org/10.1109/PVSC.2015.7355921>
- Jahandar M, Kim S, Lim DC (2021) Indoor organic photovoltaics for self-sustaining IoT devices: progress, challenges and practicalization. *Chemsuschem* 14(17):3449–3474. <https://doi.org/10.1002/cssc.202100981>
- Jia J, Dong J, Lin J, Lan Z, Fan L, Wu J (2019) Improved photovoltaic performance of perovskite solar cells by utilizing down-conversion NaYF₄: Eu³⁺ nanophosphors. *J Mater Chem C* 7(4):937–942. <https://doi.org/10.1039/C8TC05864D>
- Jordan DC, Kurtz SR (2013) Photovoltaic degradation rates—an analytical review. *Prog Photovoltaics Res Appl* 21(1):12–29. <https://doi.org/10.1002/pip.1182>
- Jordan D, Nagle JP (1994) New generation of high-efficiency solar cells: development, processing and marketing. *Prog Photovoltaics Res Appl* 2(2):171–176. <https://doi.org/10.1002/pip.4670020212>
- Kafle B, Goraya BS, Mack S, Feldmann F, Nold S, Rentsch J (2021) TOPCon—technology options for cost efficient industrial manufacturing. *Sol Energy Mater Sol Cells* 227:111100. <https://doi.org/10.1016/j.solmat.2021.111100>
- Kakiage K, Aoyama Y, Yano T, Oya K, Fujisawa J, Hanaya M (2015) Highly-efficient dye-sensitized solar cells with collaborative sensitization by silyl-anchor and carboxy-anchor dyes. *Chem Commun* 51(88):15894–15897. <https://doi.org/10.1039/C5CC06759F>
- Khan MR, Hanna A, Sun X, Alam MA (2017) Vertical bifacial solar farms: physics, design, and global optimization. *Appl Energy* 206:240–248. <https://doi.org/10.1016/j.apenergy.2017.08.042>
- Kirner S, Mazzarella L, Korte L, Stannowski B, Rech B, Schlattmann R (2015) Silicon heterojunction solar cells with nanocrystalline silicon oxide emitter: insights into charge carrier transport. *IEEE J Photovolt* 5(6):1601–1605. <https://doi.org/10.1109/JPHOTOV.2015.2479461>
- Kobayashi E et al (2016) Light-induced performance increase of silicon heterojunction solar cells. *Appl Phys Lett* 109(15):153503. <https://doi.org/10.1063/1.4964835>
- Kumar A, Mondal S, Soman A, Antony A (2014) Laser fired ohmic contacts in silicon using pulse modulated CW laser. In: 2014 IEEE 2nd international conference on emerging electronics (ICEE), pp 1–4. <https://doi.org/10.1109/ICEmElec.2014.7151214>
- Kumar A, Holuszko M, Espinosa DCR (2017) E-waste: an overview on generation, collection, legislation and recycling practices. *Resour Conserv Recycl* 122:32–42. <https://doi.org/10.1016/j.resconrec.2017.01.018>
- Kumar A, Markose KK, Khorakiwala IM, Singha B, Nair PR, Antony A (2019) Studies on the PEDOT:PSS/n-Si hybrid heterojunction diode, pp 423–427. https://doi.org/10.1007/978-3-319-97604-4_65
- Kurias KM, Jasna M, Menon MRR, Antony A, Jayaraj MK (2019) Fabrication of CNT-PEDOT:PSS/Si heterojunction carrier selective solar cell. *AIP Conf Proc* 2082(1):050008. <https://doi.org/10.1063/1.5093868>

- Lamb WF et al (2021) A review of trends and drivers of greenhouse gas emissions by sector from 1990 to 2018. *Environ Res Lett* 16(7):73005. <https://doi.org/10.1088/1748-9326/abee4e>
- Latanussa CEL, Ardenne F, Blengini GA, Mancini L (2016) Life cycle assessment of an innovative recycling process for crystalline silicon photovoltaic panels. *Sol Energy Mater Sol Cells* 156:101–111. <https://doi.org/10.1016/j.solmat.2016.03.020>
- Lee TD, Ebong AU (2017) A review of thin film solar cell technologies and challenges. *Renew Sustain Energy Rev* 70:1286–1297. <https://doi.org/10.1016/j.rser.2016.12.028>
- Lee C, Lee S, Kim G-U, Lee W, Kim BJ (2019) Recent advances, design guidelines, and prospects of all-polymer solar cells. *Chem Rev* 119(13):8028–8086. <https://doi.org/10.1021/acs.chemrev.9b00044>
- Lee SH, Lee DW, Lim K, Shin W, Kim J (2019) Copper–nickel alloy plating to improve the contact resistivity of metal grid on silicon heterojunction solar cells. *Electron Mater Lett* 15(3):314–322. <https://doi.org/10.1007/s13391-019-00134-x>
- Lee K et al (2020) Neutral-colored transparent crystalline silicon photovoltaics. *Joule* 4(1):235–246. <https://doi.org/10.1016/j.joule.2019.11.008>
- Leijtens T, Bush KA, Prasanna R, McGehee MD (2018) Opportunities and challenges for tandem solar cells using metal halide perovskite semiconductors. *Nat Energy* 3(10):828–838. <https://doi.org/10.1038/s41560-018-0190-4>
- Li J et al (2021) A brief review of high efficiency III-V solar cells for space application. *Front Phys* 8. <https://doi.org/10.3389/fphy.2020.631925>
- Lim KB, Sek SK (2017) Examining the impacts of oil price changes on economic indicators: a panel approach, p 080016. <https://doi.org/10.1063/1.4981000>
- Liu J, Yao Y, Xiao S, Gu X (2018) Review of status developments of high-efficiency crystalline silicon solar cells. *J Phys D: Appl Phys* 51(12). <https://doi.org/10.1088/1361-6463/aaac6d>
- Markose KK, Anjana R, Subha PP, Antony A, Jayaraj MK (2016) Enhancement of a-Si:H solar cell efficiency by $Y_2O_3 : Yb^{3+}, Er^{3+}$ near infrared spectral upconverter. *Proc. SPIE* 9937:99370X-99370X–10. <https://doi.org/10.1117/12.2237549>
- Markose KK, Anjana R, Antony A, Jayaraj MK (2018) Synthesis of Yb^{3+}/Er^{3+} co-doped Y_2O_3 , YOF and YF_3 UC phosphors and their application in solar cell for sub-bandgap photon harvesting. *J Lumin* 204:448–456. <https://doi.org/10.1016/j.jlumin.2018.08.005>
- Markose KK, Anjana R, Jayaraj MK (2020a) Upconversion nanophosphors: an overview, pp 47–102. https://doi.org/10.1007/978-981-15-3314-3_2
- Markose KK et al (2020) Novel boron-doped p-type Cu_2O thin films as a hole-selective contact in c-Si solar cells. *ACS Appl Mater Interfaces* 12(11):12972–12981. <https://doi.org/10.1021/acsami.9b22581>
- Markose KK, Jasna M, Subha PP, Antony A, Jayaraj MK (2020) Performance enhancement of organic/Si solar cell using CNT embedded hole selective layer. *Sol Energy* 211:158–166. <https://doi.org/10.1016/j.solener.2020.09.024>
- Mayer AC, Scully SR, Hardin BE, Rowell MW, McGehee MD (2007) Polymer-based solar cells. *Mater Today* 10(11):28–33. [https://doi.org/10.1016/S1369-7021\(07\)70276-6](https://doi.org/10.1016/S1369-7021(07)70276-6)
- Mazzarella L, Kirner S, Stannowski B, Korte L, Rech B, Schlattmann R (2015) p-type microcrystalline silicon oxide emitter for silicon heterojunction solar cells allowing current densities above 40 mA/cm². *Appl Phys Lett* 106(2):023902. <https://doi.org/10.1063/1.4905906>
- Mazzarella L, Kirner S, Stannowski B, Korte L, Rech B, Schlattmann R (2015) P-type microcrystalline silicon oxide emitter for silicon heterojunction solar cells allowing current densities above 40 mA/cm². *Appl Phys Lett* 106:2. <https://doi.org/10.1063/1.4905906>
- Meemongkolkiat V et al. (2006) Investigation of modified screen-printing Al pastes for local back surface field formation. In: 2006 IEEE 4th world conference on photovoltaic energy conference, pp 1338–1341. <https://doi.org/10.1109/WCPEC.2006.279678>
- Melskens J, Van De Loo BWH, Macco B, Black LE, Smit S, Kessels WMM (2018) Passivating contacts for crystalline silicon solar cells: from concepts and materials to prospects. *IEEE J Photovolt* 8(2):373–388. <https://doi.org/10.1109/JPHOTOV.2018.2797106>

- Michaels H, Benesperi I, Freitag M (2021) Challenges and prospects of ambient hybrid solar cell applications. *Chem Sci* 12(14):5002–5015. <https://doi.org/10.1039/D0SC06477G>
- Mikolášek M (2017) Silicon heterojunction solar cells: the key role of heterointerfaces and their impact on the performance. In: Nanostructured solar cells. InTech, Rijeka, p 4. <https://doi.org/10.5772/65020>
- Miller RG, Sorrell SR (2014) The future of oil supply. *Philos Trans R Soc A: Math, Phys Eng Sci* 372(2006):20130179. <https://doi.org/10.1098/rsta.2013.0179>
- Mitra S, Ghosh H, Saha H, Ghosh K (2019) Recombination analysis of tunnel oxide passivated contact solar cells. *IEEE Trans Electron Devices* 66(3):1368–1376. <https://doi.org/10.1109/TED.2018.2890584>
- Moldovan A, Feldmann F, Zimmer M, Rentsch J, Benick J, Hermle M (2015) Tunnel oxide passivated carrier-selective contacts based on ultra-thin SiO₂ layers. *Sol Energy Mater Sol Cells* 142:123–127. <https://doi.org/10.1016/j.solmat.2015.06.048>
- Montzka SA, Dlugokencky EJ, Butler JH (2011) Non-CO₂ greenhouse gases and climate change. *Nature* 476(7358):43–50. <https://doi.org/10.1038/nature10322>
- Nakamura J, Asano N, Hieda T, Okamoto C, Katayama H, Nakamura K (2014) Development of heterojunction back contact Si solar cells. *IEEE J PhotovoltS* 4(6):1491–1495. <https://doi.org/10.1109/JPHOTOV.2014.2358377>
- Nayak M, Mandal S, Pandey A, Mudgal S, Singh S, Komarala VK (2019) Nickel oxide hole-selective heterocontact for silicon solar cells: role of SiO_x interlayer on device performance. *Solar RRL* 3(11):1900261. <https://doi.org/10.1002/solr.201900261>
- nextmsc (2021) Photovoltaic market by technology (thin film, mono Si and multi Si), system (high concentration photovoltaic (HCPV) and low concentration photovoltaic (LCPV)), and application (industrial, residential and commercial): global opportunity analysis and indus
- Nicolai M, Zanuccoli M, Feldmann F, Hermle M, Fiegna C (2018) Analysis of silicon solar cells with poly-Si/SiO_x carrier-selective base and emitter contacts. *IEEE J PhotovoltS* 8(1):103–109. <https://doi.org/10.1109/JPHOTOV.2017.2775142>
- NREL (2020) Best research-cell efficiency chart. U.S. Department of Energy. <https://www.nrel.gov/pv/cell-efficiency.html>
- O'Regan B, Grätzel M (1991) A low-cost, high-efficiency solar cell based on dye-sensitized colloidal TiO₂ films. *Nature* 353(6346):737–740. <https://doi.org/10.1038/353737a0>
- Oberbeck L, Alvino K, Goraya B, Jubault M (2020) IPVF's PV technology vision for 2030. *Prog Photovoltaics Res Appl* 28(11):1207–1214. <https://doi.org/10.1002/pip.3305>
- Ohl RS (1941) Light-sensitive electric device, US Patent, 2:402, 602
- Olejarnik P, IEA—International Energy Agency (2009) World energy outlook 2009, p 20
- Olibet S, Vallat-Sauvain E, Ballif C (2007) Model for a-Si:H/c-Si interface recombination based on the amphoteric nature of silicon dangling bonds. *Phys Rev B* 76(3):035326. <https://doi.org/10.1103/PhysRevB.76.035326>
- Padi SP, Khokhar MQ, Chowdhury S, Cho E-C, Yi J (2021) Nanoscale SiO_x tunnel oxide deposition techniques and their influence on cell parameters of TOPCon solar cells. *Trans Electr Electron Mater* 22(5):557–566. <https://doi.org/10.1007/s42341-021-00356-7>
- Padoan FCMS, Altamari P, Pagnanelli F (2019) Recycling of end of life photovoltaic panels: a chemical prospective on process development. *Sol Energy* 177:746–761. <https://doi.org/10.1016/j.solener.2018.12.003>
- Patel MT, Khan MR, Sun X, Alam MA (2019) A worldwide cost-based design and optimization of tilted bifacial solar farms. *Appl Energy* 247:467–479. <https://doi.org/10.1016/j.apenergy.2019.03.150>
- Peibst R et al (2014) A simple model describing the symmetric I–V characteristics of p polycrystalline Si/n monocrystalline Si, and n polycrystalline Si/p monocrystalline Si junctions. *IEEE J PhotovoltS* 4(3):841–850. <https://doi.org/10.1109/JPHOTOV.2014.2310740>
- Powalla M et al (2013) High-efficiency Cu(In, Ga)Se₂ cells and modules. *Sol Energy Mater Sol Cells* 119:51–58. <https://doi.org/10.1016/j.solmat.2013.05.002>

- Qi B, Wang J (2012) Open-circuit voltage in organic solar cells. *J Mater Chem* 22(46):24315. <https://doi.org/10.1039/c2jm33719c>
- Rauer M et al (2011) Investigation of aluminum-alloyed local contacts for rear surface-passivated silicon solar cells. *IEEE J PhotovoltS* 1(1):22–28. <https://doi.org/10.1109/JPHOTOV.2011.2161864>
- Raval MC, Madugula Reddy S (2020) Industrial silicon solar cells. In: *Solar cells*. IntechOpen. <https://doi.org/10.5772/intechopen.84817>
- Raval MC, Solanki CS (2013) Review of Ni-Cu based front side metallization for c-Si solar cells. *J Solar Energy* 2013:1–20. <https://doi.org/10.1155/2013/183812>
- Reddy MR (2003) Space solar cells—tradeoff analysis. *Sol Energy Mater Sol Cells* 77(2):175–208. [https://doi.org/10.1016/S0927-0248\(02\)00320-3](https://doi.org/10.1016/S0927-0248(02)00320-3)
- Rehman A, Lee S (2014) Review of the potential of the Ni/Cu plating technique for crystalline silicon solar cells. *Materials* 7(2):1318–1341. <https://doi.org/10.3390/ma7021318>
- Reiter S et al (2016) Parasitic absorption in polycrystalline Si-layers for carrier-selective front junctions. *Energy Procedia* 92:199–204. <https://doi.org/10.1016/j.egypro.2016.07.057>
- Richter A, Hermle M, Glunz SW (2013) Reassessment of the limiting efficiency for crystalline silicon solar cells. *IEEE J PhotovoltS* 3(4):1184–1191. <https://doi.org/10.1109/JPHOTOV.2013.2270351>
- Richter A, Benick J, Feldmann F, Fell A, Hermle M, Glunz SW (2017) n-Type Si solar cells with passivating electron contact: Identifying sources for efficiency limitations by wafer thickness and resistivity variation. *Sol Energy Mater Sol Cells* 173:96–105. <https://doi.org/10.1016/j.solmat.2017.05.042>
- Richter A et al (2021) Design rules for high-efficiency both-sides-contacted silicon solar cells with balanced charge carrier transport and recombination losses. *Nat Energy* 6(4):429–438. <https://doi.org/10.1038/s41560-021-00805-w>
- Rienäcker M et al (2016) Recombination behavior of photolithography-free back junction back contact solar cells with carrier-selective polysilicon on oxide junctions for both polarities. *Energy Procedia* 92:412–418. <https://doi.org/10.1016/j.egypro.2016.07.121>
- Rienacker M et al (2017) Junction resistivity of carrier-selective polysilicon on oxide junctions and its impact on solar cell performance. *IEEE J PhotovoltS* 7(1):11–18. <https://doi.org/10.1109/JPHOTOV.2016.2614123>
- Ritchie H (2017) How long before we run out of fossil fuels? *Our World in Data*. <https://ourworldindata.org/>
- Romeo A, Artegiani E (2021) CdTe-based thin film solar cells: past, present and future. *Energies* 14(6):1684. <https://doi.org/10.3390/en14061684>
- Romer U et al (2015) Ion implantation for poly-Si passivated back-junction back-contacted solar cells. *IEEE J PhotovoltS* 5(2):507–514. <https://doi.org/10.1109/JPHOTOV.2014.2382975>
- Rudmann D et al (2004) Efficiency enhancement of Cu(In, Ga)Se₂ solar cells due to post-deposition Na incorporation. *Appl Phys Lett* 84(7):1129–1131. <https://doi.org/10.1063/1.1646758>
- Sahoo, SK, Manoharan B Sivakumar N (2018) Introduction. In *Perovskite photovoltaics*. Elsevier, pp 1–24. <https://doi.org/10.1016/B978-0-12-812915-9.00001-0>
- Saitoh T, Uematsu T, Matsukuma K, Kida Y, Morita K (1987) Design and fabrication of 20%_percent-efficiency, medium-resistivity silicon solar cells. In: *19th IEEE photovoltaic specialists conference*, p 1518
- Schneiderlöchner E, Preu R, Lüdemann R, Glunz SW (2002) Laser-fired rear contacts for crystalline silicon solar cells. *Prog Photovoltaics Res Appl* 10(1):29–34. <https://doi.org/10.1002/ppp.422>
- Scully J (2021) LONGi solar pushes n-type TOPCon cell to record 25.09% conversion efficiency. *pv tech*
- Sek SK, Teo XQ, Wong YN (2015) A comparative study on the effects of oil price changes on inflation. *Procedia Econ Financ* 26:630–636. [https://doi.org/10.1016/S2212-5671\(15\)00800-X](https://doi.org/10.1016/S2212-5671(15)00800-X)
- Seo B, Kim JY, Chung J (2021) Overview of global status and challenges for end-of-life crystalline silicon photovoltaic panels: a focus on environmental impacts. *Waste Manage* 128:45–54. <https://doi.org/10.1016/j.wasman.2021.04.045>

- SHAW V (2021) The weekend read: life after PERC. *PV Magazine*
- Smith DD, Reich G, Baldrias M, Reich M, Boitnott N, Bunea G (2016) Silicon solar cells with total area efficiency above 25 %. In: 2016 IEEE 43rd photovoltaic specialists conference (PVSC), pp 3351–3355. <https://doi.org/10.1109/PVSC.2016.7750287>
- Solar PV panels market size & share report, 2020–2027 (2020) Grand View Research, p 120
- Soman A, Antony A (2019) Colored solar cells with spectrally selective photonic crystal reflectors for application in building integrated photovoltaics. *Sol Energy* 181:1–8. <https://doi.org/10.1016/j.solener.2019.01.058>
- Soman A, Antony A (2021) A critical study on different hydrogen plasma treatment methods of a-Si: H/c-Si interface for enhanced defect passivation. *Appl Surf Sci* 553:149551. <https://doi.org/10.1016/j.apsusc.2021.149551>
- Song T, Kanevce A, Sites JR (2016) Emitter/absorber interface of CdTe solar cells. *J Appl Phys* 119(23):233104. <https://doi.org/10.1063/1.4953820>
- Spear WE, Le Comber PG (1975) Substitutional doping of amorphous silicon. *Solid State Commun* 17(9):1193–1196. [https://doi.org/10.1016/0038-1098\(75\)90284-7](https://doi.org/10.1016/0038-1098(75)90284-7)
- Statistical Review of World Energy 2016 (2016) BP. <https://www.bp.com/en/global/corporate/energy-economics/statistical-review-of-world-energy/downloads.html>
- Steinkemper H, Feldmann F, Bivour M, Hermle M (2015) Numerical simulation of carrier-selective electron contacts featuring tunnel oxides. *IEEE J Photovolt S* 5(5):1348–1356. <https://doi.org/10.1109/JPHOTOV.2015.2455346>
- Sterling HF, Swann RCG (1965) Chemical vapour deposition promoted by r.f. discharge. *Solid-State Electron* 8(8):653–654. [https://doi.org/10.1016/0038-1101\(65\)90033-X](https://doi.org/10.1016/0038-1101(65)90033-X)
- Stevens P (2020) Energy demand, hit by coronavirus crisis, is set to see record drop this year, IEA says. CNBC
- Stoker L (2021) N-type cell efficiency race continues as JinkoSolar sets new record of 25.25%. *pv tech*
- Svarc J (2021) Most efficient solar panels 2021 —clean energy reviews. *Clean Energy Rev.* <https://www.cleanenergyreviews.info/blog/most-efficient-solar-panels>
- Swanson RM (1986) Point-contact solar cells: modeling and experiment. *Solar Cells* 17(1):85–118. [https://doi.org/10.1016/0379-6787\(86\)90061-X](https://doi.org/10.1016/0379-6787(86)90061-X)
- Swanson RM (1986) Point contact silicon solar cells, Proc. SPIE 0706, Photovoltaics for commercial solar power applications. <https://doi.org/10.1117/12.937229>
- Teran AS et al (2016) Energy harvesting for GaAs photovoltaics under low-flux indoor lighting conditions. *IEEE Trans Electron Devices* 63(7):2820–2825. <https://doi.org/10.1109/TED.2016.2569079>
- The Paris Agreement (2015). <https://unfccc.int/process-and-meetings/the-paris-agreement/the-paris-agreement> (accessed Feb 10, 2022)
- Thirsk R, Kuipers A, Mukai C, Williams D (2009) The space-flight environment: the International Space Station and beyond. *Can Med Assoc J* 180(12):1216–1220. <https://doi.org/10.1503/cmaj.081125>
- Tomasi A et al (2017) Simple processing of back-contacted silicon heterojunction solar cells using selective-area crystalline growth. *Nat Energy* 2(5):17062. <https://doi.org/10.1038/nenergy.2017.62>
- Tous L et al. (2012) Large area copper plated silicon solar cell exceeding 19.5% efficiency. *Energy Procedia* 21(2011):58–65. <https://doi.org/10.1016/j.egypro.2012.05.008>
- Tu Y et al (2021) Perovskite solar cells for space applications: progress and challenges. *Adv Mater* 33(21):2006545. <https://doi.org/10.1002/adma.202006545>
- ur Rehman A, Lee SH, Bhopal MF, Lee SH (2016) Ni/Cu/Ag plated contacts: a study of resistivity and contact adhesion for crystalline-Si solar cells. *Electron Mater Lett* 12(4):439–444. <https://doi.org/10.1007/s13391-016-4003-2>
- Urrejola E, Peter K, Plagwitz H, Schubert G (2011) Silicon diffusion in aluminum for rear passivated solar cells. *Appl Phys Lett* 98(15):153508. <https://doi.org/10.1063/1.3579541>

- Urrejola E, Peter K, Plagwitz H, Schubert G (2011) Effect of gravity on the microstructure of Al-Si alloy for rear-passivated solar cells. *J Appl Phys* 110(5):056104. <https://doi.org/10.1063/1.3633510>
- Vallati A, de L Vollaro R, Tallini A, Cedola L (2015) Photovoltaics noise barrier: acoustic and energetic study. *Energy Procedia* 82:716–723. <https://doi.org/10.1016/j.egypro.2015.11.797>
- Van Aken BB, Carr AJ (2014) Relating indoor and outdoor performance of bifacial modules. In: 2014 IEEE 40th Photovoltaic Specialist Conference (PVSC), pp 1381–1383. <https://doi.org/10.1109/PVSC.2014.6925175>
- Van Aken BB et al (2017) Bifacial aspects of industrial n-Pasha solar cells. *Jpn J Appl Phys* 56(8S2):08MB03. <https://doi.org/10.7567/JJAP.56.08MB03>
- van Cleef MWM et al (1998) Photocarrier collection in a-SiC:H/c-Si heterojunction solar cells. *J Non-Cryst Solids* 227–230:1291–1294. [https://doi.org/10.1016/S0022-3093\(98\)00210-5](https://doi.org/10.1016/S0022-3093(98)00210-5)
- Vivar M, Morilla C, Antón I, Fernández JM, Sala G (2010) Laser grooved buried contact cells optimised for linear concentration systems. *Sol Energy Mater Sol Cells* 94(2):187–193. <https://doi.org/10.1016/j.solmat.2009.08.022>
- von Schneidemesser E et al (2015) Chemistry and the linkages between air quality and climate change. *Chem Rev* 115(10):3856–3897. <https://doi.org/10.1021/acs.chemrev.5b00089>
- Wan Y et al (2016) Magnesium fluoride electron-selective contacts for crystalline silicon solar cells. *ACS Appl Mater Interfaces* 8(23):14671–14677. <https://doi.org/10.1021/acsami.6b03599>
- Wang X, Barnett A (2019) The evolving value of photovoltaic module efficiency. *Appl Sci* 9(6):1227. <https://doi.org/10.3390/app9061227>
- Wenham SR, Green MA (1996) Silicon solar cells. *Prog Photovoltaics Res Appl* 4(1):3–33. [https://doi.org/10.1002/\(SICI\)1099-159X\(199601/02\)4:1%3C3::AID-PIP117%3E3.0.CO;2-S](https://doi.org/10.1002/(SICI)1099-159X(199601/02)4:1%3C3::AID-PIP117%3E3.0.CO;2-S)
- Wenham SR, Honsberg CB, Green MA (1994) Buried contact silicon solar cells. *Sol Energy Mater Sol Cells* 34(1–4):101–110. [https://doi.org/10.1016/0927-0248\(94\)90029-9](https://doi.org/10.1016/0927-0248(94)90029-9)
- Wilson et al. 2020 Wilson GM et al. (2020) The 2020 photovoltaic technologies roadmap. *J Phys D: Appl Phys* 53(49). <https://doi.org/10.1088/1361-6463/ab9c6a>
- Wolf M (1963) Drift fields in photovoltaic solar energy converter cells. *Proc IEEE* 51(5):674–693. <https://doi.org/10.1109/PROC.1963.2260>
- World Adds Record New Renewable Energy Capacity in 2020 (2021) IRENA
- Wright B, Madumelu C, Soeriyadi A, Wright M, Hallam B (2020) Evidence for a light-induced degradation mechanism at elevated temperatures in commercial N-type silicon heterojunction solar cells. *Solar RRL* 4(11):2000214. <https://doi.org/10.1002/solr.202000214>
- Würfel P (2005) *Physics of solar cells*, 2nd edn. WILEY-VCH, Verlag. <https://doi.org/10.1002/9783527618545.ch5>
- Wurfel U, Cuevas A, Würfel P (2015) Charge carrier separation in solar cells. *IEEE J Photovolt* 5(1):461–469. <https://doi.org/10.1109/JPHOTOV.2014.2363550>
- Xu X et al (2021) An overview of high-performance indoor organic photovoltaics. *Chemsuschem* 14(17):3428–3448. <https://doi.org/10.1002/cssc.202100386>
- Yablonoitch E, Cody GD (1982) Intensity enhancement in textured optical sheets for solar cells. *IEEE Trans Electron Devices* 29(2):300–305. <https://doi.org/10.1109/T-ED.1982.20700>
- Yablonoitch E, Gmitter T, Swanson RM, Kwark YH (1985) A 720 mV open circuit voltage SiO_x:c-Si:SiO_x double heterostructure solar cell. *Appl Phys Lett* 47(11):1211–1213. <https://doi.org/10.1063/1.96331>
- Yamaguchi M (2001) Radiation-resistant solar cells for space use. *Sol Energy Mater Sol Cells* 68(1):31–53. [https://doi.org/10.1016/S0927-0248\(00\)00344-5](https://doi.org/10.1016/S0927-0248(00)00344-5)
- Yan D, Cuevas A, Bullock J, Wan Y, Samundsett C (2015) Phosphorus-diffused polysilicon contacts for solar cells. *Sol Energy Mater Sol Cells* 142:75–82. <https://doi.org/10.1016/j.solmat.2015.06.001>
- Yang L et al (2011) High efficiency screen printed bifacial solar cells on monocrystalline CZ silicon. *Prog Photovoltaics Res Appl* 19(3):275–279. <https://doi.org/10.1002/pip.1018>
- Yang Y, Mielczarek K, Aryal M, Zakhidov A, Hu W (2012) Nanoimprinted polymer solar cell. *ACS Nano* 6(4):2877–2892. <https://doi.org/10.1021/nn3001388>

- Yang G, Ingenito A, van Hameren N, Isabella O, Zeman M (2016) Design and application of ion-implanted polySi passivating contacts for interdigitated back contact c-Si solar cells. *Appl Phys Lett* 108(3):033903. <https://doi.org/10.1063/1.4940364>
- Yeop Myong S, Won Jeon S (2015) Design of esthetic color for thin-film silicon semi-transparent photovoltaic modules. *Sol Energy Mater Sol Cells* 143:442–449. <https://doi.org/10.1016/j.solmat.2015.07.042>
- Yoshikawa K et al (2017) Exceeding conversion efficiency of 26% by heterojunction interdigitated back contact solar cell with thin film Si technology. *Sol Energy Mater Sol Cells* 173:37–42. <https://doi.org/10.1016/j.solmat.2017.06.024>
- Yoshikawa K et al (2017) Silicon heterojunction solar cell with interdigitated back contacts for a photoconversion efficiency over 26% *Nat Energy* 2(5). <https://doi.org/10.1038/nenergy.2017.32>
- Young DL et al (2016) Interdigitated back passivated contact (IBPC) solar cells formed by ion implantation. *IEEE J PhotovoltS* 6(1):41–47. <https://doi.org/10.1109/JPHOTOV.2015.2483364>
- Yu C, Xu S, Yao J, Han S (2018) Recent advances in and new perspectives on crystalline silicon solar cells with carrier-selective passivation contacts. *Crystals* 8(11):430,1–18. <https://doi.org/10.3390/cryst8110430>
- Zeng Y et al (2017) Theoretical exploration towards high-efficiency tunnel oxide passivated carrier-selective contacts (TOPCon) solar cells. *Sol Energy* 155:654–660
- Zhang Y et al (2011) Bulk heterojunction solar cells based on a new low-band-gap polymer: morphology and performance. *Org Electron* 12(7):1211–1215. <https://doi.org/10.1016/j.orgel.2011.04.001>
- Zhang Y et al (2016) A large-volume manufacturing of multi-crystalline silicon solar cells with 18.8% efficiency incorporating practical advanced technologies. *RSC Adv* 6(63):58046–58054. <https://doi.org/10.1039/C6RA05765A>
- Zhang Y, Wang L, Chen D, Kim M, Hallam B (2021) Pathway towards 24% efficiency for fully screen-printed passivated emitter and rear contact solar cells. *J Phys D Appl Phys* 54(21):214003. <https://doi.org/10.1088/1361-6463/abe900>
- Zhang M et al (2021) Single-layered organic photovoltaics with double cascading charge transport pathways: 18% efficiencies. *Nat Commun* 12(1):309. <https://doi.org/10.1038/s41467-020-20580-8>
- Zhao J, Wang A, Green MA (1990) 24% efficient PERL structure silicon solar cells. In: *IEEE conference on photovoltaic specialists*, pp 333–335. <https://doi.org/10.1109/PVSC.1990.111642>
- Zhong CL, Luo LE, Tan HS, Geng KW (2014) Band gap optimization of the window layer in silicon heterojunction solar cells. *Sol Energy* 108:570–575. <https://doi.org/10.1016/j.solener.2014.08.010>

Physics and Technology of Carrier Selective Contact Based Heterojunction Silicon Solar Cells



Joaquim Puigdollers , Cristobal Voz , and Eloi Ros 

1 Conceptual Solar Cell: Light Absorber Plus Two Selective Contacts

1.1 Solar Cell Characteristics

In the following pages we will describe the operation of a photovoltaic solar cell. A solar cell is a solid-state device based on a semiconductor that transforms light energy (usually from the Sun) into electrical energy. There are many types of solar cells, both from the point of view of structure and geometry, as well as the semiconductor used to make them. Despite this dispersion of semiconductors, crystalline silicon is still the most widely used compound for the manufacture of solar cells and photovoltaic modules. The first solar cells based on crystalline silicon were based on the junction between two doped semiconductors (p-type semiconductor/n-type semiconductor), in what is considered a p–n junction. An explanation widely used to explain the operation of a solar cell is to consider that charge carriers diffuse in the p–n junction creating an electric field. That is, the electrons of the n-type semiconductor move towards the p-type semiconductor and the holes of the p-type semiconductor toward n-type, creating a space charge region in which the difference in electric charge creates an electric field in the junction. This electric field would be responsible for

J. Puigdollers (✉) · C. Voz · E. Ros
Departament d'Enginyeria Electrònica, Universitat Politècnica de Catalunya, c/Jordi Girona 1-3,
Campus Nord C4, 08034 Barcelona, Spain
e-mail: joaquim.puigdollers@upc.edu

C. Voz
e-mail: cristobal.voz@upc.edu

E. Ros
e-mail: eloi.ros@upc.edu

separating the carriers, electrons and holes, photogenerated in the junction when it is illuminated.

This explanation, although widely used in textbooks, does not allow us to understand the operation of most solar cells, both solar cells based on inorganic semiconductors, such as crystalline silicon, and solar cells based on emerging materials such organic or perovskite semiconductors.

Thus, for example, in the particular case of crystalline silicon, in which the silicon wafer has a thickness ranging between 200 and 300 μm , the p–n junction located a few microns from the illuminated surface (and with a space charge region of a few tens of nm) is responsible for separating the carriers that are absorbed in the junction and accelerating them towards the contacts, one of them located 200–300 microns away! It seems obvious that with only the p–n junction it is not possible to explain the solar cell based on crystalline silicon.

Figure 1, obtained from the National Renewable Energy Laboratory (NREL, Denver, USA) (NREL Homepage 2021), shows the records of photovoltaic conversion efficiencies obtained for solar cells fabricated with different light absorbing semiconductors (silicon, GaAs, QD, perovskites, ...), different geometries (single junction, multi-junction) and different technologies (thin films, single crystal). Conversion efficiency is the electrical energy provided by the solar cell when illuminated with a power of 100 mW/cm^2 .

Despite the dispersion of materials, technologies and structures used to manufacture solar cells, all of them have an electrical behavior when illuminated, similar to that shown in Fig. 2. It is the current–voltage characteristic of a diode in the dark (pink curve) shifted towards the negative current axis (green curve). This electrical behavior is generally characterized by three parameters, the open circuit voltage (V_{oc}), that is, the voltage at the ends of the contacts when they are open circuit (no

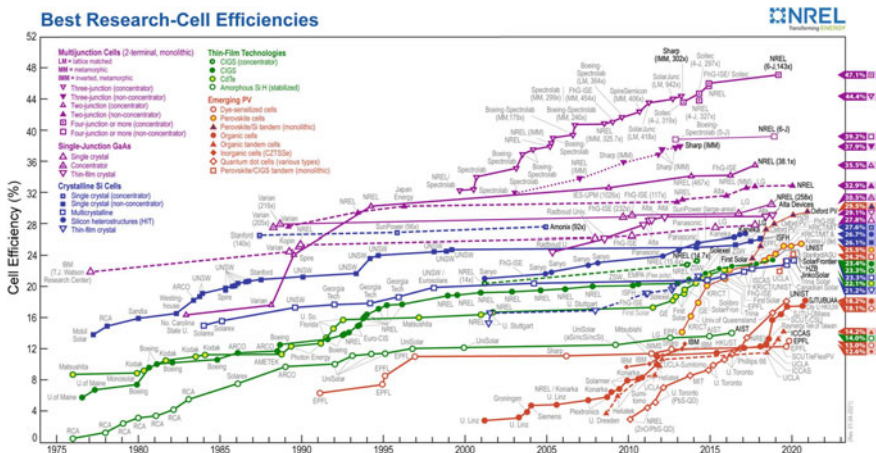
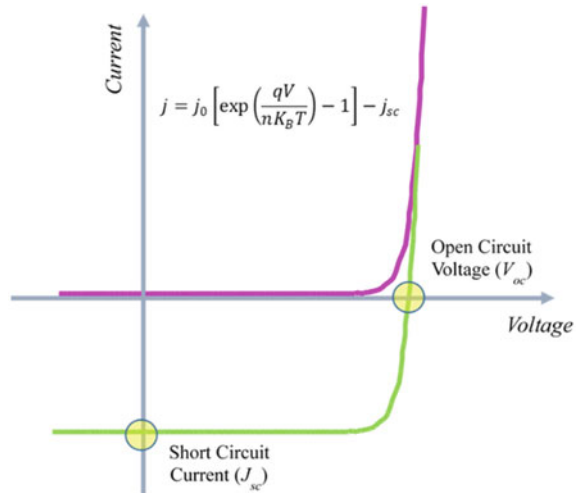


Fig. 1 Record efficiencies of solar cells fabricated using different semiconductors, technologies and structures

Fig. 2 Electrical behavior of a solar cell, in dark (pink) and illumination (green) conditions



current circulates between the contacts), the short-circuit current (I_{sc}), the current that flows through the electrodes when they are short-circuited (i.e. no voltage applied, no electric field between the electrodes), and the fill factor (FF). The equations that describe this behavior are shown in the inset of the Fig. 2. These equations will be justified at the end of the chapter.

This electrical behavior exhibited by all solar cells can be explained with a simple model composed of a light absorbing layer (semiconductor) sandwiched between two selective layers that act as filters for photogenerated carriers in the semiconductor (Würfel and Würfel 2016). The solar cell is finished with two electrodes (anode and cathode) that are usually metallic compounds and allow the solar cell to be connected to the external circuit. The absorber is made up of a semiconductor compound. Throughout this chapter we will describe different strategies for making selective contacts. Now we can anticipate that the p–n junction is a selective contact, probably the selective contact that presents the greatest benefits, which is why it has been widely studied.

The scheme of an absorber with two selective contacts allows us to qualitatively explain the operation of a solar cell, however, the concepts used also allow us to explain the electrical behavior of any electronic device or system that involves the transport of electrical charge to an external circuit. Batteries, super-capacitors, fuel cells, etc., would be examples of this. In all cases, the equilibrium of the electrochemical potentials, separated by external means from their equilibrium position, makes it possible to explain the transfer of electric charge.

1.2 Why Electrons Flow?

Before describing how a solar cell works, let's take a moment to describe why electrons move when a voltage difference is applied to the electrodes connected to the ends of a compound, which in our case will be a semiconductor. To do this, we will review some concepts that will be useful to describe the movement of electrons.

The Fermi level (E_F), or in a more general view, the electrochemical potential (μ), is defined as the average energy of the outer electrons of an element or molecule (Cahen and Kahn 2003). When a voltmeter is connected to the system, what is measured is the difference between its Fermi levels (between its electrochemical potentials). The value of an electrochemical potential is always a relative measure, which means that only the differences between the electrochemical potentials are meaningful. Throughout this introductory and more general chapter, we will not distinguish between the Fermi level and the electrochemical potential. Later, when we focus on crystalline silicon, we will use the term Fermi level.

The Fermi level is often identified as the work function of a compound. In the case of metals or semiconductors, it is easy to make this analogy. In the case of electrolytes and other compounds it cannot be done in such straightforward way. The energy needed to remove an electron from the surface of a material is defined as the work function. In other words, it is the energy to bring an electron attached to an atom, with a certain energy E_1 , negative in our case, to zero energy. The zero energy value is known as the vacuum level. This work function is represented on many occasions as the electrochemical potential of the material, its Fermi level (E_F). Applying a positive voltage to a material with respect to a reference will result in a change of its electrochemical potential to higher values with respect to the reference. Conversely, applying a negative voltage with respect to a reference will result in a shift to lower energies (Fig. 3).

Let's imagine we have two electrodes connected to a material that has electronic states, as shown in Fig. 4. The two electrodes can be considered charge reservoirs (both for electrons and for holes). Electrons are negatively charged and therefore, are subject to an electric potential, they will tend to the position of lowest energy. Electrons will minimize their energy by moving to lower energy positions (along the energy axis). For the hole, the objective will be the same, to find positions of lower energy (which translates into going up with respect to the energy axis). Electrodes are defined by their Fermi level or electrochemical potential, μ_1 and μ_2 respectively.

What happens when a positive V_{21} voltage is applied between the two electrodes? The electrochemical potentials of *electrode 2* and *electrode 1* will be separated by an energy value eV_{21} from their initial position. The positive terminal will change the electrochemical potential of the *electrode 2* a value of eV_{21} with respect to the *electrode 1* terminal, as shown in Fig. 4.

Each contact will seek to bring the channel into equilibrium with itself. This is accomplished by the flowing of electrons from high energy electronic state to lower energy electronic state. *Electrode 2* keeps pulling electrons and *electrode 1* keeps filling electrons. We focus on the particular case that the charge carriers are electrons,

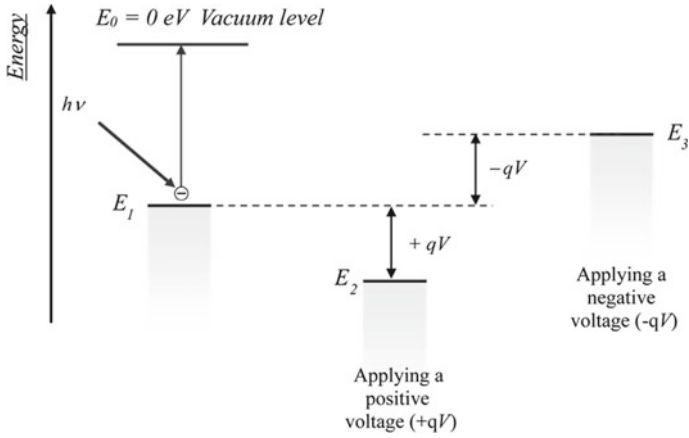


Fig. 3 Definition of work function. Consequences of voltage application on the electrochemical potential of a compound

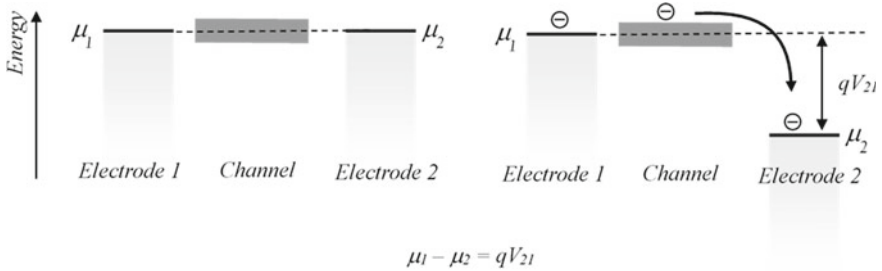


Fig. 4 Application of a voltage in a structure formed by a conductive channel and two electrodes

but the arguments presented here are also valid for holes. An excellent description of why electrons flow can be found in the works published by S. Datta (Datta 2012).

The number of carriers (electrons or holes) available for electrical conduction present in the channel is obtained by multiplying the number of electronic states $g(E)$ by the Fermi–Dirac occupancy factor $f(E)$. In the upper part of Fig. 5 a typical distribution of electronic states for a semiconductor with crystalline and disordered structure is shown. In the case of a disordered semiconductor a band tail state distribution is observed at the edge of the conduction and valence bands. The dependence of the occupancy factor is plotted as a function of temperature. In the lower part the scheme already shown in Fig. 4 is redrawn, but replacing the channel with a possible distribution of states. The occupancy factor in the semiconductor is omitted for clarity, but the occupancy factors are drawn on the *electrodes 1* and *2*. In general, the electrodes are made of metal, with a high density of electronic states, so the number of carriers available for conduction will be determined by the channel.

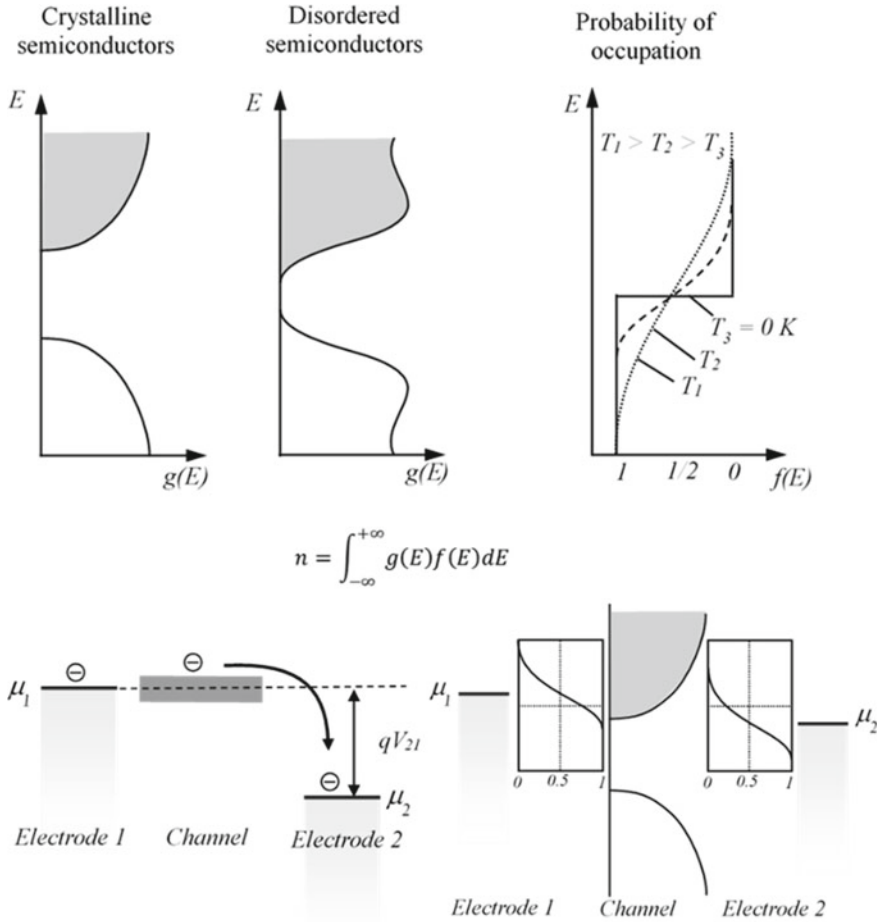


Fig. 5 From left to right. (Top) distribution of density-of-states for crystalline and disordered semiconductors. (Center) the number of carriers (electrons, for example) will be given by the product of the density-of-states $g(E)$ and the probability of occupation $f(E)$. (Bottom) scheme explaining the flow of electrons, taking into account the probability of occupation at the electrodes (channel probability of occupation is omitted for clarity)

1.3 Ideal Solar Cell: Light Absorber Plus Two Selective Contacts

An ideal solar cell is made up of a light absorbent material (semiconductor) sandwiched between two selective contacts (Würfel and Würfel 2016). The solar cell will be finished with two electrodes (generally metallic) that allow interconnection to an external circuit.

Absorber. The absorber material, where the photogenerated electrons and holes are generated, is made up of a semiconductor. A semiconductor is a material that has an energy gap between the electron conduction level and the hole conduction level (it would correspond to the conduction band and the valence band of an inorganic semiconductor—such as the case of crystalline silicon—or to the High Occupied Molecular Orbital (HOMO) Low Unoccupied Molecular Orbital (LUMO) levels for an organic semiconductor. A good semiconductor should have a bandgap free of electronic states and well-defined, steeply sloping valence and conduction bands edges.

Selective Layer. Selective layers must be selective for one type of carrier. That is, the selective electron layer must allow the flow of electrons and not allow (block) the flow of holes, while the selective layer of holes must allow the flow of holes while blocking the holes. These selective layers are also called Filters, Membranes, Electron Transport Layer (*ETL*) or Hole Transport Layer (*HTL*).

A selective layer will be defined by the existence of an energy barrier for the passage of a certain type of carrier. The creation of an energy barrier can be generated in different ways. The most common way is from the union of two materials with different job functions. After the union of two compounds with different work functions, the balance of the electrochemical potentials (Fermi levels) will occur, which will result in a separation of the vacuum levels and the creation of an energy barrier. The junction of two semiconductors with different doping levels is the standard approximation in the case of the p–n junction of crystalline silicon. However, and as we will see throughout this chapter, there are different ways to achieve energy barriers.

Electrodes. Electrodes, generally metals, will allow the electrons and holes generated in the semiconductor to be extracted. Metal is characterized by its electrical conductivity and its work function.

Now we will describe the origin of the short circuit current and the open circuit voltage. To explain this, we will focus on an ideal solar cell structure. This ideal device will consist of a semiconductor defined by a separation of the valence and conduction band (Energy gap), with an abrupt absorption edge, no defects within the gap and at the interface.

In the scheme of Fig. 6 left it is shown a semiconductor connected to two external electrodes (metals). For simplicity, let us consider that the semiconductor is intrinsic, carrier mobility is equal for electrons and holes, distribution of electronic states in the conduction and valence band are similar, in other words a symmetrical structure. When the solar cell is illuminate with photons with energy greater than the energy gap of the semiconductor, electrons and holes are generated. These electrons and holes will recombine with empty electronic states located in the metal. Semiconductor electrons with metallic holes and semiconductor holes with metallic electrons. The recombination rate will depend on the distribution of electronic states in the semiconductor and in the metal and will be given by the Fermi–Dirac statistics. As it is a symmetrical structure, there will be no charge imbalances and no voltage difference (difference in electrochemical potentials) will appear in the external metals.

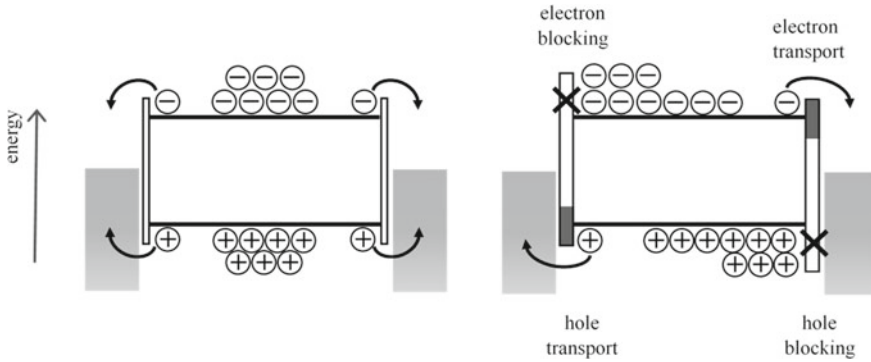


Fig. 6 Illuminated semiconductor sandwiched between two electrodes, without (left) and with (right) the inclusion of selective contacts

Let's describe what happens when we break the symmetry of the set by adding selective contacts sandwiched between the semiconductor and the metals, acting as electrodes (Fig. 6, right). These selective contacts act as electrical charge filters. A filter allows the passage of electrons and blocks the passage of holes. In the Fig. 6 it has been schematized as an energy barrier with an energy window, represented in grey color in the upper part of the energy axis. The other filter, represented by an energy window in the lower part of the energy barrier will allow the passage of holes and the blocking of electrons. As mentioned before, these filters have many names in the scientific literature. In our case, we will call them the Electron Transport Layer (*ETL*) and the Hole Transport Layer (*HTL*).

In this situation, the photogenerated electrons and holes will not recombine symmetrically as in the first case. The electrons leaving the semiconductor through the high energy window recombine with the holes leaving the semiconductor through the low energy window. The asymmetry provided by the insertion of the selective layers (*ETL* and *HTL*) have great consequences on the electrical behavior of the structure. Short circuit current and open circuit voltage are consequences of this asymmetry.

Short-Circuit Conditions. In Fig. 7 left we show a semiconductor connected to two external electrodes and in which two selective contacts *ETL* and *HTL* have been inserted between the semiconductor and the electrode. The two electrodes, usually metals, are connected with an external cable (short-circuit conditions). When illuminating the semiconductor with energy higher than the band gap ($h\nu > E_g$), photogenerated electrons and holes will recombine through the external circuit, giving rise to a current through the wire that connects the two electrodes. The electrons coming from *ETL* will recombine with the holes coming from *HTL*. In other words, the electrochemical potential of the electrons (determined by E_{Fn} and the energy window of *ETL*) will try to match the electrochemical potential of the holes (E_{Fp}), establishing a current of electrons through the external circuit. Equilibrium will never be reached, as the illumination continuously separates the electrochemical potentials

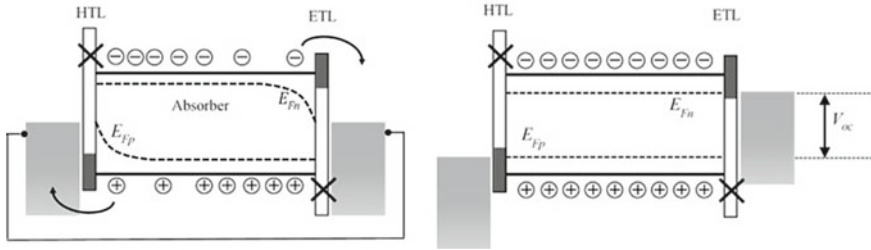


Fig. 7 Short-circuit (left) and open circuit situations (right) of an illuminated solar cell

of electrons and holes, again establishing a flow of electrons and holes that try to reach equilibrium.

In the scheme, the quasi-Fermi levels of electrons and holes (E_{Fn} , E_{Fp}) in the semiconductor are drawn with a dashed line. E_{Fn} (Chemical potential of electrons) and E_{Fp} (chemical potential of holes) describes the population of electrons and holes in the conduction and in the valence band when their populations are displaced from equilibrium. The gradient of the Fermi quasi levels along the semiconductor gives us an idea of the quality of the semiconductor and allows us to calculate the value of the generated photocurrent. For these reasons it is considered to be the driving force of the photocurrent.

Without selective contacts, electrons and holes will also recombine through the outer wire (mainly at the interface semiconductor/metal), but being a symmetrical structure there will be no defined current direction. With a single selective contact there would be a certain asymmetry in the structure that would give rise to a photocurrent, which in this case, intrinsic semiconductor and without defects, would be half the value of the photocurrent that would be obtained with both selective contacts.

The presence of electronic states in the semiconductor gap or in the semiconductor/selective contact interface would cause a recombination of the photogenerated electrons and holes without passing through the external circuit, which would result in a decrease in the generated photocurrent.

Open-Circuit Conditions. In this situation, we leave the two electrodes disconnected. When the solar cell is illuminated, a voltage appears across the electrodes (Fig. 7 right).

As in the case of a short circuit, the photogenerated electrons and holes will give rise to the creation of the quasi Fermi levels of electrons and holes (E_{Fn} , E_{Fp}). Then the electrochemical potential of the metal connected to the absorber layer through the *ETL* will balance with the average energy of the electrons (quasi Fermi level) in the semiconductor. The same will happen with the metal in contact with the semiconductor through the *HTL*. This equilibrium is achieved through the transfer of electrons and holes. The open circuit voltage will be determined by the energetic difference of the quasi-Fermi levels of electrons and holes.

As in the case of the photocurrent condition, the existence of conduction paths that allow the recombination between electrons and holes will worsen the open circuit

voltage. Such recombination will mainly occur through electronic states (defects or traps) located within the semiconductor bandgap and in surface states located at the semiconductor/selective contact interface.

It is evident that the open circuit voltage will be proportional to the energy gap of the semiconductor. The steeper the separation between the region with electronic states and the region without electronic states, the greater the V_{oc} . The slope of this transition is known as the Urbach energy. A direct relationship between Urbach energy and solar cell efficiency has been reported experimentally. The lower the Urbach energy, the higher the efficiency (Jean et al. 2017).

1.4 Making Selective Contacts

We can ask ourselves what the characteristics of the compounds must be in order for them to act as selective layers. That is, layers that allow the passage of a certain type of carrier blocking the other. In some cases, you can speculate with guarantees of success.

Doped Layers. It seems pretty obvious that the doped layers will act as selective layers. Incorporating a doped layer will behave like a filter. On the one hand, the difference in conductivity between the charge carriers (unbalance of the conductivity of the electric carrier), which will favor the transport of a certain type of electric charge over another. On the other hand, and in the case of homojunctions, the difference between the Fermi levels (electrochemical potentials) of the doped layers will translate into differences in the vacuum level, giving rise to energy barriers for a certain type of electric charge carrier. This strategy is the one that has been followed for many years in the manufacture of crystalline silicon solar cells. The p-n junction, that is, the junction of an n-type doped semiconductor with another p-type doped semiconductor is surely the most studied selective contact and one of the most efficient. A typical example would be the structure p-i-n or variations on the same concept such as p⁺-p-n or n⁻-n-p.

Heterojunction. Another approach is the use of layers with different energy gap with respect to the energy gap of the absorber layer. They are the so-called heterojunctions. An example would be the use of amorphous silicon layers doped with Boron a-Si:H (p) (or with Phosphorous a-Si:H(n)) that have an energy gap greater than that of intrinsic amorphous silicon a-Si:H(i).

The most efficient crystalline silicon solar cell reported to date, the so-called HIT (Heterojunction with Intrinsic Thin Film) uses these two concepts just mentioned. The selective contacts are formed by the junction of hydrogenated amorphous silicon (energy gap greater than that of crystalline silicon) and doped layers (creation of p-n junction).

Experimentally, it has been found that there are a wide variety of compounds that act as selective layers. In general, its efficiency is given by its ability to change the vacuum level in the selective layer/semiconductor interface and in the different

mobility between electrons and holes in the selective layer. Examples of these materials are: transition metal oxides (TMO, such as MoO_3 , V_2O_5 , WO_3 , ReO_3 , etc.), polymers (PEDOT-PSS, Spiro-OMeTad), dipoles (TiO_x , LiF, BCP, BPhen, amino acids...). Some of these approaches will be discussed throughout this chapter.

1.5 Determining the Current–Voltage Characteristic of a Solar Cell

As mentioned at the beginning of this chapter, all solar cells have a similar dependence between intensity and voltage (both in the dark and under light). In darkness, this dependence is characterized by low current when reverse biased and by an exponential increase in current for forward biases. The illuminated I–V characteristic is similar to that obtained in the dark but shifted towards negative currents (superposition principle).

We will now describe the reasons for this electrical behavior. We will begin by explaining such electrical behavior in dark conditions. In Fig. 8 we show the typical solar cell structure, composed of the absorber layer and the two selective contacts. We consider short-circuit conditions. Due to thermal generation, the electrons in the valence band will have enough energy to pass into the conduction band. Let call the the number of thermal generated electron-holes per unit time j_0 . Let call the number of electrons that recombine with holes per unit time j_{rec} . Since no voltage is applied, we will name this as $j_{rec}(0)$. At $V = 0V$ there is an equilibrium between generation and recombination, that is $j_0 = j_{rec}(0)$. This situation is described on the left of Fig. 8.

Now let’s apply a positive voltage to the solar cell, that is, a positive voltage to the anode with respect to the cathode. In other words, let’s shift up (with respect to the energy axis) the electrochemical potential of the electrode connected to the electron selective contact—cathode—and down that connected to the holes—the anode—as shown in Fig. 9 left. At the cathode, some electrons will have enough energy to

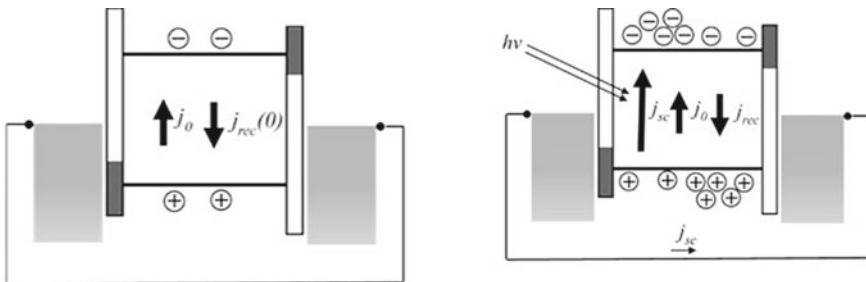


Fig. 8 Generation and recombination current in a short circuited solar cell. Under dark (left) and illumination (right) conditions. Under illumination an external current appears

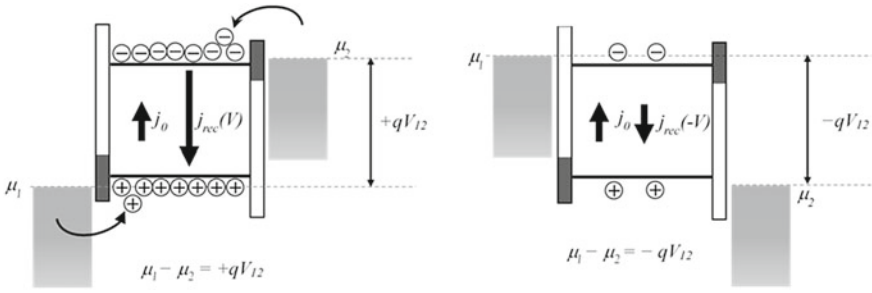


Fig. 9 Impact on the recombination current of the solar cell of an application of external voltage. Forward (left) and reverse (right) conditions. Under dark conditions

overcome the energy barrier between the electrochemical potential of the metal and the conduction band. The lower the energy barrier, the more electrons will overcome it. That is, as the positive voltage increases, the lower the energy barrier.

The application of negative voltages will have no effect on the electric current, since the energy barriers, for electrons and holes, will increase (Fig. 9 right). The number of electrons that will overcome the energy barrier will follow Boltzmann's law. A simple explanation of this law can be found in Feynman's lectures (Chap. 40) (The Feynman Lectures and on Physics, Homepage 2021) or in any textbook on statistical mechanics. Boltzmann's law states that the probability of finding a particle in a spatial arrangement depends exponentially on the (negative) potential energy of the particle divided by $K_B T$. Let n be the number of particles, K_B the Boltzmann constant, T the temperature and A a constant of proportionality, that is:

$$n = Ae^{-(potential\ energy)/K_B T} \quad (1)$$

In our scheme, by increasing the positive voltage between the anode and the cathode, the energy barrier decreases and more electrons and holes will overcome it. The number of electrons and holes that will overcome it will depend exponentially on the voltage. Electrons and holes will recombine in the absorber layer. For this reason, this component of the current is known as recombination current j_{rec} , and its dependence on the applied voltage is as follows:

$$j_{rec}(V) = Ae^{qV/K_B T} \quad (2)$$

where qV is the energy barrier. The negative sign of the electron charge has been included. In general, a factor n , called the ideality factor, is included to account for the deviation from the ideal case.

The value of the constant A is easily determined, since for a voltage equal to 0 V, the recombination current must be equal to the generation current:

$$j_{rec}(0) = j_0 \quad (3)$$

Therefore,

$$j_{rec}(V) = j_0 e^{qV/nk_B T} \quad (4)$$

The total current in dark will be the sum of the thermal generation current plus the recombination current (minus sign):

$$j = j_{rec}(V) - j_0 = j_0 e^{\frac{qV}{nk_B T}} - j_0 = j_0 \left(e^{\frac{qV}{nk_B T}} - 1 \right) \quad (5)$$

The equation that describes the electrical behavior of the solar cell under illumination conditions is obtained by adding the photogenerated current (see Fig. 8 right):

$$j = j_{rec}(V) - j_0 - j_{sc} = j_0 \left(e^{\frac{qV}{nk_B T}} - 1 \right) - j_{sc} \quad (6)$$

2 Selective Contacts and Practical Applications to Photovoltaics

We have shown that using relatively simple concepts the equation that governs the electrical behavior of a solar cell is obtained. The concepts described in this chapter must be taken into account in the design of any solar cell. The main difficulties in achieving high-efficiency solar cells lie in the synthesis of semiconductors defect-free and in finding selective contacts (*ETL* and *HTL*) compatible with the semiconductor. In recent years they have devised new strategies to achieve innovative selective contacts. In this chapter we will describe some of these approaches to making these innovative selective contacts. We will focus on solar cells, but it is obvious that their field of application is much broader.

2.1 Thin Film Carrier Selective Contacts, Hole and Electron Transport Layers

In the previous section we have shown how solar cells can be generally described as an optical absorber plus two complementary charge-carrier selective contacts (see Fig. 10). This novel approach widens the conception of photovoltaic devices (Cuevas and Yan 2013; Würfel and Würfel 2009). In this sense, traditional junctions based on doping are only a way to achieve the desired charge-carrier separation (Würfel et al. 2015). The driving-force for the motion of charge-carriers is the electrochemical potential, i.e., gradients in the quasi-Fermi levels of electrons and holes. In solar

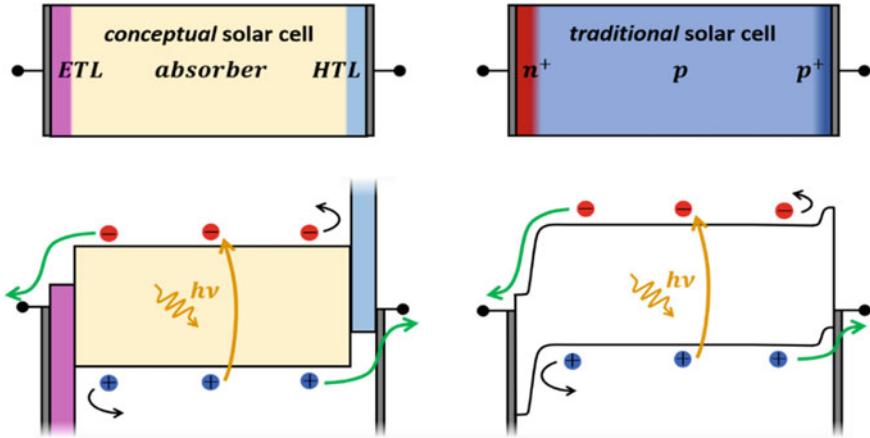


Fig. 10 Conceptual solar cell compared to a traditional silicon solar cell structure. The diffused n^+ region works pretty well as ETL, while the p^+ region (so-called back-surface-field) plays a quite efficient HTL role

cells photovoltaic power generation (output voltage together with photogenerated current) needs terminals with asymmetric properties. Unbalancing electron and hole conductivities by doping has been the regular approach, at least for silicon-based photovoltaic technologies. However, there are other ways to achieve the desired charge-carrier separation. These other options have been widely explored in alternative photovoltaic technologies, such as chalcogenides (Hsu et al. 2015), organic semiconductors (Ratcliff et al. 2011) or perovskites (Juarez-Perez et al. 2014). Thin-film layers of specific materials can efficiently extract one charge-carrier type and simultaneously block the other one. These films (sometimes stacks of several layers) are referred in the literature as hole-transport layers (HTL) and electron-transport layers (ETL), respectively (Cho et al. 2014). The term passivated carrier-selective contacts (CSC) is also well-suited, since it denotes collection of one carrier type with very low interface recombination (Muller et al. 2018). Note that in solar cells either interface recombination or carrier collection at the wrong electrode both reduce photovoltaic generation. In fact, this description above includes both amorphous/crystalline silicon heterojunction (SHJ) and tunnel oxide passivated contact (TOPCon) technologies (Battaglia et al. 2016). Although these are very different from diffused junctions, they still rely on heavily doped amorphous or polycrystalline thin silicon films. The technology to grow these films (plasma-enhanced chemical-vapor-deposition, PECVD) involves expensive equipment and the use of hazardous gas precursors. By contrast, dopant-free alternatives have indeed redefined high-efficiency silicon solar cells over the last years (Yang et al. 2017). Many materials used in emerging PV technologies have been implemented in silicon-based solar cells with remarkable success (Lin et al. 2021). These results reinforce that doped junctions are nonessential to solar cell operation. On the contrary, electrodes with differentiated work functions

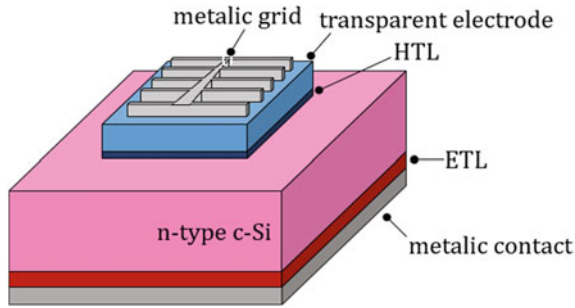


Fig. 11 Example of dopant-free silicon-based solar cell structure. The HTL and ETL selective contacts may actually consist of different stacked layers, which together provide interface passivation and effective charge-carrier separation

can effectively separate charge-carriers from the light absorber. Typically, electrodes with high work function perform well as hole-selective contacts (HTL) and those with lower values are good electron collectors (ETL) (Feldmann et al. 2015).

The acronym dopant-free asymmetric heterocontacts (DASH) was introduced to define this new kind of solar cells (Bullock et al. 2016). The basic structure could very much resemble a traditional silicon heterojunction solar cell (see Fig. 11). A transparent-conductive-oxide (TCO) serves as an antireflection coating and front electrode. The top contact is completed with a metallic grid that is typically made of evaporated silver. The grid geometry is designed to trade off the shadowed area for a lower series resistance. In this regard, there are not significant differences with respect to conventional solar cells. The back contact can be a simple aluminum layer, but the use of low work function metals can significantly improve the contact quality. This extend is discussed in more detail throughout this chapter. On the other hand, more sophisticated device structures like doping-free interdigitated-back-contact (IBC) solar cells have been already reported (Masmitjà et al. 2018).

2.2 Hole-Selective Contacts for Silicon-Based Solar Cells

Probably, first attempts to use hole-selective contacts on silicon were made with p-type organic polymers. As a clear example, the behavior of poly(3-hexylthiophene) (P3HT) described in reference (Avasthi and Sturm 2011) is consistent with the concept of hole-selective contact. The efficiency of that preliminary device was rather modest (6.5%). In later years, much better results have been reported using poly(3,4-ethylenedioxythiophene):poly(styrenesulfonate) (PEDOT:PSS) as a hole-selective contact on n-type Si (Mahato et al. 2016). Efficiencies over 16% were achieved in simple structures (He et al. 2017) and they exceeded 20% for more optimized back junctions with a passivating interlayer (Zielke et al. 2015). These first studies focused on the original combination of organic and inorganic materials to fabricate

those devices. The concept of hybrid solar cell is prior to the interest that selective contacts have gained more recently. Now, it is clear that these polymers were just performing as HTL contacts of organic nature. The main concern for selective contacts based on organic compounds is about their long-term stability.

Alternatively, films of some transition-metal-oxides (TMO) have proven to be excellent HTL contacts on silicon (see Fig. 12). These materials can be deposited by simple deposition techniques compared to the PECVD process used to grow doped silicon thin films. Thermal evaporation (Gerling et al. 2016) and atomic-layer-deposition (ALD) (Yang et al. 2020) are convenient deposition techniques, but sputtering and even solution-processing methods have been also investigated (Mews et al. 2017). Nickel oxide and copper oxide in non-stoichiometric forms are p-type semiconductors that can be used to replace boron-doped silicon films as hole-selective contacts (Nayak et al. 2019; Zhang et al. 2016). The low electron affinity of these materials also helps to block electrons (discontinuity at the conduction band edge), while their wide band gap results in very good transparency. In any case, the best results have been achieved with other TMO materials that are actually n-type. Exceptional power conversion efficiencies of 23.5% have been achieved with molybdenum oxide (MoO_3) as a hole-selective contact on n-type Si (Dréon et al. 2020). Also very remarkable efficiencies have been reported for both vanadium oxide (V_2O_5) and tungsten oxide (WO_3) (Masmitjà et al. 2017; Bivour et al. 2015). At first sight, such a good HTL performance for materials that are n-type causes perplexity. Nevertheless, the working principle has been widely described in the literature (Bullock et al. 2014; Messmer et al. 2018). The extremely high work function of these TMO materials is able to induce a strong hole inversion layer on n-type silicon. The resulting band structure is then similar to a p^+n junction where electrons are blocked by the built-in energy barrier (see Fig. 13). On the contrary, holes may be extracted from Si following a multitunneling capture and emission (MTCE) mechanism to recombine with electrons from the TMO conduction band (García-Hernansanz et al. 2018). The photovoltaic conversion can be sustained in steady-state because electrons collected at the rear ETL contact flow through the external circuit into the TMO again. In addition to their high work function values, defects (oxygen vacancies) in these TMO layers are essential for an effective hole-extraction. The sub-oxidized state of these films accounts for their n-type character and provides a high density of states to sustain charge-carrier transport by the MTCE mechanism (Messmer et al. 2018). For that reason, the MoO_x , WO_x or VO_x formulae are often used in the literature to denote that these materials are used in non-stoichiometric forms. One important advantage of using TMO layers is their higher transparency compared to doped thin silicon films. The bandgap higher than 3 eV for all these TMO materials results in devices with higher spectral response at short wavelengths ($\lambda < 400\text{nm}$). For instance, a direct comparison between MoO_x and p-doped a-Si:H layers evidences that the J_{sc} value increases by more than 1 mA/cm^2 (Battaglia et al. 2014).

It is worth mentioning that many works maintain an intrinsic a-Si:H passivating layer between c-Si and the TMO layer (Bullock et al. 2016; Dréon et al. 2020; Geissbühler et al. 2015). As for traditional silicon heterojunction devices, this buffer is used to reduce interface recombination. However, this approach reduces technological

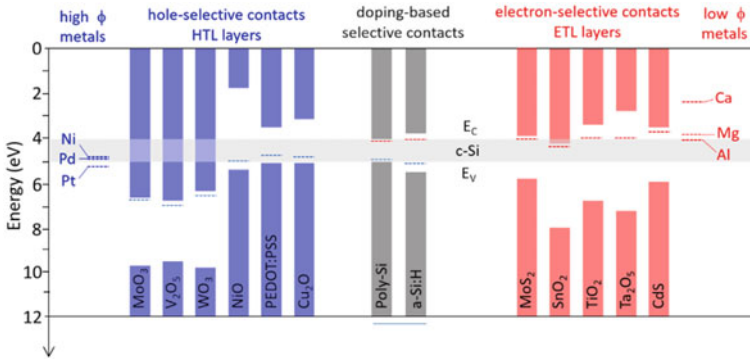
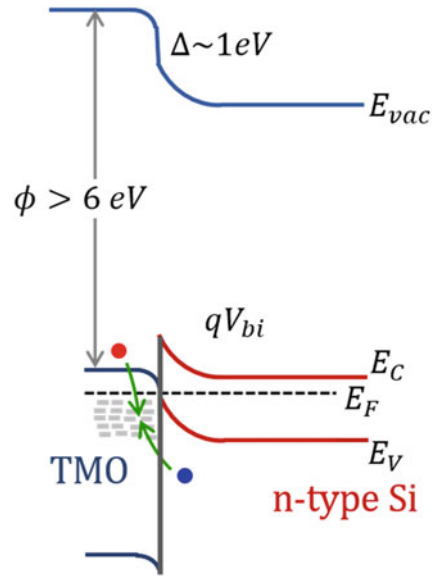


Fig. 12 Some HTL (left) and ETL materials (right) investigated as an alternative to doped thin silicon films (center) for heterojunction solar cells. High work function metals are preferred for hole-selective contacts (anode) and the contrary applies to electron-selective contacts (cathode)

Fig. 13 Proposed band diagram for a high work function TMO layer deposited on n-type Si. Defects (oxygen vacancies) are essential for an efficient hole extraction by the MTCE recombination mechanism. A strong interface dipole may be typically present at the highly inverted Si surface



interest because of its more complex fabrication route. Alternative passivating layers that could be chemically grown, e.g. silicon oxide (LuisG et al. 2017), or deposited by ALD may have more industrial interest. In any case, it has been shown that a thin SiO_x interlayer spontaneously forms at the c-Si/TMO interface during deposition. This effect explains the relatively good surface passivation that can be readily achieved without any intended passivating interlayer (Gerling et al. 2017). Particularly, vanadium oxide seems to be perform quite well in this regard (Almora et al. 2017).

2.3 *Electron-Selective Contacts for Silicon-Based Solar Cells*

The extraordinary results achieved with HTL contacts on silicon have motivated a great interest to find complementary ETL solutions. This research pursues an integral solution to fabricate doping-free high-efficiency silicon solar cells. Molybdenum disulfide in the form of monolayer (2D material) was investigated as an ETL contact for p-type Si solar cells with modest results (Tsai et al. 2014). The chalcogenide technology also inspired researchers to fabricate p-type Si solar cells with an ETL contact of cadmium sulfide (Cai et al. 2019). However, there are major concerns about the use of cadmium to fabricate solar cells.

In the last years, low work function metal oxides (also a few nitrides) of safe and abundant elements have attracted much more attention. These alternative ETL materials can be obtained by standard thin-film deposition techniques like sputtering (Zhong et al. 2019), ALD (Yang et al. 2018) or solution processing (Zheng et al. 2019). The resulting layers are typically non-stoichiometric, which is actually good to have a semiconducting rather than insulating behavior. Tin oxide and tantalum oxide have been used as ETL contacts on n-type silicon solar cells achieving rather good efficiencies (Zheng et al. 2019; Wan et al. 2017a). Similarly, nitrides of titanium and tantalum worked really well in recent works (Yang et al. 2018, 2019). Nevertheless, the most studied solution is probably the use of thin titanium oxide layers deposited by ALD. Efficiencies higher than 21% have been reported on n-type c-Si with a rear ETL contact of TiO_x (Yang et al. 2016a). The industrial feasibility of this solution has been already investigated (Yang et al. 2017), demonstrating good compatibility with thermal steps like firing and annealing. The potential of this ETL material has been demonstrated in partial-rear-contact (PRC) solar cells that exceeded 23% conversion efficiency (Bullock et al. 2019). However, such point-contact configurations (similar to classical PERC devices) involve more complex fabrication routes. All these record solar cells were obtained with a standard diffused p-junction at the front side. In any case, full dopant-free n-type silicon solar cells exceeding 20% efficiency have been reported combining an HTL of MoO_x with an ETL of TiO_x (Bullock et al. 2018).

The intercalation of a thin intrinsic a-Si:H passivating layer is also usual here to improve ETL contacts. As mentioned before, solutions that could circumvent such complex PECVD deposition are more interesting. Differently to what happened for some materials, spontaneous oxidation of silicon by TiO_x seems not enough for good interface passivation. Thus, the formation of a passivated tunnel SiO_x interface needs additional chemical or thermal processing (Yang et al. 2017). An alternative solution may be the deposition of an ultra-thin alumina layer (AlO_x) by ALD. Furthermore, the complete $\text{AlO}_x/\text{TiO}_x$ stack can be deposited in the same ALD system with a great process compatibility (Masmitjà et al. 2018).

It is important noting that these ETL materials are not really capable of inducing electron inversion on p-type Si. Thus, their practical use is generally limited to electron-selective contacts at the rear side of n-type Si solar cells. By contrast, the high work function materials (MoO_x , WO_x , VO_x) mentioned in the previous section were indeed able to work very effectively as HTL contacts on n-type Si. That is the

reason why most silicon solar cells with carrier-selective contacts reported in the literature are fabricated on n-type wafers. Nevertheless, some works have shown the possibility to replace the Al-BSF contacts of industrial p-type Si solar cells with MoO_x layers (Nasser et al. 2021). This limitation for the use of many ETL materials on p-type Si is explained by their less extreme work function values. Note that the work function of TiO_x is close to the conduction band edge of Si, while for MoO_x it goes much deeper than its valence band edge. In this sense, low work function metallic electrodes can be used to reinforce the electron selectivity of ETL materials (Allen et al. 2017). However, metals like calcium or magnesium may be relatively complex to evaporate and they are definitely not very stable. Alternatively, ultrathin layers (~1 nm) of alkali-metal-fluoride (LiF, KF, CsF) salts have been proposed as a solution to produce low work function electrodes with standard aluminum contacts (Bullock et al. 2016). Particularly, the combination of TiO_x with a LiF/Al electrode has performed extraordinarily well as the electron-selective contact of high-efficiency solar cells (Bullock et al. 2019). According to the literature (Bullock et al. 2016), from the Si side the dipolar LiF interlayer causes an apparent reduction of the aluminum work function (see Fig. 14). Consequently, electrons accumulate near the Si surface and they can be much more easily extracted. Since alkali-metal-fluoride salts are basically insulators, the thickness of these interlayers must be controlled with nanometer resolution to allow electron tunneling. Therefore, this step of vacuum evaporation adds complexity to the fabrication route. Recently, conjugated polyelectrolytes deposited by spin-coating have emerged as alternative dipolar interlayers (He et al. 2018). This attractive approach is further discussed throughout the rest of this chapter.

3 Carrier Selective Contacts Based on Dipoles

3.1 Dipolar Interfaces for Enhanced Charge Carrier Selectivity

There are many factors involved in the transport properties of a Metal/Semiconductor junction. In one of the simplest points of view the difference in work function between the metal and the semiconductor leads to charge transfer from the metal to the semiconductor and vice versa (see Fig. 15). When the metal contacts the semiconductor, the Fermi levels in the two materials must be equal at thermal equilibrium. In addition, the vacuum level must be continuous. This picture helps understand why generally low work function metals are preferred to make an electron ohmic contact, as in the case of Calcium or Magnesium. And why larger work function metals such as Palladium, Gold or Platinum are a better option for a hole contact.

In the case of n doped crystalline silicon, if the work function of the metal is smaller than that of the semiconductor, it produces a downward band bending that

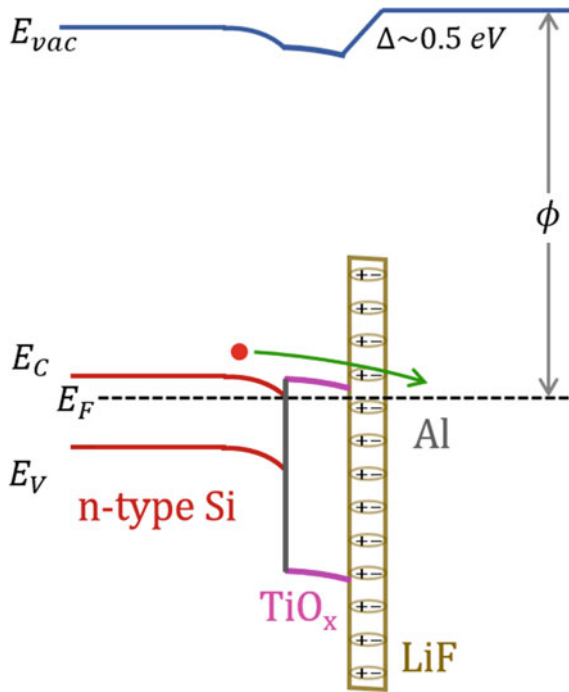


Fig. 14 Proposed band diagram for an electron-selective contact on n-type c-Si composed of a $\text{TiO}_x/\text{LiF}/\text{Al}$ stack. The dipolar LiF interlayer causes an apparent reduction in the work function of the Al cathode

accumulates electrons and gives superior electron selectivity (Fig. 15a). Simultaneously when the work function of the metal is larger than that of the semiconductor, it provokes electron migration from the semiconductor up to equilibrium by leaving a depleted zone with a larger hole density at the junction corresponding to an upwards band bending at the interface enhancing hole extraction (Fig. 15b). In this simple case the energy barrier (see Fig. 15b) can be approximated by use of the Schottky–Mott rule where the difference between work function and electronic affinity corresponds to the height of the barrier $\phi_{BN} = \phi_m - X_s$ of a Schottky junction. Which similarly would be applied to a p type semiconductor $q\phi_{BP} = E_G - q(\phi_m - X_s)$ (Sze and Lee 2016).

In the case of the majority carrier accumulation Fig. 15a the excess electron charge in the semiconductor is localized at the interface as a surface charge density. In this situation, a positive voltage applied to the junctions allows electrons to easily flow from the semiconductor into the metal. On the other hand, for a negative voltage applied to the junction an effective barrier height for electrons arises of approximately $\phi_{BN} = \phi_n$ (Neamen 2012).

From these criteria one can generally predict the barrier formation depending on the materials used. However, the dependence is not as strong as predicted by

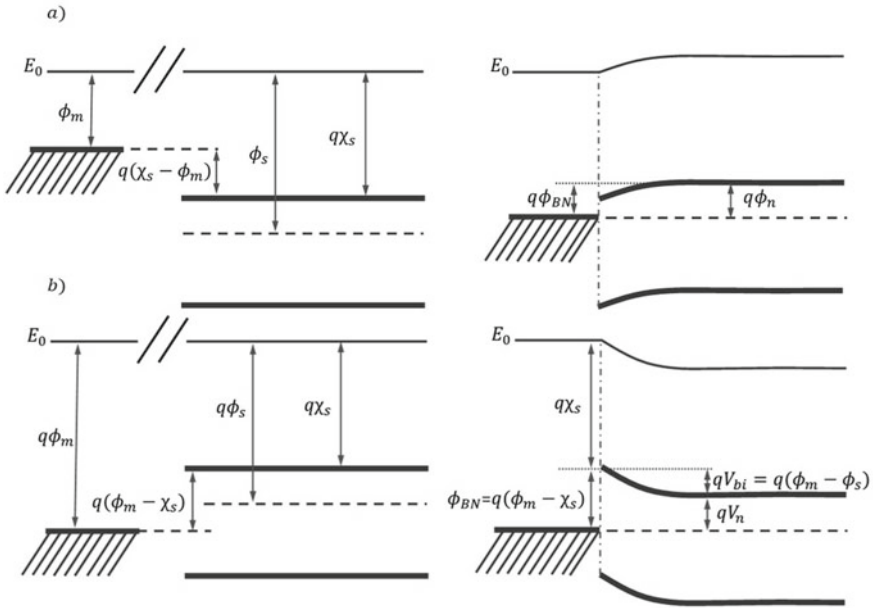


Fig. 15 Effect of the work function of the metal in the equilibrium state of metal/semiconductor junction **a** $\phi_m \ll \chi_s$ accumulation **b** $\phi_m \gg \chi_s$ depletion

previous equations and the height of the barrier is therefore poorly estimated by this rule. This phenomenon is often referred to as “Fermi Level Pinning” which is almost completely insensitive to the work function of the metal.

Using the though experiment of contacting two materials with similar or equal work function we should expect from Schottky–Mott criteria a null band bending at the interface (see Fig. 16a). However, precisely one of the most notorious problems of making ohmic contacts in Silicon solar cells, particularly in mature technologies such as Back Surface Field or Passivated Emitter Rear Cell (PERC) is that similar work function metals such as Aluminum (i.e., $\phi_{Al} = 4.1\text{eV}$, $\phi_{Si} = 4.2\text{eV}$) is not providing a satisfactory carrier injection unless the interface is either specifically post-treated by annealing or passivated by an insulator. Therefore, indicating the presence of an energy barrier caused by the Pinning of the interface.

Fermi Level Pinning (FLP) is a spontaneous effect that occurs when there are chargeable states in the semiconductor right at the interface, with energy levels inside the semiconductor’s gap (Bardeen 1947). These states can either be a consequence of chemical bonding between the metal and the semiconductor or they can be caused by the abrupt end of the mono crystalline net as in the case of crystalline Silicon. Because of the large density of defects in the interface between the semiconductor and metal, a large quantity of charge donated from the metal is absorbed at the interface by these traps that can act both as donor and acceptor. The semiconductor is then virtually deprived from the specific metal features with independent of the

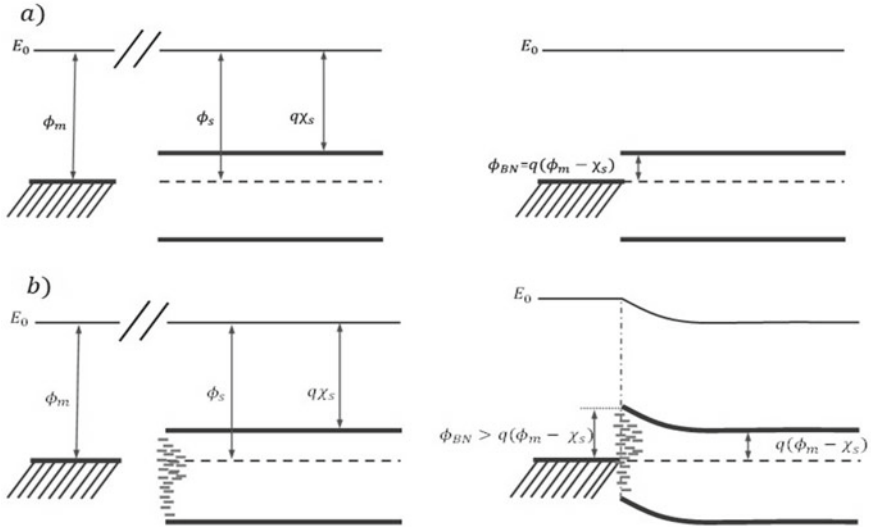


Fig. 16 Effect of surface states on a metal/semiconductor junction with equal work function $\phi_m = \phi_s$, **a** ideal thought experiment **b** real pinned semiconductor surface

barrier height to the work function of the metals. As a result, non-null band bending becomes prominent at the junction (see Fig. 16b). Furthermore, the height of this barrier depends on the surface states more than the metal properties.

Presence of an insulating layer between the semiconductor and the metal can help preventing the pinning of the surface decreasing the charge transfer from the metal to the semiconductor. In a similar manner to Metal Induced Gap States (MIGS), deposition of an insulator can partially neutralize the surface charge traps by chemically binding to the dangling bonds where the abrupt semiconductor net ended. Moreover, the conduction band of the insulating layer is several electron volts over the Fermi level of the metal, therefore not allowing a free electron flow (i.e., wave function superposition) from the metal to the semiconductor.

The schematic of a Voltage biased Metal/Insulator/Semiconductor junction can help illustrating the effect that external polarization has on the surface charge distribution with the presence of an insulator. On one hand, when a positive voltage bias is applied to the junction the insulator is polarized and a negative charge density is drawn to the semiconductor interface, corresponding to a downward band bending (see Fig. 17b). On the other hand, a negative bias applied to the junction electrostatically promotes a positive charge density to be attracted to the semiconductor surface and a corresponding upwards band bending (see Fig. 17c). Surface charge modification comes with the potential drop in the insulator (i.e. $q\Delta$) and consequent dielectric polarization. In this case the continuity of the vacuum level applies through the polarized layer and a dipole shift in vacuum level is caused by the applied voltage bias.

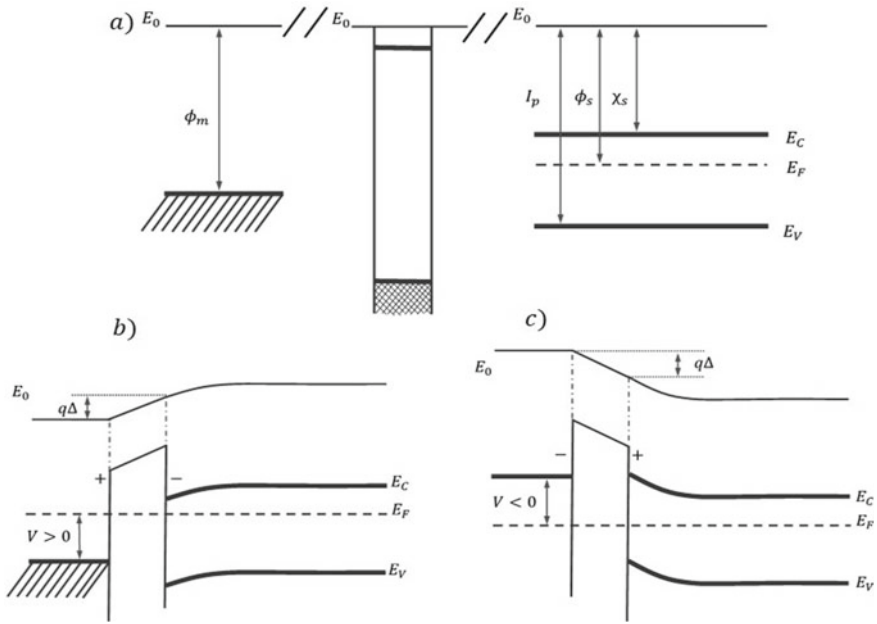


Fig. 17 Effect of a bias potential in the equilibrium state of metal/insulator/semiconductor junction **a** isolated **b** $V > 0$ accumulation, **c** $V < 0$ depletion

An interesting and relatively novel approach is the use of dipole layers or self-polarized films that can produce a similar behavior to the surface charge density without the need of an external polarization. A pseudo two-dimensional array of ordered molecular dipoles produces an internal Voltage that modifies the interface properties of the electrode by introducing a shift in the perceived work function of the metal in these sorts of Metal/Dipole/semiconductor Junctions.

In this scenario the direction in which the dipoles are arranged dictate whether the apparent work function will be larger or smaller. For instance, when the dipoles are arranged with the positive charge density sided by the semiconductor the apparent work function will be smaller than the metal work function $\phi' = \phi_m - q\Delta$. Promoting a charge transfer from the metal to the semiconductor, therefore there is an electron accumulation corresponding to a downward band bending at the interface enhancing the electron extraction (see Fig. 18a). However, when the negative charge density is sided by the semiconductor, the apparent work function will be larger than the metal work function $\phi' = \phi_m + q\Delta$. Promoting electron migration from the semiconductor to the metal, therefore depleting the interface corresponding to an upwards band bending and enhancing the hole extraction (see Fig. 18b). Equilibrium band alignment of the semiconductor is a fundamental aspect of these type of selective layers due to the importance of charge transfer in increasing selectivity.

The dipole strength and orientation will therefore promote either electron accumulation or depletion at the interface between the metal. However, due to the insulating

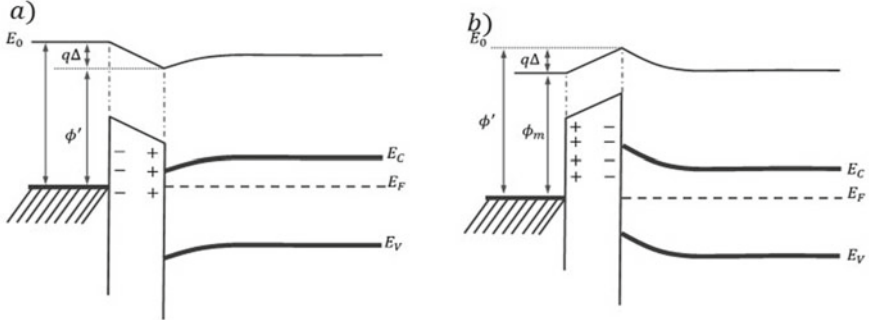


Fig. 18 Effect of a dipole layer in the vacuum level shift and corresponding equilibrium states, **a** accumulation, **b** depletion

nature of many of this dipole layers and the dependence on the dipole strength of the doping, several conduction mechanisms must be included in a MDS junction.

Further extending the case of an ETL over an n doped semiconductor which is generally the reported use of these materials in crystalline Silicon (e.g. MgF₂ (Wan et al. 2016a), MgO (Wan et al. 2017b) PEI (Ros et al. 2019)), the orientation Metal /(-/+)/Semiconductor promotes an electron accumulation at the Semiconductor interface (as illustrated in Fig. 18a). This situation is very closely related to textbook n/n⁺ junction with non-rectifying behavior. In conclusion, a majority carrier ohmic contact where selectivity comes from the difference in the doping densities between electrons and holes $\sigma_n \propto n_s \gg \sigma_p \propto p$, with n_s being the electron indirect surface doping expressed as

$$n_s = n_i \exp\left(\frac{(E_F - E_i(x=0))}{kT}\right) \quad (7)$$

For a low to moderate indirect doping, the effect of the dipole is competing against Fermi level Pinning and therefore majority carriers must be injected via thermionic emission over the barrier at the pinned interface (see Fig. 19a).

$$J_n = A^* T^2 \exp\left(-\frac{e\phi_{BN}}{kT}\right) \left[\exp\left(\frac{qV}{kT}\right) - 1 \right] \quad (8)$$

A weak doping (i.e., low surface potential modification) could be caused by deficiency of dipole orientation or a lack in thickness of the film (Butler and Walsh 2014). Straightforward to understand as the dipole layer inner voltage will be the line integral of the electric field within the film.

However, if dipole strength is enough to provide accumulation at the semiconductor interface, then the barrier becomes very narrow and the tunneling current must become dominant (see Fig. 19b).

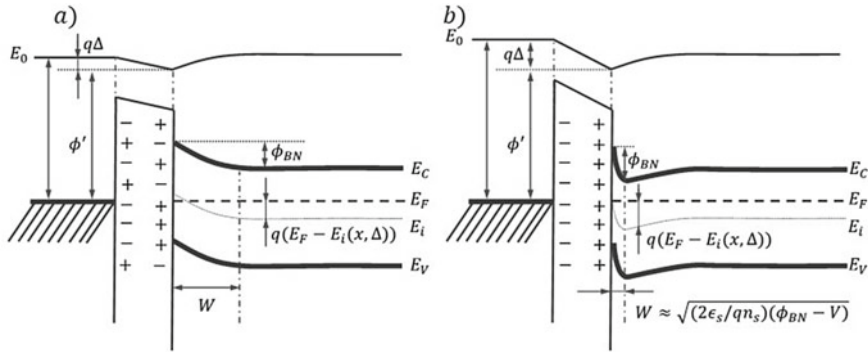


Fig. 19 Effect of the dipole strength in the Metal/Dipole/semiconductor junction, **a** low dipole strength and depleted surface, **b** high dipole strength and electron accumulation providing an ohmic contact

$$I_{\text{tun}} \propto \exp\left(-2W\sqrt{2m_n(q\phi_{BN} - qV)/\hbar^2}\right) \quad (9)$$

In this expression the width of the barrier W can be approximated as $\sqrt{(2\epsilon_s/qn_s)(\phi_{BN} - V)}$ (Sze and Lee 2016), which allows for the tunnel current to be proportional to the exponential of the square root of the interface doping n_s . Which by means of n_s definition is related to charge transfer from the metal into the semiconductor promoted by the vacuum level shift in the dipole.

Nevertheless, while indirect doping is fundamental to overcome Fermi Level Pinning and provide an Ohmic contact with low contact resistance, it is consistently observed in the literature that the thickness dependence of specific contact resistance in these previously analyzed structures (i.e., n-Silicon/Dipole/Aluminum) have an optimum in the range of one nanometer (Fig. 21).

While the injection into the semiconductor improves with the dipole strength and with the thickness of the dipole layer, the insulating nature of these materials present one of the main drawbacks in this technology, injection through the dipole layer. Direct tunneling through the dipole layer into the conduction band is often the conduction mechanism by which these junctions seem to operate, and this can be seen in the thickness dependence of the specific contact resistance. Nevertheless, other mechanisms can be also part of the outcome current.

Thermionic emission of electrons with energies sufficient to overcome the metal–insulator barrier (Fig. 20b).

Fowler–Norheim tunneling in which carrier tunnel through only a partial width of the barrier. In this case, both the average potential barrier height and the tunneling distance are reduced with respect to direct tunneling (Fig. 20c).

Frenkel–Poole emission which due to the emission of trapped electrons into the conduction band of an insulator (Fig. 20d).

Finally other mechanisms could also apply to conduction in dipole layers such as hopping, or trap assisted tunneling.

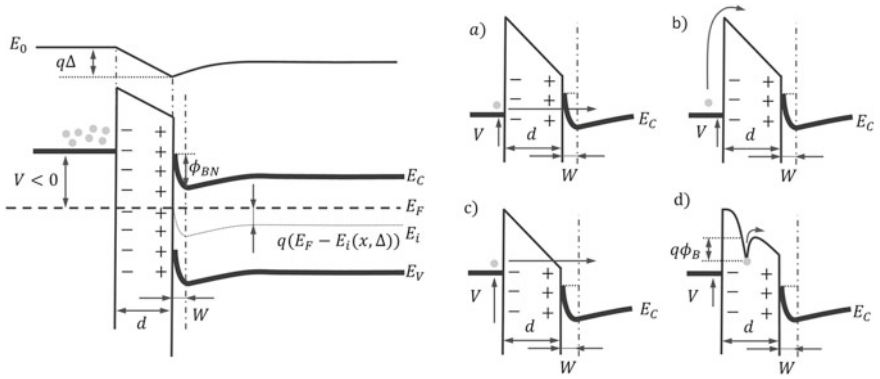


Fig. 20 Main conduction mechanisms through an insulating layer, **a** direct tunneling, **b** Thermionic emission, **c** Fowler–Nordheim tunneling, **d** Frenkel–Poole emission

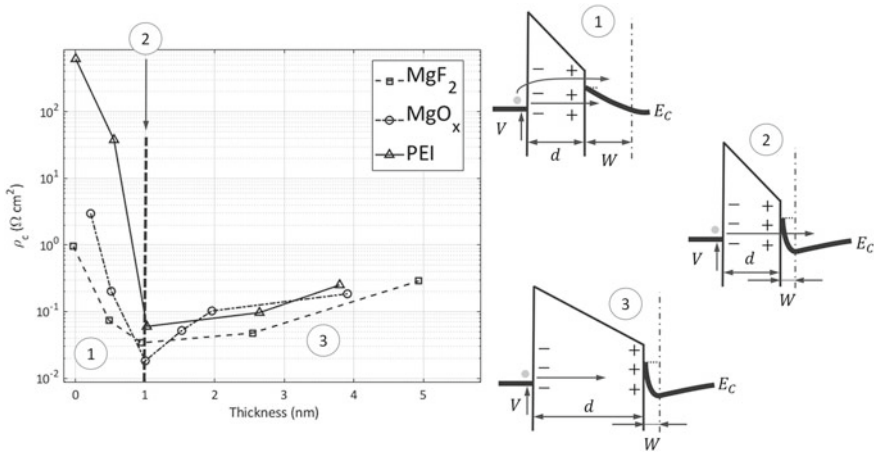


Fig. 21 Specific contact resistance of MgF_2 (Wan et al. 2016a), MgO (Wan et al. 2017b) and PEI as a function of thickness

As a conclusion for a given Metal/Dipole/Semiconductor junction, the dipole potential $q\Delta$ will induce a shift in the vacuum level of the metal and promote an indirect doping of the interface with the semiconductor enhancing the selectivity of one type of charge carrier with respect to the other. Furthermore, the dipole induced doping competes against the Fermi level pinning, narrowing the barrier and allowing a tunneling contact with low contact resistance. Even though the effect of the dipole is enhanced by orientation and dipole layer thickness, conduction through the dipole layer in these types of structures is a thickness limiting factor allowing only the direct tunneling thickness range. When thickness undergoes a certain limit (e.g., 1 nm for MgF_2 , MgO and PEI) the width of the barrier does not allow tunneling as the main

conduction mechanism and carriers must be partially injected via thermionic emission over the pinned surface. These different stages of the junction are summarized in Fig. 21.

Under the optimum thickness corresponds to the thermionic emission regime (Fig. 21(1)) where the contact resistance of the structure is predominantly determined by the injection over a strongly pinned surface. As the Thickness increases the indirect doping of the semiconductor surface the barrier becomes narrow and lower and an optimum contact is achieved (Fig. 21(2)). With a thick enough dipole layer, the resistance of the structure is determined by conduction through the generally insulating layer via direct tunneling as one of the main mechanisms amongst other (Fig. 21(3)).

3.2 *Novel Materials as Carrier Selective Contacts*

This interesting and relatively novel approach to enhance the carrier selectivity using dipole layers was triggered by the use of the interlayer, poly[(9,9-bis(3'-(N,N-dimethylamino)propyl)-2,7-fluorene)-alt-2,7-(9,9-dioctyl-fluorene)] (PFN) in Organic Solar Cells (OSC) (He et al. 2011, 2012). Due to the presence of a significant interfacial electric dipole moment at the PFN interface this was suggested to play an important role in the mechanism of improved selectivity (Chen et al. 2020). In a sense these technologies accomplish good Ohmic contacts by mimicking the effect of low work function metals in the charge distribution of a heterojunction. (e.g., magnesium (Mg) with 3.7 eV (Wan et al. 2016b), or calcium (Ca) with 2.9 eV (Allen et al. 2017)). Nevertheless, providing a good ohmic contact for electrons with Silicon at the cost of an infinite surface recombination velocity is not a perfect fit for a photovoltaic application. Even if passivation can be addressed by use of a passivating layer such as intrinsic amorphous silicon (Wan et al. 2016b) or silicon oxide (Zhang et al. 2018), some of these metals are highly reactive and therefore affect the structure by inducing chemical changes in the passivating film.

A wide library of materials has been used in PV devices, and while for some of them there is still discussion whether their main working principle is the built in potential due to molecular dipole moment, it is consistently observed that they modify the electrode surface potential, while having an insulator like behaviour that obligates to use them in ultra-thin films.

Inorganic molecular dipoles can range from straight forward Alkali or alkaline earth salts, for instance Lithium Fluoride (Zhang et al. 2014a; Kim et al. 2013), MgF_2 (Wan et al. 2016a) and a wide range of alkali or alkaline earth Metallic compounds such as oxides (e.g. MgO_x (Stuckenholtz et al. 2015) (Wan et al. 2017b)) carbonates (e.g., Cs_2CO_3 (Zhang et al. 2015; Wu et al. 2016)) and hydroxides (e.g., $BaOH_2$ (Hossain et al. 2017)).

Organic molecules and polymers are vastly the largest group of dipoles available in the literature. Extensive research can be found on these materials also because of the success of their application in Organic Light Emitting Diodes as Hole/Electron injection layers (An et al. 2019; Ohisa et al. 2018; Lee et al. 2013). They can range from simple organic molecules (e.g. 8-hydroxyquinolinolato-lithium (Zhang et al. 2014b)), organic acids and derivatives (e.g., phosphonic, benzoic and dicarboxylic acids (Rühle et al. 2005)), biologic organic molecules such as amino acids (e.g., Glycine, Histidine, tryptophan (Reichel et al. 2018; Würfel et al. 2016)), Self-Assembled Monolayers (SAMs) (Ford et al. 2014; Lin et al. 2017; Ali et al. 2020) and conjugated polyelectrolytes (e.g. PFN, PEIE, PEI (He et al. 2011, 2012; Ros et al. 2019; Khan et al. 2014; Ji et al. 2020)).

As a counter example, Transition metal oxides such as Titanium Oxide (Yang et al. 2016b) and chromium oxide (Lin et al. 2018). While they can be used as a selective layer in combination with silicon and both type of films possesses a similar insulating nature which forces them to be used in the range of ultrathin films. There is not any evidence pointing that titanium oxide or chromium oxide actively modify the work function of the metallic electrode, therefore the mechanism by which they operate as selective contacts is different to dipole layers. They operate under conduction through conduction band and therefore can be used in larger thickness allowing better blocking properties.

Dipole voltage formation mechanism comes from an internal order between dipoles when used in thin film (Butler and Walsh 2014; Wang et al. 2018). The internally ordered array of dipoles behaves in a similar manner to a polarized insulator with internal dipoles in the bulk canceling each other and surface charge densities at the interfaces with the metal and semiconductor. In this picture, self-assembled monolayers (Fig. 22b) have the highest internal degree of order which can help maximize charge at the interfaces, the length of the aliphatic chain between the anchor and head groups can determine conduction through the MDS junction as in Fig. 20. Inorganic salts and other compounds such as lithium fluoride or organic molecules as Glycine are straightforward molecular dipoles (Fig. 22a). Orientation in these molecules must be a spontaneous process that might be correlated to surface charge and surface crystal structure and could potentially be affected by layer crystallization and dipole cancelation. Conjugated polyelectrolytes have a high degree of disorder due to their amorphous nature. Nevertheless, active charge sites of the CP can be electrostatically attracted to a particular surface forming an effective high-density array of dipoles (Fig. 22c).

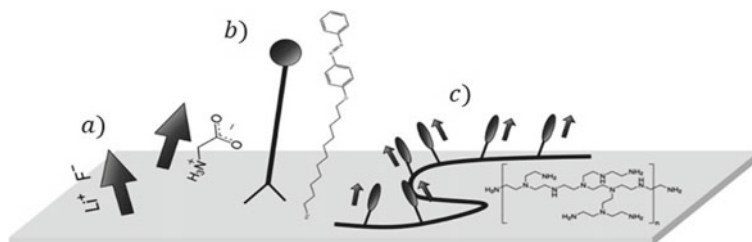


Fig. 22 Schematic representation and example of different type of dipoles **a** inorganic molecular dipole LiF and organic molecular dipole glycine **b** 11-(4-(phenyldiazenyl)phenoxy)undecane-1-tiol. Self assembled monolayer **c** branched Polyethylimine (b-PEI)

Finally, from the chemical perspective, there are many features that can be tuned when designing a dipole interlayer. For example, permanent dipole moment can be enhanced by breaking bond symmetry with strongly electronegative functional groups such as F^- , CN^- (Chen et al. 2020) as well promoting orientation using different wetting layers.

Some of the results of solar cells using carrier selective contacts based on Dipoles in current state of the art have been summarized in following Table 1 including different absorber technologies such as Silicon, Perovskite, and OPV. Interestingly enough, dipole selective contacts are able to provide functional solar cells with significant efficiencies as well as perform with multiple technologies.

4 Summary

This chapter redefines the concept of solar cell as an optical absorber plus two complementary charge-carrier selective contacts. It is demonstrated that p-n junctions are non-essential for photovoltaic generation, but a particular method to separate photo-generated charge-carriers. Heterojunction silicon solar cells have traditionally used heavily doped layers for charge-carrier separation. Here, the most important alternative selective contacts of safe and abundant materials are presented. These new solar cell structures can be fabricated following more simple fabrication routes with important technological advantages.

Table 1 Summary of devices using dipole selective contacts with different absorbers and architectures

Absorber	ETL	HTL	V_{oc}	FF	J_{sc}	PCE	Ref
n-Silicon	L-hystidine	p^+ diffusion	625	76.3	36.8	17.5	(Reichel et al. 2018)
n-Silicon	a-Si:H(i)/b-PEI	a-Si:H(i)/a-Si:H(p)	720	72.9	37	19.4	(Ji et al. 2020)
n-Silicon	a-Si:H(i)/a-Si:H(n)/LiF	a-Si:H(i)/a-Si:H(p)	690	~72	33.62	17.13	(Kim et al. 2013)
n-Silicon	LiF	PEDOT:PSS	570	68	28.71	10.86	(Zhang et al. 2014a)
n-Silicon	a-Si:H/MgF ₂	p^+ diffusion	687	77.3	37.8	20.1	(Wan et al. 2016a)
n-Silicon	Cs ₂ CO ₃ :PEI	PEDOT:PSS	621	68.4	32.2	13.7	(Zhang et al. 2015)
n-Silicon	MgO _x	p^+ diffusion	628.8	80.6	39.5	20	(Wan et al. 2017b)
n-Silicon	a-Si:H(i)/a-Si:H(n)/PFN	V ₂ O ₅	670	76.4	33.6	17.2	(Ros et al. 2019)
n-Silicon	a-Si:H(i)/PFN	V ₂ O ₅	590	78.2	30.1	13.9	(Ros et al. 2019)
n-Silicon (IBC)	Cs ₂ CO ₃	WO _x	539	61.3	37.67	12.44	(Wu et al. 2016)
n-Silicon (IBC)	Cs ₂ CO ₃	MoO _x	594	66.13	38.42	15.09	(Wu et al. 2016)
n-Silicon (IBC)	Cs ₂ CO ₃	V ₂ O ₅	610	70	38.85	16.59	(Wu et al. 2016)
Perovskite	m-TiO ₂ /H OCO-R-NH ₃ ⁺ I ⁻	Spiro-OMeTAD/Au	900	70	18	12	(Ogomi et al. 2014)
Perovskite	m-TiO ₂ /sinapoyl malate	Co (II)/(III)/Au	1130	77	23.6	20.5	(Cao et al. 2018)
Perovskite	m-TiO ₂ /glycine	Spiro-OMeTAD/Au	960	64	21.37	13.14	(Shih et al. 2017)
Perovskite (IBC)	OMeTP	CITP	550	36.7	9.87	1.96	(Lin et al. 2017)
P3HT:ICBA	PEIE/Al	PEDOT:PSS	775	65	9.1	4.6	(Khan et al. 2014)
P3HT:ICBA	PEIE/Ag	PEDOT:PSS	762	63	9.4	4.5	(Khan et al. 2014)
P3HT:ICBA	PEIE/Au	PEDOT:PSS	733	64	7.5	3.5	(Khan et al. 2014)
PCDTBT:PCBM	PFN/Al	PEDOT:PSS	900	62	12.1	6.55	(He et al. 2011)

References

- Ali F, Roldán-Carmona C, Sohail M, Nazeeruddin MK (2020) Applications of self-assembled monolayers for perovskite solar cells interface engineering to address efficiency and stability. *Adv Energy Mater* 10
- Allen TG, Bullock J, Zheng P et al (2017) Calcium contacts to n-type crystalline silicon solar cells. *Prog Photovoltaics Res Appl* 25:636–644. <https://doi.org/10.1002/pip.2838>
- Almora O, Gerling LG, Voz C et al (2017) Superior performance of V_2O_5 as hole selective contact over other transition metal oxides in silicon heterojunction solar cells. *Sol Energy Mater Sol Cells* 168:221–226. <https://doi.org/10.1016/j.solmat.2017.04.042>
- An D, Liu H, Wang S, Li X (2019) Modification of ITO anodes with self-assembled monolayers for enhancing hole injection in OLEDs. *Appl Phys Lett* 114. <https://doi.org/10.1063/1.5086800>
- Avasthi S, Sturm JC (2011) Charge separation and minority carrier injection in P3HT-silicon heterojunction solar cells. In: 2011 37th IEEE photovoltaic specialists conference. IEEE, pp 002487–002489
- Bardeen J (1947) Surface states and rectification at a metal semi-conductor contact. *Phys Rev* 71:717–727. <https://doi.org/10.1103/PhysRev.71.717>
- Battaglia C, de Nicolás SM, De Wolf S et al (2014) Silicon heterojunction solar cell with passivated hole selective MoO_x contact. *Appl Phys Lett* 104:113902. <https://doi.org/10.1063/1.4868880>
- Battaglia C, Cuevas A, De Wolf S (2016) High-efficiency crystalline silicon solar cells: status and perspectives. *Energy Environ Sci* 9:1552–1576. <https://doi.org/10.1039/C5EE03380B>
- Bivour M, Temmler J, Steinkemper H, Hermle M (2015) Molybdenum and tungsten oxide: high work function wide band gap contact materials for hole selective contacts of silicon solar cells. *Sol Energy Mater Sol Cells* 142:34–41. <https://doi.org/10.1016/j.solmat.2015.05.031>
- Bullock J, Cuevas A, Allen T, Battaglia C (2014) Molybdenum oxide MoO_x : a versatile hole contact for silicon solar cells. *Appl Phys Lett* 105:232109. <https://doi.org/10.1063/1.4903467>
- Bullock J, Hettick M, Geissbühler J et al (2016) Efficient silicon solar cells with dopant-free asymmetric heterocontacts. *Nat Energy* 1:15031. <https://doi.org/10.1038/nenergy.2015.31>
- Bullock J, Wan Y, Xu Z et al (2018) Stable dopant-free asymmetric heterocontact silicon solar cells with efficiencies above 20%. *ACS Energy Lett* 3:508–513. <https://doi.org/10.1021/ACS.ENERGYLETT.7B01279>
- Bullock J, Wan Y, Hettick M et al (2019) Dopant-free partial rear contacts enabling 23% silicon solar cells. *Adv Energy Mater* 1803367. <https://doi.org/10.1002/aeam.201803367>
- Butler KT, Walsh A (2014) Ultra-thin oxide films for band engineering: design principles and numerical experiments. In: *Thin Solid Films*. Elsevier, pp 64–68
- Cahen D, Kahn A (2003) Electron energetics at surfaces and interfaces: concepts and experiments. *Adv Mater* 15:271–277. <https://doi.org/10.1002/adma.200390065>
- Cai L, Wang W, Jin L, et al (2019) 12.29% low temperature-processed dopant-free CdS/p-Si heterojunction solar cells. *Adv Mater Interfaces* 6:1900367. <https://doi.org/10.1002/ADMI.201900367>
- Cao J, Lv X, Zhang P et al (2018) Plant sunscreen and Co(II)/(III) porphyrins for UV-resistant and thermally stable perovskite solar cells: from natural to artificial. *Adv Mater* 30. <https://doi.org/10.1002/adma.201800568>
- Chen L, Chen Q, Wang C, Li Y (2020) Interfacial dipole in organic and perovskite solar cells. *J Am Chem Soc* 142:18281–18292. <https://doi.org/10.1021/jacs.0c07439>
- Cho JM, Kim JR, Kim H et al (2014) Effects of hole and electron transporting interlayers for inverted polymer solar cells. *J Nanosci Nanotechnol* 14:6028–6032. <https://doi.org/10.1166/JNN.2014.8783>
- Cuevas A, Yan D (2013) Misconceptions and misnomers in solar cells. *IEEE J PhotovoltS* 3:916–923. <https://doi.org/10.1109/JPHOTOV.2013.2238289>
- Datta S (2012) *Lessons from nanoelectronics : a new perspective on transport*. World Scientific Publishing Co

- Dréon J, Jeangros Q, Cattin J et al (2020) 23.5%-efficient silicon heterojunction silicon solar cell using molybdenum oxide as hole-selective contact. *Nano Energy* 70:104495. <https://doi.org/10.1016/j.nanoen.2020.104495>
- Feldmann F, Ritzau K-U, Bivour M et al (2015) High and low work function materials for passivated contacts. *Energy Procedia* 77:263–270. <https://doi.org/10.1016/j.egypro.2015.07.037>
- Ford WE, Gao D, Knorr N et al (2014) Organic dipole layers for ultralow work function electrodes. *ACS Nano* 8:9173–9180. <https://doi.org/10.1021/nn502794z>
- García-Hernansanz R, García-Hemme E, Montero D et al (2018) Transport mechanisms in silicon heterojunction solar cells with molybdenum oxide as a hole transport layer. *Solar Energy Mater Solar Cells* 185. <https://doi.org/10.1016/j.solmat.2018.05.019>
- Geissbühler J, Werner J, Martin de Nicolas S et al (2015) 22.5% efficient silicon heterojunction solar cell with molybdenum oxide hole collector. *Appl Phys Lett* 107:081601. <https://doi.org/10.1063/1.4928747>
- Gerling LG, Mahato S, Morales-vilches A et al (2016) Transition metal oxides as hole-selective contacts in silicon heterojunctions solar cells. *Sol Energy Mater Sol Cells* 3:109–115. <https://doi.org/10.1016/j.solmat.2015.08.028>
- Gerling LGLG, Voz C, Alcubilla R, Puigdollers J (2017) Origin of passivation in hole-selective transition metal oxides for crystalline silicon heterojunction solar cells. *J Mater Res* 32:260–268. <https://doi.org/10.1557/jmr.2016.453>
- He Z, Zhong C, Huang X et al (2011) Simultaneous enhancement of open-circuit voltage, short-circuit current density, and fill factor in polymer solar cells. *Adv Mater* (deerfield Beach, Fla) 23:4636–4643. <https://doi.org/10.1002/adma.201103006>
- He Z, Zhong C, Su S et al (2012) Enhanced power-conversion efficiency in polymer solar cells using an inverted device structure. *Nat Photonics* 6:593–597. <https://doi.org/10.1038/nphoton.2012.190>
- He J, Gao P, Yang Z, et al (2017) Silicon/organic hybrid solar cells with 16.2% efficiency and improved stability by formation of conformal heterojunction coating and moisture-resistant capping layer. *Adv Mat* 29:1606321. <https://doi.org/10.1002/ADMA.201606321>
- He J, Zhang W, Ye J, Gao P (2018) 16% efficient silicon/organic heterojunction solar cells using narrow band-gap conjugated polyelectrolytes based low resistance electron-selective contacts. *Nano Energy* 43:117–123. <https://doi.org/10.1016/j.nanoen.2017.11.025>
- Hossain J, Kasahara K, Harada D et al (2017) Barium hydroxide hole blocking layer for front- and back-organic/crystalline Si heterojunction solar cells. *J Appl Phys* 122:055101. <https://doi.org/10.1063/1.4985812>
- Hsu W, Sutter-Fella CM, Hettick M, et al (2015) Electron-selective TiO₂ contact for Cu(In,Ga)Se₂ solar cells. *Sci Rep* 2015 5(1 5):1–7. <https://doi.org/10.1038/srep16028>
- Jean J, Mahony T, Bozyigit D et al (2017) Radiative efficiency limit with band tailing exceeds 30% for quantum dot solar cells. *ACS Energy Lett* 2:2616–2624. <https://doi.org/10.1021/acsenenergylett.7b00923>
- Ji W, Allen T, Yang X et al (2020) Polymeric electron-selective contact for crystalline silicon solar cells with an efficiency exceeding 19%. *ACS Energy Lett* 5:897–902. <https://doi.org/10.1021/acsenenergylett.0c00110>
- Juarez-Perez EJ, Wußler M, Fabregat-Santiago F et al (2014) Role of the selective contacts in the performance of lead halide perovskite solar cells. *J Phys Chem Lett* 5:680–685. <https://doi.org/10.1021/jz500059v>
- Khan TM, Zhou Y, Dindar A et al (2014) Organic photovoltaic cells with stable top metal electrodes modified with polyethylenimine. In: *ACS Applied Materials and Interfaces*. American Chemical Society, pp 6202–6207
- Kim S, Lee J, Dao VA et al (2013) Effects of LiF/Al back electrode on the amorphous/crystalline silicon heterojunction solar cells. *Mater Sci Eng B: Solid-State Mater Adv Technol* 178:660–664. <https://doi.org/10.1016/j.mseb.2012.10.029>

- Lee W, Seo J, Woo H (2013) Conjugated polyelectrolytes: a new class of semiconducting material for organic electronic devices. *Polymer* 54:5104–5121. <https://doi.org/10.1016/j.polymer.2013.07.015>
- Lin X, Jumabekov AN, Lal NN et al (2017) Dipole-field-assisted charge extraction in metal-perovskite-metal back-contact solar cells. *Nat Commun* 8:613. <https://doi.org/10.1038/s41467-017-00588-3>
- Lin W, Dréon J, Zhong S et al (2021) Dopant-free bifacial silicon solar cells. *Solar RRL* 5:2000771. <https://doi.org/10.1002/SOLR.202000771>
- Lin W, Wu W, Liu Z et al (2018) Chromium trioxide hole-selective heterocontacts for silicon solar cells. In: 2018 IEEE 7th World conference on photovoltaic energy conversion, WCPEC 2018—a joint conference of 45th IEEE PVSC, 28th PVSEC and 34th EU PVSEC. Institute of Electrical and Electronics Engineers Inc., pp 2045–2047
- Luis G G, Masmitja G, Ortega P et al (2017) Passivating/hole-selective contacts based on V_2O_5/SiO_x stacks deposited at ambient temperature. *Energy Procedia* 124:584–592. <https://doi.org/10.1016/j.egypro.2017.09.294>
- Mahato S, Gerling LG, Voz C et al (2016) PEDOT:PSS as an alternative hole selective contact for ITO-free hybrid crystalline silicon solar cell. *IEEE J PhotovoltS* 6:934–939. <https://doi.org/10.1109/JPHOTOV.2016.2557072>
- Masmitja G, Gerling LG, Ortega P et al (2017) V_2O_x -based hole-selective contacts for c-Si interdigitated back-contacted solar cells. *J Mater Chem A* 5. <https://doi.org/10.1039/c7ta01959a>
- Masmitja G, Ortega P, Puigdollers J et al (2018) Interdigitated back-contacted crystalline silicon solar cells with low-temperature dopant-free selective contacts. *J Mater Chem A* 6:3977–3985. <https://doi.org/10.1039/C7TA11308K>
- Messmer C, Bivour M, Schön J et al (2018) Numerical simulation of silicon heterojunction solar cells featuring metal oxides as carrier-selective contacts. *IEEE J PhotovoltS* 1:1–9. <https://doi.org/10.1109/JPHOTOV.2018.2793762>
- Mews M, Lemaire A, Korte L (2017) Sputtered tungsten oxide as hole contact for silicon heterojunction solar cells. *IEEE J PhotovoltS* 7:1209–1215. <https://doi.org/10.1109/JPHOTOV.2017.2714193>
- Muller R, Richter A, Hermle M, et al (2018) Passivating and carrier-selective contacts—basic requirements and implementation, pp 2064–2069. <https://doi.org/10.1109/pvsc.2017.8366202>
- Nasser H, Es F, Borra MZ et al (2021) On the application of hole-selective MoO_x as full-area rear contact for industrial scale p-type c-Si solar cells. *Prog Photovoltaics Res Appl* 29:281–293. <https://doi.org/10.1002/PIP.3363>
- Nayak M, Mandal S, Pandey A et al (2019) Nickel oxide hole-selective heterocontact for silicon solar cells: role of SiO_x interlayer on device performance. *Solar RRL* 3:1900261. <https://doi.org/10.1002/SOLR.201900261>
- Neamen DA (2012) *Semiconductor physics and devices: basic principles*. McGraw-Hill
- NREL Homepage (2021). <https://www.nrel.gov/pv/cell-efficiency.html>, last accessed 2021/08/01
- Ogomi Y, Morita A, Tsukamoto S et al (2014) All-solid perovskite solar cells with $HOCO-R-NH_3^+I^-$ anchor-group inserted between porous titania and perovskite. *J Phys Chem C* 118:16651–16659. <https://doi.org/10.1021/jp412627n>
- Ohisa S, Kato T, Takahashi T et al (2018) Conjugated polyelectrolyte blend with polyethyleneimine ethoxylated for thickness-insensitive electron injection layers in organic light-emitting devices. *ACS Appl Mater Interfaces* 10:17318–17326. <https://doi.org/10.1021/acsami.8b00752>
- Ratcliff EL, Zacher B, Armstrong NR (2011) Selective interlayers and contacts in organic photovoltaic cells. *J Phys Chem Lett* 2:1337–1350. <https://doi.org/10.1021/JZ2002259>
- Reichel C, Würfel U, Winkler K et al (2018) Electron-selective contacts via ultra-thin organic interface dipoles for silicon organic heterojunction solar cells. *J Appl Phys* 123. <https://doi.org/10.1063/1.5010937>
- Ros E, Barquera Z, Ortega PR et al (2019) Improved electron selectivity in silicon solar cells by cathode modification with a dipolar conjugated polyelectrolyte interlayer. *ACS Applied Energy Materials* 2:5954–5959. <https://doi.org/10.1021/acsaem.9b01055>

- Rühle S, Greenshtein M, Chen S-G et al (2005) Molecular adjustment of the electronic properties of nanoporous electrodes in dye-sensitized solar cells. *J Phys Chem B* 109:18907–18913. <https://doi.org/10.1021/jp0514123>
- Shih YC, Lan YB, Li CS et al (2017) Amino-acid-induced preferential orientation of perovskite crystals for enhancing interfacial charge transfer and photovoltaic performance. *Small* 13. <https://doi.org/10.1002/sml.201604305>
- Stuckenholtz S, Büchner C, Heyde M, Freund HJ (2015) MgO on Mo(001): local work function measurements above pristine terrace and line defect sites. *J Phys Chem C* 119:12283–12290. <https://doi.org/10.1021/jp512575n>
- Sze SM, Lee MK (2016) *Semiconductor devices physics and technology*
- The Feynman Lectures on Physics, Homepage (2021). <https://www.feynmanlectures.caltech.edu/>, last accessed 2021/08/01
- Tsai M-L, Su S-H, Chang J-K et al (2014) Monolayer MoS₂ heterojunction solar cells. *ACS Nano* 8:8317–8322. <https://doi.org/10.1021/NN502776H>
- Wan Y, Samundsett C, Bullock J et al (2016a) Magnesium fluoride electron-selective contacts for crystalline silicon solar cells. *ACS Appl Mater Interfaces* 8:14671–14677. <https://doi.org/10.1021/acsami.6b03599>
- Wan Y, Samundsett C, Yan D et al (2016b) A magnesium/amorphous silicon passivating contact for n-type crystalline silicon solar cells. *Appl Phys Lett* 109. <https://doi.org/10.1063/1.4962960>
- Wan Y, Karuturi SK, Samundsett C et al (2017a) Tantalum oxide electron-selective heterocontacts for silicon photovoltaics and photoelectrochemical water reduction. *ACS Energy Lett* 3:125–131. <https://doi.org/10.1021/ACSENERGYLETT.7B01153>
- Wan Y, Samundsett C, Bullock J et al (2017b) Conductive and stable magnesium oxide electron-selective contacts for efficient silicon solar cells. *Adv Energy Mater* 7. <https://doi.org/10.1002/aenm.201601863>
- Wang C, Luo Y, Zheng J et al (2018) Spontaneous interfacial dipole orientation effect of acetic acid solubilized PFN. *ACS Appl Mater Interfaces* 10:10270–10279. <https://doi.org/10.1021/acsami.8b00975>
- Wu W, Bao J, Jia X et al (2016) Dopant-free back contact silicon heterojunction solar cells employing transition metal oxide emitters. *Phys Status Solidi-Rapid Res Lett* 10:662–667. <https://doi.org/10.1002/pssr.201600254>
- Würfel U, Cuevas A, Würfel P (2015) Charge carrier separation in solar cells. *IEEE J PhotovoltS* 5:461–469. <https://doi.org/10.1109/JPHOTOV.2014.2363550>
- Würfel U, Seßler M, Unmüßig M et al (2016) How molecules with dipole moments enhance the selectivity of electrodes in organic solar cells—a combined experimental and theoretical approach. *Adv Energy Mater* 6. <https://doi.org/10.1002/aenm.201600594>
- Würfel P, Würfel U (2009) *Physics of solar cells: from principles to new concepts*, second Up. Wiley-VCH Verlag GmbH & Co., Weinheim, Germany
- Würfel P, Würfel U (2016) *Physics of solar cells: from basic principles to advanced concepts*
- Yang X, Bi Q, Ali H et al (2016a) High-performance TiO₂-based electron-selective contacts for crystalline silicon solar cells. *Adv Mater* 28:5891–5897. <https://doi.org/10.1002/adma.201600926>
- Yang X, Zheng P, Bi Q, Weber K (2016) Silicon heterojunction solar cells with electron selective TiO_x contact. *Sol Energy Mater Sol Cells* 150:32–38. <https://doi.org/10.1016/j.solmat.2016.01.020>
- Yang X, Weber K, Hameiri Z, De WS (2017) Industrially feasible, dopant-free, carrier-selective contacts for high-efficiency silicon solar cells. *Prog Photovoltaics Res Appl* 25:896–904. <https://doi.org/10.1002/PIP.2901>
- Yang X, Aydin E, Xu H et al (2018) Tantalum nitride electron-selective contact for crystalline silicon solar cells. *Adv Energy Mater* 8:1800608. <https://doi.org/10.1002/aenm.201800608>
- Yang X, Liu W, De Bastiani M et al (2019) Dual-function electron-conductive, hole-blocking titanium nitride contacts for efficient silicon solar cells. *Joule* 3:1314–1327. <https://doi.org/10.1016/J.JOULE.2019.03.008>

- Yang X, Xu H, Liu W et al (2020) Atomic layer deposition of vanadium oxide as hole-selective contact for crystalline silicon solar cells. *Adv Electron Mater* 6:2000467. <https://doi.org/10.1002/AELM.202000467>
- Zhang Y, Cui W, Zhu Y et al (2015) High efficiency hybrid PEDOT:PSS/nanostructured silicon Schottky junction solar cells by doping-free rear contact. *Energy Environ Sci* 8:297–302. <https://doi.org/10.1039/c4ee02282c>
- Zhang X, Wan Y, Bullock J et al (2016) Low resistance Ohmic contact to p-type crystalline silicon via nitrogen-doped copper oxide films. *Appl Phys Lett* 109:052102. <https://doi.org/10.1063/1.4960529>
- Zhang Y, Liu R, Lee ST, Sun B (2014a) The role of a LiF layer on the performance of poly(3,4-ethylenedioxythiophene):poly(styrenesulfonate)/Si organic-inorganic hybrid solar cells. *Appl Phys Lett* 104. <https://doi.org/10.1063/1.4866968>
- Zhang Y, Zu F-S, Lee S et al (2014b) Heterojunction with organic thin layers on silicon for record efficiency hybrid solar cells. *Adv Energy Mater* 4. <https://doi.org/10.1002/aenm.201300923>
- Zhang Z, Liao M, Tong H et al (2018) Tunnel oxide—magnesium as electron-selective passivated contact for n-type silicon solar cell. *Solar RRL* 2. <https://doi.org/10.1002/solr.201800241>
- Zheng Y, Jiang B, Gao Z et al (2019) Optimization of SnO₂-based electron-selective contacts for Si/PEDOT:PSS heterojunction solar cells. *Sol Energy* 193:502–506. <https://doi.org/10.1016/j.solener.2019.09.077>
- Zhong S, Morales-Masis M, Mews M et al (2019) Exploring co-sputtering of ZnO: Al and SiO₂ for efficient electron-selective contacts on silicon solar cells. *Sol Energy Mater Sol Cells* 194:67–73. <https://doi.org/10.1016/J.SOLMAT.2019.02.005>
- Zielke D, Niehaves C, Lövenich W et al (2015) Organic-silicon solar cells exceeding 20% efficiency. *Energy Procedia* 77:331–339. <https://doi.org/10.1016/j.egypro.2015.07.047>

Perovskite Solar Cells: Concepts and Prospects



C. V. Mary Vijila, Aldrin Antony, and M. K. Jayaraj

1 Introduction to Metal–Organic Perovskites

Perovskites are materials having the chemical formula ABX_3 . The first perovskite, calcium titanate ($CaTiO_3$), was discovered in 1839 by German mineralogist Gustav Rose. Materials with a similar chemical structure were named perovskites after Russian mineralogist Lev A. Perovski. These oxides exhibited excellent magnetic properties, electrical conductivity, and ferroelectric properties. Organometal halides-based perovskites have recently gained much attention in optoelectronic devices. The electrical and optical properties of these materials are most suitable for photovoltaics and other optoelectronic device applications. They are named hybrid perovskites since they contain both organic and inorganic components. In addition, it is even possible to tune their electrical and optical properties by using mixed organic (mixture of methylammonium CH_3NH_3) and inorganic cations (mixture of Pb, Sn) and mixed halides (I, Cl, and Br).

C. V. M. Vijila (✉) · A. Antony
Department of Physics, Cochin University of Science and Technology, Kochi, Kerala 682022,
India
e-mail: maryvijilacv157@cusat.ac.in

A. Antony
Centre of Excellence in Advanced Materials, Cochin University of Science and Technology,
Kochi, Kerala 682022, India

M. K. Jayaraj
University of Calicut, Malappuram, Kerala 673635, India

1.1 Crystal Structure

Perovskites, having general chemical formula ABX_3 , commonly occur in a cubic structure as shown in Fig. 1a, where cations ‘A’ with an oxidation state +1 located at the corners of the cube, cation B with an oxidation state +2 at the body centre, and anions X with an oxidation state -1 at the face centres. Alternatively, it is an octahedral arrangement in three-dimensional space, Fig. 1b. BX_6 anions with an oxidation state -4 form the octahedral units. Cations A placed inside the voids of the octahedral arrangement have an oxidation state +1. The perovskites acquire symmetric cubic structure only if the radii of ions A, B, and X satisfy Goldschmidt tolerance factor t given by the equation,

$$t = \frac{R_A + R_X}{\sqrt{2}(R_B + R_X)} \approx 1 \quad (1)$$

Here, R_A , R_B , and R_X represent the radii of ions A, B, and X, respectively. To satisfy the requirement for cubic lattice (α phase), cation A must be of considerable size than B (lead or tin). Methylammonium (CH_3NH_3) ion is large enough to hold the crystal in a cubic structure. The cubic structure exists for the values of t lying between 0.89 and 1. Smaller t leads to less symmetrical tetragonal (β) or orthorhombic (γ) crystal structures. The tolerance factor > 1 , will destabilize the three-dimensional structure of perovskite and will lead to a non-perovskite (δ) phase. Γ phase is more stable than α and β phases at zero kelvin since it is not easy to satisfy $t = 1$ at low temperatures. At a finite temperature, transitions between these phases occur (Yin et al. 2015). The unit cell parameter, ‘a’ of cubic perovskite $CH_3NH_3PbX_3$, varies with the size of X anion as 6.27, 5.92, and 5.68 Å for X = I, Br, and Cl, respectively (Jung and Park 2015).

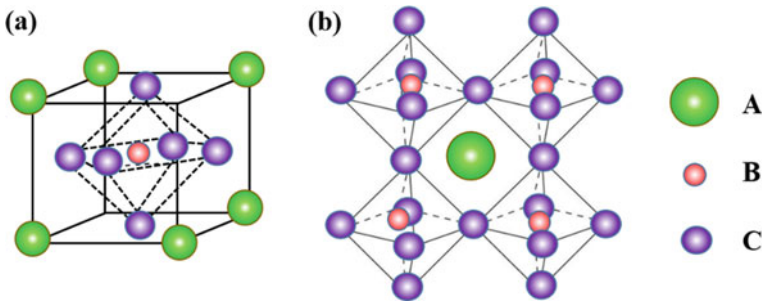


Fig. 1 Crystal structure of perovskite ABX_3

1.2 Methylammonium Lead Iodide

Methylammonium lead iodides ($\text{CH}_3\text{NH}_3\text{PbI}_3$) are the most commonly used material in solar cell application due to their optimum low bandgap compared to other halide perovskites. The experimental value of the energy bandgap is 1.55 eV. $\text{CH}_3\text{NH}_3\text{PbI}_3$ stabilizes in tetragonal crystal structure with $14/m$ space group under ambient temperatures and transforms into an orthorhombic structure (space group Pnma) at low temperatures (Poglitsch and Weber 1987). The lattice parameters corresponding to tetragonal structure are $a = 8.86 \text{ \AA}$, $b = 12.66 \text{ \AA}$, $c = 8.86 \text{ \AA}$ and for orthorhombic structure the values are, $a = 8.86 \text{ \AA}$, $b = 12.62 \text{ \AA}$, $c = 8.58 \text{ \AA}$ (Kim et al. 2014). $\text{CH}_3\text{NH}_3\text{PbI}_3$ exhibits a p or n -type nature due to the presence of different defects. Two major kinds of defects in perovskites are the Schottky defect (the presence of an equal number of positive and negative vacancies) and the Frenkel defect consisting of an equal number of vacancies and the same ion in the interstitials. The formation energy of different defects in perovskites is low. The relative quantity of precursors such as methylammonium iodide ($\text{CH}_3\text{NH}_3\text{I}$) and lead iodide (PbI_2) determine different defects. Schottky defects will not form any trap states within the bandgap. However, Frenkel defects form shallow levels near the energy gap and result in unintentional p or n -type doping. Thus by varying the atomic composition of precursors, we can synthesize doped perovskites (Kim et al. 2014).

1.3 Mixed Halides and Mixed Cation Perovskites

In the perovskite ABX_3 structure, we mix different halides (X anions), organic, and inorganic (A and B) cations to tune their properties. Methylammonium lead iodides ($\text{CH}_3\text{NH}_3\text{PbI}_3$, MAPbI_3) with an energy bandgap of 1.55 eV have application in solar cells. The band gaps of $\text{CH}_3\text{NH}_3\text{PbBr}_3$ and $\text{CH}_3\text{NH}_3\text{PbCl}_3$ are 2.3 eV and 3.11 eV, respectively. Due to higher bandgaps, they could find application in tandem solar cells. By mixing different halide groups, we can tune the bandgap in between this range. Sn and Ge can be used as B site substitutes since they are from the same 14th group as Pb. Partial substitution of Sn for Pb can lower the bandgap. Transition metals like Cu, Mn, Fe, Co, and Ni are also possible alternatives. Nevertheless, their smaller ionic radii compared to Pb lead to layered structures (Boix et al. 2015). There can be many monoammonium and diammonium ion substitutes for the A site. However, to form a 3D material or fit into octahedral voids of BX_6 anions, the ionic radii have to satisfy the Goldschmidt tolerance factor. Organic cations at the 'A' site do not determine band structure but can cause expansion and contraction to the lattice depending on their size. Methylammonium (CH_3NH_3^+) is the smallest among possible organic cations. A slightly larger cation formamidinium $\text{CH}(\text{NH}_2)_2^+$ will cause a decrease in bandgap to 1.48 eV (Eperon et al. 2014). Other larger monoammonium and diammonium cations such as ethane 1, 2—diammonium ($^+\text{H}_3\text{N}(\text{CH}_2)_2\text{NH}_3^+$, EDA^{2+}), propane 1, 3—diammonium ($^+\text{H}_3\text{N}(\text{CH}_2)_3\text{NH}_3^+$,

PDA²⁺) and hexane 1, 6—diammonium (⁺H₃N(CH₂)₆NH₃⁺, HDA²⁺) lead to 2D or hybrid 2D, 3D structures with better stability towards moisture and heat (Lu et al. 2017).

2 Properties of Perovskites

2.1 Optical Properties

High light absorption coefficient: A very high optical absorption coefficient ($10^4 - 10^5 \text{ cm}^{-1}$) is a desirable characteristic that makes perovskites a promising material for solar cells. A perovskite film having a thickness of only 500 nm can absorb about 15% of incident sunlight. The absorption coefficient is determined by the nature of transition—direct or indirect types and joint density of states in the conduction band and valence bands. Figure 2a-c shows a schematic illustration of the absorption mechanisms in Si, GaAs, and halide perovskites, respectively. Transitions from p to p and s orbitals of Si represent its optical absorption close to the band edge. The probability of this transition is very low since silicon is an indirect bandgap material. GaAs and halide perovskites have a direct bandgap with different electronic structures. The bottom of the perovskite conduction band consists of degenerate p bands, which are less dispersed. Less dispersed p bands lead to a higher density of states (DOS) and a greater transition probability. Besides, the band edge transition of CH₃NH₃PbBr₃ is from the s orbital of Pb and p orbital of I to the p orbital of Pb. The transition probability is considerable between the orbitals of the same element (Pb s to Pb p). Thus the absorption coefficient of halide perovskites is about one order greater than that for GaAs.

Bandgap tuning: The bandgap of CH₃NH₃PbI₃ (MAPbI₃) is around 1.5 eV, which is not the optimum for the fabrication of high-efficiency solar cells according to the Shockley-Queisser limit. Tuning of bandgap by replacing cations and anions can extend the absorption to longer wavelengths. Swapping of methylammonium (MA⁺) cation with formamidinium CH(NH₂)₂⁺ (FA⁺) reduces the bandgap by about 0.07 eV and extends the absorption wavelength. Replacing Pb²⁺ partially with Sn²⁺ in MAPbI₃ reduces the bandgap to 1.17 eV. Changing halide anions result in modifying the bandgap. In tetragonal MAPbX₃, bandgap varies as 1.55, 1.78, and 1.55 eV for I⁻, Br⁻ and Cl⁻ respectively. It is 1.55, 2, and 3.11 eV in cubic structure for I⁻, Br⁻ and Cl⁻ respectively. Figure 3 shows the variation in the bandgap, valence band maximum (VBM), and conduction band minimum (CBM) by ion swapping (Jung and Park 2015).

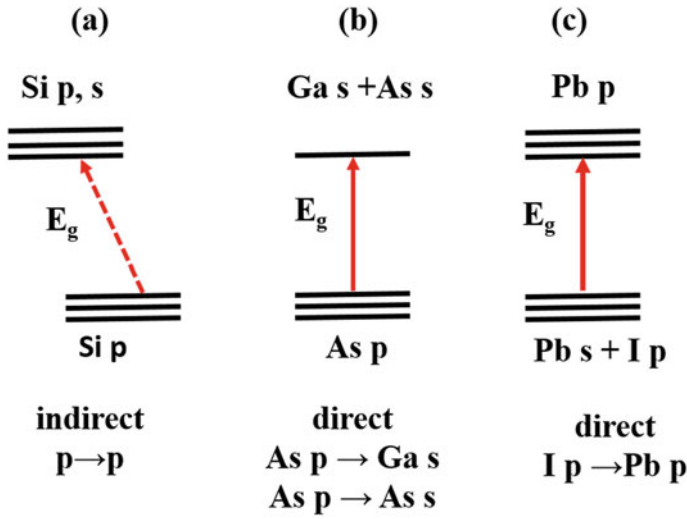
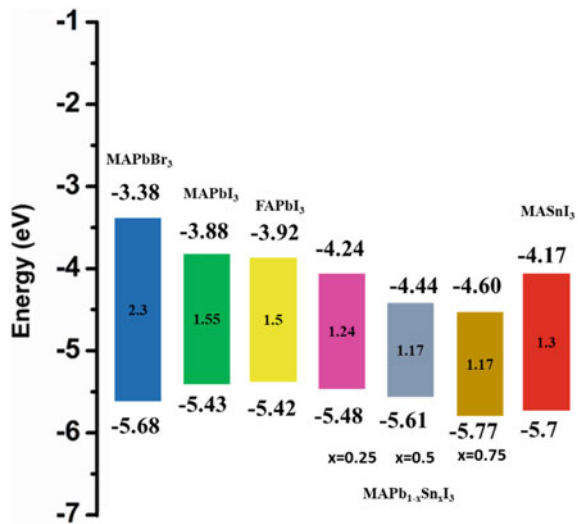


Fig. 2 Schematic diagram of optical absorption in **a** indirect bandgap semiconductor silicon, **b** direct bandgap semiconductor GaAs and **c** $CH_3NH_3PbI_3$

Fig. 3 Energy band diagram of different organic metal halides



2.2 Electrical Properties

Ambipolar Conductivity, Carrier Mobility, and Diffusion Length: Balanced effective mass, m^* of electrons, and holes in perovskites provide them ambipolar conductivity. The effective mass of electron or hole is given by,

$$m^* = \hbar^2 \left[\frac{\partial^2 \varepsilon(k)}{\partial k^2} \right]^{-1} \quad (2)$$

Here, $\varepsilon(k)$ is the energy dispersion function. A more dispersive band near the band edge gives a low effective mass of electron or hole. For direct bandgap semiconductors such as GaAs, the top of the valence band (VBM) consists of p orbital of arsenic and is less dispersed. The bottom of the conduction band (CBM) consists of s orbitals of gallium and arsenic hence more dispersed since it is at higher energy. Thus, the effective mass of electrons in the more dispersed conduction band is lower than that of the hole. However, in the case of $\text{CH}_3\text{NH}_3\text{PbI}_3$ perovskites, the situation is reversed. The CBM of $\text{CH}_3\text{NH}_3\text{PbI}_3$ consists of p orbitals of Pb, and the VBM consists of a mixture of s orbitals of Pb and p orbitals of I. Strong s – p coupling in VBM makes its upper part dispersive. Moreover, the CBM formed by p bands is dispersive since they are at higher energy. Hence the electron and hole m^* of perovskite are balanced (Yin et al. 2015).

The distance that a free carrier can cover before recombination is known as diffusion length. The diffusion length of polycrystalline $\text{CH}_3\text{NH}_3\text{PbI}_{3-x}\text{Cl}_x$ and $\text{CH}_3\text{NH}_3\text{PbI}_3$ are 10 and 4 μm , respectively. Single crystal perovskites $\text{CH}_3\text{NH}_3\text{PbI}_3$ have even longer diffusion lengths $\sim 175 \mu\text{m}$. Carrier mobility of $\text{CH}_3\text{NH}_3\text{PbI}_3$ films prepared by different methods are different and is about $20 \text{ cm}^2 \text{ V}^{-1} \text{ s}^{-1}$ (Dong et al. 2015; Adinolfi et al. 2017).

3 3D and Low Dimensional Structures

Low dimensional perovskites, including 0-dimensional quantum dots and nanocrystals, 1—dimensional nano-rods and nanowires, and 2—dimensional nanosheets and platelets, display different optical and stability properties compared to their bulk counterpart. As mentioned earlier in Sect. 1.1, 3D perovskites consist of three-dimensionally arranged BX_6^{4-} octahedral units. Here, cations A occupy the octahedral voids. The chemical formula for three-dimensional perovskite thus becomes ABX_3 . These bulk perovskites have low exciton binding energy ranging between 20–50 meV, resulting in weakly bound excitons and inefficient radiative recombination. Bulk perovskites are unstable and decompose into their precursors in the presence of moisture, oxygen, high temperatures, and UV rays, leading to degradation of device performance.

Introducing larger organic cations such as derivatives of phenylamine inside 3D perovskite structure transforms them into forms with alternating organic and inorganic layers. These are generally known as 2D perovskites and consist of pure 2D and quasi 2D perovskites. The chemical formula for a 2D perovskite is $\text{R}_2\text{A}_{n-1}\text{M}_n\text{X}_{3n+1}$. Here, R represents a long chain organic cation that neither satisfies the tolerance factor nor fits into the octahedral voids of MX_6 units, thus separating each metal halide layer from the other. In the formula, A represents smaller organic cation such

as methylammonium that satisfies the tolerance factor, and n gives the number of consecutive inorganic layers. $n = 1$ results R_2MX_4 corresponding to pure 2D and $n = \infty$ result in AMX_3 , bulk 3D perovskite. Figure 4 shows the perovskite structures with $n = 1, 2$, and infinity. These alternatives are highly stable in ambient conditions and high temperatures. The superior stability of 2D perovskites is due to hydrophobic, long-chain organic cations that protect inorganic layers. Also, the energy to disrupt these structures is higher than their 3D analogues. Organic and inorganic units form covalent, ionic bonds in between them. In addition, the Van der Waals force between adjacent long-chain organic cations also provides extra stability towards ambient conditions. These interactions include the covalent and ionic bonds within the inorganic layer, interactions between organic and inorganic components, and the weak van der Waals forces within the organic layer. Besides, the long-chain organic cations extend to a broader space interacting via van der Waals force with each other. However, the organic layers surrounding inorganic sheets will reduce the mobility of charge carriers (Ma et al. 2018).

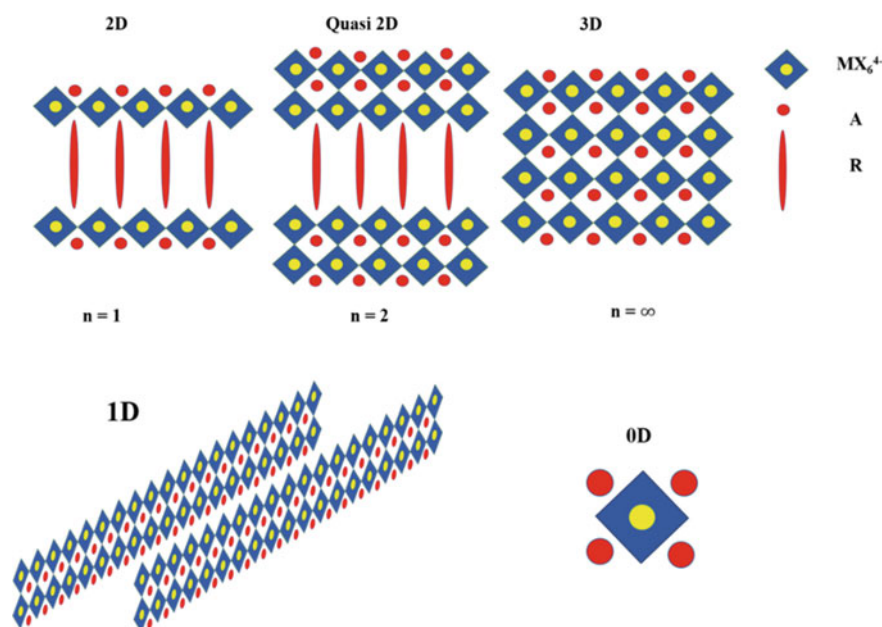


Fig. 4 Structural diagrams of perovskites with different dimensions ($n = 1$, pure 2D structure, $n = \infty$, 3D structure $1 < n < \infty$, quasi 2D or quasi 1D structure and 0D structure)

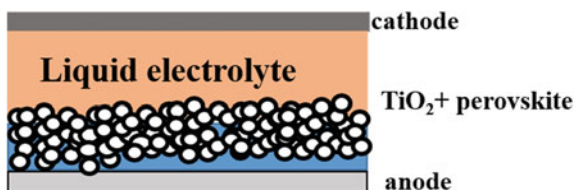
4 Perovskite Sensitized Solar Cells Using Liquid Electrolyte

Dye-sensitized solar cells (DSSCs) generally use organic dye molecules to sensitize a wide bandgap photo-electrode. Nevertheless, their absorption coefficient is very low. Perovskites are direct bandgap semiconductors with an exceptionally high absorption coefficient and bandgap tunability. The absorption coefficient of perovskite nanocrystals is about one order greater than that of N719, a commonly used organic dye in DSSCs. Nano-crystalline perovskite particles act as sensitizers in perovskite sensitized solar cells. In 2009, the first perovskite sensitized solar cell was fabricated by Miyasaka et al. (Kojima et al. 2009). A schematic diagram of the perovskite-based dye-sensitized solar cell is shown in Fig. 5. A photo-electrode (anode) is formed on Fluorine doped tin dioxide (FTO) (its transparency and conductivity are well known) by coating a mesoporous TiO_2 film from commercially available nano-crystalline TiO_2 paste by screen printing and sintering at 480°C . A nano-crystalline perovskite film is formed over mesoporous TiO_2 by spin coating precursor solution of perovskite ($\text{CH}_3\text{NH}_3\text{PbX}$ and PbX_2 in N, N—dimethylformamide) and drying. A counter electrode (cathode) is prepared by Pt coated FTO glass. A $5\ \mu\text{m}$ separator film separates the two electrodes. An electrolyte solution of lithium halide and halogen redox couple fills up the space between two electrodes.

4.1 Operating Principle

Mesoporous TiO_2 adsorbs perovskite nanocrystals onto its large surface area. Figure 6 shows the band structure of perovskites $\text{CH}_3\text{NH}_3\text{PbI}_3$, $\text{CH}_3\text{NH}_3\text{PbBr}_3$, and TiO_2 layers. When light is incident on the cell, the perovskite sensitizers absorb photons and get oxidized by an exciting electron from the valence band to the conduction band. The values of conduction band levels of perovskites are $-4\ \text{eV}$ and $-3.36\ \text{eV}$ for $\text{CH}_3\text{NH}_3\text{PbI}_3$ and $\text{CH}_3\text{NH}_3\text{PbBr}_3$, respectively. This allows the transport of excited electrons from the conduction level of perovskite to that of the TiO_2 at $-4.1\ \text{eV}$. These electrons get extracted to the external circuit through the load resistance. The electrolyte (lithium halide—halogen redox couple) regenerates the oxidized perovskites by donating electrons. Figure 7a shows the perovskite sensitized solar cell circuit, and Fig. 7b represents the photocurrent—voltage characteristics of perovskite solar cells with $\text{CH}_3\text{NH}_3\text{PbBr}_3$ and $\text{CH}_3\text{NH}_3\text{PbI}_3$ as sensitizers.

Fig. 5 The device structure of a perovskite sensitized solar cell with liquid electrolyte



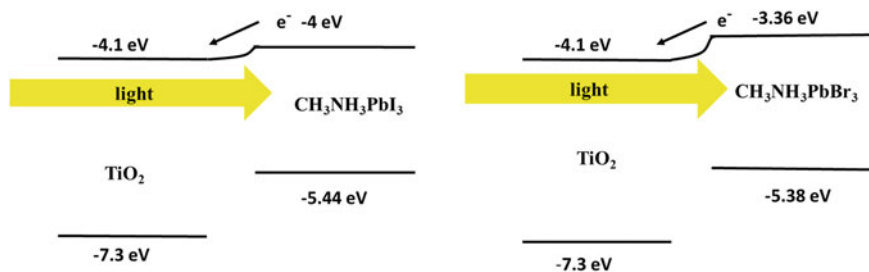


Fig. 6 Energy band diagram and motion of electron of solar cells

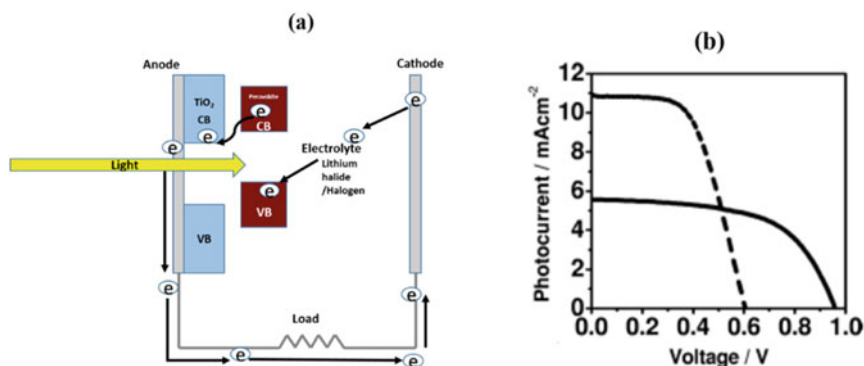


Fig. 7 a Principle of operation of a perovskite sensitized solar cell having liquid electrolyte. b Photocurrent and Voltage characteristics of perovskite solar cell with $\text{CH}_3\text{NH}_3\text{PbBr}_3$ (solid) and $\text{CH}_3\text{NH}_3\text{PbI}_3$ (dashed) as sensitizers. [Reprinted with permission from (Kojima et al. 2009) Copyright (2009) © American Chemical Society]

Table 1 summarizes the characteristics of the solar cells sensitized with $\text{CH}_3\text{NH}_3\text{PbBr}_3$ and $\text{CH}_3\text{NH}_3\text{PbI}_3$, respectively (data obtained from (Kojima et al. 2009)). The efficiencies of perovskite sensitized solar cells are higher than the conventional organic dye-based cells.

Table 1 Short circuit current density J_{SC} , open-circuit voltage V_{OC} , fill factor FF, and power conversion efficiencies of solar cells with $\text{CH}_3\text{NH}_3\text{PbBr}_3$ and $\text{CH}_3\text{NH}_3\text{PbI}_3$ sensitizers (Kojima et al. 2009)

Perovskite	$J_{SC}(\text{mA}/\text{cm}^2)$	$V_{oc}(\text{V})$	FF	η (%)
$\text{CH}_3\text{NH}_3\text{PbBr}_3$	5.57	0.96	0.59	3.31
$\text{CH}_3\text{NH}_3\text{PbI}_3$	11.0	0.61	0.57	3.81

5 Perovskite Quantum Dot Sensitized Solar Cells

Quantum dot sensitized solar cells are identical to dye-sensitized solar cells. Here, perovskite quantum dots sensitizes the n-type wide bandgap semiconductor instead of organic dyes. 2–3 nm-sized perovskite quantum dots are deposited over nanocrystalline TiO_2 using a spin coating method. The power conversion efficiency of perovskite quantum dot sensitized solar cells is ~6.54%, the highest efficiency among organic quantum dot sensitizers.

Limitations: The major drawback of perovskite sensitized solar cells is their longterm instability due to the dissolution of perovskite into the liquid electrolyte used as the redox couple to regenerate perovskite particles (Im et al. 2011).

6 All-Solid-State Perovskite Sensitized Heterojunction Solar Cells

If a solid electrolyte replaces the liquid counterpart, it can improve the stability of perovskite solar cells. In 2012, Park and his coworkers used 2,2',7,7'-tetrakis-(N,N-di-p-methoxyphenyl-amine)—9,9'-spirobifluorene (spiro-MeOTAD as a solid electrolyte in perovskite sensitized solar cells. Here a thin layer of perovskite particles is deposited at the interface between hole and electron transporting layers.

Device structure and working: Fig. 8a shows the device structure of a solid-state perovskite sensitized solar cell and (b) the band structure of perovskite, hole, and electron transporting layers. TiO_2 paste is coated on FTO using a doctor's blade and annealed at 550 °C to form a mesoporous TiO_2 film of 1.5 μm thickness. A thin layer of perovskite film is formed over TiO_2 by spin coating the precursor solution ($\text{CH}_3\text{NH}_3\text{I}$ and PbI_2 in γ -butyrolactone). A hole transporting layer of spiro—MeOTAD is coated over this by spin coating. Then a 60 nm thick gold film is evaporated over this as a counter electrode. When light is incident, the light harvester absorbs it and excites an electron from the valence band to the conduction band. The excited electron in the conduction band of the perovskite layer injects into the conduction band of an electron conducting material, TiO_2 . Similarly, the hole in the valence band goes to HOMO (highest occupied molecular orbital) of the hole transport material, spiro—MeOTAD. The power conversion efficiency (PCE) of such a solar cell is 9.7%. Photocurrent and open-circuit voltage obtained were 17 mA/cm^2 and 0.888 V respectively (Kim et al. 2012).

Limitations: In perovskite sensitized solar cells, the $\text{CH}_3\text{NH}_3\text{PbX}_3$ sensitizes the TiO_2 photo-anode. It requires a driving force to transfer electrons from perovskite into TiO_2 and causes energy losses in the cell, which reduces overall efficiency (Lee et al. 2012).

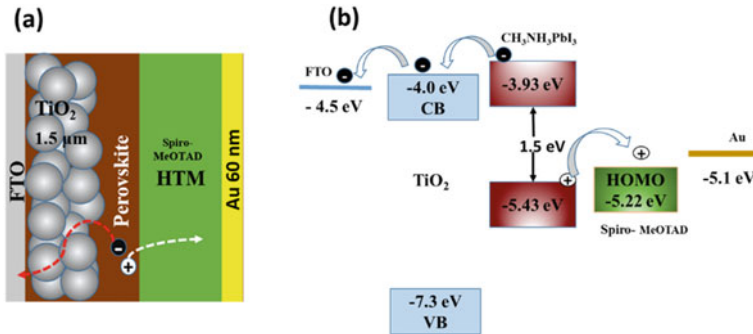


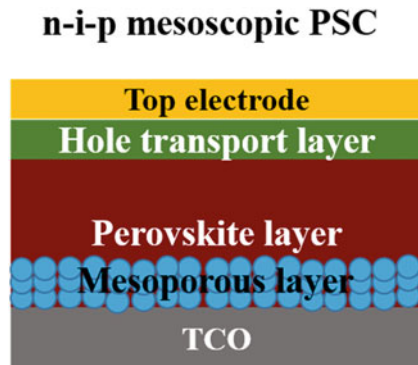
Fig. 8 **a** Device structure and **b** schematic of charge movement through various layers of a perovskite sensitized solar cell with a solid electrolyte

7 Meso-Super Structured Solar Cells (MSSC)

A non-conducting Al_2O_3 scaffold can eliminate losses in TiO_2 based solar cells. Perovskite is coated over the mesoporous—super structured alumina. Figure 9 shows the structure of such a solar cell, and Fig. 10 is a schematic representation of the electron and hole motion in TiO_2 based sensitized solar cells and Al_2O_3 based solar cells. Electrons in perovskite will not be transmitted into the conduction band of insulating alumina since it is at higher energy. Electron conduction takes place fastly through perovskite than through an *n*-type TiO_2 . Since there is no photo-anode (*n*-type) sensitized by perovskite, and Al_2O_3 acts only as a scaffold layer for depositing perovskite, the device is called “meso—super structured solar cell” (MSSC). The PCE of an MSSC formed on Al_2O_3 is 10.9% (Lee et al. 2012).

Limitations: Contact can occur between silver electrode and highly conducting perovskite absorber ($10^{-3} Scm^{-1}$) due to a thin hole transport layer, leading to a short circuit. A thicker layer of a less conductive hole transporting spiro—MeOTAD ($10^{-5} Scm^{-1}$) over perovskite will avoid short-circuiting. However, the series resistance of the cell increases with capping layer thickness.

Fig. 9 The device structure of n-i-p mesoscopic perovskite solar cell



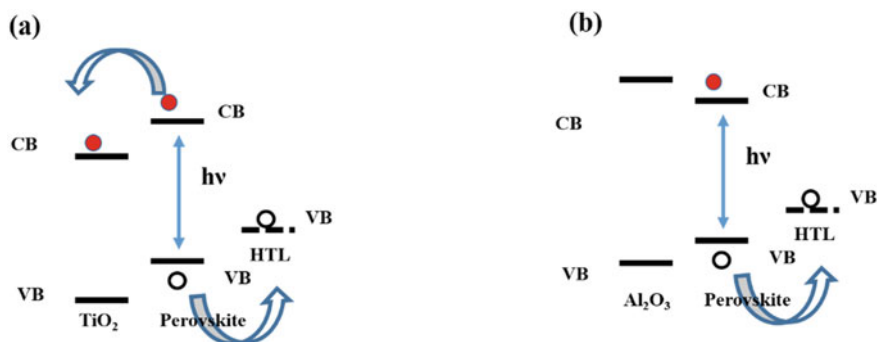


Fig. 10 Schematic representation of **a** electron and **b** hole motion in TiO_2 based perovskite sensitized solar and Al_2O_3 based MSSC

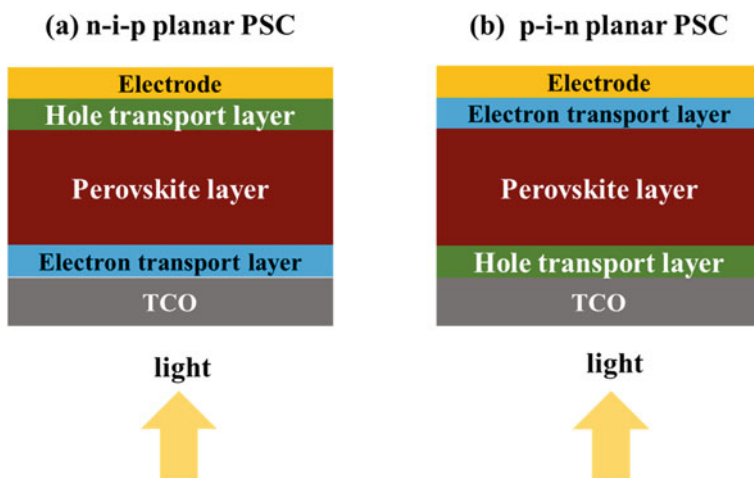


Fig. 11 The device structure of solar cells with **a** n-i-p and **b** p-i-n configurations

8 Planar Heterojunction Perovskite Solar Cells

Planar heterojunction perovskite solar cells comprise a thin film of perovskite sandwiched between the electron transport (ETL) and hole transport layers (HTL). Charge generation by light absorption and separation induced by the band alignments of ETL and HTL with the perovskite is the fundamental principle of these types of solar cells. Depending on the different layers' order in the device's incident light path, the perovskite solar cells are NIP and PIN types. A PIN is called an inverted structure in which the order of layers is HTL/perovskite/ETL, and for a regular NIP, the order is ETL/perovskite/HTL. Figure 11a and b shows the device structure of NIP and PIN type planar heterojunction perovskite solar cells, respectively.

Vapor deposition or spin coating techniques can form thin perovskite active layers. Figure 12a shows a schematic illustration for dual-source vapor deposition set up for deriving flat planar layers of perovskite films. Films get evaporated on the TiO_2 from PbI_2 and methylammonium iodide sources under vacuum. The as-deposited films are exceptionally uniform.

We can categorize the spin coating technique into one-step spin coating and two-step spin coating. Figure 12b shows a schematic diagram of perovskite film's one-step and two-step coating methods onto the TiO_2 compact layer. In one step, the equimolar solution of MAI and PbI_2 in DMA (dimethylacetamide) or DMF (dimethylformamide) is spin-coated over the substrate. In the two-step process, the first step is coating PbI_2 solution in DMF/DMA over TiO_2 film. After proper drying, the MAI solution in IPA is spin-coated and annealed to obtain MAPbI_3 film. An HTL, spiro-MeOTAD is deposited by spin coating to extract perovskite holes into the back electrode (silver). Figure 12c shows the energy band diagram of a perovskite

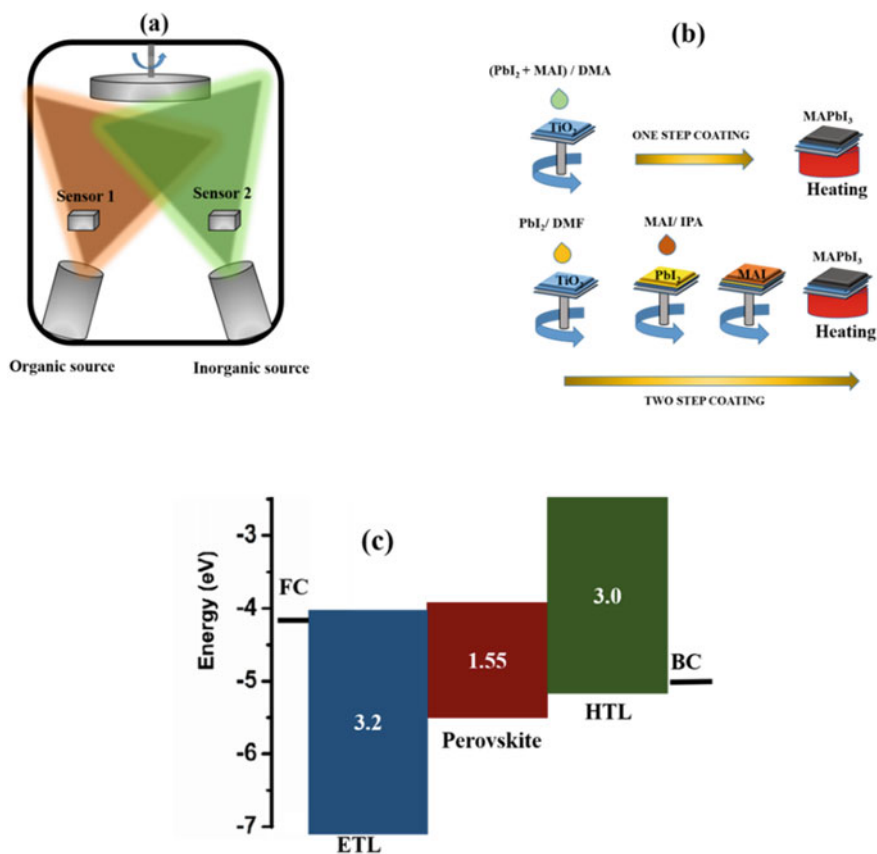


Fig. 12 a Evaporation, and b spin coating methods to deposit perovskite films (Jung and Park 2015) c Energy band diagram of a perovskite solar cell

Table 2 Performance parameters of perovskite solar cells fabricated using different deposition methods

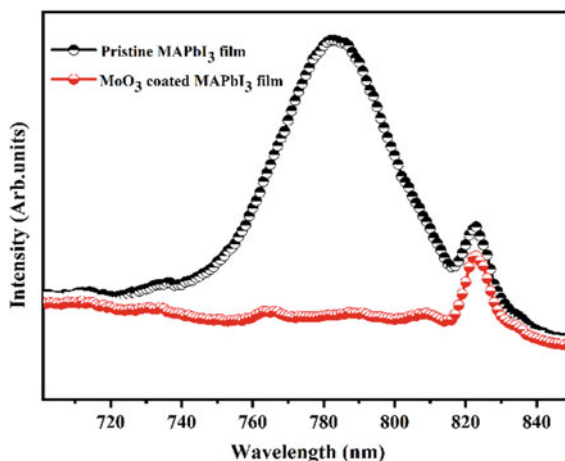
Perovskite	J_{SC} (mA/cm ²)	V_{oc} (V)	FF	η (%)
Vapour deposition	21.5	1.07	0.67	15.4 (Liu et al. 2013)
One step spin coating	19.15	0.828	0.47	7.5 (Im et al. 2015)
Two step spin coating	21.47	1.024	0.634	13.9 (Im et al. 2015)

solar cell. The free electrons resulting from light absorption get collected at the corresponding electrode by drifting through the electron transport layer. The photo-induced hole drifts to the hole transport layer (HTL) and is collected by the respective electrode. The band structure of ETL and HTL facilitates charge transport and collection. Since the perovskite active layer has ambipolar nature, the electron transport layer should extract electrons effortlessly and block the holes. Thus, a wide bandgap semiconductor with a LUMO level lying lower than the conduction level and with a HOMO level lying underneath the perovskite valence level can act as an effective ETL. Similarly, an HTL must be a wide bandgap semiconductor with its HOMO level above the valence level of perovskite to allow the passage of holes into the layer and LUMO level above the conduction level of perovskite to block approaching electrons. Table 2 illustrates the photovoltaic performances of perovskite solar cells formed by evaporation, one-step spin coating, and two-step spin coating methods.

9 Materials for Electron Transport and Hole Transport Layers

The charge transport layers, i.e., electron and hole transport layers, should be satisfying certain properties. In addition to bandgap requirements described in Sect. 8, a charge transport layer should be chemically stable and acts as a protective shield to the perovskite layer from moisture in the atmosphere. These layers must be providing high mobility for the desired kind of charge carriers. These should passivate the neighbouring perovskite layer, and the coating should not impair the absorber. The transport layer that follows the transparent electrode must transmit incident light, and its processing should be cheap. One of the ways to measure the charge extraction efficiency of a transport layer is by studying photoluminescence quenching of the perovskite active layer after the deposition of the transport layer. Light absorption by perovskite generates free carriers as well as excitons. The charges must drift to opposite directions by charge extraction layers. Then the photoluminescence intensity obtained from electron–hole and exciton recombination will be quenched (Xing et al. 2013). Figure 13 illustrates the PL quenching effect in perovskite film due to HTL (MoO_3) coating.

Fig. 13 PL spectra of pristine MAPbI₃ films and those coated with MoO₃ HTL



Two types of electron transport layer structures are there: the planar structure and the mesoporous electron transporter. A mesoporous structure provides a large surface and substrate for the controllable crystallization of perovskites, while a planar structure suppresses the charge recombination process. Table 3 gives a record of various ETL together with their properties such as electron mobility, conduction band minima, and valence band maxima. TiO₂ is the most frequently used ETL. Nevertheless, their electron mobility is low. Mesoporous TiO₂ suffers from many defects, such as deep trap states affecting its conductivity and acts as recombination centres for electrons and holes. The electronic properties of TiO₂ can be modified by doping with elements such as Mg, Nb, Y, Al, Li, and F. Some inorganic ETL that can overcome the drawbacks of TiO₂ are alpha Fe₂O₃, WO_x, SnO₂, BaSnO₂, SrTiO₃, and Zn₂SnO₄. Polymer ETLs provide a robust resistance towards humidity and thus acts as a protective layer for perovskites. 2D forms of graphene, graphene/ polymer, polyaniline (PANI), polyethylene glycol are examples of some mesoporous polymer ETLs.

There are organic as well as inorganic hole transport materials. Most commonly used organic hole transport materials are spiro—MeOTAD, poly(3,4-ethylene dioxythiophene):poly(styrene sulfonate) (PEDOT:PSS), poly-triarylamine (PTAA), poly(3,4-ethylene dioxythiophene) (PEDOT), polyaniline (PANI), polypyrrole (PPy), poly-[[9-(1-octylnonyl)-9H-carbazole-2,7-diyl]-2,5-thiophenediyl-2,1,3-benzothiadiazole-4,7-diyl-2,5-thiophenediyl] (PCDTBT), poly-[3-hexylthiophene-2,5-diyl] (P3HT), N,N'-dialkyl perylene diimide (PDI), and 4-(diethylamino)-benzaldehyde diphenylhydrazone (DEH).

Organic hole transport materials are expensive and are less stable; hence inorganic hole transport layer is practical from a commercial point of view. CuSCN, CuAlO₂, MoO_x, CuO, CuI, Cu₂O, CuGaO₃, MoS₂, NiO_x and CuS are examples of potential hole transport materials. Carbon nanotubes, graphite powder, activated carbon, graphene, and carbon black are the carbon-based materials that act as the hole

Table 3 CBM, VBM, and mobility of various electron transport layers (Lian et al. 2018; Yang et al. 2015; Zhang et al. 2009; Snaith and Ducati 2010; Li et al. 2016; Hadjarab et al. 2007; Ohtomo and Hwang 2004; Mahmood et al. 2015; Liang et al. 2015; Li et al. 2016; Xing et al. 2016)

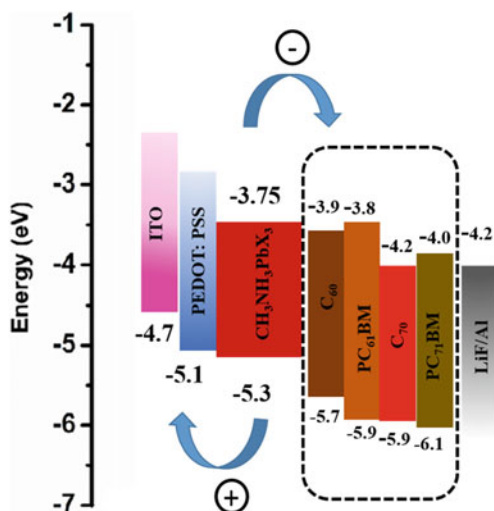
ETM	CBM (eV)	VBM (eV)	Mobility ($\text{cm}^2\text{V}^{-1} \text{s}^{-1}$)
TiO ₂	-4.1 (anatase) -3.9 (rutile) -4.1 (brookite)	-7.3 -6.9 -7.4	0.1–4
ZnO	-4.2	-7.6	205–300
SnO ₂	-4.5	-8.1	240
c-Bi ₂ S ₃	-3.86	-5.45	259
Zn ₂ SnO ₄	-4.1	-7.8	10–15
BaSnO ₃	-3.9	-7.1	~70
SrTiO ₃	-3.9	-7.1	5–8
WO ₃	-5.3	-8.3	–
PCBM	-4.1	-6.0	6.1×10^{-2}
C ₆₀	-4.5	-6.2	1.6×10^{-2}
C ₆₀ -N	-3.9	-5.7	–
C70-DPM-OE	-3.86	-5.88	3.3×10^{-4}
TDTP	-4.03	-5.43	2.7×10^{-3}
HATNASOC7-Cs	-4.16	-6.69	5.13×10^{-3}
IDIC	-3.9	-5.7	1.1×10^{-3}
CDIN	-3.79	-5.99	–
N-PDI	-3.72	-6.05	–
PFN-2TNDI	-3.84	-5.57	4.8×10^{-4}
PPDIDTT	-3.9	-5.9	1.3×10^{-2}

transport layer. Spray coating, spin coating, electrodeposition, combustion, screen printing, pulsed laser deposition, e-beam evaporation, dip coating, screen printing, sputtering are the methods utilized in HTL deposition (Singh et al. 2019).

9.1 Carbon-Based Interlayers to Improve Charge Extraction and Transport

Carbon-based interlayers between absorber and transport layers help to enhance charge extraction and suppress charge trapping. Nano forms of carbon provide the passivation of the absorber layer, protecting them from moisture. They allow efficient charge transport along with providing enhanced stability to the solar cell. Properties of nanocarbon are possible to engineer as suitable for both types of charges. Materials such as carbon quantum dots, graphene quantum dots, carbon nanotubes, and graphene act as multifunctional, environmentally amiable, and stable interlayers

Fig. 14 Energy band diagram of different carbon-based interlayers used as ETL in a solar cell (Litvin et al. 2020)



for PSCs. Fullerenes are allotropes of carbon with a fixed number of carbon atoms (C_{60} , C_{70}). Functionalization of fullerene results in PC_{60}BM and PC_{70}BM with electron extracting properties. Figure 14 shows an architecture in which derivatives of fullerene facilitate electron transport to the electrode. Thus employing fullerene interlayers improves the photovoltaic performance of PSCs. It also builds up the stability and reduces the J-V hysteresis of the device.

Graphene is the 2D form of carbon with excellent conductivity. It functions as a hole extracting material. PEDOT: PSS is a common HTL in inverted PSC architecture. However, they are hygroscopic and causes stability issues if it is adjacent to the perovskite layer. A thin layer of graphene between perovskite and PEDOT: PSS provides extra stability to the device. Carbon nanotubes in different compounds such as P3HT-CNTs blend, spiro MeOTAD-CNTs blend, spiro MeOTAD/spiro MeOTAD—CNTs blend, CNTs transferred/spiro MeOTAD, CNT spin-coated/spiro MeOTAD, Wrapped-CNTs/spiro MeOTAD, Wrapped-CNTs/PMMA, GO-CNTs/PMMA, Graphene-CNTs, etc. work as HTLs (Cai et al. 2015; Miletić et al. 2016; Lee et al. 2015; Wang et al. 2015, 2016a; Yao et al. 2018; Habisreutinger et al. 2014; Habisreutinger et al. 2014; Zhang et al. 2017).

Graphene quantum dots comprises 1 or 2 layers of graphene whose bandgap is size-tunable due to quantum confinement effects. They improve electron extraction and hence power conversion efficiency of PSC when deposited over ETL (Zhu et al. 2014). Carbon dots are different from graphene quantum dots in terms of weak crystallinity. Their properties and crystallinity depend on synthesis methods. Carbon dots function as both HTL and ETL in inverter perovskite solar cell architecture (Jin et al. 2017).

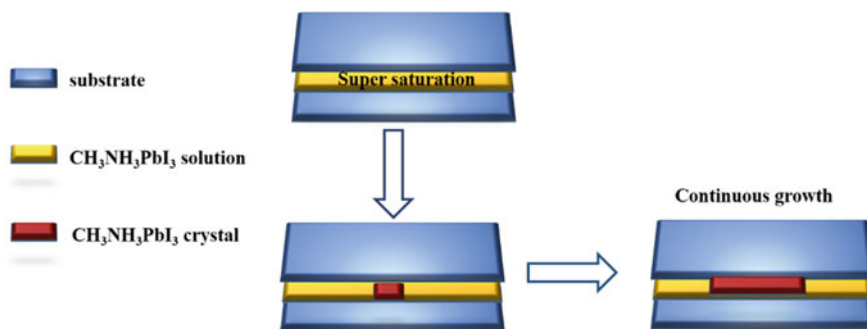


Fig. 15 Schematic illustration of diffusion facilitated space confined method to develop $\text{CH}_3\text{NH}_3\text{PbI}_3$ single crystals

9.2 Single Crystal Perovskite Solar Cells

Single crystal perovskites possess longer diffusion lengths $\sim 175 \mu\text{m}$ and reduced trap densities. Longer diffusion length will enhance the efficiency of the solar cell by effectively collecting charge carriers. The bandgap of $\text{CH}_3\text{NH}_3\text{PbI}_3$ is too large for attaining the Shockley—Queisser limit for single-junction solar cells. We can utilize the below bandgap absorption by single-crystal perovskites, narrowing the optical bandgap without changing composition. Below the bandgap, absorption is due to indirect type transition in $\text{CH}_3\text{NH}_3\text{PbI}_3$. The indirect bandgap of $\text{CH}_3\text{NH}_3\text{PbI}_3$ is smaller than its direct bandgap for about 60 meV. A PCE of 17.8% is obtainable with a single crystal perovskite (Hutter et al. 2017; Chen et al. 2017).

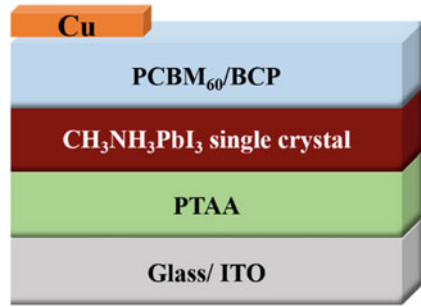
Single crystals are grown directly on HTL above ITO. Figure 15 shows a diffusion facilitated space confined method to develop $\text{CH}_3\text{NH}_3\text{PbI}_3$ single crystals. Distance between two substrates (ITO coated with PTAA—poly(triarylamine), p-type organic semiconductor) provides confinement required to grow thin-film single crystals. A supersaturated solution of perovskite precursors in γ -butyrolactone solvent formed by raising the temperature to about 100°C will grow into single crystals between the substrates (Saidaminov et al. 2015).

The single-crystal thin film develops on one of the substrates, and the other is easily removable by peeling. An electron transport layer PCBM and an electrode of copper 80 nm thick completes the structure. Silver is also used as the electrode. Figure 16 shows the design of the single-crystal perovskite solar cell.

9.3 Back Contact Perovskite Solar Cells

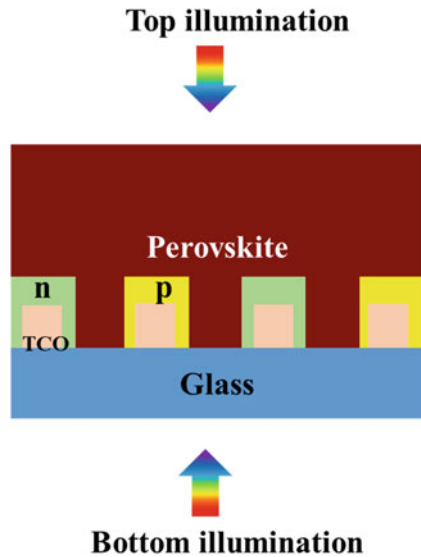
In this type of architecture, n (electron selective) and p (hole selective) electrodes are at the rear side of the cell in an interdigitated manner hence, known as interdigitated

Fig. 16 The device structure of perovskite single-crystal solar cell



back contact (IBC) cell. The absorber gets deposited over the interdigitated electrodes, and the light can be allowed to fall directly over the absorber, thus limiting the shading losses of the top electrode. Light can also be sent from the rear side also for the architecture, which uses TCOs as the rear side contacts with ETL/HTL. A large variety of electrodes are acceptable for an IBC since the transparency of electrodes is not a necessity. Figure 17 shows the device structure of a perovskite IBC. This type of architecture is common in crystalline silicon solar cells.

Fig. 17 The device structure of a perovskite back contact solar cell



10 High-Efficiency Concepts: Tandem Solar Cells

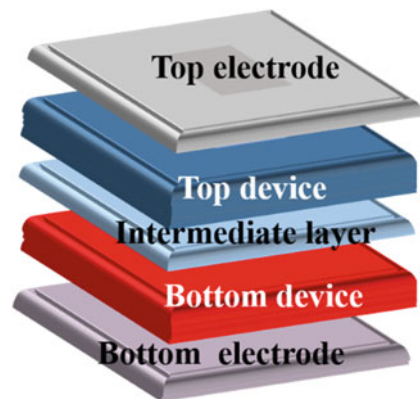
10.1 Introduction to Tandem Solar Cells

Tandem solar cells (TSC) are two or more cascaded cells with different bandgaps absorbing different wavelengths in solar spectra to improve light absorption and efficiency. The bandgap of the absorber in the uppermost layer will be the highest. Consequently, higher energy radiations are absorbed in the first layer. The low-energy radiations get penetrated to the next layer, where the absorber bandgap is further smaller. And so on, the maximum quantity of incident energy gets absorbed. Figure 18 shows a tandem structure in which there are two cascaded cells. The maximum efficiency that a single-junction solar cell can attain is 33.7%, with an absorber material of the bandgap equal to 1.34 eV. Losses in photon absorption, non-radiative recombination, and exciton dissociations make the practical values even smaller. A downside of the single-junction cell is that they are not able to absorb radiations with energy lower than their bandgap. At the same time, a tandem solar cell can absorb different wavelengths.

There are different possible configurations for tandem cells, like two-terminal (2 T) and four-terminal (4 T). In the 2 T configuration, all the cells are electrically in series, as shown in Fig. 19a. Perovskite-CZTSSe (CZTS) cells were the first reported in 2 T with 4.4% efficiency (Todorov et al. 2014). Furthermore, now its efficiency has reached above 23%. In 4 T perovskite tandem cell configuration, the top perovskite cell connects independently to bottom silicon or CZTS cells by mechanical stacking, as in Fig. 19b.

Moreover, the efficiency secured from this configuration is above 25% (Bailie et al. 2015). 4 T has multiple designs including, a series-parallel tandem (SPT) configuration (Fig. 19c), which gives similar power outputs equal to 4 T configuration. Here, the top and bottom strings of cells are combined separately before connecting the top-bottom layers in parallel (Futscher and Ehrler 2016). Another design is reflecting

Fig. 18 The device structure of tandem solar cell with two cascaded cells



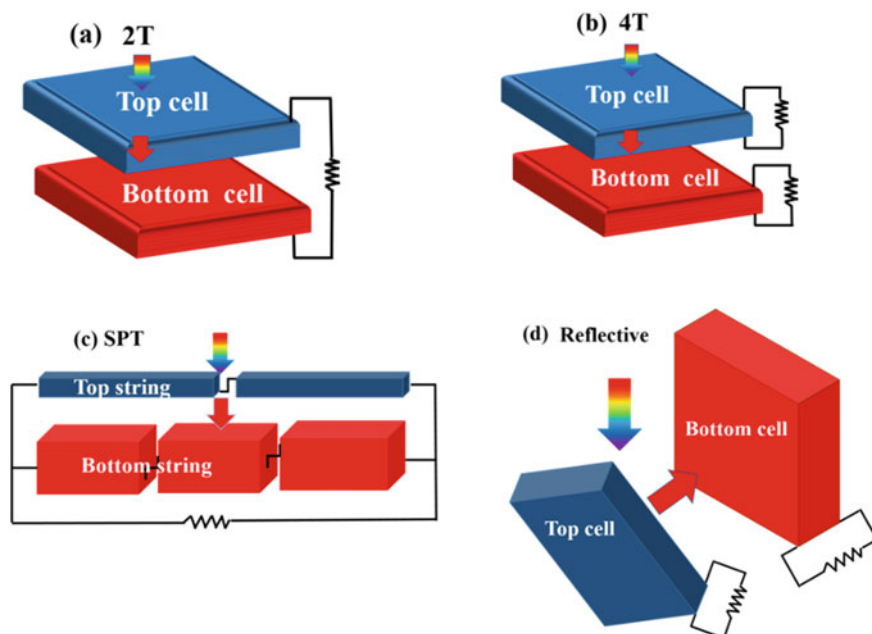


Fig. 19 Different tandem cell configurations **a** 4-terminal configuration (4 T) **b** 2-terminal tandem (2 T) **c** Series—parallel tandem **d** Reflective tandem

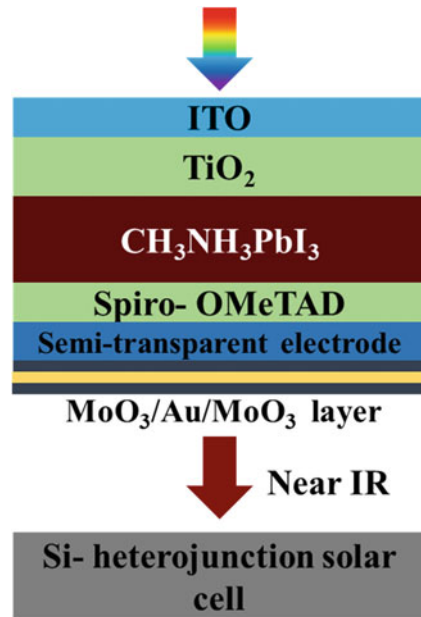
one. Here, longer wavelength light from the top layer gets reflected in the bottom layer instead of a transmission. Figure 19d shows a reflecting type of configuration.

Low-cost processing methods, easy tunability of bandgaps, direct bandgap, high absorption coefficients, long carrier lifetime and diffusion length, ambipolar conductivity, and higher efficiencies of perovskite solar cells make these materials a promising candidate in the field of TSCs. Perovskites are used in all the configurations mentioned above and with several other materials as a top or bottom cell component. Leading perovskite-based TSC architectures are perovskite-silicon, perovskite—copper indium gallium selenide (CIGS), perovskite-organic, and perovskite-perovskite.

10.2 Perovskite-Si TSC

Silicon is a much-established material in photovoltaic applications, both in the laboratory and industry, and currently holds more than 95% of the market share. Consequently, the majority of the perovskite TSC is made over silicon solar cells (Zhang et al. 2020). The maximum efficiency attained by single-junction silicon solar cells is 26.6%, and further marginal improvement in the single-junction cell efficiency will be difficult. Figure 20 shows the device structure of 2 T mechanically

Fig. 20 The device structure of perovskite–Si tandem solar cell

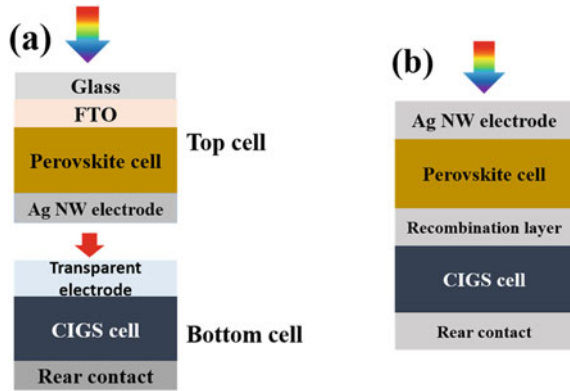


stacked perovskite–Silicon TSC. It is a stacked semi-transparent perovskite solar cell over a heterojunction silicon SC. For the transparent perovskite cell, TiO₂ film on ITO coated glass electrode acts as an ETL and spiro–MeOTAD as an HTL. A gold nanomesh sandwiched between two molybdenum trioxide (MoO₃) layers (MoO₃/Au/MoO₃) formed using thermal evaporation acts as a transparent bottom electrode for perovskite top cell. The upper MoO₃ layer acts as an antireflection coating. Light is incident to the top cell; perovskite absorbs a short wavelength and transmits the longer wavelength to the bottom silicon cell. The individual efficiencies of the perovskite and silicon cells are 18.3% and 23.3%, respectively. Moreover, the combination yields 27% PCE (Wang et al. 2020). The newest efficiency reported by Helmholtz Centrum Berlin for two junctions, two-terminal 1 cm² perovskite–silicon tandem solar cells is 29.16% (Green et al. 2020).

10.3 Perovskite-CIGS TSC

Perovskites are the best suitable top cell for CIGS to form tandem cell configuration. The perovskite–CIGS TSC can have a mechanically stacked structure or a monolithically integrated TSC, as shown in Fig. 21a and b, respectively. Due to fewer options for transparent electrodes, monolithic TSC is more efficient than mechanically stacked one. The highest efficiency obtained from a 4 T perovskite–CIGS spectral splitting TSC consisting of a perovskite top cell with Eg 1.59 eV and CIGS bottom cell with Eg 1.08 eV is 28% (Nakamura et al. 2020).

Fig. 21 Schematic diagram of stacked tandem perovskite cell over CIGS bottom cell **a** mechanically stacked and **b** monolithically integrated structures



10.4 Perovskite-Perovskite TSC (Flexible—Lightweight)

All perovskite TSCs are appropriate for flexible and lightweight applications. It provides the advantage of low-cost fabrication and high efficiency. The lowest bandgap of lead halide perovskite is 1.5 eV which is higher than the optimum value of the Shockley Queisser limit. Partial or complete substitution of Pb with Sn having a similar electronic structure and ionic radius can narrow the bandgap and helps to achieve SQ limit to provide highly efficient all-perovskite-based tandem solar cells. Mixed Pb–Sn perovskite can tune the bandgap between 1.6 to 1.2 eV. Usually, an inverted PIN device structure is preferred for a mixed Pb–Sn perovskite solar cells instead of a widely used NIP structure, crystalline-TiO₂/ mesoporous-TiO₂/ Pb–Sn halide perovskite/ poly (3-hexylthiophene)(P3HT)/ gold because of the low power conversion efficiency of NIP (14.04%) compared to that of their PIN counterpart (21.1%). Pb–Sn perovskite has better contact above PEDOT:PSS than TiO₂ or other ETLs, resulting in higher efficiency for an inverted PIN structure. An ideal perovskite-perovskite TSC consists of a wide bandgap perovskite top cell stacked over a narrow bandgap bottom cell and transparent electrodes surrounding the cells. Practically, there arises difficulty in matching bandgaps of top and bottom sub-cells to derive an optimal current. Figure 22a shows an all perovskite TSC containing various functional and recombination layers (Lin et al. 2019). These layers protect the dissolution of the top cell while fabricating the bottom cell using solution processing technique and provides bandgap matching for optimal current. Figure 22b gives the progress of all perovskite tandem solar cells over past years.

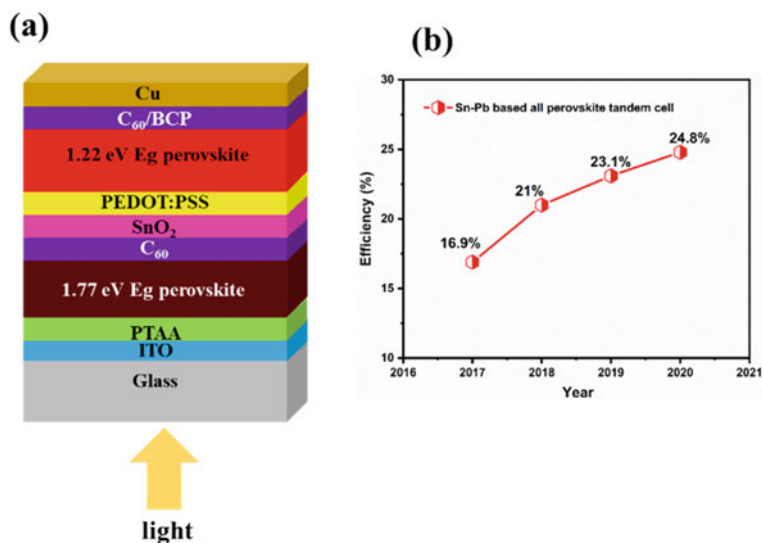


Fig. 22 a Schematic of an ideal all perovskite tandem cell b A real TSC consisting of intermediate functional layers c Progress in the efficiency of monolithic all—perovskite tandem solar cells (Gu et al. 2020; Eperon et al. 2016; Zhao et al. 2018; Tong et al. 2019; Lin et al. 2019)

10.5 Critical Issues Regarding Perovskite Tandem Solar Cells and Remedies

Several factors are contributing to power loss in perovskite-based tandem solar cells. The refractive index mismatch between perovskite film ($n = 2$) and silicon ($n = 4$) results in optical losses. Textured silicon will trap the light and reduce the reflection loss (Albrecht et al. 2016). However, the fabrication of such a TSC over texture is a bit difficult. The difference in refractive indices of air, glass, and transparent electrodes also contribute to the reflection losses (Mailoa et al. 2015). Antireflection coatings such as MgF_2 and LiF can minimize the effect (Albrecht et al. 2016; Duong et al. 2016). Layers such as HTL, ETL, transparent electrodes, and antireflection coatings absorb photons and result in parasitic absorption loss. Using transparent electrodes with substantial carrier mobility and low carrier concentration can reduce this type of power loss (Duong et al. 2016; Yang Michael et al. 2015). The power conversion efficiency of a solar cell depends on the sheet resistance of transparent electrodes and the transport layers. It has to be made optimum by device design and material selection. The current mismatch of different cells in TSC can result in power loss. Current matching between the top and bottom cells requires proper energy alignment between different transport layers and thickness optimization of the absorber layers (Futscher and Ehrler 2017). The prime challenge in TSC is its stability in ambient conditions, as in the case of single-junction perovskite solar cells.

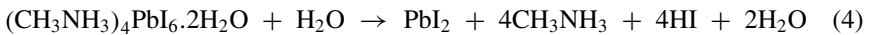
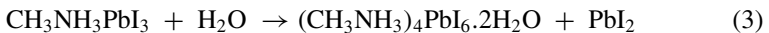
11 Challenges in Commercializing Perovskite Solar Cells

11.1 Toxicity of Lead

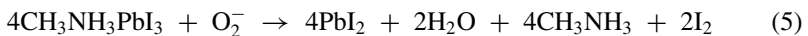
Lead present in perovskite solar cells is a toxic metal and can affect human health. Lead reaches the human body either through inhalation, injection, or contact with skin. After in-taking, blood will transport this toxic metal into the liver, kidney, lungs, and nervous tissues. Lead poisoning affects the nervous system, bones, lungs, and liver. Neurological disorders, cataracts, heart and renal diseases, and decreased fertility are some of the effects of lead poisoning. Continuous exposure to lead can deposit lead phosphate in bones. Children are more prone to lead poisoning. Methylammonium lead iodide perovskite degrades into PbI_2 , $\text{Pb}(\text{OH})_2$, and HI. HI will acidify the medium and is most dangerous (Babayigit et al. 2016; Schileo and Grancini 2020). Lead-free alternatives were explored, but their performances were inferior.

11.2 Lack of Stability

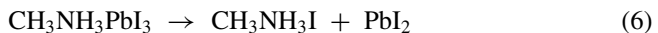
Sensitivity towards moisture, oxygen, light, and heat remains an obstacle in the commercialization path of perovskites. Perovskite readily decomposes into precursors on exposure to water and most of the other polar solvents. Under 50% relative humidity, it will degrade slowly in 10 days, while the degradation will be rapid when exposed to 80% relative humidity. Reacting with water $\text{CH}_3\text{NH}_3\text{PbI}_3$ will result in a hydrate complex as given below.



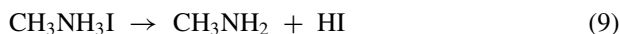
Oxygen and light also have a degrading effect on perovskite films. Oxygen diffuses into perovskite crystal within minutes and becomes highly reactive O_2^- near iodine vacancies. It will decompose photo-excited perovskite as follows (Duong et al. 2016).



Under thermal stress of 40 °C, $\text{CH}_3\text{NH}_3\text{PbI}_3$ undergo following reactions,



Above 80 °C $\text{CH}_3\text{NH}_3\text{I}$ undergo the following reactions



Proper encapsulation methods are inevitable to tackle these degradation issues.

11.3 Scalability Issues

Compared to other thin-film photovoltaic technologies, perovskite solar cell research has achieved power conversion efficiencies greater than 22% within a short period. The low cost of production using solution processing is suitable for commercializing this technology. However, the drop in power conversion efficiency while scaling up is higher in perovskite solar cells than in other thin-film photovoltaics. The monolithic interconnection of cells is also a challenge for the production of perovskite solar modules. There are several solution-based techniques for large-area deposition of perovskites. Blade coating, slot dye coating, inkjet printing, spray coating, electrodeposition, and screen printing are some of these. However, all these methods face challenges: (1) obtain a uniform coverage over the substrate, (2) uniform chemical composition, (3) low surface roughness, and (4) high crystallinity. The spin coating can fabricate (10 × 10 cm) solar cell modules, but the power conversion efficiency is lower than an equivalent smaller device. The vapour phase deposition method is also a scalable coating technique for perovskite thin films. Nevertheless, the vacuum technology used will raise the cost of production (Li et al. 2018). Table 4 compares the performance of perovskite modules and their single-cell counterpart fabricated using different techniques.

11.4 Current–Voltage Hysteresis

Ion migration is another mechanism causing J-V hysteresis. According to DFT calculations, the activation energies of iodine vacancies and iodine interstitial defects are very low ~0.08 eV. Under a bias voltage or photo voltage, they can drift towards electrodes in a short time. But methylammonium and lead vacancies have higher activation energies, 0.46 eV and 0.8 eV, respectively, resulting in slower migration and hysteresis (Azpiroz et al. 2015). Thus hysteresis behaviour depends on the composition of perovskite (Kang and Park 2019).

Organic–inorganic halide perovskites possess ferroelectric properties. MAPbI_3 exhibits different polarization under forward and reverse biases. For example, a MAPbI_3 based perovskite solar cell having a PIN structure generates an electric

Table 4 Comparison of the performance of perovskite modules fabricated using different scalable techniques

Method	PCE of single cell with area $\leq 10 \text{ cm}^2$ (%)	PCE of module with area $\geq 10 \text{ cm}^2$ (%)
Blade coating	19.5 (Tang et al. 2017)	14.1 (Yang et al. 2017)
Slot dye coating	14.7 (Qin et al. 2017)	–
Inkjet printing	12.3 (Paquin et al. 2015)	–
Spray coating	18.3 (Heo et al. 2016)	15.5 (Heo et al. 2016)
Electrodeposition	14.6 (Huang et al. 2015)	–
Screen printing	15.6 (Rong et al. 2017)	Priyadarshi et al. 2016)

field due to polarization opposing the built-in electric field during a forward scan suppressing the charge extraction. While during a reverse scan, the polarization electric field will enhance the built-in potential facilitating the charge collection. Ferroelectric polarization and the resulting hysteresis are higher in the perovskite planar structures due to the ordered dipole array that can develop here. But perovskite embedded in mesoporous TiO_2 or Al_2O_3 forms randomly oriented dipoles weakening ferroelectric domains, hence hysteresis (Chen et al. 2015).

11.5 Lead-Free Perovskites for Photovoltaics

11.6 Tin Based Perovskites

The first option for toxic metal lead in perovskites is Sn which lies in the same group (group 14) as Pb in the periodic table. Both p-type (MASnI_3) and n-type (FASnI_3) are obtainable. Sn perovskites are sensitive to air. Sn has 2+ and 4+ oxidation states but oxidizes into Sn^{4+} state in ambient atmosphere. FASnI_3 is extra stable compared to MASnI_3 . All inorganic CsSnX_3 are also employable in solar cell applications. The power conversion efficiency of different halides are 12.96%, 10.46% and 9.66% for CsSnI_3 , CsSnBr_3 , and CsSnCl_3 respectively (Ghosh and Pradhan 2019). Tin also has some toxic effects as it is a carcinogen and has effects like neurotoxicity. Since Sn in perovskites is less stable, they will easily release HI, causing acidification (Babayigit et al. 2016).

11.7 Germanium Based Perovskites

Another element from group 14, Ge, possesses similar electronic characteristics as that of lead. CsGeX₃ has a lower bandgap (1.6 eV) than their Pb and Sn counterparts hence finds application in solar cell technology. In addition, Ge is less toxic compared to lead and tin. Nevertheless, Ge-perovskites face a similar or worse stability issue as Sn, getting oxidized to a 4 + oxidation state in air.

11.8 Other Lead-Free Perovskites

Bismuth Bi³⁺ has a similar electronic configuration as Pb²⁺ and is a better replacement option for lead in perovskites. Bi perovskites having chemical formula A₃BiX₆ and A₃Bi₂X₉ are more stable compared to Sn-based perovskites. Here A is an organic or an inorganic cation with 1 + oxidation state (Cs⁺, CH₃NH₃⁺), and X is a halide anion with oxidation state - 1 (I⁻, Br⁻, Cl⁻). The bandgap of Bi-based perovskite is large (1.9 – 2.2 eV) for solar cell applications. Doping with Ga, In, and Ru can lower the bandgap (Mao et al. 2019). Antimony is another choice in Pb-free perovskites. A₃Sb₂X₉ has layered 2D structures with a bandgap of 2 eV (Jiang et al. 2018). Copper is also used to eliminate the usage of Pb. A₂CuX₄ is the structure of copper-based perovskites. Double perovskites are recently understudying for lead-free materials. They form a 3D structure with chemical formula is A₂M⁺M³⁺X₆. Here A = cation with 1 + oxidation state, M⁺ = Cu⁺, Ag⁺, Na⁺, and M³⁺ = Bi³⁺, In³⁺ and X⁻ = I⁻, Br⁻, Cl⁻ (Slavney et al. 2016; Ravi et al. 2018).

11.9 Protection Methods for Perovskite Solar Cells

The stability of perovskite solar cells depends on the absorber layer, contacts, and interfaces. Ion migration that results in I-V hysteresis is also essential. Chemical or molecular engineering, applying hydrophobic buffer layers, and interface engineering can improve the stability of PSCs. The formation energy of bulk MAPbI₃ is 0.11–0.14 eV and can degrade into precursors if kept at 85 °C (0.093 eV), required by IEC 61,646 climatic chamber tests (international standards). However, the corresponding bromide perovskite, MAPbBr₃, exhibits exceptional stability under the same conditions due to higher bond strength. Thus chemical engineering by introducing Br into MAPbI₃ forming MAPb(I_{1-x}Br_x)₃ has proved to enhance the stability of perovskite against moisture and heat (Noh et al. 2013).

However, the bandgap will further increase with Br addition. Layered perovskites, 2D or quasi 2D formed by partial substitution of MA cation with long-chain organic cations like (PEA)₂(MA)₂[Pb₃I₁₀], where PEA = C₆H₅(CH₂)₂NH₃⁺ also exhibits enhanced stability towards moisture (Smith et al. 2014).

The low interaction energy of cation and iodide ions results in the easy generation of defects. The activation energy for vacancy-assisted ion (I^-) migration is 0.44–0.58 eV. The drift and accumulation of ionic defects at the interfaces between perovskite and transport layers screen the electric field. Then I^- can turn into I_2 by injecting electrons to TiO_2 , causing $MAPbI_3$ and PCE to degrade. A layer of Sb_2S_3 coated between perovskite and TiO_2 can inhibit this conversion and enhance the stability of the device (Ito et al. 2014). $TiO_2/ MAPbI_3/$ spiro—MeOTAD structure exhibits severe I-V hysteresis due to I^- migration and its action on the transport layers. Changing the transport layers with less reactive ones gives structures such as $NiO/ MAPbI_3/ PCBM$ and $PEDOT: PSS/ MAPbI_3/ PCBM$ to negligible hysteresis (Kim et al. 2015). Electron transport layer TiO_2 is highly unstable under UV illumination (Leijtens et al. 2013). ZnO doped with F and Sn has shown enhanced UV stability (Jiang et al. 2016). Spiro—MeOTAD is the most commonly used HTL in perovskite solar cells. It is doped with a p-type lithium bistrifluoromethanesulfonimide (Li-TFSI) to enhance hole mobility.

Nevertheless, doping reduces their stability (Liu et al. 2014), and the cost of Spiro-MeOTAD is also high. Cu doped NiO_x as an HTL has shown high PCE and enhanced stability (Kim et al. 2015) and is more stable and easy to deposit. The addition of a buffer layer can protect PSC from moisture-induced instability. HTL itself works as a buffer layer. Spiro-MeOTAD cannot endure mechanical stress caused due to morphological changes and induce cracks through which moisture reaches the perovskite layer. A thin layer of Al_2O_3 between perovskite and spiro—MeOTAD has shown better protection (Guarnera et al. 2015). Poly(3-hexylthiophene) (P3HT) can act as HTL as well as a better buffer layer (Yang et al. 2015).

12 Techniques for Large Area Perovskite Solar Cells

There are a large number of techniques employed to obtain large-scale perovskite films. Some of these are solution processing techniques such as spin coating, blade coating, slot dye coating, inkjet printing, spray coating, electrodeposition, screen printing, and vapour phase deposition.

Spin coating is the technique used for producing thin films in a smaller area (1×1 cm). A larger film of dimensions 10×10 cm also can be obtained. A solution of precursors, methylammonium halide and lead halide in N, N dimethylformamide (DMF) or γ -butyrolactone (GBL), or dimethyl sulfoxide (DMSO) forms the ink used for coating. Dropping a small amount of this ink over a spinning substrate will result in smooth films. Spinning speed, acceleration, and time of rotation determine the quality and thickness of the perovskite films. Spinning at high speeds and annealing after deposition will remove the solvents. Spin coating yields very high efficiency (22.1%) solar cells at smaller scales (0.1 cm^2). But scaling up from 0.1 cm^2 to 1 cm^2 result in 10–15% efficiency drop (Chen et al. 2015; Yang et al. 2015). In the blade coating, the liquid is loaded on the substrate, and a knife spreads it. Parameters such as the quantity of ink, coating speed, and knife determine the thickness of the

film. Slot die coating is also one of the techniques that can fabricate large-scale thin films. It has a slot die head with an upstream die and a downstream die. The coating solution is injected into the slot-die head through a feed slot and then delivered onto the substrate through the coating head (Ruschak 1976).

Inkjet printing uses nozzles to disperse the ink to the substrate. Perovskites solar cells of area 0.04 cm^2 are already fabricated using this technique. This technique has the potential to be applied in large-scale modules. Spray coating results in perovskite films of high quality over a large area. Here, tiny drops of ink get sprayed on the preheated substrate that helps to evaporate excess solvents. About 15.5% of efficient modules are obtained by this method (Heo et al. 2016). Processing parameters such as substrate temperature, flow rate, annealing treatments, and gas carrier determine the quality of the film. Electrodeposition can form large-area perovskite thin films in 2 steps. The first step is the electrodeposition of PbO or PbO₂ over a conducting substrate. Reacting this with organic halide will result in the formation of perovskite. In screen printing, the ink is transferred to the substrate using a patterned mesh screen. An emulsion of exposed photosensitive polymer blocks the unwanted mesh area. This method has been used to develop perovskite solar cell modules resulting in an efficiency of 10.8% (Priyadarshi et al. 2016). Vacuum deposition methods such as chemical vapour deposition (CVD), sublimation, vapour assisted sequential processing is available for large area PSC fabrication (Liu et al. 2013; Chen et al. 2014).

12.1 Current Status of Perovskite Solar Cells

Organic–inorganic halide perovskites were first employed in the photovoltaic application by Miyasaka in 2009. The structure of the first perovskite-based solar cell was a liquid electrolyte perovskite sensitized solar cell. Since then there were massive changes in structure and as a result in their performance and reached its present status as illustrated in Table 5.

Table 5 Current status of efficiencies and other cell parameters measured under the global AM1.5 spectrum (1000 W/m^2) at $25 \text{ }^\circ\text{C}$ (Green et al. 2020, 2021)

Perovskite cell classification	Efficiency (%)	Area (cm^2)	V_{oc} (V)	J_{SC} (mA/cm^2)
Single-junction terrestrial cell	21.6 ± 0.6	1.0235	1.193	21.64
Perovskite/Si (2-terminal) tandem solar cell	29.15 ± 0.7	1.060	1.897	19.75
Perovskite/CIGS tandem solar cell	24.2 ± 0.7	1.045	1.768	19.24
Perovskite/perovskite tandem solar cell	24.2 ± 0.8	1.041	1.986	15.93

12.2 *Other Applications of Perovskites*

The most intriguing property of organic–inorganic halide perovskites is that they have varied applications other than photovoltaics such as photodetectors, Light-emitting diodes (LED), and light converting layers in white light LED, laser, waveguides, resistive memory, field—effect transistors, and artificial synapses [97–104]. Owing to their excellent absorption, they were first used in solar cells and LEDs. However, their properties are tuneable and suitable for all other optical and electronic device applications. Compositional engineering and different morphologies allow one to attain the characteristics that an application demands. Low dimensional perovskites (2D or quasi 2D) can act as a passivating layer between absorption and transport layers that will match the bandgaps resulting in smooth carrier injection into transport layers (Wang et al. 2016b; Cho et al. 2018). A perovskite LED has the same structure that of a solar cell. Electrons injected from ETL and holes from HTL undergo radiative recombination. Quantum confinement in low dimensional perovskites can overcome the limitations of 3D perovskites (Yang et al. 2018). Properties of perovskites such as high drift mobility of charge carriers, photo-induced polarization, and efficient charge collection are convenient for this application. Low-cost solution-processed perovskite thin films have sensitivity towards light signals and also possess a low noise current. Spin coating perovskite between dielectric and evaporated gold mirrors and perovskite nanowires integrated on-chip can work as lasers (Deschler et al. 2014; Liu et al. 2017). Polycrystalline microwires of organic–inorganic perovskite can operate as a waveguide with negligible loss. Nanowires with different halogen groups can guide different wavelengths.

13 Summary

The chapter “Perovskite solar cells: concepts and prospects” introduces organic–inorganic halide perovskite materials and their unique properties. It proceeds by demonstrating every development in the perovskite solar cell up to present status. The chapter discusses critical issues in commercializing perovskite solar cells and the possible solutions. It also presents different applications of perovskite materials other than solar cells.

References

- Adinolfi V, Peng W, Walters G, Bakr OM, Sargent EH (2017) The Electrical and Optical Properties of Organometal Halide Perovskites Relevant to Optoelectronic Performance, 1700764, 1–13
- Albrecht S, Saliba M, Correa Baena JP, Lang F, Kegelmann L, Mews M, Steier L, Abate A, Rappich J, Korte L, Schlattmann R, Nazeeruddin MK, Hagfeldt A, Grätzel M, Rech B (2016) Monolithic perovskite/silicon-heterojunction tandem solar cells processed at low temperature. *Energy Environ Sci* 9:81–88
- Azpiroz JM, Mosconi E, Bisquert J, De Angelis F (2015) Defect migration in methylammonium lead iodide and its role in perovskite solar cell operation. *Energy Environ Sci* 8:2118–2127
- Babayigit A, Ethirajan A, Muller M, Conings B (2016) Toxicity of organometal halide perovskite solar cells. *Nat Mater* 15:247–251
- Baillie CD, Christoforo MG, Mailoa JP, Bowring AR, Unger EL, Nguyen WH, Burschka J, Pellet N, Lee JZ, Grätzel M, Noufi R, Buonassisi T, Salbeck J, Scharber MR, McGehee MD (2015) Semi-transparent perovskite solar cells for tandems with silicon and CIGS. *Energy Environ Sci* 8:956–963
- Boix PP, Agarwala S, Koh TM, Mathews N, Mhaisalkar SG (2015) Perovskite solar cells: beyond methylammonium lead iodide. *J Phys Chem Lett* 6(5):898–907
- Cai M, Tiong VT, Hreid T, Bell J, Wang H (2015) An efficient hole transport material composite based on poly(3-hexylthiophene) and bamboo-structured carbon nanotubes for high performance perovskite solar cells. *J Mater Chem A* 3:2784–2793
- Chen Q, Zhou H, Hong Z, Luo S, Duan HS, Wang HH, Liu Y, Li G, Yang Y (2014) Planar heterojunction perovskite solar cells via vapor-assisted solution process. *J Am Chem Soc* 136:622–625
- Chen HW, Sakai N, Ikegami M, Miyasaka T (2015) Emergence of hysteresis and transient ferroelectric response in organo-lead halide perovskite solar cells. *J Phys Chem Lett* 6:164–169
- Chen W, Wu Y, Yue Y, Liu J, Zhang W, Yang X, Chen H, Bi E, Ashraful I, Grätzel M, Han L (2015) Efficient and stable large-area perovskite solar cells with inorganic charge extraction layers. *Science* 350:944–948
- Chen Z, Dong Q, Liu Y, Bao C, Xiao X, Bai Y, Deng Y, Huang J, Fang Y, Lin Y, Tang S, Wang Q (2017) Thin single crystal perovskite solar cells to harvest below-bandgap light absorption. *Nat Commun* 8:1–7
- Cho KT, Grancini G, Lee Y, Oveisi E, Ryu J, Almora O, Tschumi M, Schouwink PA, Seo G, Heo S, Park J, Jang J, Paek S, Garcia-Belmonte G, Nazeeruddin MK (2018) Selective growth of layered perovskites for stable and efficient photovoltaics. *Energy Environ Sci* 11:952–959
- Choi J, Han JS, Hong K, Kim SY, Jang HW (2018) Organic-inorganic hybrid halide perovskites for memories, transistors, and artificial synapses. *Adv Mater* 30:1–21
- Deschler F, Price M, Pathak S, Klintberg LE, Jarausch DD, Higler R, Hüttner S, Leijtens T, Stranks SD, Snaith HJ, Atature M, Phillips RT, Friend RH (2014) High photoluminescence efficiency and optically pumped lasing in solution-processed mixed halide perovskite semiconductors. *J Phys Chem Lett* 5:1421–1426
- Dong Q, Fang Y, Shao Y, Mulligan P, Qiu J, Cao L, Huang J (2015) Electron-hole diffusion lengths > 175 nm in solution-grown CH₃NH₃PbI₃ single crystals. *Science* 347(80):967–970
- Duong T, Lal N, Grant D, Jacobs D, Zheng P, Rahman S, Shen H, Stocks M, Blakers A, Weber K, White TP, Catchpole KR (2016) Semitransparent perovskite solar cell with sputtered front and rear electrodes for a four-terminal tandem. *IEEE J Photovoltaics* 6:679–687
- Eperon GE, Stranks SD, Menelaou C, Johnston MB, Herz LM, Snaith HJ (2014) Formamidinium lead trihalide: a broadly tunable perovskite for efficient planar heterojunction solar cells. *Energy Environ Sci* 7:982–988
- Eperon GE, Leijtens T, Bush KA, Prasanna R, Green T, Wang JT, McMeekin DP, Volonakis G, Milot RL, May R, Palmstrom A, Slotcavage DJ, Belisle RA, Patel JB, Parrott ES, Sutton RJ, Ma W, Moghadam F, Conings B, Babayigit A, Boyen HG, Bent S, Giustino F, Herz LM, Johnston MB, McGehee MD, Snaith HJ (2016) Perovskite-perovskite tandem photovoltaics with optimized band gaps. *Science* 354:861–865

- Fu Y, Zhu H, Schrader AW, Liang D, Ding Q, Joshi P, Hwang L, Zhu XY, Jin S (2016) Nanowire lasers of formamidinium lead halide perovskites and their stabilized alloys with improved stability. *Nano Lett* 16:1000–1008
- Futscher MH, Ehrler B (2016) Efficiency limit of Perovskite/Si tandem solar cells. *ACS Energy Lett* 1:863–868
- Futscher MH, Ehrler B (2017) Modeling the performance limitations and prospects of perovskite/Si tandem solar cells under realistic operating conditions. *ACS Energy Lett* 2:2089–2095
- Gao R, Li G, Han Y, Xi Y, Ji T, Tian Y, Tian B, Hao Y, Wu Y, Cui Y (2020) Carrier lifetime exceeding 81 ns in single crystalline perovskite nanowires enable large on-off ratio photodetectors. *Org Electron* 83:105744
- Ghosh S, Pradhan B (2019) Lead-free metal halide perovskite nanocrystals: challenges. *Appl Future Aspects ChemNanoMat* 5:300–312
- Green MA, Dunlop ED, Hohl-Ebinger J, Yoshita M, Kopidakis N, Hao X (2020) Solar cell efficiency tables (version 56). *Prog Photovoltaics Res Appl* 28:629–638
- Green M, Dunlop E, Hohl-Ebinger J, Yoshita M, Kopidakis N, Hao X (2021) Solar cell efficiency tables (version 57). *Prog Photovoltaics Res Appl* 29:3–15
- Gu S, Lin R, Han Q, Gao Y, Tan H, Zhu J (2020) Tin and mixed lead-tin halide perovskite solar cells: progress and their application in tandem solar cells. *Adv Mater* 32:1–16
- Guarnera S, Abate A, Zhang W, Foster JM, Richardson G, Petrozza A, Snaith HJ (2015) Improving the long-term stability of perovskite solar cells with a porous Al₂O₃ buffer layer. *J Phys Chem Lett* 6:432–437
- Guner T, Demir MM (2018) A review on halide perovskites as color conversion layers in white light emitting diode applications. *Phys Status Solidi Appl Mater Sci* 215:1–11
- Habisreutinger SN, Leijtens T, Eperon GE, Stranks SD, Nicholas RJ, Snaith HJ (2014) Carbon nanotube/polymer composites as a highly stable hole collection layer in perovskite solar cells. *Nano Lett* 14:5561–5568
- Habisreutinger SN, Leijtens T, Eperon GE, Stranks SD, Nicholas RJ, Snaith HJ (2014) Enhanced hole extraction in perovskite solar cells through carbon nanotubes. *J Phys Chem Lett* 5:4207–4212
- Hadjarab B, Bouguelia A, Trari M (2007) Optical and transport properties of lanthanum-doped stannate BaSnO₃. *J Phys D Appl Phys* 40:5833–5839
- Heo JH, Lee MH, Jang MH, Im SH (2016) Highly efficient CH₃NH₃PbI_{3-x}Cl_x mixed halide perovskite solar cells prepared by re-dissolution and crystal grain growth via spray coating. *J Mater Chem A* 4:17636–17642
- Huang JH, Jiang KJ, Cui XP, Zhang QQ, Gao M, Su MJ, Yang LM, Song Y (2015) Direct conversion of CH₃NH₃PbI₃ from electrodeposited PbO for highly efficient planar perovskite solar cells. *Sci Rep* 5:1–8
- Hutter EM, Gélvez-Rueda MC, Osherov A, Bulović V, Grozema FC, Stranks SD, Savenije TJ (2017) Direct-indirect character of the bandgap in methylammonium lead iodide perovskite. *Nat Mater* 16:115–120
- Im JH, Lee CR, Lee JW, Park SW, Park NG (2011) 6.5% Efficient Perovskite Quantum-Dot-Sensitized Solar Cell. *Nanoscale* 3:4088–4093
- Im J, Kim H, Park N, Morphology-photovoltaic property correlation in perovskite solar cells: One-step versus two-step deposition of CH₃NH₃PbI₃ Morphology-photovoltaic property correlation in perovskite solar cells: One-step versus two-step deposition, 081510
- Ito S, Tanaka S, Manabe K, Nishino H (2014) Effects of surface blocking layer of Sb₂S₃ on nanocrystalline TiO₂ for CH₃NH₃PbI₃ perovskite solar cells. *J Phys Chem C* 118:16995–17000
- Jiang W, Yang T, Gao Y, Gao X (2016) Enhanced stability of CH₃NH₃PbI₃ thin films deposited on FTZO. *Chem Lett* 45:819–821
- Jiang F, Yang D, Jiang Y, Liu T, Zhao X, Ming Y, Luo B, Qin F, Fan J, Han H, Zhang L, Zhou Y (2018) Chlorine-incorporation-induced formation of the layered phase for antimony-based lead-free perovskite solar cells. *J Am Chem Soc* 140:1019–1027

- Jin J, Chen C, Li H, Cheng Y, Xu L, Dong B, Song H, Dai Q (2017) Enhanced performance and photostability of perovskite solar cells by introduction of fluorescent carbon dots. *ACS Appl Mater Interfaces* 9:14518–14524
- Jung HS, Park NG (2015) Perovskite solar cells: From materials to devices. *Small* 11:10–25
- Kang DH, Park NG (2019) On the current-voltage hysteresis in perovskite solar cells: dependence on perovskite composition and methods to remove hysteresis. *Adv Mater* 31:1–23
- Kim HS, Lee CR, Im JH, Lee KB, Moehl T, Marchioro A, Moon SJ, Humphry-Baker R, Yum JH, Moser JE, Grätzel M, Park NG (2012) Lead iodide perovskite sensitized all-solid-state submicron thin film mesoscopic solar cell with efficiency exceeding 9%. *Sci Rep* 2:1–7
- Kim J, Lee SH, Lee JH, Hong KH (2014) The role of intrinsic defects in methylammonium lead iodide perovskite. *J Phys Chem Lett* 5:1312–1317
- Kim JH, Liang PW, Williams ST, Cho N, Chueh CC, Glaz MS, Ginger DS, Jen AKY (2015) High-performance and environmentally stable planar heterojunction perovskite solar cells based on a solution-processed copper-doped nickel oxide hole-transporting layer. *Adv Mater* 27:695–701
- Kim HS, Jang IH, Ahn N, Choi M, Guerrero A, Bisquert J, Park NG (2015) Control of I-V hysteresis in $\text{CH}_3\text{NH}_3\text{PbI}_3$ perovskite solar cell. *J Phys Chem Lett* 6:4633–4639
- Kojima A, Teshima K, Shirai Y, Miyasaka T (2009) Organometal halide perovskites as visible-light sensitizers for photovoltaic cells. *J Am Chem Soc* 131:6050–6051
- Lee MM, Teuscher J, Miyasaka T, Murakami TN, Snaith HJ (2012) Efficient hybrid solar cells based on meso-superstructured organometal halide perovskites. *Science* 338:643–647
- Lee J, Menamparambath MM, Hwang JY, Baik S (2015) Hierarchically structured hole transport layers of Spiro-OMeTAD and multiwalled carbon nanotubes for perovskite solar cells. *Chemsuschem* 8:2358–2362
- Leijtens T, Eperon GE, Pathak S, Abate A, Lee MM, Snaith HJ (2013) Overcoming ultraviolet light instability of sensitized TiO_2 with meso-superstructured organometal tri-halide perovskite solar cells. *Nat Commun* 4:1–8
- Li DB, Hu L, Xie Y, Niu G, Liu T, Zhou Y, Gao L, Yang B, Tang J (2016) Low-temperature-processed amorphous Bi_2S_3 film as an inorganic electron transport layer for perovskite solar cells. *ACS Photonics* 3:2122–2128
- Li Y, Lu K, Ling X, Yuan J, Shi G, Ding G, Sun J, Shi S, Gong X, Ma W (2016) High performance planar-heterojunction perovskite solar cells using amino-based fulleropyrrolidine as the electron transporting material. *J Mater Chem A* 4:10130–10134
- Li Z, Klein TR, Kim DH, Yang M, Berry JJ, Van Hest MFAM, Zhu K (2018) Scalable fabrication of perovskite solar cells. *Nat Rev Mater* 3:1–20
- Lian J, Lu B, Niu F, Zeng P, Zhan X (2018) Electron-transport materials in perovskite solar cells. *Small Methods* 2:1800082
- Liang PW, Chueh CC, Williams ST, Jen AKY (2015) Roles of fullerene-based interlayers in enhancing the performance of organometal perovskite thin-film solar cells. *Adv Energy Mater* 5:1–7
- Lin R, Xiao K, Qin Z, Han Q, Zhang C, Wei M, Saidaminov MI, Gao Y, Xu J, Xiao M, Li A, Zhu J, Sargent EH, Tan H (2019) Monolithic all-perovskite tandem solar cells with 24.8% efficiency exploiting comproportionation to suppress Sn(II) oxidation in precursor ink. *Nat Energy* 4:864–873
- Lin R, Xiao K, Qin Z, Han Q, Zhang C, Wei M, Saidaminov MI, Gao Y, Xu J, Xiao M, Li A, Zhu J, Sargent EH, Tan H (2019) Monolithic all-perovskite tandem solar cells with 24.8% efficiency exploiting comproportionation to suppress Sn(II) oxidation in precursor ink. *Nat Energy* 4:864–873
- Litvin AP, Zhang X, Berwick K, Fedorov AV, Zheng W, Baranov AV (2020) Carbon-based interlayers in perovskite solar cells. *Renew Sustain Energy Rev* 124:109774
- Liu M, Johnston MB, Snaith HJ (2013) Efficient planar heterojunction perovskite solar cells by vapour deposition. *Nature* 501:395–398

- Liu J, Wu Y, Qin C, Yang X, Yasuda T, Islam A, Zhang K, Peng W, Chen W, Han L (2014) A dopant-free hole-transporting material for efficient and stable perovskite solar cells. *Energy Environ Sci* 7:2963–2967
- Liu P, He X, Ren J, Liao Q, Yao J, Fu H (2017) Organic-inorganic hybrid perovskite nanowire laser arrays. *ACS Nano* 11:5766–5773
- Lu J, Jiang L, Li W, Li F, Pai NK, Scully AD, Tsai CM, Bach U, Simonov AN, Cheng YB, Spiccia L (2017) Diammonium and monoammonium mixed-organic-cation perovskites for high performance solar cells with improved stability. *Adv Energy Mater* 7(18):1700444
- Ma S, Cai M, Cheng T, Ding X, Shi X, Alsaedi A, Hayat T, Ding Y, Tan Z, Dai S (2018) Two-dimensional organic-inorganic hybrid perovskite: from material properties to device applications. *Sci China Mater* 61:1257–1277
- Mahmood K, Swain BS, Kirmani AR, Amassian A (2015) Highly efficient perovskite solar cells based on a nanostructured WO_3 - TiO_2 core-shell electron transporting material. *J Mater Chem A* 3:9051–9057
- Mailoa JP, Bailie CD, Akey AJ, Hoke ET, Johlin EC, Nguyen WH, Sofia SE, McGehee MD, Buonassisi T (2015) Optical loss analysis of monolithic perovskite/Si tandem solar cell, 2015 IEEE 42nd Photovolt. Spec Conf PVSC 2015:1–3
- Mao L, Teicher SML, Stoumpos CC, Kennard RM, Decrescent RA, Wu G, Schuller JA, Chabynyc ML, Cheetham AK, Seshadri R (2019) Chemical and structural diversity of hybrid layered double perovskite halides. *J Am Chem Soc* 141:19099–19109
- Miletić T, Pavoni E, Trifiletti V, Rizzo A, Listorti A, Colella S, Armaroli N, Bonifazi D (2016) Covalently functionalized SWCNTs as tailored p-type dopants for perovskite solar cells. *ACS Appl Mater Interf* 8:27966–27973
- Nakamura M, Tada K, Kinoshita T, Bessho T, Nishiyama C, Takenaka I, Kimoto Y, Higashino Y, Sugimoto H, Segawa H (2020) Perovskite/CIGS spectral splitting double junction solar cell with 28% power conversion efficiency. *Iscience*. 23:101817
- Noh JH, Im SH, Heo JH, Mandal TN, Il Seok S (2013) Chemical management for colorful, efficient, and stable inorganic-organic hybrid nanostructured solar cells. *Nano Lett* 13:1764–1769
- Ohtomo A, Hwang HY (2004) A high-mobility electron gas at the $\text{LaAlO}_3/\text{SrTiO}_3$ heterointerface. *Nature* 427:423–426
- Ouyang Z, Abrams H, Bergstone R, Li Q, Zhu F, Li D (2020) Rapid layer-specific annealing enabled by ultraviolet LED with estimation of crystallization energy for high-performance perovskite solar cells. *Adv Energy Mater* 10:1–10
- Paquin F, Rivnay J, Salleo A, Stingelin N, Silva C (2015) Multi-phase semicrystalline microstructures drive exciton dissociation in neat plastic semiconductors. *J Mater Chem C* 3:10715–10722
- Poglitich A, Weber D (1987) Dynamic disorder in methylammoniumtrihalogenoplumbates (II) observed by millimeter-wave spectroscopy. *J Chem Phys* 87:6373–6378
- Priyadarshi A, Haur LJ, Murray P, Fu D, Kulkarni S, Xing G, Sum TC, Mathews N, Mhaisalkar SG (2016) A large area (70 cm^2) monolithic perovskite solar module with a high efficiency and stability. *Energy Environ Sci* 9:3687–3692
- Qin T, Huang W, Kim JE, Vak D, Forsyth C, McNeill CR, Cheng YB (2017) Amorphous hole-transporting layer in slot-die coated perovskite solar cells. *Nano Energy* 31:210–217
- Ravi VK, Singhal N, Nag A (2018) Initiation and future prospects of colloidal metal halide double-perovskite nanocrystals: $\text{Cs}_2\text{AgBiX}_6$ ($X = \text{Cl}, \text{Br}, \text{I}$). *J Mater Chem A* 6:21666–21675
- Rong Y, Hou X, Hu Y, Mei A, Liu L, Wang P, Han H (2017) Synergy of ammonium chloride and moisture on perovskite crystallization for efficient printable mesoscopic solar cells. *Nat Commun* 8:14555
- Ruschak KJ (1976) Limiting flow in a pre-metered coating device. *Chem Eng Sci* 31:1057–1060
- Saidaminov MI, Abdelhady AL, Murali B, Alarousu E, Burlakov VM, Peng W, Dursun I, Wang L, He Y, MacUlán G, Goriely A, Wu T, Mohammed OF, Bakr OM (2015) High-quality bulk hybrid perovskite single crystals within minutes by inverse temperature crystallization. *Nat Commun* 6:1–6

- Schileo G, Grancini G (2020) Halide perovskites: current issues and new strategies to push material and device stability. *Jphys Energy*. 2:021005
- Senanayak SP, Abdi-Jalebi M, Kamboj VS, Carey R, Shivanna R, Tian T, Schweicher G, Wang J, Giesbrecht N, Di Nuzzo D, Beere HE, Docampo P, Ritchie DA, Fairen-Jimenez D, Friend RH, Srinringhaus H (2020) A general approach for hysteresis-free, operationally stable metal halide perovskite field-effect transistors. *Sci Adv* 6:1–13
- Singh R, Singh PK, Bhattacharya B, Rhee H (2019) Review of current progress in inorganic hole-transport materials for perovskite solar cells. *Appl Mater Today* 14:175–200
- Slavney AH, Hu T, Lindenberg AM, Karunadasa HI (2016) A bismuth-halide double perovskite with long carrier recombination lifetime for photovoltaic applications. *J Am Chem Soc* 138:2138–2141
- Smith IC, Hoke ET, Solis-Ibarra D, McGehee MD, Karunadasa HI (2014) A layered hybrid perovskite solar-cell absorber with enhanced moisture stability. *Angew Chemie Int Ed* 53:11232–11235
- Snath HJ, Ducati C (2010) SnO₂-Based dye-sensitized hybrid solar cells exhibiting near unity absorbed photon-to-electron conversion efficiency. *Nano Lett* 10:1259–1265
- Tang S, Deng Y, Zheng X, Bai Y, Fang Y, Dong Q, Wei H, Huang J (2017) Composition engineering in doctor-blading of perovskite solar cells. *Adv Energy Mater* 7:1–7
- Thien GSH, Talik NA, Yap BK, Nakajima H, Tunmee S, Chanlek N, Goh BT (2020) Improvement of MAPbI₃ perovskite blend with TiO₂ nanoparticles as ReRAM device. *Ceram Int* 46:29041–29051
- Todorov T, Gershon T, Gunawan O, Sturdevant C, Guha S (2014) Perovskite-kesterite monolithic tandem solar cells with high open-circuit voltage. *Appl Phys Lett* 105:173902
- Tong J, Song Z, Kim DH, Chen X, Chen C, Palmstrom AF, Ndione PF, Reese MO, Dunfield SP, Reid OG, Liu J, Zhang F, Harvey SP, Li Z, Christensen ST, Teeter G, Zhao D, Al-Jassim MM, van Hest M, Beard MC, Shaheen SE, Berry JJ, Yan Y, Zhu K (2019) Carrier lifetimes of >1 μs in Sn-Pb perovskites enable efficient all-perovskite tandem solar cells. *Science* 364:475–479
- Wang X, Li Z, Xu W, Kulkarni SA, Batabyal SK, Zhang S, Cao A, Wong LH (2015) TiO₂ nanotube arrays based flexible perovskite solar cells with transparent carbon nanotube electrode. *Nano Energy* 11:728–735
- Wang F, Endo M, Mouri S, Miyauchi Y, Ohno Y, Wakamiya A, Murata Y, Matsuda K (2016a) Highly stable perovskite solar cells with an all-carbon hole transport layer. *Nanoscale* 8:11882–11888
- Wang Z, Liu J, Xu ZQ, Xue Y, Jiang L, Song J, Huang F, Wang Y, Zhong YL, Zhang Y, Cheng YB, Bao Q (2016b) Wavelength-tunable waveguides based on polycrystalline organic-inorganic perovskite microwires. *Nanoscale* 8:6258–6264
- Wang F, Geng W, Zhou Y, Fang HH, Tong CJ, Loi MA, Liu LM, Zhao N (2016c) Phenylalkylamine passivation of organolead halide perovskites enabling high-efficiency and air-stable photovoltaic cells. *Adv Mater* 28:9986–9992
- Wang Z, Zhu X, Zuo S, Chen M, Zhang C, Wang C, Ren X, Yang Z, Liu Z, Xu X, Chang Q, Yang S, Meng F, Liu Z, Yuan N, Ding J, Liu S, Yang D (2020) 27%-efficiency four-terminal perovskite/silicon tandem solar cells by sandwiched gold nanomesh. *Adv Funct Mater* 30:1–8
- Xing G, Mathews N, Sun S, Lim SS, Lam YM, Graetzel M, Mhaisalkar S, Sum TC (2013) Long-range balanced electron-and hole-transport lengths in organic-inorganic CH₃NH₃PbI₃. *Science* 342:344–347
- Xing Y, Sun C, Yip HL, Bazan GC, Huang F, Cao Y (2016) New fullerene design enables efficient passivation of surface traps in high performance p-i-n heterojunction perovskite solar cells. *Nano Energy* 26:7–15
- Yang M, Zhou Y, Zeng Y, Jiang CS, Padture NP, Zhu K (2015) Square-centimeter solution-processed planar CH₃NH₃PbI₃ perovskite solar cells with efficiency exceeding 15%. *Adv Mater* 27:6363–6370
- Yang J, Siempelkamp BD, Liu D, Kelly TL (2015) Investigation of CH₃NH₃PbI₃ degradation rates and mechanisms in controlled humidity environments using in situ techniques. *ACS Nano* 9:1955–1963

- Yang M, Li Z, Reese MO, Reid OG, Kim DH, Siol S, Klein TR, Yan Y, Berry JJ, Van Hest MFAM, Zhu K (2017) Perovskite ink with wide processing window for scalable high-efficiency solar cells. *Nat Energy* 2:1–9
- Yang X, Zhang X, Deng J, Chu Z, Jiang Q, Meng J, Wang P, Zhang L, Yin Z, You J (2018) Efficient green light-emitting diodes based on quasi-two-dimensional composition and phase engineered perovskite with surface passivation. *Nat Commun* 9:2–9
- Yang WS, Noh JH, Jeon NJ, Kim YC, Ryu S, Seo J, Il Seok S (2015) High-performance photovoltaic perovskite layers fabricated through intramolecular exchange. *Science* 348:1234–1237
- Yang Michael Y, Chen Q, Hsieh YT, Bin Song T, De Marco N, Zhou H, Yang Y (2015) Multi-layer transparent top electrode for solution processed perovskite/Cu(In,Ga)(Se,S)₂ four terminal tandem solar cells. *ACS Nano* 9:7714–7721
- Yao D, Zhang C, Pham ND, Zhang Y, Tiong VT, Du A, Shen Q, Wilson GJ, Wang H (2018) Hindered formation of Photoinactive δ -FAPbI₃ phase and hysteresis-free mixed-cation planar heterojunction perovskite solar cells with enhanced efficiency via potassium incorporation. *J Phys Chem Lett* 9:2113–2120
- Yin WJ, Yang JH, Kang J, Yan Y, Wei SH (2015) Halide perovskite materials for solar cells: a theoretical review. *J Mater Chem A* 3:8926–8942
- Zhang Q, Dandeneau CS, Zhou X, Cao C (2009) ZnO nanostructures for dye-sensitized solar cells. *Adv Mater* 21:4087–4108
- Zhang R, Chen Y, Xiong J, Liu X (2017) Synergistic carbon-based hole transporting layers for efficient and stable perovskite solar cells. *J Mater Sci* 53:4507–4514
- Zhang Z, Li Z, Meng L, Lien SY, Gao P (2020) Perovskite-based tandem solar cells: get the most out of the sun. *Adv Funct Mater* 30:2001904
- Zhao D, Chen C, Wang C, Junda MM, Song Z, Grice CR, Yu Y, Li C, Subedi B, Podraza NJ, Zhao X, Fang G, Xiong R-G, Zhu K, Yan Y (2018) Efficient two-terminal all-perovskite tandem solar cells enabled by high-quality low-bandgap absorber layers. *Nat Energy* 3:1093–1100
- Zhu Z, Ma J, Wang Z, Mu C, Fan Z, Du L, Bai Y, Fan L, Yan H, Phillips DL, Yang S (2014) Efficiency enhancement of perovskite solar cells through fast electron extraction: the role of Graphene quantum dots. *J Am Chem Soc* 136:3760–3763

Radiation Hardness, a New Characterization Technique and Bistability Regarding Methylammonium Containing Perovskite Solar Cells



H. C. Neitzert, G. Landi, F. Lang, J. Bundesmann, A. Denker, S. Albrecht, N. Nickel, P. C. Ramamurthy, and A. Sambandam

1 Introduction

Perovskite solar cell technology is already rivalling conventional c-Si technology for terrestrial applications. Record efficiencies of 23.7% have been reported for single cells (Green et al. 2019) and more than 17% efficiencies for mini-modules (Green et al. 2018). Even more promising results have been reported on Tandem type solar cells either in combination with crystalline silicon (Zhang et al. 2018a) or with CIGS (Jost et al. 2019). In the first case the single cell record efficiencies have already been reached. For the important field of solar cells in space, flexible and lightweight solar cells—as possible to be realized with perovskite—are very attractive, but in this case, especially a good resistance to high energy particle radiation is required. Early space solar cells, starting with the first application in 1958 on the Vanguard satellite mission (Easton and Votav 1959), have all been crystalline silicon based. This material is however rather sensible to high energy particle irradiation (Neitzert

H. C. Neitzert (✉) · G. Landi
Department of Industrial Engineering, Salerno University, Fisciano, Italy
e-mail: neitzert@unisa.it

G. Landi
Institute for Polymers, Composites and Biomaterials, CNR, Portici, Italy

F. Lang · J. Bundesmann · A. Denker · S. Albrecht · N. Nickel
Helmholtz Zentrum Berlin Für Materialien Und Energie, Berlin, Germany

A. Denker
Department of Physics, Beuth Hochschule, Berlin, Germany

P. C. Ramamurthy
Department of Materials Engineering, Indian Institute of Science, Bangalore, India

A. Sambandam
Department of Chemistry, National Institute of Technology, Tiruchirappalli, India

et al. 2006, 2008), although specific strategies have been developed to minimize the radiation induced damage in Silicon based solar cells (Khan et al. 2003). The most efficient solar cell type with crystalline silicon absorber—namely the crystalline silicon/amorphous silicon heterojunction solar cell (Fahrner et al. 2006)—have also been tested under space-like radiation conditions and show very similar strong degradation as the conventional Silicon p-n homojunction solar cells (Neitzert et al. 2006; Scherff et al. 2006). Amorphous hydrogenated Silicon based thin-film solar cells, either as single junction cells (Klaver 2007) or as part of a micro-morph Tandem cell (Neitzert et al. 2010) or a triple-junction amorphous thin film solar cell (Sato et al. 2012) are more radiation-tolerant than crystalline Silicon devices, but have an initial efficiency below 13%, what limits their possible application in space, especially when compared to the state-of-the-art multi-junction III-V based solar cells with nowadays more than 27% initial efficiency, that were for example very successfully used in the last MARS-rover experiment (Stella et al. 2005). Nevertheless, there is still a large interest in developing foldable, low-cost and lightweight solar cell arrays with at least 20% stabilized efficiency and perovskite could be a good candidate for this purpose.

2 Perovskite Solar Cell Radiation Hardness Investigation

2.1 Solar Cell Preparation and Characterization

For this study Perovskite solar cells with a planar inverted staggered structure were used with the layer sequence: glass/ITO/PEDOT:PSS/CH₃NH₃PbI₃/PCBM/BCP/Ag. This configuration has the advantage of only a very small hysteresis in the solar characteristics under illumination. The solar cell preparation was done, as follows: After the ITO coated glass cleaning, a PEDOT:PSS layer (60 nm thick) was deposited on this substrate by spin coating. This layer had then been annealed for 20 min at 150 °C. Subsequently, a stoichiometric CH₃NH₃PbI₃ precursor solution containing 1.1 M of PbI₂ and CH₃NH₃I has been prepared in a mixed solvent of γ -butyrolactone and dimethyl sulfoxide with a volume ratio of 70 vol.% to 30 vol.%. These solutions were stirred for 12 h at 60 °C and spin-coated in a 3-step-sequence on top of the PEDOT:PSS layer. In a last step, 150 μ l toluene were then dripped on top of the perovskite layer. Spin coating was performed in a nitrogen atmosphere. Subsequently, the CH₃NH₃PbI₃ layer was crystallized for 10 min at 100 °C. The resulting perovskite absorber thickness was 350 nm. Then an electron selective contact was formed by spin coating of an about 50 nm thick PC₆₁BM layer on top of the active layer. After annealing for 10 min at 100 °C then a thin layer of bathocuproine (BCP) was spin coated from an ethanol solution. After a 15 min

long annealing step at 70 °C, 100 nm thick Ag electrical contacts were thermally evaporated using a shadow mask. More technological details can be found in Lang et al. (2016).

In Fig. 1a the device structure is schematically shown, together with the indication of the direction of the light and proton beam irradiation. In the cross-sectional SEM-micrograph of the solar cell (see Fig. 1b, the polycrystalline nature of the perovskite layer and the relatively large grainsize are clearly seen. The current density—voltage ($J - V$) characteristics with and without illumination (under AM1.5G condition) and the internal and external quantum efficiency spectra for a typical as-grown solar cell are shown in Fig. 1d and e respectively. In the J-V light characteristics only a very small hysteresis between reverse scan and forward scan is observed and a stabilized efficiency of about 12% has been measured (see inset of Fig. 1d).

Additionally in Fig. 1c simulation results are given, that show the depth distribution of the proton irradiation induced defects for various proton energies. It can be seen, that for a proton energy of 68 MeV, a defect maximum—corresponding to the projected range of the ions—at almost 2 cm is found and for lower depths an almost constant defect profile can be expected. This means, that this proton energy is quite suitable for the investigations, because the radiation hardness of encapsulated devices can be measured and the defect profile in the active layers of the solar cells is constant.

2.2 *Influence of Proton Irradiation on the Solar Cell Characteristics and Parameters*

In order to directly check the radiation hardness of the perovskite solar cells, the solar cells have been illuminated with constant light during proton irradiation and the light current density—voltage characteristics has been continuously measured and the relevant parameters have been determined. In Fig. 2a the development of these parameters, normalized to their initial value is shown as a function of the proton fluence. It can be observed, that the open circuit voltage (V_{oc}) and the fill factor (FF) do not degrade at all up to the maximum fluence value of 10^{13} protons/cm². The short-circuit current density (J_{sc}) and in consequence also the solar cell efficiency (η) start to decrease for lower fluence values and reach about 60% of the original values at the maximum fluence of 10^{13} protons/cm². As comparison, the development of the degradation of a commercial crystalline silicon photodiode normalized J_{sc} value at the same proton energy of 68 MeV has been also plotted in Fig. 2a. It is clearly seen, that the degradation of the silicon device starts much earlier.

An important fraction of the degradation of the perovskite solar cell is due to the decrease of the optical transmittance of the ITO coated glass substrate and not due to the active layer degradation. The effect of the proton irradiation for two different irradiation levels is shown in Fig. 2b. Using this data, the comparison in Fig. 1d between Silicon and Perovskite device J_{sc} degradation can be corrected in order to

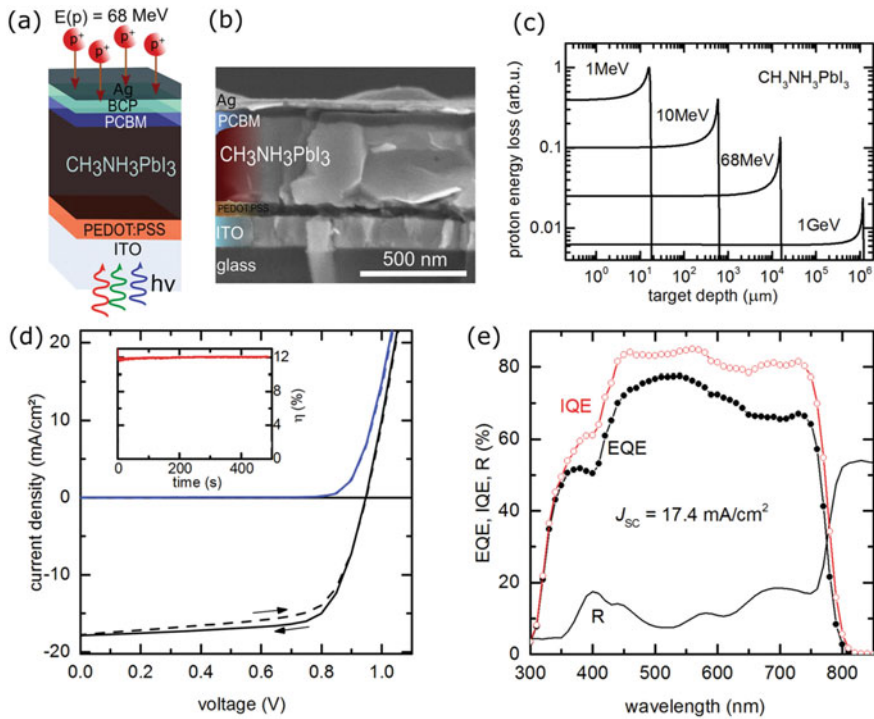


Fig. 1 Reprinted with kind permission; Original article: Lang et al. Adv. Mat. 2016 (Lang et al. 2016). **a** A sketch of the perovskite solar cell. **b** Cross-sectional SEM micrograph of an inverted perovskite solar cell consisting of the layer stack glass/ITO/PEDOT:PSS/CH₃NH₃PbI₃/PCBM/BCP/Ag. The device was illuminated through the glass substrate. **c** Depth profile of the irradiation induced defects for proton beams with different energies in the perovskite CH₃NH₃PbI₃. The simulation was performed using SRIM (Ziegler et al. 2010). **d** Current–voltage characteristics of the perovskite solar cell before irradiation, taken in the dark (blue curve) and under AM1.5G illumination (black curve). The scan direction of the voltage is indicated by arrows. Only a very small hysteresis between reverse scan (solid lines) and forward scan (dashed lines) is observed. The stabilized efficiency from maximum power point tracking is shown in the inset. **e** External (EQE) and internal (IQE) quantum efficiencies. The specular reflection (R) is shown as black solid line

compare the active layer degradation only. Doing this correction for the perovskite J_{sc} values, at a fluence value of 10^{13} protons/cm² a decrease to only 80% of the initial value is obtained (indicated by the red mark in Fig. 2a). This means, that the degradation rate of Perovskite solar cells is about 2 orders of magnitude lower than that of Silicon photodetectors.

In conclusion it has been found, that perovskite solar cells may be a valid alternative to nowadays used space solar cells. At least in terms of radiation hardness.

Due to the high proton energy, used for the radiation stability tests, the solar cells are directly after the irradiation activated and we could characterize them under

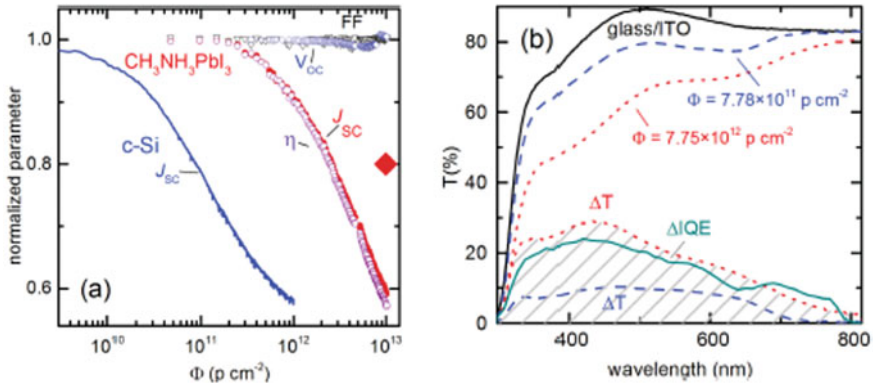
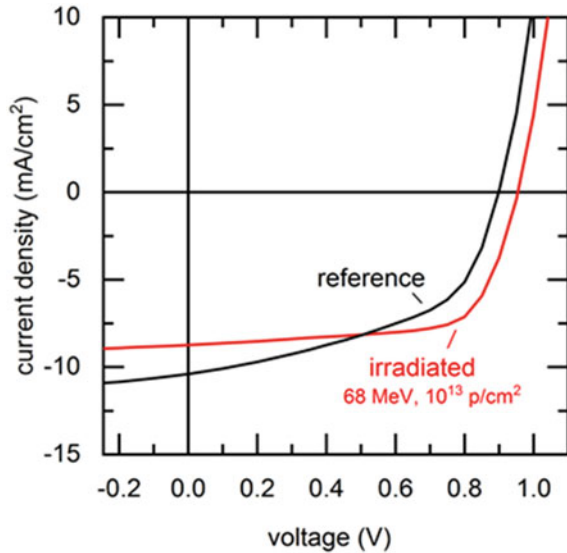


Fig. 2 Reprinted with kind permission: Original article: Lang et al. Adv. Mat. 2016 (Lang et al. 2016) **a** Monitoring of the solar cell parameters (normalized to the initial value) of a perovskite solar cell during irradiation with 68 MeV protons with a maximum fluence of 10^{13} protons/cm². For comparison the monitoring of a crystalline silicon photodiode short circuit (J_{sc}) current during irradiation with 68 MeV protons up to a fluence of 10^{12} protons/cm² has been added. **b** Change of the optical transmission spectral characteristics of the ITO-coated glass substrates, used for the realization of the investigated perovskite solar cells

standard conditions (AM1.5G) therefore only after a certain time, when the radioactivity decreased to low enough values. Therefore we compared the irradiated devices to reference samples that had not been irradiated. Both devices—with very similar properties before the tests—however, did undergo some long-time degradation. In Fig. 3 the light $J - V$ characteristics of a non-irradiated perovskite cell is compared to a cell, that was irradiated with 10^{13} protons/cm² at 68 MeV. While the short-circuit current of the irradiated cell is slightly lower than that of the reference cell, can we observe a higher open-circuit voltage and surprisingly also a higher fill factor in the case of the irradiated solar cell.

It should be noted that we tested recently also a new class of Perovskite solar cells, based on a Triple-Cation Perovskite. This optimized solar cells with $\text{Cs}_{0.05}\text{MA}_{0.17}\text{FA}_{0.83}\text{Pb}(\text{I}_{0.83}\text{Br}_{0.17})_3$ as active layer had a high initial efficiency of 19.4%. Also in this case, we found a very stable behavior with only minor degradation, when compared to non-irradiated references (Lang et al. 2019). A direct comparison of the radiation induced current decrease of the Perovskite solar cells during irradiation to commercial SiC based Schottky diodes, revealed that the Perovskite based devices are also more stable than this wide-bandgap material, which in literature is reported to possess a good radiation-hardness (Canepa et al. 1964).

Fig. 3 Comparison of the current–voltage characteristics under AM1.5G illumination conditions of a non-irradiated reference (black trace) and a with 68 MeV protons (fluence of 10^{13} protons/cm²) irradiated CH₃NH₃PbI₃ solar cell. Both displayed curves have been measured about 2 weeks after the irradiation. The initial efficiency before irradiation of both cells was about 12.0%



3 Low Frequency Noise Spectroscopy as Perovskite Solar Cell Characterization Tool

Analysis of the electrical low frequency noise spectra at different temperatures has been shown to be a valuable tool for the characterization of complex electronic systems. In a common research between the Optoelectronics Group and the CNR-SPIN group at Salerno University this technique has been originally applied to the understanding of electrical interconnections in carbon nanotube networks with percolative transport, embedded into various organic matrix materials (Barone et al. 2015). The same technique has been successfully applied also to the investigation of the electronic structure and degradation of organic solar cells (Barone et al. 2014) and of silicon solar cells with different levels of proton induced degradation (Landi et al. 2016). In the last case it could be shown that important parameters, as electronic state densities and defect level energetic positions, can be determined using this innovative measurement technique.

Applying the noise spectroscopy technique to the characterization of perovskite solar cells, a detailed electronic defect model has been developed, that contributed to understand the relation between the electronic defect structure and the device performance (Landi et al. 2017). In Fig. 4 it is for example demonstrated, that for two different classes of Perovskite solar cells, with large differences in the perovskite grain sizes in the absorber layer, that result in a different defect concentration, a strong correlation between the solar cell conversion efficiency and the value of the electronic noise level can be observed (Landi et al. 2017).

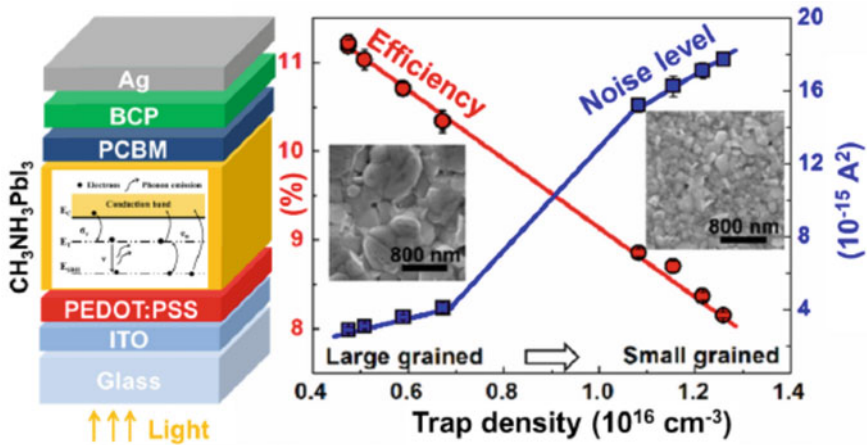


Fig. 4 Reprinted with kind permission: Original article: Landi et al. *Adv. Sci.* 2017 (Landi et al. 2017). Schematic structure (with sketch of the electron recombination and trapping mechanisms) of a perovskite solar cell and relation between the solar cell efficiency (red dots) and the current noise level (blue dots) as a function of the trap density in solar cells with different grain sizes (see SEM images in the inset)

Another interesting application of low-frequency noise-spectroscopy is the identification of different current-transport mechanisms at different temperatures in solar cells. In a recent research, we could show, that noise spectroscopy is a useful tool for understanding the temperature stress induced modifications regarding for example the internal barrier heights in polymer solar cells (Landi et al. 2018). Perovskite is a material which exists in different crystalline configurations. Dependent on the temperature, orthorhombic, tetragonal and cubic configurations are found. While the tetragonal to cubic phase transition is found at a temperature slightly above room temperature does the orthorhombic to tetragonal transition take place at about 160 K.

This transition is clearly seen in noise measurements, with a pronounced increase of the voltage-noise amplitude at this transition temperature (see Fig. 5) (Barone et al. 2016). The unexpected additional noise, with a peak at 155 K is due to a structural reorganization of the perovskite material in this temperature range, which results in a random distribution of microscopic phases, to which a random resistor network can be associated. The $1/f$ noise with a quadratic bias current dependence can then be explained by a random fluctuation of the resistor values between the values, which are characteristic for the tetragonal and the orthorhombic phase. A detailed analysis of this transition and of the noise behavior in the orthorhombic and tetragonal phases can be found in Barone et al. (2016). It would be interesting in the future to extend this research also for the investigation of the tetragonal to cubic transition. This transition is very close to the normal operating temperature of perovskite solar cells in terrestrial applications (Barone et al. 2014).

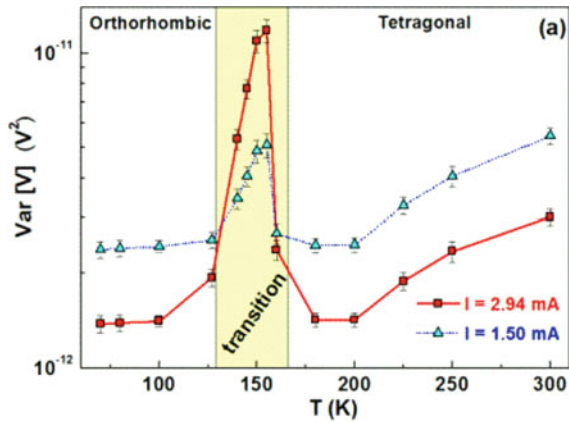


Fig. 5 Reprinted with kind permission: Original article: Landi et al., IPRS Symp. San Francisco 2018 (Landi et al. 2018). **a** Voltage-noise amplitude for a perovskite solar cell for two different bias current values as a function of the measurement temperature. The different Perovskite crystalline phases are indicated

4 Perovskite Solar Cell Based Highly Reproducible Electronic Switching Device

Recently the same perovskite films, applied for the realization of thin-film solar cells have various other electronic applications. Besides the realization of relatively fast photodiodes for communication purposes (Whitfield et al. 2016) also very efficient light emitting diodes (LEDs) (Zhang et al. 2018b) and in combination of both devices for example opto-couplers (Zhao et al. 2018) have been reported. Another interesting electronic application is the realization of electronic memories, that are based on intrinsic bistable behavior of some perovskite solar cells. This research has been performed in collaboration between Salerno University, the CNR-IPCB institute at Portici and research groups from Tiruchirappalli and Bangalore Universities (Landi et al. 2018).

For this purpose, we exploited the strong hysteretic behavior of the conventional—non inverted—perovskite solar cell, whose structure is shown in Fig. 6a with the subsequent layer and processing sequence: A fluorine-doped tin oxide (FTO) glass substrate was covered with a blocking layer of TiO_2 , deposited by spin-coating. Then about 600 nm thick $\text{CH}_3\text{NH}_3\text{PbI}_3$ absorber layer was formed by sequential deposition of PbI_2 and $\text{CH}_3\text{NH}_3\text{I}$ in a two-step spin-coating process. First PbI_2 was dissolved in DMF at 70 °C and then spin-coated onto the TiO_2 coated FTO glass substrate. Then $\text{CH}_3\text{NH}_3\text{I}$ was dissolved in isopropyl alcohol and then spin-coated sequentially on the as coated wet films (without prior thermal drying of the PbI_2 film). The substrate was then heated to 70 °C for 5 min. Then the hole transporting layer,

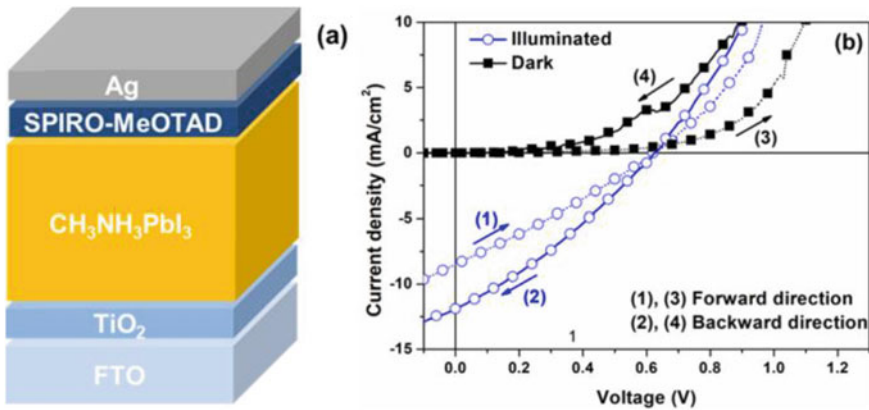


Fig. 6 Reprinted with kind permission. Original article; Landi et al., IEEE J-EDS 2018 (Landi et al. 2018). **a** Schematic illustration of the cross-section of the device structure. **b** Current density–voltage characteristics measured at 300 K under dark conditions (full symbols) and under one sun illumination (open symbols) for the perovskite solar cell at a scan rate of 10 mV/s. Dotted and solid lines refer to performed forward and backward voltage scans, respectively. The arrows indicate the voltage scan directions

a Spiro-OMeTAD compound was deposited by spin-coating and finally, silver as back contact, with an area of 0.04 cm² was deposited by thermally evaporation. The deposition of the perovskite film, and of the hole-transport layer), the metal contact deposition and the electrical measurement were all done under nitrogen atmosphere while all prior fabrication processes up to the TiO₂ layer deposition were done under ambient atmosphere. More details regarding the device realization and measurement conditions can be found in Li et al. (2015).

The non-optimized solar cells had in this case a typical conversion efficiency of 2.2% and in the electrical characteristics with and without illumination, shown in Fig. 6b for the dark $J - V$ and for the phot $J - V$ characteristics a large hysteresis can be observed.

In Fig. 7 the $J - V$ characteristics measured in forward and in backward sweep directions under dark conditions are shown. A “butterfly” shape owing to the four combinations of resistance states between the two resistive memory elements is observed. It is worth noting that the switching of the perovskite solar cell occurs only when the opposite polarity of the bias voltage has been applied before. This means that the ReRAM device operates in bipolar mode. Normally, the bipolar switching is due to the influence of the external electric field on the migration of the charged defects (Landi et al. 2018). A comparison of a large variety of materials, utilized for the realization of ReRAM devices can be for example found in Eames et al. (2015).

The operation of the non-illuminated solar cell as electronic memory is demonstrated in the voltage- and the resulting current-trace, shown in Fig. 8a during six cycles, starting with a reset pulse of -1 V, then a read period at +0.5 V, a subsequent set pulse of +1 V and finally another read period at 0.5 V. A highly reproducible

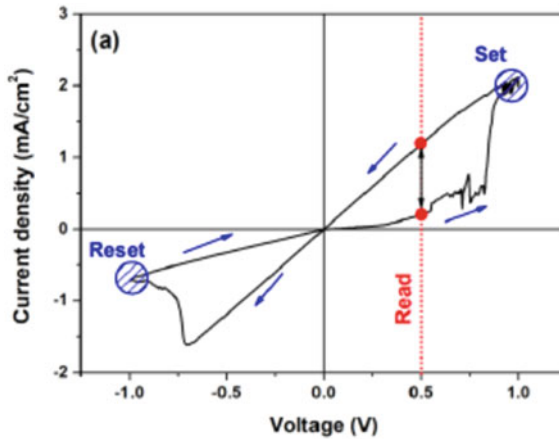


Fig. 7 Reprinted with kind permission: Original article: Landi et al., IEEE J-EDS 2018 (Landi et al. 2018). **a** Current–voltage characteristics measured under dark conditions for the FTO/TiO₂/CH₃NH₃PbI₃/SPIRO-OMeTAD/Ag structure solar cell device with switching direction of applied voltages: 0 V → +1 V → 0 V → -1 V → 0 V

behavior is observed with clearly different read current values, dependent on the prior application of set- or reset-pulses. In Fig. 8b a zoom into a single cycle is shown, indicating also the time constants that best describe best the current transients during the single phases.

5 Summary

It has been shown, that thin-film perovskite solar cells can be an interesting alternative to nowadays space solar cell technologies, combining high efficiency, simple technology and good stability, when exposed to space radiation. Two particular further research activities at Salerno University, regarding perovskite solar cells, are shortly described: Low-frequency noise spectroscopy has been shown to give valuable information on the perovskite electronic defect structure and the low-temperature phase transition and electronic memory operation with very good reproducibility has been achieved, using the hysteretic behavior of a non-inverted perovskite solar cell.

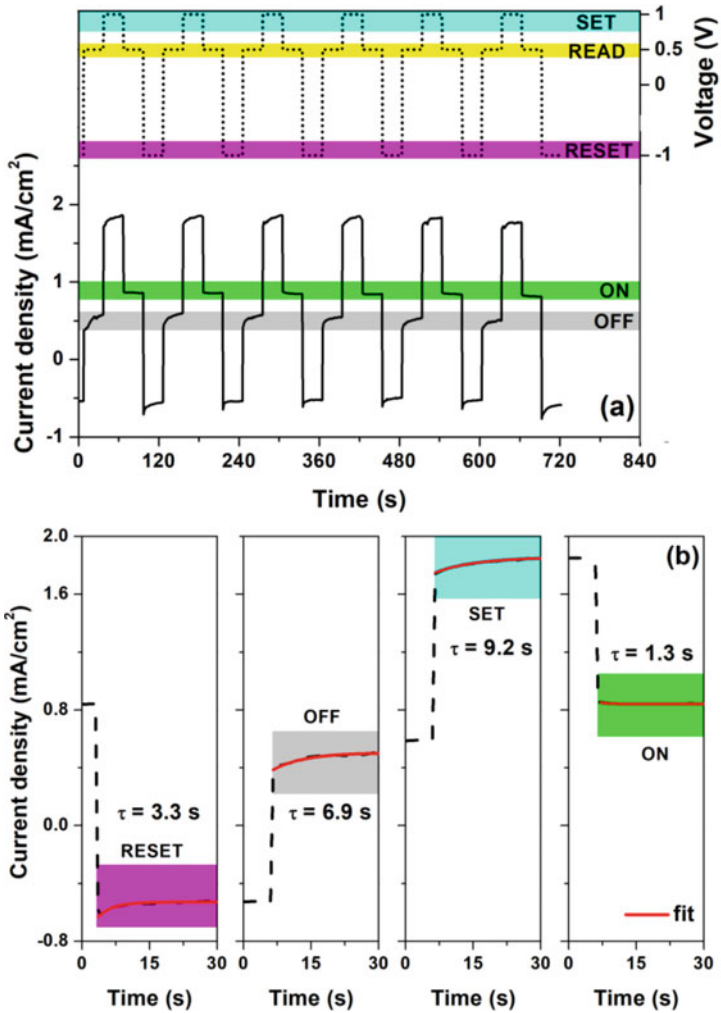


Fig. 8 Reprinted with kind permission: Original article: Landi et al., IEEE J-EDS 2018 (Landi et al. 2018). **a** Time evolution of the voltage control signal applied to the device (dotted line in right y-axis) during the write-read-erase pulse cycles (specifically, 1 V to write, 0.5 V to read, then -1 V to erase and 0.5 V to read), and the corresponding current–density response (solid line in left y-axis). **b** Current–density transients after the reset, read and set events. The solid curves are the best fit obtained by using the following exponential decay function $y = y_0 + Aexp(-t/\tau)$





References

- Arjen Klaver (2007) Irradiation-induced degradation of amorphous silicon solar cells in space. Ph.D. thesis, Delft University of Technology
- Brus VV, Lang F, Bundesmann J, Seidel S, Denker A, Rech B, Landi G, Neitzert HC, Rappich J, Nickel NH (2017) Defect Dynamics in proton irradiated $\text{CH}_3\text{NH}_3\text{PbI}_3$ perovskite solar cells. *Adv Electron Mat* 3:1600438
- Barone C, Landi G, Mauro C, Neitzert HC, Pagano S (2015) Universal crossover of the charge carrier fluctuation mechanism in different polymer/carbon nanotubes composites. *Appl Phys Lett* 107:143106
- Barone C, Lang F, Mauro C, Landi G, Rappich J, Nickel NH, Rech B, Pagano S, Neitzert HC (2016) Unravelling the low-temperature metastable state in perovskite solar cells by noise spectroscopy. *Sci Rep* 6:34675
- Barone C, Landi G, De Sio A, Neitzert HC, Pagano S (2014) Thermal ageing of bulk heterojunction polymer solar cells investigated by electric noise analysis. *Sol Energy Mat Sol Cells* 122:40–45
- Canepa PC, Malinaric P, Campbell RP, Ostroski J (1964) High temperature nuclear particle detector. *IEEE Trans Nucl Sci* 11:262–270
- Eames C, Frost JM, Barnes PRF, O'Regan BC, Walsh A, Islam MS (2015) Ionic transport in hybrid lead iodide perovskite solar cells. *Nat Commun* 6:7497
- Easton RL, Votav MJ (1959) Vanguard I IGY satellite (1958 Beta). *Rev Sci Instrum* 30:70–75
- Fahrner WR, Muehlbauer M, Neitzert HC (2006) Silicon Heterojunction solar cells. *Trans Tech Publications, Ueticon-Zuerich*
- Green MA, Hishikawa Y, Dunlop ED, Levi DH, Hohl-Ebinger J, Ho-Baillie AWY (2018) Solar cell efficiency tables (version 52). *Prog Photovolt Res Appl* 26:427–436
- Green MA, Hishikawa Y, Dunlop ED, Levi DH, Hohl-Ebinger J, Ho-Baillie AWY (2019) Solar cell efficiency tables (Version 53). *Prog Photovolt Res Appl* 27:3–12
- Jost M, Bertram T, Koushik D, Marquez J, Verheijen M, Heinemann MD, Köhnen E, Al-Ashouri A, Braunger S, Lang F, Rech B, Unold T, Creatore M, Lauermann I, Kaufmann CA, Schlatmann R, Albrecht S (2019) 21.6%-Efficient monolithic perovskite/Cu(In,Ga)Se₂ tandem solar cells with thin conformal hole transport layers for integration on rough bottom cell surfaces. *ACS Energy Lett* 4:583–590
- Khan A, Yamaguchi M, Ohshita Y, Dharmaraso N, Araki K, Khanh VT, Itoh H, Ohshima T, Imaizumi M, Matsuda S (2003) Strategies for improving radiation tolerance of Si space solar cells. *Sol Energy Mat Sol Cells* 75:271–276
- Lang F, Shargaleva O, Brus VV, Neitzert HC, Rappich J, Nickel NH (2018) Influence of radiation on the properties and the stability of hybrid perovskites. *Adv Mat* 30:201702905
- Lang F, Jost M, Bundesmann J, Denker A, Albrecht S, Landi G, Neitzert HC, Rappich J, Nickel NH (2019) Efficient minority carrier detrapping mediating the radiation hardness of triple-cation perovskite solar cells under proton irradiation. *Energy Environ Sci* 12:1634–1647
- Lang F, Nickel N, Bundesmann J, Seidel S, Denker A, Albrecht S, Brus V, Rappich J, Rech B, Landi G, Neitzert HC (2016) Radiation hardness and self-healing of perovskite solar cells. *Adv Mat* 28:8726–8731
- Landi G, Barone C, De Sio A, Pagano S, Neitzert HC (2013) Characterization of polymer:fullerene solar cells by low-frequency noise spectroscopy. *Appl Phys Lett* 102:223902
- Landi G, Barone C, Mauro C, Pagano S, Neitzert HC (2016) A noise model for the evaluation of defect states in solar cells. *Sci Rep* 6:29685
- Landi G, Barone C, Mauro C, Pagano S, Neitzert HC (2018) Evaluation of silicon, organic, and perovskite solar cell reliability with low-frequency noise spectroscopy. In: *Proceedings of the IEEE International Reliability Physics Symposium, San Francisco 2018*, pp 6C.31–6C.36
- Landi G, Subbiah V, Reddy KS, Sorrentino A, Sambandam A, Ramamurthy PC, Neitzert HC (2018) Evidence of bipolar resistive switching memory in perovskite solar cell. *IEEE J Electron Dev Soc* 6:454–463

- Landi G, Neitzert HC, Barone C, Mauro C, Lang F, Albrecht S, Rech B, Pagano S (2017) Correlation between electronic defect states distribution and device performance of perovskite solar cells. *Adv Sci* 4:1700183
- Li D, Dong G, Li W, Wang L (2015) High performance organic-inorganic perovskite-optocoupler based on low-voltage and fast response perovskite compound photodetector. *Sci Rep* 5:7902
- Miyazawa Y, Ikegami M, Chen H-W, Ohshima T, Imaizumi M, Hirose K, Miyasaka T (2018) Tolerance of Perovskite Solar Cell to High-Energy Particle Irradiations in Space Environment. *iScience* 2:148–155
- Neitzert HC, Labonia L, Citro M, Delli VP, Mercaldo L (2010) Degradation of micromorph silicon solar cells after exposure to 65 MeV protons. *Phys Stat Sol (c)* 7:1065–1068
- Neitzert HC, Ferrara M, Fahrner W, Scherff M, Bobeico E, Roca F, Tucci M, Serenelli L (2006) Stability under space conditions of silicon based homojunction and heterojunction solar cells. *Mat Sci Eng B* 154:263–268
- Neitzert HC, Ferrara M, Kunst M, Denker A, Kertesz Z, Limata B, Gialanella L, Romano M (2008) Electroluminescence efficiency degradation of crystalline silicon solar cells after irradiation with protons in the energy range between 0.8 MeV and 65 MeV. *Phys Stat Sol (b)* 245:1877–1883
- Sato S-I, Beernink K, Ohshima T (2012) Degradation behavior of flexible a-Si/a-SiGe/a-SiGe triple junction solar cells irradiated with 20–350 keV protons. In: *Proceedings of the 38th IEEE Photovoltaic Specialists Conference*, pp 2856–2861
- Scherff M, Drzymalla R, Goesse R, Fahrner WR, Ferrara M, Neitzert HC, Opitz-Coutureau J, Denker A, Stangl R, Limata B, Gialanella L, Romano M (2006) Proton damage in amorphous silicon / crystalline silicon heterojunction solar cells—measurement and simulation. *J Electrochem Soc* 153:G1117–G1121
- Stella PM, Ewell RC, Hoskin JJ (2005) Design and performance of the MER (Mars Exploration Rovers) solar arrays. In: *Proceedings of the 31st IEEE Photovoltaic Specialist Conference*, Lake Buena Vista, 3.-7. January 2005, pp 626–630
- Whitfield PS, Herron N, Guise WE, Page K, Cheng YQ, Milas I, Crawford MK (2016) Structures, phase transitions and tricritical behavior of the hybrid perovskite methyl ammonium lead iodide. *Sci Rep* 6:35685
- Zhang D, Najafi M, Zardetto V, Dörenkämper M, Zhou X, Veenstra S, Geerligs LJ, Aernouts T, Andriessen R (2018a) High efficiency 4-terminal perovskite/c-Si tandem cells. *Sol Energy Mat Sol Cells* 188:1–5
- Zhang M, Zhang F, Wang Y, Zhu L, Hu Y, Lou Z, Hou Y, Teng F (2018b) High-performance photodiode-type photodetectors based on polycrystalline formamidinium lead iodide perovskite thin films. *Sci Rep* 8:11157
- Zhao B, Bai S, Kim V, Lamboll R, Shivanna R, Auras F, Richter JM, Yang L, Dai L, Alsari M, She X-J, Liang L, Zhang J, Lilliu S, Gao P, Snaith HJ, Wang J, Greenham NC, Friend RH, Di D (2018) High-efficiency perovskite-polymer bulk heterostructure light-emitting diodes. *Nat Photonics* 12:783–789
- Zhu L, Zhou J, Guo Z, Sun Z (2015) An overview of materials issues in resistive random access memory. *J Mater* 1:285–295
- Ziegler JF, Ziegler MD, Biersack JP (2010) The Stopping and Range of Ions in Mater, Nuclear Instruments and Methods in Physics Research Section B—Beam Interactions with Materials and Atoms 268:1818–1823

Tackling the Challenges in High Capacity Silicon Anodes for Li-Ion Cells



Merin K. Wilson , A. Abhilash , S. Jayalekshmi , and M. K. Jayaraj 

1 Introduction

1.1 Energy: A Burning Issue

Demand for energy is increasing day by day due to intense population explosion, economic growth and advances and modernization in life style. Heavy dependence on fossil fuels for power generation especially in the automobile sector is causing severe environmental issues related to atmospheric pollution, green-house effect, acid rain and ozone layer depletion. Fossil fuels are also getting depleted at an alarmingly faster rate and hence attempts to switch to renewable energy sources for power generation are in full swing all over the world. Developing efficient renewable energy sources that would meet the increasing fuel demand of modern society by providing clean and pollution free power, keeping global environment safe and green is inevitable for the healthy survival of human race on earth (Liu et al. 2017).

M. K. Wilson (✉) · A. Abhilash · S. Jayalekshmi
Department of Physics, Cochin University of Science and Technology, Cochin, Kerala 682022,
India
e-mail: merinkwilson@cusat.ac.in

S. Jayalekshmi
e-mail: jayalekshmi@cusat.ac.in

M. K. Jayaraj
University of Calicut, Malappuram, Kerala 673635, India

1.2 Electrochemical Energy Resources

Solar energy and wind energy constitute most viable renewable energy sources, capable of solving all issues related to global energy crisis. Intermittent or time dependent nature of these energy sources is a critical challenge associated with them. Solar energy is not directly available during night time and wind pattern varies from season to season and is often strong enough for power generation only for a small period of time. Sporadic nature of these energy sources makes it mandatory to have efficient and economic storage systems for storing the generated electric power. Storage batteries constitute the most promising types of energy storage systems (Nitta et al. 2015). Presently available batteries, especially rechargeable ones, are sufficient for the power requirements of most of the portable devices, such as flashlights, smart phones, laptops and medical implants. Some small sized cars can also be powered using presently available rechargeable batteries. When it comes to powering applications of heavy vehicles and systems requiring high energy density, improvements in battery performance in terms of cell voltage, energy density, power density, operational stability and safety have to be achieved using viable and cost-effective approaches (Fujita et al. 2021).

Different types of commercialized batteries, both primary and rechargeable, are widely being used power sources and the history of development of batteries as versatile energy storage systems is quite inspiring and illustrates the breakthroughs and innovations in battery research (Raccichini et al. 2019). Lithium ion cells have emerged as the most promising types of rechargeable cells and offer high energy density, excellent cycling stability and environmental safety for powering portable electronic devices and small sized automobiles. Extensive research activities are in full swing globally to tap the full potential of lithium ion cells and extend their application scenario to areas requiring higher energy, power and cell voltage by identifying ideal types of electrode and electrolyte materials.

1.3 Batteries—A Brief Overview

Electricity is one of the profound and path breaking discoveries in the last 400 years and conversion of chemical energy to electrical energy is one of the most popular and efficient ways of storing energy. Technically coined term for such a device is “battery” or collection of electrochemical cells. The word “battery” is derived from the old French word “baterie”, which means “action of beating”. In the 1700s, scientists coined the term “battery” to describe a collection of electrochemical cells connected together and capable of producing the appropriate voltage and capacity. Each cell has a positive and negative electrode, abbreviated as cathode and anode, separated by an ion permeable dielectric membrane called a separator, which insulates both electrodes and prevents an electric short within the cell. In an electrolyte solution, both electrodes are subjected to chemical reactions and the dissociated salt present in

the electrolyte helps in migration of ions between the two electrodes. If we connect both electrodes externally, an electric current will flow in the external circuit due to the liberation of electrons from the chemical reaction taking place inside the cell. Amount of electrical energy stored per volume or mass and power of the cell depend on the cell's potential and capacity and also on the chemical properties of the electrodes and electrolyte (Paul et al. 2021).

Italian physicist Alessandro Volta in 1800, created the first modern day battery when he built what came to be known as 'Voltaic pile', providing static electric current, which later led to the development of continuous source of electricity. In the same year, Sir Humphry Davy, the creator of the 'miner's safety lamp', began researching the chemical effects of electricity and noticed the decomposition of electrolyte material when electrical current passed through it. 'Electrolysis' was the name given to this process later on. Humphry Davy created the first electric lamp in 1809 by connecting two wires to a battery and connecting the other ends of the cables with a charcoal strip. The first arc lamp was created when charged carbon glowed. In 1815, Davy devised the miner's safety lamp, which was designed to aid in deep mining where combustible gases such as methane could exist. Davy's laboratory helper, Michael Faraday, went on to extend Davy's work and become famous in his own lines.

The first electric battery viable for mass production was designed by Dr. William Cruickshank in the year 1802. He arranged soldered square sheets of copper together with sheets of zinc having equal dimension. These sheets were placed in a long rectangular wooden box and cement was used for sealing the box. Metal plates were held in position by the grooves in the wooden box. The box was then filled with an electrolyte of brine or watered-down acid. This arrangement resembles that of the flooded battery, still in use. This flooded design had the advantage of not drying up as quickly as Volta's disc layout and provided more energy.

1.4 Primary and Secondary Batteries

Batteries are broadly classified into primary and secondary batteries, both having their own characteristic properties and applications. Primary batteries are non-rechargeable and are use-and-throw type. It is highly possible that one day, rechargeable batteries may replace primary batteries in all applications, but in certain areas such as military applications, rescue missions and forest fire services, high capacity offering primary batteries play an important role. For wild life photography applications in remote areas where recharging of battery is impossible or difficult, primary batteries offer efficient, long duration operation with high capacity compared to secondary batteries, presently available. In special areas which need high capacity to size ratio, such as in some medical applications like pacemaker implants which last for 5–10 years and draw only 10–20 microampere (μA) current, primary batteries are the suitable choice. Many hearing aid batteries are also primary ones, with a capacity in the range 70–600 mAh and are good for 5–14 days before a replacement

is needed. Secondary batteries offer less capacity to size ratio and at an average last only for 20–25 hr. High specific energy, long storage time and instant readiness give primary batteries more advantage over other similar storage devices. They may be transported to remote regions and used right away, even if they have been stored for a long time.

Even though they are easily accessible, they have several drawbacks which include the following:

- Low performance under load conditions due to high internal resistance, eventually causing the voltage to collapse.
- Expensive when in continuous use because of the use and throw nature.
- Discarding of partially used batteries is a common trend in modern society, resulting in economic and safety issues.

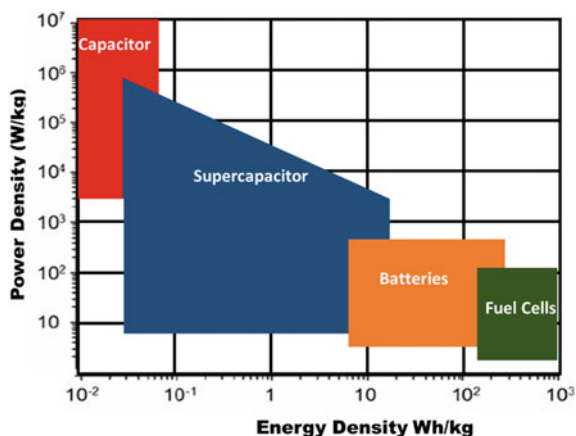
Secondary batteries are the other type of batteries. Main advantage of secondary batteries is that they can be recharged and used again. Many portable electronic devices and even electric automobiles are powered by rechargeable batteries. Electrode reactions are reversible in rechargeable batteries and recharging is done by passing current through them in the opposite direction to that of discharge current. They store electrical energy in them and hence also known as storage batteries or accumulators. High energy density, high discharge rate, smooth discharge curves, and outstanding low-temperature performance characterise them. The most common rechargeable batteries include,

- Lead-acid (oldest)
- Nickel-cadmium (ultra-fast charging)
- Nickel metal hydride
- Lithium-ion.

1.5 New Era of Rechargeable Batteries

Until the invention of rechargeable cell in 1859 by the French physician Gaston Planté, there was only one category of batteries, termed later as primary batteries which could not be recharged. Secondary cell invented by Planté was based on lead acid chemistry, which is used even today.

Concept of nickel–cadmium cell (Ni–Cd) was developed by Waldmar Jungner of Sweden in 1899 in which nickel was used for the positive electrode and cadmium for the negative electrode. High cost of the materials compared to lead, adversely affected the development of Ni–Cd batteries. After two years, Thomas Edison developed a cell, using iron in the place of cadmium, and this cell was called nickel iron (Ni–Fe) or ‘Edison cell’. It is one of the most robust types of cells. Overcharging, overdischarging, and short-circuiting are all tolerated very well by this battery. It is considered as one of the heaviest types of battery till date and is used in those applications where weight of battery does not matter. It finds applications in solar

Fig. 1 Ragone plot

and wind energy systems. Low specific energy, temperature dependence and high self-discharge rate have however limited the long term use of nickel–iron battery.

Until the invention of lithium based batteries world’s favorite battery was nickel based one, taking over the market for many years, because of its user friendly and environmentally benign nature (Shen 2017) and other advantageous aspects of high specific energy and low maintenance cost (Chu et al. 2018). Contemporary research activities in battery field are mainly on improving lithium based systems (Aghamohammadi et al. 2021). Ragone plot shown in Fig. 1, gives comparison of power density and energy density of different energy storage systems and clearly demonstrates the promising nature of battery systems.

2 Lithium Batteries—A Brief History

Lithium batteries having more attractive features over nickel-based ones have dominated energy storage market since the past few decades. Light weight, higher electrochemical potential and preferred values of specific energy make lithium, a desirable choice for the anode (Deng 2015). Pioneering work in the field of lithium batteries began in 1912 under GN Lewis. First non- rechargeable type of lithium batteries became commercially available in 1970’s, with lithium metal being used as the anode. Attempts towards developing rechargeable lithium ion batteries began in 1980’s and these types of batteries with lithium cobalt oxide used as the cathode active material were commercialized by Sony & Asahi Kasei in 1991. John B. Goodenough, M. Stanley Whittingham, and Akira Yoshino were jointly awarded the Nobel Prize in Chemistry 2019 for the development of lithium-ion batteries (Kim et al. 2019).

These batteries have several advantages which include (Bruce et al. 2008):

- Low self-discharge.

- Nominal cell voltage of 3.60 V is suitable for directly powering mobile phones, tablets, laptops and digital cameras.
- Rechargeable.
- High energy density and appreciable power capability.
- Possibility to design the batteries in a variety of types.

Major drawbacks of lithium based battery systems include:

- Safety issues: Quick charging may lead to explosion or fire.
- Ageing.
- High production cost.
- High internal resistance, which leads to voltage drop at the terminals when load is connected and reduces the maximum current that can be drawn from the cell.
- Use of lithium insertion materials as anode and cathode limits charge storing capacity and energy density of the cell.

Li-ion cells offer much higher energy density compared to other types of electrochemical cells. These batteries have found their way into the hybrid electric vehicle market with ever-increasing popularity and are also gradually starting to make entry into larger-scale energy storage systems for renewable energy sources such as solar power. Li-ion batteries capable of delivering 200 MWs of power are installed globally for grid applications and this number is expected to increase drastically, since the need to manage the intermittency of renewable energy resources is becoming inevitable at a faster rate. There are still some limitations for Li-ion batteries as well and these mainly include capacity fading, self-discharge and reduced cycle life. Most recently, remarkable interest is growing in the field of lithium–sulfur batteries (LSBs) (Manoj et al. 2019) due to extremely high theoretical energy density (2500 Wh/kg) and the natural abundance of sulfur (Li et al. 2018).

2.1 Common Terminologies

Capacity: Capacity of a cell is the amount of electric charge it can deliver at the rated voltage. According to the state of the cell (charging or discharging) capacity is called charge capacity or discharge capacity. It is measured in units of ampere-hour (A-h). Capacity increases with increase in the amount of electrode material contained in the cell. So a smaller cell has lesser capacity than a larger cell with the same chemistry even though they develop the same open circuit voltage.

Fraction of the stored charge that can be delivered by a cell depends on.

- Chemistry of the cell
- Rate at which the charge is delivered (current)
- Required terminal voltage
- Storage period
- Ambient temperature.

Higher the discharge rate, lower will be the capacity of the cell. Various processes which can cause capacity loss of the cell are

- Internal self-discharge occurs when cells are stored for an extended period of time or when there are irreversible side reactions that consume charge carriers without creating current.
- When cells are recharged side reactions can occur which reduce the capacity of the subsequent discharge. Most of the cell capacity gets lost and the cell stops power generation after many recharges.
- Cell efficiency varies due to internal energy losses and limitations on the rate at which ions pass through the electrolyte.

C-rate: Charge discharge rate or C-rate is the rate at which a cell is being charged or discharged. When the cell is cycled electrochemically, C-rate is often employed to explain the time frame for either one full charge or discharge. It is defined as the ratio of discharge current to the theoretical current drawn under which the cell would deliver its nominal rated capacity in one hour. A 1C discharge rate would supply the cell's rated capacity in 1 hr, and a 2C discharge rate that the cell will get discharged twice as fast (30 min) and so on. A 1C discharge rate on a 1.6 Ah cell means a discharge current of 1.6A and a 2C rate would mean a discharge current of 3.2 A.

Theoretical capacity: It is defined as the capability of the cell to provide current to an external circuit and is found out in terms of the quantity of active material present in the cell. It is expressed in coulombs or ampere-hours and is related to the total electricity involved in the electrochemical reaction.

Theoretical energy density: It is a measure of energy stored in the cell in terms of mass or volume and is expressed as the ratio of its power to mass or size.

Open circuit voltage: It is defined as the voltage of a cell under no load conditions and is usually a close approximation of the theoretical voltage.

Closed circuit voltage: It is the cell voltage under a load condition.

Nominal voltage: Nominal voltage is the generally accepted operating voltage of the cell (For example, 1.5 V for zinc manganese dioxide cell).

Cycle: One charge-discharge sequence of a cell is defined as a cycle.

Coulombic efficiency: It is the ratio of discharge capacity after the full charging of a cell, to its charge capacity during the same cycle.

Operating voltage: Voltage of a battery under load is known as its operating voltage.

Battery lifetime: For rechargeable cells, life time means the time duration for which the cells can deliver sufficient amount of energy or power to the external circuit until no chemical reaction occurs internally or in other words it is the number of charge/discharge cycles possible before the cell fails to operate satisfactorily. For non-rechargeable cells, lifetime is the time duration for the devices to become fully discharged, because by definition, chemical reactions occurring in these cells are irreversible.

Self-discharge: When stored at room temperature (20–30°C) disposable batteries typically lose 8 to 20 percent of their initial charge per year. This is known as the

“self-discharge” rate. This is due to the fact that non-current producing chemical reactions can occur within the cells even when there is no load. These types of side reactions are reduced when they are stored at lower temperatures, but some of them may get damaged by freezing. For rechargeable cells, self-discharge rate is generally much lower (Braga et al. 2017).

2.2 Comparison of Batteries with Other Energy Storage Systems

Developments in battery technology have revolutionized the arenas of technological innovations and batteries have gained an important role in our day to day life. Different types of batteries that can be used for various purposes have been designed and developed over the past years and are serving as the best types of energy storage systems (Li et al. 2019a). In spite of many advantageous aspects ascribed to batteries, there are certain limitations as well, which need special addressing.

Energy storage: Batteries can store energy for a long time. On comparing with secondary batteries, primary ones can store more energy. For secondary cells, self-discharge is lower. Lead, nickel and lithium based secondary cells require periodic charging to compensate the lost energy.

Specific energy (capacity): On comparing with fossil fuels, batteries have less energy storage capability. For gasoline, energy by mass is over 12,000 Wh/Kg. On the other hand, lithium batteries carries only 200 Wh/kg. However battery delivers energy more efficiently than a thermal engine.

Responsiveness: One of the best advantages of battery is that it is ready to deliver energy even on short notice. In a battery, power flows within a fraction of seconds on comparison with other energy sources. A steam engine takes hours to build up steam and a fuel cell takes few minutes to gain power. In this respect, batteries are much better power sources than other energy sources.

Power bandwidth: Secondary batteries have very wide bandwidth. They can easily and effectively handle small and large loads, a property similar to that of diesel engines. On comparing a fuel cell with a battery, one can see that the former has narrow bandwidth and can handle only a specific load.

Environment: Batteries run clean and stay cool. Most sealed cells have no vents, run quietly and do not vibrate. Internal combustion engine (ICE) and large fuel cells require cooling fans and compressors in sharp contrast with a battery (Blomgren 2017).

Efficiency: Batteries are highly efficient. Li-ion battery has 99% efficiency and the discharge loss of this battery is less compared to others. Fuel cells and ICE have energy efficiency of 20-60% and 25-30% respectively. Charging efficiency of a battery depends on its ability to accept charge.

Installation: On comparing with ICE, and thermal engines, sealed batteries operate at any position and they possess a good shock and vibration tolerance. ICE must be

positioned in an upright way and should be mounted on shock absorbing dampers. Thermal engines work satisfactorily with air intake manifold and exhaust mufflers.

Operating cost: In most of the portable devices, lithium and nickel based batteries are widely used as they seem to be best suited. For wheeled mobility and stationary applications lead acid batteries are economical (Li et al. 2019b). Price and weight of batteries make them impractical for electric power generation in large vehicles. Cost of drawing energy from a battery is three times higher than getting it from AC grid.

Even with small limitations, battery plays an important role in storing energy. Ongoing advancements in battery technology are expected to find suitable solutions for these limitations.

3 Li-Ion Cell: Structure and Components

Fundamental unit of battery is called a cell. A cell consists of two electrodes, electrolyte and separator. Positive and negative electrodes are commonly called as cathode and anode respectively. Efficient working of a Li-ion cell is the result of continuous shuttling of Li-ions through the electrolyte across the separator. Schematic diagram representing discharging of a Li-ion cell is given in Fig. 2a. Electrodes and electrolyte of a cell with their relative electron energies at thermodynamic stable equilibrium are shown schematically in Fig. 2b. Anode is the reductant where oxidation takes place and cathode is the oxidant where reduction takes place. Energy separation between lowest unoccupied molecular orbital (LUMO) and the highest occupied molecular orbital (HOMO) of the electrolyte is its thermodynamic stability window (E_g). Electrolyte will be a good ionic conductor and the two electrodes, good electronic conductors. Separator is an insulating membrane inserted between the electrodes to avoid physical contact and the short circuit of the cell (Goodenough and Park 2013).

Let the electrochemical potentials of anode and cathode be represented by μ_A and μ_C respectively. An anode with μ_A above the LUMO will reduce the electrolyte and a cathode with μ_C below the HOMO will oxidize the electrolyte unless a passivation layer creates a barrier for electron transfer at the electrode-electrolyte interface (Jinisha et al. 2017a). This passivation layer at the electrode- electrolyte boundary is called solid electrolyte interface (SEI) and gives kinetic stability to the junction.

Interface layer attains thermodynamic stability due to the electrochemical potentials μ_A and μ_C within the window of the electrolyte (E_g). Open circuit voltage V_{oc} of a cell must be less than the window of the electrolyte and is given by

$$eV_{oc} = \mu_A - \mu_C \leq E_g \quad (1)$$

where e is the magnitude of electron charge. SEI layer can give stability provided the value $eV_{oc} - E_g$ is not too large (Goodenough and Kim 2010).

The active components of the cell consist of

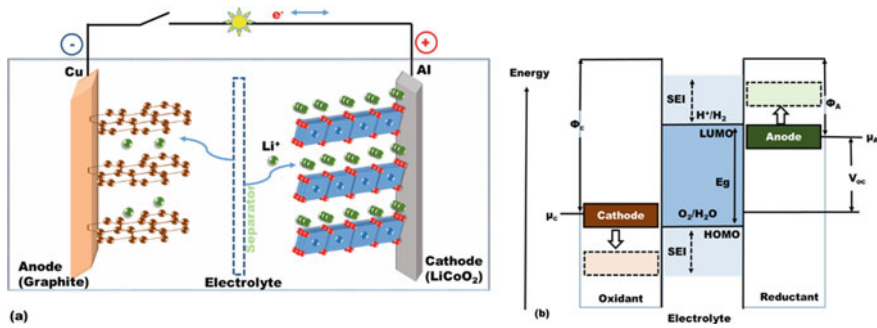


Fig. 2 (a) Schematic diagram of the first Li-ion cell (LiCoO₂/Li + electrolyte/graphite) (b) Schematic open-circuit energy diagram of an aqueous electrolyte. Φ_A and Φ_C are the anode and cathode work functions respectively. E_g is the window of the electrolyte for thermodynamic stability. The condition $\mu_A > \text{LUMO}$ and/or $\mu_C < \text{HOMO}$ requires kinetic stability and is maintained by formation of the SEI layer

- A non-aqueous electrolyte of high lithium ion conductivity at ambient temperatures, capable of allowing thermodynamically stable V_{oc} .
- A negative electrode commonly known as anode with electrochemical potential μ_A .
- A positive electrode commonly known as cathode with electrochemical potential μ_C .

3.1 Electrolytes

An ideal electrolyte must satisfy several requirements as follows:

- Must have large electrolyte window E_g with good match with the electrochemical potential of anode and cathode.
- Must satisfy retention of the electrode-electrolyte interface during cycling when electrode particles change their volume.
- Should have Li-ion conductivity $\sigma_{ionic} \sim 10^{-3} S/cm$ over ambient temperature range of cell operation.
- Must have very low electronic conductivity $\sigma_{electronic} \sim 10^{-10} S/cm$.
- Should have transference number $(\frac{\sigma_{ionic}}{\sigma_{Total}}) \approx 1$, where $\sigma_{Total} = \sigma_{ionic} + \sigma_{electronic}$.

3.2 Electrodes

In general cathode is the positive electrode and anode is the negative electrode. Electrode should be a perfect conductor of electrons and electrolyte should provide an easy path way for the ionic conduction through the separator (Jinisha et al. 2017b). Criteria

for selecting an electrode material should be based on the following factors like cost, energy density, power density, cycle life, operational safety and environmental safety.

3.3 Different Types of Cathode Materials

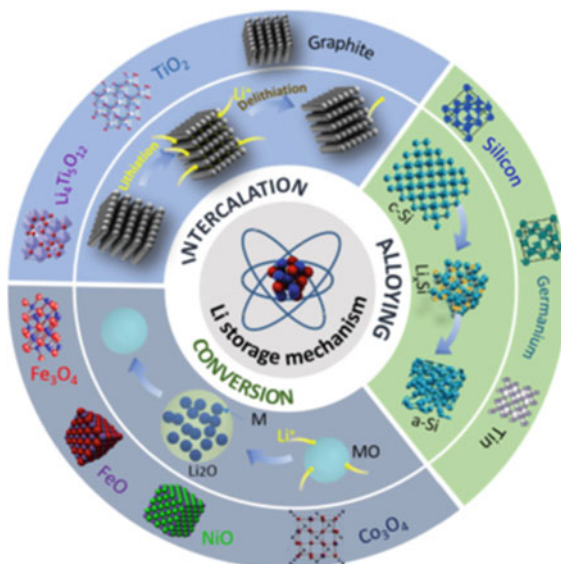
- Layered oxides
- Spinel oxides
- Polyanion oxides.

Selection criteria and properties of various types of cathode materials and electrolytes are discussed in detail in chapters six and eight.

4 Different Types of Anode Materials

There are three types of reaction processes occurring at anode materials of Li-ion cells. They are (1) intercalation or insertion, (2) conversion and (3) alloying. According to these reaction mechanisms, anode materials are classified into three different groups as represented schematically in Fig. 3.

Fig. 3 Schematic illustration of different reaction mechanisms of anode materials in Li-ion cells. (Reprinted with permission from Xu et al. (2017), copyright (2021) © Elsevier)



4.1 Intercalation Type Anode Materials

Intercalation is referred to as insertion between layers. Common anode materials showing insertion type reaction are graphite and TiO_2 (Fang et al. 2019). During charging, insertion of Li-ions into the d-spacing lattices of graphite or TiO_2 takes place and de-intercalation or removal of ions occur during the discharge process (Wang et al. 2019a). Insertion of Li-ions into the spinel $\text{Li}_4\text{Ti}_5\text{O}_{12}$ (LTO) results in its transformation to rock-salt type $\text{Li}_7\text{Ti}_5\text{O}_{12}$ with almost zero strain but with a low specific capacity of 175 mAh/g (Gangaja et al. 2020). Although anode materials in this group possess limited specific capacity, good cycling stability and negligible volume expansion on lithiation are their remarkable advantages (Winter et al. 1998).

4.2 Conversion Type Anode Materials

Anode materials based on transition metal oxides like Fe_3O_4 , FeO , Co_3O_4 and NiO , offer high energy densities. These types of materials are quite significant due to their environmental friendliness, low cost and the possibility of adopting simple preparation techniques. Electrode materials in the group undergo a reversible redox reaction process during charging and discharging of the cell. However, they have disadvantages of low initial coulombic efficiencies (ICE), formation of unstable solid electrolyte interface (SEI) layers and poor cycling stability due to large volume expansion upon lithium insertion and poor electronic/ionic conductivities.

4.3 Alloying Type Anode Materials

These type of anode materials are typically of lithium metal alloys, Li_xM_y ($\text{M} = \text{Si}, \text{Sn}, \text{Ge}, \text{Al}, \text{Mg}, \text{Sb}$), and owing to their ability to store lithium, are of great attention as high capacity anode materials in lithium-ion cells. Specific capacity of these type of anode materials is far ahead of the theoretical capacity of graphite, which is intercalation type and a comparison of performance parameters of various types of anode materials is shown in Table 1. Alloying type anode materials undergoes compound phase formation with lithium upon lithiation. Alloying and de-alloying of anode material occurs at the electrode during charging and discharging (Kwon et al. 2016). One of the disadvantages of this process is volume expansion of the anode material up to 300% upon lithiation, which adversely affects the performance of the cell (Sun and Gong 2001). Accompanying changes result in cracking and pulverization of the electrode and consequently limiting its lifetime to only a few charge–discharge cycles (Xu et al. 2017).

Table 1 Comparison of reaction mechanisms, densities, lithiation/delithiation processes, theoretical specific capacities, volume changes (ΔV) and potentials of various representative anode materials. Reprinted with permission from Xu et al. (2017), Copyright (2021) © Elsevier

Reaction mechanisms	Anode Materials	Lithiation/Delithiation Processes	Specific capacity (mAh/g)	Volume change (%)	Potential Vs Li/Li ⁺
Intercalation	C	$6C + Li \leftrightarrow LiC_6$	372	12	0.05
	Li ₄ Ti ₅ O ₁₂	$LTO + 3Li \leftrightarrow Li_7Ti_5O_{12}$	175	1	1.6
	Fe ₃ O ₄	$Fe_3O_4 + 8Li \leftrightarrow 3Fe + 4Li_2O$	924	93	0.8
Conversion	FeO	$FeO + 2Li \leftrightarrow Fe + Li_2O$	744	90	1.0
	Co ₃ O ₄	$Co_3O_4 + 8Li \leftrightarrow 3Co + 4Li_2O$	890	100	1.1
	NiO	$NiO + 2Li \leftrightarrow Ni + Li_2O$	718	100	0.6
	Si	$Si + 4.4Li \leftrightarrow Li_{4.4}Si$	4200	300	0.4
Alloying	Sn	$Sn + 4.4Li \leftrightarrow Li_{4.4}Sn$	994	260	0.6
	Ge	$Ge + 4.4Li \leftrightarrow Li_{4.4}Ge$	1600	370	0.4

5 Silicon Anode

5.1 Advantages

Silicon is a promising anode material for next generation Li-ion cells since it possesses the highest theoretical storage capacity around 3500–4200 mAh/g, relatively low and safe discharge potential and natural abundance compared to all other established anode materials. It is the second richest element in earth's crust and is quite cost-effective. It is an intrinsic semiconductor with a band gap of 1.12 eV and electrical conductivity around 10^{-3} S/cm at room temperature. Electrical conductivity of Si is sensitive to its chemical structure and can be effectively tailored by doping process. Depending on the type of hetero-atoms introduced into Si, doped silicon will be n-type or p-type semi-conductor. Conductivity and band gap of doped Si can be tuned by changing the type and concentration of hetero-atoms. Doped Si can be used to make porous Si by chemical etching (Kwon et al. 2019).

Although silicon possesses many advantages, there are some challenges in developing silicon-based Li-ion cells due to the large volume change of Si anode around 300% during lithium intercalation/de-intercalation (Zuo et al. 2017). Induced stress and strain from this volume change result in electrode fracture and electrical isolation during repeated cycling, leading to delamination of the deposited film from the current collector (Fukata et al. 2017). Further to this, electrode is subjected to mechanical fracturing, leading to instability of the solid-electrolyte interphase (SEI) layers that are formed during the intercalation/de-intercalation processes. Failure mechanisms of Si anode are illustrated in Fig. 4 (Rahman et al. 2016).

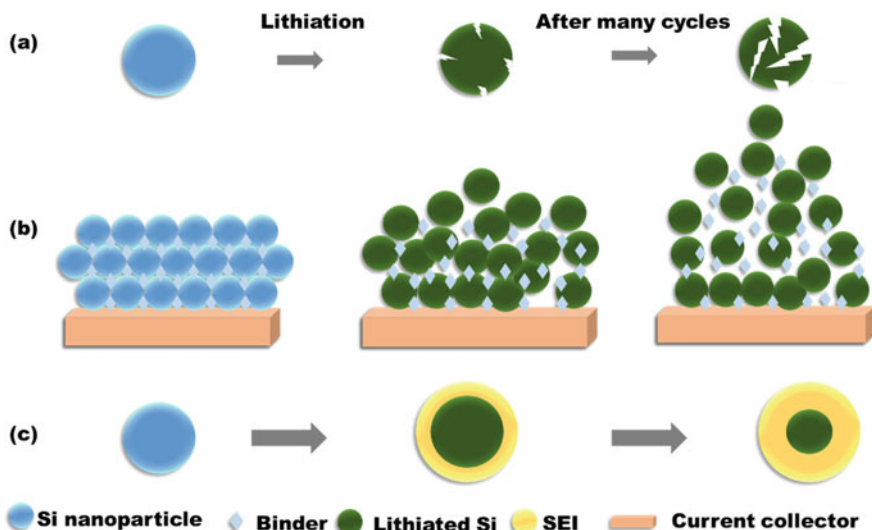


Fig. 4 Failure mechanisms of Si electrode: (a) cracking and pulverization; (b) volume expansion and loss of electrical contacts and (c) formation of excessive SEI layer

5.2 Challenges in Si Anode

Volume expansion: Volume expansion is one of the major challenges in silicon-based electrodes for Li-ion batteries. Reaction mechanism in silicon anode is alloying. Mostly all the alloying type anode materials suffer from drastic performance decay due to volume expansion within a limited number of charge–discharge cycles. Uncontrolled volume expansion results in pulverization and cracking of the electrode. Finally, it leads to loss of electrical contacts and permanent damage to the cell (Ge et al. 2013a). Structural stability of the electrode after every cycle is the key factor contributing towards the overall cycle life and cycling stability. Si particle at the beginning of lithium intercalation with radius $R_1 \sim 200$ nm might become a larger spherical particle with radius $R_2 \sim 1.49R_1$, with about 330% volume expansion (Lin et al. 2012). In order to accommodate the volume changes, void space with a thickness of about 100 nm is needed, without destroying the electrode structure (Ge et al. 2013b). Morphological changes during lithiation have been studied using in situ synchrotron tomography. There are three phases consisting of (i) solid phase with 55% volume (ii) the electrolyte phase with 44% volume, created by the pores filled with electrolyte and (iii) the gas phase with 1% volume, constituted by electrolyte-free pores. Electrode cracking begins during the 1st charging, from the bottom of the electrode. This could be owing to the presence of the inflexible stainless steel connector nearby, as well as the higher volume change at the electrode's bottom. During the ensuing discharge procedure, large cracks filled with electrolyte or gas get closed. At the bottom part of the electrode, cracks are larger

and less reversible, implying that permanent changes in the electrode structure and the resulting Si particle disconnections are more intense (Wang et al. 2019b).

Conductivity of the electrode: Silicon is a semiconductor with comparatively low electrical conductivity. Most important characteristic of an ideal electrode material is infinite electrical conductivity and perfect non-conductivity for ions (Kulova et al. 2016). Low electrical conductivity of silicon is another challenge in developing silicon-based anode materials for rechargeable batteries (Park et al. 2009). Improved electrochemical performance of Si anodes due to the influence in conductivity by doping (Ma et al. 2016) and by adding carbonaceous materials and conducting polymers has been reported (Pradeep et al. 2014). Different conducting polymers including polypyrrole with electrical conductivity around 2–100 S/cm, polyaniline with conductivity in the range, 10^{-5} –6.7 S/cm and poly(3,4-ethylenedioxythiophene): poly(4-styrene sulfonate) (PEDOT: PSS) with conductivity around 10 – 10^3 S/cm, all of which are endowed with advantageous features of high electrical conductivity, structural flexibility and the availability of cost-effective and simple synthesis techniques are highly promising for developing Si based anodes (Yao et al. 2011).

Formation of excessive SEI layer: Solid electrolyte interface is an electronically insulating layer of decomposed electrolyte at the electrode–electrolyte interface. Hence formation of thicker SEI layer on lithiation is another challenge for Si based cells. Decomposition of electrolyte will result in the formation of solid compounds and these products accumulate in the pores of electrodes (Gao et al. 2019). This will end up in a thicker and unstable SEI layer formation, since silicon anode is unstable due to its large volume expansion. Unstable SEI layer affects coulombic efficiency and long cycle life of electrodes (Hsieh and Liu 2019). Formation of the passive layer prevents the occurrence of further side reactions of liquid electrolyte. Growth of the SEI layer is unavoidable. As a result, it is critical to keep SEI layers constant during cycles to provide high coulombic efficiencies and long electrode cycle life (Tao et al. 2019).

6 Development in Silicon-Based Anode Materials

Studies on anode materials undergoing alloying type reaction mechanism to form alloys electrochemically with lithium metal at room temperature started in the 1970s. Theoretical capacity of silicon is around 4200 mAh/g due to the formation of Li-Si alloys at high temperature. However, upon lithiation, silicon powder tends to show poor performance due to irreversible volume expansion. Developing effective strategies to resolve problems related to volume expansion is identified as the major challenge for realizing silicon-based Li-ion cells (Zuo, et al. 2018).

6.1 Si Thin Films and Si Nanostructured Materials

In the 2000s, investigations were initiated on silicon thin films and Si nanowires for applications as anode materials for Li-ion cells. Different growth techniques including sputtering, electron beam evaporation and chemical vapour deposition (Mukanova et al. 2018) have been utilized to deposit amorphous thin films of silicon (Salah et al. 2018). Amorphous Si thin film electrodes of thickness 50 nm have been grown by chemical vapour deposition (CVD) using disilane as precursor on molybdenum (300 nm thick)/glass substrates. These films when used as anodes, are reported to give maximum capacity of 1330 mAh/g at 0.1 mA/g for 30 cycles. In 2008, performance of Si thin film electrodes has been further improved to provide a discharge capacity of 3000 mAh/g at 0.5 C for 53 cycles. RF magnetron sputtering is another promising method utilized to deposit 75 nm thick silicon film on copper and when this film is used as anode, better columbic efficiency of 76% and maximum capacity near to the theoretical capacity of 4135 mAh/g have been reported to be achieved. Although this film has shown good capacity, cycling stability is poor due to cracking and pulverization resulting from volume expansion (Ababtain et al. 2018). Surface roughness of the substrate is an important factor in the case of silicon thin films. Performance improvement is observed for silicon anode deposited on well-etched substrate with a specific capacity of 1500 mAh/g at 1C rate after 400 cycles.

Influence of carbon on the electrochemical properties of SiO/C thin film anodes is illustrated in Fig. 5 and these anodes are reported to show specific capacity of 960 mAh/g at 1 A/g and 82% capacity retention after 750 cycles (Cao et al. 2019).

Si nanowires (Si NWs) of diameter 89 nm, grown directly onto stainless steel current collector by vapour liquid solid (VLS) method have been used as Li cell anodes, and the schematic diagram illustrating the growth mechanism is shown in Fig. 6. Anodes based on Si NWs are reported to achieve an exceptionally high discharging capacity near to the theoretical capacity of 4277 mAh/g during the first charging cycle with a capacity retention of 75% after 10 cycles. Delamination of the electrode is small and the electrode does not break into small particles (Liu et al. 2019). Silicon NWs are expected to release the mechanical stress induced by volume expansion by providing an anisotropic route (Kohandehghan et al. 2013). Moreover, advantageous structural features of one dimensional Si nanowire facilitate better charge transportation. Silicon NWs grown via metal-assisted chemical etching and CVD are found to give an initial discharge capacity of 2500 mAh/g. The fast rate of capacity fading in Si NWs may be due to the limited surface area accessible to the electrolyte and the continual formation of SEI at the interface between electrode and electrolyte (Roy and Srivastava 2015). Mechanism of improved stability of Si NWs is also shown in Fig. 6d. Reductive breakdown of Si precursor in an alumina template followed by etching of the alumina template can be used to generate Si nanotubes (NTs) and anodes based on Si nanotubes are found to exhibit average initial charge/discharge capacity of 3448 mAh/g at 600 mA/g. Li-ion full cell consisting of LiCoO₂ cathode and Si nanotubes anode is reported to show initial capacity around 3000 mAh/g and capacity retention of 89% after 200 cycles at 1C.

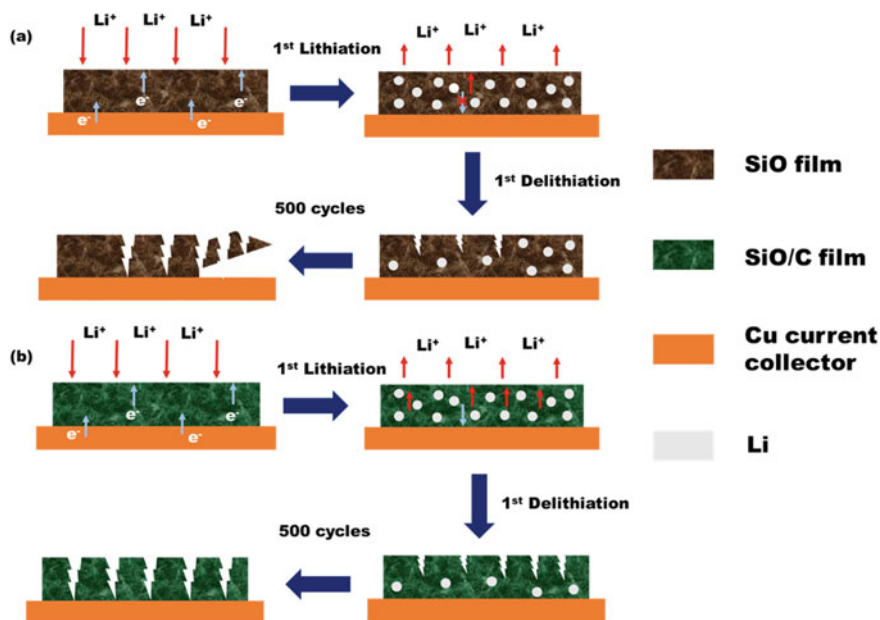


Fig. 5 Schematic illustration of the role of SiO/C film in improving the electrochemical performance

7 Si Composite Materials

In 1990s, making composites of silicon with carbonaceous materials has been identified as a promising method to tackle the challenges encountered in silicon-based anode materials for Li-ion cells (Kaskhedikar and Maier 2009). Methodologies to improve the electrochemical performance using different strategies are being investigated which include (1) modification of silicon using carbonaceous materials, metals and metal oxides (Cai and Wang 2009) (2) hierarchical structure construction consisting of nanoparticles embedded networks, core-shell and yolk-shell (Zhu et al. 2020). Eventually, the goal is to develop more porous, conducting electrode (Kasukabe et al. 2016) architecture with good structural stability on lithiation to achieve better electrochemical performance (Fu et al. 2013).

7.1 Nano/Micro Dimensional Si Particles Embedded in a Network

Composite Si nanoparticles embedded in network type anodes utilize the matrix to accommodate large volume expansion. These types of anodes can withstand substantial Si expansion while maintaining the electrode's structural integrity and enhancing

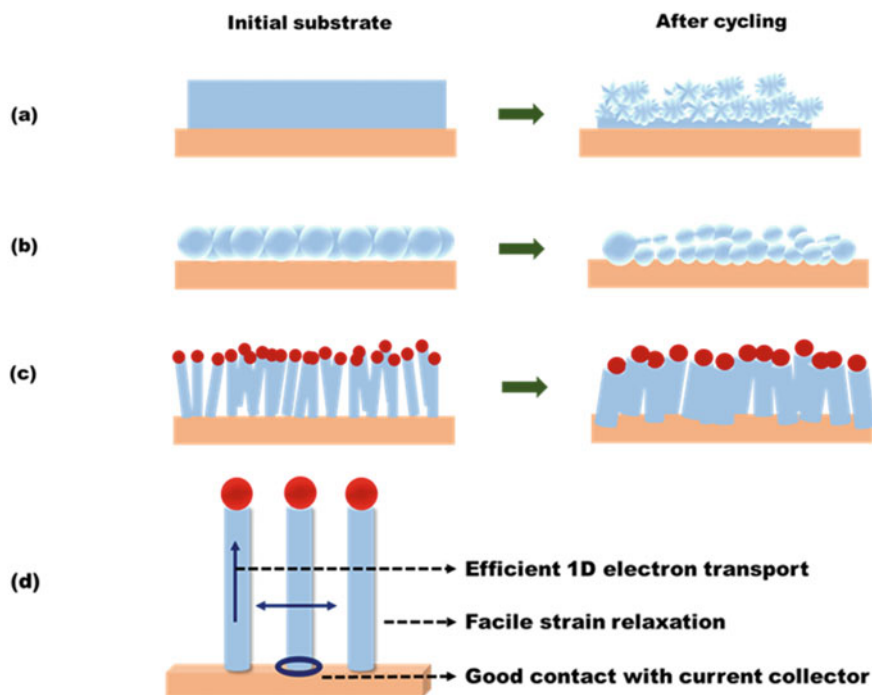


Fig. 6 Schematic of morphological changes that occur in (a) Si thin films, (b) Si nanoparticles and (c) Si NWs and (d) Growth mechanism of Si NWs directly on the current collector

structural stability by reducing Si aggregation (Li et al. 2015). In Si-carbon nanocomposite systems (Lee et al. 2019), carbonaceous materials like graphite and carbon nanotubes (CNTs) and conducting polymers are used as the networks to replace inactive matrices (Fu et al. 2016). Carbon nanotubes can be used as conductive additives with improved stress absorption during volume change (Tokur et al. 2016). Composites of Si with CNTs are reported to show an initial capacity of 940 mAh/g. In 2010, S. L. Chou's group has reported improved electrochemical performance of silicon-based anodes by using Si/graphene composite anode, prepared by simple physical mixing and has obtained a capacity of 1168 mAh/g with coulombic efficiency of 93% up to 30 cycles. H. C. Tao and co-workers have developed self-supporting Si/reduced graphene oxide (RGO) nanocomposite, capable of giving a specific capacity of 1040 mAh/g at 50 mA/g with a capacity retention of 94% after 50 cycles. Yi and co-workers have reported their work on micro-sized Si-C composite anode consisting of interconnected Si and carbon nanoscale building blocks. This Si-C composite anode is shown to exhibit a reversible capacity of 1459 mAh/g after 200 cycles at 1 A/g current rate with a capacity retention of 97.8%.

Recently, 3D sandwich-like Si/polyaniline/graphene nanoarchitecture anode has been developed using an easy and scalable approach of in situ polymerisation (Huang et al. 2018). Schematic illustration of this synthesis procedure is shown in Fig. 7.

These anodes are shown to give initial discharge/ charge capacity of 2708 mAh/g and 1725 mAh/g at 160 mA/g respectively with initial coulombic efficiency 63.7%. This architecture has been improved by introducing a few layers of black phosphorus (FLBP) as stress absorbing material with silicon nanoparticles (Roy et al. 2019) and the schematic diagram, showing this effect is given in Fig. 8. Due to the unique properties and puckered structure of FLBP, a capacity of 3386 mAh/g at 0.1A/g after 250 cycles and ICE about 78% have been reported for the cells based on nanostructured Si anode with improved architecture. It has been established that FLBP can definitely influence the electrochemical performance of the anode material on lithiation and delithiation and also provide flexible, strain-absorbing and electrically conducting network.

Development of nano/microstructured silicon by boron doping and carbon nanotubes (CNT) wedging has been identified as a viable technique for realizing highly promising Si based anodes and the process is schematically illustrated in Fig. 9. Anodes based on B-Si/CNT are reported to show improved stability, high reversible capacity around 2424 mAh/g at 2000 mA/g and 88.2% capacity retention

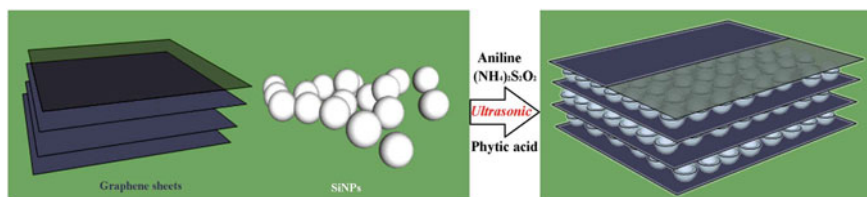


Fig. 7 Growth process for 3D sandwich-like Si/polyaniline/graphene nano-architecture. Reprinted with permission from Huang et al. (2018), copyright (2021) © Elsevier

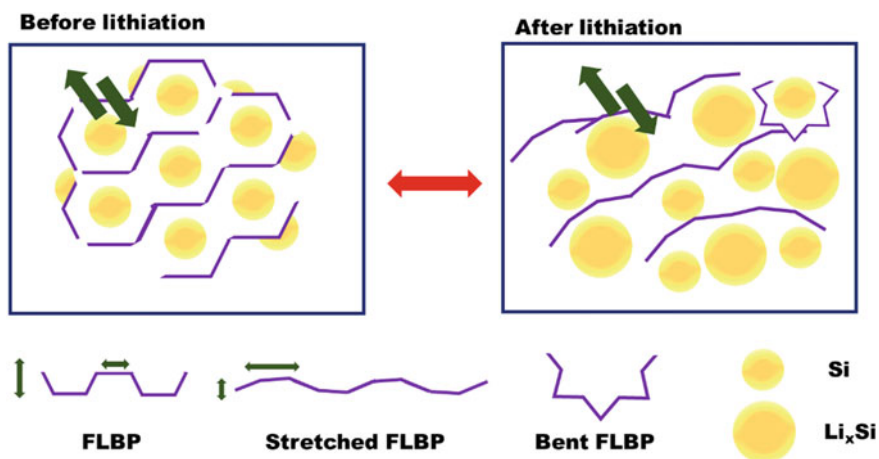


Fig. 8 Schematic diagram, bringing out the primary benefit of using FLBP additive to nanostructured Si anode

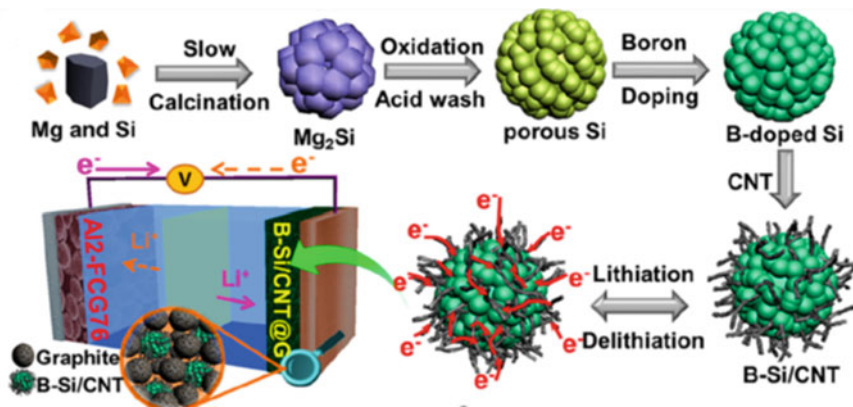
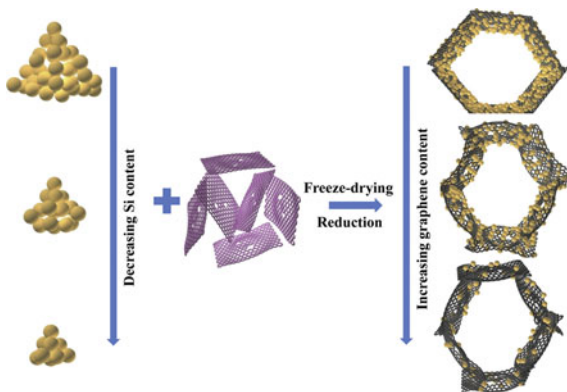


Fig. 9 Schematic illustration of the synthesis of B – Si/CNT (Li et al. 2019c)

after 200 cycles in half cell configuration. In the full cell configuration, it is observed that coulombic efficiency of 96% and specific capacity of 180 mAh/g at 180 mA/g can be maintained after 300 cycles with a capacity retention of 82.5% (Li et al. 2019c).

Variation of Si and graphene weight percentages in the distribution of silicon nanoparticles on graphene sheets has been studied through rapid freezing process (Hu et al. 2018). Schematic illustration of the process is given in Fig. 10. An improved rate performance is observed on the addition of multi walled carbon nanotubes (MWCNTs). Even at high C-rate of 5C, average specific capacity is maintained at 458 mAh/g. Addition of MWCNTs contributes to better conductivity of the electrode and long MWCNTs getting distributed uniformly inside the anode will act as nanopores to attach silicon nanoparticles on graphene framework, improving the structural stability of the electrode. In-situ X-ray synchrotron tomography has been used to study the morphological changes during cycling (1st discharge, 2nd charge, 2nd discharge) of Si/C paper anode (Vanpeene et al. 2017).

Fig. 10 Schematic illustration of synthesis process of Si nanoparticles on graphene sheets with different Si content. Reprinted with permission from Hu et al. (2018), copyright (2021) © Elsevier



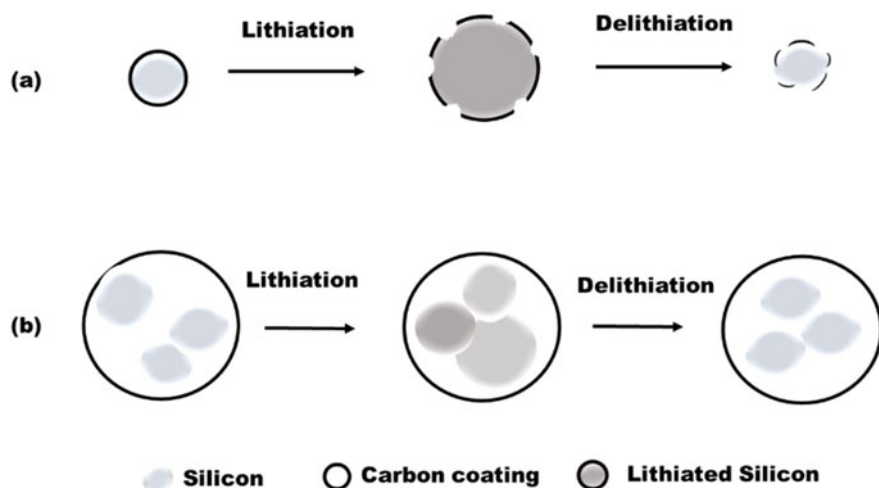


Fig. 11 Schematic representation of (a) conventional carbon coating on Si particles, (b) empty space carbon coating

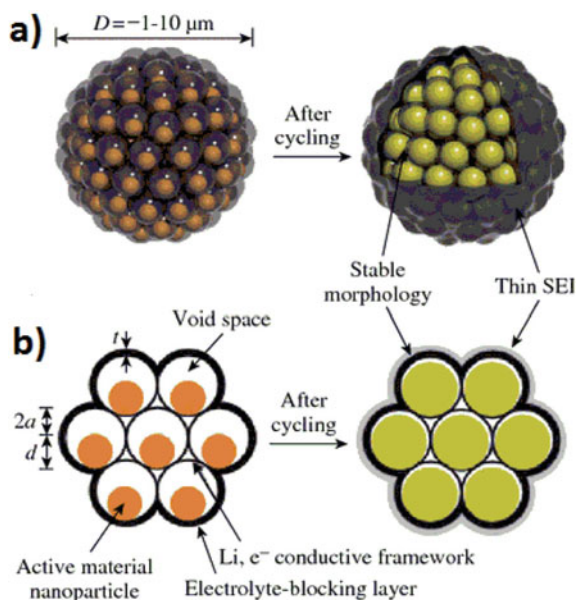
7.2 Core–Shell Structured Si Composites

A widely adopted strategy towards the challenges related to volume expansion of Si anode is the core–shell hierarchical structure (Luo et al. 2019) with silicon core and porous conducting material shell. The advantage of empty space carbon coating can be schematically represented as shown in Fig. 11. Synthesis process includes making of silicon/silica nanoparticles, carbonaceous coating of the core through calcination and final etching or removal of impurities (Shao et al. 2013).

Solid Si/C core–shell anodes are reported to show capacity around 1800 mAh/g at a current density of 100 mA/g for 50 cycles without much capacity fading in the work conducted by Dan Sha and co-workers. In this work, each single silicon particle is coated with a thin porous carbon shell by simple hydrothermal approach. This composite electrode shows excellent cycling stability and rate capability. Nanostructured Si/porous carbon electrode is found to deliver a capacity of 1607 mAh/g at a current rate of 0.4 A/g after 100 cycles. J. Source and team have reported their work on amorphous silicon /carbon nanostructured anode, synthesized using two-stage laser pyrolysis (Source et al. 2016). It has been shown to retain specific capacity of 1250 mAh/g at current rate of C/5 after 500 cycles. A simple hydrothermal process has been employed to synthesize core–shell type $\text{SiO}_2 @ \text{Fe}_2\text{O}_3 @ \text{C}$ composite electrode by employing SiO_2 as a template. This composite anode is reported to have good electrochemical reversibility and stability with an initial charge–discharge capacity of 640 mAh/g and 1020 mAh/g respectively (Hou et al. 2017).

A yolk-shell structure is a self-supporting carbon shell with an improved capacity of 2833 mAh/g at 400 mA/g over 1000 cycles with a capacity retention of 74% and

Fig. 12 Schematic representation of pomegranate structured Si-C composite electrode: (a) 3D view and (b) 2D cross-sectional view of one micro-particle before and after lithiation. Reprinted with permission from Zuo et al. (2017), copyright (2021) © Elsevier



coulombic efficiency 99%. It is also similar to pomegranate structured Si-C composite electrode illustrated in Fig. 12. For this electrode, owing to good electrical conductivity and structural stability, specific capacity is retained at 1160 mAh/g after 1000 cycles at a current rate of 0.5 C.

Development of a yolk-shell structure with controllable space buffer layer grown around large size industrial silicon has been reported. This electrode configuration having Si@void@C exhibits good cycling stability and high coulombic efficiency with a capacity of 950 mAh/g at a current rate of 100 mA/g after 100 cycles. Details are schematically given in Fig. 13 (Jiao et al. 2018).

Development of Si core covered with mesoporous shell carbon spheres (SCMSC) using simple methods is a common strategy adopted to accommodate volume expansion. Schematic illustration of this process is given in Fig. 14. This type of electrode is reported to exhibit an initial discharge capacity of 2450 mAh/g at a current rate of 0.166 A/g and 99.2% of coulombic efficiency over 100 cycles (Prakash et al. 2019).

Introducing germanium coating to silicon brings about significant improvement in electrochemical performance. Growth of micron/sub-micron sized Si@Ge@C core-shell electrode using simple techniques has been reported. Germanium is also an attractive material owing to its theoretical capacity of 1600 mAh/g and reduced trend towards pulverization on lithiation, compared to silicon. Difference in lithiation potential will allow subsequent release of stress/strain in the core-shell electrode, alleviating mechanical disintegration. This electrode is shown to deliver a high specific capacity of 900 mAh/g at a current rate of 2A/g. Carbon and Ge rich electrodes are mostly spherical in shape with good structural stability after 10 cycles at a low current rate of 200 mA/g (Mishra et al. 2018).



Fig. 13 Schematic illustration of lithiation and delithiation processes of (a) Si@C, (b) traditional yolk-shell Si@void@C and (c) as-prepared industrial Si@void@C with interconnected porous carbon network. Reprinted with permission from Jiao et al. (2018), copyright (2021) © Elsevier

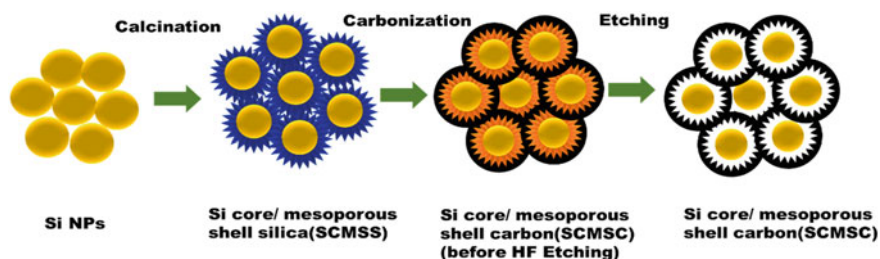


Fig. 14 Schematic representation for the synthesis of Si core/mesoporous shell carbon (SCMSC) via Si core/mesoporous shell silica (SCMSS)

8 Current Trends in Silicon-Based Composites and Hybrid Materials

Nano/micro-structured hybrid materials:

Most recently, micro/nano-structured materials are found to offer better electrode performance, owing to good structural stability and improved conductivity (Yi et al. 2019). Qi Liang Pan and team have synthesized Si@N-doped C /reduced graphene oxide (rGO) composite anode by polymer network method, as illustrated in Fig. 15. This composite anode is found to deliver capacity of 867.4 mAh/g and 479.1 mAh/g at current rates of 0.1 and 2 A /g respectively after 100 cycles. This electrode consists

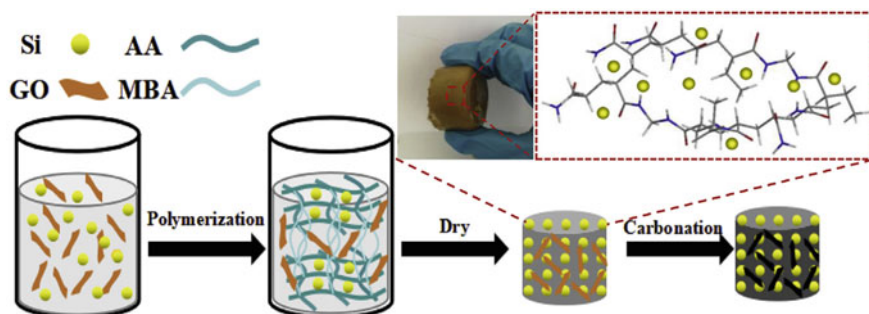


Fig. 15 Schematic illustration of the growth process of Si@NC/rGO composite. Reprinted with permission from Pan et al. (2019) Copyright (2021) © Elsevier

of carbon covered Si nanoparticles embedded in a network of rGO sheets and is found to show an ICE of 69% (Pan et al. 2019).

Modification of nanostructured silicon by making composites with $\text{Fe}_2\text{O}_3/\text{C}$ as shown in Fig. 16, using simple solvo-thermal method is a promising approach to identify high quality, Si based anode materials. Performance of core-shell structured Si@ $\text{Fe}_2\text{O}_3/\text{C}$ nanocomposite is compared with that of pristine Si and Si@C (Fe_2O_3 removed by HCl etching). Fe_2O_3 can contribute towards capacity enhancement and stabilizing of the SEI layer, which in turn enhance cycling stability of the electrode. This composite electrode is found to deliver an initial capacity of 2941mAh/g at current rate of 0.1A/g and ICE is 68.5%. After 300 cycles, it retains 680 mAh/g at 1A/g and 423 mAh/g at 10 A/g current rates. High rate capability is due to improved structural stability and conductivity and stable SEI formation (Wang et al. 2019c).

Method of graded silicon concentration is used by varying the concentration of Si in the layered electrode in a graded manner to solve the interfacial delamination problem and the process is shown in Fig. 17 with improved electrochemical performance of silicon. Graded electrode shows ICE of 76% in contrast to 66% of a homogeneous silicon electrode. Thickness of the transition layer for the graded electrode is optimized as 25 μm and the graded electrode is found to deliver a capacity of 1263 mAh/g after 20 cycles (Guo et al. 2019).

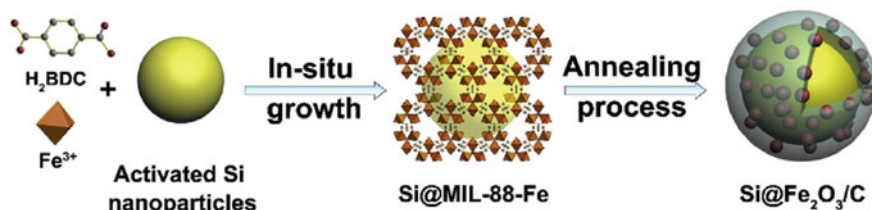


Fig. 16 Schematic illustration of the synthesis of core-shell structured Si@ $\text{Fe}_2\text{O}_3/\text{C}$ composite. Reprinted with permission from Wang et al. (2019c), copyright (2021) © Elsevier

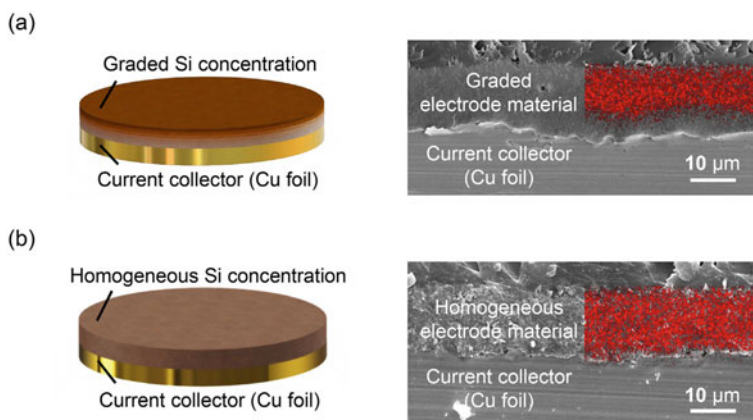


Fig. 17 Schematic and cross-sectional energy-dispersive X-ray spectroscopy (EDS) mapping of Si element for (a) graded and (b) homogeneous Si-based electrodes. Reprinted with permission from Guo et al. (2019), copyright (2021) © Elsevier

Architecture having ant nest like, porous, 3D interconnected silicon nanofilaments and continuous nanopores, which can effectively accommodate volume expansion during cycling and prevent pulverization and cracking of electrodes has been developed using Mg-Si alloy, as illustrated in Fig. 18. A layer of 5- 8 nm thick carbon is also coated on the ant nest microscale porous silicon to give AMPSi@C.

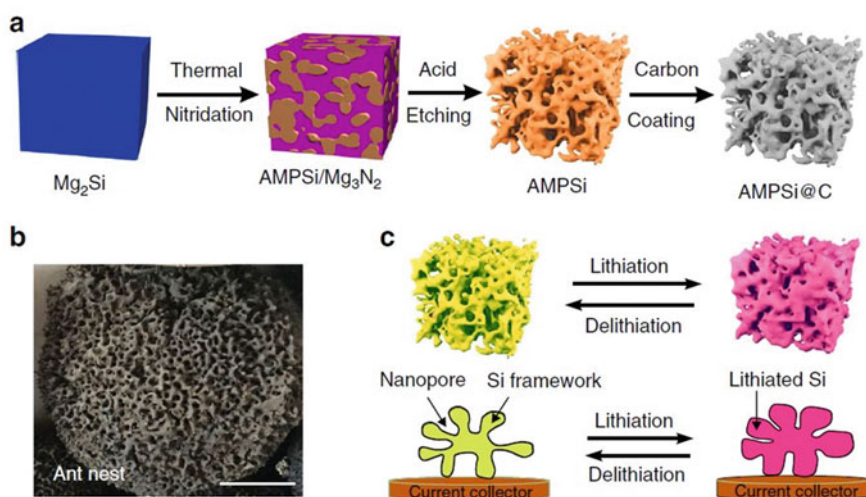


Fig. 18 Design and schematic showing the synthesis method of AMPSi. (a) Schematic showing the preparation of AMPSi and AMPSi@C. (b) Photograph of an ant nest. (c) Schematic diagrams illustrating the lithiation/delithiation process of the ant-nest-like microscale porous Si particles showing inward volume expansion and stable Si framework retention during cycling. (PMID- 30,926,799)

Cycling performance of the electrode in both half-cell and full-cell configurations is shown in Fig. 19. This AMPSi@C electrode is found to deliver initial capacity of 2134 mAh/g at 0.1 C and 1271 mAh/g at 0.5C current rate ($1C = 4200 \text{ mA/g}$) with high initial coulombic efficiency of 80%. In half cell configuration, the anode maintains 1271 mAh/g at current 2100 mA/g after 1000 cycles with a capacity retention of 90%. Full cell configuration against $\text{LiNi}_{1/3}\text{Co}_{1/3}\text{Mn}_{1/3}\text{O}_2$ cathode is found to maintain a capacity of 134 mAh/g at the current rate of 0.5C ($1C = 160 \text{ mA/g}$) for 400 cycles with a capacity retention of 84% (An et al. 2019). Galvanostatic charge discharge curves and cycling performance of the electrode for different current density show quite higher rate capability and good cycling stability.

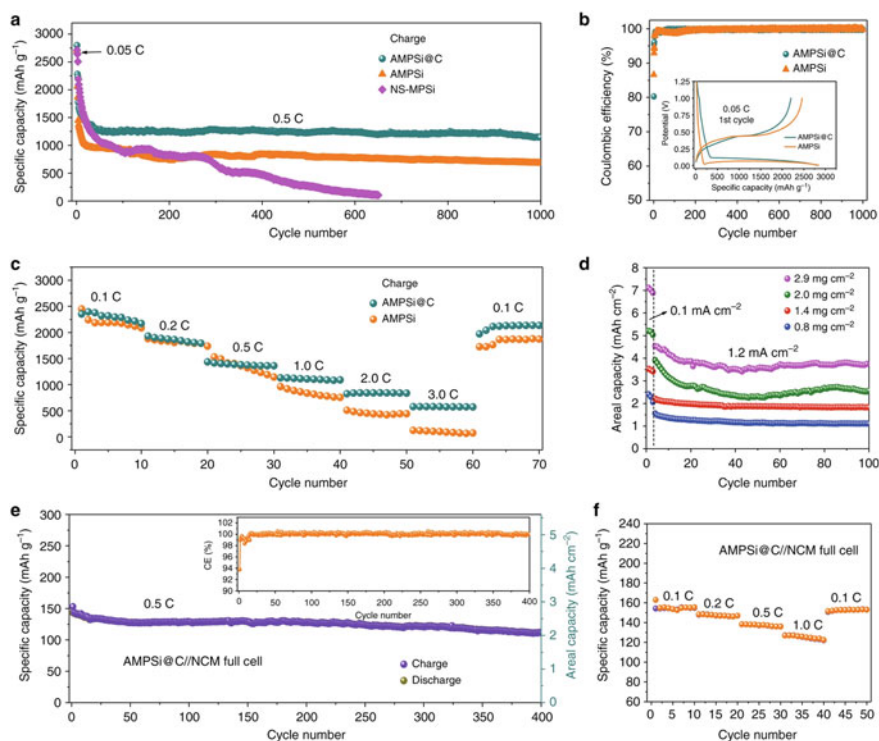
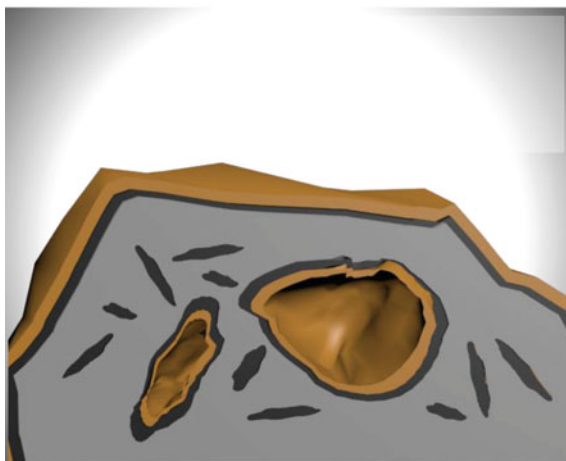


Fig. 19 Electrochemical characterization of anodes in half-cell or full-cell configurations. **(a)** Cycling stability test of AMPSi@C at 0.5 C after the activation process in the first three cycles at 0.05 C ($1C = 4.2 \text{ A/g}$) in the half-cell with areal mass loading of 0.8 mg/cm^2 . **(b)** Comparison of CE between AMPSi and AMPSi@C electrode. (inset being the galvanostatic charge discharge curve). **(c)** Rate capability performance of AMPSi@C and AMPSi at various current densities from 0.1 to 3 C. **(d)** Areal capacities vs. cycling number of the AMPSi@C anodes with different mass loadings at a current density of 1.2 mA/cm^2 (the initial three cycles are carried out at 0.1 mA/cm^2). **(e)** Full-cell charge at 0.5 C ($1C = 160 \text{ mA/g}$) with prelithiated AMPSi@C anode and a $\text{LiNi}_{1/3}\text{Co}_{1/3}\text{Mn}_{1/3}\text{O}_2$ cathode. Inset shows the corresponding CE Vs cycle number. **(f)** Rate performance of the full cell (An et al. 2019)

Fig. 20 Schematic illustration of cross-sectional MGS providing detailed characteristics of each component (Ma et al. 2019)



Results of simulations and mathematical calculations are compared with experimental data of macro-pore coordinated graphite Si (MGS) composite electrodes. From mathematical calculations, volume expansion of Si in mesopores causes pulverization and breaking and will ultimately lead to loss of contacts. Si containing macropores can accommodate volume expansion of Si layers. In the experimental part, macro pores in graphite-Si composite are filled with Si layers to avoid electrode swelling and mesopores are filled with carbon called ‘carbon blocking’.

Si layers are filled in macropores of graphite via thermal decomposition of monosilane (silicon blocking) (Fig. 20). In the full cell configuration, against LiCoO_2 cathode, this electrode retains high specific capacity of 527 mAh/g with ICE of 93% (Ma et al. 2019).

Developing hierarchically porous, rice husk(RH) derived honeycomb structure of carbon which can accommodate volume expansion of silicon and offer transportation highways for Li-ions (Wang et al. 2020) is emerging as a cost-effective and environmentally friendly approach for identifying high quality Si based anodes. Citric acid (CA) and the binder carboxy methyl cellulose (CMC) coated on Si particles anchored to RH are found to improve both structural and SEI layer stability of the anode. Si@CA@RH electrode is reported to show a stable capacity of 2126 mAh/g with columbic efficiency of 99.5% after 250 cycles at 1 A/g. Excellent cycling performance of full cell assembled with Si@CA@RH anode and LiFePO_4 cathode has also been observed.

9 Summary

Silicon anodes have drawn extreme attention for developing the next generation Li-ion cells due to their high theoretical capacity suitable for applications in hybrid

electric vehicles, which require high energy density. Earth abundance, environmental friendliness and low production cost are other advantageous factors, making silicon the most sought after anode material. However, volume expansion of Si up to 300% on lithiation leading to pulverization and cracking of electrode with the loss of electrical contacts, formation of unstable and thick SEI layer and low electrical conductivity are the striking drawbacks, hindering full utilization of the promising features of Si anode. This review is intended to provide a comprehensive analysis of the various viable strategies, available to tackle the limitations of Si anode, which include modification strategies, chemical etching and hierarchical structure construction. Recently, tremendous progress has been achieved in improving the performance of Si-based anodes by developing hierarchical structures, nano architecture and nano structured hybrid materials. Devoted research efforts are needed to improve structural stability and high rate performance of silicon anodes.

References

- Manoj M, Muhamed Ashraf C, Jasna M, Anilkumar KM, Jinisha B, Pradeep VS, Jayalekshmi S (2019) Biomass-derived, activated carbon-sulfur composite cathode with a bifunctional interlayer of functionalized carbon nanotubes for lithium-sulfur cells. *J Colloid Interface Sci* 535:287–299
- Ababtain K, Babu G, Susarla S, Gullapalli H, Masurkar N, Ajayan PM, Arava LMR (2018) Porous graphene current collectors filled with silicon as high-performance lithium battery anode. *Mater Res Express* 5(1):014004
- Aghamohammadi H, Hassanzadeh N, Eslami-Farsani R (2021) A review study on the recent advances in developing the heteroatom-doped graphene and porous graphene as superior anode materials for Li-ion batteries. *Ceram Int* 47(16):22269–22301
- An Huang R, Guo Y, Chen Z, Zhang X, Wang J, Yang B (2018) An easy and scalable approach to synthesize three-dimensional sandwich-like Si/Polyaniline/Graphenenanoarchitecture anode for lithium ion batteries. *Ceram Int* 44(4):4282–4286
- An W, Gao B, Mei S, Xiang B, Fu J, Wang L, Zhang Q, Chu PK, Huo K (2019) Scalable synthesis of ant-nest-like bulk porous silicon for high-performance lithium-ion battery anodes. *Nat Commun* 10(1):1–11
- Blomgren GE (2017) The development and future of lithium ion batteries. *J Electrochem Soc* 164(1):A5019–A5025
- Braga MH, Grundish NS, Murchison AJ, Goodenough JB (2017) Alternative strategy for a safe rechargeable battery. *Energy Environ Sci* 10(1):331–336
- Bruce PG, Scrosati B, Tarascon JM (2008) Nanomaterials for rechargeable lithium batteries. *Angew Chemie Int Ed* 47(16):2930–2946
- Cai C, Wang Y (2009) Novel nanocomposite materials for advanced li-ion rechargeable batteries. *Materials (basel)* 2(3):1205–1238
- Cao Z, Xia B, Xie X, Zhao J (2019) Influences of co-sputtered carbon on the electrochemical performance of SiO/C thin film anodes for lithium-ion batteries. *Electrochim Acta* 313:311–320
- Chu H, Wu Q, Huang J (2018) Rice husk derived silicon/carbon and silica/carbon nanocomposites as anodic materials for lithium-ion batteries. *Colloids Surf A Physicochem Eng Asp* 558(August):495–503
- Deng D (2015) Li-ion batteries: basics, progress, and challenges. *Energy Sci Eng* 3(5):385–418
- Fang R, Xiao W, Miao C, Mei P, Zhang Y, Yan X, Jiang Y (2019) Enhanced lithium storage performance of core-shell structural Si@TiO₂/NC composite anode via facile sol-gel and in situ N-doped carbon coating processes. *Electrochim Acta* 317:575–582

- Fu K, Yildiz O, Bhanushali H, Wang Y, Stano K, Xue L, Zhang X, Bradford PD (2013) Aligned carbon nanotube-silicon sheets: a novel nano-architecture for flexible lithium ion battery electrodes. *Adv Mater* 25(36):5109–5114
- Fu C, Song C, Liu L, Zhao W, Xie X (2016) High reversible silicon/graphene nanocomposite anode for Lithium-Ion batteries. *Int J Electrochem Sci* 11(1):154–164
- Fujita T, Chen H, Wang K, He C, Wang Y, Dodbiba G, Wei Y (2021) Reduction, reuse and recycle of spent Li-ion batteries for automobiles: a review. *Int J Miner Metall Mater* 28(2):179–192
- Fukata N, Subramani T, Jevasuwan W, Dutta M, Bando Y (2017) Functionalization of silicon nanostructures for energy-related applications. *Small* 13(45):1–13
- Gangaja B, Nair S, Santhanagopalan D (2020) Surface—engineered Li 4 Ti 5 O 12 nanostructures for high—power Li—Ion batteries, no 0123456789, pp 1–11
- Gao X, Wang F, Gollon S, Yuan C (2019) Micro silicon-graphene-carbon nanotube anode for full cell lithium-ion battery. *J Electrochem Energy Convers Storage* 16(1)
- Ge M, Rong J, Fang X, Zhang A, Lu Y, Zhou C (2013a) Scalable preparation of porous silicon nanoparticles and their application for lithium-ion battery anodes. *Nano Res* 6(3):174–181
- Ge M, Fang X, Rong J, Zhou C (2013b) Review of porous silicon preparation and its application for lithium-ion battery anodes. *Nanotechnology* 24(42)
- Goodenough JB, Kim Y (2010) Challenges for rechargeable Li batteries. *Chem Mater* 22(3):587–603
- Goodenough JB, Park KS (2013) The Li-ion rechargeable battery: a perspective. *J Am Chem Soc* 135(4):1167–1176
- Guo Z, Zhou L, Yao H (2019) Improving the electrochemical performance of Si-based anode via gradient Si concentration. *Mater Des* 177:107851
- Hou Y, Yuan H, Chen H, Shen J, Li L (2017) The preparation and lithium battery performance of core-shell SiO₂@Fe₃O₄@C composite. *Ceram Int* 43(14):11505–11510
- Hsieh CC, Liu WR (2019) Effects of nitrogen doping on Si/carbon composite anode derived from Si wastes as potential active materials for Li ion batteries. *J Alloys Compd* 790:829–836
- Hu X, Jin Y, Zhu B, Liu Z, Xu D, Guan Y, Sun M, Liu F (2018) Tuning density of Si nanoparticles on graphene sheets in graphene-Si aerogels for stable lithium ion batteries. *J Colloid Interface Sci* 532:738–745
- Jiao Z, Gao Y, Liu S, Huang S, Jiang Y, Chen Z, Zhao B (2018) Controlled scalable synthesis of yolk-shell structured large-size industrial silicon with interconnected carbon network for lithium storage. *Electrochim Acta* 283:1702–1711
- Jinisha B, Km A, Manoj M, Pradeep VS, Jayalekshmi S (2017a) Development of a novel type of solid polymer electrolyte for solid state lithium battery applications based on lithium enriched poly (ethylene oxide) (PEO)/ poly (vinyl pyrrolidone) (PVP) blend polymer. *Electrochim Acta* 235:210–222
- Jinisha B, Anilkumar KM, Manoj M, Abhilash A, Pradeep VS (2017b) Poly (ethylene oxide) (PEO) -based , sodium ion-conducting , solid polymer electrolyte films , dispersed with Al 2 O 3 filler, for applications in sodium ion cells
- Kaskhedikar NA, Maier J (2009) Lithium storage in carbon nanostructures. *Adv Mater* 21(25–26):2664–2680
- Kasukabe T, Nishihara H, Iwamura S, Kyotani T (2016) Remarkable performance improvement of inexpensive ball-milled Si nanoparticles by carbon-coating for Li-ion batteries. *J Power Sources* 319:99–103
- Kim T, Song W, Son DY, Ono LK, Qi Y (2019) Lithium-ion batteries: outlook on present, future, and hybridized technologies. *J Mater Chem A* 7(7):2942–2964
- Kohandehghan A et al (2013) Magnesium and magnesium-silicide coated silicon nanowire composite anodes for lithium-ion batteries. *J Mater Chem A* 1(5):1600–1612
- Kulova TL, Mironenko AA, Skundin AM, Rudy AS, Naumov VV, Pukhov DE (2016) Study of silicon composite for negative electrode of lithium-ion battery. *Int J Electrochem Sci* 11(2):1370–1381

- Kwon HT, Lee CK, Jeon KJ, Park CM (2016) Silicon diphosphide: a Si-based three-dimensional crystalline framework as a high-performance Li-Ion battery anode. *ACS Nano* 10(6):5701–5709
- Kwon S, Kim KH, Kim WS, Hong SH (2019) Mesoporous Si-Cu nanocomposite anode for a lithium ion battery produced by magnesiothermic reduction and electroless deposition. *Nanotechnology* 30(40)
- Lee S-Y, Kim S-I, Yoon S (2019) Si nanoparticles coated with Co-containing N-doped carbon: preparation and characterization as Li-Ion battery anode materials. *J Nanosci Nanotechnol* 19(12):7753–7757
- Li X, Zhang G, Zhang L, Zhong M, Yuan X (2015) Silicon/graphite/carbon nanotubes composite as anode for lithium ion battery. *Int J Electrochem Sci* 10(4):2802–2811
- Li M, Zhang Y, Bai Z, Liu WW, Liu T, Gim J, Jiang G, Yuan Y, Luo D, Feng K, Yassar RS, Wang X, Chen Z, Lu J (2018) A lithium-sulfur battery using a 2D current collector architecture with a large-sized sulfur host operated under high areal loading and low E/S ratio. *Adv Mater* 30(46):1–9
- Li X, Bai Y, Wang M, Wang G, Ma Y, Li L, Xiao B, Zheng J (2019) Self-assembly encapsulation of Si in N-doped reduced graphene oxide for use as a lithium ion battery anode with significantly enhanced electrochemical performance. *Sustain Energy Fuels* 3(6):1427–1438
- Li C, Li X, Zheng YZ, Wu J, Ding H, Tao X (2019b) A cost-effective and scaleable approach for the in-situ synthesis of porous carbon-coated micrometer-sized AlSi particles as anode for lithium-ion batteries. *Chem Electro Chem* 6(9):2517–2523
- Li P, Hwang JY, Sun YK (2019c) Nano/microstructured silicon-graphite composite anode for high-energy-density li-ion battery. *ACS Nano* 13(2):2624–2633
- Lin CC, Yen YC, Wu HC, Wu NL (2012) Synthesis of porous Si particles by metal-assisted chemical etching for li-ion battery application. *J Chinese Chem Soc* 59(10):1226–1232
- Liu H, Wei Z, He W, Zhao J (2017) Thermal issues about Li-ion batteries and recent progress in battery thermal management systems: a review. *Energy Convers Manag* 150:304–330
- Liu L, Li X, Zhang G, Zhang Z, Fang C, Ma H, Luo W, Liu Z (2019) Enhanced stability lithium-ion battery based on optimized Graphene/Si Nanocomposites by templated assembly. *ACS Omega* 4(19):18195–18202
- Luo J, Ma B, Peng J, Wu Z, Luo Z, Wang X (2019) Modified chestnut-like structure silicon carbon composite as anode material for Lithium-Ion batteries. *ACS Sustain Chem Eng* 7(12):10415–10424
- Ma Y, Liu Y, Wang M, Yang z, Bai y, Yin x, Luo c, Huang Y, Li X (2016) Synergetic protection hollow silicon by nitrogen-doped carbon/reduced graphene oxide to improve the electrochemical stability as lithium-ion battery anode. *Int J Electrochem Sci* 14(6):5831–5845
- Ma J, Sung J, Hong J, Chae S, Kim N, Choi SH, Nam G, Son Y, Kim SY, Ko M, Cho J (2019) Towards maximized volumetric capacity via pore-coordinated design for large-volume-change lithium-ion battery anodes. *Nat Commun* 10(1)
- Mishra K, George K, Zhou XD (2018) Submicron silicon anode stabilized by single-step carbon and germanium coatings for high capacity lithium-ion batteries. *Carbon N Y* 138:419–426
- Mukanova A, Jetybayeva A, Myung ST, Kim SS, Bakenov Z (2018) A mini-review on the development of Si-based thin film anodes for Li-ion batteries. *Mater Today Energy* 9:49–66
- Nitta N, Wu F, Lee JT, Yushin G (2015) Li-ion battery materials: present and future. *Mater Today* 18(5):252–264
- Pan Q, Zhao J, Qu W, Liu R, Li N, Xing B, Jiang S, Pang M, Zhao L, Zhang Y, Liang W (2019) Facile synthesis of the 3D framework Si@N-doped C/reduced graphene oxide composite by polymer network method for highly stable lithium storage. *J Phys Chem Solids* 133(February):92–99
- Park M, Kim MG, Joo J, Kim K, Kim J, Ahn S, Cui Y, Cho J (2009) Silicon nanotube battery anodes. *Nano Lett* 9(11):3844–3847
- Paul P, McShane EJ, Colclasure AM, Balsara N, Brown DE, Cao C, Chen B, Chinnam P, Cui Y, Dufek EJ, Finegan D, Gillard S, Huang W, Konz ZM, Kostecki R, Liu R, Lubner S, Prasher R, Preefer M, Qian J, Rodrigues MF, Schnabel M, Son S, Srinivasan V, Steinrück H, Tanim TR, Toney M, Tong W, Usseglio-Viretta FLE, Wan J, Yusuf M, McCloskey B, Weker JN (2021) A

- review of existing and emerging methods for lithium detection and characterization in Li-Ion and Li-Metal batteries. *Adv Energy Mater* 11(17):2100372
- Pradeep VS, Graczyk-Zajac M, Riedel R, Soraru GD (2014) New insights in to the lithium storage mechanism in polymer derived SiOC anode materials. *Electrochim Acta* 119:78–85
- Prakash S, Zhang C, Park JD, Razmjooei F, Yu JS (2019) Silicon core-mesoporous shell carbon spheres as high stability lithium-ion battery anode. *J Colloid Interface Sci* 534:47–54
- Raccichini R, Amores M, Hinds G (2019) Critical review of the use of reference electrodes in Li-Ion batteries: a diagnostic perspective. *Batteries* 5(1)
- Rahman MA, Song G, Bhatt AI, Wong YC, Wen C (2016) Nanostructured silicon anodes for high-performance lithium-ion batteries. *Adv Funct Mater* 26(5):647–678
- Roy P, Srivastava SK (2015) Nanostructured anode materials for lithium ion batteries. *J Mater Chem A* 3(6):2454–2484
- Roy K, Wahid M, Puthusseri D, Patrike A, Muduli S, Vaidhyanathan R, Ogale S (2019) High capacity, power density and cycling stability of silicon Li-ion battery anodes with a few layer black phosphorus additive. *Sustain Energy Fuels* 3(1):245–250
- Salah M, Murphy P, Hall C, Francis C, Kerr R, Fabretto M (2019) Pure silicon thin-film anodes for lithium-ion batteries: a review. *J Power Sources* 414(December 2018):48–67
- Shao D, Tang D, Mai Y, Zhang L (2013) Nanostructured silicon/porous carbon spherical composite as a high capacity anode for Li-ion batteries. *J Mater Chem A* 1(47):15068–15075
- Shen Y (2017) Rice husk silica-derived nanomaterials for battery applications: a literature review. *J Agric Food Chem* 65(5):995–1004
- Sourice J, Bordes A, Boulineau A, Alper JP, Franger S, Quinsac A, Habert A, Leconte Y, Vito ED, Porcher W, Reynaud C, Herlin-Boime N, Haon C (2016) Core-shell amorphous silicon-carbon nanoparticles for high performance anodes in lithium ion batteries. *J Power Sources* 328:527–535
- Sun L, Gong K (2001) Silicon-based materials from rice husks and their applications. *Ind Eng Chem Res* 40(25):5861–5877
- Tao W, Wang P, You Y, Park K, Wang C, Li Y, Cao F, Xin S (2019) Strategies for improving the storage performance of silicon-based anodes in lithium-ion batteries. *Nano Res* 12(8):1739–1749
- Tokur M, Algul H, Ozcan S, Cetinkaya T, Uysal M, Akbulut H (2016) Closing to scaling-up high reversible Si/rGO Nanocomposite anodes for lithium ion batteries. *Electrochim Acta* 216:312–319
- Vanpeene V, Etienne A, Bonnin A, Maire E, Roué L (2017) In-situ X-ray tomographic study of the morphological changes of a Si/C paper anode for Li-ion batteries. *J Power Sources* 350:18–27
- Wang X, Xia Y, Zuo X, Schaper SJ, Yin S, Ji Q, Liang S, Yang Z, Xia S, Xiao Y, Zhu J, Müller-P, Cheng Y (2019a) Synergistic effects from super-small sized TiO₂ and SiO_x nanoparticles within TiO₂/SiO_x/carbon nanohybrid lithium-ion battery anode. *Ceram Int* 45(11):14327–14337
- Wang F, Sun L, Zi W, Zhao B, Du H (2019b) Solution synthesis of porous silicon particles as an anode material for lithium ion batteries. *Chem A Eur J* 25(38):9071–9077
- Wang Q, Guo C, He J, Yang S, Liu Z, Wang Q (2019c) Fe₂O₃/C-modified Si nanoparticles as anode material for high-performance lithium-ion batteries. *J Alloys Compd* 795:284–290
- Wang Y, Wang X, Jin H, Bai Y, Xu H (2020) The synergetic effects of a multifunctional citric acid and rice husk derived honeycomb carbon matrix on a silicon anode for high-performance lithium ion batteries. *Sustain Energy Fuels* 4(5):2583–2592
- Winter M, Besenhard JO, Spahr ME, Novák P (1998) Insertion electrode materials for rechargeable lithium batteries. *Adv Mater* 10(10):725–763
- Xu ZL, Liu X, Luo Y, Zhou L, Kim JK (2017) Nanosilicon anodes for high performance rechargeable batteries. *Prog Mater Sci* 90(July):1–44
- Yao Y, Zhang J, Xue L, Huang T, Yu A (2011) Carbon-coated SiO₂ nanoparticles as anode material for lithium ion batteries. *J Power Sources* 196(23):10240–10243
- Yi Z, Qian Y, Cao C, Lin N, Qian Y (2019) Porous Si/C microspheres decorated with stable outer carbon interphase and inner interpenetrated Si@C channel for enhanced lithium storage. *Carbon N Y* 149:664–671

- Zhu L, Chen Y, Wu C, Chu R, Zhang J, Jiang H, Zeng Y, Zhang Y, Guo H (2020) Double-carbon protected silicon anode for high performance lithium-ion batteries. *J Alloys Compd* 812:151848
- Zuo X, Zhu J, Müller- P, Cheng YJ (2017) Silicon based lithium-ion battery anodes: a chronicle perspective review. *Nano Energy* 31:113–143
- Zuo X, Wang X, Xia Y, Yin S, Ji Q, Yang Z, Wang M, Zheng X, Qiu B, Liu Z, Zhu J, Müller- P, Cheng Y (2019) Silicon/carbon lithium-ion battery anode with 3D hierarchical macro-/mesoporous silicon network: self-templating synthesis via magnesiothermic reduction of silica/carbon composite. *J Power Sources* 412(October 2018):93–104

The Renaissance of High-Capacity Cathode Materials for Lithium Ion Cells



M. Akhilash, P. S. Salini, Bibin John, and T. D. Mercy

1 Introduction

The development of improved battery technology is critical owing to the ever growing energy demand for various applications. Scientifically, a battery is a device that can convert chemical energy into electrical energy by electrochemical redox reactions (Ozawa 2009). Among the different types of cells available, Li-ion cells stand as a forerunner and market leader owing to their intriguing electrochemical properties (Fig. 1) (Tarascon and Armand 2001). Li-ion cells have high working voltage, high energy density, long cycle life and low self-discharge rate (Goodenough and Park 2013; Anoopkumar et al. 2020; Salini et al. 2020; John et al. 2018).

A typical Li-ion cell comprises cathode, anode, electrolyte and separator. Conventional cathode materials used in Li-ion cells are layered LiCoO_2 and $\text{LiMn}_{1/3}\text{Ni}_{1/3}\text{Co}_{1/3}\text{O}_2$, olivine LiFePO_4 , and spinel LiMn_2O_4 . The commonly used anode materials are graphitic and non-graphitic carbon. Lithium salt dissolved in organic solvents is used as electrolyte and polyolefin membranes are used as separator. The working of Li-ion cells is depicted in Fig. 2 (Nishi 2001). During charging of the cell, cathode undergoes oxidation releasing Li^+ and e^- . Li^+ moves towards the anode through the electrolyte while the electrons move through the external circuit towards the anode and Li^+ ions are intercalated in the graphite layers. The reverse process occurs during discharging. The reaction of LiCoO_2 as cathode and graphite as anode during the operation of a Li-ion cell is depicted in Scheme 1.

Among the different components, cathode materials play a decisive role in the performance of Li-ion cells. Considerable efforts have been made to develop new cathode materials with higher voltage and specific capacities. In this chapter, we present recent developments in the deployment of different cathodes for Li-ion

M. Akhilash · P. S. Salini · B. John (✉) · T. D. Mercy
Energy Systems Division, PCM Entity, Vikram Sarabhai Space Centre,
Thiruvananthapuram 695022, Kerala, India
e-mail: bbjohn@gmail.com

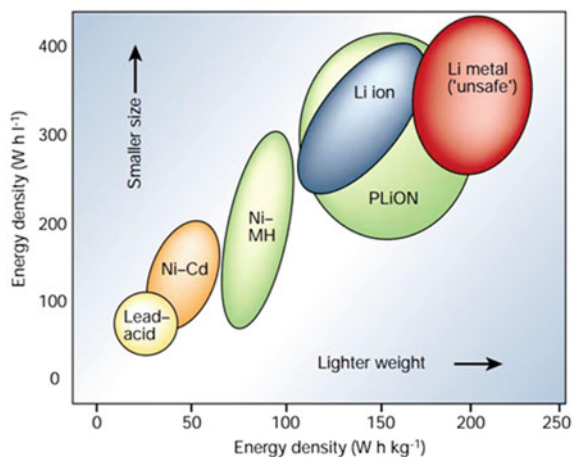


Fig. 1 Comparison of various battery technologies (Reprinted with permission from Tarascon and Armand (2001), copyright (2001) © Springer Nature)

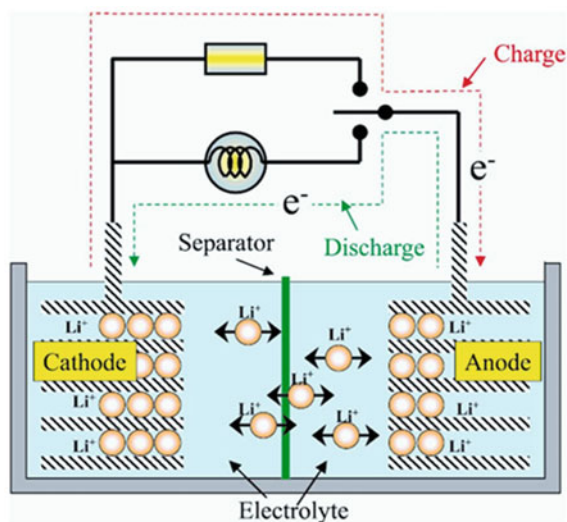
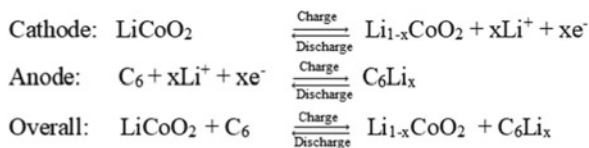


Fig. 2 Schematic illustration of working of a Li-ion cell (Reprinted with permission from Nishi (2001), Copyright (2001) © John Wiley & Sons, Inc.)

Scheme 1 Reactions that take place during charging and discharging of a Li-ion cell



cells with special thrust on the structure, significance of transition metals, doping of different metal ions and morphology of cathode materials that affect the performance of Li-ion cells.

2 Requirements of Cathode Materials for Li-Ion Cells

The parameters which determine the performance of Li-ion cells include: (1) specific energy: the product of average working voltage and specific capacity and (2) cycle life which is affected by the structural stability and electrode–electrolyte interface. The following aspects should be taken into account in the design of cathode materials for Li-ion cells (Whittingham 2004).

- The material should contain readily reducible/oxidizable ion.
- Insertion/extraction of the mobile guest species must be reversible.
- The material should react with Li^+ with a high reaction free energy for obtaining high cell voltage and high energy density.
- It should be electronically conducting for allowing the addition or removal of electrons during the entire electrochemical process.
- The material should not undergo much structural change during the electrochemical reaction.
- Morphology of the material: Small particles increase Li^+ diffusion and can enhance specific capacity and rate capability of insertion materials.
- The material should be insoluble in the electrolyte to eliminate self-discharge.
- Low cost and environment benign materials are preferred.

3 Conventional Cathode Materials for Li-Ion Cells

Tremendous research activities have been conducted in recent years for the deployment of various cathode materials for Li-ion cells. In the initial phase of lithium cells, metal chalcogenides (e.g. TiS_2 , MoS_2 etc.) and metal oxides (e.g. MnO_2 , V_2O_5 etc.) were used as the cathode that paved the way for the development of commercial Li-ion cells (Dan et al. 1995). Afterwards, the main centre of attention of research of cathode materials has been shifted to a group of structurally variant materials such as LiCoO_2 with layered hexagonal structure (Mizushima et al. 1980), spinel LiMn_2O_4 (Thackeray et al. 1983, 1984), olivine LiFePO_4 and their derivatives (Padhi et al. 1997a). Among the aforementioned groups, layered materials are used as cathode for high-energy Li-ion cells (Peres et al. 1999; Ohzuku and Makimura 2001), whereas spinel oxides and olivines are used in high-power systems (Tarascon et al. 1994; Zaghib et al. 2013). Figure 3 illustrates the working potential and specific capacity of various materials used in Li-ion cells (Tarascon and Armand 2001). Materials with a potential higher than 3 V versus Li^+/Li can be effectively employed as cathode material

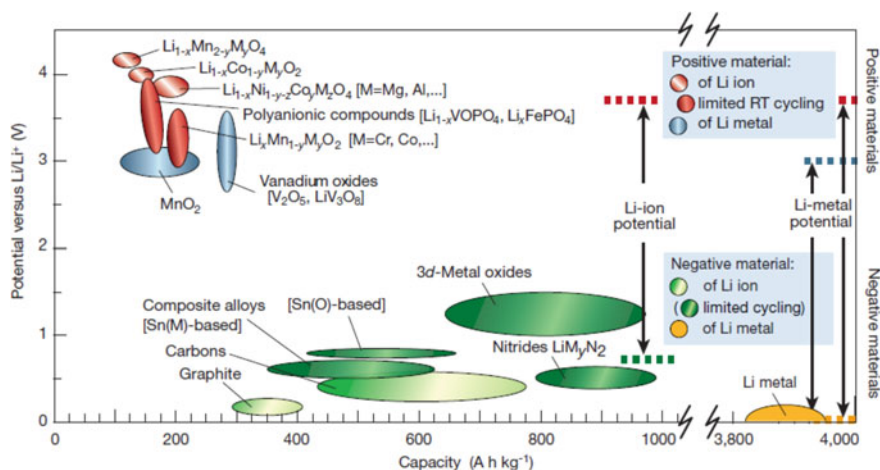


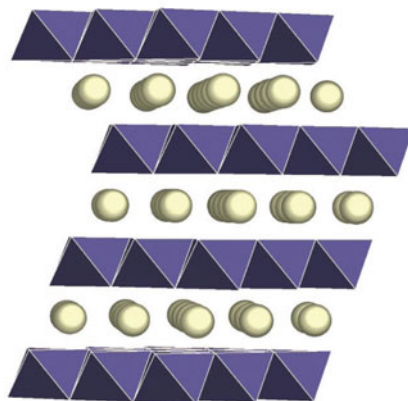
Fig. 3 Voltage versus capacity for various electrode materials of Li-ion cells (Reprinted with permission from Tarascon and Armand (2001), copyright (2001) © Springer Nature)

in Li-ion cells. The following section gives a brief description of the conventional cathode materials used in Li-ion cells.

3.1 Layered Transition Metal Oxide Cathodes

Lithium cobalt oxide, LiCoO_2 (LCO): The most commonly used cathodes in Li-ion cells is layered metal oxides, LiMO_2 ($M =$ Transition metals such as Co, Ni and Mn). Here, Li^+ and M ion occupy the alternate (111) planes of the rock salt structure (Shaju et al. 2002). Among the different layered transition metal (TM) oxides, LCO has been the most commonly used in commercial Li-ion cells. The crystal structure of LCO resembles layered $\alpha\text{-NaFeO}_2$ structure where oxygen is in a cubic close-packed arrangement. LCO unit cell consists of three CoO_2 layers with cubic close-packed oxygen array of ...ABCABC... along the c axis, and the Li^+ ions and M ions reside in the octahedral interstitial sites between them (Fig. 4) (Shao-Horn et al. 2003). The $\text{Co}^{3+/4+}$ redox couple offers a relatively increased cell voltage of ~ 4 V versus Li with a theoretical specific capacity of 274 mAh g^{-1} . LiCoO_2 can be synthesized by simple solid state reactions (Delmas et al. 1980; Ozawa 1994). LiCoO_2 showed a practical specific capacity of 140 mAh g^{-1} , that is half of its theoretical specific capacity owing to the serious phase transition from hexagonal to monoclinic phase and Co dissolution (at >4.2 V) into the electrolyte. In order to alleviate the aforementioned issues, substitution of metals such as Mg (Ven et al. 1998; Tukamoto and West 1997; Levasseur et al. 2002), Al (Ceder et al. 1998; Jang et al. 1999; Huang et al. 1999; Yoon et al. 2000; Myung et al. 2001; Amdouni et al. 2003), Fe (Alcantara et al. 1999; Kobayashi et al. 2000; Holzapfel et al. 2001), Ni (Delmas and Saadoun

Fig. 4 Layered structure of LiCoO_2 (Reprinted with permission from Shao-Horn et al. (2003), Copyright (2003) © Springer Nature)



1992; Julien et al. 2000; Ohzuku and Ueda 1997; Cho et al. 1999, 2000; Delmas et al. 1999; Madhavi et al. 2001; Gummow and Thackeray 1992), Cr (Madhavi et al. 2002), Mn (Stoyanova et al. 1994; Armstrong et al. 1999) and Li (Lavassuer et al. 2000; Imanishi et al. 2001a, b) for Co has been investigated. The main drawbacks of LiCoO_2 include toxicity and higher cost of cobalt; accelerating research to find appropriate alternatives to LiCoO_2 .

$\text{LiNi}_{0.8}\text{Co}_{0.15}\text{Al}_{0.05}\text{O}_2$ (NCA): Over the past two decades, NCA has been the main focus of interest as a cathode material and have been successfully adopted in electric vehicles launched by Tesla Motors (<https://www.tesla.com>). NCA has a theoretical specific capacity of 279 mAh g^{-1} . Experimentally, NCA has exhibited a specific capacity of $\sim 199 \text{ mAh g}^{-1}$ (which is higher compared to other conventional cathode materials) and an average voltage of 3.7 V (Martha et al. 2011).

Layered lithium nickel cobalt manganese oxide (NCM): Layered $\text{LiNi}_x\text{Co}_y\text{Mn}_z\text{O}_2$ (NCM, $x + y + z = 1$) is considered as a promising cathode for large-capacity cells due to its higher specific capacity, improved thermal stability and low cost compared to normal layered materials (YiDi et al. 2015). NCM is a solid solution of ternary mixed metal oxides LiCoO_2 , LiNiO_2 and LiMnO_2 that exist in a single phase with layered structure providing a high theoretical capacity ($\sim 275 \text{ mAh g}^{-1}$) (Jung et al. 2014). The predominant oxidation states of Ni, Co and Mn in NCM are +2, +3 and +4 respectively. The superior electrochemical performance is ascribed to Ni, while at high potentials, Co plays active role. Manganese does not take part in the redox reaction and remains electrochemically inactive, stabilizing the crystal structure (Kim and Chung 2004; Gu et al. 2011). NCM showed a sloped voltage profile with high specific capacity and energy density at higher cut-off voltage. Furthermore, high voltage is desirable to attain complete extraction of lithium that can initiate electrolyte oxidation thereby diminishing the cycling stability (Buchberger et al. 2015; Metzger et al. 2016; Gallus et al. 2014; Zheng et al. 2012; Lu et al. 2009; Andersson et al. 2002; Wandt et al. 2016). When the Ni content is low as in NCM 111, the amount of lithium that can be extracted is less resulting in lower capacity (Whittingham 2004) whereas more lithium can be

taken from the structure of Ni-rich NCMs (NCM622 and NCM811) and became the focus of research recently (Noh et al. 2013).

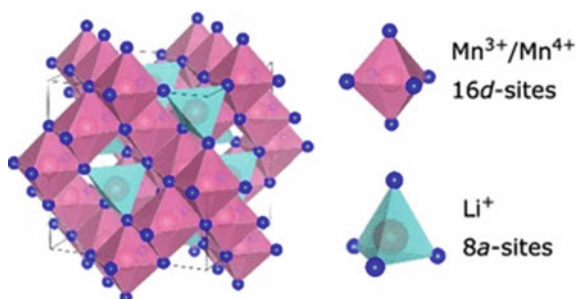
3.2 Spinel Transition Metal Oxide Cathodes

LiMn_2O_4 is a representative example of spinel cathode materials. The advantages of LiMn_2O_4 include lower cost, higher rate capability and improved thermal stability compared to LiCoO_2 . This material belongs to the space group of $\text{Fd}\bar{3}\text{m}$ where Li^+ ions and $\text{Mn}^{3+/4+}$ ions reside in the 8a tetrahedral sites and the 16d octahedral sites with oxygen based cubic close-packed array while leaving the other sites empty as in Fig. 5 (Sun et al. 2018). In this structure, MnO_6 octahedra shares edges through Mn–Mn interaction to build a rigid three-dimensional framework, that provides good electrical conductivity and Li^+ mobility resulting in high rate capability. However, at elevated temperatures, spinel LiMn_2O_4 suffers from severe capacity fade and provides a lower capacity of 120 mAh g^{-1} (Jang et al. 1996; Thackeray et al. 1998). Furthermore, LiMn_2O_4 based cells tend to self-discharge at elevated temperature and Mn dissolution into the electrolyte is another serious issue (Jang et al. 1996; Inoue and Sano 1998). Thus, surface modifications and doping of metal ions were employed to increase the structural stability and electrochemical performance of LiMn_2O_4 cathode.

3.3 Olivine Cathode Materials

Olivine type cathodes like LiFePO_4 are promising candidates owing to the abundance, low toxicity, long cycle life, and outstanding thermal stability. LiFePO_4 crystallizes in the space group of P_{nma} where oxygen atoms forms a distorted, hexagonal close-packed array and phosphorus atoms and metal ions occupy tetrahedral sites and octahedral sites respectively and one-dimensional chains of Li^+ forms along the (010) direction (Padhi et al. 1997a). The unit cell consists of FeO_6 octahedra and

Fig. 5 Crystalline structure of spinel LiMn_2O_4 (Reprinted with permission from Sun et al. (2018), copyright (2018) © Springer Nature)



PO₄ tetrahedra (Padhi et al. 1997b; Huang et al. 2001). Upon elimination of Li⁺, the generated FePO₄ phase maintains essentially similar structure as LiFePO₄ (LiFePO₄ → FePO₄ + Li⁺ + e⁻). Consequently, a flat voltage curve is observed at ~3.4 V owing to the formation of two phase, resulting in a theoretical capacity of 170 mAh g⁻¹. (PO₄)³⁻ polyanionic cluster contains strong P–O bonds that further lead to high thermal stability. On the other hand, the insulating nature of (PO₄)³⁻ groups and localized Fe^{2+/3+} couple and the one-dimensional Li⁺ diffusion channel in LiFePO₄ leads to poor electronic conductivity (10⁻⁹ S cm⁻¹) and poor Li⁺ ion conductivity at room temperature (Li et al. 2009; Wang et al. 2005). To mitigate these drawbacks, particle size reduction and coating with conducting agents are reported to be quite effective. Decreasing the particle size offers shorter lengths for Li⁺ diffusion and gives additional electrolyte/electrode interface for Li⁺ intercalation and deintercalation (Chang et al. 2009; Sun et al. 2009; Satyavani et al. 2016).

The aforementioned cathode materials are essentially lithiated TM oxides/phosphates where Li⁺ ions are deintercalated and intercalated with charge compensated by the TM redox reactions. Consequently, the specific capacity of these cathode materials is determined by the number of Li⁺ that can participate in the intercalation/deintercalation process. In that respect, lithium rich materials find considerable significance due to the availability of more number of lithium ions.

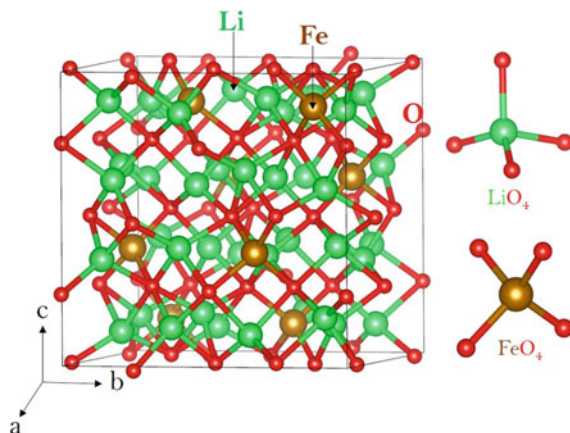
4 Lithium Rich Cathode Materials

As part of the attempts to improve the specific capacity, a plethora of cathodes have been developed in the past few years. These materials are capable of providing large amount of reversible Li⁺. The various lithium rich high capacity cathode materials are discussed in the subsequent sections.

4.1 Li₅FeO₄

Li₅FeO₄ exhibits low cost, good electrochemical stability and non-toxicity compared with LiCoO₂ and LiNiO₂. “Li-rich” antifluorite Li₅FeO₄ provides significant quantity of Li⁺ ions and is a potential material with improved electrochemical performance. Theoretically four Li⁺ ions can be removed per formula unit, in the voltage range of 3.5–4.5 V, thereby exhibiting a capacity of about 700 mAh g⁻¹ (Hirano et al. 2005; Narukawa et al. 1999; Johnson et al. 2010; Okumura et al. 2014; Park et al. 2014). Here, the extraction of Li⁺ ions is accompanied by oxygen release generating Li₂O and Fe₂O₃ rich residual product (Johnson et al. 2010). Li₅FeO₄ exists as Li₂O–Fe₂O₃ system resembling anti-fluorite structure where two among the eight cation sites are vacant. The structure constitutes crystallographic orthorhombic symmetry with space group of *Pbca* where Fe³⁺ ion substitutes three Li⁺ ions in Li₂O cubic primitive cell. Fe³⁺ ions occupy the tetrahedral voids in a close-packed array of O²⁻

Fig. 6 Crystal structure of Li_5FeO_4 (space group $Pbca$) (Kuganathan et al. 2018a)



ions, which are isolated by adjacent LiO_4 tetrahedra and vacancies as shown in Fig. 6 (Kuganathan et al. 2018a).

Hirano et al. studied the electrochemical reaction of $\text{Li}/\text{Li}_5\text{FeO}_4$ cell by XRD and Mossbauer measurements and found that during charging–discharging process, a maximum of 1.2 equivalent lithium take part in electrochemical process resulting in a capacity of 200 mAh g^{-1} in the voltage window 2–4 V. During first charge, the anti-fluorite type structure changes to an amorphous like phase and the efficiency become close to 100% after the fifth cycle (Hirano et al. 2005). A high temperature solid state method for the synthesis of Li_5FeO_4 based cathode was adopted by Liang et al. where they obtained a single phased material with a high initial specific capacity. The first cycle charge and discharge capacities were 584.5 and 210.8 mAh g^{-1} respectively (Liang et al. 2013).

Various synchrotron-radiation analysis techniques were used by Okumura et al. to analyse the bulk and surface structural changes that occur in Li_5FeO_4 . The studies showed that during first charging, a pseudo-cubic lithium iron oxide (PC-LFO) phase of $\text{Li}_\alpha\text{Fe}^{(4-\alpha)}\text{O}_2$ is formed rather than the decomposition of pristine Li_5FeO_4 . There is a non-linear change in the relative ratio of the PC-LFO phase with the charging depth. Simultaneously, the surface compound such as Li_2O covers the PC-LFO phase which played a key role in improving the electrochemical reaction (Okumura et al. 2014).

Metal doping has been explored in Li_5FeO_4 to improve the electrochemical performance. The effect of cobalt doping in Li_5FeO_4 was investigated by Imanishi et al. where they observed a phase transition as the lithium extraction progresses during charging reaction. A complete loss of anti-fluorite structure was observed when 1.5 equivalent lithium was de-intercalated from the structure, while no such phenomenon was observed in the cobalt doped samples. Cobalt doping preserves the original lattice and improved the cycling stability and 2.1 equivalents of Li^+ can be extracted from the cobalt doped sample. 1.3 equivalents of Li^+ are reversibly extracted from the Co doped compound ($\text{Li}_{5.6}\text{Fe}_{0.4}\text{Co}_{0.6}\text{O}_4$) which corresponds to a specific capacity

of 220 mAh g⁻¹. Evidences from Mossbauer spectra revealed that electrons from oxygen atom also play an important role other than iron (Imanishi et al. 2005).

Besides metal doping, carbon incorporation is studied as another method for enhancing the performance. Ding et al. prepared Li₅Fe_{1-x}Mn_xO₄/carbon nanotube (CNTs) composite cathode. The incorporation of CNTs into the precursor improves the conductivity and influence the particle size significantly. The Mn content influences the electrochemical performance of cathode which is evident from the electrochemical impedance spectroscopy (EIS) and charge–discharge measurements. Nyquist plots of EIS proved that CNTs-incorporated Li₅Fe_{0.9}Mn_{0.1}O₄ having 9 wt% CNTs displayed the best charge–discharge performance (Ding et al. 2011).

4.2 Li₆CoO₄

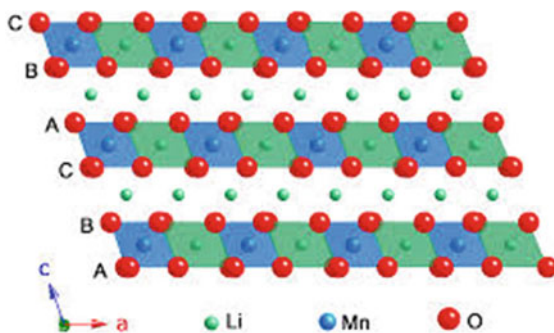
Li₆CoO₄, having anti-fluorite structure, is an appealing candidate owing to the high theoretical capacity (>900 mAh g⁻¹) (Noh and Cho 2012), 4 mol of Li⁺ ions can be electrochemically extracted from Li₆CoO₄ up to a cut-off voltage of 4.3 V versus Li⁺/Li. Compared to other materials like Li₂MoO₃ and Li₅FeO₄ that suffer from electrolyte decomposition at high voltage (>4.7 V versus Li⁺/Li), Li₆CoO₄ efficiently prevents unwanted side reactions during high voltage operation >4.3 V versus Li⁺/Li (Park et al. 2014, 2011; Thackeray et al. 2013). Narukawa et al. synthesized Li₆CoO₄ by solid state method and only one equivalent Li was deintercalated from it. The performance of Li₆CoO₄ based cathode versus Li⁺/Li was comparatively good at 0 ≤ x ≤ 0.75 and the large hysteresis in charge and discharge curves demonstrated a different mechanism for Li de-intercalation and intercalation (Narukawa et al. 1999). Even though, a large number of Li⁺ can be removed from Li₆CoO₄, its high irreversibility prevents this material from practical use in Li-ion cells.

4.3 Lithium Manganese Oxides

Lithium manganese oxides, Li–Mn–O based systems, have gained significant attention owing to their high specific energy, low cost, and low toxicity. These materials including LiMnO₂, LiMn₂O₄, Li₂MnO₃, Li₂Mn₄O₉, etc. get benefited from the possibility of exploiting multiple oxidation states for Mn within the cathode that help to attain high energy densities. Albeit layered LiMnO₂ is a promising active material for Li-ion cells, difficulty in synthesis and structural instability prevents this material from advanced applications (Kim et al. 2004).

Li₂MnO₃: Among the Mn based cathode materials, Li₂MnO₃ has received wide attention mainly due to two reasons; (1) Li₂MnO₃ is endowed with an extraordinary theoretical capacity (460 mAh g⁻¹) (Okamoto 2012) which is remarkably higher than the currently used cathodes in Li-ion cells like LiCoO₂ or LiNi_{1/3}Co_{1/3}Mn_{1/3}O₂ (270 mAh g⁻¹), LiMn₂O₄ (148 mAh g⁻¹), and LiFePO₄ (170 mAh g⁻¹), (2) Li₂MnO₃

Fig. 7 Close-packed oxygen layers in O3 structure of Li_2MnO_3 (C2/m) (Reprinted with permission from Rana et al. (2013), Copyright (2013) © WILEY-VCH Verlag GmbH & Co. KGaA, Weinheim)



has an O^{3-} layered structure in which close-packed array of oxygen are stacked in ...ABCABC... pattern (Fig. 7) (Rana et al. 2013). Li_2MnO_3 can be denoted as $\text{Li}[\text{Li}_{1/3}\text{Mn}_{2/3}]\text{O}_2$. Li_2MnO_3 belongs to C2/m space group symmetry and is an electrochemically inactive material owing to the presence of Mn(IV) (Thackeray 1997; Paik et al. 2002; Robertson and Bruce 2002). However, it can be converted into an electrochemically active material at above 4.5 V by chemical or electrochemical means by taking out Li and oxygen from the structure (Singh et al. 2012; Croy et al. 2011).

In order to utilise the entire Li^+ in Li_2MnO_3 , a clear understanding of the mechanism of lithiation/delithiation process is highly essential. Li^+ and H^+ exchange (Robertson and Bruce 2003; Armstrong et al. 2005) and instantaneous removal of Li and O (Thackeray 1997; Armstrong et al. 2006) are the two widely accepted mechanisms for the delithiation process in Li_2MnO_3 , but which one play the major role is still under discussion. The activation of Li_2MnO_3 by the extraction of lithium and oxygen by chemical treatments with HNO_3 and H_2SO_4 has been reported. Nevertheless, during the electrochemical process, a phase change occurs where the new spinel structure is formed. Both activation process results in the rearrangement of ion vacancies in the structure and allow the reversible intercalation of lithium (Thackeray 1997). Kalyani et al. for the first time developed Li_2MnO_3 by simple solid state method. The charge/discharge behaviour of the cells displayed improved performance and good capacity retention is observed for 15 cycles (Kalyani et al. 1999). Robertson et al. argued that continuous cycling led to the structural deformation of Li_2MnO_3 to LiMn_2O_4 (Robertson and Bruce 2003). Rana and his co-workers studied the structural changes in Li_2MnO_3 by X-ray absorption spectroscopy and proved that the participation of oxygen anions in redox processes and $\text{Li}^+ - \text{H}^+$ exchange are the crucial factors that affects the electrochemical performance of Li_2MnO_3 . However, during cycling structural degradation due to repetitive shearing of oxygen layers weakens the electrochemical performance of Li_2MnO_3 (Rana et al. 2013). Wang et al. reported that at a voltage >4.5 V, Li^+ is extracted from Li_2MnO_3 in the form of Li_2O leaving behind MnO_2 . During discharging, Li^+ is inserted back to MnO_2 and forms LiMnO_2 which is an active material. The usage of Li_2MnO_3 as cathode in

Li-ion cells is limited due to its poor cyclability and low first cycle efficiency (Wang et al. 2013a).

Li and Lei have synthesized nano sized Li_2MnO_3 through one step solid state reaction. The material exhibited very poor charge/discharge capacity in the first cycle. But there is a drastic increase in the discharge capacity up to 153.7 mAh/g at 39th cycle. These changes can be ascribed to manganese dissolution and the structural change from layered to the spinel (Li and Lei 2017). It is reported that nano sized Li_2MnO_3 exhibits a very high discharge capacity of $\geq 250 \text{ mAh g}^{-1}$ when activated at high potential while sub-micrometer Li_2MnO_3 shows poor electrochemical performance. The effect of manganese source on electrochemical performance of Fe- and Ni-substituted Li_2MnO_3 cathode material was studied by Tabuchi and his co-workers. They chose two manganese salts such as KMnO_4 and MnCl_2 as the manganese source and adopted the same procedure for the synthesis of the cathode material. A better electrochemical performance was obtained for the sample prepared from KMnO_4 which is due to the high degree of homogeneous distribution of Fe and Mn ions (Tabuchi et al. 2015).

Different methods are adopted by researchers to increase the capacity and the cyclability of Li_2MnO_3 . Park et al. investigated the impact of calcination temperature on the electrochemical behaviour of Li_2MnO_3 prepared by solid state method. The surface morphology and oxygen content and the electrochemical performance varied according to the calcination temperatures. The specific capacity of Li_2MnO_3 got reduced with increase in calcination temperature. The synthesized compound mainly contains Li_2MnO_3 , sub- LiMnO_2 , and sub- LiMn_2O_4 phases, as confirmed by XRD and TEM. During lithium insertion-extraction process, there is a structural transformation of Li_2MnO_3 between layered LiMnO_2 and cubic LiMn_2O_4 phases. They concluded that the lower capacity of $\text{Li}/\text{Li}_2\text{MnO}_3$ might be due to the presence of the impurity phase such as LiMnO_2 and LiMn_2O_4 (Park et al. 2007). Dong et al. introduced a new strategy for enhancing the cycle life of Li_2MnO_3 by partially substituting lithium by sodium. They followed the conventional solid state method for the preparation and studied the cycle life and rate capability of $\text{Li}_{2-x}\text{Na}_x\text{MnO}_3$ with varying composition ($0 \leq x \leq 0.20$). The studies show that $\text{Li}_{1.90}\text{Na}_{0.10}\text{MnO}_3$ delivers an initial capacity of 181 mAh g^{-1} with capacity retention of 99.3% after 45 cycles at C/10, and 98.6% after 100 cycles at C/2. The good cycling performance is attributed to the decrease in particle size and the charge transfer resistance as well as increased crystallinity and the Li-Ion diffusion coefficient (Dong et al. 2013).

Kim et al. synthesised a highly stable TiO_2 coated Li_2MnO_3 using varying amount of titanium butoxide. Although TiO_2 coated samples showed an initial capacity which is less than the sample without TiO_2 coating, after 100 cycles the TiO_2 coated samples shows a better discharge capacity than the latter. The oxidation of electrolyte and the attack of acidic species caused the electrode/electrolyte interface to degrade which resulted in the deterioration of electrochemical performance. In the case of samples coated with TiO_2 , the cathode-electrolyte interface is more stabilised thus preventing the decomposition of the electrolyte at high voltage (Kim et al. 2016). Zhao et al. successfully synthesized a composite of Li_2MnO_3 (LMO) and reduced

graphene oxide (rGO) and evaluated the effect of reduced graphene on the electrochemical properties. SEM and TEM analysis showed that LMO forms a laminated structure by distributing separately on the rGO which helps to improve electrical contact between LMO and the rGO matrix. Cyclic voltammetry and electrochemical impedance spectroscopy displayed that the charge transfer resistance is reduced in case of LMO/rGO composite when compared with LMO. Due to these reasons LMO/rGO showed an initial capacity of 284.9 mAh g^{-1} with capacity fading of 13.4% after 45 cycles. Even at a higher current density of 8C, the composite cathode delivered a specific capacity of 123.7 mAh g^{-1} (Zhao et al. 2016).

Li_3MnO_4 : Li_3MnO_4 has a wurtzite-type structure and manganese in (V) oxidation state and the structure consists of $[\text{LiO}_4]$ and $[\text{MnO}_4]$ tetrahedron, sharing corners (Yu et al. 2012; Saint et al. 2007). Only a few studies are available for Li_3MnO_4 due to its poor electrochemical performance owing to poor structural stability under cycling and low electronic conductivity. Surace et al. adopted freeze drying route (FDR) to synthesize Li_3MnO_4 and they investigated the structural, morphological and electrochemical properties and compared with the material synthesised by solid state reaction. They could reduce the average particle size (from $10 \mu\text{m}$ to $3.5 \mu\text{m}$) and crystallite size (from 100 nm to around 30 nm) which led to improved capacity and rate capability (Surace et al. 2015). The same research group carried out an analysis on fresh Li_3MnO_4 and the cycled electrodes. Studies confirmed that capacity fading in this material is due to the electrochemical activation of Li_3MnO_4 to amorphous MnO_2 during the first cycle. Amorphization causes structural instability of the material towards lithium insertion or extraction. During discharge, collapse of the structure along with reorganization of the coordination around the Mn ion liberates reactive oxygen species and this created a thick solid electrolyte interphase layer. After the first cycle, the degradation product remains amorphous and this is accountable for the subsequent capacity fall. Also, the low cycle life of the material is due to the amorphous MnO_2 formed during the first cycle (Surace et al. 2016).

Xie et al. demonstrated the effect of vanadium doping on the electrochemical performance of Li_3MnO_4 . No tangible change in crystal phase was observed on increasing the amount of vanadium, while the increased vanadium doping decreases the particle aggregation in $\text{Li}_3\text{Mn}_{1-x}\text{V}_x\text{O}_4$. The $\text{Li}_3\text{Mn}_{0.7}\text{V}_{0.3}\text{O}_4$ electrode showed a higher specific capacity and enhanced rate capability than the other ones. The respective specific capacity of $\text{Li}_3\text{Mn}_{0.7}\text{V}_{0.3}\text{O}_4$ samples was 153 mAh/g at a current density of 7 mA g^{-1} , 117 mAh g^{-1} at a current density of 14 mA g^{-1} and 90 mAh g^{-1} at a current density of 35 mA g^{-1} . Electrochemical Impedance studies inferred that appropriate amount of vanadium doping helps to decrease the resistance due to solid electrolyte interphase and charge transfer, and finally led to improved electrochemical performance of Li_3MnO_4 (Xie et al. 2013).

$\text{Li}_4\text{Mn}_5\text{O}_{12}$: $\text{Li}_4\text{Mn}_5\text{O}_{12}$ is another member of $\text{Li}_{1+x}\text{Mn}_{2-x}\text{O}_4$ family of spinel Lithium Manganese Oxide (LMO), with manganese in a tetravalent state. In spinel notation it is represented as $\text{Li}[\text{Mn}_{1.67}\text{Li}_{0.33}]\text{O}_4$ (Thackeray et al. 1996, 1987; Ivanova et al. 2013, 2011; Takada et al. 1997; Fu et al. 2014). $\text{Li}_4\text{Mn}_5\text{O}_{12}$ is a potential cathode material for Li-ion cells owing to its high theoretical capacity, three dimensional Li^+ transport pathway, good reversibility and environmental friendliness (Thackeray

et al. 1996, 1987). Generally, $\text{Li}_{1+x}\text{Mn}_{2-x}\text{O}_4$ spinel is classified as either a 3 or 4 V versus Li^+/Li (Doeff and Batteries 2013; Daniel and Besenhard 2011). But $\text{Li}_4\text{Mn}_5\text{O}_{12}$ operates only at 3 V because manganese is in tetravalent state. Hence Li^+ cannot be extracted from the structure. The tetravalent Mn stabilizes the cubic structure during lithiation over a wider range when compared to LiMn_2O_4 in the 3 V discharge range (Padhi et al. 1997a; Fu et al. 2014; Cao et al. 2013). $\text{Li}_4\text{Mn}_5\text{O}_{12}$ with porous nano/micro structure exhibits a specific capacity of 161 mAh/g in the 3 V range with good cycling stability and intriguing rate capability (Fu et al. 2014). Jiang et al. prepared $\text{Li}_4\text{Mn}_5\text{O}_{12}$ nanocrystallites through spray-drying assisted solid state reaction (Jiang et al. 2010). Tian et al. synthesised single crystalline $\text{Li}_4\text{Mn}_5\text{O}_{12}$ with the aid of nanowires by a molten salt route (Tian et al. 2007). $\text{Li}_4\text{Mn}_5\text{O}_{12}$ synthesized by ball milling technique exhibited a capacity of 158 mAh g^{-1} (Julien and Zaghbi 2004).

The main drawback of $\text{Li}_4\text{Mn}_5\text{O}_{12}$ is the difficulty to obtain it in stoichiometric ratio, because it may disproportionate into LiMn_2O_4 and LiMnO_2 at high temperature leading to its poor electrochemical performance. To solve this issue, Choi et al. used F^- substitution in O^- site with different concentrations, which suppresses the disproportionation problem and obtained good capacity for $\text{Li}_4\text{Mn}_5\text{O}_{11.85}\text{F}_{0.1}$ material (Choi and Manthiram 2007). Another disadvantage of $\text{Li}_4\text{Mn}_5\text{O}_{12}$ is its low working potential of ~ 3 V. By substituting Mn partially with $\text{Cr}^{3+/4+}$, $\text{Co}^{3+/4+}$, etc., the discharge plateau can be enhanced. Robertson et al. demonstrated the improved structural stability as well as electrochemical performance of $\text{Li}_4\text{Mn}_5\text{O}_{12}$ by Co doping in Li and Mn sites with different concentrations (Robertson et al. 2001). Le et al. used solid solution method for synthesizing Ti substituted $\text{Li}_4\text{Mn}_5\text{O}_{12}$ and investigated the structural, magnetic and electrochemical behaviour of the material (Le et al. 2011). Zinc substituted $\text{Li}_4\text{Mn}_5\text{O}_{12}$ was examined by Sharmila et al. and they studied the impedance and conductivity behaviour where improved conductivity was observed for 0.1 mol Zn doped $\text{Li}_4\text{Mn}_5\text{O}_{12}$ (Sharmila et al. 2014). Xie et al. prepared Ni and Fe dual doped $\text{Li}_4\text{Mn}_{5-x-y}\text{Ni}_x\text{Fe}_y\text{O}_{12}$ which showed a specific capacity of 133 mAh g^{-1} at 25 mA g^{-1} after 100 cycles and exhibits a high-voltage performance. Dual-cations doping effectively improves both the reversible specific capacity and operating voltage of $\text{Li}_4\text{Mn}_5\text{O}_{12}$ with excellent cycling stability (Xie et al. 2015).

$\text{Li}_4\text{Mn}_2\text{O}_5$: Among the lithium-manganese rich cathode material family, $\text{Li}_4\text{Mn}_2\text{O}_5$ exhibits the highest discharge capacity. Recently, Freire et al. reported this Li-excess $\text{Li}_4\text{Mn}_2\text{O}_5$ material with disordered rock salt-type structure having a specific capacity of 355 mAh g^{-1} . In subsequent cycles, this material retains its structure and exhibits a specific capacity of ~ 250 mAh g^{-1} . They synthesized the material by direct mechanochemical method at room temperature. Based on magnetic susceptibility measurements, Freire and his co-workers proposed a complex delithiation mechanism, which consists of the possible redox couples, $\text{Mn}^{3+}/\text{Mn}^{4+}$, O^{2-}/O^- , and $\text{Mn}^{4+}/\text{Mn}^{5+}$. According to the magnetic measurements, the electrochemical activity of $\text{Li}_4\text{Mn}_2\text{O}_5$ is not only due to the $\text{Mn}^{3+}/\text{Mn}^{4+}$ and O^{2-}/O^- redox couples, but also to the $\text{Mn}^{4+}/\text{Mn}^{5+}$ redox couple (Freire et al. 2016). Using first-principle density functional theory (DFT) calculations, Yao et al. examined the electrochemical delithiation

process of $\text{Li}_4\text{Mn}_2\text{O}_5$ that occurs through three-step reaction pathway, (i) initial Mn oxidation, $\text{Mn}^{3+} \rightarrow \text{Mn}^{4+}$ ($\text{Li}_x\text{Mn}_2\text{O}_5$, $4 > x > 2$); (ii) anionic oxidation $\text{O}^{2-} \rightarrow \text{O}^{1-}$ ($2 > x > 1$) and (iii) Mn oxidation, $\text{Mn}^{4+} \rightarrow \text{Mn}^{5+}$ ($1 > x > 0$). The final step is accompanied by Mn migration from octahedral site to adjacent tetrahedral site. Further, the studies also suggested that suitable dopants such as V and Cr can improve the cyclability of the material (Yao et al. 2018).

4.4 Integrated Li and Mn Rich Layered Oxides

Integrated Li and Mn-rich layered oxide cathodes are getting increased attention owing to their high specific capacities (up to ca. 280 mAh g^{-1}) and high working potential (2.0–4.8 V) (Thackeray et al. 2007; Yu and Zhou 2013; Kang et al. 2007; Lu et al. 2001; Johnson et al. 2004; Akhilash et al. 2021a, b). Li-, Mn-rich cathodes are represented either as $x\text{Li}_2\text{MnO}_3 \cdot (1-x)\text{LiMO}_2$ with the co-existence of Li-rich monoclinic phase (C2/m space group) or $\text{Li}_{1+x}\text{M}_{1-x}\text{O}_2$ (M = Mn, Co, Ni etc.) that denotes the rhombohedral phase (R3m space group) with the ratio of $x/(1-x)$. The second notation clearly shows the excess lithium in the layered cathode. Hence the name Li-rich cathodes (Thackeray et al. 2007). For example, the lithium rich cathode material $\text{Li}_{1.2}\text{Mn}_{0.6}\text{Ni}_{0.2}\text{O}_2$ can be represented as $0.5\text{Li}_2\text{MnO}_3 \cdot 0.5\text{Li} [\text{Mn}_{0.5}\text{Ni}_{0.5}]\text{O}_2$. As shown in Fig. 8 (Yu et al. 2013), lithium rich material comprises two phases, Li_2MnO_3 monoclinic (C2/m) and LiMO_2 rhombohedral (R3m).

The first Li-, Mn-rich cathode material $\text{Li}_{1.09}\text{Mn}_{0.91}\text{O}_2$ was synthesized by Rossouw et al. by chemical leaching from Li_2MnO_3 followed by electrochemical relithiation (Rossouw et al. 1993). Li-, Mn-rich cathode required an activation step by charging to >4.5 V during first cycle to attain high capacities (Kalyani et al. 1999; Lu et al. 2001; Kang et al. 2006; Rossouw and Thackeray 1991). The charge profile measured during the first cycle demonstrated redox centres and Li^+

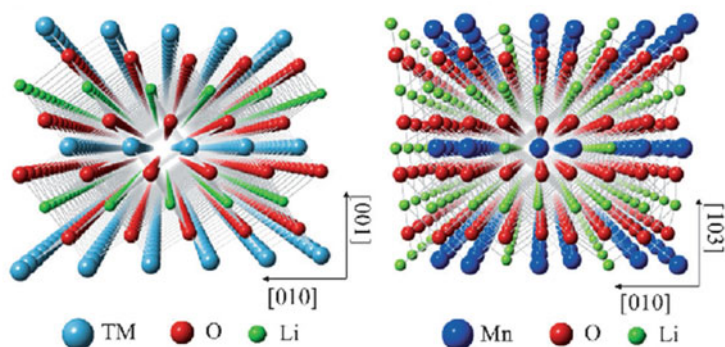


Fig. 8 Simulated view of R-3m LiTMO_2 and C2/m Li_2MnO_3 phases along [100] direction (Reprinted with permission from Yu et al. (2013), copyright (2013) © John Wiley and Sons)

intercalation sites were measured by in situ X-ray-absorption spectroscopy (XAS) and X-ray-diffraction measurements (XRD) respectively. Oxidation of $\text{Ni}^{2+/4+}$ and $\text{Co}^{3+/4+}$ occurs during initial charging similar to $\text{Li}[\text{Ni}_a\text{Co}_b\text{Mn}_c]\text{O}_2$ layered materials. Above 4.5 V, a long activation voltage plateau occurs, corresponding to O_2 evolution, and extraction of Li^+ from the TM-layer. After this lithium extraction, anionic oxidation of O^{2-} takes place at higher potential, accompanied by transition metal ion migration to Li-layer between the O^{2-} slabs. During discharge, Li^+ first enters the transition metal layer, accompanied by the reduction of Ni^{4+} , Co^{4+} and Mn^{4+} , followed by Li^+ insertion into the Li-layer with further Mn^{4+} reduction. In the later charging stages, TM migration into Li-layer causes the large capacity fading in Li, Mn-rich cathodes during cycling (Mohanty et al. 2013; Yu et al. 2014; Erickson et al. 2017).

For the first time, Lithium-manganese-cobalt oxide, $\text{Li}(\text{Co}_{1-x}\text{Li}_{x/3}\text{Mn}_{2x/3})\text{O}_2$ ($0 \leq x \leq 1$), a solid solution between Li_2MnO_3 and LiCoO_2 was prepared by Numata et al. A simple calcination method with an excess of lithium carbonate at 900–1000 °C is used to obtain the solid solution (Numata et al. 1999). The same solid solution containing LiCoO_2 and Li_2MnO_3 was prepared by Sun et al. using spray drying method at 750–900 °C. Redox titration and XPS testing results indicated that Co and Mn were at +3 and +4 respectively. Their studies revealed that the specific capacity decreased with increase in Li_2MnO_3 content. These materials showed an excellent electrochemical cycling performance when charged to 4.5 V (Sun et al. 2006).

Lim et al. synthesized Lithium-manganese rich NMC based cathode material $\text{Li}_2\text{MnO}_3\text{-LiNi}_{1/3}\text{Co}_{1/3}\text{Mn}_{1/3}\text{O}_2\text{-LiNiO}_2$ by co-precipitation method by using metal oxide precursors. Results revealed that when charged in the voltage range of 2–4.6 V, a specific capacity of 248.8 mAh g^{-1} was obtained for $\text{Li}[\text{Li}_{0.20}\text{Ni}_{0.133}\text{Co}_{0.133}\text{Mn}_{0.534}]\text{O}_2$ material (Lim et al. 2009). Wu and Manthiram reported a novel lithium-manganese rich cathode, $\text{Li}[\text{Li}_{(1-x)/3}\text{Mn}_{(2-x)/3}\text{Ni}_{x/3}\text{Co}_{x/3}]\text{O}_2$, which is a solid solution between $(1-x)\text{Li}_2\text{MnO}_3$ and $x\text{LiNi}_{1/3}\text{Mn}_{1/3}\text{Co}_{1/3}\text{O}_2$. Electrochemical evaluation in the voltage window 2–4.8 V at C/20, showed an initial capacity of 227 mAh g^{-1} for $x = 0.7$ and 253 mAh g^{-1} for $x = 0.4$. There is an initial capacity decrease of 63 and 75 mAh g^{-1} for $x = 0.7$ and 0.4, respectively (Wu and Manthiram 2006).

The influence of metal oxide coating and metal ion doping in lithium rich cathode materials has been studied by various researchers. Metal oxide such as Al_2O_3 reduces initial capacity loss to 41 mAh g^{-1} (Wu and Manthiram 2006). Liu and Manthiram used surface coating on $\text{Li}[\text{Li}_{0.2}\text{Mn}_{0.54}\text{Ni}_{0.13}\text{Co}_{0.13}]\text{O}_2$ with 2 wt% Al_2O_3 , 2 wt% RuO_2 and 1 wt% $\text{Al}_2\text{O}_3 + 1$ wt% RuO_2 (Liu and Manthiram 2010). The surface coated materials showed enhanced electrochemical performance, particularly with 1 wt% $\text{Al}_2\text{O}_3 + 1$ wt% RuO_2 , exhibiting a specific capacity of 280 mAh g^{-1} at C/20 with 94.3% capacity retention in 30 cycles. Li et al. used AlF_3 coating, which enhances the coulombic efficiency of $\text{Li}_{1.17}\text{Ni}_{0.25}\text{Mn}_{0.58}\text{O}_2$ from 76.4 to 89.5% (Li et al. 2012). Incorporation of LiFePO_4 into the Li, Mn-rich oxides decreases its irreversible capacity (Gallagher et al. 2011). Yu and Zhou substituted Mn with Ru and observed a reduction in irreversible capacity (Yu and Zhou 2012). Na-stabilized $\text{Li}_{1.2-x}\text{Na}_x[\text{Co}_{0.13}\text{Ni}_{0.13}\text{Mn}_{0.54}]\text{O}_2$ material prepared by He et al. using

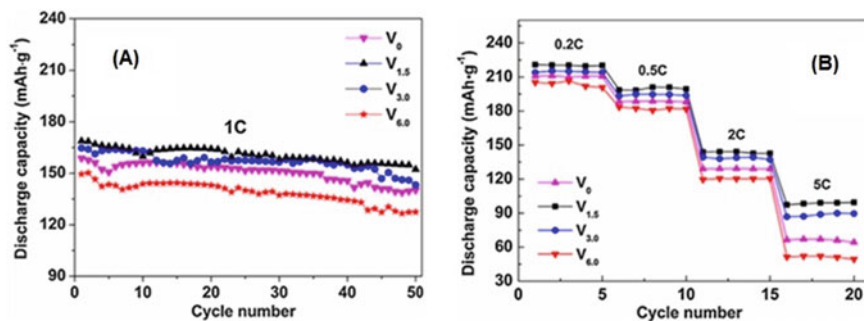


Fig. 9 a Cycling performance and b rate capability of $\text{Li}_{1.2}\text{Mn}_{0.52-x/3}\text{Co}_{0.08-x/3}\text{Ni}_{0.2-x/3}\text{V}_x\text{O}_2$ (Reprinted with permission from Lu et al. (2016), copyright (2016) © Elsevier)

polymer pyrolysis method has delivered a coulombic efficiency of 87% (He et al. 2013). Liao et al. used LiV_2O_5 to reduce the irreversible capacity loss, which acts as both coating and Li-insertion host (Liao et al. 2014). Cao et al. synthesized a porous Li-, Mn-rich layered oxide material which delivered a specific capacity of 245 mAh g^{-1} and coulombic efficiency of 87% (Cao et al. 2015). Zheng et al. synthesised a layered/spinel composite, $0.75\text{Li}_{1.2}\text{Ni}_{0.2}\text{Mn}_{0.6}\text{O}_2 \cdot 0.25\text{LiNi}_{0.5}\text{Mn}_{1.5}\text{O}_4$, which showed a specific capacity of $\sim 135 \text{ mAh g}^{-1}$ at 2000 mA g^{-1} , as compared to 82 mAh g^{-1} for $\text{Li}_{1.2}\text{Ni}_{0.2}\text{Mn}_{0.6}\text{O}_2$ (Zheng et al. 2015). Lu et al. prepared V doped Li-rich $\text{Li}_{1.2}\text{Mn}_{0.52-x/3}\text{Co}_{0.08-x/3}\text{Ni}_{0.2-x/3}\text{V}_x\text{O}_2$ by solid state thermal decomposition method. Minor amount of V doping ($x = 0.015$) expands the inter slab spacing of layered oxide, which promote the lithium-ion diffusion. The V ions in the crystal lattices improved the capacity retention (90.2% after 50 cycles at 1C rate) (Fig. 9a), improved the rate capability; at 5C exhibiting a capacity of 99.0 mAh g^{-1} (Fig. 9b). However, excessive doping leads to poor electrochemical performance (Lu et al. 2016).

Deng et al. reported a layered/spinel hetero structured Li-rich cathode, $\text{Li}_{1.140}\text{Mn}_{0.622}\text{Ni}_{0.114}\text{Co}_{0.124}\text{O}_2$, synthesised by solvothermal method, which exhibited 280 mAh g^{-1} at 1C and 206 mAh g^{-1} at 10C (Deng et al. 2016). Ming et al. studied doping of Nb and F on $\text{Li}_{1.2}\text{Mn}_{0.54}\text{Ni}_{0.13}\text{Co}_{0.13}\text{O}_2$. They synthesized $\text{Li}_{1.2}\text{Mn}_{0.54-x}\text{Nb}_x\text{Co}_{0.13}\text{Ni}_{0.13}\text{O}_{2-6x}\text{F}_{6x}$ ($x = 0, 0.01, 0.03, 0.05$) by the conventional high temperature solid state method. XRD analysis revealed that Nb and F doping increased the interplanar spacing. The replacement of O by highly electronegative F suppressed structural change of Li_2MnO_3 during initial charge process. The addition of Nb in Mn site well controls the migration of transition metal ions during charge-discharge cycling and it also maintains the stability of structure. The Nb^{5+} and F^- co-doping boost the initial coulombic efficiency, discharge capacity and cycling performance and reduce voltage fading (Ming et al. 2018). The cycling performance is shown in Fig. 10.

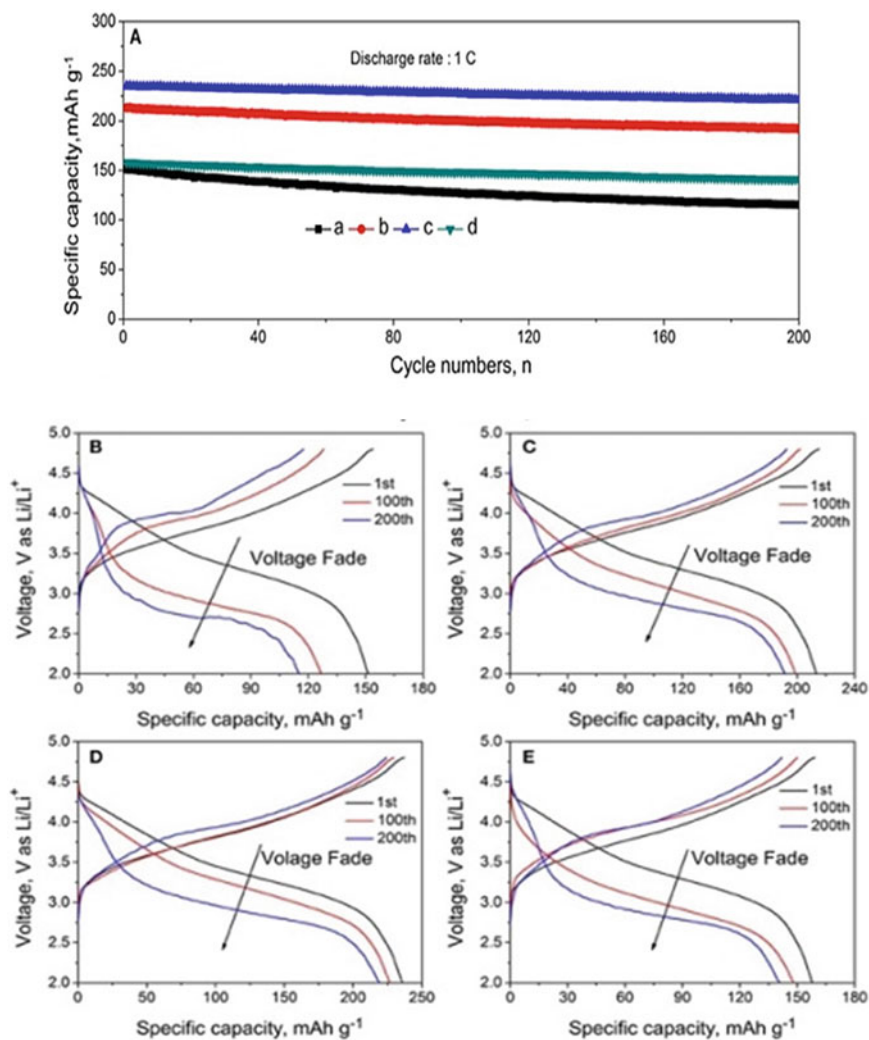


Fig. 10 a Specific capacity versus cycle number and b–e charge–discharge curves of $\text{Li}_{1.2}\text{Mn}_{0.54-x}\text{Nb}_x\text{Co}_{0.13}\text{Ni}_{0.13}\text{O}_{2-6x}\text{F}_{6x}$ ($x = 0, 0.01, 0.03, \text{ and } 0.05$) at 1C between 2.0 and 4.8 V (vs. Li^+/Li) at room temperature (Ming et al. 2018)

Li_2MnO_3 coating on $\text{Li}_{1.2}\text{Mn}_{0.54}\text{Co}_{0.13}\text{Ni}_{0.13}\text{O}_2$ nano/micro hierarchical micro-rods suppresses its voltage decay and provides superior electrochemical performance. Surface-modified $\text{Li}_{1.2}\text{Mn}_{0.54}\text{Co}_{0.13}\text{Ni}_{0.13}\text{O}_2$ micro rods showed improved initial coulombic efficiency (76.4%) and it delivered a high specific capacity of 159.6 mAh g⁻¹ at 10C (Xie et al. 2019). Redel et al. synthesized Li-rich layered oxide ($x\text{Li}_2\text{MnO}_3 \cdot (1-x)\text{LiMn}_{0.5}\text{Ni}_{0.25}\text{Co}_{0.25}\text{O}_2$ or $\text{Li}[\text{Li}_y\text{Mn}_{1-y-2z}\text{Ni}_z\text{Co}_z]\text{O}_2$), which crystallizes within C2/m space group with nanometric spherical morphology.

$\text{Li}[\text{Li}_{0.2}\text{Mn}_{0.6}\text{Ni}_{0.1}\text{Co}_{0.1}]\text{O}_2$ material delivers $\sim 350 \text{ mAh g}^{-1}$ for the first discharge and 250 mAh g^{-1} on subsequent cycles (Redel et al. 2019).

4.5 Li_2RuO_3

Li_2RuO_3 is a promising candidate for Li-ion cells, because it is an electrochemically active material with low capacity fade and high theoretical capacity and also due to its novel anionic redox process ($2\text{O}^{2-} \leftrightarrow (\text{O}_2)^{n-}$) (Sathiya et al. 2013). Its practical voltage plateau is lower than that of LiCoO_2 . Reversible oxygen redox process plays a major role in Li_2RuO_3 , which enhances its capacity. Experimental studies show that, though both lithium can be extracted from this material, only one of them is repeatedly cyclable (Moore et al. 2003; James and Goodenough 1988; Kobayashi et al. 1995).

Li_2RuO_3 has a layered monoclinic structure with space group $C2/c$. (Fig. 11) (Kuganathan et al. 2019). Here, the TM ions reside in the octahedral cage of O atoms and form a planar triangular arrangement and the Li^+ are accommodated between the transition-metal-oxide planes (Kobayashi et al. 1995). Moore et al. investigated the electrochemical performance of Li_2RuO_3 and observed that in the first charging process, there are two working plateaus and provides a specific capacity of $\sim 270 \text{ mAh g}^{-1}$ (Moore et al. 2003). Sathiya et al. studied the electrochemical behaviour of $\text{Li}_2\text{Ru}_{1-y}\text{Mn}_y\text{O}_3$ and reported sustainable reversible capacities more than 220 mAh g^{-1} around 3.6 V versus Li^+/Li (Sathiya et al. 2013). Yao et al. made a novel hybrid Na^+/Li^+ cell using Li_2RuO_3 as a cathode material owing to its distinctive structure accommodating both Li^+ and Na^+ (Yao et al. 2015).

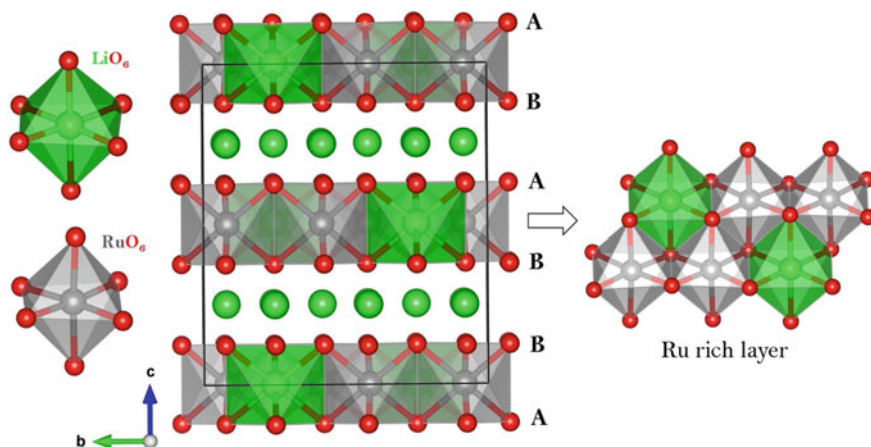


Fig. 11 Crystal structure of Li_2RuO_3 (space group $C2/c$) (Kuganathan et al. 2019)

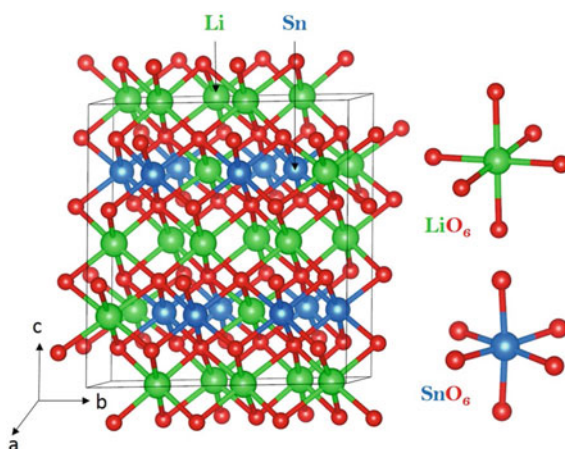
Even though Li_2RuO_3 exhibits large specific capacity and excellent rate capability, it suffers from severe voltage decay and capacity fading upon prolonged cycling. Tarascon and his co-workers proposed a tactic of partially substituting Ru^{4+} by Sn^{4+} to decrease voltage decay and enhance cycling stability (Sathiya et al. 2015). Boron doping has been adopted by Xia's group to enhance electrochemical performance of Li_2RuO_3 and also to control the reversibility of oxygen redox (Li et al. 2017). Arunkumar et al. synthesized over-lithiated $\text{Li}_{2+x}\text{Ru}_{1-x}\text{CoO}_3$ material by aliovalent Co doping in Li_2RuO_3 , at the Ru site which enhances the Li^+ extraction and electrochemical lithium reversibility compared to those associated with pristine Li_2RuO_3 (Arunkumar et al. 2016). Sarkar et al. reported electrochemical performance of Li_2RuO_3 and Li_2IrO_3 and their solid solution $\text{Li}_2\text{Ru}_{1-x}\text{Ir}_x\text{O}_3$ ($0 \leq x \leq 1$). The solid solution of composition $\text{Li}_2\text{Ru}_{0.90}\text{Ir}_{0.10}\text{O}_3$ exhibited an improved cyclic behaviour with discharge capacity of $198.30 \text{ mAh g}^{-1}$ at 40 mA g^{-1} (Sarkar et al. 2014). Chromium doped Li_2RuO_3 cathode exhibited significantly augmented capacity due to $\text{Cr}^{3+}/\text{Cr}^{6+}$ redox reaction and superior activity of oxygen redox reaction (Liu et al. 2017).

4.6 Li_2SnO_3

Li_2SnO_3 is a potential cathode for Li-ion cells due to its high specific capacity (over 200 mAh g^{-1}) and its high energy density. The material crystallizes in monoclinic structure with space group C2/c (Fig. 12). In this, both Sn and Li form octahedrons with six oxygen atoms and the material consists of layers in the ab plane with an A–B stacking sequence (Kuganathan et al. 2018b).

Wang et al. synthesized Li_2SnO_3 by a hydrothermal route which exhibited improved capacity and cycling stability (Wang et al. 2013b). The structure of Li_2SnO_3

Fig. 12 Crystal structure of Li_2SnO_3 (space group C2/c) (Kuganathan et al. 2018b)



was determined using high-energy X-ray diffraction and intra-layer Li–Sn intermixing was observed in the material (Wang et al. 2016). Recently, Howard and Holzworth have studied computationally the Li^+ ion diffusion mechanism in both Li_2SnO_3 and Li_2SnS_3 (Howard and Holzworth 2016). Li_2SnO_3 exhibited poor structural stability during cycling. Wang et al. prepared carbon-doped Li_2SnO_3 ($\text{Li}_2\text{SnO}_3/\text{C}$) nanocomposite by sol–gel method and carbothermic reduction process and the results showed that $\text{Li}_2\text{SnO}_3/\text{C}$ exhibited better electrochemical properties than Li_2SnO_3 (Wang et al. 2012).

From several literature reports reviewed, it is concluded that modifications, mainly doping and surface coating, in the cathode material resulted in significant improvement in structural stability of cathode materials and stabilization of the average voltage and also decreased the capacity fading.

5 Summary

Cathode materials are one of the main decisive components which decide the energy density and lifespan of Li-ion cells. Conventional cathode materials suffer from major drawbacks such as low capacity, low thermal stability (in delithiated state), severe capacity degradation at high current rate and poor cycle stability. Lithium rich transition metal oxides have been recently emerged as promising cathode material for increasing the capacity and energy density of Li-ion cells. Humongous amount of research have been dedicated to the development of lithium rich cathodes including Li_2MnO_3 , $x\text{Li}_2\text{MnO}_3 \cdot (1 - x)\text{LiMO}_2$, $\text{Li}_4\text{Mn}_2\text{O}_5$, Li_2RuO_3 , etc. Nevertheless, the practical application of these lithium rich cathode materials are still hindered due to their capacity fading and voltage decay upon cycling and unsatisfactory rate capability. There is scope for improving the performance of these materials via doping of cations, surface coating, adopting suitable synthesis route and controlling the process temperature and voltage window and so on. With the advances in the research on these cathode materials, it is sure that some of these materials will definitely make their way to practical lithium ion cells with improved energy density.

Acknowledgements The authors acknowledge Director, VSSC for granting permission to publish this chapter.

References

- Akhilash M, Salini PS, Jalaja K, John B, Mercy TD (2021a) Synthesis of $\text{Li}_{1.5}\text{Ni}_{0.25}\text{Mn}_{0.75}\text{O}_{2.5}$ cathode material via carbonate co-precipitation method and its electrochemical properties. *Inorg Chem Commun* 126:108434
- Akhilash M, Salini PS, John B, Mercy TD (2021b) A journey through layered cathode materials for lithium ion cells—from lithium cobalt oxide to lithium-rich transition metal oxides. *J Alloys Compd* 869:159239
- Alcantara R, Jumas JC, Lavela P, Fourcade JO, Vincente CP, Tirado JL (1999) X-ray diffraction, ^{57}Fe Mössbauer and step potential electrochemical spectroscopy study of $\text{LiFe}_y\text{Co}_{1-y}\text{O}_2$ compounds. *J Power Sources* 81/82:547
- Amdouni N, Zarrouk H, Soulette F, Julien C (2003) $\text{LiAl}_y\text{Co}_{1-y}\text{O}_2$ ($0.0 \leq y \leq 0.3$) intercalation compounds synthesized from the citrate precursors. *Mater Chem Phys* 80:205
- Andersson AM, Abraham DP, Haasch R, MacLaren S, Liu J, Amine K (2002) Surface characterization of electrodes from high power lithium-ion batteries. *J Electrochem Soc* 149:A1358
- Anoopkumar V, John B, Mercy TD (2020) Potassium-ion batteries: key to future large-scale energy storage? *ACS Appl Energy Mater* 3(10):9478–9492
- Armstrong AR, Robertson AD, Gitzendanner R, Bruce PG (1999) The layered intercalation compounds $\text{Li}(\text{Mn}_{1-y}\text{Co}_y)\text{O}_2$: positive electrode materials for lithium-ion batteries. *J Solid State Chem* 145:549
- Armstrong AR, Robertson AD, Bruce PG (2005) Overcharging manganese oxides: extracting lithium beyond Mn^{4+} . *J Power Sources* 146:275
- Armstrong AR, Holzapfel M, Novak P, Johnson CS, Kang SH, Thackeray MM, Bruce PG (2006) Demonstrating oxygen loss and associated structural reorganization in the lithium battery cathode $\text{Li}[\text{Ni}_{0.2}\text{Li}_{0.2}\text{Mn}_{0.6}]\text{O}_2$. *J Am Chem Soc* 128:8694
- Arunkumar P, Jeong WJ, Won S, Im WB (2016) Improved electrochemical reversibility of over-lithiated layered Li_2RuO_3 cathodes: understanding aliovalent Co^{3+} substitution with excess lithium. *J Power Sources* 324:428. <https://doi.org/10.1016/j.jpowsour.2016.05.013>
- Buchberger I, Seidlmayer S, Pokharel A, Piana M, Hattendorff J, Kudejova P, Gilles R, Gasteiger HA (2015) Aging analysis of graphite/ $\text{LiNi}_{1/3}\text{Mn}_{1/3}\text{Co}_{1/3}\text{O}_2$ cells using XRD, PGAA, and AC impedance. *J Electrochem Soc* 162:A2737
- Cao J, Xie J, Cao G, Zhu T, Zhao X, Zhang S (2013) Electrochemical properties of $0.5\text{Li}_2\text{MnO}_3 \cdot 0.5\text{Li}_4\text{Mn}_5\text{O}_{12}$ nanotubes prepared by a self-templating method. *Electrochim Acta* 111:447–454
- Cao CW, Xi LJ, Leung KL, Wang M, Liu Y, Ma RG, Yang SL, Lu ZG, Chung CY (2015) Facile synthesis of porous Li-rich layered $\text{Li}[\text{Li}_{0.2}\text{Mn}_{0.534}\text{Ni}_{0.133}\text{Co}_{0.133}]\text{O}_2$ as high-performance cathode materials for Li-ion batteries. *RSC Adv* 5:30507
- Ceder G, Chiang YM, Sadoway DR, Aydinol MK, Jang YI, Huang B (1998) Identification of cathode materials for lithium batteries guided by first-principles calculations. *Nature* 392:694
- Chang ZR, Lv HJ, Tang HW, Li HJ, Yuan XZ, Wang H (2009) Synthesis and characterization of high-density LiFePO_4/C composites as cathode materials for lithium-ion batteries. *Electrochim Acta* 54:4595–4599
- Cho J, Jung HS, Park YC, Kim GB, Lim HS (2000) Electrochemical properties and thermal stability of $\text{Li}_x\text{Ni}_{1-x}\text{Co}_x\text{O}_2$ cathode materials. *J Electrochem Soc* 147:15
- Cho J, Kim G, Lim HS, J (1999) Effect of preparation methods of $\text{LiNi}_{1-x}\text{Co}_x\text{O}_2$ cathode materials on their chemical structure and electrode performance. *Electrochem Soc* 146:3571
- Choi W, Manthiram A (2007) Influence of fluorine substitution on the electrochemical performance of 3 V spinel $\text{Li}_4\text{Mn}_5\text{O}_{12-\eta}\text{F}_\eta$ cathodes. *Solid State Ion* 178(27–28):1541–1545
- Croy JR, Kang SH, Balasubramanian M, Thackeray MM (2011) Li_2MnO_3 -based composite cathodes for lithium batteries: a novel synthesis approach and new structures. *Electrochem Commun* 13:1063
- Dan P, Mengeritsky E, Geronov Y, Aurbach D, Weissman I (1995) Performances and safety behaviour of rechargeable AA-size $\text{Li}/\text{Li}_x\text{MnO}_2$ cell. *J Power Sources* 54:143

- Daniel C, Besenhard JO, Hand book of battery materials. Wiley-VCH, Germany
- Delmas C, Saadoun I (1992) Electrochemical and physical properties of the $\text{Li}_x\text{Ni}_{1-y}\text{Co}_y\text{O}_2$ phases. *Solid State Ion* 53–56:370
- Delmas C, Menetrier M, Croguennec L, Saadoun I, Rougier A, Poullier C, Prado G, Grune M, Fournes L (1999) An overview of the $\text{Li}(\text{Ni}, \text{M})\text{O}_2$ systems: syntheses, structures and properties. *Electrochim Acta* 45:243
- Delmas C, Fouassier C, Hagemuller P (1980) Structural classification and properties of the layered oxides. *Phys. B+ C* 99(1–4):81–85
- Deng YP, Fu F, Wu ZG, Yin ZW, Zhang T, Li JT, Huang L, Sun SG (2016) Layered/spinel heterostructured Li-rich materials synthesized by a one-step solvothermal strategy with enhanced electrochemical performance for Li-ion batteries. *J Mater Chem A* 4:257–263
- Ding K, Wang L, Li J, Jia H, He X (2011) Preparation of $\text{Li}_5\text{Fe}_{1-x}\text{Mn}_x\text{O}_4/\text{CNT}$ materials for Li-ion batteries. *Int J Electrochem Sci* 6:6165–6176
- Doeff MM (2013) Batteries: overview of battery cathodes, springer encyclopedia of sustainability science and technology. Springer Science + Business Media, New York, pp 709–739
- Dong X, Xu Y, Xiong L, Sun X, Zhang Z (2013) Sodium substitution for partial lithium to significantly enhance the cycling stability of Li_2MnO_3 cathode material. *J Power Sources* 243:78–87
- Erickson EM, Schipper F, Penki TR, Shin JY, Erk C, Chesneau FF, Markovsky B, Aurbach D (2017) Review—recent advances and remaining challenges for lithium ion battery cathodes. *J Electrochem Soc* 164:A6341–A6348
- Freire M, Kosova NV, Jordy C, Chateigner D, Lebedev OI, Maignan A, Pralong V (2016) A new active Li–Mn–O compound for high energy density Li-ion batteries. *Nat Mater* 15:173–177
- Fu Y, Jiang H, Hu Y, Zhang L, Li C (2014) Hierarchical porous $\text{Li}_4\text{Mn}_5\text{O}_{12}$ nano/micro structure as superior cathode materials for Li-ion batteries. *J Power Sources* 261:306
- Gallagher KG, Kang SH, Park SU, Han SY (2011) $x\text{Li}_2\text{MnO}_3 \cdot (1-x)\text{LiMO}_2$ blended with LiFePO_4 to achieve high energy density and pulse power capability. *J Power Sources* 196:9702
- Gallus DR, Schmitz R, Wagner R, Hoffmann B, Nowak S, Cekic-Laskovic I, Schmitz RW, Winter M (2014) The influence of different conducting salts on the metal dissolution and capacity fading of NCM cathode material. *Electrochim Acta* 134:393–398
- Goodenough JB, Park KS (2013) The Li-ion rechargeable battery: a perspective. *J Am Chem Soc* 135:1167–1176
- Gu YJ, Chen YB, Liu H-Q, Wang Y-M, Wang C-L, Wu H-K (2011) Structural characterization of layered $\text{LiNi}_{0.85-x}\text{Mn}_x\text{Co}_{0.15}\text{O}_2$ with $x = 0, 0.1, 0.2$ and 0.4 oxide electrodes for Li batteries. *J Alloys Compd* 509:7915–7921
- Gummow RJ, Thackeray MM (1992) Lithium-cobalt-nickel-oxide cathode materials prepared at 400°C for rechargeable lithium batteries. *Solid State Ion* 53–56:681
- He W, Yuan DD, Qian JF, Ai XP, Yang HX, Cao YL (2013) Enhanced high-rate capability and cycling stability of Na-stabilized layered $\text{Li}_{1.2}[\text{Co}_{0.13}\text{Ni}_{0.13}\text{Mn}_{0.54}]\text{O}_2$ cathode material. *J Mater Chem A* 1:11397
- Hirano A, Matsumura T, Ueda M, Imanishi N, Takeda Y, Tabuchi M (2005) Electrochemical properties and Mössbauer effect of anti-fluorite type compound, Li_5FeO_4 . *Solid State Ion* 176:2777–2782
- Holzapfel M, Schreiner R, Ott A (2001) Lithium-ion conductors of the system $\text{LiCo}_{1-x}\text{Fe}_x\text{O}_2$: a first electrochemical investigation. *Electrochim Acta* 46:103
- Howard J, Holzwarth NAW (2016) First-principles simulations of the porous layered calcogenides $\text{Li}_{2+x}\text{SnO}_3$ and $\text{Li}_{2+x}\text{SnS}_3$. *Phys Rev B* 94:064108
<https://www.tesla.com>. Accessed July 2018
- Huang H, SubbaRao GV, Chowdari BVR (1999) $\text{LiAl}_x\text{Co}_{1-x}\text{O}_2$ as 4 V cathodes for lithium ion batteries. *J Power Sources* 81:690
- Huang H, Yin SC, Nazar L (2001) Approaching theoretical capacity of LiFePO_4 at room temperature at high rates. *Electrochem Solid-State Lett* 4:A170

- Imanishi N, Fujii M, Hirano A, Takeda Y, Inaba M, Ogumi Z (2001b) Structure and electrochemical behaviors of Li_xCoO_2 ($x > 1$) treated under high oxygen pressure. *Solid State Ion* 140:45
- Imanishi N, Inoue Y, Hirano A, Ueda M, Takeda Y, Sakaebe H, Tabuchi M (2005) Antifluorite compounds, $\text{Li}_{5+x}\text{Fe}_{1-x}\text{Co}_x\text{O}_4$, as a lithium intercalation host. *J Power Sources* 146:21–26
- Imanishi N, Fujii M, Hirano A, Takeda Y (2001a) Synthesis and characterization of nonstoichiometric LiCoO_2 . *J Power Sources* 97/98:287
- Inoue T, Sano M (1998) An investigation of capacity fading of manganese spinels stored at elevated temperature. *J Electrochem Soc* 145:3704
- Ivanova SV, Zhecheva E, Nihtianova D, Stoyanova R (2011) Nano-domain structure of $\text{Li}_4\text{Mn}_5\text{O}_{12}$ spinel. *J Mater Sci* 46:7098–7105
- Ivanova SV, Zhecheva E, Nihtianova D, Mladenov ML, Stoyanova R (2013) Electrochemical intercalation of Li^+ into nanodomain $\text{Li}_4\text{Mn}_5\text{O}_{12}$. *J Alloys Compd* 561:252–261. <https://doi.org/10.1016/j.jallcom.2013.02.022>
- James ACWP, Goodenough JB (1988) Structure and bonding in lithium ruthenate, Li_2RuO_3 . *J Solid State Chem* 74:287–294
- Jang DH, Shin YJ, Oh SM (1996) Dissolution of spinel oxides and capacity losses in 4 V $\text{Li}/\text{Li}_x\text{Mn}_2\text{O}_4$ cells. *J Electrochem Soc* 143(7):2204–2211
- Jang YI, Huang B, Wang H, Sadoway DR, Ceder G, Chiang YM, Liu H, Tamura H (1999) $\text{LiAl}_y\text{Co}_{1-y}\text{O}_2$ (R–m) intercalation cathode for rechargeable lithium batteries. *J Electrochem Soc* 146:862
- Jiang YP, Xie J, Cao GS, Zhao XB (2010) Electrochemical performance of $\text{Li}_4\text{Mn}_5\text{O}_{12}$ nanocrystallites prepared by spray-drying-assisted solid state reactions. *Electrochim Acta* 56:412
- John B, Sandhya CP, Gouri C (2018) The role of nanosized materials in lithium ion batteries. *Nanomater: Phys, Chem, Biol Appl* (Apple Academic Press, USA)
- Johnson CS, Kang SH, Vaughey JT, Pol SV, Balasubramanian M, Thackeray MM (2010) Li_2O removal from Li_5FeO_4 —a cathode precursor for lithium-ion batteries. *Chem Mater* 22:1263–1270
- Johnson CS, Kim JS, Lefief C, Li N, Vaughey JT, Thackeray MM (2004) The significance of the Li_2MnO_3 component in ‘composite’ $x\text{Li}_2\text{MnO}_3 \cdot (1-x)\text{LiMn}_{0.5}\text{Ni}_{0.5}\text{O}_2$ electrodes. *Electrochem Commun* 6(10):1085–1091
- Julien CM, Zaghbi K (2004) Electrochemistry and local structure of nano-sized $\text{Li}_{4/3}\text{Me}_{5/3}\text{O}_4$ (Me–Mn, Ti) spinels. *Electrochim Acta* 50:411–416
- Julien C, Camacho-Lopez MA, Mohan T, Chitra S, Kalyani P, Gopukumar S (2000) Combustion synthesis and characterization of substituted lithium cobalt oxides in lithium batteries. *Solid State Ion* 135(1–4):241–248
- Jung SK, Gwon H, Hong J, Park KY, Seo DH, Kim H, Hyun J, Yang W, Kang K (2014) Understanding the degradation mechanisms of $\text{LiNi}_{0.5}\text{Co}_{0.2}\text{Mn}_{0.3}\text{O}_2$ cathode material in lithium ion batteries. *Adv Energy Mater* 4:1300787
- Kalyani P, Chitra S, Mohan T, Gopukumar S (1999) Lithium metal rechargeable cells using Li_2MnO_3 as the positive electrode. *J Power Sources* 80:103–106
- Kang SH, Johnson CS, Vaughey JT, Amine K, Thackeray MM (2006) The effects of acid treatment on the electrochemical properties of $0.5\text{Li}_2\text{MnO}_3 \cdot 0.5\text{LiNi}_{0.44}\text{Co}_{0.25}\text{Mn}_{0.31}\text{O}_2$ electrodes in lithium cells. *J Electrochem Soc* 153:A1186–A1192
- Kang SH, Kempgens P, Greenbaum S, Kropf AJ, Amine K, Thackeray MM (2007) Interpreting the structural and electrochemical complexity of $0.5\text{Li}_2\text{MnO}_3 \cdot 0.5\text{LiMO}_2$ electrodes for lithium batteries ($\text{M} = \text{Mn}_{0.5-x}\text{Ni}_{0.5-x}\text{Co}_{2x}$, $0 \leq x \leq 0.5$). *J Mater Chem* 17(20):2069–2077
- Kim KS, Lee SW, Moon HS, Kim HJ, Cho BW, Cho WI, Choi JB, Park JW (2004) Electrochemical properties of Li–Cr–Mn–O cathode materials for lithium secondary batteries. *J Power Sources* 129:319–323
- Kim SJ, Kim MC, Kwak DH, Kim DM, Lee GH, Choe HS, Park KW (2016) Highly stable TiO_2 coated Li_2MnO_3 cathode materials for lithium-ion batteries. *J Power Sources* 304:119–127
- Kim JM, Chung HT (2004) The first cycle characteristics of $\text{Li}[\text{Ni}_{1/3}\text{Co}_{1/3}\text{Mn}_{1/3}]\text{O}_2$ charged up to 4.7 V. *Electrochim Acta* 49:937–944

- Kobayashi H, Kawamoto KY, Tabuchi M, Nakamura O, Takano M (1995) Structure and lithium deintercalation of $\text{Li}_{2-x}\text{RuO}_3$. *Solid State Ion* 82:25–31
- Kobayashi H, Shigemura H, Tabuchi M, Sakaebe H, Ado K, Kageyama H, Hirano A, Kanno R, Wakita M, Morimoto S, Nasu S (2000) Electrochemical properties of hydrothermally obtained $\text{LiCo}_{1-x}\text{Fe}_x\text{O}_2$ as a positive electrode material for rechargeable lithium batteries. *J Electrochem Soc* 147:960
- Kuganathan N, Iyngaran P, Chreneos A (2018a) Lithium diffusion in Li_5FeO_4 . *Sci Rep* 8:5832
- Kuganathan N, Kordatos A, Chreneos A (2018b) Li_2SnO_3 as a cathode material for lithium-ion batteries: defects, lithium ion diffusion and dopants. *Sci Rep* 8:12621
- Kuganathan N, Kordatos A, Chreneos A (2019) Defect chemistry and Li-ion diffusion in Li_2RuO_3 . *Sci Rep* 9:550. <https://doi.org/10.1038/s41598-018-36865-4>
- Lavassuer S, Menetrier M, Suard E, Delmas C (2000) Evidence for structural defects in non-stoichiometric HT- LiCoO_2 : electrochemical, electronic properties and ^7Li NMR studies. *Solid State Ion* 128:11
- Le MLP, Strobel P, Colin CV, Pagnier T, Alloin F (2011) Spinel-type solid solutions involving Mn^{4+} and Ti^{4+} : crystal chemistry, magnetic and electrochemical properties. *J Phys Chem Solids* 72:124–135
- Levasseur S, Ménétrier M, Delmas C (2002) On the dual effect of Mg doping in LiCoO_2 and $\text{Li}_{1+x}\text{CoO}_2$: structural, electronic properties, and ^7Li MAS NMR studies. *Chem Mater* 14(8):3584–3590
- Li S, Lei D (2017) Synthesis and electrochemical characterization of nanosized Li_2MnO_3 cathode material for lithium ion batteries. *AIP Conf Proc* 1890:040037
- Li Z, Zhang D, Yang F (2009) Developments of lithium-ion batteries and challenges of LiFePO_4 as one promising cathode material. *J Mater Sci* 44:2435–2443
- Li B, Yan HJ, Zuo YX, Xia DG (2017) Tuning the reversibility of oxygen redox in lithium-rich layered oxides. *Chem Mater* 29:2811
- Li GR, Feng X, Ding Y, Ye SH, Gao XP (2012) AlF_3 -coated $\text{Li}(\text{Li}_{0.17}\text{Ni}_{0.25}\text{Mn}_{0.58})\text{O}_2$ as cathode material for Li-ion batteries. *Electrochim Acta* 78:308
- Liang L, Luo J, Chen M, Wang L, Li J, He X (2013) Synthesis and characterization of novel cathode material Li_5FeO_4 for Li-ion batteries. *Int J Electrochem Sci* 8:6393–6398
- Liao SX, Shen CH, Zhong YJ, Yan WH, Shi XX, Pei SS, Guo XD, Zhong BH, Wang XL, Liu H (2014) Influence of vanadium compound coating on lithium-rich layered oxide cathode for lithium-ion batteries. *RSC Adv* 4:56273. <https://doi.org/10.1039/C4RA10097B>
- Lim JH, Bang H, Lee KS, Amine K (2009) Electrochemical characterization of Li_2MnO_3 – $\text{Li}[\text{Ni}_{1/3}\text{Co}_{1/3}\text{Mn}_{1/3}]\text{O}_2$ – LiNiO_2 cathode synthesized via co-precipitation for lithium secondary batteries. *J Power Sources* 189(1):571–575
- Liu S, Wang J, Tian Z, Li Q, Tian X, Cui Y, Yang Y (2017) Chromium doped Li_2RuO_3 as a positive electrode with superior electrochemical performance for lithium ion batteries. *Chem Commun* 53:11913–11916
- Liu J, Manthiram A (2010) Functional surface modifications of a high capacity layered $\text{Li}[\text{Li}_{0.2}\text{Mn}_{0.54}\text{Ni}_{0.13}\text{Co}_{0.13}]\text{O}_2$ cathode. *J Mater Chem* 20(19):3961–3967
- Lu Z, MacNeil DD, Dahn JR (2001) Layered cathode materials $\text{Li}[\text{Ni}_x\text{Li}_{(1/3-2x/3)}\text{Mn}_{(2/3-x/3)}]\text{O}_2$ for lithium-ion batteries. *Electrochem Solid-State Lett* 4(11):A191–A194
- Lu YC, Mansour AN, Yabuuchi N, Shao-Horn Y (2009) Probing the origin of enhanced stability of “ AlPO_4 ” nanoparticle coated LiCoO_2 during cycling to high voltages: combined XRD and XPS studies. *Chem Mater* 21:4408–4424
- Lu C, Yang S, Wu H, Zhang Y, Yang X, Liang T (2016) Enhanced electrochemical performance of Li-rich $\text{Li}_{1.2}\text{Mn}_{0.52}\text{Co}_{0.08}\text{Ni}_{0.2}\text{O}_2$ cathode materials for Li-ion batteries by vanadium doping. *Electrochimica Acta* 209:448–455
- Madhavi S, SubbaRao GV, Chowdari BVR, Li SFY (2002) Effect of Cr dopant on the cathodic behavior of LiCoO_2 . *Electrochim Acta* 48:219
- Madhavi S, SubbaRao GV, Chowdari BVR, Li SFY (2001) Effect of aluminium doping on cathodic behaviour of $\text{LiNi}_{0.7}\text{Co}_{0.3}\text{O}_2$. *J Power Sources* 93:156

- Martha SK, Haik O, Zinigrad E, Exnar I, Drezen T, Miners JH, Aurbach D (2011) On the thermal stability of olivine cathode materials for lithium-ion batteries. *J Electrochem Soc* 158(10):A1115
- Metzger M, Strehle B, Solchenbach S, Gasteiger HA (2016) Origin of H₂ evolution in LIBs: H₂O reduction versus electrolyte oxidation. *J Electrochem Soc* 163:A798
- Ming L, Zhang B, Cao Y, Zhang JF, Wang CH, Wang XW, Li H (2018) Effect of Nb and F co-doping on Li_{1.2}Mn_{0.54}Ni_{0.13}Co_{0.13}O₂ cathode material for high-performance lithium-ion batteries. *Front Chem* 6:76
- Mizushima K, Jones PC, Wiseman PJ, Goodenough JB (1980) Li_xCoO₂ (0 < x < 1): a new cathode material for batteries of high energy density. *Mater Res Bull* 15:783–789
- Mohanty D, Kalnaus S, Meisner RA, Rhodes KJ, Li JL, Payzant EA, Wood DL, Daniel C (2013) Structural transformation of a lithium-rich Li_{1.2}Co_{0.1}Mn_{0.55}Ni_{0.15}O₂ cathode during high voltage cycling resolved by in situ X-ray diffraction. *J Power Sources* 229:239–248
- Moore GJ, Johnson CS, Thackeray MM (2003) The electrochemical behavior of xLiNiO₂·(1-x)Li₂RuO₃ and Li₂Ru_{1-y}Zr_yO₃ electrodes in lithium cells. *J Power Sources* 119–121:216
- Myung ST, Kumagai N, Komaba S, Chung HT (2001) Effects of Al doping on the microstructure of LiCoO₂ cathode materials. *Solid State Ion* 139:47
- Narukawa S, Takeda Y, Nishijima M, Imanishi N, Yamamoto O, Tabuchi M (1999) Anti-fluorite type Li₆CoO₄, Li₅FeO₄, and Li₆MnO₄ as the cathode for lithium secondary batteries. *Solid State Ion* 122:59–64
- Nishi Y (2001) The development of lithium ion secondary batteries. *Chem Rec* 1(5):406–413
- Noh M, Cho J (2012) Role of Li₆CoO₄ Cathode additive in Li-ion cells containing low coulombic efficiency anode material. *J Electrochem Soc* 159(8):A1329–A1334
- Noh HJ, Youn S, Yoon CS, Sun YK (2013) Comparison of the structural and electrochemical properties of layered Li[Ni_xCo_yMn_z]O₂ (x = 1/3, 0.5, 0.6, 0.7, 0.8 and 0.85) cathode material for lithium-ion batteries. *J Power Sources* 233:121–130
- Numata K, Sakaki C, Yamanaka S (1999) Synthesis and characterization of layer structured solid solutions in the system of LiCoO₂–Li₂MnO₃. *Solid State Ion* 117(3–4):257–263
- Ohzuku T, Makimura Y (2001) Layered lithium insertion material of LiCo_{1/3}Ni_{1/3}Mn_{1/3}O₂ for lithium-ion batteries. *Chem Lett* 30:642–643
- Ohzuku T, Ueda A (1997) Phenomenological expression of solid-state redox potentials of LiCoO₂, LiCo_{1/2}Ni_{1/2}O₂, and LiNiO₂ insertion electrodes. *J Electrochem Soc* 144:2780
- Okamoto Y (2012) Ambivalent effect of oxygen vacancies on Li₂MnO₃: a first-principles study. *J Electrochem Soc* 159:A152
- Okumura T, Shikano M, Kobayashi H (2014) Effect of bulk and surface structural changes in Li₅FeO₄ positive electrodes during first charging on subsequent lithium-ion battery performance. *J Mater Chem A* 2:11847–11856
- Ozawa K (1994) Lithium-ion rechargeable batteries with LiCoO₂ and carbon electrodes: the LiCoO₂/C system. *Solid State Ion* 69:212–221
- Ozawa K (2009) Lithium ion rechargeable batteries: materials, technology, and new applications. Wiley-VCH Verlag GmbH & Co. KGaA, Weinheim
- Padhi AK, Nanjundaswamy KS, Goodenough JB (1997a) Phospho-olivines as positive-electrode materials for rechargeable lithium batteries. *J Electrochem Soc* 144:1188–1194
- Padhi A, Nanjundaswamy KS, Goodenough JB (1997b) Phospho-olivines as positive-electrode materials for rechargeable lithium batteries. *J Electrochem Soc* 144:1609
- Paik Y, Grey CP, Johnson CS, Kim JS, Thackeray MM (2002) Lithium and deuterium NMR studies of acid-leached layered lithium manganese oxides. *Chem Mater* 14:5109
- Park SH, Sato Y, Kim JK, Lee YS (2007) Powder property and electrochemical characterization of Li₂MnO₃ material. *Mater Chem Phys* 102:225–230
- Park MS, Lim YG, Kim JH, Kim YJ, Cho J, Kim JS (2011) A novel lithium-doping approach for an advanced lithium ion capacitor. *Adv Energy Mater* 1:1002
- Park MS, Lim YG, Hwang SM, Kim JH, Kim JS, Dou SX, Cho J, Kim YJ (2014) Scalable integration of Li₅FeO₄ towards robust, high-performance lithium-ion hybrid capacitors. *ChemSusChem* 7:3138–3144


- Peres JP, Weill F, Delmas C (1999) Lithium/vacancy ordering in the monoclinic Li_xNiO_2 ($0.50 \leq x \leq 0.75$) solid solution. *Solid State Ion* 116:19–27
- Rana J, Stan M, Kloepsch R, Li J, Schumacher G, Welter E, Zizak I, Banhart J, Winter M (2013) Structural changes in Li_2MnO_3 cathode material for Li-ion batteries. *Adv Energy Mater* 4:1300998
- Redel K, Kulka A, Plewa A, Molenda J (2019) High-performance Li-rich layered transition metal oxide cathode materials for Li-ion batteries. *J Electrochem Soc* 16(3):A5333–A5342
- Robertson AD, Bruce PG (2002) The origin of electrochemical activity in Li_2MnO_3 . *Chem Commun* 23:2790
- Robertson AD, Bruce PG (2003) Mechanism of electrochemical activity in Li_2MnO_3 . *Chem Mater* 15:1984
- Robertson AD, Armstrong AR, Bruce PG (2001) Low temperature lithium manganese cobalt oxide spinels, $\text{Li}_{4-x}\text{Mn}_{5-2x}\text{Co}_x\text{O}_{12}$ ($0 \leq x \leq 1$), for use as cathode materials in rechargeable lithium batteries. *J Power Source* 97–98:332–335
- Rossouw MH, Liles DC, Thackeray MM (1993) Synthesis and structural characterization of a novel layered lithium manganese oxide, $\text{Li}_{0.36}\text{Mn}_{0.91}\text{O}_2$, and its lithiated derivative, $\text{Li}_{1.09}\text{Mn}_{0.91}\text{O}_2$. *J Solid State Chem* 104:464
- Rossouw MH, Thackeray MM (1991) Lithium manganese oxides from Li_2MnO_3 for rechargeable lithium battery applications. *Mater Res Bull* 26:463–473
- Saint JA, Doeff MM, Reed J (2007) Synthesis and electrochemistry of Li_3MnO_4 : Mn in the +5 oxidation state. *J Power Sources* 172:189–197
- Salini PS, Gopinadh SV, Kalpakasser A, John B, Mercy TD (2020) Toward greener and sustainable Li-ion cells: an overview of aqueous-based binder systems. *ACS Sustain Chem Eng* 8(10):4003–4025
- Sarkar S, Mahale P, Mitra S (2014) Lithium rich composition of Li_2RuO_3 and $\text{Li}_2\text{Ru}_{1-x}\text{Ir}_x\text{O}_3$ layered materials as Li-ion battery cathode. *J Electrochem Soc* 161(6):A934–A942
- Sathiyam M, Rousse G, Ramesha K, Laisa CP, Vezin H, Sougrati MT, Doublet ML, Foix D, Gonbeau D, Walker W, Prakash AS, Ben Hassine M, Dupont L, Tarascon JM (2013) Reversible anionic redox chemistry in high-capacity layered-oxide electrodes. *Nat Mater* 12:827
- Sathiyam M, Abakumov AM, Foix D, Rousse G, Ramesha K, Saubanere M, Doublet ML, Vezin H, Laisa CP, Prakash AS, Gonbeau D, VanTendeloo G, Tarascon JM (2015) Origin of voltage decay in high-capacity layered oxide electrodes. *Nat Mater* 14:230
- Satyavani TVSL, Srinivas Kumar A, Subba Rao PSV (2016) Methods of synthesis and performance improvement of lithium iron phosphate for high rate Li-ion batteries: a review. *Eng Sci Technol, Int J* 19:178–188
- Shaju KM, SubbaRao GV, Chowdari BVR (2002) Performance of layered $\text{Li}(\text{Ni}_{1/3}\text{Co}_{1/3}\text{Mn}_{1/3})\text{O}_2$ as cathode for Li-ion batteries. *Electrochim Acta* 48(2):145–151
- Shao-Horn Y, Croguennec L, Delmas C, Nelson EC, O’Keefe MA (2003) Atomic resolution of lithium ions in LiCoO_2 . *Nat Mater* 2(7):464–467
- Sharmila S, Janarthanan B, Gomathi B (2014) Impedance and conductivity analysis of Zn doped $\text{Li}_4\text{Mn}_5\text{O}_{12}$. *IJRSET* 3:9537–9544
- Singh G, Thomas R, Kumar A, Katiyar RS (2012) Electrochemical behavior of Cr-doped composite $\text{Li}_2\text{MnO}_3\text{--LiMn}_{0.5}\text{Ni}_{0.5}\text{O}_2$ cathode materials. *J Electrochem Soc* 159:A410
- Stoyanova R, Zhecheva E, Zarkova L (1994) Effect of Mn-substitution for Co on the crystal structure and acid delithiation of $\text{LiMn}_y\text{Co}_{1-y}\text{O}_2$ solid solutions. *Solid State Ion* 73:233
- Sun Y, Shiosaki Y, Xia Y, Noguchi H (2006) The preparation and electrochemical performance of solid solutions $\text{LiCoO}_2\text{--Li}_2\text{MnO}_3$ as cathode materials for lithium ion batteries. *J Power Sources* 159(2):1353–1359
- Sun CS, Zhou Z, Xu ZG, Wang DG, Wei JP, Bian XK, Yan J (2009) Improved high-rate charge/discharge performances of LiFePO_4/C via V-doping. *J Power Sources* 193:841–845
- Sun R, Jakes P, Eurich S, van Holt D, Yang S, Homberger M, Simon U, Kungl H, Eichel R-A (2018) Secondary-phase formation in spinel-type LiMn_2O_4 -cathode materials for lithium-ion batteries:

- quantifying trace amounts of Li_2MnO_3 by electron paramagnetic resonance spectroscopy. *Appl Magn Reson* 49(4):415–427
- Surace Y, Simões M, Karvonen L, Yoon S, Pokrant S, Weidenkaff A (2015) Freeze drying synthesis of Li_3MnO_4 cathode material for Li-ion batteries: a physico-electrochemical study. *J Alloys Compd* 644:297–303
- Surace Y, Simões M, Pokrant S, Weidenkaff A (2016) Capacity fading in Li_3MnO_4 : a post-mortem analysis. *J Electroanal Chem* 766:44–51
- Tabuchi M, Kitta M, Kageyama H, Shibuya H, Imaizumi J (2015) Mn source effects on electrochemical properties of Fe- and Ni-substituted Li_2MnO_3 positive electrode material. *J Power Sources* 279:510–516
- Takada T, Hayakawa H, Akiba E, Izumi F, Chakoumakos BC (1997) Novel synthesis process and structure refinements of $\text{Li}_4\text{Mn}_5\text{O}_{12}$ for rechargeable lithium batteries. *J Power Sources* 68(2):613–617
- Tarascon JM, Armand M (2001) Issues and challenges facing rechargeable lithium batteries. *Nature* 414(6861):359–367
- Tarascon JM, McKinnon WR, Coowar F, Bowmer TN, Amatucci G, Guyomard D (1994) Synthesis conditions and oxygen stoichiometry effects on Li insertion into the spinel LiMn_2O_4 . *J Electrochem Soc* 141:1421–1431
- Thackeray M (1997) Manganese oxides for lithium batteries. *Prog Solid State Chem* 25:1–71
- Thackeray MM, David WIF, Bruce PG, Goodenough JB (1983) Lithium insertion into manganese spinels. *Mater Res Bull* 18:461–472
- Thackeray MM, Johnson PJ, de Picciotto LA, Bruce PG, Goodenough JB (1984) Electrochemical extraction of lithium from LiMn_2O_4 . *Mater Res Bull* 19:179–187
- Thackeray MM, de Picciotto LA, de Kock A, Johnson PJ, Nicholas VA, Adendorff KT (1987) Spinel electrodes for lithium batteries—a review. *J Power Sources* 21(1):1–8. [https://doi.org/10.1016/0378-7753\(87\)80071-X](https://doi.org/10.1016/0378-7753(87)80071-X)
- Thackeray MM, Mansuetto MF, Johnson CS (1996) Thermal stability of $\text{Li}_4\text{Mn}_5\text{O}_{12}$ electrodes for lithium batteries. *J Solid State Chem* 125(2):274–277. <https://doi.org/10.1006/jssc.1996.0297>
- Thackeray MM, Kang S-H, Johnson CS, Vaughey JT, Benedek R, Hackney SA (2007) *J Mater Chem* 17(30):3112–3125
- Thackeray MM, Chan MKY, Trahey L, Kirklín S, Wolverton C (2013) Vision for designing high-energy, hybrid Li ion/ $\text{Li}-\text{O}_2$ cells. *J Phys Chem Lett* 4:3607
- Thackeray MM, Shao-Horn Y, Kahian AJ, Kepler KD, Skinner E, Vaughey JT, Hackney S (1998) Structural fatigue in spinel electrodes in high voltage (4 V) $\text{Li}/\text{Li}_x\text{Mn}_2\text{O}_4$ cells. *Electrochem Solid-State Lett* 1:7
- Tian Y, Chen DR, Jiao XL, Duan YZ (2007) Facile preparation and electrochemical properties of cubic-phase $\text{Li}_4\text{Mn}_5\text{O}_{12}$ nanowires. *Chem Commun* 20:72
- Tukamoto H, West AR (1997) Electronic conductivity of LiCoO_2 and its enhancement by magnesium doping. *J Electrochem Soc* 144:3164
- Van der Ven A, Aydinol MK, Ceder G (1998) First-principles evidence for stage ordering in Li_xCoO_2 . *J Electrochem Soc* 145:2149
- Wandt J, Freiberg A, Thomas R, Gorlin Y, Siebel A, Jung R, Gasteiger HA, Tromp M (2016) Transition metal dissolution and deposition in Li-ion batteries investigated by operando X-ray absorption spectroscopy. *J Mater Chem A* 4:18300–18305
- Wang GX, Yang L, Chen Y, Wang JZ, Bewlay S, Liu HK (2005) An investigation of polypyrrole- LiFePO_4 composite cathode materials for lithium-ion batteries. *Electrochim Acta* 50:4649–4654
- Wang Q, Huang Y, Miao J, Zhao Y, Wang Y (2012) Synthesis and properties of carbon-doped Li_2SnO_3 nanocomposite as cathode material for lithium-ion batteries. *Mater Lett* 71:66–69
- Wang R, He XQ, He LH, Wang FW, Xiao RJ, Gu L, Li H, Chen L (2013a) Atomic structure of Li_2MnO_3 after partial delithiation and re-lithiation. *Adv Energy Mater* 3:1358
- Wang Q, Huang Y, Zhao Y, Zhang W, Wang Y (2013b) Preparation of Li_2SnO_3 and its application in lithium-ion batteries. *Surf Interface Anal* 45:1297–1303. <https://doi.org/10.1002/sia.5274>

- Wang Z, Ren Y, Ma T, Zhuang W, Lu S, Xu G, Abouimrane A, Amine K, Chen Z (2016) Probing cation intermixing in Li_2SnO_3 . *RSC Adv* 6:31559–31564. <https://doi.org/10.1039/C6RA00977H>
- Whittingham MS (2004) Lithium batteries and cathode materials. *Chem Rev* 104(10):4271–4302
- Wu Y, Manthiram A (2006) High capacity, surface-modified layered $\text{Li}[\text{Li}_{(1-x)/3}\text{Mn}_{(2-x)/3}\text{Ni}_{x/3}\text{Co}_{x/3}]\text{O}_2$ cathodes with low irreversible capacity loss. *Electrochem Solid-State Lett* 9(5):A221–A224
- Xie S, Yu Z, Liu H, Wu S (2013) Effects of V doping on the electrochemical performance of Li_3MnO_4 for lithium ion batteries. *Solid State Ion* 262:102–105
- Xie Y, Chen S, Yang W, Zou H, Lin Z, Zhou J (2019) Improving the rate capability and decelerating the voltage decay of Li-rich layered oxide cathodes by constructing a surface-modified microrod structure. *J Alloy Compd* 772:230–239
- Xie Z, Eikhuemelo H, Zhao J, Cain C, Xu W, Wang Y (2015) Ni and Fe dual-doped $\text{Li}_4\text{Mn}_5\text{O}_{12}$ spinels as cathode materials for high-voltage Li-ion batteries. *J Electrochem Soc* 162(8):A1523–A1529
- Yao Y, Yang P, Bie X, Wang C, Wei Y, Chen G, Du F (2015) High capacity and rate capability of a layered Li_2RuO_3 cathode utilized in hybrid Na^+/Li^+ batteries. *J Mater Chem A* 3:18273–18278
- Yao Z, Kim S, He J, Hegde VI, Wolverton C (2018) Interplay of cation and anion redox in $\text{Li}_4\text{Mn}_2\text{O}_5$ cathode material and prediction of improved $\text{Li}_4(\text{Mn}, \text{M})_2\text{O}_5$ electrodes for Li-ion batteries. *Sci Adv* 4:6754
- YiDi Z, Yi L, XinHui X, XiuLi W, ChangDong GU, Jiang Ping TU (2015) High-energy cathode materials for Li-ion batteries: a review of recent developments. *Sci China Technol Sci* 58:1809–1828
- Yoon W, Lee KK, Kim KB (2000) Structural and electrochemical properties of $\text{LiAl}_y\text{Co}_{1-y}\text{O}_2$ cathode for Li rechargeable batteries. *J Electrochem Soc* 147:2023
- Yu HJ, Zhou HS (2012) Initial coulombic efficiency improvement of the $\text{Li}_{1.2}\text{Mn}_{0.567}\text{Ni}_{0.166}\text{Co}_{0.067}\text{O}_2$ lithium-rich material by ruthenium substitution for manganese. *J Mater Chem* 22:15507. <https://doi.org/10.1039/C2JM33484D>
- Yu H, Zhou H (2013) High-energy cathode materials ($\text{Li}_2\text{MnO}_3\text{--LiMO}_2$) for lithium-ion batteries. *J Phys Chem Lett* 4(8):1268–1280
- Yu Z, Xie S, Liu X, Cui Y, Liu H (2012) Electrochemical evaluation of Li_3MnO_4 used as cathode materials for lithium ion batteries. *Solid State Ion* 72–78
- Yu H, Ishikawa R, So YG, Shibata N, Kudo T, Zhou H, Ikuhara Y (2013) Direct atomic-resolution observation of two phases in the $\text{Li}_{1.2}\text{Mn}_{0.567}\text{Ni}_{0.166}\text{Co}_{0.067}\text{O}_2$ cathode material for lithium-ion batteries. *Angew Chem Int Ed* 52:5969–5973
- Yu X, Lyu Y, Gu L, Wu H, Bak SM, Zhou Y, Amine K, Ehrlich SN, Li H, Nam K-W (2014) Understanding the rate capability of high-energy-density Li-rich layered $\text{Li}_{1.2}\text{Ni}_{0.15}\text{Co}_{0.1}\text{Mn}_{0.55}\text{O}_2$ cathode materials. *Adv Energy Mater* 4:1300950-n/a
- Zaghib K, Mauger A, Groult H, Goodenough JB, Julien CM (2013) Advanced electrodes for high power Li-ion batteries. *Materials* 6:1028–1049
- Zhao W, Xiong L, Xu Y, Xiao X, Wang J, Ren Z (2016) Magnesium substitution to improve the electrochemical performance of layered Li_2MnO_3 positive-electrode material. *J Power Sources* 330:37–44
- Zheng H, Sun Q, Liu G, Song X, Battaglia VS (2012) Correlation between dissolution behavior and electrochemical cycling performance for $\text{LiNi}_{1/3}\text{Co}_{1/3}\text{Mn}_{1/3}\text{O}_2$ -based cells. *J Power Sources* 207:134–140
- Zheng Z, Wu ZG, Zhong YJ, Shen CH, Hua WB, Xu BB, Yu C, Zhong BH, Guo XD (2015) A further electrochemical investigation on solutions to high energetical power sources: isomeric compound $0.75\text{Li}_{1.2}\text{Ni}_{0.2}\text{Mn}_{0.6}\text{O}_2\cdot 0.25\text{LiNi}_{0.5}\text{Mn}_{1.5}\text{O}_4$. *RSC Adv* 5:37330

Lithium-Ion Pouch Cells: An Overview



Sumol V. Gopinadh, V. Anoopkumar, Md. Jamal Nawaz Ansari, Deepak Srivastava, Arjun Raj M., Bibin John , Aiswarya Samridh, P. S. Vijayakumar, and T. D. Mercy

1 Introduction

Lithium-ion batteries (LIBs) have emerged as a key power source for various applications due to their high operating voltage, high energy density, high columbic efficiency, low self-discharge, low maintenance and prolonged cycle life (John and Cheruvally 2017; John et al. 2018; Salini et al. 2020; Vamsi et al. 2021). Another stunning feature which boosts their demand is the design flexibility. They can be manufactured in different formats such as cylindrical, prismatic, pouch etc. (Dai et al. 2020). Among the different battery packs, the pouch model has become an attractive and dependable choice among the battery manufacturers, particularly because of its light weight, high energy density, design flexibility and low manufacturing cost (Kim 2007). Unlike the traditional battery pack of LIBs, which occupy large portions of the mass and volume of the devices they power, the pouch pack is absolutely devoid of any hard metallic enclosure; instead they use only flexible laminated aluminium foil to house the cell components and therefore it can efficiently fit the available space in the devices with more than 90% packaging efficiency, the highest among battery packs ever exist (Murashko and Pyrh 2013).

Generally, pouch cell comprises of layered construction of internal electrode stack, which is enclosed in a flexible laminate material. Each layer of the laminate film contributes to different properties so as to meet the critical performance requirements. For example, the innermost layer is composed of heat sealable and electrolyte resistant polymer such as modified polypropylene, which serves as a thermal adhesive layer for pouch sealing, the middle layer is usually aluminium, which provides superior gas and water barrier properties to laminated film and also

S. V. Gopinadh · V. Anoopkumar · Md. J. N. Ansari · D. Srivastava · A. Raj M. · B. John (✉) · A. Samridh · P. S. Vijayakumar · T. D. Mercy
Energy Systems Division, PCM Entity, Vikram Sarabhai Space Centre,
Thiruvananthapuram-695022, Kerala, India
e-mail: bbjohn@gmail.com

brings weight reduction and slimness. Moreover, it helps in easy reshaping of the pack and quick heat dissipation from the cell. The exterior stratum is usually a polyamide or polyester such as nylon or polyethylene terephthalate (PET), for ensuring scratch resistance, electrical insulation and mechanical durability of the laminate and also permits package labelling or marking (Zeng et al. 2018). Compared to other battery packs, pouch module necessities only minimal usage of cell packaging materials, which makes the cells more attractive over metallic body prismatic cells of the same chemistry type, especially in terms of cost and gravimetric energy density. Pouch cells can be based on different cathode/anode chemistries and a range of electrolyte types such as dry polymer, gel and liquid electrolytes (Bowles et al. 2009). General structure of a pouch cell is depicted in Fig. 1 (Du et al. 2015). Lithium-ion pouch cell comprises a stack of individual anode and cathode, each electrode separated by a non-conductive, porous separator. Electrical contact is brought about by welding metallic tabs to the current collectors in the stack in such a way that they are protruding outward to allow external connection (Kepler et al. 2014). The entire assembly is then enclosed in a pouch pack. Although this slim package has numerous advantages associated with their construction, they are more vulnerable to damages compared to cells encased in metallic case and poses issues in performance, particularly in rechargeable format (Wünsch et al. 2019). However, being influenced from the innumerable positive traits of pouch module, many battery researchers have devoted their attention in the development and implementation of pouch module in a wide range of applications. This chapter summarizes various aspects of lithium ion pouch cells.

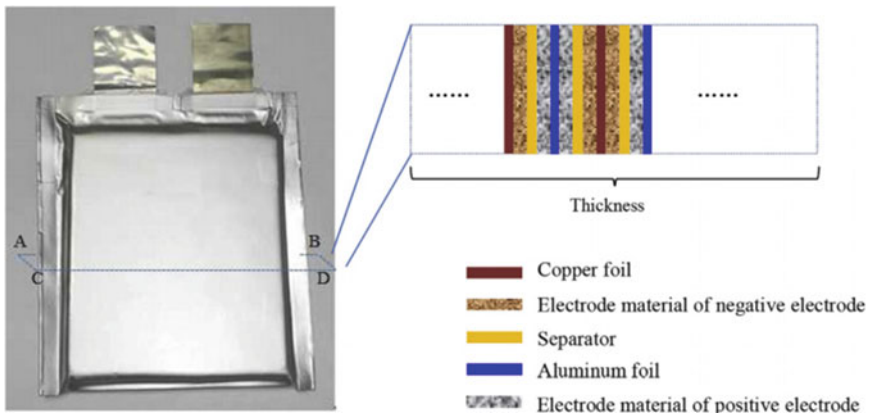


Fig. 1 Structure of a pouch-type lithium-ion cell. (Reprinted with permission from Copyright © 2014 Elsevier Masson SAS)

2 Method of Manufacturing of Lithium-Ion Pouch Cell

There is no generalised method for the fabrication of pouch cells; each manufacturer follows slightly different process for fabrication. A typical example is shown in Fig. 2 (Tagawa and Brodd 2009). The core stack of lithium-ion pouch cell is made by sequentially winding (Z folding)/stacking the individual anode and cathode, together with interposed non-conductive and porous separator, in a predetermined number of times. The current collectors of each electrode of the stack are then welded with metallic tabs, usually aluminium (for cathode) and copper (for anode) of sufficient thickness and size (Kepler et al. 2014; Tagawa and Brodd 2009). The electrode stack is then enclosed in a pouch case, the upper and lower portion of which is created by roughly folding a rectangular composite film (Al laminate). A tray like groove is created through a pressing process for receiving the electrode assembly (Kim et al. 2015). Such a cup shape helps to keep the electrode and electrolyte material intact during handling. The pouch is then sealed along three edges by applying pressure and temperature, which is higher than melting point of the innermost polymer layer, around the edges of the polymer laminate, with an electrolyte inlet left therein for the activation of the cell. This inlet is resealed only after the formation cycle so as to facilitate the residual gas to escape, which may otherwise cause the pouch pack to swell. During sealing it is necessary to maintain sufficient sealing width in order to effectively prevent the ingress of corrosive agents, such as moisture and oxygen, from entering the operating environment of the battery and also prevent the egress of the electrolyte. The fourth edge is normally formed by folding the laminated aluminium foil and therefore does not involve heat sealing. The welded tabs are extending through the enclosure seal to the outside of the cell to enable external connection for charging and discharging of the cell. During high temperature heat sealing operation, the innermost layer melts completely and therefore there is a chance that the middle aluminum layer may expose and comes in contact with metal constituting the electrode tabs. Therefore, prior to heat sealing, a separate insulating sleeve is usually wrapped around the sealing area of the tab, where it adheres to the sealing surfaces of the pack (Kim 2007; Jacobs and Dasgupta 2001). Such an extra component not only prevent the short circuit arising out of the direct contact between metal tab and aluminum layer, but also reinforce the adhesion between tab and innermost layer of the pouch pack, which is also a crucial task, as these sandwiched contact area is more vulnerable to sealing unpredictability and thus arises a possibility of the seepage of the liquid electrolyte through it (Tagawa and Brodd 2009; Jacobs and Dasgupta 2001). Once the sealing process is over, all the lateral cut edges are either folded or covered with flame/heat resistant resin, since there exist a chance for the exposed metal layer to be corroded and also be short circuited by direct contact between metal exposed along edge of the pouch pack and the hard case or a battery box of an electronic device or tab material (Kim et al. 2013).

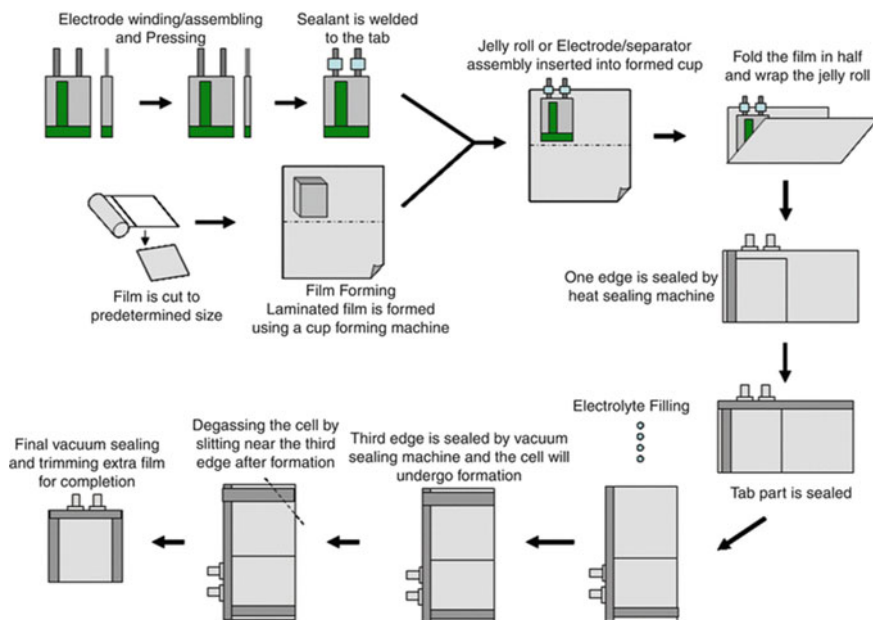


Fig. 2 General method for manufacturing of pouch cell. (Reprinted with permission from Tagawa and Brodd (2009), copyright (2009) © Springer Nature)

3 Heat Sealing of Pouch Cell Pack

Heat sealing is a widely accepted joining technique in packaging. If the strength of sealing is not sufficiently high enough to provide excellent barrier to moisture, gas, and electrolyte, the life of the cell has to be compromised. High seal strength (HSS) ensures safety and reliability, because it permits the cell to accommodate the gas formed as a result of charge–discharge process without being bursted. Therefore, in pouch design, HSS is one of the crucial factors. The HSS is primarily determined by sealing temperature and secondarily by the sealing dwell time (Malsen et al. 2008). Generally speaking, the temperature of heat sealing should be maintained between a particular temperature level, the lower limit of which should be above the melting point of innermost layer and the upper limit should be below the melting temperature of outermost layer. If it is not so, it will lead to improper sealing and for outermost layer, high temperature will change the crystallinity of the layer and damage the bonding strength with adjacent aluminium layer. While considering the heat seal temperature within the allowed temperature limit, the HSS initially increases with heat-sealing temperature as it assists enough melting of the sealant layer and thus allowing the efficient utilization of hot tack capacity. Moreover, the thorough melting of the sealant layer fills the sealing region, thus maximising the adhesive strength. However, further increase of the sealing temperature will reduce the melt viscosity of the sealant and causes the material to overflow through the heat-sealing area.

Therefore, additional improvement in heat strength could not be achieved (Guo and Fan 2016).

Apart from heat-sealing temperature, heat sealing dwell time also affects the sealing strength. Sufficient dwell time is necessary to guarantee the proper attainment of applied heat by the sealant material, however the required duration varies with magnitude of temperature applied. When the sealing temperature is below the melting point of the sealant material, increase in dwell time cannot enhance the sealing efficiency (Guo and Fan 2016). Therefore, optimal sealing temperature and dwell time is to be identified to achieve better sealing strength. For a laminate pouch casing consisting of polypropylene (PP, melting point: 160–165 °C) as innermost layer, and polyethylene terephthalate (PET, melting point: 240–250 °C) as outermost layer, the optimal sealing temperature and dwell time are reported to be 170 °C and 3 s, respectively (Malsen et al. 2008). Apart from the sealing temperature and dwell time, other two factors such as sufficient sealant layer thickness and external pressure during sealing are also necessary for ensuring high-quality sealing. High external pressure leads to improved contact between the heat seal layers and prevents deconsolidation during melting. Likewise, sealing strength increases with increase in thickness of sealant layer, though it increases the minimum heat-sealing temperature (Guo and Fan 2016).

4 Thermal Management in Pouch Cell

Electrochemical process in lithium-ion cells is usually accompanied with continuous and substantial amount of heat generation. Once accumulated, this will lead to sudden increase of cell temperature, which in turn accelerates many side reactions and ends up in inexorable catastrophes such as performance degradation, explosion etc. (Fan et al. 2013). Unlike the cells with hard casing, pouch cells are much more temperature sensitive and for the same reason if the heat generated from the cell is not properly dissipated, the cells may easily catch fire and hurt the user at a faster pace than the other battery envelops do. Therefore, to secure the battery operation and extend the battery life, the pouch package necessitates thermal management measures. Studies have shown that heat dissipation in pouch cells can effectively be done either by modifying the internal structural design (cell shape, tab configuration etc.) or by using external cooling systems (Kim et al. 2019; Kosch et al. 2017; Zhang et al. 2017).

Different tab arrangements lead to difference in current density, heat generation rate (HGR) and thermal resistances, which in turn results in different temperature distributions (Zhang et al. 2017). Any non-uniformity in the above mentioned parameters not only affects the safety characteristics of the battery but also ruin the electrochemical performance. For example, non-uniform current and temperature distribution will result in under-utilization of active materials, thereby decreasing its energy density and initiate localized aging. Figure 3 illustrates the effect of different tab positions on the current distribution in positive current collector and temperature

distribution in pouch cell. Uniform current and temperature distribution will take place when the tabs are placed on the middle of the top and the bottom side (battery B in Fig. 3). Therefore, this design can effectively dissipate the heat and thus easily lower the maximum temperature of the cell. Therefore, this configuration is identified to be most favorable thermal design for lithium ion pouch cell (Zhang et al. 2017; Song et al. 2018). When the tabs are put on the same side, maximum temperature increases and minimum temperature decreases. As a result, such arrangements may result in non-uniform temperature distribution and high surface temperature on pouch pack (Zhang et al. 2017). Apart from the tab configuration, tab dimension also plays a crucial role in controlling the battery temperature and thus safety of the whole battery. It is reported that the use of wider and thicker tab can considerably reduce the cell temperature due to low current density of the thicker tabs. Moreover, higher tab width can also lead to uniform distribution of current density, potential and temperature and thus can lead to more uniform utilization of the active material. All of these improvements can bring excellent output voltage and capacity of the cell (Samba et al. 2014). On the contrary, tab height has no significant role on the thermal behaviour of the battery. Too much tab height will also reduce the energy density of pouch cell (Mei et al. 2018).

Heat dissipation rate can also be accelerated by the utilization of external thermal management systems. Large surface area of pouch cells allows them to be easily impregnated with exterior battery management system (Hu et al. 2011). Different concept of cooling systems viz. phase change materials, liquid or fin cooling methods etc. have been designed and developed for pouch cell to ensure the operational safety without sacrificing the cell performance (Mei et al. 2018; Bai et al. 2019; Patil et al. 2018). Huo et al. suggested that the placement of a mini-channel cold plate on the surface of pouch cell as an ideal method to reduce the maximum temperature of the battery. Equidistantly distributed cooling channels along the width of aluminium cold plate permits the liquids to flow uninterruptedly over the surface of pouch cell and thereby maintaining temperatures of the pouch pack within the ideal ranges. The

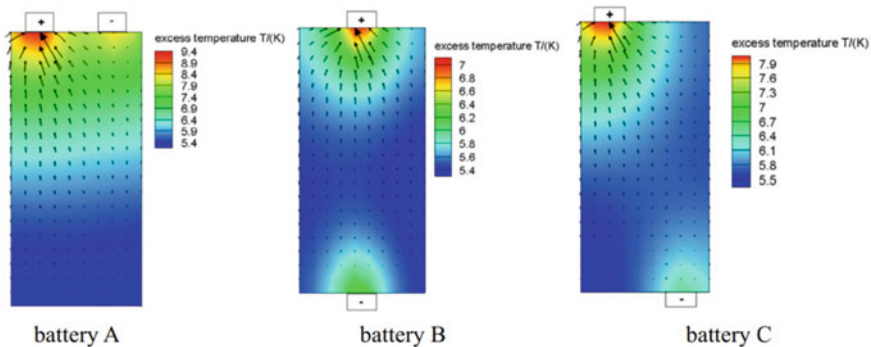


Fig. 3 Current distribution in positive current collector and temperature distribution in pouch cell with different tab design, at the last moment of discharge ($t = 3600$ s) at 1 C rate. (Reprinted with permission from Song et al. (2018), copyright (2018) © Elsevier Ltd.)

authors suggested that a more satisfactory result can be obtained when the number of cooling channels as well as inlet flow rate of the liquid increases. In addition, flow direction of the liquid also affects the performance of the cooling system; the best results were obtained when water was allowed to flow into the channels on the side of the electrodes (Huo et al. 2015). However, these techniques will add to additional price and make the battery system more complex. In contrast, a thermal management system with air cooling is less problematic. Recently, an air cooling system consisting of double silica cooling plate together with copper mesh is reported to have better heat dissipation and temperature steadiness in pouch battery, which is due to the desirable thermal conductivity of the copper mesh. In this set up, each pouch pack in the battery is covered with silica impregnated copper mesh and exposed to air source. Cooling effect was thoroughly studied by fixing different number of fans at different locations and observed that obvious improvement can be achieved only when two fans were placed at the face side of the battery rather than at other locations (Li et al. 2019). The major challenge arising out of the deployment of such cooling plates on the cell surface is the decrease in the specific energy and energy density due to the extra volume and weight of cooling accessories. Vortex generation technique is recently identified to be one of effective key solution for addressing the thermal concerns of battery where improvements in local heat transfer up to 460% as observed by other strategies, can be achieved. However, the performance varies with the shape of vortex generators. Among the different vortex generator geometries such as delta wing, delta winglet, rectangular rib and rectangular winglet, the one with delta winglet shape is seemed to be beneficial for the enhanced heat transfer rate. The vortices of the delta winglet enable mixing of cold and hot air between the top and bottom thermal layers effectively. Moreover, this particular geometry can considerably improve heat transfer in both upstream and downstream domain in an uninterrupted way (Xie et al. 2019).

Apart from the surface cooling, tab cooling techniques is also gaining attention in pouch thermal management. Recent work by Haunt et al. suggested that tab cooling of the pouch cell can extend the cell life up to three fold more than that being cooled by surface techniques. At higher discharge rates, the surface cooling cause uneven impedance and currents among the layers, which cause non-uniform ageing and reduction in usable capacity. However, when the cells are cooled via tabs, the capacity loss was negligible. The difference between the two types of cooling strategies originates from the way in which the thermal management system interacts with operation of batteries. In surface cooling, thermal gradient is perpendicular to the layers, while in tab cooling, it is in-plane with the layers and therefore leads to more homogenous temperature distribution (Hunt et al. 2016).

5 Failure Mode of Pouch Cell

Although sealed pouch cells present a light weight solution to the battery pack, it is easily vulnerable to certain kind of damages than cells enclosed in rigid metallic

cases. The major challenges associated with the pouch geometry are (1) volume expansion during charge–discharge cycle and (2) laminate corrosion. Gaseous products formed as a result of charge–discharge process or abusive condition leads to permanent swelling of the pouch cell and the structure changes to a pillow-shaped geometry (Bond et al. 2017) (https://batteryuniversity.com/learn/archive/pouch_cell_small_but_not_trouble_free). The gas formed not only reshape the pouch case but also initiate debonding process at the cohesive zones in the sealing part as shown in Fig. 4, especially when the pressure exerted by the gas surpass the critical value. In severe case, it results in the leakage of highly flammable electrolytes and gaseous reaction products and this could result in failure of the pouch cell (Chen et al. 2018). Another serious issue which is in conjunction with swelling includes the performance degradations such as capacity fade and efficiency decrease (Choi et al. 2018). The gases responsible for swelling also exert some pressure on the separator which leads to breakdown of the pores in separator resulting in lower Li^+ conductivity and higher heat generation. Increased temperature would further cause the decomposition of active material and electrolyte which lead to gas generation and subsequently to thermal runaway (Sarkar et al. 2019; Dube 2011). Further, during bulging, the electrode layers lose their contact with the separator layer, causing a rise in internal impedance. All of these scenarios eventually become a root cause for the degradation of cell performance and safety concerns (Bond et al. 2017). Also, volume expansion of the cell creates mechanical stresses on the device or equipment where they power and slowly damage them (Lee et al. 2004). In order to prevent the early failure of cells and the possible disastrous effects, provision must be given to alleviate the severe volume expansion when designing the battery compartment of the pouch cells.

Mitigation against this scenario can be done in different ways; primary remedy is the provision of compressive surface pressure (restraining) on the flat pouch surface.

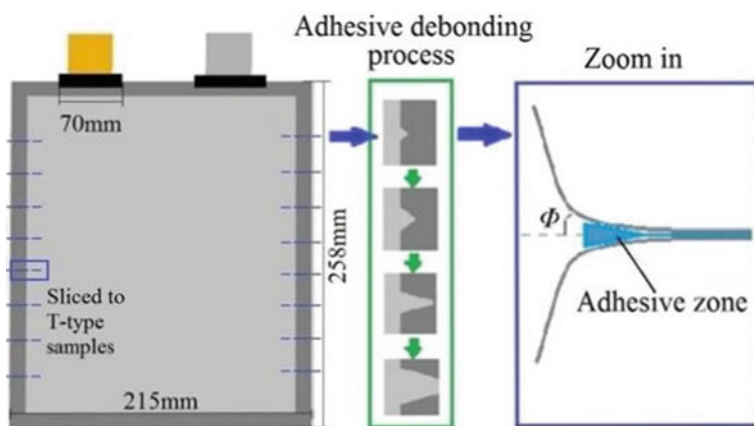


Fig. 4 Schematic of the debonding process of adhesive bonded interface in a pouch cell. (Reprinted with permission from Chen et al. (2018), copyright (2018) © Elsevier Ltd.)

Except external pressure, a pouch cell has no option to control its expansion, therefore restraining is indispensable in the cell level as well as in the battery module so as to deliver performance equivalent to lithium-ion cells that employ the metallic case. Restraining offers effective constraint to the surface of the cell and prevents delamination during charge–discharge process; thereby assuring improved cycle life (Wünsch et al. 2019; Choi et al. 2018; Dube 2011; Jeevarajan and Duffield 2014). Moreover, when the cells are clamped, any produced gas is pushed away from the electrode stack into the excess volume of the pouch. Therefore, the gas does not get much access to the electrode surfaces to initiate further side reactions with electrode surface (Aiken et al. 2014). In space application also restraining is a necessary criterion. Unlike the conventional lithium-ion pouch cells for terrestrial use, the same for space applications should have to cope with harsh environment of space. Due to the lack of external pressure, pouch cell based on aluminium foil are more likely to swell under vacuum conditions than in normal atmosphere. However, under restrained condition, the cell is not only capable to guarantee long term endurance but also become capable of withstanding all the challenges imposed by the sub-atmospheric space environments. The importance of restraining in pouch module is evidenced from experimental results of Judith et al. Their studies on the cycling performance of lithium-ion pouch cells under vacuum of 0.1 psi and restrained conditions observed that restrained cells can prevent the irreversible capacity loss approximately four fold better than unrestrained cells. After a continuous 30 cycles at 0.1 psi, restrained cells showed only 16.7% irreversible capacity loss while unrestrained cells showed 73% loss (Fig. 5) (Jeevarajan and Duffield 2014).

Even though restraining is a promising strategy against volume expansion, there will not be any additional improvement in the durability performance of battery cell when the constrained pressure is either above or below a certain level (Choi et al. 2018; Mussa et al. 2018). Higher pressure of stack hinders the kinetic and mass transport rate of electrochemical reactions (Mussa et al. 2018). Therefore, for assuring extended battery life it is necessary to optimize the restraining conditions. In one such

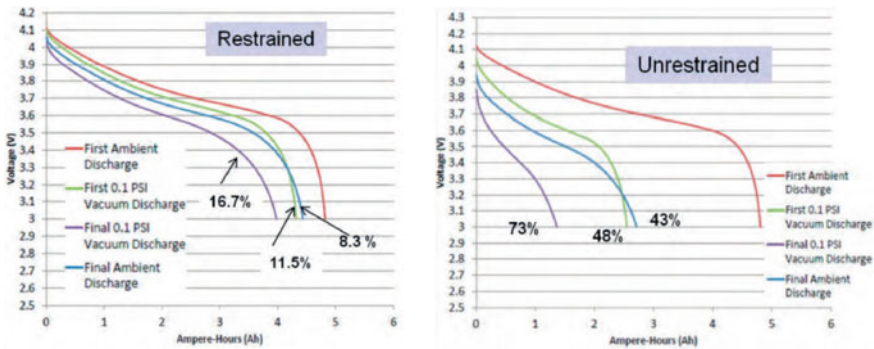


Fig. 5 Cycling performance of lithium-ion pouch cells under vacuum (0.1 psi) in unrestrained conditions and in restrained conditions. (Reprinted with permission from Jeevarajan and Duffield (2014), copyright (2014) © Elsevier Ltd.)

attempt, Choi et al. subjected a pouch cell to various restraining pressure and found that excessively high initial external pressure will induce a plastic deformation on the structure and steadily degrade the structural safety of the pouch cell. Therefore, the external pressure applied should be chosen at the minimum level of requirement so as to guarantee a satisfactory electrochemical performance of the pouch cell. Additionally, the authors observed that thickness of the cell varies during cycling and the amount of swelling is influenced by the magnitude of external pressure applied and the properties of the constraining structure. When there is no constrained pressure, severe increase in cell thickness and dramatic fading of capacity are observed due to delamination of layers. Therefore, to prevent layer delamination, a slight amount of external pressure (20 kPa) is advisable, however when the initial external pressure is increased to 40 kPa, the cell showed similar swelling behaviour as well as capacity fade tendency, as that of the cell kept under 20 kPa, until the end of life during the power cycle test, indicating the unnecessary of high restraining pressure i.e. pressure which is higher than a particular level cannot bring any additional improvement (Choi et al. 2018).

Apart from restraining, pouch cell for space applications can also be reinforced by replacing conventionally used aluminium laminate with stainless steel sandwiched trilayer laminate, because even in the unrestrained condition also, the latter neither swell nor lose their capacity during the charge/discharge cycles in vacuum and also show high tolerance to vibration and pyroshock experienced during launch time (Ooto et al. 2014). However, for terrestrial applications, aluminium laminate is preferable as it offers superior electrochemical performance under atmospheric condition than steel laminated one if it is restrained properly.

Some studies have shown that resin potting technique can also provide high tolerance in vacuum and therefore suggested for flight batteries. However, all the resins do not provide same level of protection against vacuum environment. Some studies have shown that polyurethane based resins can no longer prevent the pouch cells from being swelled up in vacuum while epoxy resins can. This is due to high permeability of polyurethane which causes electrolyte leakage and leads to premature deterioration. On the contrary, epoxy-based resin potted pouch cell showed improved rigidity and excellent charge–discharge cycle life performance and it was successfully used in a small scientific satellite called “REIMEI” (Hu et al. 2011).

Blending of control electrolyte with some additives is also identified to be a very effective strategy for suppressing the bulging tendency of pouch cell as it can control the parasitic reactions and can thus reduce or prevent the creation of gases during formation as well as subsequent cycles (Aiken et al. 2014). With the aid of Archimedes’ In Situ Gas Analyzer (AISGA), Aiken et al. measured and compared the volume of gas expelled from pouch cells containing different electrolyte additives such as vinylene carbonate (VC), 1,3-propane sultone (PS), succinonitrile (SN), lithium bis(oxalato) borate (LiBOB), prop-1-ene 1,3-sultone (PES) and fluoroethylene carbonate (FEC) or their combinations. The inference was that no other additives or additive combination can offer such a least gas formation in NMC/graphite pouch cell as effectively as a mixture of 2% VC + 2% PES does. However, when these

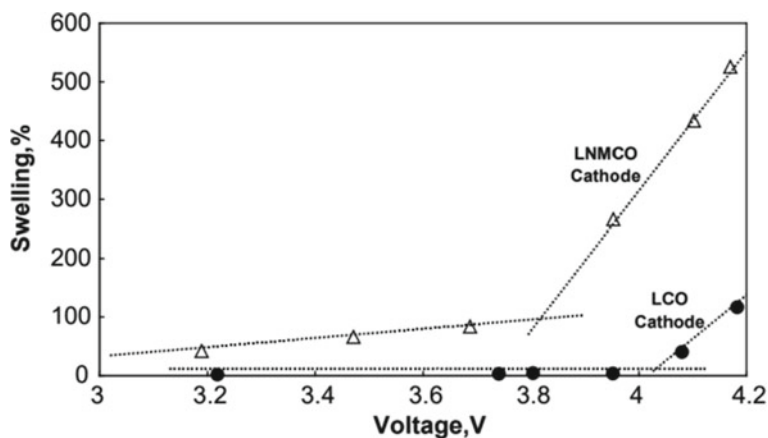


Fig. 6 Comparative study of the swelling of pouch cell with NMC-811 and LCO after 4 h storage test 90 °C as function of electrode potential. (Reprinted with permission from Lee et al. (2004), copyright (2004) © Elsevier)

additives are used alone, no satisfactory result could be observed (Aiken et al. 2014; Rieger et al. 2016; Xia et al. 2014).

Some additives like vinyl ethylene carbonate (VEC) and ethylene sulphite (ES) can delay the kinetics of gas production but cannot provide any kind of reduction in the gas volume (Aiken et al. 2014). Apart from VC and PES, some other additives such as Triazine-(BF₃)₃ (Aiken et al. 2014), LiPO₂F₂ (Ma et al. 2018) and lithium bis(fluorosulfonyl) imide (LiFSI) (Wang et al. 2015) are also reported to be better for NMC/Graphite pouch cells. The degree of swelling of pouch packaging can also be ameliorated by the proper selection of electrode materials. Some electrode materials, especially cathode materials are likely to accelerate the gas forming reaction even at a much lower voltage. For example LiNi_{0.8}Mn_{0.1}Co_{0.1}O₂ (NMC-811) cathode based pouch cell displays higher percentage of swelling than that of the LiCoO₂ (LCO) based pouch cell (Fig. 6). The latter shows SoC or voltage independent swelling behaviour and thus opens the possibility of such cells to be charged at a higher voltage without being swelled up (Lee et al. 2004).

6 Trend and Opportunities of Pouch Cell

Unlike the other enduringly popular cell designs such as cylindrical and prismatic cells, the pouch cells can easily be applied for various applications. The high design flexibility, high energy density, slimness and cost effectiveness of the pouch pack permits the manufacturers to produce sleek-looking gadgets with promising electrochemical performance at low cost. All these features have undoubtedly increased the market trend or the penetration rate of these soft pack batteries in the field of

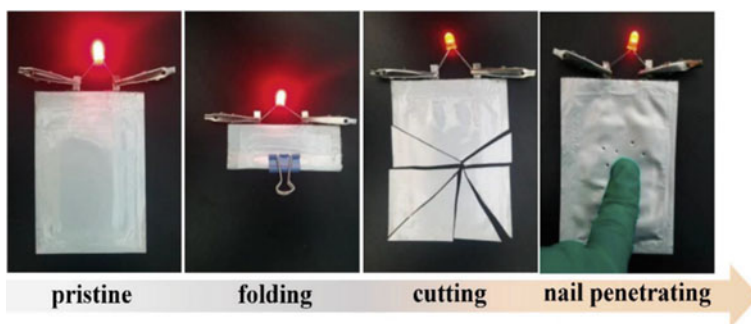


Fig. 7 Demonstration of solid-state Li metal pouch cell under bending conditions and working normally after being cut into many pieces and after nail test. (Reprinted with permission from Hu et al. (2020), copyright (2020) © Elsevier)

new energy storage systems. Additionally, the pouch packaging is suitable even for the most neonate and challenging areas such as all-solid-state batteries, metal air batteries and Li metal anode batteries (Yue et al. 2018; Lu et al. 2020; Gao et al. 2020; Jiang et al. 2020; Hu et al. 2020; Niu et al. 2019). As these are in the infancy state, many trials are still being pursued. The observations from pouch cells can directly guide the design of new battery technology for practical applications, as pouch pack provides larger current and capacity than coin cells (normally employed for R&D applications) and also offer a pressure-free environment during cycling (Shi et al. 2019). Moreover, the aforesaid battery technologies have demonstrated excellent electrochemical performance with pouch casing even under harsh conditions. In one such example Hu et al. showed that solid state Li pouch cell when subjected to devastating conditions such as cut into pieces, being folded, and nail penetrated, the cells could still exhibit high reliability, safety and performance similar to a pristine cell (Fig. 7) (Hu et al. 2020).

The outstanding packaging efficiency and geometric flexibility of pouch cells make them more attractive for space applications too, as these applications seek weight reduction in their module. Polymer pouch cell have been tested for some spacesuit applications (Darcy 2007). Due to the flexibility, it can be easily configured into the small and miniature spacecrafts. In 2005, pouch cell powered small scientific piggyback satellite “REIMEI” (Fig. 8) was launched by the Dnepr rocket into a nearly sun synchronous polar orbit and it was orbiting around the earth till 2018 (Hu et al. 2011). Lithium-ion pouch cells are also used in wearable devices, smartphones, speakers and electric vehicles.

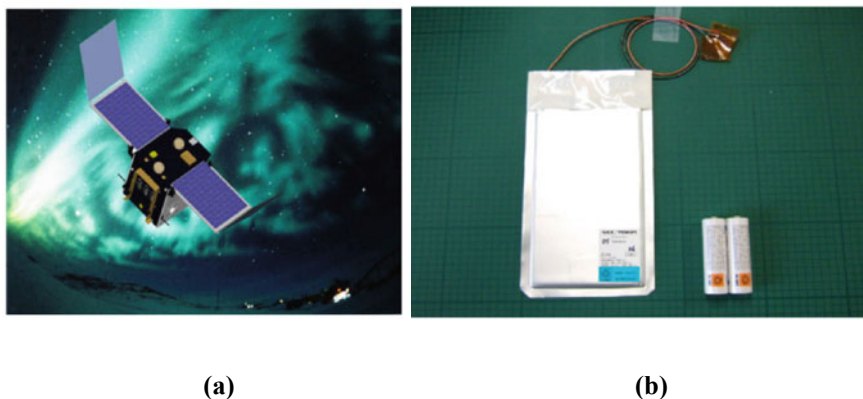


Fig. 8 **a** Image of “REIMEI” and **b** pouch cell used for the “REIMEI”. (Reprinted with permission from Hu et al. (2011), copyright (2011) © Elsevier)

7 Summary

Pouch type lithium-ion batteries are a class of thin battery technology which have now been a popular choice for the battery manufacturers on account of their light weight, high energy density and cost effectiveness over the cells contained in metal cans. It can be fabricated in any shape and size according to the design requirement and thus it can easily conform to the shape of the device they power; assuring high packaging efficiency of the battery. It can easily cope with any type of battery technology such as solid state batteries, metal air batteries, Li metal batteries etc. However, due to the low mechanical stability of the pack, their characteristics are strongly affected by environmental conditions. They are more vulnerable to swell or change their shape in response to the pressure exerted by the gaseous by-products and the magnitude of external pressure felt over the pouch surface. Inflated cell gradually become poor in electrochemical performance and also damage the gadgets which they power. However, by adopting suitable design modifications, the pouch technology can be successfully implemented in ground as well as in space applications.

Acknowledgements The authors thank Director, VSSC for granting permission to publish this chapter.

References

Aiken CP, Xia J, Wang DY, Stevens DA, Trussler S, Dahn JR (2014) An apparatus for the study of in situ gas evolution in Li-Ion pouch cells. *J Electrochem Soc* 161:A1548–A1554

- Bai F, Chen M, Song W, Yu Q, Li Y, Feng Z, Ding Y (2019) Investigation of thermal management for lithium-ion pouch battery module based on phase change slurry and mini channel cooling plate. *Energy* 167:561–574
- Bond T, Zhou J, Cutler J (2017) electrode stack geometry changes during gas evolution in pouch-cell-type lithium ion batteries. *J Electrochem Soc* 164:A6158–A6162
- Bowles PG, Eweka, EI, Giwa CO, Ritichie AG (2009) Pouch cell construction. US Patent US 7,629,077 B2, assigned to Qinetiq Limited
- Chen Y, Liu Y, Gong W, Zhang B (2018) Sealing life prediction of Li-ion pouch cell under uncertainties using a CZM-based degradation model. *Int J Adhes Adhes* 84:378–386
- Choi YH, Lim HK, Seo JH, Shin WJ, Choi JH, Park JH (2018) Development of standardized battery pack for next-generation phev's in considering the effect of external pressure on lithium-ion pouch cells. *SAE Inter J Alter Power* 7(3):195–206
- Dai F, Xiao Q, Yang L, Cai M, Zeng SH (2020) Making a pouch format cell and attaching a tab to the electrode. US Patent 10629941B2, assigned to GM global technology operation
- Darcy E (2007) Screening Li-ion batteries for internal shorts. *J Power Sources* 174:575–578
- Du S, Jia M, Cheng Y, Tang Y, Zhang H, Ai L, Zhang K, Lai Y (2015) Study on the thermal behaviors of power lithium iron phosphate (LFP) aluminum-laminated battery with different tab configurations. *Int J Therm Sci* 89:327–336
- Dube WP (2011) Expanadable battery pack containment device for pouch battery cells. US Patent 2011/0177377 A1, assigned to Boulder Electric Vehicle
- Fan L, Khodadadi JM, Pesaran AA (2013) A parametric study on thermal management of an air-cooled lithium-ion battery module for plug-in hybrid electric vehicles. *J Power Sources* 238:301–312
- Gao KN, Wang HR, He MH, Li YQ, Cui ZH, Mao Y, Zhang T (2020) Interfacial integration and roll forming of quasi-solid-state Li–O₂ battery through solidification and gelation of ionic liquid. *J Power Sources* 463:228179
- Guo Z, Fan Y (2016) Heat seal properties of polymer-aluminum-polymer composite films for application in pouch lithium-ion battery. *RSC Adv* 6:8971–8979
https://batteryuniversity.com/learn/archive/pouch_cell_small_but_not_trouble_free
- Hu J, He P, Zhang B, Wang B, Fan LZ (2011) Development and on-orbit operation of lithium-ion pouch battery for small scientific satellite 'REIMEI.' *J Power Sources* 196:8755–8763
- Hu J, He P, Zhang B, Wang B, Fan LZ (2020) Porous film host-derived 3D composite polymer electrolyte for high-voltage solid state lithium batteries. *Energy Storage Mater* 26:283–289
- Hunt IA, Zhao Y, Patel Y, Offer J (2016) Surface cooling causes accelerated degradation compared to tab cooling for lithium-ion pouch cells. *J Electrochem Soc* 163:A1846–A1852
- Huo Y, Rao Z, Liu X, Zhao J (2015) Investigation of power battery thermal management by using mini-channel cold plate. *Energy Convers Manag* 89:387–395
- Jacobs JK, Dasgupta S (2001) Lithium battery structure incorporating lithium pouch cells. US Patent 6,296,967 B1, Electrofuel Inc
- Jeevarajan JA, Duffield BE (2014) Performance and safety of lithium-ion polymer pouch cells. *J Sp Saf Eng* 1:10–16
- Jiang T, He P, Wang G, Shen Y, Nan CW, Fan LZ (2020) Solvent-free synthesis of thin, flexible, nonflammable garnet-based composite solid electrolyte for all-solid-state lithium batteries. *Adv Energy Mater* 10:1–10
- John B, Cheruvally G (2017) Polymeric materials for lithium-ion cells. *Polym Adv Technol* 28:1528–1538
- John B, Sandhya CP, Gouri C (2018) The role of nanosized materials in lithium ion batteries. *Nanomater: Phys, Chem, Biol Appl* 18
- Kepler KD, Vermeulen R, Hailey P, Larson A (2014) Li-ion pouch cell and a cell module. US Patent 2014/0205882 A1, assigned to Farasis Energy, Inc
- Kim H-K, Choi JH, Lee K-J (2019) A numerical study of the effects of cell formats on the cycle life of lithium ion batteries. *J Electrochem Soc* 166:A1769–A1778

- Kim CS, Lee HY, Cho MH, Kang SB (2013) Pouch-type battery with improved safety by coating sealing unit with flame retardant and heat resistant resin composition prepared by mixing flame retardant material and heat resistant material to thermoplastic resin or thermosetting resin and production method thereof. US Patent 2013/0071696A1, assigned to EIG LTD
- Kim J, Lee H, Kim C, Oh J (2015) Pouch-type battery and method of assembling for the same. US Patent US 8,936,653 B2, assigned to Samsung SDI Co., Ltd
- Kim JH (2007) Pouch type lithium secondary battery. US Patent 7201998B2, assigned to Samsung SDI Co., Ltd
- Kosch S, Rheinfeld A, Erhard SV, Jossen A (2017) An extended polarization model to study the influence of current collector geometry of large-format lithium-ion pouch cells. *J Power Sources* 342:666–676
- Lee KH, Song EH, Lee JY, Jung BH, Lim HS (2004) Mechanism of gas build-up in a Li-ion cell at elevated temperature. *J Power Sources* 132:201–205
- Li X, He F, Zhang G, Huang Q, Zhou D (2019) Experiment and simulation for pouch battery with silica cooling plates and copper mesh based air cooling thermal management system. *Appl Therm Eng* 146:866–880
- Lu J, Zhou J, Chen R, Fang F, Nie K, Qi W, Zhang JN, Yang R, Yu X, Li H, Chen L (2020) 4.2 V poly(ethylene oxide)-based all-solid-state lithium batteries with superior cycle and safety performance. *Energy Storage Mater.* <https://doi.org/10.1016/j.ensm.2020.07.026>
- Ma L, Ellis L, Glazier SL, Ma X, Liu Q, Li J, Dahn JR (2018) LiPO₂F₂ as an electrolyte additive in Li[Ni_{0.5}Mn_{0.3}Co_{0.2}]O₂/graphite pouch cells. *J Electrochem Soc* 165:A891–A899
- Malsen Jv, Tenpierik MJ, Looman RHJ, Cauberg JJM (2008) Heat seal strength of barrier films used in vacuum insulation panels at room temperature and at–130°C. *J Plast Film Sheeting* 24:35–52
- Mei W, Chen H, Sun J, Wang Q (2018) Numerical study on tab dimension optimization of lithium-ion battery from the thermal safety perspective. *Appl Therm Eng* 142:148–165
- Murashko K, Pyrh J (2013) Three-Dimensional Thermal Model of a Lithium Ion Battery for Hybrid Mobile Working Machines: Determination of the Model Parameters in a Pouch. *Cell* 28:335–343
- Mussa AS, Klett M, Lindbergh G, Lindström RW (2018) Effects of external pressure on the performance and ageing of single-layer lithium-ion pouch cells. *J Power Sources* 385:18–26
- Nie M, Xia J, Ma L, Dahn JR (2015) A comparative study of pyridine-boron trifluoride, Pyrazine-(BF₃)₂ and Triazine-(BF₃)₃ as electrolyte additives for lithium-ion cells. *J Electrochem Soc* 162:A2066–A2074
- Niu C, Lee H, Chen S, Li Q, Du J, Xu W, Zhang JG, Whittingham MS, Xiao J, Liu J (2019) High-energy lithium metal pouch cells with limited anode swelling and long stable cycles. *Nat Energy* 4:551–559
- Ooto H, Koide K, Ohira K, Yamamoto M, Abe H, Toyota H, Shimada T, Takahashi Y, Hirose K (2014) Development of stainless steel laminate li-ion pouch cells. *Eur Sp Power Conf* 2–6
- Patil MS, Panchal S, Kim N, Lee MY (2018) Cooling performance characteristics of 20 Ah lithium-ion pouch cell with cold plates along both surfaces. *Energies* 11
- Rieger B, Schlueter S, Erhard SV, Schmalz J, Reinhart G, Jossen A (2016) Multi-scale investigation of thickness changes in a commercial pouch type lithium-ion battery. *J Energy Storage* 6:213–221
- Salini PS, Gopinadh SV, Kalpakasseri A, John B, Mercy TD (2020) Toward greener and sustainable Li-ion cells: an overview of aqueous-based binder systems. *ACS Sustain Chem Eng* 8:4003–4025
- Samba A, Omar N, Gualous H, Capron O, Van den Bossche P, Van Mierlo J (2014) Impact of tab location on large format lithium-ion pouch cell based on fully coupled tree-dimensional electrochemical-thermal modeling. *Electrochim Acta* 147:319–329
- Sarkar A, Shrotriya P, Chandra A (2019) Modeling of separator failure in lithium-ion pouch cells under compression. *J Power Sources* 435:226756
- Shi P, Cheng XB, Li T, Zhang R, Liu H, Yan C, Zhang XQ, Huang JQ, Zhang Q (2019) Electrochemical diagram of an ultrathin lithium metal anode in pouch cells. *Adv Mater* 31:1–8
- Song W, Chen M, Bai F, Lin S, Chen Y, Feng Z (2018) Non-uniform effect on the thermal/aging performance of lithium-ion pouch battery. *Appl Therm Eng* 128:1165–1174

- Tagawa K, Brodd RJ (2009) Production processes for fabrication of lithium-ion batteries. In: Yoshio M, Brodd RJ, Kozawa A (eds) *Lithium-ion batteries*. Springer, New York, NY. https://doi.org/10.1007/978-0-387-34445-4_8.
- Vamsi A, Ansari JN, Sundaresan MK, Chitaranjan PA, John B, Samridh A, Mercy TD (2021) Structural design and testing of pouch cells. *J Ener Sys* 5(2):80–91
- Wang DY, Xiao A, Wells L, Dahn JR (2015) Effect of mixtures of lithium hexafluorophosphate (LiPF₆) and lithium bis(fluorosulfonyl)imide (LiFSI) as salts in Li[Ni_{1/3}Mn_{1/3}Co_{1/3}]O₂/Graphite Pouch Cells. *J Electrochem Soc* 162:A169–A175
- Wünsch M, Kaufman J, Uwe D (2019) Investigation of the influence of different bracing of automotive pouch cells on cyclic lifetime and impedance spectra. *J Energy Storage* 21:149–155
- Xia J, Ma L, Aiken CP, Nelson KJ, Chen LP, Dahn JR (2014) Comparative study on prop-1-ene-1,3-sultone and vinylene carbonate as electrolyte additives for Li(Ni_{1/3}Mn_{1/3}Co_{1/3})O₂/graphite pouch cells. *J Electrochem Soc* 161:A1634–A1641
- Xie J, Xie Y, Yuan C (2019) Numerical study of heat transfer enhancement using vortex generator for thermal management of lithium ion battery. *Int J Heat Mass Transf* 129:1184–1193
- Yue H, Li J, Wang Q, Li C, Zhang J, Li Q, Li X, Zhang H, Yang S (2018) Sandwich-like poly(propylene carbonate)-based electrolyte for ambient-temperature solid-state lithium ion batteries. *ACS Sustain Chem Eng* 6:268–274
- Zeng F, Chen J, Yang F, Kang J, Cao Y, Xiang M (2018) Effects of polypropylene orientation on mechanical and heat seal properties of polymer-aluminum-polymer composite films for pouch lithium-ion batteries. *Materials* 11(1):144
- Zhang X, Chang X, Shen Y, Xiang Y (2017) Electrochemical-electrical-thermal modeling of a pouch-type lithium ion battery: An application to optimize temperature distribution. *J Energy Storage* 11:249–257

An Overview of Polymer Based Electrolytes for Li-Ion Battery Applications



Soumya Ravi and M. K. Jayaraj

1 Introduction

Li-Ion batteries (LIBs) have become an indispensable part of our daily power requirements enabling the use of wide range of mobile electronic devices and tools. Electrolytes serve as key components in Li-Ion battery technology as they are vital in making the electronic devices conductive by permitting the transport of ions from cathode to anode upon charging and reverse process during discharge. In LIBs, electrolytes undertakes the role of a medium that enables hassle free movement of Li-Ions back and forth between the cathode and anode and hence should possess high ionic conductivity. The basic components of an electrolyte in a battery include soluble salts, acids or other bases in liquid, gelled and dry forms.

The electrolytes used currently in batteries are the outcome of many years of research and development and play a significant role in providing good performance for various applications. Significant innovations in battery chemistry and technology is the need of the hour to cater to the novel challenges in energy storage requirements for hybrid electric vehicles, power tools and stand-by power sources for communications and modern aircrafts. The batteries looked-for require higher voltages and higher energy content. Moreover, they are prone to exposure to extremes of temperature with the requisite of providing long cycle, storage life and assured user safety. A new class of electrolytes is essential to cater to these requirements. The emerging electrolytes are not only expected to impart good ionic conduction over a wide range of ambient temperatures but also cater to the need of superior chemical stability and compatibility with the more reactive electrode materials in

S. Ravi (✉)

Centre of Excellence in Advanced Materials, Cochin University of Science and Technology,
Kochi, Kerala, India

e-mail: svravi88@cusat.ac.in

M. K. Jayaraj

University of Calicut, Thenjipalam, Malappuram, Kerala, India

order to realize higher battery-specific energy and power. Considering these factors, research and technology is favoring the use of high specific energy electrode materials, such as layer–layer composite, layer–spinel composites made of $\text{Li}[\text{Co}, \text{Ni}, \text{Mn}]\text{O}_2$ (Mizushima et al. 1980; Rougier et al. 1996; Hy et al. 2014), layer-olivine phosphates like LiCoPO_4 (Lloris et al. 2002) having specific capacity in the range of 250–300 mAh/g in comparison to 140 mAh/g for LiCoO_2 cathodes. There is also demand for higher capacity Li alloy-based anodes such as Li–Sn (Xu et al. 2013) and Li–Si (Ryou et al. 2013) alloys. The present state-of-art electrolytes based on lithium hexafluorophosphate (LiPF_6) dissolved in linear and cyclic carbonate solvent mixtures with functional additives have turned out to be insufficient in these new higher energy density electrochemical systems and no compromise over capacity or power could be thought about (Xu 2004). A step further ahead, researchers began utilizing sulfur or air as an even higher theoretical capacity cathode pairing with pure Li as an anode to achieve even higher energy density. The need of compatible electrolytes is inevitable for developing such higher energy density systems. Hence the development and usage of new electrolytes will depend on their compatibility with the as mentioned electrode materials which in effect count on a proper understanding of electrolytes and their interaction with the electrodes.

Most of the electrolytes in Li based batteries employ aprotic or non-aqueous organic carbonate solvents like Ethylene Carbonate (EC) in which Li salts are dissolved. Other electrolyte systems make use of lithium salts dissolved in ionic liquids (IL), solids/ceramics, polymers, and aqueous based systems which have their own merits but what limits their utilization to an extent are their lower ionic conductivities, higher production costs, safety and toxicity concerns (Aurbach 1999; Henderson 2014; Gores et al. 2011).

2 Electrolyte Properties

Early research on electrolytes used in Li-Ion batteries (LIBs) relied mainly on Li salts with few anions such as hexafluoroarsenate (AsF_6^-), perchlorate (ClO_4^-), hexafluorophosphate (PF_6^-), tetrafluoroborate (BF_4^-) and trifluoromethanesulfonate or triflate (Tf) (CF_3SO_3^-) (Fig. 1) (Pistoia 1971; Desjardins et al. 1985; Besenhard and Eichinger 1976; Koch 1981). Most of these anions were initially used based on the understanding of their ability to generate strong superacids which are considered to be stronger than sulfuric acid (Olah et al. 2009). The stronger the acidity, the weaker the coordination of the anions with the associated protons (H^+ cations). Therefore the ionic association tendency of anions to coordinate Li^+ cations will be more resulting in the replacement of the acid protons with Li^+ cations giving rise to the corresponding lithium salts (Koppel et al. 1994; Barthel et al. 1996). With more advancement in LIB technology, lithium salts like LiAsF_6 and LiClO_4 became less popular due to safety and toxicity issues. It was also found that the electrolytes made from LiTf suffered from low conductivity issues. Gradually with the advent of graphite anodes and commercialization of LIBs, LiPF_6 and LiBF_4 dissolved in

aprotic solvents like EC or dimethylene carbonate (DMC), became more popular with ultimately LiPF_6 gaining prominence as the most widely used Li salt in electrolytes (Huang et al. 1994; Johansson 2007; Dudley et al. 1991). In fact it is not the best candidate in any of its properties of paramount importance to batteries like: ionic conductivity-relatively good, hygroscopic, thermal stability-somewhat poor but its success as the most dominant salt arises from the fact that it strikes the best balance of these properties and enables the formation of an appropriate Solid Electrolyte Interface (SEI) along with solvents such as EC or DMC developed on the graphite anode in addition to a suitable protective layer formed on the aluminum cathode current collector. The use of LiBF_4 is also common since it operates well in LIBs at extreme temperatures (-20 – 80 °C) but exhibits only moderate conductivity (Takami et al. 2002; Zhang et al. 2003). All this clearly indicates the intricacies of the criteria to be fulfilled by the Li salt with regard to the several components of the cell (Andersson et al. 2002).

Electrolyte in LIBs must fulfill an extensive and challenging range of properties some of these as listed below.

I. Solubility. A reasonably high lithium salt solubility in the electrolyte solvents is a prerequisite to provide adequate charge carriers for rapid ionic conduction, as well as to prevent precipitation. It is vital to differentiate the solubility of salt from crystalline solvate formation. A salt may be readily soluble, but also leads to a crystalline solvate phase with a high melting point (T_m) giving rise to the solvates formed in the electrolyte which gradually extracts the salt from the electrolyte solution affecting the conductivity to drop. This becomes more evident in the case of cell operation at lower temperatures (Younesi et al. 2015). The Li dissolution in non-aqueous solvents, occurs through solvent- Li^+ interfaces (Scheers et al. 2010). The interaction of solvent

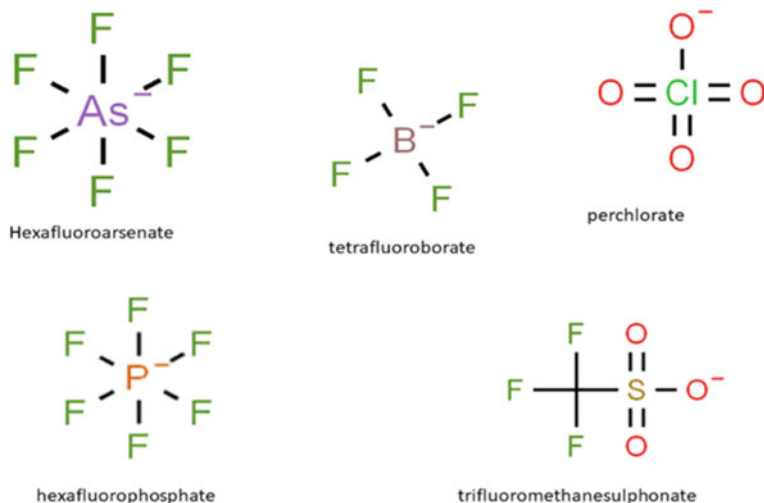


Fig. 1 Chemical structures of anions commonly used in electrolyte

and Li^+ involves two processes; (i) Li^+ gets dissociated from the anion, overcoming the lattice energy of the salt and (ii) coordination bonds between Li^+ ions and the electron-lone pairs of the solvent molecules are subsequently formed. The extent of Li^+ –anion interaction is extremely crucial besides solvent properties like viscosity and polarity. A strong cation–anion interactions lead to high lattice energies resulting in poor solubility of the salts in relevant aprotic solvents which is why many simple salts like Li_2O , LiF , LiCl etc. are restricted from electrolyte usage. Li salts like triflates made of weakly coordinating anions (WCA) to reduce Li^+ –anion interaction are also preferred. They are developed through delocalization of negative charge over the whole anion via electron-drawing substituents like $-\text{F}$ or $-\text{CF}_3$ (Johansson et al. 2004).

II. Ionic Conductivity. A high Li^+ cation transport rate is crucial for high power output as the Li^+ cation mobility within the bulk electrolyte often serves as one of the main sources of impedance for the battery. The selection of a lithium salt's anion is an influencing factor that determines the electrolyte's conductivity. This is due to the variations in the Li^+ cation solvation and ionic association interactions due to the differences in anion structure and coordination strength. Although electrolyte conductivity is the paramount parameter to be considered, it is actually the Li^+ cation mobility that is calculated from the product of the total ionic conductivity and Li^+ cation transference or transport number (i.e., T_{Li^+} , t_{Li^+}). This value tells about the measure of the fraction of the current contributed by the Li^+ . It is estimated to be less than 0.5 in non-aqueous electrolytes from impedance measurements. The electrolyte conductivity increases as a function of salt concentration with increase in solvation of Li salt in solvent as the number of charge carriers increases. Based on Stokes–Einstein equation, the ionic conductivity of liquid electrolytes depends on the dissociation of ions in the solvents and could be improved by enhancing the ion-dissociation in solvents with high dielectric constant and low viscosity.

$$D = \frac{kT}{6\pi\eta R} \quad (1)$$

where D = Diffusion coefficient, η = solvent viscosity, k = Boltzman Coefficient, T = Temperature, R = solute radius. In totality, the conductivity of any aprotic/nonaqueous Li-salt based electrolyte depends on the salt concentration, anion, solvent composition and the temperature. For instance, the conductivity of LiClO_4 in propylene carbonate (PC) attains a maximum value of 1.5 mS cm^{-1} at a low salt concentration of 0.08 M, with further increase in the concentration results in a drop in the conductivity. The same conductivity of 15 mS cm^{-1} is achieved in a solvent combination of EC/PC at a salt concentration of 1 M (Chen et al. 2000).

III. SEI Formation. The SEI refers to a passivation layer formed at the interface between the electrode surface and the electrolyte when the both electrolyte components and electrode material(s) degrade or react (Zaghib et al. 1995). Only a limited amount of materials is expected to react, with the as formed SEI layer restricting further electrode–electrolyte reactions and aiding the smooth movement

of Li^+ cations within the electrolytes and electrodes offering low impedance. The lithium salt(s), whether as a bulk salt or an additive, can considerably influence the SEI's components properties, and stability (Ryou et al. 2012). The popularity of graphite anode relies on the formation of this SEI which acts as a barrier for electron transfer between anode and the electrolyte resulting in kinetic stability of the cell and prevents exfoliation that occurs due to solvent intercalation during cycling.

IV. Stability. Electrolytes must, in general, be stable in the sense that it has to be non-reactive with all other cell components within the electrochemical potential window for the battery charge/discharge reactions (Lee et al. 2005). Electrolytes also need to be stable at extremes of temperatures, to deliver thousands of charge/discharge cycles with low capacity fading. From a thermodynamic stability point of view, battery should contain an electrochemical stability window (ESW), located beyond the oxidation and reduction potential window of the cathode and anode respectively. The difference between the LUMO and HOMO of the electrolyte defines the theoretical ESW which is determined by the coordination between Li-salt and solvent. ESW is strongly temperature dependent with even a slight increase in temperature, in some cases, resulting in a significant decrease in stability (Zheng et al. 2005). The electrolyte need to be stable in contact with the reaction products developed during cycling. This is mostly relevant in the case of Li-S, Li-O₂ in which new reaction species or intermediate products are formed in each discharge cycle which can degrade the electrolyte and cause battery failure unlike in conventional LIBs based on intercalation electrodes. Many F-containing anions hydrolyze upon exposure to water, specifically at elevated temperatures giving rise to the formation of HF which can degrade the electrolyte and also cause serious safety concerns. This leads to additional costs associated with the salt's synthesis, storage, and handling. The formation of HF could strongly impact the cycling behavior and lifetime of batteries when performed at high temperature and/or at high potential windows (>4.8 V versus Li/Li⁺) (Lux et al. 2012).

V. Donor Number. For any battery electrolyte, Guttmann Donor number (DN) (Gutmann 1976), is an often used quantitative measure for solvents showing their electron donating properties and hence ability to interact with acceptors such as protons, Li^+ and other cations thereby solvating them. The higher DN, the higher basicity of the solvent resulting in stronger interaction with Li^+ and hence most anions have relatively small DN. For instance, the DN for the PF_6^- and AsF_6^- is 2.5 with tetrabutyl ammonium (TBA^+) as the counter cation in PC at 25 °C measured using a solvatochromic method while that of ClO_4^- is 8.4 under the same conditions. This is one of the reasons for lesser solubility of ClO_4^- in PC compared to PF_6^- . In recent studies, DN is found to be significant in the case of Li-O₂ batteries where it is found to influence the, discharge reaction pathways and the capacity of the cells (Jeong et al. 2008). In the case of Li-S cells, it influences the solubility of the intermediate polysulphide species formed in every discharge cycle (Suo et al. 2013).

2.1 Conventional Non-Aqueous Liquid Electrolytes

The electrolyte system in any battery system assumes the role of a medium for the transport of ions between the pair of electrodes. As discussed in the previous section, vast majority of the electrolytes used in secondary batteries is made up of electrolytic solutes (salts) dissolved in organic liquids operating in the service temperature range. Being sandwiched in between the electrodes and in close interaction with them, this interface between electrolyte and electrodes direct the performance of a battery system. In batteries, the chemical behavior of the cathode and anode determines the energy output whereas the electrolyte controls the rate of mass flow within the battery and tells us how fast the energy could be released. All the Faradaic processes happen at the electrodes and no net chemical change should occur to the electrolyte during the operation of the battery. A typical non-aqueous liquid electrolyte used in rechargeable lithium make use of LiPF_6 dissolved in a mixture of ethylene carbonate (EC)/propylene carbonate and linear carbonates like dimethyl carbonate (DMC), diethyl carbonate (DEC) (Tarascon and Guyomard 1994). A mixture of two or more solvents is preferred over single solvent formulation primarily because individual formulation often does not alone meet the diverse and contradictory requirement of battery operation. Hence solvents with varied chemical and physical properties are used together to perform various functions simultaneously. A mixture of salts is however not used since anion choice is limited and performance improvement is not readily demonstrated. An ideal electrolyte solvent must adhere to the following criteria:

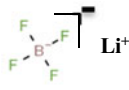

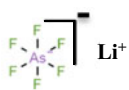
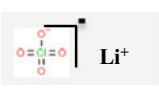
- It should have a high dielectric constant and dissolve sufficient concentration of salts.
- Possess low viscosity (η) to facilitate smooth ion transport.
- Remain inert to all cell components especially the charged surface of cathode and anode during cell operation.
- Should have a low melting point (T_m) and high boiling point (T_b) and remain liquid over a wide range of temperature. The flash point also needs to be high (T_f) so that it remains safe.

The use of a non-aqueous solvent that has active protons and solvate lithium salts quite efficiently is often ruled out because the strongly reducing anode and strongly oxidizing cathode which initiates the reduction of proton and the oxidation of the corresponding anions fall within 2.0–4.0 V versus Li whereas the charged potential of the cathode and anode in rechargeable lithium devices ranges between 3.0–4.5 V and 0.0–0.2 V respectively. Hence solvents with polar groups which have sufficiently good solvation like carbonyl ($\text{C}=\text{O}$), nitrile ($\text{C}=\text{N}$), sulfonyl ($\text{S}=\text{O}$) and ether linkage ($-\text{O}-$) are conventionally considered (Fry 1989).

The interest in alkyl carbonates as solvents gained prominence with development in Li-ion batteries. Propylene carbonate (PC) with its high anodic stability made it a promising solvent in first generation of commercial Li-ion cells with LiCo_xO_2 as

cathode and petroleum coke as anode (Harris 1958). However, EC with its high dielectric constant and low viscosity brought the real renaissance in using alkyl carbonates as lithium electrolyte solvents since it was understood that it could not only improve the bulk ionic conductivity but also interfacial properties like less polarization on various cathode surfaces (Surampudi et al. 1993). EC assumed a unique place in electrolyte system when Dahn et al. in 1990 studied the fundamental difference between the two on how they affected the reversibility of Li-Ion intercalation/deintercalation on graphite anodes. EC was found to be more effective in the formation of an effective SEI on graphite anode that prevented further electrolyte decomposition on the electrode. On the other hand, with PC co-intercalation, the graphite anode eventually exfoliated and disintegrated. PC was also found to favor the formation of Li dendrite like structures via its reaction with Li and caused non uniformity on Li surface. This gradually resulted in the formation of Li crystals which are isolated from the lithium anode during the discharge processes. These dendrites as well as isolated lithium crystals react with the solvent and cause serious safety hazards and internal shorts (Dahn et al. 1991). The first commercialized rechargeable lithium battery used a combination of EC/PC mixture as the solvent in which LiPF_6 was dissolved. Attempts to use ethers as solvents did not gain much momentum as they were unstable against oxidation caused on the surface of the charged cathode. It was realized that the electrolyte must have a oxidative stability up to ~ 5 V vs Li for a Li-Ion cell that uses graphite as anode and LiMO_2 metal oxides as cathode (4 V), the. In order to achieve this, the use of a linear carbonate, dimethyl carbonate (DMC) as cosolvent with EC was formulated (Guyomard and Tarascon 1993). Linear carbonates can form homogenous mixture with EC at any ratio and the resultant mixed electrolytes take the synergistic advantages of both solvents like high anodic stability of EC on cathode surfaces, high lithium solvation of EC, melting temperature suppression of EC, low viscosity, hence better ion transport and high ionic conductivity of DMC are imparted to the resultant electrolyte. Such a mixture of solvents also benefit from high electrochemical stability window: it remains stable up to 5 V on a spinel cathode. Other linear carbonates like diethyl carbonate (DEC), ethylmethyl carbonate (EMC), propylmethyl carbonate (PMC) etc. were also used. These mixture of solvents made of EC and linear carbonates with LiPF_6 emerged as state of art electrolyte in Li-Ion cells (Ein-Eli et al. 1996; Chu et al. 1997; Koetschau et al. 1995). Another interesting way of improving the electrolyte performance was by the introduction of fluorine atoms into the solvent molecules. Fluorinated organic solvents exhibit different physical properties compared to commonly used organic solvents due to the high electronegativity, superior ionic potential and poor polarizability of the fluorine atom. In truth, partially a fluorinated organic solvent demonstrates high polarity compared to perfluoro-organic solvents. Direct fluorination of EC and PC were carried out and improvement in the cycling efficiency was obtained (McMillan et al. 1999). Since fluorine was involved in the process, there were concerns regarding the formation of HF and subsequent safety hazards which limited their usage in practical application. Table 1 mentions the various Li salts and their conductivities in commonly employed solvents.

Table 1 Different Li salts, their decomposition temperatures and ionic conductivity in commonly used organic solvents PC and EC/DMC used in LIBs

Salt	Structure	M. wt.	T _m /°C	T _{decomp} /°C	σ/mS cm ⁻¹ (1 M, 25 °C)	
					PC	EC/DMC
LiBF ₄		-93.9	293	>100	3.4	4.9
LiPF ₆		151.9	200	~80	5.8	10.7
LiAsF ₆		195.9	340	>100	5.7	11.1
LiClO ₄		106.4	234	>100	5.6	8.4
Li Imide	LiN(CF ₃ SO ₂) ₂	286.9	234	>100	5.1	9.0

2.2 Characteristics of High Voltage Electrode–Electrolyte Interface

LIBs always seek improvement in the energy and power density, cycle life and safety to range their applications from small scale like in electronic devices to large scale such as in pure-electric vehicles. Increasing the specific capacity and operating potential of the cathode materials is one of the key approaches to promote the energy and power density of LIBs. Therefore many novel cathode materials have been successfully proposed such as nickel-rich layered oxides (LiNi_{1-x}M_xO₂ M = Co, Mn and Al), lithium-rich layered oxides (Li_{1+x}M_{1-x}O₂ M = Mn, Ni, Co, etc.) and high-voltage spinel oxides (LiNi_{0.5}Mn_{1.5}O₄) (Rozier and Tarascon 2015; Song et al. 2017; Kim et al. 2016). However, these cathode materials suffer from poor cycling stability at higher potentials which practically hinders its application in LIBs. The continuous electrolyte oxidation is mainly responsible for the capacity fading of high voltage LIBs. The commercialized carbonate-based electrolyte oxidizes when the cell operating voltage goes beyond 4.5 V, resulting in continuous increase in the interfacial reaction resistance and generation of harmful by-products, like HF, which hastens the dissolution of transition metal ions from cathode materials. Improving the interfacial stability of high voltage cathode/electrolyte is crucial for the practical application of high voltage LIBs (Kim et al. 2016; Park et al. 2014). The redox stability of electrolytes (containing lithium salt and mix-solvents) depends not only

on the lowest oxidation/reduction stability solvent, but also on the stability of the component that lies next to the electrode surface. Moreover, the composition of the interfacial electrolyte near the electrode depends strongly on the electrode material. The electrolyte component of the most widely used electrolyte (1 M LiPF₆/EC:DMC = 3:7) near a graphite electrode was extensively studied by Vatamanu et al. (2012) using molecular dynamic (MD) simulation and observed that upon increasing the electrode potential i.e., charging process, the less polar DMC solvent is partially replaced in the interfacial electrolyte layer by the more polar ethylene carbonate (EC) solvent. At higher potential values, the surface becomes affluent in the minority EC than in DMC. This result elucidates that the detected electrolyte oxidation decomposition products arises mainly from EC than DMC, though the former shows higher oxidation stability than the latter. Sulfone-based electrolytes have high oxidation stability compared to conventional carbonates. The interfacial electrolyte component of trimethyl sulfonate (TMS)/DMC mixed-solvent doped with LiPF₆ salt was also studied consequently. TMS was shown to have higher polarity and stronger binding energy with Li⁺ than that of DMC. As a result, when the negative electrode potential increases, the electrode surface gets loaded with higher proportions of TMS molecules. On the other hand at positive electrode/cathode surface, the ratio of TMS/DMC was found to be similar to the bulk components (Xing et al. 2012). The change in the interfacial electrolyte component as a function of electrode potential obtained from the MD simulation helps to predict the electrochemical stability of the electrolyte, and more importantly, to design an ideal interfacial electrolyte layer with high reaction inertness, or to form a high stability solid electrolyte interphase (SEI) film and cathode electrolyte interphase (CEI) film on the anode and cathode surfaces, respectively (Watanabe et al. 2008).

The critical role of anions in affecting the electrolyte oxidation stability has also received considerable attention in recent years. The oxidation decomposition rate of propylene carbonate (PC)-based electrolyte greatly depends on the lithium salts being used, indicating that salt anions are in fact involved in electrolyte oxidation. Moreover, studies also reveal that apart from more polar solvent, a higher accumulation of PF₆-anions on the positively charged surfaces can also be observed, signifying the possibility of anions participating in the oxidation reaction with the neighboring polar solvent (Arakawa and Yamaki 1995). The idea to replace carbonate-based electrolytes with high anodic stability salt and a solvent could drastically solve the instability of the high voltage cathode/electrolyte interphase. However, the practical application of these novel electrolytes in LIBs takes longer since they must consider compatibility with the graphite anode and the Al current collector, influence on interphasal reaction kinetics, safety, cost etc. Majority of the novel non-carbonate/LiPF₆ electrolytes appear in a highly concentrated state, which shows improved anodic stability than in a dilute state. Dahn et al. (Xia et al. 2016) showed that LiPF₆/EC-free-linear alkyl carbonate-based electrolytes with a small amount of film-forming additive, such as vinylene carbonate (VC), achieved higher capacity retention of high voltage LIBs. They also suggest that further optimizing the linear alkyl carbonate electrolytes with appropriate co-additives may open a plausible path to the successful commercial utilization of high voltage LIBs. Without using EC as co-solvent and replacing LiPF₆

with a high stable salt lithium bis(fluorosulfonyl)-amide (LiFSA), Wang et al. (2016) reported stable and fast charge/discharge cycling of 5 V $\text{LiNi}_{0.5}\text{Mn}_{1.5}\text{O}_4$ /graphite cells. The high concentration LiFSA/DMC electrolyte with salt-to-solvent molar ratio of 1:1.1 shows great stability, with high voltage cathode, graphite anode and an Al current collector, in effect giving a significantly improved cyclic performance of high voltage LIBs as shown in Fig. 2.

Sun et al. (2017) proposed the use of three novel half borate lithium salts, such as lithium difluoro-2-methyl-2-fluoromalonateborate (LiDFMFMB), lithium difluoro-2-ethyl-2-fluoromalonateborate (LiDFEFMB), and lithium difluoro-2-propyl-2-fluoromalonateborate (LiDFPFMB) (Fig. 3) in high voltage LIBs. The ionic conductivity of the half borate lithium salts occur in the following order of $\text{LiDFMFMB} > \text{LiDFEFMB} > \text{LiDFPFMB}$. As the alkyl chain length of the anions increase, the mobility of the anions is found to increase.

Cyclic voltammetry was performed to investigate the redox stability of these new salts on a natural graphite anode and a high voltage spinel $\text{LiNi}_{0.5}\text{Mn}_{1.5}\text{O}_4$ (LNMO)

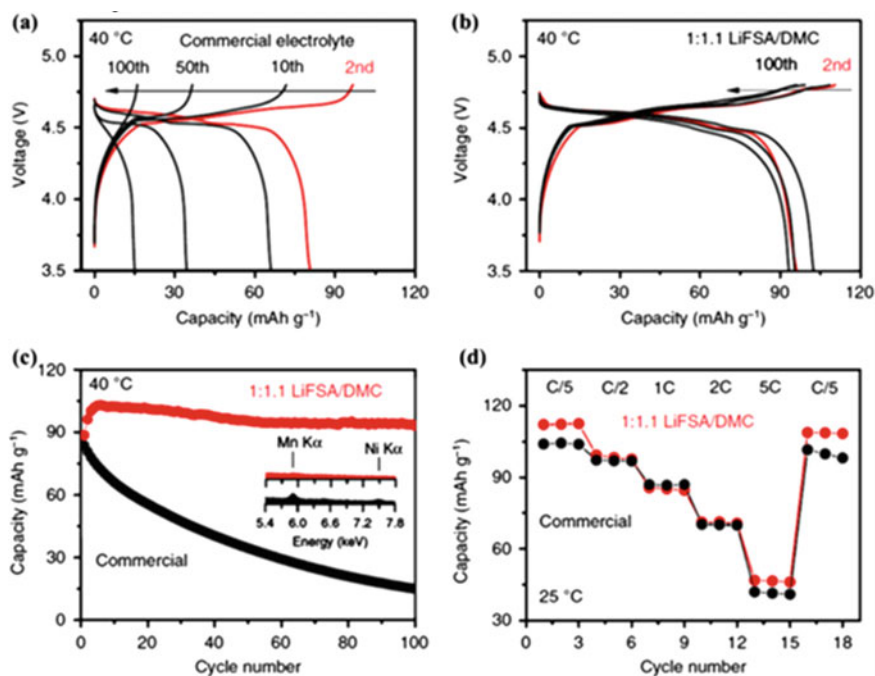


Fig. 2 Performance of a high-voltage $\text{LiNi}_{0.5}\text{Mn}_{1.5}\text{O}_4$ /natural graphite battery. Charge–discharge voltage curves of $\text{LiNi}_{0.5}\text{Mn}_{1.5}\text{O}_4$ /graphite full cell using **a** a commercial 1.0 mol dm^{-3} $\text{LiPF}_6/\text{EC}:\text{DMC}$ (1:1 by vol) electrolyte and **b** a lab-made superconcentrated 1:1.1 LiFSA/DMC electrolyte at a C/5 rate and 40 °C. **c** Discharge capacity retention of the full cells at a C/5 rate. **d** Discharge capacity of the full cell at various C-rates and 25 °C. All charge–discharge cycling tests were conducted with a cut-off voltage of 3.5–4.8 V. The 1C-rate corresponds to 147 mA g^{-1} on the weight basis of the $\text{LiNi}_{0.5}\text{Mn}_{1.5}\text{O}_4$ electrode (Wang et al. 2016)

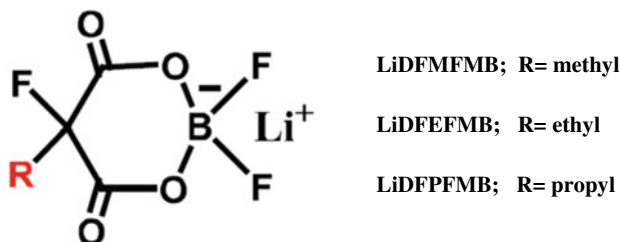


Fig. 3 Lithium difluoro-2-methyl-2-fluoromalonateborate

cathode, which showed that three new salts reduced/oxidized on the graphite/LNMO surface when the electrode potential initially decreased/increased, and significantly, created SEI and CEI film on the graphite and LNMO surfaces, respectively. Therefore, the new salt-based electrolytes presented good cycling stability with high coulombic efficiencies in both graphite and LNMO based half-cells and full cells. Another successful way of improving the characteristics of interfacial stability of high voltage cathode is the use of CEI film-forming additives. Such electrolyte additive does not bring any change in the physicochemical properties of the electrolyte like its ionic conductivity or viscosity. Some of the additives, in addition to improving the interfacial stability of graphite/electrolyte also enhance the thermal stability of LiPF_6 , taking up HF and reducing the risk of flammability of electrolytes. For instance, an electrolyte additive based on a highly fluorinated phosphate ester structure tris(hexafluoro-iso-propyl) phosphate (HFIP) was found to stabilize carbonate-based electrolytes on 5 V $\text{LiNi}_{0.5}\text{Mn}_{1.5}\text{O}_4$ cathode surfaces (Cresce and Xu 2011). The sacrificial oxidation of HFIP occurs before oxidation of the bulk electrolyte components, passivating the reactive sites on the cathode surface, resulting in improved cyclic stability of the $\text{LiNi}_{0.5}\text{Mn}_{1.5}\text{O}_4/\text{Li}$ half-cell. In addition, HFIP also provided excellent protective SEI on the graphitic anode. Such protective CEI layer prevents electrolyte decomposition and cathode degradation.

3 Solid Polymer Electrolytes (SPEs): Components and Ion Transport Studies

The need for electric vehicles (EVs) has become indispensable in a view to reduce greenhouse emissions and the use of fossil fuels. LIBs have been identified as one of the best options to power such large scale applications with essential requirements like high energy density, exceptional safety, long lifecycle, and extensive operating temperature range (Goodenough and Kim 2010). It is well understood that the electrolyte sandwiched between the anode and the cathode has a key role to play towards the success of LIBs used for powering EVs. In extreme thermal, mechanical and electrical conditions, the use of flammable/combustible organic electrolytes pose a threat to the safety features of LIBs (Tarascon and Armand 2001). A sustainable

strategy to evade this limitation of existing LIBs is to replace the state-of-the-art, alkyl carbonate-based liquid electrolytes, with solid electrolytes (SEs), which paves a way towards building intrinsically safer, and possibly eco-friendly, lithium battery systems. SE materials mainly include solid polymer electrolytes (SPEs), inorganic solid electrolytes (ISEs), and their composite/hybrid versions (Kalhoff et al. 2015). In this section we mostly stick on to solid polymer electrolytes (SPEs) and their possibilities as electrolyte membranes.

3.1 Components of SPEs

SPEs offer advantages of cost effectiveness, ease of processing to fabricate ultra-thin films, facile patterning and integration to give flexible battery design. SPEs also rule out the possibility of the use of separators which act as membrane separating cathode and anode to avoid shorting. Solid polymer electrolytes (SPEs) comprises of lithium salts (Li^+ , X^- , $\text{X}^- =$ monovalent anion) with low dissociation energy, polymer matrices with high donor number (DN), solid additives like Al_2O_3 as fillers, low-molecular-weight plasticizers like, PEGDME (Arya and Sharma 2017; Fan et al. 2018). The polymer electrolytes in which plasticizers are added to enhance ionic transport to impart more ionic conductivity falls under the category of Gel polymer electrolytes (GPEs) though they can be broadly treated as a sub category of SPEs (Song et al. 1999). Lithium salts embedded on polymer matrices, and/or other solid additives, have improved mechanical properties and lesser fire-induced hazards compared to those added with plasticizers (GPEs), though the former tends to be less ionic conductive. SPEs possess many merits over conventional liquid electrolytes such as low reactivity (kinetically) with polarized electrodes, no risk of electrolyte leakage and release of harmful/toxic gases, slower Li dendrite formation. In contrast to ISEs which have better ionic conductivity than SPEs, the SPEs can attenuate the interfacial resistance and improve the electrode–electrolyte compatibility (Bachman et al. 2016) (Fig. 4).

3.2 Ionic Transport Mechanism in SPE

The chemical properties of SPEs are intrinsically different from that of liquid organic electrolytes. In conventional liquid electrolytes, both cations and anions are mobile and contribute to the ionic conductivity. The mobility of these ions also varies in solvents and hence individual contribution to conductivity varies over a wide range. The ions solvate and move in the solvent, hence by improving the ionic dissociation in the solvents one can improve the ionic conductivity. On the other hand, only one type of ion is mobile in SPEs and in order for ion transport it requires to overcome the electrostatic forces and other interaction with the lattice or polymer structure in general. Ionic mobility and diffusion coefficient vary with compositional variation

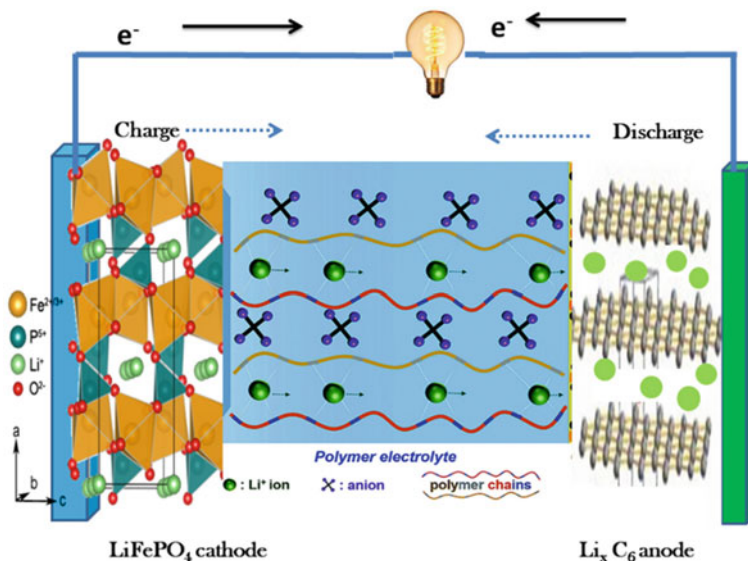


Fig. 4 Representation of LIB comprising LiFePO_4 cathode, graphite anode and a polymer electrolyte

in the polymer, in other words ionic conductivity is highly dependent on the amorphous/crystalline structural frame of the host polymer matrix. The space provided by the free volume of the polymer allows the ions to move within the matrix and conductivity above the glass transition temperature could be achieved where the ions are free to move. Polymers thus act as host for ionic transport. Ionic transport could be viewed to have diffusive liquid-like behavior in SPE (Druger et al. 1983; Harris et al. 1986; Bunde et al. 2005). Ionic conductivity of the SPE is measured by electrochemical impedance spectroscopy (EIS) in a certain frequency range using an AC impedance analyzer. It is understood that the ionic conduction mechanism in polyether based media occur via amorphous phases. The local structural relaxations associated to the glass transition occurring in these amorphous domains contribute to the ionic motion. It is understood that the lithium ions are coordinated on the segments of a polymeric chain by ether oxygen atoms in a similar manner in which they complex with crown ethers or other oligo-ether based solvents (Druger et al. 1983). A continuous segmental rearrangement occur with the gradual replacement of ligands in the solvation medium of Li-Ions giving rise to the long range net displacement of Li-Ions.

We need to understand the ionic transport mechanism at macroscopic level, i.e., ionic conductivity-temperature dependence and at microscopic level i.e. Li^+ transport mechanism. In 1889, Arrhenius proposed an empirical Eq. (2) for the description of temperature (T , K) dependence of reaction rate (k , rate constant) (Stoeva et al. 2003). This equation has been extended to express the relationship between ionic conductivity (σ , S cm^{-1}) and temperature in Eq. (3). In both equations, E_a , and R represent, activation energy (J mol^{-1}), and ideal gas constant ($\text{J mol}^{-1} \text{K}^{-1}$),

respectively. In 2009, Frech et al. (Petrowsky and Frech 2009) gave a modified Arrhenius equation that introduces the temperature dependence of the dielectric constant ($\epsilon(T)$) into the pre-exponential factor in order to terminate the non-Arrhenius factors as in Eq. (4).

$$k(T) = A \exp\left(-\frac{E_a}{RT}\right) \quad (2)$$

$$\sigma(T) = \sigma_0 \exp\left(-\frac{E_a}{RT}\right) \quad (3)$$

$$\sigma(T, \epsilon) = \sigma_0[\epsilon(T)] \exp\left(-\frac{E_a}{RT}\right) \quad (4)$$

These are mostly applied to inorganic electrolytes with ordered structures (such as Li_3N , and $\beta\text{-Al}_2\text{O}_3$), as well as in crystalline polymer electrolytes. However, for amorphous materials such as silicates, phosphates and chalcogenide glasses and, polymer electrolytes in particular, the σ - T dependences deviate from the typical Arrhenius behavior (i.e. a linear correlation between the logarithm of conductivity and the inverse of temperature). In these cases, the Vogel–Tamman–Fulcher (VTF) and Williams–Landel–Ferry (WLF) equations are adopted as given in Eqs. (5) and (6) respectively (Ikeda and Aniya 2010; Williams et al. 1955). In both expressions, A , B , C_1 , and C_2 are constants, T_0 is the ideal glass transition temperature, and T_s is a reference temperature. Effectively, the WLF equation can be converted into the VTF equation when $C_1 = B/(T - T_s)$ and $C_2 = T_s - T_0$.

$$\sigma(T) = AT^{1/2} \exp\left(-\frac{B}{T - T_0}\right) \quad (5)$$

$$\log \frac{\sigma(T)}{\sigma(T_s)} = C_1 \frac{T - T_s}{C_2 + T - T_s} \quad (6)$$

It was Armand (1986) who suggested the use of VTF equation to correlate the σ - T dependence of Li-ion conducting polymer electrolytes. VTF equation is extensively used for studying the ionic transport phenomena in SEs for rechargeable LIBs.

In general, the Arrhenius equation gives a microscopic illustration of ionic transport whereby it is achieved by the hopping of ionic species from existing occupied sites to vacant sites. For instance, in the crystalline $\text{LiAsF}_6/\text{poly}(\text{ethylene oxide})$ (PEO) electrolyte, the ion motion is mainly contributed by the hopping of Li^+ cations in the PEO semi-helical skeleton. That is, ion transport is facilitated by intra- or inter-chain hopping via the Li–O bonds breaking/forming (Armand 1986). By contrast, the VTF equation depicts the segmental motion of a polymer chain, instead of the diffusivity or mobility of the ion species. According to the free-volume theory developed by Cohen and Turnbull (1959), molecular transport occurs only at the moment when voids have a volume larger than a certain critical volume. The expansivity of the

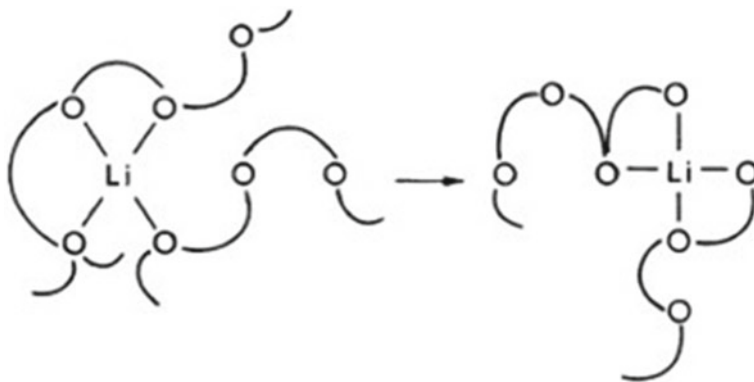


Fig. 5 Diffusion pathway of Li^+ in PEO according to dynamic percolation model by Ratner et al. Reprinted with permission from M. A. Ratner and D. Shriver: Ion Transport in Solvent-Free Polymers. Chem. Rev. 88(1). (Reprinted with permission from (Ratner and Shriver 1988), copyright (1988) © American Chemical Society)

materials with the increase of temperature yields free volume, which allows the ionic carriers, solvated molecules, or polymer chains to move. Ratner and Shriver (1988) developed a dynamic percolation model for explaining ion transport in polymer electrolytes (PEs). This microscopic model features the ionic motion via hopping between neighboring positions, where the Li^+ cations are transferred by a complete exchange of ligand surrounded in the local coordination environment as in Fig. 5.

The mechanism of ion transport in these electrolytes is rather complicated, due to the co-existence of multiple phases and structures, thus different models are required for simulating the diffusion of ionic species and accompanying mechanism. However, for PEs, there is a general agreement that lowering the glass transition temperature T_g crucial for increasing the mobility of polymer segments, thus leading to an improved ionic conductivity.

3.3 Polyethylene Oxide (PEO) Based and Non PEO Based Electrolytes

Polyethylene oxide (PEO) is a poly ether compound with chemical structure $\text{H}-(\text{O}-\text{CH}_2-\text{CH}_2)_n-\text{OH}$. It is also known as Polyethylene glycol (PEG) based on the molecular weight of PEO. PEO has a molecular weight of $20,000 \text{ g mol}^{-1}$ whereas PEG is an oligomer of ethylene oxide with $\text{MW} < 20,000 \text{ g mol}^{-1}$. PEO based materials are considered potential candidates of polymer hosts in SPEs for realizing high energy density secondary Li-Ion batteries. They have several advantages like ease of processability high safety, good electrochemical stability, cost effectiveness and exceptional compatibility with Li salts (Jung et al. 2017). The repeating units of PEO, ethylene oxide ($-\text{CH}_2\text{CH}_2\text{O}-$), are appropriately spaced ether solvating

units (low entropy change) that have excellent solvation abilities ($DN = 22$), thus permitting the formation of the favored lithium salt/PEO complex and providing a sufficient concentration of charge carriers. Moreover, it presents optimal conditions for Li^+ dissociation, and high chain flexibility. However, they suffer from insufficient ionic conductivity due to the semi-crystalline nature of the ethylene Oxide (EO) chains. The stiff structure restrains the ionic transition especially at low temperature. Nevertheless they are still one of the best choices of polymer host material and research is always on to develop approaches to reduce the crystallinity of the structure and hence improve the ionic conductivity. This includes polymer blending, modifying and making PEO derivatives etc. (Judez et al. 2017; Devaux et al. 2015; Khurana et al. 2014).

It was the study by Wright (1975) regarding the ionic conductivity of PEO complexes with alkali metal salts and later Armand (1986) suggestion that PEO could be used in electrochemical devices that paved the way for the development of SPE to be used in Li batteries.

The ionic conductivity of the PEO is contributed by the ionic transport happening in the amorphous region of PEO, thereby the ionic motion ability in the PEO segment need to be increased (Fig. 6a). The Li-Ions are understood to move in the PEO chain via both interchain and intrachain hopping as illustrated in Fig. 6b. The ionic conductivity reached practically useful values ($\sim 10^{-4}$ S/cm) at temperatures of 60–80 °C (Armand et al. 1979). Most commonly used and traditional approach adopted to improve the problem of ionic conductivity is the use of plasticizer to reduce the crystallinity and increase the amorphous phase content of Li salt in polymer electrolytes. Such a use of plasticizer, most commonly organic aprotic solvents deviate them from SPEs and make them GPEs which are not regarded as pristine SPEs.

Adopting a chemical modification of the polymer matrix as is one of the feasible approach. Poly(styrene-*b*-ethylene oxide) block copolymers have been widely studied and comprising PS segment confers mechanical stiffness and a PEO block provides solvation and transport properties. As the PS block content increases, both T_m and crystallinity (χ_c) decrease regardless of the length of the PEO chain, while the Young's modulus and tensile strength increase. The decreased melting transition compared to PEO could allow the operating of polymer cells at relatively low temperatures (25 °C) (Ping et al. 2017). Chintapalli et al. (2016) studied the conductivity of a PS-*b*-PEO/LiTFSI system with high salt content and found the maximum ionic conductivity of the copolymer to be about twice that of the corresponding PEO based one. Another strategy for overcoming the above-mentioned challenges involves cross-linking of PEO with other polymers. For example, cross-linked PE and PEO enhance the ionic conductivity of SPEs to as high as 2.3×10^{-4} S cm^{-1} at 25 °C, a value that was proportionally increased with the addition of low molecular weight PEGDME as plasticizer (Khurana et al. 2014).

Addition of inorganic fillers to reduce the crystallinity is a possible strategy to improve the conductivity of PEO based electrolytes. It is remarkable that the overall performance of an SPE does not rely only on the chosen polymer host, but also on the selection of Li salt. Generally, anions with highly delocalized negative charge are selected as counterparts of lithium salts, which could improve the amorphicity and

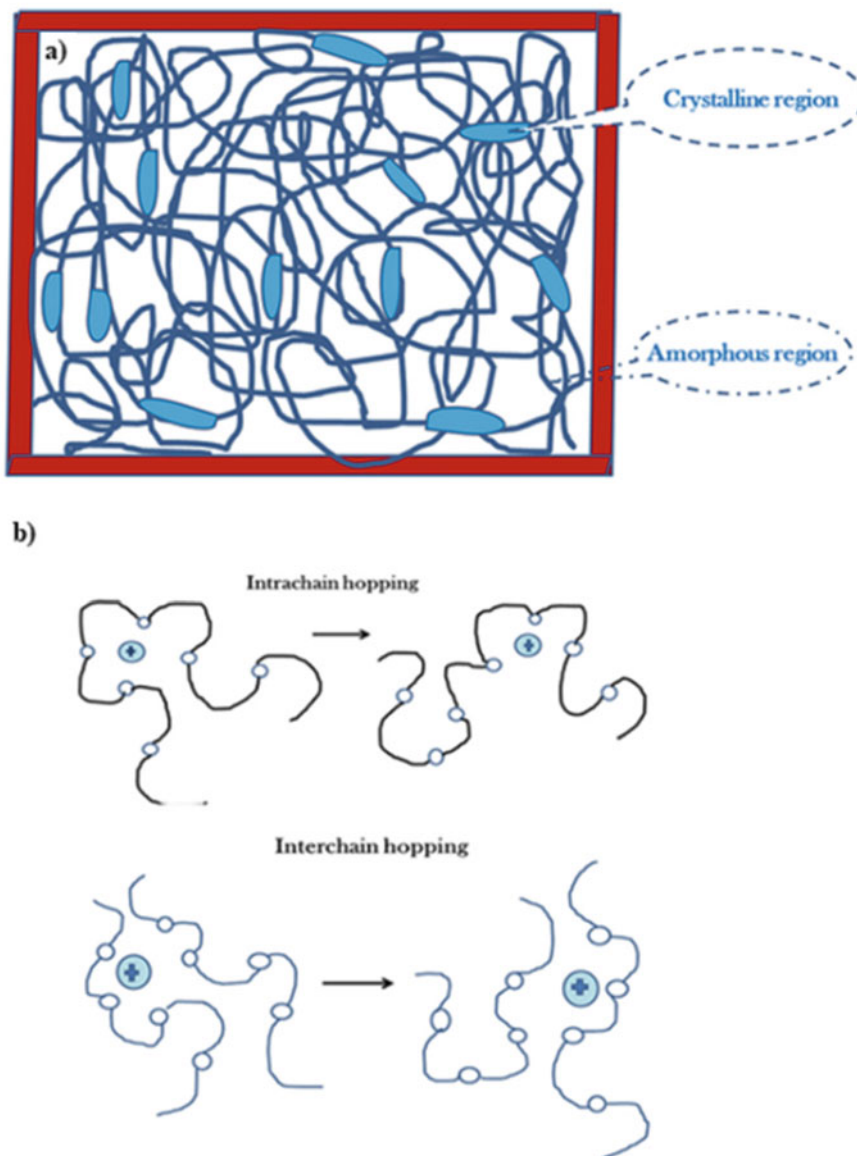


Fig. 6 a An illustration showing amorphous and crystalline regions in PEO b Li-Ion transport mechanism in PEO via intrachain and interchain hopping

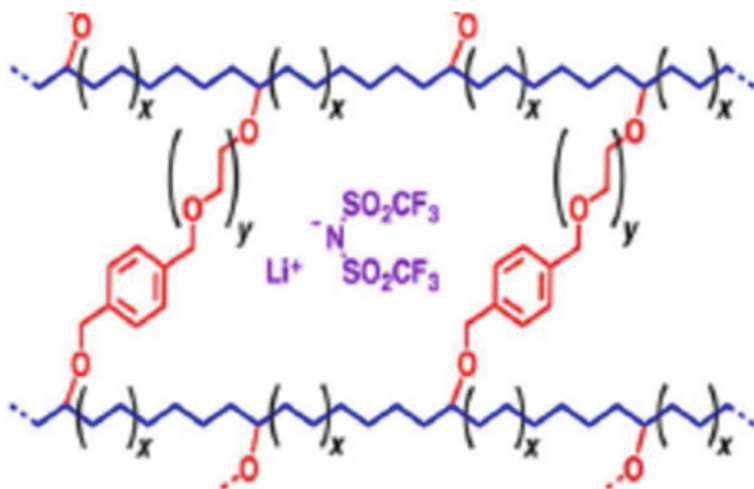


Fig. 7 Chemical structure of a PE-PEO cross-linked SPE with LiTFSI as salt. <https://pubs.acs.org/doi/10.1021/ja502133j>. (Reprinted with permission from (Judez et al. 2018), copyright (2014) © American Chemical Society (ACS))

ionic conductivity of SPEs. Among all the investigated candidates, $\text{LiN}(\text{CF}_3\text{SO}_2)_2$ known as lithium bis(trifluoromethanesulfonyl)imide (LiTFSI) has been employed as a dominative salt in SPEs, due to its low lattice energy ($T_m = 233\text{ }^\circ\text{C}$) and highly delocalized negative charge of the anion, which promotes the dissociation and dissolution of lithium salt in the polymer host, thus enhancing the ionic conductivity (Fig. 7) (Judez et al. 2018; Judez et al. 2017; Zhang et al. 2014).

In spite of the great advances in the performance of PEO-based batteries, the poor compatibility between PEO-based electrolytes and high-voltage electrodes ($>4\text{ V}$ versus Li/Li^+) due to the substandard anodic stability of PEO paves way for alternative polymer matrices. Among the variety of candidates to replace PEO, polycarbonates (PCs), are identified as feasible materials (Mindemark et al. 2018). Generally, polycarbonate-based polymer electrolytes show higher transference number T_{Li^+} due to the weaker carbonyl group oxygen– Li^+ interaction and/or the absence of chelating effects. Unlike EO-based PEs, PC-based PEs show poor conductivities at a low-salt concentration, although a high salt concentration results in a strong plasticizing effect and therefore fast Li-ion transport and hence improved conductivity. Tominaga and Yamazaki (2014) proved that high conductivity and lithium transference number T_{Li^+} (0.54) values were obtained for poly(ethylene carbonate) (PEC)/LiFSI electrolytes, which were further improved upon the addition of 1 wt% TiO_2 nanoparticles. Within this family of polymers, acrylate derivatives with the ester moiety have been widely studied. Poly(methyl methacrylate) (PMMA)-based SPEs, showing enhanced interface stability, is restricted by their poor mechanical flexibility ($T_g \approx 100\text{ }^\circ\text{C}$). The use of a more flexible ether-modified polysiloxane

partner in a blend with LiTFSI could render a more conductive (3.1×10^{-6} at 20 °C) and flexible (T_g of PMMA, 62 °C) polymer electrolytes (Cznotka et al. 2015).

Poly(acrylonitrile) (PAN) and poly(vinylidene fluoride) (PVdF) based host matrices, guarantee good mechanical properties and in general lead to higher stabilities towards electrochemical oxidation (Sharma and Thakur 2013; Tamilselvi and Hema 2016). However, conductivity problems may arise from their semi-crystalline structure. Thus, they are mainly applied to enhance the mechanical properties of other materials as well as in combination with fillers. Research on composite/hybrid electrolyte which consists of inert (inactive) or Li-conducting inorganic ceramic filler (active), embedded in an organic polymer matrix is steadily gaining popularity in SPEs. Such systems have advantage of either providing high ionic conductivity at low temperatures from ceramic phase when active, or of interfacial interactions between the nano-filler and the polymer, giving rise to lower crystallinity fraction, lower T_g and higher T_{Li^+} even when inactive. They have synergistic interfacial properties and improved mechanical stability derived from the polymeric structure (Sharma and Thakur 2010).

In conclusion, while the primary importance of the polymer host is indisputable, it has been observed that those can be tuned by physical and chemical processes leading to better properties of the SPEs (ionic conductivity, thermal properties and stability towards electrochemical oxidation). Furthermore, the structural nature of the lithium salt assumes a pivotal role in elevating the electrochemical performance of cells.

4 Gel Polymer Electrolytes (GPEs)

It is well realized from previous sections that the highly flammable nature of liquid electrolytes result in fires or explosions in cases of unusual heat generation such as short circuits or local overheating. Polymer electrolytes are understood to be safe and more reliable electrolyte systems. However, poor ionic conductivity at room temperature is one of the limiting factors in most of the SPEs which regulates their practical application in LIBs at ambient temperature. For this reason, most of the recent research has been engrossed on gel polymer electrolytes (GPEs) that exhibit higher ionic conductivities than SPEs. GPE is defined as an electrolyte that consists of a lithium salt dissolved in polymer along with suitable amount of organic solvent in it. The ionic conductivities of GPEs can be improved to almost the same level of liquid electrolyte by incorporating a lithium salt and a large amount of organic solvent into a matrix polymer that can form a stable and free-standing film. Inorganic filler is often used as the plasticizer to enhance the amorphous phase in the polymer. The electrochemical and mechanical properties of GPEs are dependent on the type and composition of the constituents (i.e. lithium salt, organic solvent, polymer and inorganic filler).

4.1 Constituents of GPEs

Any GPE consist of the Lithium salt dissolved in the organic solvent that is incorporated into the polymer matrix by various techniques like solution casting, hot melting, and immersion of porous membrane of the polymer matrix into the liquid electrolyte etc. (Wang et al. 2014; Kong et al. 2007; Kim et al. 2008). Most commonly used Li salts in liquid electrolytes such as LiPF_6 , LiClO_4 and LiBF_4 are employed out of which LiPF_6 offers overall good physicochemical properties in terms of good Li dissociation and ionic conductivity though superficial thermal stability. A major shortcoming of LiPF_6 is low thermal stability and high moisture sensitivity as compared with other lithium salts. It decomposes at high temperature and produces highly acidic PF_5 gas that reacts with water to generate HF. Therefore, the GPEs prepared with LiPF_6 exhibit high ionic conductivity but low thermal stability. LiClO_4 has safety concerns due to the fact that it is highly reactive with most organic species at high temperature and high charging current (Hossain 1995). Nonetheless, it is still being used in preparing GPEs. On the other hand, LiCF_3SO_3 is thermally stable, non-toxic and insensitive to moisture as compared with LiPF_6 . Its critical limiting factor is low ion conductivity as compared with other lithium salts, which is due to its low dissociation in organic solvents. $\text{Li}(\text{CF}_3\text{SO}_2)_2\text{N}$ has high ionic conductivity, thermal stability and is a safe salt. The high ion conductivity can be credited to its high degree of dissociation. The high dispersion of anionic charge marks it more easily dissociated into cations and anions. It melts at around 236 °C without thermal decomposition. However this salt is known to corrode Al current collector which restricts its application (Schmidt et al. 2001).

The organic solvents must meet the usual criteria as in the case of liquid electrolyte like high dielectric constant, low viscosity, electrochemically stability in the potential range of 0–4.5 V versus Li/Li^+ , low melting temperature, high boiling point, low volatility to remain safe. A synergistic effect in ionic conductivity is attained when cyclic carbonates and linear carbonates are mixed, as the advantages of each individual solvent are imparted to the resultant mixture. Among various cyclic carbonate-based solvents for preparing the GPEs, EC is the basic and indispensable component, as it can form an effective protective film on a graphitic anode which inhibits any further electrolyte decomposition on the surface of the anode. Such protective film formation cannot be realized with PC as a result of which exfoliation of graphite occurs due to the co-intercalation of PC into the graphite. Organic solvents usually undergo decomposition due to their tendency to reduce at low potential. This can be overcome by adding a small amount of additives such as vinylene carbonate (VC) and fluoroethylene carbonate (FEC). They also help to form an even and ionic-conductive solid electrolyte interphase (SEI) layer at the surface of a carbon anode.

The role of the polymer is to sustain a solid-state film that supports ion migration in organic solvents. Numerous types of polymers, such as PEO, polyacrylonitrile (PAN), poly(vinylidene fluoride) (PVdF), poly(vinylidene fluoride-co-hexafluoropropylene) (PVdF-HFP), poly(methyl methacrylate) (PMMA) and poly(vinyl chloride) (PVC),

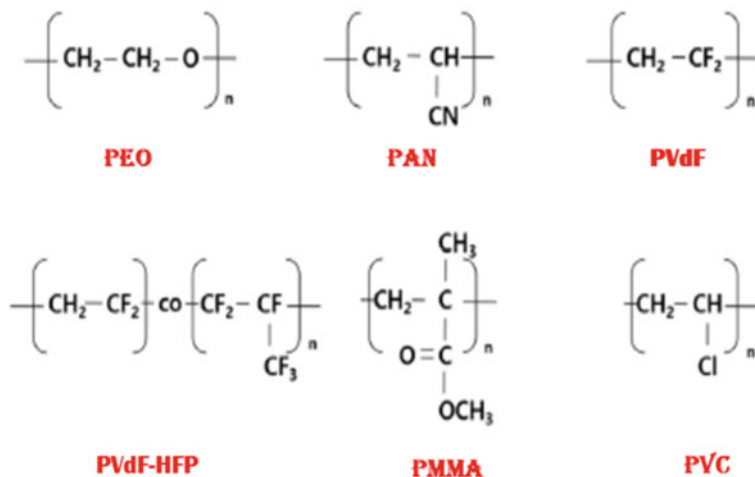


Fig. 8 Chemical Structures of various polymers used in GPEs

are mainly used in developing GPEs (Fig. 8) (Weston and Steele 1982; Watanabe et al. 1982; Capiglia et al. 2001; Sukeshini et al. 1996).

The ionic conductivities of the most widely used PEO-based polymer electrolytes is found to improve upon addition of plasticizers. In addition to reducing the crystallinity and increasing the segmental motion of the polymer chain, the organic plasticizers can also enhance ion dissociation. Low-molecular-weight polyethers, organic solvents and ionic liquids are generally used as plasticizers for the purposes. Adding poly(ethylene glycol) (PEG) as a low-molecular-weight polyether to PEO–LiCF₃SO₃ complexes increased the ionic conductivity, however, the existence of hydroxyl end groups negatively affected the interfacial properties at the electrode and electrolyte interface. An increase of ionic conductivity with the addition of PEG can be attributed to the decrease in the crystallinity and the increase of free volume in PEO (Ito et al. 1987). A GPE containing PEO and a conventional LiPF₆-based liquid electrolyte was prepared by in situ polymerization using UV irradiation. The gel polymer electrolyte revealed a high ionic conductivity value of $3.3 \times 10^{-3} \text{ S cm}^{-1}$ and lithium transference number of 0.76 at room temperature. A Li/LiFePO₄ cell using this GPE exhibited good cycling stability with excellent capacity retention of 81% after 500 cycles.

The presence of polar side chain in PAN attracts lithium ions and organic solvents, making it suitable as a matrix polymer for preparing GPEs. Abraham et al. prepared a GPE comprising of EC, PC, LiClO₄ immobilized in PAN which exhibited a high ionic conductivities of 1.1×10^{-3} and $1.7 \times 10^{-3} \text{ S cm}^{-1}$ at -10°C and 20°C , respectively (Li et al. 2017). As the PAN matrix is devoid of oxygen atoms, a lithium transference number higher than 0.5 was also reported GPEs based on PAN are prepared by soaking the porous PAN membrane in organic electrolytes such as LiPF₆-EC/DMC, LiBF₄-EC/DMC and LiClO₄-EC/DMC. High ionic conductivities of the order of

$2.0 \times 10^{-3} \text{ S cm}^{-1}$ and sufficient electrochemical stability over 5.0 V could be achieved which paves its application in high-voltage lithium-ion polymer batteries. The preparation of PAN-based GPEs usually involves the heating of PAN dissolved in EC or PC at high temperatures. When PAN and lithium salt are fully dissolved in organic solvents, the solution is cast and then subjected cooling at room temperature. Regardless of several advantages of PAN-based GPEs, comprising high ionic conductivity, electrochemical stability high lithium transference number, the poor compatibility with lithium metal has inhibited their practical applications (Abraham and Alamgir 1990).

PVdF and its copolymer are potential host polymers for preparing GPEs due to their unique properties like high dielectric constant which allows a high degree of salt dissociation and thus a high concentration of charge carriers, high oxidative stability due to the strong electron-withdrawing $-\text{CF}_2-$ group. It was understood from a study by Tsuchida et al. that the ionic conductivities of the GPEs consisting of PVdF, LiClO_4 and plasticizers like EC, PC, DMF, γ -BL, PEG, PPG, was strongly influenced by the ionic mobility within the material. Hence, the viscosity of the plasticizer was the governing parameter rather than its dielectric constant for achieving high ionic conductivity (Min et al. 2003). PVdF-HFP copolymer is rich in amorphous domains which could entrap large amounts of liquid electrolyte, and crystalline regions capable of offering enough mechanical support for the processing of free-standing films, eliminating the need for cross-linking. The porous PVdF-HFP membrane is initially prepared under atmospheric conditions and GPE is obtained by injecting liquid electrolyte into the porous membrane. While PVdF homopolymer does not swell well, the presence of HFP quite increases the electrolyte uptake. A solution casting of PVdF-HFP containing 12% of HFP in carbonate solutions resulted in films capable of swelling up to 60% by volume, which maintained good mechanical properties and high ionic conductivity ($1 \times 10^{-3} \text{ S cm}^{-1}$) (Capiglia et al. 2001). A porous and chemically cross-linked GPE based on PVdF-HFP copolymer as a matrix was reported by Cheng et al. (2004). In this study, PEG was used as a plasticizer and polyethylene glycol methacrylate (PEGDMA) as a chemical cross-linking oligomer. GPEs based on PVdF-HFP/PEG/PEGDMA with a composition in the ratio 5:3:2 demonstrated a high ambient ionic conductivity of $1 \times 10^{-3} \text{ S cm}^{-1}$ and a high tensile modulus value of 52 MPa due to the presence of porous network structures. They are found to be electrochemically stable up to 5.0 V versus Li/Li^+ in the presence of 1 M LiPF_6 -EC/DEC (Cheng et al. 2004). PMMA based GPE was first reported by Iijima et al. who found that PMMA could be used as a gelation agent and an ionic conductivity of the order of $10^{-3} \text{ S cm}^{-1}$ could be achieved at 15 wt% PMMA. A main disadvantage of PMMA-based GPEs is their poor mechanical strength when plasticized with large amounts of organic solvents, which limits their application as electrolytes in rechargeable lithium batteries (Rajendran and Uma 2000). Some studies proved that copolymerization of PMMA with other polymers gave rise to GPEs with better mechanical and electrical properties. GPEs based on PMMA copolymerized with polyacrylonitrile, polystyrene and polyethylene to form a terpolymer showed enhanced mechanical strength to develop free-standing films. The ionic conductivity reached $1.4 \times 10^{-3} \text{ S cm}^{-1}$ in the GPE containing 27 wt%

terpolymer, 64 wt% LiClO₄-EC/PC and 9 wt% fumed silica at room temperature to give homogeneous films that exhibited good mechanical properties (Kim and Sun 1998). Since an amorphous polymer structure is always desirable for achieving high ionic conductivity, amorphous PVC finds use as a host polymer for GPEs. PVC complexed with LiTFSI and plasticized using organic solvents such as dibutyl phthalate (DBP) and dioctyl adipate (DOA) is used as GPE. The plasticizing effect was understood in terms of reduction in the mechanical modulus by about one to two orders of magnitude compared to pure PVC. Ionic conductivities varied from 10⁻⁷ to 10⁻⁴ S cm⁻¹ at 25 °C when the weight ratio of PVC was changed from 0.67 to 0.17. The lithium transference number varied from 0.54 to 0.98 depending on the composition and temperature (Sukeshini et al. 1996). The GPE developed with 15 wt% PVC, 40 wt% EC, 40 wt% PC and 5 wt% LiClO₄ exhibited an ionic conductivity of 1.2 × 10⁻³ S cm⁻¹ at 20 °C. PVC-based GPEs is known to display high mechanical strength even if the content of plasticizing solvents is very high (Alamgir and Abraham 1993). PVC could also be used to enhance the mechanical strength of PMMA-based GPEs. The GPEs based on PVC/PMMA blend offered a phase-separated structure consisting of a PVC-rich phase and an electrolyte-rich phase. At the blend ratio of PVC/PMMA = 3/2, it was observed that the mechanical properties and ionic conductivity increased. At this ratio, the polarity of the liquid electrolyte was elevated and the domain size of the electrolyte-rich phase reduced. The lithium-ion cell assembled with carbon anode, blended GPE and LiCoO₂ cathode gave a discharge capacity of 111 mAh g⁻¹ at 2C-rate with good capacity retention (Kim et al. 2000).

Another major component of interest in GPEs is the inorganic fillers that are integrated into the polymer matrix to improve the electrical and mechanical properties. GPEs usually exhibit high ionic conductivities exceeding 10⁻³ S cm⁻¹ at room temperature upon the addition of large amount of liquid electrolyte into a matrix polymer. However, incorporating larger amounts of liquid electrolyte can be detrimental to mechanical properties of GPEs and cause poor compatibility with the lithium electrode. This can be overcome using inorganic fillers such as SiO₂, Al₂O₃, γ-LiAlO₂, TiO₂, ZrO₂, CeO₂ and BaTiO₃ (Borghini et al. 1995; Liu et al. 2003; Woo et al. 2018). The particle size of the inorganic filler is an important parameter that affects the ion transport and ionic conductivity. Park et al. demonstrated that incorporating Al₂O₃ as a filler augmented the electrochemical stability of the PEO-based polymer electrolyte. The hydrogen bonding between surface group of Al₂O₃ and the perchlorate anion in the Li salt resulted in the stability enhancement. A composite polymer electrolyte made with two fillers Al₂O₃ and BaTiO₃ showed better ionic conductivity which can be attributed to both the reduction of crystallinity and the increase in charge carrier concentration. Ferroelectric inorganic fillers such as BaTiO₃ possess permanent dipole and they are capable of reducing the interfacial resistance between the electrode and electrolyte. A composite GPE was prepared by an in situ cross-linking reaction between reactive SiO₂ particles dispersed in the PAN membrane and electrolyte precursor containing tri(ethylene glycol)diacrylate. The cross-linked composite polymer electrolyte encapsulated electrolyte solution efficiently without leakage and offered good thermal stability in addition to favorable

interfacial characteristics toward electrodes. Inorganic clay with high strength and stiffness also finds application as inert filler for reinforcing the mechanical strength of GPEs (Shin et al. 2015).

4.2 *Ionic Conduction in GPES*

GPEs inherited majority of their properties and merits like ionic conduction and electrochemical stability on carbonaceous anode and metal oxide cathode from bulk liquid electrolytes; nonetheless features like safety, tolerance against electrical and mechanical instabilities and dimensional stability are dealt by the polymer matrix encapsulating them. The ionic mobility and hence the ion conduction is determined mainly upon the motion of ions in the liquid electrolyte which is embedded in the solid polymer matrix. Most of the GPEs are understood to consist of a two-phase separated gel consisting of swollen polymer chains and the Li salt solution in organic solvents retained in the cavities of porous polymer. Both these phases contribute to carrier migration. Gelation happens in a stepwise manner in which the pores gets filled with electrolyte solution initially followed by their penetration into polymer to swell the polymer chains. The porosity and pore size of the polymer thus determine the swelling condition of the gel. The interaction between the carriers and polymer chains in the swollen polymer affects the carrier concentration and mobility and hence the ionic conductivity. As far as the polymer substrate is concerned, its porosity, pore size, amorphousness, chain structure and degree of polymerization matters while from the aspect of electrolyte solution, the degree of dissociation of Li salt, viscosity, concentration and dielectric constant would attribute to the carrier migration characteristics. A porous polymer membrane allows smooth movement of electrolyte solution trapped in the cavities into the polymer from resulting in homogenous network chains appropriate for ion transport (Figs. 9 and 10) (Saito et al. 2003).

4.3 *Characteristics of GPEs*

The essential parameters that determine the efficacy of GPEs include their ionic conductivity, electrochemical stability, Lithium transference number and the mechanical strength to find practical large scale application in Li batteries. Ionic conductivity of GPEs is the most important characteristic that affects battery performance. The ionic conductivity of a GPE for lithium-ion battery application should be higher than 10^{-3} S cm^{-1} at room temperature. The migration of lithium ions between two electrodes and diffusion of lithium ions in the electrodes are crucial for the fast charge–discharge of LIBs at high current rates. Unless a rapid and facile transport of Li-Ions occur between the electrodes, a high capacity cannot be achieved.

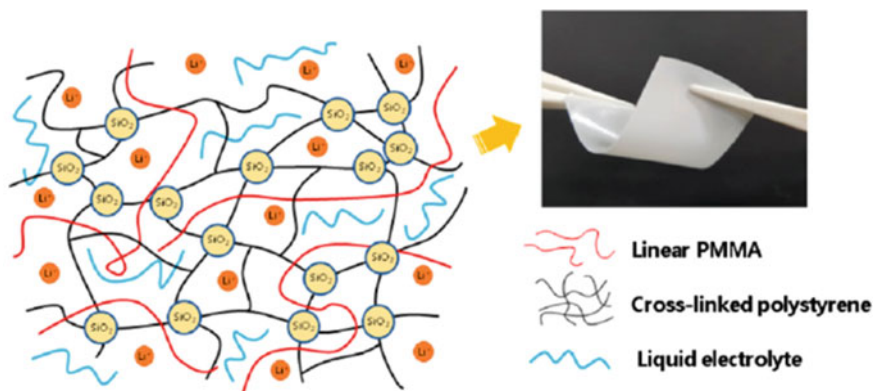
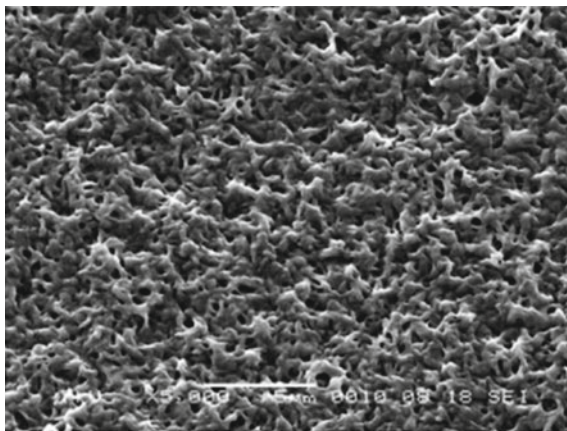


Fig. 9 An illustration of composite GPE based on PMMA/polystyrene with SiO_2 as inorganic fillers. Liquid electrolyte is 1 M LiTFSI in TEGDME. (Reprinted with permission from (Woo et al. 2018), copyright (2017) © American Chemical Society (ACS))

Fig. 10 SEM photograph of GPE composed of PVdF-HFP polymer. The porous network enables smooth movement of electrolytes trapped in the cavities into the polymer and hence improves ionic conductivity. (Reprinted with permission from (Saito et al. 2003), copyright (2003) © Elsevier)



Ionic conductivity of the GPE can be measured by electrochemical impedance spectroscopy (EIS) in a certain frequency range using an AC impedance analyser. For conductivity measurement, GPE film is sandwiched between two blocking electrodes such as stainless-steel electrodes and the bulk resistance (R_b) is obtained by the intercept on the real axis of AC impedance spectrum (Nyquist plot) of the cell (Oh et al. 2006). The ionic conductivity can be calculated by equation:

$$\sigma = \frac{t}{R_b A} \quad (7)$$

where σ is the ionic conductivity, t is the thickness of the gel polymer electrolyte, film; A is the area of gel polymer electrolyte in contact with blocking electrodes.

The operating voltage of the LIB is decided by the electrochemical stability window of the electrolyte. Linear sweep voltammetry (LSV) is employed to evaluate the electrochemical stability window of the GPE, which is the range of potential that does not involve in oxidative and reductive decomposition reactions. A potentiostat scans the potential of a working electrode at a constant rate with respect to the reference electrode. When the current increases rapidly, it gives a decomposition voltage of the electrolyte. A platinum or stainless-steel electrode is often used as a working electrode, and lithium metal is used as reference and counter electrodes. GPEs should be electrochemically stable up to at least 4.5 V versus Li/Li⁺, because the lithium-ion batteries with lithium metal oxide cathodes such as LiCoO₂, LiNiO₂ and LiNi_xCo_yMn_{1-x-y}O₂ reach a voltage of 4.3 V when fully charged. Since the GPE is sandwiched between anode and cathode in the cell, no chemical reactions should occur when the GPE come into direct contact with electrodes. So like the conventional liquid electrolytes and SPEs, the GPEs should also continue to be inert to the charged surfaces of the electrodes during cell operation.

Lithium ions are the charge carriers in LIBS and henceforth they should have a higher mobility than the anions. The fraction of the current carried by Li⁺ ions can be determined from the lithium transference number (t_{Li^+}) given by the equation.

$$t_{Li^+} = \frac{\sigma^+}{\sigma^+ + \sigma^-} = \frac{\mu^+}{\mu^+ + \mu^-} \quad (8)$$

The conductivity ratio is also expressed in terms of ionic mobility since lithium salt dissociates to form the same number of cations and anions. When the lithium transference number is low, the overall resistance of the cell increases due to the concentration polarization of the anions in the electrolyte, resulting in reduced capacity and poor power density. The lithium transference number in the GPE usually ranges between 0.2 and 0.5. Various methods are employed to measure transference number such as AC impedance, DC polarization measurement, Tubandt's method, Hittorf's method and the pulsed field gradient NMR (PFG NMR) technique. The most commonly used method for determining the lithium transference number is a combination of AC impedance and DC polarization measurements of the symmetric Li/gel polymer electrolyte/Li cell using the following equation:

$$t^+ = \frac{I_s(V - I_0 R_0)}{I_0(V - I_s R_s)} \quad (9)$$

where V is the applied voltage to the cell, I_0 and I_s are the initial and steady state current, respectively, and R_0 and R_s are the interfacial resistances before and after the polarization, respectively. The cell is polarized by applying a DC voltage and the time evolution of the current flow is monitored. The initial and steady-state currents flowing in the cell are monitored. AC impedance measurements of the cell are done before and after DC polarization and the initial and steady-state interfacial resistances are measured. The lithium transference number is dependent on various

factors including temperature, salt type and concentration, types of polymer, organic solvent and inorganic filler (Jung et al. 2017). The anions can be effectively covalent bonded to polymer backbone making it immobile and thereby improving the Li transference number. GPE not only function as the electrolyte but also as a separator between two electrodes in the cell. The mechanical strength of GPE plays a vital role in the manufacture of batteries. To facilitate easy fabrication of battery, with reproducibility along with mechanical reliability during assembling, storage and usage, the mechanical stability of GPE is the most important factor to be considered when battery technology scales from laboratory to mass production. Most of the GPEs reported so far have exhibited poor mechanical properties, which has restricted their application without a supportive membrane in LIBs. Increasing the amount of organic solvent improves ionic conductivity but leads to a decrease in mechanical strength. While considering this connection, ionic conductivity and mechanical properties should be optimized within a suitable range. The mechanical strength of the GPEs can be augmented by addition of inorganic fillers and in situ chemical cross-linking (Evans et al. 1987). The thickness of GPE is also an important factor that affects battery performance such as rate capability and energy density. By enhancing the mechanical strength of GPEs, the thickness can be reduced and battery could be made more compact. In general, the film thickness should be less than 30 μm taking it into account, the thickness of conventional polyolefin separators used in LIBs. The mechanical strength of a GPE can be evaluated from the strain–stress curve by tensile test. For maintaining good interfacial characteristics and better contacts with electrodes in the cell during charge and discharge cycles, GPE should also retain adequate adhesive properties and flexibility. Thermally stability of GPEs also serves as a major requirement to have a suitable temperature range of operation in Li batteries (Zhang et al. 2011; Park et al. 2017). A comparison of conventional liquid electrolytes, SPEs and GPEs is illustrated in Table 2.

Table 2 Comparison of various types of liquid and solid electrolytes used in LIBs. *Note* Pyr₁₄-TFSI: 1-butyl-1-methyl pyrrolidinium bis(trifluoromethane) sulfonyl imide

Liquid			GPE	SPE
	Organic electrolyte	Ionic electrolyte		
Composition	Li salt + organic solvent	Li salt + ionic liquid	Li salt + organic solvent + polymer + inorganic filler	Li salt + polymer
Ionic conductivity @ RT (S/cm ⁻¹)	$\sim 10^{-2}$	$\sim 10^{-3}$	$\sim 10^{-3}$	$\sim 10^{-5}$
Safety	Poor	Good	Relatively good	Excellent
Example	LiPF ₆ + EC/DMC	LiTFSI + Pyr ₁₄ -TFSI	LiPF ₆ + EC/PC + PVdF-HFP	LiBF ₄ + PEO

5 Summary

The importance and role of electrolytes used in LIBs and general properties required for any electrolyte in LIBs are explained. The various electrolyte salts and solvents that are conventionally used to offer the demand of high voltage electrode–electrolyte interface for practical and large scale application is outlined. The ionic transport mechanism in SPEs is rather complicated and follows a different route as compared with conventional liquid electrolytes which restricts its ionic conductivity. But taking in to account the merits of safety, ability to develop compact and flexible battery designs, relevance of SPEs to meet the future application in electric vehicles is realized with focus on PEO based and non-PEO based electrolytes. GPEs on the other hand could overcome many of the demerits of SPEs mainly the ionic conductivity since they have organic liquid electrolytes incorporated into the polymer skeleton encapsulating them. The use of inorganic fillers also helped to improve the amorphousness of the polymer to facilitate proper ion migration and transport. Ionic conductivity comparable to liquid electrolytes of the order of $10^{-3} \text{ S cm}^{-1}$ could be achieved in GPEs which pave way for its usage in large scale applications. The mechanical and thermal stability of these systems offer possibilities for flexible compact battery design. With advantages of safety, cost-effectiveness and flexible battery design, SPEs is expected to dominate the electrolyte technology and there by its usage in secondary energy storage devices sometime in the near future.

References

- Abraham KM, Alamgir M (1990) Li^+ -conductive solid polymer electrolytes with liquid-like conductivity. *J Electrochem Soc* 137(5):657
- Alamgir M, Abraham KM (1993) Li ion conductive electrolytes based on poly(vinyl chloride). *J Electrochem Soc* 140(6):L96–L97
- Andersson AM, Herstedt M, Bishop AG, Edstrom K (2002) The influence of lithium salt on the interfacial reactions controlling the thermal stability of graphite anodes. *Electrochim Acta* 47(12):1885–1898
- Arakawa M, Yamaki J (1995) Anodic oxidation of propylene carbonate and ethylene carbonate on graphite electrodes. *J Power Sources* 54(2):250–254
- Armand M (1986) Polymer electrolytes. *Annu Rev Mater Res* 16:245–261
- Armand MB, Chabagno JM, Duclot MJ (1979) Polyethers as solid electrolytes, in fast ion transport in solids: electrodes and electrolytes. *Proc Int Conf* 131–136
- Arya A, Sharma AL (2017) Polymer electrolytes for lithium ion batteries: a critical study. *Ionics* 23(3):497–540
- Aurbach D (1999) *Non aqueous Electrochemistry*, 1st edn. Marcel Dek, New York
- Bachman JC, Muy S, Grimaud A, Chang H-H, Pour N, Lux SF, Paschos O, Maglia F, Lupart S, Lamp P (2016) Inorganic solid-state electrolytes for lithium batteries: mechanisms and properties governing ion conduction. *Chem Rev* 116(1):140–162
- Barthel J, Gores HJ, Kraml L (1996) Effects of electronegative substituents of anions on ion-pair formation. Temperature dependence of the conductivity of lithium fluoroacetate and alkali-metal acetate solutions in dimethyl sulfoxide. *J Phys Chem* 100(4):1283–1287

- Besenhard JO, Eichinger G (1976) High energy density lithium cells: part I. Electrolytes and anodes. *J Electroanal Chem Interfacial Electrochem* 68(1):1–18
- Borghini MC, Mastragostino M, Passerini S, Scrosati B (1995) Electrochemical and structural studies of petroleum coke in carbonate-based electrolytes. *J Electrochem Soc* 142(7):2118–2122
- Bunde A, Dieterich W, Maass P, Meyer M (2005) Ionic transport in disordered materials. In: Heitjans P, Kärger J (eds) *Diffusion in condensed matter*. Springer, Berlin, Heidelberg. https://doi.org/10.1007/3-540-30970-5_20
- Capiglia C, Saito Y, Kataoka H, Kodama T, Quartarone E, Mustarelli P (2001) Structure and transport properties of polymer gel electrolytes based on PVdF–HFP and $\text{LiN}(\text{C}_2\text{F}_5\text{SO}_2)_2$. *Solid State Ion* 131(3):291–299
- Chen HP, Fergus JW, Jang BZ (2000) The effect of ethylene carbonate and salt concentration on the conductivity of propylene carbonate/lithium perchlorate electrolytes. *J Electrochem Soc* 147(2):399–406
- Cheng CL, Wan CC, Wang YY (2004) Preparation of porous, chemically cross-linked, PVdF-based gel polymer electrolytes for rechargeable lithium batteries. *J Power Sources* 134(2):202–210
- Chintapalli M, Le TNP, Venkatesan NR, Mackay NG, Rojas AA, Thelen JL, Chen XC, Devaux D, Balsara NP (2016) Structure and ionic conductivity of polystyrene-block-poly(ethylene oxide) electrolytes in the high salt concentration limit. *Macromolecules* 49(5):1770–1780
- Chu AC, Josefowicz JY, Farrington GC (1997) Electrochemistry of highly ordered pyrolytic graphite surface film formation observed by atomic force microscopy. *J Electrochem Soc* 144(12):4161–4169
- Cohen MH, Turnbull D (1959) Molecular transport in liquids and glasses. *J Chem Phys* 31(5):1164–1169
- Cresce A, Xu K (2011) Electrolyte additive in support of 5 V Li ion chemistry. *J Electrochem Soc* 158(3):A337–A342
- Cznotka E, Jeschke S, Vettikuzha P, Wiemhöfer HD (2015) Semi-interpenetrating polymer network of poly(methyl methacrylate) and ether-modified polysiloxane. *Solid State Ion* 274:55–63
- Dahn JR, von Sacken U, Juzkow MW, Al-Janaby H (1991) Rechargeable LiO_2 /carbon cells. *J Electrochem Soc* 138(8):2207–2211
- Desjardins CD, Cadger TG, Salter RS, Donaldson G, Caser EJ (1985) Lithium cycling performance in improved lithium hexafluoroarsenate/2-methyl tetrahydrofuran electrolytes. *J Electrochem Soc* 132(3):529–533
- Devaux D, Glé D, Phan TNT, Gignes D, Giroud E, Deschamps M, Denoyel R, Bouchet R (2015) Optimization of block copolymer electrolytes for lithium metal batteries. *Chem Mater* 27(13):4682–4692
- Druger SD, Nitzan A, Ratner MA (1983) Dynamic bond percolation theory: a microscopic model for diffusion in dynamically disordered systems. I. Definition and one-dimensional case. *J Chem Phys* 79(6):3133–3142
- Druger SD, Ratner MA, Nitzan A (1983) Polymeric solid electrolytes: dynamic bond percolation and free volume models for diffusion. *Solid State Ion* 9–10:1115–1120
- Dudley JT, Wilkinson DP, Thomas G, LeVae R, Woo S, Blom H, Horvath C, Juzkow MW, Denis B, Juric P, Aghakian P, Dahn JR (1991) Conductivity of electrolytes for rechargeable lithium batteries. *J Power Sources* 35(1):59–82
- Ein-Eli Y, Thomas SR, Koch VR (1996) New electrolyte system for Li-ion battery. *J Electrochem Soc* 143(9):L195–L198
- Evans J, Vincent CA, Bruce PG (1987) Electrochemical measurement of transference numbers in polymer electrolytes. *Polymer* 28(13):2324–2328
- Fan L, Wei S, Li S, Li Q, Lu Y (2018) Recent progress of the solid-state electrolytes for high-energy metal-based batteries. *Adv Energy Mater* 8(11):1702657, 1–31
- Fry AJ (1989) *Synthetic organic electrochemistry*, 2nd edn. Wiley, London
- Goodenough JB, Kim Y (2010) Challenges for rechargeable Li batteries. *Chem Mater* 22(3):587–603

- Gores HJ, Barthel J, Zugmann S, Moosbauer D (2011) Handbook of battery materials. Wiley-VCH Verlag GmbH & Co., KGaA, Weinheim, Germany
- Gutmann V (1976) Solvent effects on the reactivities of organometallic compounds. *Coord Chem Rev* 18(2):225–255
- Guyomard D, Tarascon JM (1993) Rechargeable $\text{Li}_{1+x}\text{Mn}_2\text{O}_4$ /carbon cells with a new electrolyte composition: potentiostatic studies and application to practical cells. *J Electrochem Soc* 140(11):3071–3081
- Harris WS (1958) Electrochemical studies in cyclic esters. PhD thesis, University of California, Berkeley, CA
- Harris CS, Nitzan A, Ratner MA, Shriver DF (1986) Particle motion through a dynamically disordered medium: the effects of bond correlation and application to polymer solid electrolytes. *Solid State Ion* 18–19:151–155
- Henderson WA (2014) Electrolytes for lithium and lithium-ion batteries, 1st edn. Springer, New York
- Hossain S (1995) Linden D (ed) Handbook of batteries, 2nd edn, ch 36. McGraw-Hill, New York
- Huang CK, Surampudi S, Shen DH, Halpert G (1994) Effect of electrolyte composition on carbon electrode performance. *Proc Electrochem Soc* 94(4):105–110
- Hy S, Felix F, Rick J, Su W-N, Hwang BJ (2014) Direct in situ observation of Li_2O evolution on Li-rich high-capacity cathode material, $\text{Li}[\text{Ni}_x\text{Li}_{(1-2x)/3}\text{Mn}_{(2-x)/3}]\text{O}_2$ ($0 \leq x \leq 0.5$). *J Am Chem Soc* 136(3):999–1007
- Ikeda M, Aniya M (2010) Bond strength—coordination number fluctuation model of viscosity: an alternative model for the Vogel–Fulcher–Tammann equation and an application to bulk metallic glass forming liquids. *Materials* 3:5246–5262
- Ito Y, Kanehori K, Miyauchi K, Kodu T (1987) Ionic conductivity of electrolytes formed from PEO– LiCF_3SO_3 complex low molecular weight poly(ethylene glycol). *J Mater Sci* 22:1845–1849
- Jeong SK, Seo HY, Kim DH, Han HK, Kim JG, Lee YB, Iriyama Y, Abe T, Ogumi Z (2008) Suppression of dendritic lithium formation by using concentrated electrolyte solutions. *Electrochem Commun* 10(4):635–638
- Johansson P (2007) Electronic structure calculations on lithium battery electrolyte salts. *Phys Chem Chem Phys* 9(12):1493–1498
- Johansson P, Nilsson H, Jacobsson P, Armand M (2004) Novel Hückel stabilised azole ring-based lithium salts studied by ab initio Gaussian-3 theory. *Phys Chem Chem Phys* 6:895–899
- Judez X, Zhang H, Li C, González-Marcos JA, Zhou Z, Armand M, Rodriguez-Martinez LM (2017) Lithium bis(fluorosulfonyl)imide/poly(ethylene oxide) polymer electrolyte for all solid-state Li–S cell. *J Phys Chem Lett* 8(9):1956–1960
- Judez X, Zhang H, Li C, González-Marcos JA, Zhou Z, Armand M, Rodriguez-Martinez LM (2017) Lithium bis(fluorosulfonyl)imide/poly(ethylene oxide) polymer electrolyte for all solid-state Li–S cell. *J Phys Chem Lett* 8:1956–1960
- Judez X, Piszcz M, Coya E, Li C, Aldalur I, Oteo U, Zhang Y, Zhang W, Rodriguez-Martinez LM, Zhang H (2018) Stable cycling of lithium metal electrode in nanocomposite solid polymer electrolytes with lithium bis(fluorosulfonyl)imide. *Solid State Ion* 318:95–101
- Jung YC, Park MS, Kim DH, Ue M, Eftekhari A, Kim DW (2017) *Sci Rep* 7:17482
- Jung YC, Lee SM, Choi JH, Jang SS, Kim DW (2017) Room-temperature performance of poly(ethylene ether carbonate)-based solid polymer electrolytes for all-solid-state lithium batteries. *Sci Rep* 7:17482
- Kalhoff J, Eshetu GG, Bresser D, Passerini S (2015) Safer electrolytes for lithium-ion batteries: state of the art and perspectives. *ChemSusChem* 8(13):2154–2175
- Khurana R, Schaefer J, Archer LA, Coates GW, Schaefer JL, Coates GW (2014) Suppression of lithium dendrite growth using cross-linked polyethylene/polyethylene oxide electrolytes: a new approach for practical lithium–metal polymer batteries. *J Am Chem Soc* 136(20):7395–7402
- Kim DW, Sun YK (1998) Polymer electrolytes based on acrylonitrile-methyl methacrylate-styrene terpolymers for rechargeable lithium-polymer batteries. *J Electrochem Soc* 145(6):1958–1964

- Kim HT, Kim KB, Kim SW, Park JK (2000) Li-ion polymer battery based on phase-separated gel polymer electrolyte. *Electrochim Acta* 45(24):4001–4007
- Kim W, Cho JJ, Kang Y, Kim DW (2008) Study on cycling performances of lithium-ion polymer cells assembled by in situ chemical cross-linking with star-shaped siloxane acrylate. *J Power Sources* 178(2):837–841
- Kim S, Cho W, Zhang XB, Oshima Y, Choi JW (2016) A stable lithium-rich surface structure for lithium-rich layered cathode materials. *Nat Commun* 7(13598):1–8
- Kim U-H, Lee EJ, Yoon CS, Myung ST, Sun YK (2016) Compositionally graded cathode material with long-term cycling stability for electric vehicles application. *Adv Energy Mater* 6(22):1601417
- Koch VR (1981) Status of the secondary lithium electrode. *J Power Sources* 6(4):357–370
- Koetschau I, Richard MN, Dahn JR, Soupart JB, Rousche JC (1995) The electrochemical society, orthorhombic LiMnO_2 as a high capacity cathode for Li-ion cells. *J Electrochem Soc* 142(9):2906–2910
- Kong L, Zhan H, Li Y, Zhou Y (2007) In situ fabrication of lithium polymer battery basing on a novel electro-polymerization technique. *Electrochem Commun* 9(10):2557–2563
- Koppel IA, Taft RW, Anvia F, Zhu S-Z, Hu LQ, Sung K-S, Desmarteau DD, Yagupolskii LM, Yagupolskii YL, Igat'ev NV, Kondratenko NV, Volkonskii AY, Vlasor VM, Notario R, Maria PC (1994) The gas-phase acidities of very strong neutral Brønsted acids. *J Am Chem Soc* 116(7):3047–3057
- Lee H, Cho JJ, Kim J, Kim HJ (2005) Comparison of voltammetric responses over the cathodic region in LiPF_6 and LiBETI with and without HF. *J Electrochem Soc* 152(6):A1193–A1198
- Li W, Pang Y, Liu J, Liu G, Wang Y, Xia Y (2017) A PEO-based gel polymer electrolyte for lithium ion batteries. *RSC Adv* 7:23494–23501
- Liu Y, Lee JY, Hong L (2003) Morphology, crystallinity, and electrochemical properties of in situ formed poly(ethylene oxide)/ TiO_2 nanocomposite polymer electrolytes. *J Appl Polym Sci* 89(10):2815–2822
- Lloris JM, Pérez Vicente C, Tirado JL (2002) Improvement of the electrochemical performance of LiCoPO_4 5 V material using a novel synthesis procedure. *Electrochem Solid-State Lett* 5(10):A234–A237
- Lux SF, Lucas IT, Pollak E, Passerini S, Winter M, Kostecki R (2012) The mechanism of HF formation in LiPF_6 based organic carbonate electrolytes. *Electrochem Commun* 14(1):47–50
- McMillan R, Slegel H, Shu ZX, Wang W (1999) Fluoroethylene carbonate electrolyte and its use in lithium ion batteries with graphite anode. *J Power Sources* 81–82:20–26
- Min HS, Ko JM, Kim DW (2003) Preparation and characterization of porous polyacrylonitrile membranes for lithium-ion polymer batteries. *J Power Sources* 119–121:469–472
- Mindemark J, Lacey MJ, Bowden T, Brandell D (2018) Beyond PEO-alternative host materials for Li^+ -conducting solid polymer electrolytes. *Prog Polym Sci* 81:114–143
- Mizushima K, Jones PC, Wiseman PJ, Goodenough JB (1980) Li_xCoO_2 ($0 < x < -1$): a new cathode material for batteries of high energy density. *Mater Res Bull* 15(6):783–789
- Oh JS, Kang Y, Kim DW (2006) Lithium polymer batteries using the highly porous membrane filled with solvent-free polymer electrolyte. *Electrochim Acta* 52(4):1567–1570
- Olah GA, Prakash GKS, Molnár Á, Sommer J (2009) *Superacid chemistry*, 1st edn. Wiley, Hoboken, NJ
- Park JS, Meng X, Elam JW, Hao S, Wolverton C, Kim C, Cabana J (2014) Ultrathin lithium-ion conducting coatings for increased interfacial stability in high voltage lithium-ion batteries. *Chem Mater* 26(10):3128–3134
- Park SR, Jung YC, Shin WK, Ahn KH, Lee CH, Kim DW (2017) Cross-linked fibrous composite separator for high performance lithium-ion batteries with enhanced safety. *J Membr Sci* 527:129–136
- Petrowsky M, Frech R (2009) Temperature dependence of ion transport: the compensated Arrhenius equation. *J Phys Chem B* 113(17):5996–6000

- Ping J, Pan H, Hou PP, Zhang MY, Wang X, Wang C, Chen J, Wu D, Shen Z, Fan XH (2017) Solid polymer electrolytes with excellent high-temperature properties based on brush block copolymers having rigid side chains. *ACS Appl Mater Interfaces* 9(7):6130–6137
- Pistoia G (1971) Nonaqueous batteries with LiClO_4 -ethylene carbonate as electrolyte. *J Electrochem Soc* 118(1):153–158
- Rajendran S, Uma T (2000) Characterization of plasticized PMMA– LiBF_4 based solid polymer electrolytes. *Bull Mater Sci* 23:27–29
- Ratner MA, Shriver DF (1988) Ion transport in solvent-free polymers. *Chem Rev* 88(1):109–124
- Rougier A, Gravereau P, Delmas C (1996) Optimization of the composition of the $\text{Li}_{1-z}\text{Ni}_{1+z}\text{O}_2$ electrode materials: structural, magnetic, and electrochemical studies. *J Electrochem Soc* 143(4):1168–1175
- Rozier P, Tarascon JM (2015) Review-Li-rich layered oxide cathodes for next-generation Li-ion batteries: chances and challenges. *J Electrochem Soc* 162(14):A2490–A2499
- Ryou MH, Kim J, Lee I, Kim S, Jeong YK, Hong S, Ryu JH, Kim TS, Park JK, Lee H, Choi JW (2013) Mussel-inspired adhesive binders for high-performance silicon nanoparticle anodes in lithium-ion batteries. *Adv Mater* 25(11):1571–1576
- Ryou MH, Lee JN, Lee DJ, Kim WK, Jeong YK, Choi JW, Park JK, Lee YM (2012) Effects of lithium salts on thermal stabilities of lithium alkyl carbonates in SEI layer. *Electrochim Acta* 83:259–263
- Saito Y, Stephan AM, Kataoka H (2003) Ionic conduction mechanism of lithium gel polymer electrolytes investigated by conductivity and diffusion coefficient. *Solid State Ion* 160:149–153
- Scheers J, Johanssona P, Szczecinski P, Wieczorek W, Armand M, Jacobsson P (2010) Benzimidazole and imidazole lithium salts for battery electrolytes. *J Power Sources* 195(18):6081–6087
- Schmidt M, Heider U, Kuehner A, Oesten R, Jungnitz M, Ignatev N, Sartori P (2001) Lithium fluoroalkylphosphates: a new class of conducting salts for electrolytes for high energy lithium-ion batteries. *J Power Sources* 97/98:557–560
- Sharma AL, Thakur AK (2010) Improvement in voltage, thermal, mechanical stability and ion transport properties in polymer–clay nanocomposites. *J Appl Polym Sci* 118(5):2743–2753
- Sharma AL, Thakur AK (2013) Plastic separators with improved properties for portable power device applications. *Ionics* 19(5):795–809
- Shin WK, Yoo JH, Choi W, Chung KY, Jang SS, Kim DW (2015) Cycling performance of lithium-ion polymer cells assembled with a cross-linked composite polymer electrolyte using a fibrous polyacrylonitrile membrane and vinyl-functionalized SiO_2 nanoparticles. *J Mater Chem A* 3:12163–12170
- Song JY, Wang YY, Wan CC (1999) Review of gel-type polymer electrolytes for lithium-ion batteries. *J Power Sources* 77(2):183–197
- Song BH, Li WD, Oh SM, Manthiram A (2017) Long-life nickel-rich layered oxide cathodes with a uniform Li_2ZrO_3 surface coating for lithium-ion batteries. *ACS Appl Mater Interfaces* 9(11):9718–9725
- Stoeva Z, Martin-Litas I, Staunton E, Andreev YG, Bruce PG (2003) Ionic conductivity in the crystalline polymer electrolytes $\text{PEO}_6\cdot\text{LiXF}_6$, X = P, As, Sb. *J Am Chem Soc* 125(15):4619–4626
- Sukeshini AM, Nishimoto A, Watanabe M (1996) Transport and electrochemical characterization of plasticized poly(vinyl chloride) solid electrolytes. *Solid State Ion* 86–88:385–393
- Sun XG, Wan S, Guang HY, Fang YX, Reeves KS, Chi M, Dai S (2017) New promising lithium malonateborate salts for high voltage lithium ion batteries. *J Mater Chem A* 5:1233–1241
- Suo L, Hu YS, Li H, Armand M, Chen L (2013) A new class of solvent-in-salt electrolyte for high-energy rechargeable metallic lithium batteries. *Nat Commun* 4(1481):1–9
- Surampudi S, Shen DH, Huang CK, Narayanan SR, Attia A, Halpert G, Peled E (1993) Effect of cycling on the lithium/electrolyte interface in organic electrolytes. *J Power Sources* 43(1–3):21–26
- Takami N, Ohsaki T, Hasebe H, Yamamoto M (2002) Laminated thin Li-ion batteries using a liquid electrolyte. *J Electrochem Soc* 149(1):A9–A12

- Tamilselvi P, Hema M (2016) Structural, thermal, vibrational, and electrochemical behavior of lithium ion conducting solid polymer electrolyte based on poly(vinyl alcohol)/poly(vinylidene fluoride) blend. *Polym Sci Ser A* 58:776–784
- Tarascon JM, Armand M (2001) Issues and challenges facing rechargeable lithium batteries. *Nature* 414:359–367
- Tarascon JM, Guyomard D (1994) New electrolyte compositions stable over the 0 to 5 V voltage range and compatible with the $\text{Li}_{1+x}\text{Mn}_2\text{O}_4$ /carbon Li-ion cells. *Solid State Ion* 69(3):293–305
- Tominaga Y, Yamazaki K (2014) Fast Li-ion conduction in poly(ethylenecarbonate)-based electrolytes and composites filled with TiO_2 nanoparticles. *Chem Commun* 50(34):4448–4450
- Vatamanu J, Borodin O, Smith GD (2012) Molecular dynamics simulation studies of the structure of a mixed carbonate/ LiPF_6 electrolyte near graphite surface as a function of electrode potential. *J Phys Chem C* 116(1):1114–1121
- Wang X, Gong C, He D, Xue Z, Chen C, Liao Y, Xie X (2014) Gelled microporous polymer electrolyte with low liquid leakage for lithium-ion batteries. *J Membr Sci* 454:298–304
- Wang JH, Yamada Y, Sodeyama K, Chiang CH, Tateyama Y, Yamada A (2016) Superconcentrated electrolytes for a high-voltage lithium-ion battery. *Nat Commun* 7:12032
- Watanabe M, Kanba M, Nagaoka K, Shinohara I (1982) Ionic conductivity of hybrid films based on polyacrylonitrile and their battery application. *J Appl Electrochem* 27(11):4191–4198
- Watanabe Y, Kinoshita SI, Wada S, Hoshino K, Morimoto H, Tobishima SI (2008) Electrochemical properties and lithium ion solvation behavior of sulfone-ester mixed electrolytes for high-voltage rechargeable lithium cells. *J Power Sources* 179(2):770–779
- Weston JE, Steele BCH (1982) Effects of preparation method on properties of lithium salt-poly(ethylene oxide) polymer electrolytes. *Solid State Ion* 7(1):81–88
- Williams ML, Landel RF, Ferry JD (1955) The temperature dependence of relaxation mechanisms in amorphous polymers and other glass-forming liquids. *J Am Chem Soc* 77(14):3701–3707
- Woo HS, Moon YM, Seo S, Lee HT, Kim DW (2018) Semi-interpenetrating polymer network composite gel electrolytes employing vinyl-functionalized silica for lithium-oxygen batteries with enhanced cycling stability. *ACS Appl Mater Interfaces* 10(1):687–695
- Wright PV (1975) Electrical conductivity in ionic complexes of poly(ethylene oxide). *Br Polym J* 7(5):319–327
- Xia J, Petibon R, Xiong D, Ma L, Dahn JR (2016) Enabling linear alkyl carbonate electrolytes for high voltage Li-ion cells. *J Power Sources* 328:124–135
- Xing LD, Vatamanu J, Borodin O, Smith GD, Bedrov D (2012) Electrode/electrolyte interface in sulfolane-based electrolytes for Li ion batteries: a molecular dynamics simulation study. *J Phys Chem C* 116:23871–23881
- Xu K (2004) Nonaqueous liquid electrolytes for lithium-based rechargeable batteries. *Chem Rev* 104(10):4303–4417
- Xu L, Kim C, Shukla AK, Dong A, Mattox TM, Milliron DJ, Cabana J (2013) Monodisperse Sn nanocrystals as a platform for the study of mechanical damage during electrochemical reactions with Li. *Nano Lett* 13(4):1800–1805
- Younesi R, Veith GM, Johansson P, Edstrom K, Veggea T (2015) Lithium salts for advanced lithium batteries: Li-metal, Li- O_2 , and Li-S. *Energy Environ Sci* 8(7):1905–1922
- Zaghib K, Tatsumi K, Abe H, Ohsaki T, Sawada Y, Higuchi S (1995) Electrochemical behavior of an advanced graphite whisker anodic electrode for lithium-ion rechargeable batteries. *J Power Sources* 54(2):435–439
- S.S. Zhang., K. Xu., and T.R. Jow.: Low-temperature performance of Li-ion cells with a LiBF_4 -based electrolyte. *J Solid State Electrochem.* 7, 147–151(2003).
- Zhang P, Yang LC, Li LL, Ding ML, Wu YP, Holze R (2011) Enhanced electrochemical and mechanical properties of P(VDF-HFP)-based composite polymer electrolytes with SiO_2 nanowires. *J Membr Sci* 379(1–2):80–85

- Zhang H, Li L, Feng W, Zhou Z, Nie J (2014) Polymeric ionic liquids based on ether functionalized ammoniums and perfluorinated sulfonimides. *Polymer* 55(16):3339–3348
- Zheng H, Qin J, Zhao Y, Abe T, Ogumi Z (2005) Temperature dependence of the electrochemical behavior of LiCoO_2 in quaternary ammonium-based ionic liquid electrolyte. *Solid State Ion* 176(29):2219–2226

Carbon Based Composites for Supercapacitor Applications



Mannayil Jasna, Muraleedharan Pillai Manoj,
and Madambi Kunjukutan Ezhuthachan Jayaraj

1 Introduction

The possibility of electrical charge storage on the surface was discovered from the phenomena related to the rubbing of amber in early times. In the mid-eighteen century, such phenomenon was understood from investigations on physics of so-called “static electricity” and the development of various “electrical machines”. Development of the Leyden jar and discovery of charge separation and storage mechanism (i.e., the charge is stored on both surfaces of the Leyden jar separated by a layer of glass) was of significant impact for the origin of physics of electricity and then for electronics, electrochemical and electrical engineering (Yu et al. 2013). In early developments and technological applications until the middle of this century, this discovery was referred to as the “condenser”. In later terminology, such a device in different personifications is denoted to as a “capacitor,” and its ability for charge storage per volt is indicated to as its “capacitance”. In battery terminology, the word “capacity,” suggests the amount of Faradaic charge storage (unit is coulombs or watt-hours), which should not be baffled with “capacitance” (unit is farads), which relates to capacitors. In 1957, Becker, General Electric Company observed the electric double-layer capacitor effect, experimenting with porous carbon electrodes devices (Becker 1957). The device exhibited exceptionally high capacitance, and they concluded that energy was stored in the carbon pores even though the mechanism was unknown. In 1966, while working on fuel cell designs, a group of researchers at Standard Oil of Ohio accidentally rediscovered the effect (Boos

M. Jasna (✉)
Cochin University of Science and Technology, Kochi, Kerala, India
e-mail: jma@cusat.ac.in

M. P. Manoj
Department of Applied Physics, University of Eastern Finland, Kuopio, Finland

M. K. E. Jayaraj
University of Calicut, Malappuram, Kerala 673635, India

1968). Nippon Electric Company (NEC) accommodated the term ‘Supercapacitor,’ in 1978 and used it to deliver backup power for sustaining computer memory (Conway 1999a).

The increase in world’s population and worldwide economic growth and usage of consuming appliances of human beings on energy leads to the development of alternative/renewable energy sources. According to the World Energy Council, it is estimated that, by 2050, the world will necessitate doubling its energy supply (www.worldenergy.org). This opens up more challenges to human health, the environment and thus disclose a need for the development of high-power, sustainable, energy conversion and storage devices such as batteries and supercapacitors for widespread applications ranging from consumer optoelectronics like mobile phone, laptops, etc. to hybrid electric vehicles (Service 2003; Textiles 2007; Jost et al. 2013; Le et al. 2013; Lee et al. 2013; Chen et al. 2012; Burk 2000; Zhang and Zhao 2009).

Energy storage devices have an essential role in handling the issues related to renewable energy resources by providing the power grid system. Ragone plot for different energy storage devices is shown in Fig. 1. Supercapacitors (SCs), so-called electric double-layer capacitors or ultracapacitors) are promising energy storage devices due to their high power density, fast discharging time, and long cycle life (Meng et al. 2014; Yan et al. 2017; Yu et al. 2017; Li et al. 2013; Naoi et al. 2012). A supercapacitor consists of two electrodes, an electrolyte, and a separator which avoids the physical contact between the two electrodes, as shown in Fig. 2. The electrode material is the key element of a supercapacitor (Li et al. 2013; Naoi et al. 2012). Supercapacitors can be used in combination with batteries to meet the start-up power and act as temporary energy storage devices by giving high power capability to store energy from braking.

Fig. 1 Ragone plot for different energy storage devices

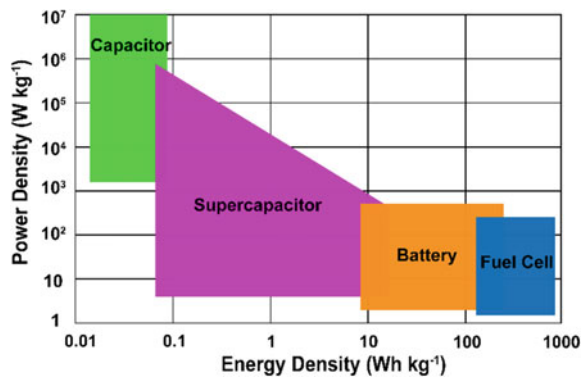
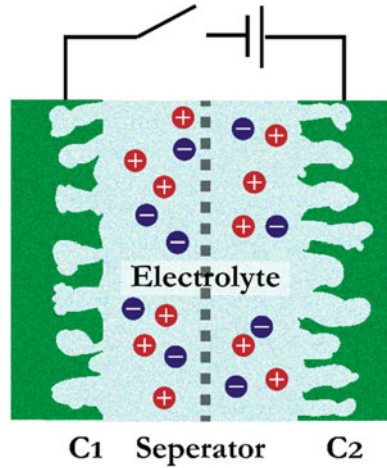


Fig. 2 Structure of a supercapacitor



2 Classification of Supercapacitors

Supercapacitors have a higher capacitance and energy density than normal capacitors due to a bigger electrode surface area and a thin double layer. Supercapacitors are divided into three types based on their energy storage mechanisms: Electrochemical double-layer capacitors, pseudo-capacitors, and hybrid supercapacitors as shown in Fig. 3.

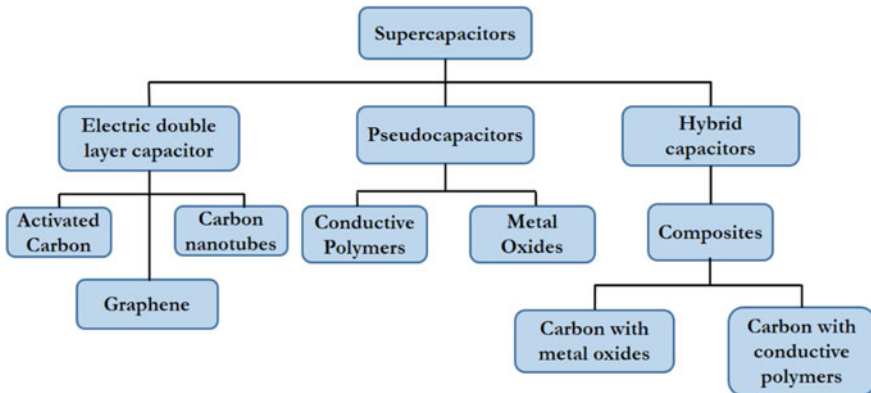


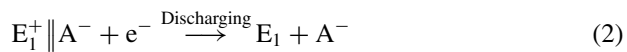
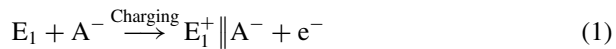
Fig. 3 Taxonomy of supercapacitors along with electrode materials

2.1 EDLC Supercapacitors

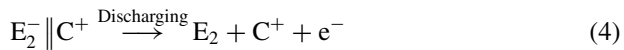
The energy storage mechanism in an electrochemical double-layer capacitor (EDLC) is accomplished via reversible ion adsorption at the electrode/electrolyte interface, as shown in Fig. 4. In EDLC, charge storage is a non-faradic process since no chemical reaction or charge transfer occurs across the electrode. The applied voltage forms an electric field between the electrodes during charging, forcing the electrically charged ions in the electrolyte to move to the electrodes with opposite polarity, generating two different charged layers with only a few molecular diameters in thickness. Large surface area and high porosity materials are critical for achieving high capacitance because they can store moving ions. A schematic diagram of the working of EDLC is shown in Fig. 4.

If E_1 and E_2 can be represented as two electrode surfaces, anion as A^- , cation as C^+ , and the electrode/electrolyte interface as \parallel , electrochemical charge/discharge processes can be expressed as Eqs. (1), (2), (3) and (4) (Wang et al. 2012)

At the positive electrode,



At the negative electrode,



Overall charging and discharging processes can be given in the Eqs. (5) and (6)

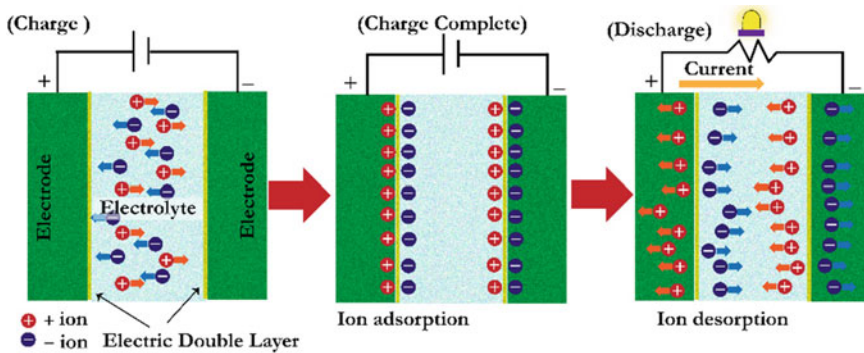
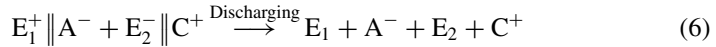


Fig. 4 Schematic diagram of working of EDLC (Yi et al. 2018)



As shown in Fig. 4, since the double layer is formed at both electrode/electrolyte interface, the whole capacitor can be considered two capacitors connected in series. C_T represents the whole capacitance which can be expressed as Eq. (7),

$$\frac{1}{C_T} = \frac{1}{C_1} + \frac{1}{C_2} \quad (7)$$

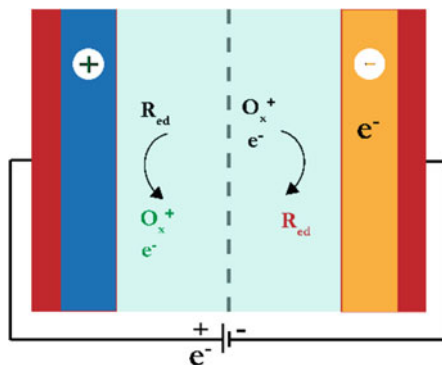
If the two electrodes are the same, i.e. $C_1 = C_2$, the total capacitance (device capacitance) will be half of either electrode's capacitance, and the corresponding capacitor is known as symmetric capacitors. If $C_1 \neq C_2$ (two electrodes are of different materials), the corresponding capacitors are known as asymmetric supercapacitors.

In EDLC, due to the non-Faradic process, no swelling is observed in the active material like in batteries during charging and discharging processes. The huge surface area of electrodes in EDLC supercapacitors allows for high current delivery, resulting in a power density that is several orders of magnitude higher than that of batteries (Simon and Gogotsi 2010). In most commercial EDLCs, activated carbon (AC), a low-cost and abundant carbon source, is often employed. ACs can provide specific capacitance of around 100–120 F/g with organic electrolyte (Simon and Gogotsi 2010). To further enhance the capacitance value of EDLC, advanced carbon nanostructures like mesoporous carbon, carbon nanotubes (CNTs), and graphene, etc., were explored. These carbon nanomaterials are mostly expensive than ACs; but, their specific capacitance values exceed that of ACs. Zhu et al. produced KOH-activated graphene that exhibits a specific capacitance of 166 F/g in organic electrolytes (Zhu et al. 2011). Furthermore, EDLC materials' good electrical conductivity can lower electrode internal resistance, and the electrolyte's better wettability will promote ion mobility into carbon electrode pores, boosting capacitive performance. Carbon materials are thus considered potential electrode materials in EDLC capacitors because they provide a number of benefits, including low cost, non-toxic nature, simplicity of processing, good electrical conductivity, and a large charge storage surface area.

2.2 Pseudo-Capacitors

Charge storage in a pseudo-capacitor differs from that of an EDLC capacitor. When a voltage is supplied, a reversible faradic (oxidation and reduction) process on the active electrode material occurs, like what occurs in batteries. Electron charge transfer happens between the electrode and the electrolyte. Unlike batteries, however, charging and discharging in pseudocapacitive materials takes seconds

Fig. 5 Schematic diagram of pseudo-capacitor



or minutes. Ruthenium oxide (RuO_2) is one of the most comprehensively explored pseudo-capacitive materials as this ruthenium metal has multiple redox phases [i.e., $\text{Ru(IV)}/\text{(III)}$ and $\text{Ru(III)}/\text{Ru(II)}$] in a proton-rich solvent such as sulfuric acid (H_2SO_4). This precious metal can facilitate more electron transfers for superior capacitance (Conway 1999b). Hu et al. reported a specific capacitance of 1300 F/g in H_2SO_4 electrolyte for hydrous RuO_2 nanotubes arrayed electrodes (Hu et al. 2006). Although the RuO_2 electrode material has good electrochemical properties, its high cost, toxicity, and availability limit its use in supercapacitors. In this respect, research focused on developing non-toxic and inexpensive materials such as cobalt oxide, nickel oxide, Fe_3O_4 , MnO_2 , and conductive polymers where the redox processes occur, is necessary. Due to the faradic response mechanism, the pseudo-capacitor has a greater specific capacitance value and energy density than EDLC. For example, Gao et al. synthesized cobalt oxide nanowire arrays that showed a specific capacitance of 570–700 F/g (Gao et al. 2010). Also, nickel oxide nanoflowers exhibited a specific capacitance of around 600–760 F/g (Kim et al. 2013; Yuan et al. 2009). However, because the faradic process is generally slower than the non-faradic process, the power density of a pseudo-capacitor is lower than that of an EDLC, and it also suffers from a lack of cycling stability, like that of batteries, due to redox processes occurring at the electrode. Figure 5 shows the schematic diagram of pseudo-capacitor.

2.3 Hybrid Capacitors

As the name implies, a hybrid capacitor has an asymmetrical electrode configuration, i.e., a carbon electrode and a pseudo-capacitive electrode material. Although one plays a leading role, both faradic and non-faradic processes occur simultaneously in a hybrid capacitor. Recently, a lot of research has been done on hybrid supercapacitors. Hybrid supercapacitors take advantage of the benefits of both electrode materials in terms of performance voltage, energy, and power densities of the entire cell. To attain substantial capacitance in both mechanisms, the electrode

materials must have a wide surface area, an acceptable pore size distribution, and good conductivity. Mainly composites are used as hybrid supercapacitor electrode materials which can overcome demerits involved in EDLC and pseudocapacitive materials. Composite materials consist of carbon materials with either conducting polymer or metal oxides to form a single electrode that involves both EDLC and pseudocapacitive mechanisms. In composite electrodes, carbon materials provide a capacitive double layer of charge and greater specific surface area and increase the contact between pseudocapacitive materials and electrolytes. Pseudocapacitive material improves the capacitance in the composite electrode through Faradaic reaction. Currently, two different types of composites are binary and ternary composites are being used as electrodes. A binary composite electrode contains two different electrode materials, whereas a ternary composite electrode includes three various electrode materials to form a single electrode. Consequently, composite materials will be the most prominent electrode materials for the next-generation energy storage devices. Hybrid supercapacitors also offer a lot of potential for future energy storage systems in terms of increasing energy and power density.

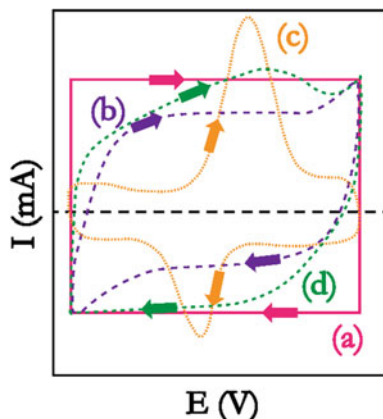
3 Different Techniques for the Evaluation of Supercapacitors

The electrochemical performance of the supercapacitor cells depends on the charging rates, voltage ranges, and calculation method of electrochemical parameters and should closely match presently established and accepted calculation procedures. The specific capacitance of a supercapacitor electrode depends on the type of electrochemical measurements such as two-electrode or three-electrode configuration. Capacitance is usually significantly higher when using a three-electrode system, while a two-electrode configuration provides the device-level performance. In a two-electrode configuration, test cells are constructed using two active electrodes, electrolyte and a separator which avoid the physical contact between the two electrodes. Finally, metal plates connect the two electrodes and their separator to form test cells. There are different analysis techniques for evaluating the electrochemical performance of the supercapacitor cells and discussed in the following sections.

3.1 *Cyclic Voltammetry*

Cyclic voltammetry evaluates the quantitative and qualitative information regarding the electrochemical phenomena happening within the active materials of the working electrodes. This is done by applying a potential range to the working electrode with respect to the fixed potential of the reference electrode, which sweeps between the two preset potentials. Electrolyte's operating stability determines the potential range.

Fig. 6 Illustration of CV curves of (a) ideal capacitor, (b) EDLC, (c) pseudocapacitive, and (d) hybrid materials



Voltage sweep produces a time-dependent current (I), and a cyclic voltammogram (CV) curve can be obtained by plotting this current versus applied potential for evaluating the capacitance of the test cells. Figure 6 gives a detailed picture of the CV curves of different supercapacitors. The CV of the ideal capacitors looks like a rectangular shape, as shown in Fig. 6a, but EDLC shows a deformed rectangular shape (Fig. 6b). Pseudocapacitor displays redox peaks in the CV curve due to the faradaic reaction that occurs in the active materials (Fig. 6c). Hybrid capacitors show the deformed rectangular shape along with redox peaks (Fig. 6d). From the CV curves, capacitance can be evaluated using the following equation (Kim et al. 2013).

$$C = \frac{\int i dV}{2V\Delta V} \quad (8)$$

where $\int i dV$ is the total area under the CV curve, V is the scan rate (mV s^{-1}), and ΔV is the potential window.

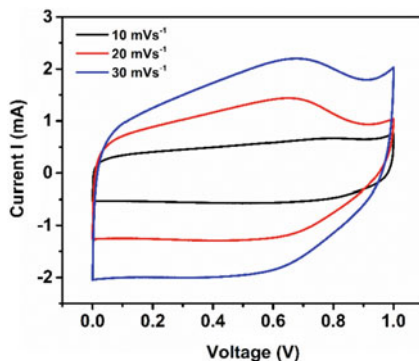
Specific capacitance of the electrode is given by

$$C_s = \frac{C}{m} \quad (9)$$

where C_s the specific capacitance (F/g) is, C is the capacitance calculated from Eq. (8) and m is the mass of the active material.

The capacitance of the electrode varies with respect to potential scan rates. High potential scan rates distort the rectangular shape of CV curves. The Fig. 7 shows the CV curves of PANI/MWCNT hybrid materials at different scan rates.

Fig. 7 The CV curves of PANI/MWCNT composite at various scan rates (Mannayil et al. 2018)



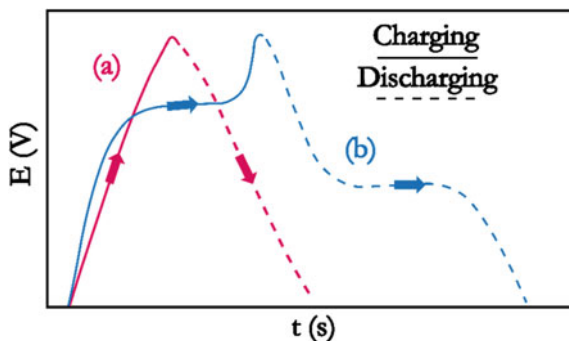
3.2 Galvanostatic Charge Discharge (GCD)

Besides CV, the galvanostatic charge discharge (GCD) technique is also used to determine the capacitance of the material. GCD provides an accurate capacitance value and measures potential versus time by applying constant current density. Here the electrode is charged to an upper value of the applied potential and then discharged to the lower value of the potential to evaluate the capacitance of the material. Figure 8 illustrates the GCD profile of the EDLC and pseudo-capacitor.

Similar to CV curves, GCD profiles also have dissimilar behavior for different materials, and hence equations for evaluating the capacitance of the materials are also different. For EDLC materials, the charge–discharge plot is linear, while pseudo-capacitive materials show a non-linear behavior in GCD plot. For EDLC, capacitance can be determined using Eq. (10) (Stoller and Ruoff 2010). Here, the slope of the discharge part is used for the calculation of capacitance.

$$C = \frac{I}{dV/dt} \quad (10)$$

Fig. 8 Schematic diagram of GCD plots for **a** EDLC and **b** pseudo-capacitor



where C is the capacitance of the materials (in F), I is the applied current (mA) and dV/dt is the slope of the discharge part of the GCD curve. For pseudo-capacitor, capacitance value can be determined using the Eq. (11)

$$C = \frac{I(\Delta t)}{\Delta V} \quad (11)$$

where C is the capacitance of the material (F), I is the applied current (mA), Δt is the discharge time (s), and ΔV is the voltage difference (V) in the discharge part of the GCD curve. For calculating the specific capacitance, Eq. (9) can be used, i.e., Eq. (9) can be modified as follows:

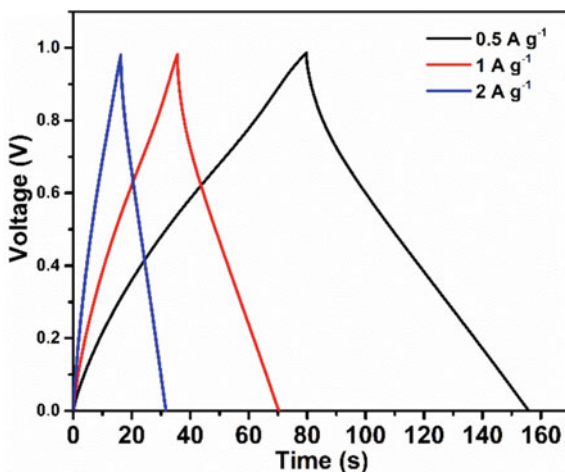
$$C_s = \frac{I(\Delta t)}{m\Delta V} \quad (12)$$

where m is the mass of active material. As in the case of scan rate-dependent capacitance, it also depends on the current density. At higher current densities, rapid discharge occurs and hinders the electrochemical properties of the electrode due to material degradation. At lower current densities, more self-discharge and leakage current is induced, which affects the commercialization of the device. Figure 9 shows the GCD profiles of the PANI/MWCNT composites.

Usually, supercapacitor structure is considered equivalent to a circuit comprising of two capacitors connected in series. Therefore, the total capacitance (F) of the capacitors in series is given by

$$\frac{1}{C_T} = \frac{1}{C_1} + \frac{1}{C_2} \quad (13)$$

Fig. 9 GCD profile of the PANI/MWCNT composite on carbon cloth at different current densities (Mannayil et al. 2018)



Hence, the total capacitance of the symmetric supercapacitor test cells is $C_T = \frac{C_E}{2}$ and the capacitance of the single electrode is given by

$$C_E = 2C_T \quad (14)$$

where C_E is the capacitance of the single electrode. Equation (14) is applicable if the mass of the combined electrode is added in the capacitance calculation.

In Fig. 9, a voltage drop IR is observed at the starting point of the discharge curve, which denotes the internal resistance of the device. This potential variation increases at higher current densities, which reduces the power density of the device (Choi et al. 2010).

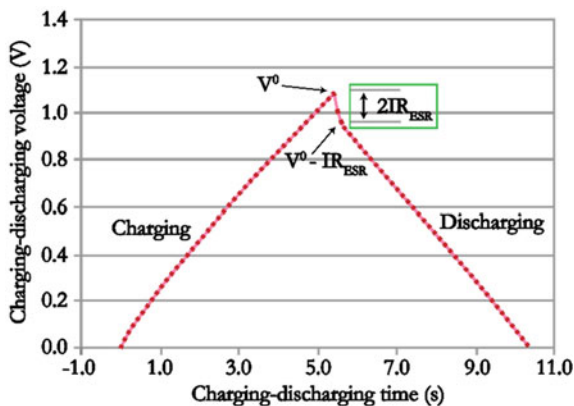
3.3 *Electrochemical Impedance Spectroscopy (EIS)*

Most supercapacitors in practical applications exhibit some internal resistances rather than ideal capacitive behavior. Understanding the internal resistances offered by supercapacitors provides in-depth knowledge about the power performance of the device, which is very useful in commercial applications. The main resistance is the equivalent series resistance (ESR), which is contributed by the resistances of all cell components, i.e., electrolyte resistance, contact resistance between electrodes and current collectors (Zhao et al. 2010; Conway 1999c). This ESR value significantly affects the power density of a cell. ESR value depends on the current density at which the cell can be charged and discharged. ESR value increases as the current density of the charging and discharging of the cell increases, resulting in power reduction and energy dissipation. Two techniques can control the ESR (Kim et al. 2015) which include Galvanostatic charge–discharge techniques and electrochemical impedance spectroscopy (EIS).

In the GCD technique, the discharge process is monitored in the specified potential range with respect to time, as mentioned in the earlier section. In the GCD plot, a sudden drop at the initial discharge is observed called IR drop, as shown in Fig. 10. ESR can be determined by dividing the change in potential at the initial discharge process (i.e., IR drop) by doubling the current applied. This technique can be applied for both three-electrode and two-electrode device level systems.

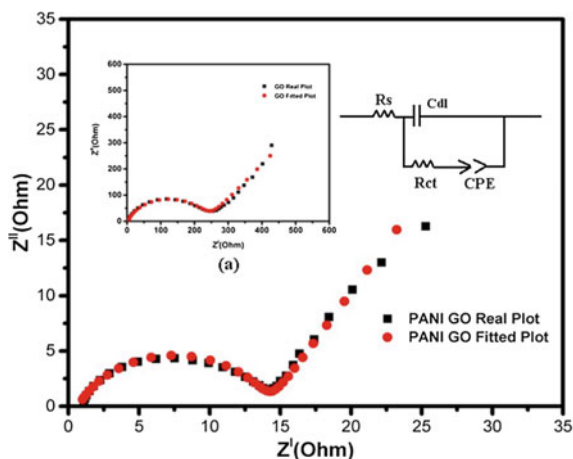
Another technique is the EIS, which is one of the most important techniques used to evaluate the internal resistances of the device quantitatively. Besides ESR, EIS also offers in-depth knowledge about other electrical characteristics of the cell. In this technique, a small magnitude alternating current (AC) (say 5–10 mV) is applied to supercapacitors within the frequency range of 0.01 Hz to 1 MHz. The response is plotted as a Nyquist plot, which contains imaginary resistance (Z'') versus real resistance (Z') from higher frequency range to lower. The plot consists of a linear region in the lower frequency range and a semi-circle at the high-frequency range. The diameter of the semi-circle signifies the interfacial charge transfer resistance

Fig. 10 Schematic representation of GCD plot. IR drop is marked in the box



(R_{ct}) and a straight line at the lower frequency range indicates the ionic resistance offered by the electrolyte (Kotz and Carlen 2000; Wang et al. 2005). As interfacial charge transfer resistance decreases, the power density of the cell increases. R_{ct} can be calculated by fitting the EIS spectra with equivalent circuit (as shown in Fig. 11). Moreover, more vertical line at lower frequency corresponds to lower ionic diffusion resistance, which also increases the electrochemical properties of the cells. Figure 11 shows the Nyquist plot for the GO/PANI composite electrode.

Fig. 11 Nyquist plots of GO and PANI-GO symmetric cells in the frequency range of 20 kHz–10 MHz (Reprinted with permission from Manoj et al. (2017), copyright (2017) © Springer Nature)



4 Supercapacitor Parameters

4.1 Energy Density and Power Density

Galvanostatic charge–discharge technique is one of the familiar techniques to investigate the energy and power densities of the supercapacitors. Particularly, the energy density of supercapacitor decreases with an increase in power density, and therefore these are inversely proportional to each other. The energy density and power densities are two key tools for investigating the electrochemical performance of supercapacitors. These two parameters have been widely used to assess the electrochemical performance of electrode materials and provide the overall performance of the device. The energy and power densities of the electrochemical cell can be calculated from the following equations (Wang et al. 2005, 2006; Li et al. 2016).

$$E = (1/2 \times 3.6)C \times (\Delta V)^2 \quad (15)$$

$$P = (E/t) \times 3600 \quad (16)$$

where E is the energy density in Wh kg^{-1} , C is the specific capacitance of the device in F g^{-1} , ΔV is the voltage window, P is the power density in W kg^{-1} , t is the discharge time in s. Energy density depends on the specific capacitance of the supercapacitor cells as well as the voltage range of the electrolyte. The voltage window of the electrolytes varies upon the nature of the electrolyte. It is less than 1 V for aqueous electrolytes such as H_2SO_4 , KOH , etc. and less than 3 V for organic electrolytes such as LiClO_4 , and greater than 3 V for ionic liquid-based electrolytes. Hence the energy density of the supercapacitor cells can also be enhanced by the use of high voltage withstandable electrolytes.

4.2 Coulombic Efficiency

Coulombic efficiency (CE) is defined as the ratio of discharging time and charging time at constant charge–discharge current densities. CE can be determined using the equation (Stoller and Ruoff 2010; Park et al. 2002; Mallika and Saravana Kumar 2011; Wang et al. 2007).

$$\eta = (t_D/t_C) \times 100\% \quad (17)$$

where t_D is the discharging time (s), t_C is the charging time (s), and η is the coulombic efficiency (%). The coulombic efficiency is calculated by the cyclic stability method

using charge–discharge techniques by making a comparison between the first and the end cycle. Hence, the CE is usually used for evaluating the cyclic stability of the device.

5 Stability of the Electrode Materials

Supercapacitors provide an auspicious alternative to batteries, particularly due to their outstanding power density and rapid charging rate capability. The stability of the electrode materials is a key parameter to rank the electrochemical performances of supercapacitors. Nevertheless, the cyclic stability and the stability of the electrode materials are essential properties that must be considerably improved to boost the reliability and durability of supercapacitor cells in practical applications. The Charge–discharge technique has been used to evaluate the stability of the electrode materials. Many researchers reported the cyclic stability of the electrodes and capacitance retention after several cycles (Wang et al. 2006; Liang et al. 2007). The stability of the electrode materials can be enhanced by the addition of carbon material which provides rapid ion diffusion pathways and avoids the degradation of the active materials during several charge/discharge cycles. Cyclic stability of the PANI–GO composite (Manoj et al. 2017) was evaluated by the charge–discharge method for 1000 cycles within the potential range of 0–2.5 V. After 1000 cycles composite electrode retained 84.8% of its initial specific capacitance, confirming the remarkable stability of the composite electrode.

The stability of the electrodes can be enhanced by using 3D structured current collectors like nickel foam or carbon cloth which offers better adhesion to the active materials. Hierarchically ordered mesoporous carbon/graphene (OMC/G) composites have been used as supercapacitor electrodes which showed excellent cyclic stability of 96% after 5000 cycles (Song et al. 2016). Here, the ordered mesoporous structure in the OMC/G composites provides more accessibility of the electrolyte and offers rapid ion diffusion pathways; meanwhile, graphene facilitates the charge transport during the charging/discharging process due to its high conductivity, thereby leading to an excellent electrochemical performance.

6 Critical Factors Affecting the Performance of Supercapacitors

Many factors affect the supercapacitor performance, including the nature of the electrolyte, type of electrodes, current collectors, etc. Properties of electrode materials such as porosity, surface area, etc., significantly affect the electrochemical performance of the supercapacitors. Materials having high surface area provide more sites for ion adsorption or redox reaction process, resulting in higher energy and power

densities. Similarly, pore size distribution in the electrode materials and the ionic radii of the electrolyte ions affects the electrochemical process. Mesopores are favorable to rapid diffusion and increase the accessibility of electrolytes, which can increase the electroactive surface area and thereby lead to the excellent electrochemical performance of the device. Another important parameter that affects the supercapacitor performance is the electrolyte. Electrolytes should have high ionic conductivity for involving the redox reaction process or ion adsorption on the electrode surface. Moreover, the potential window of the electrolyte is related to the energy density of the supercapacitors. The electrolyte having a high potential window provides high energy density. For example, aqueous electrolytes have high ionic conductivity than organic electrolytes, but their potential window is less than 1 V. Hence, electrolytes having high ionic conductivity along with a better potential window will be favorable for the efficient energy storage system.

7 Carbon Materials for Supercapacitor Electrodes

Carbon is an extremely attractive material for supercapacitor electrodes as it is most abundant and cost-effective. A wide variety of dimensionality (0–3D) and capability for the existence of different forms from powder to fibers are available due to its degree of graphitization. Moreover, carbon-based materials have attractive properties like high conductivity, eco-friendliness, and simple design. Various forms of carbon materials like activated carbon (AC), CNTs, Graphene, etc., have been widely used for supercapacitor electrode applications due to their large surface area, cost-effective, and well-known electrode production technologies.

In carbon materials, the charge storage mechanism is an electric double layer (EDLC) formed at the electrode/electrolyte interface. The specific capacitance of the carbon electrodes depends on the surface area called the electrochemical surface area, where the ions are adsorbed during the charging process. Moreover, carbon has pronounced advantages in supercapacitor applications: the activation process can easily design their porosity and morphology. Thus highly porous materials can be formed whose surface area may range from a few hundred to more than $2000 \text{ m}^2 \text{ g}^{-1}$ (Lee et al. 2006; Kyotani 2000; Noked et al. 2009). The pores in carbons can be categorized into three: macropores having a diameter greater than 50 nm, mesopores having diameter between 50 and 2 nm, and micropores with diameter less than 2 nm (Bansal and Goyal 2005). Desired porosity of the electrode materials is very important, which gives the high specific surface area, and supercapacitors deliver a high specific capacity of ion adsorption. Moreover, porosity determines the rate of ion diffusion through the pores of the electrodes during the charge/discharge processes.

Generally, activated carbon is utilized as electrode material in commercially available supercapacitors. AC can be synthesized by the thermal or chemical activation process of carbonaceous precursors like woods, coals, coconut-derived shells, etc. The activation process using potassium hydroxide (KOH) is one of the most prevalent techniques for the low-cost production of AC. The activation process creates pores

which increase the surface area and contributes to the capacitance performance of AC. Activated carbon electrodes can store specific capacitance around 200 F/g using aqueous electrolytes and ~150 F/g using organic electrolytes (Frackowiak 2007). Wang et al. achieved a specific capacitance of 160 F/g for KOH-treated AC with 6 M KOH as electrolyte. They studied the variation of specific capacitance with respect to the pore structure of AC (Nguyen et al. 2013). Wen et al. (Wen et al. 2009) reported the capacitance performance of the polymeric activated carbon with a specific capacitance of 225 F/g.

Recently, graphitic allotropes of carbon such as carbon nanotubes (Simon and Gogotsi 2008; Carbon et al. 2010), fullerenes (Dresselhaus et al. 1996), and graphene (Huang et al. 2012; Chen and Dai 2013; Sheng et al. 2012) have been investigated as electrode materials. CNT and graphene have been widely explored as supercapacitor electrodes due to their unique morphology, high surface area, high electrical conductivity, and mechanical strength. They may subdue the disadvantages of the conventional activated carbon, having poor electrical conductivity and mechanical strength. The electrochemical performance of CNT depends on its morphology and purity, and the specific capacitance ranges between 15 and 200 F/g (Liu et al. 2010).

8 Limitations of Carbon Materials Based Supercapacitors

Carbon-based materials have unique properties such as high electrical conductivity, high surface area, and high mechanical strength, very suitable for supercapacitor electrode applications. Carbon nanostructures-based supercapacitor electrodes have the limitations of low specific capacitance, agglomeration, and difficulty in processing. Since the carbon materials show EDLC behavior where the ions are adsorbed on the electrode/electrolyte interface forming a double layer, capacitance contribution is low when compared to pseudo-capacitors. Moreover, carbon materials have the inherent property of agglomeration, which seriously affects the electrochemical performance of the device. Carbon materials have poor processibility due to their inherent agglomeration nature, so it is difficult to make a uniform coating of the carbon materials on the current collector. Hence the carbon electrode has to be modified to avoid agglomeration and improve the electroactive surface area of the electrode to obtain an efficient energy storage system.

9 Carbon Based Composites for Supercapacitors

Composite materials can overcome the shortcomings of carbon materials by integrating them with redox-active materials such as conducting polymers or metal oxides. Numerous reports in recent times have highlighted that carbon composites are the promising elements in supercapacitor electrodes. Hassan et al. reported the 3D composite of PANI/graphene with a specific capacitance of 448 F/g at a

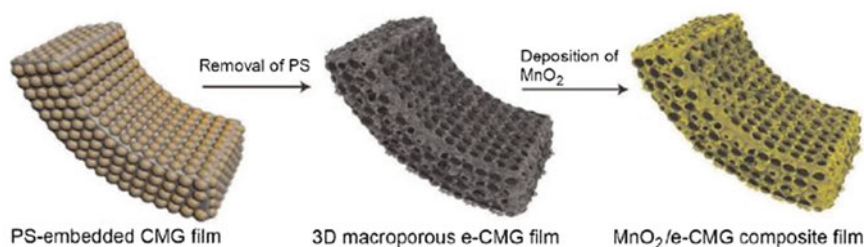


Fig. 12 Schematic representation of the fabrication of 3D macroporous films e-CMG film and a subsequent deposition process of MnO₂ for MnO₂/e-CMG film. (Reprinted with permission from Choi et al. (2012). Copyright (2012) © American Chemical Society)

current density of 0.5 A/g using a three-electrode system. They observed that the graphene/PANI composite has capacitance retention of about 81% after 5000 cycles (Hassan et al. 2014). Bong et al. fabricated a 3D framework of graphene for high-performance supercapacitor application. They reported asymmetric supercapacitor of MnO₂/embossed chemically modified graphene (e-CMG) composite (Fig. 12), and e-CMG and the composite showed a specific capacitance of 389 F/g at a current density of 1 A/g (Choi et al. 2012). Yanjie et al. fabricated ordered mesoporous carbon (OMC)/graphene composite via solvent-evaporation-induced self-assembly (EISA) method for supercapacitor electrodes. The composite electrode showed capacitance of 329.5 F/g in 6 M KOH electrolyte at a current density of 0.5 A/g using a three-electrode configuration. The obtained OMC/G composites showed final capacitance retention of approximately 96% after 5000 cycles and displayed good cyclic stability (Song et al. 2016).

Manoj et al. reported PANI/GO composite electrodes synthesized by the in-situ oxidative polymerization method. They observed a specific capacitance of 810 F/g at a current density of 0.2 A/g using a three-electrode system (Fig. 13). This high capacitance value is due to the ordered arrangement of PANI nanorods on GO sheets. The composite shows a specific capacitance of 132 F/g at a high current density of 5 A/g and also exhibited a good rate capability (Manoj et al. 2017).

Symmetric supercapacitor cells assembled using Mn₃O₄ graphene composite showed a specific capacitance of 94 F/g with capacitance retention of 95% after 5000 cycles at a current density of 5 A/g (Fig. 14) (Anilkumar et al. 2017). Asymmetric supercapacitor assembled using graphene/CNT, and graphene/CNT–PANI composite electrodes (Fig. 15) obtained the highest energy density of 188.4 Wh kg⁻¹ and maximum power density of 200.5 kW kg⁻¹. The supercapacitor was charged up to 4 V, and capacitance dropped by 18% after 1000 cycles which showed good cyclic stability of the electrodes (Cheng et al. 2013).

MnO₂ decorated hierarchical porous carbon fiber/graphene supercapacitor electrode was synthesized via the electrospinning method. Electrode showed capacitance of 210 F g⁻¹ at a current density of 1 mA cm⁻², the high energy density of 24–19 Wh kg⁻¹, and good rate capability (capacitance of 170 F g⁻¹ retained at a high current density of 20 mA cm⁻²) in a 6 M KOH aqueous solution (Lee and Kim

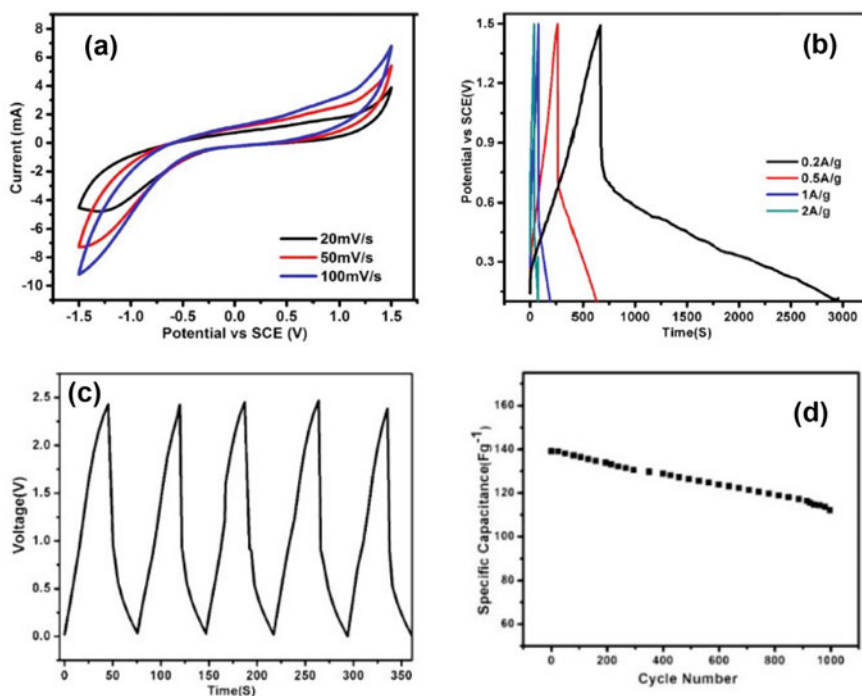


Fig. 13 **a** GCD and **b** CV curves of the PANI–GO composites at a current density of 0.2 A/g using a three-electrode system, **c** GCD curve of the PANI–GO composite at a current density of 5 A/g, and **d** Specific capacitance versus cycle number. (Reprinted with permission from Manoj et al. (2017) Copyright (2017), © Springer Nature)

2016). Graphene-like activated carbon sheets from jute were synthesized and electrochemically characterized for supercapacitor application. The composite showed a specific capacitance of 476 F/g and 200 F/g at a current density of 0.2 A/g and 10 A/g, respectively, in 0.5 M H₂SO₄ solution using a three-electrode configuration (Ojha et al. 2017). PANI/CNT/MoS₂ composite was synthesized by the chemical oxidative polymerization method. The composite electrode showed a specific capacitance of 350 F/g with 5% MoS₂ at 1 A/g in 1 M H₂SO₄ solution using a two-electrode configuration. The voltage window was 0–0.8 V. The role of MoS₂ on PANI/CNT MoS₂ composite in supercapacitor performance was analyzed (Thakur et al. 2017). Wujun et al. reported fiber-shaped hybrid supercapacitor based on transition metal oxide nanorods/reduced graphene oxide (rGO) by a wet-spinning method. They fabricated an all-solid-state asymmetric supercapacitor with MnO₂ nanorod/rGO as the positive electrode and MoO₃ nanorods/rGO as the negative electrode in H₃PO₄/poly(vinyl alcohol) (PVA) electrolyte. This asymmetric supercapacitor exhibited a superior volumetric energy density of 18.2 mWh cm⁻³ at a power density of 76.4 mW cm⁻³ at

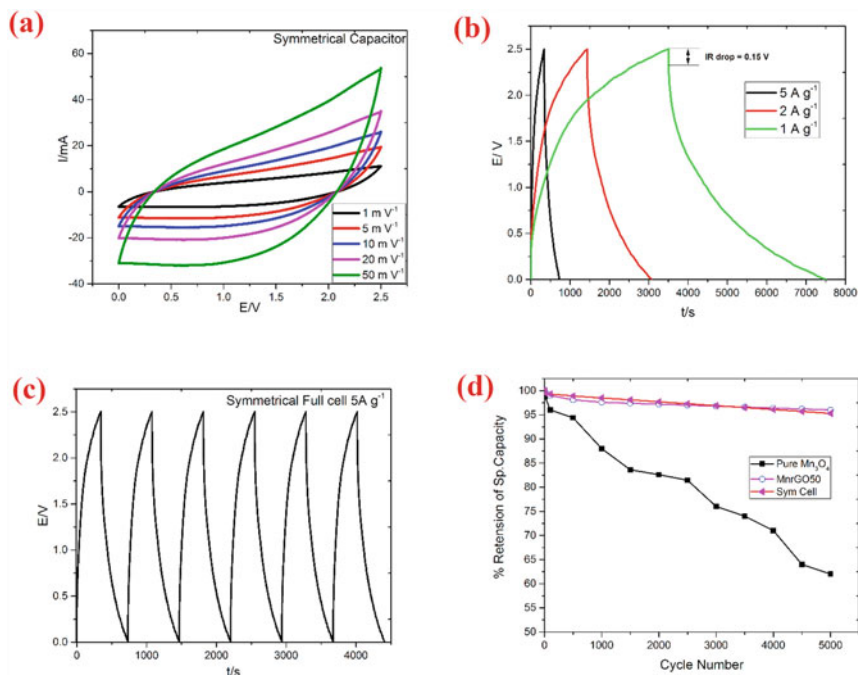


Fig. 14 **a** CV and **b** GCD curves of the Mn_3O_4 graphene composite supercapacitor, **c** GCD curve at a current density of 5 A/g , and **d** percentage of capacitance retention versus cycle number. (Reprinted with permission from Anilkumar et al. (2017), Copyright (2017), © Elsevier)

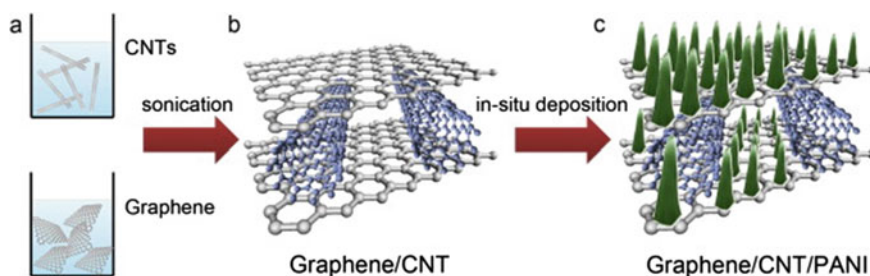


Fig. 15 Illustration of the fabrication process of graphene/CNT and graphene/CNT-PANI composites. **a** Graphene and CNTs are first mixed in ethanol. **b** Graphene and CNT suspensions are mixed by ultrasonication and formation of graphene/CNT composite by vacuum filtration method. **c** Graphene/CNT-PANI composite formation via in-situ polymerization. (Reprinted with permission from Cheng et al. (2013), copyright (2013) © Elsevier)

a high voltage of 1.6 V and exhibited significant cycling stability and excellent flexibility (Ma et al. 2017). Nanostructured graphene/polyaniline (PANI) nanofibre supercapacitor electrode materials were synthesized using the hydrothermal method. The diameter of PANI nanofiber was 50–100 nm. The composites showed high specific capacitances of 532.3 F/g at a scan rate of 2 mV/s and good cyclic performances with capacitance retention of ~99.6%. Here the ultrathin layer—structure provides active materials to participate in the interfacial electrochemical reactions (Wang et al. 2017a). The double-layer capacitance of CNT can be enhanced by introducing pseudocapacitive materials, such as conducting polymers, metal doping, etc. Yaping et al. fabricated all-solid-state supercapacitors using Ag-doped PEDOT:PSS composites as electrodes and PVA/H₃PO₄ gel as electrolyte (Fig. 16). The composite was fabricated by drop-casting Ag-doped PEDOT:PSS solution on aligned CNT arrays. The supercapacitor showed a high specific capacitance of 64 mF/cm² (corresponding to 85.3 F/g) with capacitance retention of 98% even under a tensile strain as high as 480%. The reason for high stretchability is that the aligned CNT electrodes were strongly bundled together with polymeric chains of electrolyte (Zhu et al. 2018). Fabrication of supercapacitor on conducting substrates can omit the transfer and coating procedure in the traditional method and act as a current collector. Zhou et al. reported a supercapacitor made of graphene nanowalls (GNW) on nickel foam with a capacitance of 0.053 F cm⁻³ at a scan rate of 50 mV/s using a three-electrode system. The electrode exhibited tiny degradation (<10%) after 800 charge/discharge cycles (Zhou et al. 2018). An all-solid-state flexible supercapacitor was assembled using MWCNTs/PEDOT as electrodes and the PVA–H₃PO₄ gel as electrolyte. The device showed a real capacitance of 32.06 mF/cm² and demonstrated potential in wearable electronics (Chen et al. 2019). Wang et al. (Wang et al. 2017b) constructed PANI–CNT@zeolite imidazolate framework-67 on carbon cloth for flexible supercapacitor electrodes. The composite showed a high specific capacitance of 3511 mF cm⁻² at 10 mV/s with excellent capacitance retention of 83% after 1000 charge/discharge cycles at 0.5 mA cm⁻².

Recent reports on carbon composite-based supercapacitors give new pathways for efficient energy storage devices in terms of high power density, enhanced energy density, and long cycle life.

10 Challenges of Supercapacitors

Supercapacitors can be considered as future energy storage systems owing to their amazing properties of wide operational temperature window, rapid charging/discharging, and long cycle life. But some disadvantages of supercapacitors are high self-discharge and voltage loss which will reduce the shelf life of the supercapacitors. Moreover, supercapacitors are not suitable for long-term energy storage and also have a high cost. These issues limit wide applications of supercapacitors.

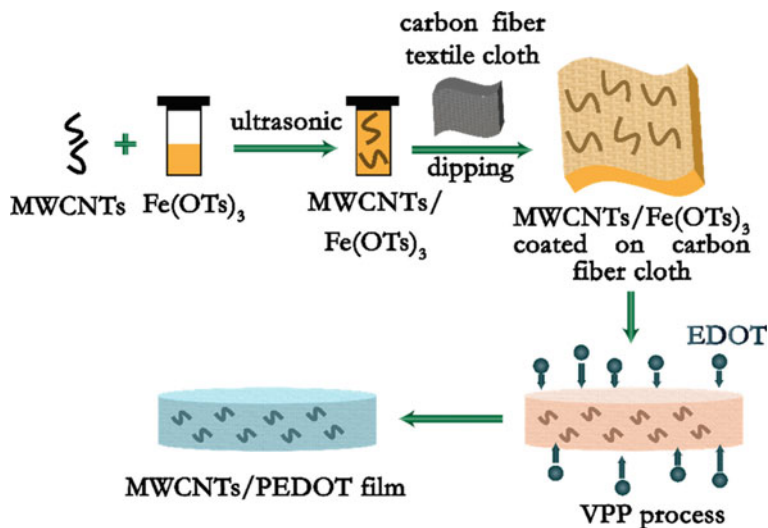


Fig. 16 Schematic diagram of the fabrication of MWCNT/PEDOT flexible electrodes

10.1 Self-Discharge Characteristics

Self-discharge of SCs is a serious problem that limits their practical applications. When several studies have been made to overcome the disadvantages of supercapacitors like low energy density and high cost, little efforts were made in discussing the self-discharge issue of supercapacitors. Self-discharge mechanism is defined as a spontaneous reduction of the voltage of the charged supercapacitors with time in an open circuit. The high self-discharge rate of supercapacitors is mainly due to the faradaic reaction of electrolyte impurities or functional group present on the electrode surface, charge redistributions due to the loss of adsorbed ions on the electrode surface caused by the concentration gradient in the electrolyte, and ohmic leakage caused due to the improper sealing of the electrodes (Black and Andreas 2009; Zhang et al. 2020; Andreas 2015; Conway et al. 1997; Liu et al. 1997).

Different self-discharge mechanisms have been found for different systems. The self-discharge mechanism for each system should be analyzed for determining the self-discharge rate of the supercapacitors. Since the self-discharge due to the ohmic leakage is related to the potential driving model, the self-discharge characteristic behavior of ohmic leakage is modeled according to the following equation (Black and Andreas 2009; Andreas 2015; Conway et al. 1997),

$$V = V_0 \exp\left(-\frac{t}{RC}\right) \quad (18)$$

where V is the cell voltage during the self-discharge, V_0 is the initial cell voltage of the charged supercapacitor, t is the time, and RC represent the time constant of the self-discharge process. Other important contributors to the self-discharge are the diffusion-controlled or activation-controlled faradaic processes. By taking the diffusion-controlled faradaic process, the self-discharge process is modeled as per the following equation (Conway et al. 1997),

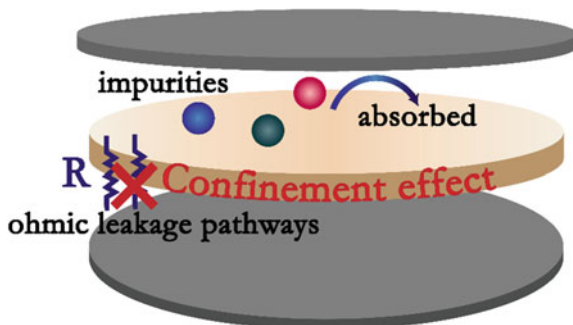
$$V = V_0 - m\sqrt{t} \quad (19)$$

where m is the diffusion factor which denotes the rate of ion diffusion near the electrode surface.

Based on the self-discharge mechanism, some attempts have been made to reduce self-discharge by adding additives, tuning ion transport by employing ion-exchange membranes, and using modified electrodes. Xia et al. suggested an electrorheological (ER) method to reduce the self-discharge rate (Xia et al. 2018). They introduced liquid crystal 4-*n*-pentyl-4'-cyanobiphenyl in the electrolyte as an additive and reduced the decay rate of cell potential and leakage current by 80%. The electrostatic interaction between a single-walled carbon nanotube and the electrolytic ions is also described to study the effect of surface chemistry on the self-discharge process. Some efforts had been made in subduing the self-discharge of supercapacitors by employing a cation exchange membrane rather than a porous separator. They described that the ion exchange membrane avoids shuttling of ions through the separator (Lee et al. 2017). Even though the self-discharge studies of supercapacitors are improved to some extent through these strategies, it is still far from state of the art, particularly in high-temperature circumstances.

Recently, researchers have found an effective way of suppressing the self-discharge rate of supercapacitors by using layered materials like clay. Wang et al. introduced the ‘mud pies’ strategy to prepare clay@ionic liquid-based solid-state electrolyte for suppressing self-discharge (Fig. 17) (Wang et al. 2019). They found very low self-discharge with cell potential decay around only 28.9% within 60 h and also showed a low potential decay rate even at a high temperature of 75 °C.

Fig. 17 Schematic illustration of the inhibited self-discharge phenomenon due to confinement effect of ion transfer



Here, clay ionic liquid-based solid-state electrolyte avoids the shuttling of the impurity ions via Si–O bond present in the clay and encourages the selective penetration of electrolyte ions. Hence the layered structure of the bentonite clay decays the diffusion-controlled faradaic process and the ohmic leakage by providing good sealing between the electrodes due to the high mechanical strength of the solid-state electrolyte. This strategy opens a way to analyze the self-discharge mechanism, which will lead to extremely low self-discharge supercapacitors with high electrochemical performance.

11 Summary

In brief, supercapacitors have a significant role in alternative energy technology with exceptional electrochemical performance such as high power density and energy density and excellent cyclic stability. Carbon materials with high specific surface area show high cyclic stability, but their low capacitances and energy density limits practical applications. Carbon-based composite materials show high specific capacitance along with high cyclic stability, but the major challenge faced is the fabrication of binder-free electrodes to improve the capacitance value further. The review shows that challenges faced for the design and development of highly efficient supercapacitors to be used in various applications requiring high energy densities. In the future, researchers should focus on ternary composite electrode materials to develop binder-free electrodes providing more active sites for high-performance supercapacitor electrodes with high cyclic stability. The chapter concluded that self-discharge studies of supercapacitors are critical to analyzing the performance of the device. Some methods show an excellent route to tune the self-discharge mechanism and provide a new idea for developing low self-discharge high-performance supercapacitors.

References

- Andreas HA (2015) Self-discharge in electrochemical capacitors: a perspective article. *J Electrochem Soc* 162(5):A5047–A5053
- Anilkumar KM, Manoj M, Jinisha B, Pradeep VS, Jayalekshmi S (2017) Mn₃O₄/reduced graphene oxide nanocomposite electrodes with tailored morphology for high power supercapacitor applications. *Electrochim Acta* 236:424–433
- Bansal RC, Goyal M (2005) Activated carbon adsorption. CRC Press, Boca Raton
- Becker HI (1957) Low voltage electrolytic capacitor. US patent 2800616, p 148
- Black J, Andreas HA (2009) Effects of charge redistribution on self-discharge of electrochemical capacitors. *Electrochim Acta* 54(13):3568–3574
- Boos DL (1968) Electrolytic capacitor having carbon paste electrodes. United States Pat. Off., pp 1–6
- Burk A (2000) Ultracapacitors: why, how, and where is the technology. *J Power Sources* 91(1):37–50
- Carbon C, et al (2010) High-rate electrochemical capacitors based on ordered mesoporous silicon carbide-derived carbon. 4(3):1337–1344

- Chen T, Dai L (2013) Carbon nanomaterials for high-performance supercapacitors. *Mater Today* 16(7–8):272–280
- Chen T et al (2012) An integrated ‘energy wire’ for both photoelectric conversion and energy storage. *Angew Chem Int Ed* 51(48):11977–11980
- Chen Y, Yang W, Yang D, Wangyang P, Li X (2019) Facile synthesis and electrochemical performances of multi-walled carbon nanotubes/poly(3,4-ethylenedioxythiophene) composite films as electrodes for fabric supercapacitors. *J Mater Sci Mater Electron* 30(7):6350–6357
- Cheng Q, Tang J, Shinya N, Qin LC (2013) Polyaniline modified graphene and carbon nanotube composite electrode for asymmetric supercapacitors of high energy density. *J Power Sources* 241:423–428
- Choi JW, McDonough J, Jeong S, Yoo JS, Chan CK, Cui Y (2010) Stepwise nanopore evolution in one-dimensional nanostructures. *Nano Lett* 10(4):1409–1413
- Choi BG, Yang M, Hong WH, Choi JW, Huh YS (2012) 3D macroporous graphene frameworks for supercapacitors with high energy and power densities. *ACS Nano* 6(5):4020–4028
- Conway BE (1999b) *Electrochemical supercapacitors: scientific fundamentals and technological application*. Academic Plenum Publishers, New York
- Conway BE, Pell WG, Liu TC (1997) Diagnostic analyses for mechanisms of self-discharge of electrochemical capacitors and batteries. *J Power Sources* 65(1–2):53–59
- Conway BE (1999a) *Electrochemical supercapacitors scientific fundamentals and technological applications*. Plenum Press, New York
- Conway BE (1999c) *Electrochemical supercapacitors*. Plenum Publishing, New York
- Dresselhaus MS, Dresselhaus G, Eklund PC (1996) *Science of fullerenes and carbon nanotubes: their properties and applications*. Elsevier, Amsterdam
- Frackowiak E (2007) Carbon materials for supercapacitor application. *Phys Chem Chem Phys* 9(15):1774–1785
- Gao Y, Chen S, Cao D, Wang G, Yin J (2010) Electrochemical capacitance of Co_3O_4 nanowire arrays supported on nickel foam. *J Power Sources* 195(6):1757–1760
- Hassan M et al (2014) Hierarchical assembly of graphene/polyaniline nanostructures to synthesize free-standing supercapacitor electrode. *Compos Sci Technol* 98:1–8
- Hu CC, Chang KH, Lin MC, Wu YT (2006) Design and tailoring of the nanotubular arrayed architecture of hydrous RuO_2 for next generation supercapacitors. *Nano Lett* 6(12):2690–2695
- Huang Y, Liang J, Chen Y (2012) An overview of the applications of graphene-based materials in supercapacitors. *Small* 8(12):1805–1834
- Jost K et al (2013) Knitted and screen printed carbon-fiber supercapacitors for applications in wearable electronics. *Energy Environ Sci* 6(9):2698–2705
- Kim BK, Chabot V, Yu A (2013) Carbon nanomaterials supported $\text{Ni}(\text{OH})_2/\text{NiO}$ hybrid flower structure for supercapacitor. *Electrochim Acta* 109:370–380
- Kim BK, Sy S, Yu A, Zhang J (2015) Electrochemical supercapacitors for energy storage and conversion. In: *Handbook of clean energy systems*, pp 1–25
- Kotz R, Carlen MJ (2000) Principles and applications of electrochemical capacitors. *Electrochim Acta* 45:2483–2498
- Kyotani T (2000) Control of pore structure in carbon. *Carbon (NY)* 38(2):269–286
- Le VT et al (2013) Coaxial fiber supercapacitor using all-carbon material electrodes. *ACS Nano* 7(7):5940–5947
- Lee DG, Kim BH (2016) MnO_2 decorated on electrospun carbon nanofiber/graphene composites as supercapacitor electrode materials. *Synth Met* 219:115–123
- Lee J, Kim J, Hyeon T (2006) Recent progress in the synthesis of porous carbon materials. *Adv Mater* 18(16):2073–2094
- Lee J et al (2017) Asymmetric tin-vanadium redox electrolyte for hybrid energy storage with nanoporous carbon electrodes. *Sustain Energy Fuels* 1(2):299–307
- Lee JA, et al (2013) Ultrafast charge and discharge bicroiled yarn supercapacitors for textiles and microdevices. *Nat Commun* 4

- Li Y, Li Z, Shen PK (2013) Simultaneous formation of ultrahigh surface area and three-dimensional hierarchical porous graphene-like networks for fast and highly stable supercapacitors. *Adv Mater* 25(17):2474–2480
- Li X et al (2016) Facile synthesis of MoS₂/reduced graphene oxide@polyaniline for high-performance supercapacitors. *ACS Appl Mater Interfaces* 8(33):21373–21380
- Liang YY, Li HL, Zhang XG (2007) Solid state synthesis of hydrous ruthenium oxide for supercapacitors. *J Power Sources* 173(1):599–605
- Liu T, Pell WG, Conway BE (1997) Self-discharge and potential recovery phenomena at thermally and electrochemically prepared RuO₂ supercapacitor electrodes. *Electrochim Acta* 42(23–24):3541–3552
- Liu C, Li F, Lai-Peng M, Cheng HM (2010) Advanced materials for energy storage. *Adv Mater* 22(8):28–62
- Ma W et al (2017) Flexible all-solid-state asymmetric supercapacitor based on transition metal oxide nanorods/reduced graphene oxide hybrid fibers with high energy density. *Carbon (NY)* 113:151–158
- Mallika S, Saravana Kumar R (2011) Review on ultracapacitor-battery interface for energy management system. *Int J Eng Technol* 3(1):37–43
- Mannayil J, Manoj M, Jayalekshmi S, Jayaraj MK (2018) PANI/MWCNT composite electrode for supercapacitor applications. 25
- Manoj M, Anilkumar KM, Jinisha B, Jayalekshmi S (2017) Polyaniline–graphene oxide based ordered nanocomposite electrodes for high-performance supercapacitor applications. *J Mater Sci Mater Electron* 28(19):14323–14330
- Meng Q, Wu H, Meng Y, Xie K, Wei Z, Guo Z (2014) High-performance all-carbon yarn micro-supercapacitor for an integrated energy system. *Adv Mater* 26(24):4100–4106
- Naoi K, Ishimoto S, Miyamoto JI, Naoi W (2012) Second generation ‘nanohybrid supercapacitor’: evolution of capacitive energy storage devices. *Energy Environ Sci* 5(11):9363–9373
- Nguyen TD, Ryu JK, Bramhe Sachin N, Kim TN (2013) Performance of electric double layers capacitor using activated carbon materials from rice husk as electrodes. *Korean J Mater Res* 23(11):643–648
- Noked M, Avraham E, Bohadana Y, Soffer A, Aurbach D (2009) Development of anion stereoselective, activated carbon molecular sieve electrodes prepared by chemical vapor deposition. *J Phys Chem C* 113(17):7316–7321
- Ojha K, Kumar B, Ganguli AK (2017) Biomass derived graphene-like activated and non-activated porous carbon for advanced supercapacitors. *J Chem Sci* 129(3):397–404
- Park JH, Ko JM, Park OO, Kim DW (2002) Capacitance properties of graphite/polypyrrole composite electrode prepared by chemical polymerization of pyrrole on graphite fiber. *J Power Sources* 105(1):20–25
- Service RF (2003) Electronic textiles charge ahead. *Am Assoc Adv Sci*
- Sheng K, Sun Y, Li C, Yuan W, Shi G (2012) Ultrahigh-rate supercapacitors based on electrochemically reduced graphene oxide for ac line-filtering. *Sci Rep* 2:3–7
- Simon P, Gogotsi Y (2010) Materials for electrochemical capacitors. *Nanoscience and technology: a collection of reviews from Nature journals*, pp 320–329
- Simon P, Gogotsi Y (2008) Materials for electrochemical capacitors. *Nat Mater* 7(11):845–854
- Song Y, Li Z, Guo K, Shao T (2016) Hierarchically ordered mesoporous carbon/graphene composites as supercapacitor electrode materials. *Nanoscale* 8(34):15671–15680
- Stoller MD, Ruoff RS (2010) Best practice methods for determining an electrode material’s performance for ultracapacitors. *Energy Environ Sci* 3(9):1294–1301
- Textiles E (2007) A logical step. *Nat Mater* 6:328–329
- Thakur AK, Deshmukh AB, Choudhary RB, Karbhal I, Majumder M, Shelke MV (2017) Facile synthesis and electrochemical evaluation of PANI/CNT/MoS₂ ternary composite as an electrode material for high performance supercapacitor. *Mater Sci Eng B Solid-State Mater Adv Technol* 223:24–34

- Wang YG, Wang ZD, Xia YY (2005) An asymmetric supercapacitor using RuO₂/TiO₂ nanotube composite and activated carbon electrodes. *Electrochim Acta* 50(28):5641–5646
- Wang YG, Cheng L, Xia YY (2006) Electrochemical profile of nano-particle CoAl double hydroxide/active carbon supercapacitor using KOH electrolyte solution. *J Power Sources* 153(1):191–196
- Wang G, Qu M, Yu Z, Yuan R (2007) LiNi_{0.8}Co_{0.2}O₂/MWCNT composite electrodes for supercapacitors. *Mater Chem Phys* 105(2–3):169–174
- Wang G, Zhang L, Zhang J (2012) A review of electrode materials for electrochemical supercapacitors. *Chem Soc Rev* 41(2):797–828
- Wang R et al (2017a) Hydrothermal synthesis of nanostructured graphene/polyaniline composites as high-capacitance electrode materials for supercapacitors. *Sci Rep* 7(174):1–9
- Wang L, Yang H, Pan G, Miao L, Chen S, Song Y (2017b) Polyaniline-carbon nanotubes@zeolite imidazolate framework67-carbon cloth hierarchical nanostructures for supercapacitor electrode. *Electrochim Acta* 240:16–23
- Wang Z et al (2019) Extremely low self-discharge solid-state supercapacitors: via the confinement effect of ion transfer. *J Mater Chem A* 7(14):8633–8640
- Wen ZB et al (2009) An activated carbon with high capacitance from carbonization of a resorcinol–formaldehyde resin. *Electrochem Commun* 11(3):715–718
- Xia M, Nie J, Zhang Z, Lu X, Wang ZL (2018) Suppressing self-discharge of supercapacitors via electrorheological effect of liquid crystals. *Nano Energy* 47:43–50
- Yan J, et al (2017) Flexible MXene/graphene films for ultrafast supercapacitors with outstanding volumetric capacitance. *Adv Funct Mater* 27(30)
- Yi F, Ren H, Shan J, Sun X, Wei D, Liu Z (2018) Wearable energy sources based on 2D materials. *Chem Soc Rev* 47(9):3152–3188
- Yu A, Chabot V, Zhang J (2013) Electrochemical supercapacitors for energy storage and delivery: fundamentals and applications. Taylor & Francis, Abingdon
- Yu Y, Zhong J, Sun W, Kumar R, Koratkar N (2017) Solid-state hybrid fibrous supercapacitors produced by dead-end tube membrane ultrafiltration. *Adv Funct Mater* 27(24)
- Yuan C, Zhang X, Su L, Gao B, Shen L (2009) Facile synthesis and self-assembly of hierarchical porous NiO nano/micro spherical superstructures for high performance supercapacitors. *J Mater Chem* 19(32):5772–5777
- Zhang LL, Zhao XS (2009) Carbon-based materials as supercapacitor electrodes. *Chem Soc Rev* 38(9):2520–2531
- Zhang W et al (2020) Self-discharge of supercapacitors based on carbon nanotubes with different diameters. *Electrochim Acta* 357:136855
- Zhao S, Wu F, Yang L, Gao L, Burke AF (2010) A measurement method for determination of dc internal resistance of batteries and supercapacitors. *Electrochem Commun* 12(2):242–245
- Zhou H et al (2018) Preparation of graphene nanowalls on nickel foam as supercapacitor electrodes. *Micro Nano Lett* 13(6):842–844
- Zhu Y et al (2018) Ag-doped PEDOT:PSS/CNT composites for thin-film all-solid-state supercapacitors with a stretchability of 480%. *J Mater Chem A* 6(3):941–947
- Zhu Y, et al (2011) Carbon-based supercapacitors produced by activation of graphene. *Science* 332(6037):1537–1541

Wearable Supercapacitors



Kowsik Sambath Kumar , Deepak Pandey , Rajkumar Gurjar ,
and Jayan Thomas 

1 Introduction

In recent times flexible and wearable electronics has been rapidly growing in the areas of wearable body sensors, health monitors, flexible displays, portable and wearable energy storage devices (Choi et al. 2016; Huang et al. 2016). For the realization of fully flexible and wearable electronic gadgets, the power source to run these gadgets must also be fully flexible and be able to integrate with the fabrics of the wearer. Therefore, a need arises to develop flexible batteries and supercapacitors which are thin, safe and have good mechanical reliability in terms of twisting, stretching and warping (Jost et al. 2015; Kim et al. 2015). Besides flexibility, these energy storage devices should also be lightweight, small, and with good electrochemical performances (Tang et al. 2016; Vlad et al. 2015).

Supercapacitors are a class of energy storage devices which can offer high power density, long cycle life and fast charge discharge ability compared to batteries (Huang et al. 2016; Shao et al. 2015). In contrast to batteries that store charges in the electrode volume, supercapacitors store charges only on the electrode surface through ion adsorption or surface redox reactions. Supercapacitors are broadly classified into three different types based on the different charge storage mechanisms: (1) electrical double-layer capacitors (EDLCs), (2) pseudocapacitor, and (3) hybrid capacitors (Vlad et al. 2015; Huang et al. 2016; Conway and Pell 2003). EDLCs store the charges through an electrostatic field across a double layer between the electrode surface and the electrolyte. Usually, carbon-based electrode material exhibits

K. Sambath Kumar · D. Pandey · R. Gurjar · J. Thomas (✉)

Department of Materials Science and Engineering, University of Central Florida, Orlando, FL 32816, USA

e-mail: Jayan.Thomas@ucf.edu

NanoScience Technology Center, University of Central Florida, Orlando, FL 32826, USA

J. Thomas

CREOL, College of Optics and Photonics, University of Central Florida, Orlando, FL 32816, USA

EDLC behavior. The electrochemical behavior of EDLCs is determined by the electrical conductivity of active material, pore structure, and specific surface area of the electrode structure. On the other hand, for pseudocapacitors, charge storage is usually achieved by fast and reversible redox reactions. These redox reactions typically occur only on the surface of the electrodes, which enables faster rate kinetics. Theoretical capacitance, electrical conductivity and geometric configuration of the electrodes govern the overall electrochemical performance of the pseudocapacitors. Hybrid supercapacitors are a combination of EDLCs or pseudocapacitors along with a battery electrode. Such supercapacitors store the charges, which is a combination of capacitive as well as battery-type storage. Such supercapacitors try to bring the best of both supercapacitors and batteries. Along with a good power density, these hybrid devices could also impart reasonably good energy density.

The structural design of a supercapacitor is comprised of the electrodes (anode and cathode), electrolyte, separator, and packaging material. Electrodes are generally considered as the most critical part of the supercapacitors and thus have been extensively studied. So far, a wide range of electrode materials has been developed and studied, which include carbon-based materials (Zhang and Zhao 2009), metal oxides/hydroxides (Forouzandeh et al. 2020), and conducting polymers (Mastragostino et al. 2002). Several carbon materials such as activated carbon particles, carbon nanotubes, carbon fibers, carbon nanofibers, graphene, etc., show typical EDLC behavior and are important for supercapacitor applications. However, there must be no functional group present on such materials; otherwise, they show redox-type behavior. On the other hand, MnO_2 , RuO_2 , CuO , Co_3O_4 , MoO_3 , Fe_2O_3 , etc., are some of the commonly used metal oxide electrode materials. Polyaniline (PANI) and polypyrrole are some of the widely used conducting polymers used as pseudocapacitor materials. In general, EDLC materials have better rate capability, higher power density and longer cycle life than pseudocapacitive materials. However, when it comes to specific capacitance and energy density, pseudocapacitive materials outperform EDLC materials by several-fold.

The conventional design of supercapacitor is stiff and cumbersome. However, in recent years a frontier of science has focused on developing thin and flexible supercapacitor (FSC) electrodes with superior electrochemical and mechanical properties (Huang et al. 2016; Huang et al. 2016; Yu et al. 2015). In earlier studies, the geometric shape and sizes of supercapacitors were quite simple. With the development of flexible electronics, flexible supercapacitors with diversified micro-structures and macro features have been reported recently (Shao et al. 2015; Park et al. 2013; Chen and Dai 2014). Each of the components in a flexible supercapacitor like electrodes, electrolyte, separator and packing shell must also be flexible. This is the most significant difference between a conventional (rigid) and a wearable/flexible supercapacitor, which offers the FSCs variability in shapes. The first step in fabricating a flexible supercapacitor is the development of a flexible electrode with good electrochemical performance. This means the active material deposition on a flexible substrate could resist different types of mechanical strains like pulling, twisting, and bending. A myriad of shapes and functional features have been shown by researchers that become complex over time. There have been many promising studies published as

review articles that often focus on a single type of configuration. For e.g., Peng et al. reviewed several articles on two-dimensional nanomaterials for flexible supercapacitors (Peng et al. 2014). Similarly, Park et al. have discussed CNT film-based supercapacitor devices (Park et al. 2013). Liu et al. introduced the application of inorganic nanowires in flexible electronics (Liu et al. 2015). Though these studies have tried to cover a broad range of research, they are limited to a specific category of supercapacitors.

In this chapter, flexible supercapacitors are well categorized and systematically discussed based on the type of their substrates, different types of deposition processes, their assembly and packaging, followed by their application. Based on the macroscopic patterns and the type of substrates, these flexible supercapacitors could be categorized into three different types: (1) 1-dimensional (1D), (2) 2-dimensional (2D), and (3) 3-dimensional (3D). The 1D flexible supercapacitors are generally fiber-type flexible supercapacitors. Such a design helps the device to be used in cable-based applications. The 2D design is a paper-type supercapacitor which is thin and flexible. They are ideal for integration in flat and flexible display panels and sensors. The third category is the 3D porous flexible supercapacitors. They possess a little more thickness than the paper-type supercapacitors, but still, the flexibility is not compromised. Based on the fabrication methods, mechanical properties and electrochemical performance, these supercapacitors are further divided into subcategories discussed in the following sections. Such a hierarchical and detailed discussion is essential to understanding the correct classification and comparison of flexible supercapacitors. It helps the readers know the most recent advancement in flexible supercapacitors' design and electrochemical performance.

2 Electrode Material for Flexible Supercapacitors

For making electrodes to design a flexible supercapacitor, material with high stability, superior mechanical integrity, and good electrochemical properties are ideal for deposition on a flexible substrate (Huang et al. 2015; Li et al. 2016; Liu et al. 2015) while choosing material for flexible supercapacitors, it is essential to look into factors like proper adhesion to current collectors, reduced delamination for bending/twisting and stability of the crystal structure during the charge and discharge cycle. Based on these parameters, various materials are discussed in the following subsections.

Carbon based electrode materials. As we discussed previously, the majority of the flexible supercapacitors employ carbon-based materials exhibiting EDLC behavior like graphene, carbon nanotubes, carbon nano fibers, carbide-derived carbons, and activated carbon, where the surface area and porosities play a major role in electrochemical performance (Yu et al. 2015; Li et al. 2015; Wang et al. 2015). These carbon-based materials show excellent cycling stability along with good mechanical integrity, which makes them an ideal choice for making flexible supercapacitors. However, carbon-based materials do suffer from low intrinsic specific

capacitance, which is a huge obstacle in making a high energy density supercapacitor. To overcome this problem, surface modifications like exfoliation, surface activation, S-doping, or N-doping have been proven to be effective strategies (Yu et al. 2015; Tran et al. 2016). Several oxygen functional groups are present on the surface of graphene nanosheets and other carbon materials that could alter the electrical and physiochemical properties of the material for the desired use (Zarrin et al. 2016). Surface charge storage properties and ionic conductivity could be significantly enhanced by modulating the material for a large surface area to volume ratio and ion-accessible porosity (Wang et al. 2015; Wee et al. 2017). Several efforts have been made to increase the specific surface area by modifying the surface morphology to impart more nanostructuring of carbon-based material (Yu et al. 2015; Bonaccorso et al. 2015; Yoo et al. 2011). Methods like exfoliation of restacked graphene could also help to increase the specific surface area, thereby increasing the double-layer capacitance. For e.g., a 22-fold increase can be seen in the specific capacitance of graphene carbon fiber electrodes after surface activation (Yu et al. 2015). Superior flexibility and high energy density (0.35 mWh cm^{-3}) were achieved using the surface activated electrode in a solid-state device. Graphene can also be deposited on carbon fibers by electrophoretic deposition as shown in Fig. 1 (Cherusseri et al. 2019). Using such a deposition method, a unique vertical alignment of graphene can be obtained on carbon fibers. This structure has been termed as Vertically attached Graphene on Carbon Fibers (VGCF). Such an arrangement can impart high capacitance to carbon fibers and electrodes can deliver a high gravimetric capacitance of 333.3 F g^{-1} . Besides electrochemical properties, optical properties like transmittance have also been investigated for graphene electrodes (Li et al. 2015). Such properties are helpful in designing flexible and transparent film-type supercapacitors. A free-standing graphene paper with high transparency was prepared using prism-like graphene building blocks. The fabricated transparent electrode with microstructure graphene showed a high power density of 190 mW cm^{-3} and a volumetric energy density of $430 \mu \text{ Wh cm}^{-3}$. The electrode also exhibited a superior life cycle of 20,000 cycles with high-capacity retention of 95.4%.

Metal-based electrode materials. In recent years, the scientific community has invested a lot of effort to develop metal-based materials like Metal Nitrides/oxides/carbides/sulfides (Huang et al. 2016; Wang et al. 2017; Liao et al. 2015; Lv et al. 2016; Zeng et al. 2015; Su et al. 2015). These metal nitrides/carbides/sulfides are separately often termed as MXenes (Venkateshalu et al. 2020; Kumar et al. 2018), while some common metal oxides are RuO_2 , MnO_2 , Fe_2O_3 , Co_3O_4 , etc. Compared to the carbon-based materials, which often show EDLC charge storage, these metal-based electrode materials exhibit pseudocapacitive charge storage. RuO_2 was the first material to be found exhibiting pseudocapacitive charge storage, with high proton conductivity and high capacitance. Not only in the individual state, but these materials can also form complexes with other pseudocapacitive materials to boost their electrochemical performance. RuO_2 can form a highly conductive and ultrathin film with PEDOT:PSS (polystyrene sulfonate) using the aerosol-jet spraying technique to make high-performing transparent and flexible

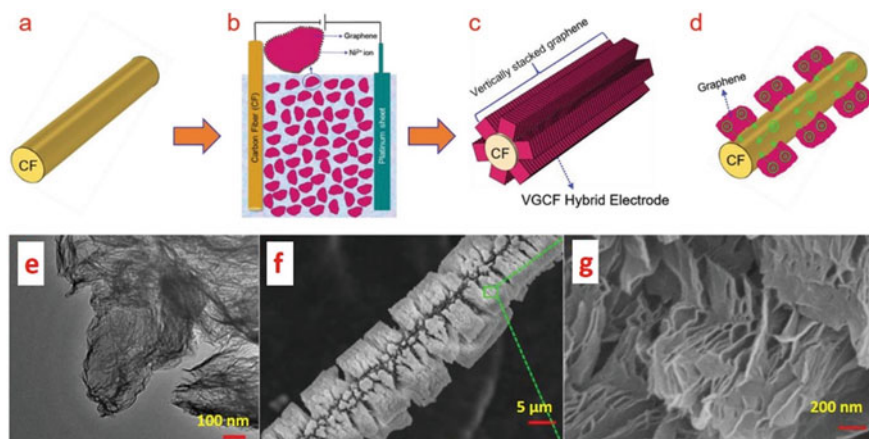


Fig. 1 **a–d** Schematics of electrophoretic deposition of graphene flakes on flexible carbon fibers. **a** bare carbon fiber. **b** electrophoretic deposition **c** Vertical attachment of graphene on carbon fibers **d** charge conduction through VGCF structure. **e** TEM image of graphene flake attached. **f** SEM micrograph of graphene flakes vertically attached to carbon fibers. **g** Zoomed in image (green box) of the area, showing alignment of graphene flakes. (Reprinted with permission from (Cherusseri et al. 2019) copyright (2019) © John Wiley and Sons)

supercapacitors (Zhang et al. 2016) Another highly popular pseudocapacitive material ideal for flexible supercapacitors is MnO_2 . Its low cost, environmental friendliness and high capacitance have recently made it very popular for boosting the energy density of flexible energy storage devices (Yu et al. 2016; Qian et al. 2015; Zhang et al. 2016). These pseudocapacitive materials often offer high capacitance due to their redox behavior but may lack high surface area compared with carbon-based materials. Another issue is their lower cycle life since their charge storage mechanism involves partial intercalation of the bulk material. Due to this reason, with every cycle of charge and discharge, the crystal lattice of these materials undergoes cyclic strain of expansion and contraction. To overcome these problems, these materials can be used in conjunction with more stable substrates, which can offer high surface area. They can also show higher endurance to cyclic strains during charge–discharge cycles. For e.g., MnO_2 also can be used in conjunction with metal–organic frame works as a substrate, achieving a three-fold increase in capacitance (Zhang et al. 2016). This has been made possible by synergistic effects of high surface area with micropores offered by the MOF as an electrode and high pseudocapacitance of MnO_2 . Similarly, Mn_3O_4 nano walls can be grown electrochemically on carbon fibers, as shown in Fig. 2 (Sambath Kumar et al. 2019). These nano walls are very stable and can retain almost 100% of its capacitance for up to 7500 cycles. Such an arrangement can impart a gravimetric capacitance of 300.7 F g^{-1} to the carbon fiber cloth.

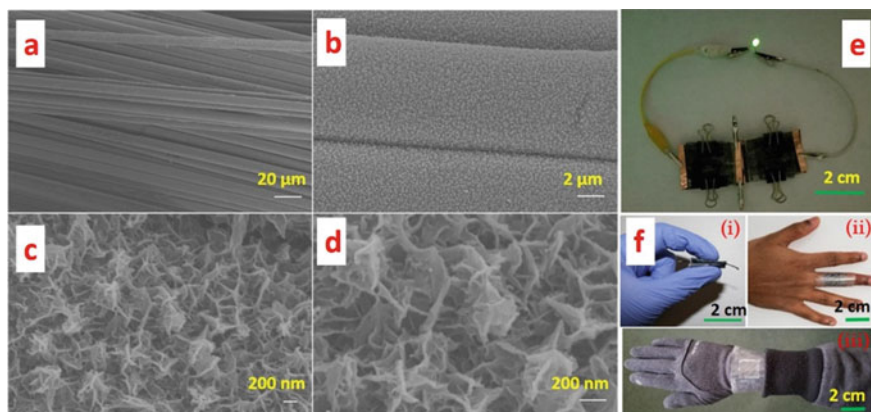


Fig. 2 Growing Mn_3O_4 nano walls on carbon fibers through electrochemical deposition. **a–d** SEM image of Mn_3O_4 nano walls grown on carbon fibers at different magnifications. **e** Assembled two Mn_3O_4 carbon fiber-based supercapacitors in series, lightening an LED. **f** Mn_3O_4 carbon fiber supercapacitor (i) bent to 180° , (ii) rolled around figures, (iii) integrated on a cloth. (Reprinted with permission from (Sambath Kumar et al. 2019) copyright (2019) © American Chemical Society)

Though many synthesizing technologies are available to develop electrodes with desired material morphology, electrodes with high capacitance and high rate capability with well-designed pore structure and elaborate surface decoration are ideal (Wang et al. 2017; Zeng et al. 2015). A hierarchical structure of $\text{Fe}_2\text{O}_3/\text{PPy}$ nano arrays synthesized on a conductive carbon cloth can be created, which could be used for flexible supercapacitors (Wang et al. 2017). This structure demonstrated a high areal capacitance of 382.4 mF cm^{-2} at a current density of 0.5 mA cm^{-2} . In a similar hierarchical structure synthesis, Ti-doped Fe_2O_3 and PEDOT were prepared in the form of core–shell nanorods, which exhibited very good ion diffusion with a superior capacitance of 1.15 F cm^{-2} and an exceptionally high cycle life of 3000 cycles (Zeng et al. 2015). MnO_2 based inorganic ink was also developed to print electrodes on conductive paper, making it into a flexible supercapacitor. This device showed a high capacitance of 91.7 mF cm^{-2} and retained over 98.9% of its performance after 10,000 cycles at 4 A g^{-1} revealing high potentials of directly printing flexible electrodes. Such a technology could be very easily scaled up for a large industrial production. Device performance can also be enhanced by improving substrate and synthesis method. MnS nanoparticles have been hydrothermally grown on carbon fiber ensuring strong contact between the nanoparticles and the fiber. This electrode delivered a high capacitance of 465 F g^{-1} . High cycling stability was observed in the electrochemical studies which showed over 92.47% retention after 10,000 charging cycles (Javed et al. 2016).

Conductive polymers. Conductive polymers promise low cost, lightweight, high specific capacitance, and high conductivity materials for flexible supercapacitors. With an appropriate doping agent and adequate concentration, the electronic conductivity of these polymers can reach as high as 10^4 S cm^{-1} , which is superior to that

of metal oxide-based materials. Many conductive polymers can exhibit very high capacitance; for e.g., 1284 F g⁻¹ for PANI, 480 F g⁻¹ for Polypropylene (PPy), and 210 F g⁻¹ for PEDOT (Liu et al. 2014; Song et al. 2015; Huang et al. 2015; Wang et al. 2015). However, many of these conducting polymers often suffer from poor cycling stability due to structural pulverization and counter-ion drain effect, which pose a significant hurdle to the large-scale commercial application of these polymers (Liu et al. 2014; Song et al. 2015). In order to circumvent this problem, fabrication of PPy with designed morphology or structure can help. Compared to a microstructure, a nanostructure provides much higher capacitance, energy density and power density due to increased interfacial surface area and better ion transport. The synthesis of composite electrodes where metal-based materials are combined with carbon-based materials improves cycling stability, energy density and power density (Khosrozadeh et al. 2016; Wan et al. 2017).

A functionalized partially exfoliated graphite substrate with the decoration of MnO₂ nanosheets can enhance the cycling stability of PPy, retaining more than 97% of its capacitance after 10,000 cycles in an aqueous electrolyte (Song et al. 2015). Moreover, interweaving MOF crystals having micropores and PANI chains, a highly conductive flexible electrode with the ultra-high areal capacitance of 2146 mF cm⁻² at 10 mV s⁻¹ can be obtained (Wang et al. 2015). Hybridizing layered double hydroxides (LDH) in the form of a shell material could also help improve the life cycle and impart better charge mobility in conducting polymers. Hence a core-shell system of PPy/LDH where PPy nanoarrays form a core and LDH materials form the shell can help in the fabrication of high-performing flexible supercapacitor by the synergistic effect of both (Shao et al. 2015).

3 Design of Flexible Supercapacitors

As flexible electronics are becoming popular, flexible supercapacitors are also developed in all shapes and sizes. Many flexible electronic items like display boards or thin screens need a flexible sheet-like power device to cater to their energy needs. On the other hand, products like wearable smart jackets and jeans with sensors and integrated displays require a fiber-type energy storage device to power their needs. Based on shapes and sizes, the flexible supercapacitors have been categorized into the following types: (1) 1D yarn/fiber-shaped flexible electrodes, (2) 2D paper type flexible electrodes, and (3) 3D porous flexible electrodes. Each of these categories is discussed in detail below.

1D substrates. 1D yarn type, also known as fiber-shaped flexible electrode or flexible supercapacitor, is now being popularly used in smart fabrics to weave the power source directly with the sensors and micro-electronics integrated with them. Based on today's precise and adaptable weaving technologies, it has now become possible to integrate them into our smart clothes (Yu et al. 2015). A set of such power fibers known as "yarn" is mechanically robust, meaning it should be able to withstand not only bending but also twisting and stretching. Fiber-shaped electrodes

can be easily made with different types of textile yarns like cotton fibers, carbon materials, Kevlar fibers, metal wires, and polymer nanofibers. There are multiple deposition technologies that can be used to deposit active material on these yarns like dipping, electrodeposition, chemical deposition, hydrothermal deposition, etc.

Typically, there are two types of fiber-based supercapacitor designs. In a type 1 structure, the individual anodes and cathodes are in the form of a fiber (where the active material is deposited on a filament-type substrate). These individual anode and cathode fibers are twisted around each other, with an electrolyte layer covering each of them. In another design, which is type 2, a filament type electrode and a paper-like electrode ('membrane electrode' also known as 'film electrode') are used as inner and outer electrodes in the form of a wrap-around a coaxial cable. Both of these electrodes are separated with the help of a porous separator and an electrolyte. If a liquid electrolyte is applied, a separator is always necessary to avoid short-circuiting of the two electrodes during mechanical strains (bending/twisting). However, if the electrolyte is a polymer gel-like PVA/H₃PO₄, then no separator is needed since the gel is thick and viscous enough to avoid the contact of anode and cathode (Choi et al. 2014; Lee et al. 2013). In comparison to the liquid electrolyte, gel-based electrolytes are more popular because the liquid electrolytes have a tendency to leak, while the gel-based electrolytes are intact with the yarn even during high bending and twisting.

These 1-D fiber-type supercapacitors should be highly flexible and demonstrate good electrochemical performance. However, the flexibility should not come at the cost of reduced mechanical strength. Such a characteristic is mainly dependent on the type of substrate used for the fiber electrodes. With evolving micro-manufacturing, different types of fiber yarns are available with varying properties as per their usage. They come in the form of plastic fibers, metal fibers, carbon-based micro and nano fibers, natural fibers like cotton, linen, and bamboo yarns, etc. Further, these fibers are coated with electrochemically active materials using different deposition techniques like dipping and drying, electrochemical deposition, physical and chemical vapor deposition, and other chemical processes.

Plastic fiber substrates: Inexpensive, highly flexible and mechanically robust plastic fibers are a common choice of 1-D substrate to make cheap and flexible supercapacitors. Graphite carbon nanoparticles of a diameter about 20 nm, can be deposited easily in the form of pen ink to make flexible anodes (Fu et al. 2012). However, these plastic fibers also serve as a good current collector if some sort of a conducting film like that of gold or copper is also deposited before depositing the active material. The graphite carbon nanoparticles can further be coated in the form of a uniform film and can offer a high specific surface area of about 27 m² g⁻¹. Flexible electrodes prepared using such inks can exhibit specific capacitance of upto 20 mF cm⁻² (0.504 mF cm⁻¹) in addition to maximum power and energy density of 9070 μW cm⁻² and 2.7 μW h cm⁻², respectively. Some research groups have also reported using carbon nanotubes (CNT)–PANI composite material to coat these plastic fibers (Bae et al. 2011). In such cases, a closely packed and highly aligned CNT film can be wound around a plastic fiber upon which a PANI film can be electrodeposited. The CNTs deep embedded in this film form a matrix composite of the active material. The CNTs are highly electrically conducting thus serve as an

excellent current collector. PANI stores the electrical charge using the redox mechanism. PANI itself has good electrical conductivity; therefore, it can act as a bridging agent for a facile transfer of charges to the current collector layer. Using such a composite active material on a plastic fiber, a specific capacitance of 255.5 F g^{-1} , can be obtained. However, this value is strongly affected by the ratio of the CNT vs. PANI used. Some reports have also utilized metal oxides/hydroxides as active material on plastic fibers (Bae et al. 2011; Toupin et al. 2004). However, the plastic fibers must be first coated with a conductive Au film upon which active materials like MnO_2 or ZnO can be coated. Though the theoretical capacitance of MnO_2 is very high, the inherent brittleness of such metal oxides limits their loading on the fiber-shaped electrodes.

Metal fiber substrates: Though plastic fibers are inexpensive and easily obtainable, their nonconductive behavior makes them less attractive as they only serve the purpose of providing a substrate for material deposition. Moreover, the cost of Au film deposition using processes like magnetron sputtering to make them a conducting current collector may outweigh the benefit of being cheap. To counter this problem, a better solution is metallic fibers (including wires and yarns). Researchers have reported using steel fiber yarns instead as a substrate which is both flexible, mechanically strong, and electrically conducting (Huang et al. 2015). Choosing a set of electrochemically active materials like reduced graphene oxide (rGO), MnO_2 and PPy in turns to make a rGO/ MnO_2 /PPy composite over these steel fibers have resulted in flexible and strong, electrochemically active supercapacitor electrodes. This electrode provided a high electrochemical capacitance of 36.6 mF cm^{-1} and areal capacitance of 486 mF cm^{-2} in $1 \text{ M Na}_2\text{SO}_4$. Using a PVA/ H_3PO_4 gel electrolyte and a symmetric assembly, the capacitance of a solid-state device still reached 31 mF cm^{-1} and 411 mF cm^{-2} . Some researchers have also used Au wire and Ni fiber as a substrate for the fabrication of flexible electrodes (Wang et al. 2014; Li et al. 2013). Using rGO as active material on Au wire and Co_3O_4 nanowire on Ni fibers, flexible supercapacitor electrodes have been developed with high electrochemical performance. The rGO coated Au nanowire exhibited a maximum linear capacitance of 101.9 mF cm^{-2} and a corresponding areal capacitance of 6.49 mF cm^{-2} . The capacitance could be further enhanced with increased mass loading, but a problem lies in the higher thickness of these metallic fibers. The ratio of the active material coating diameter vs. the diameter of the fiber itself is very low. This means that a large area and the weight of the current collector fiber results in a lower gravimetric capacitance. In addition, metallic fibers are also prone to parasitic side reactions when the device is in operation. Any uncoated area over the length of the fibers can result in immediate reactions involving corrosion of the current collector and evolution in the electrolyte. These factors must be accounted before choosing the metallic fiber substrates for making flexible supercapacitor electrodes.

Carbon fiber substrates: An alternative to plastic and metallic fibers is carbon fibers. It would be appropriate to say that the carbon fibers overcome the shortcomings of both plastic fibers and metallic fibers. Unlike the insulating plastic fibers and heavy metallic fibers, carbon fibers are electrically conducting, highly flexible, lightweight and even stronger than steel fibers. On top of that, they are chemically

inert, which makes sure that they do not engage in parasitic reactions. These characteristics make carbon fibers an excellent choice of substrate for making flexible supercapacitors. However, to some extent, carbon fibers can store electrochemical charges as well, but their pore structure may not be well developed or may possess a low surface area (less than $30 \text{ m}^2 \text{ g}^{-1}$). Thus, to make them into flexible electrodes, electrochemically active material can be deposited on them. Other carbon-based materials like CNTs have been deposited on the carbon fibers to improve their electrochemical activity (Le et al. 2013). CNT solution can be directly sprayed on these carbon fibers to obtain CNT film deposition on the electrodes. CNTs are known for their high electrical conductivity and specific surface area that can provide a large number of facile charge storage and transportation sites. A higher amount of CNT loading leads to a larger capacitance in a prepared bundle electrode. However, excessive CNT loading results in aggregation of CNT on the fibers leading to higher diffusion resistance, poor cycling performance, low power density and rigidity in the electrode. An appropriate CNT loading on carbon fibers with PVA/ H_3PO_4 gel electrolyte and carbon nanofiber films on top in a coaxial geometry enabled to develop a flexible fiber-shaped supercapacitor. Such a device can give a linear capacitance of 6.3 mF cm^{-1} and areal capacitance of 86.8 mF cm^{-2} . Though these values are decent, they are not high enough for many practical applications. Another approach is to use high capacitance redox materials like metal oxides/hydroxides and conducting polymers (Liu et al. 2015; Zhai et al. 2015). MnO_2 nano particles can be easily deposited on carbon fibers using electrochemical deposition since carbon fibers are electrically conducting. The areal capacitance of MnO_2 deposited carbon fibers is significantly enhanced compared to bare carbon fibers due to the redox behavior of the MnO_2 . However, the electrical conductivity of metal oxides is very poor, which increases the overall resistance because of the voltage drops in the form of the IR loss. To overcome this problem conducting polymers like PPy can be wrapped around the metal oxides and hydroxides for better conductivity and further enhancement in charge storage ability. A carbon fiber/ MnO_2 /PPy bundle electrode can show an areal specific capacitance of 3.95 F cm^{-2} at a current density of 50 mA cm^{-2} .

Two-dimensional substrate. Paper-like 2D flexible electrodes/supercapacitors are devices which are geometrically in the form of a thin sheet. They are highly flexible and are appropriate for integrating and powering foldable mobile phones, foldable display screens, digital cameras and laptops. They are constructed using a flexible packing shell, a flexible current collector and a separator and paper-type flexible electrodes (Lee et al. 2013; Lu et al. 2014; Zhang et al. 2015). Even though the concept of 2D paper-like electrodes and supercapacitors is relatively new, thin and flexible electrodes have existed for a long time. When electrochemically active material is in the form of a powder and is coated on a foil of metals like (Al, Cu and Ni foil) for electrochemical energy storage, these electrodes do come in the category of flexible, foldable 2D paper electrodes.

Depending on the substrates, the reported paper-like electrodes can be broadly classified into two main categories: (1) Free standing paper-like electrodes and (2) Flexible substrate-supported electrodes. Both of them have been discussed in detail below.

Free-standing 2D (paper-like) electrodes: In this category, the electrode active material does not need a separate substrate to hold itself. The electrode material forms a robust network structure of fiber-type shapes closely entangled to each other with a well-defined pore system. This type of structure can typically be shown by CNTs and CNFs (carbon nano fibers), which possess an excellent length to diameter ratio and can be formed into a conductive carbon film. Similarly, graphene with a 2D ultrathin structure can be combined with electrically conducting long-chain polymers to make a similar conducting film (Peng et al. 2014; Hu et al. 2010; Geetha et al. 2006). These conductive carbon films do not require a separate substrate or a separate current collector, as they possess good mechanical strength, high flexibility, and also good electrical conductivity by itself. However, if the mechanical strength or cohesion is low between the filaments/flakes, some types of conducting polymer binders can be used (Yan et al. 2011; Meng et al. 2009; Niu et al. 2011). These conducting carbon films can be directly used as supercapacitor flexible electrodes, however, their capacitance, energy and power density depend on a number of factors like the electrical conductivity of the material, binder used, specific surface area, pore size, etc. In order to further improve their performance, metal oxides and hydroxides can be coated on them, which can impart their pseudocapacitive properties to the existing capacitance and energy density. Since freestanding 2D electrodes do not need a separate substrate or a current collector, this greatly helps in weight reduction; thus, higher gravimetric capacitance can be achieved. The CNT or graphene-based film electrodes can be prepared by chemical vapor deposition (CVD) or filtration method (Park et al. 2013; Cao and Wei 2013; Liu et al. 2015). They are discussed below.

- *Free-standing films of CNTs:* There are several factors like length, diameter, crystallization, organization state, and chirality which affect the electrical conductivity, specific surface area, and pore size of the free-standing films of CNT (Park et al. 2013). In reality, these factors almost entirely decide the electrochemical properties of CNT film, given that CNTs are pure carbon-based materials, which exhibit a pure EDLC mechanism. Both single-walled CNTs (SWCNT) and multi-walled CNTs (MWCNT) have gained a lot of attention recently for their electrochemical energy storage properties. Some researchers believe that MWCNT has superior electrochemical properties like capacitance compared to the SWCNT (Frackowiak et al. 2001; Hughes and Spinks 2005), while others hold an opposite view (Zhao et al. 2009). It is hard to draw a conclusion between the two by just using the experimental results due to other factors (like CNT length and crystallization) which strongly influence the electrochemical properties of CNT. The CVD growth method can easily prepare SWCNT film electrodes. This approach does not require any current collector or a substrate to provide a platform for its growth. A symmetric supercapacitor assembled using two such identical film electrodes exhibited a high gravimetric capacitance of 140 F g^{-1} (Niu et al. 2011). The simple reason for such a high gravimetric capacitance is the lack of substrate and a current collector. This assembled symmetric device delivered a high energy density of 43.7 Wh kg^{-1} and a power density of 197.3 kW kg^{-1} . In another method, SWCNT

film electrodes were prepared by the filtration method (Barisci et al. 2000). The filtered SWCNT film electrodes had an areal density of 10.2–19.4 g cm⁻² and they delivered a gravimetric capacitance of 18.0–40.7 F g⁻².

- *Free-standing Graphene films*: Graphene is another important carbon material that can be used to form free-standing films. Typically, the filtration method is used to form a freestanding graphene film. The electrochemical properties of these graphene-based freestanding films are affected by the physiochemical and dispersion state of graphene flakes (Zhang et al. 2012; Tan and Lee 2013). For e.g. if graphene flakes are not carefully designed/modified, the resulting free-standing graphene film can only impart a gravimetric capacitance of 67 F g⁻¹ (Sumboja et al. 2013). On the other hand, when urea reduced free-standing graphene film was prepared, the gravimetric capacitance was found to be 172 F g⁻¹ at a charge–discharge current density of 0.5 A g⁻¹ (Lei et al. 2012). Also, when oxygen-containing surface functional groups were left untreated, the gravimetric capacitance obtained went upto 255 F g⁻¹. The cycling data for these electrodes were evaluated at 3 A g⁻¹. Almost 94% of the capacitance was retained after 1200 cycles. In some methods activating agents like KOH can be used to improve specific surface area (Zhang et al. 2012). A surface area of 2400 m² g⁻¹ with superior electrical conductivity can be obtained by using KOH activation process.

Flexible substrate supported 2D (paper-like) electrodes: In this category, active materials like metal oxides/metal hydroxides, conductive polymers and their composites can be deposited on a thin, metallic, or another conducting substrate. If the substrate is not conducting like plastic or simple paper, then a conducting film of Au, Cu, etc., can be first deposited as a current collector layer. However, if the active material itself is conducting enough like that of CNTs, then no separate coating is required.

- *Flexible metal foil supported*: Flexible thin metal substrates are very common since we have often seen that active material can be easily coated on conductive metal foils (like Cu, Al, Stainless steel foils) to evaluate their electrochemical properties (be in a three-electrode or an assembled 2 electrode system). Researchers, while developing this kind of electrode, focus on two things: (1) choosing the right flexible metal foil, which is highly pliant and can take a series of bending cycles without any permanent failure in the foil itself. (2) Finding an appropriate method for depositing the active material, which does not peel off the substrate after multiple bending cycles. In fact, the tightly integrated bonding between the active material and the metal substrate is important to reduce the contact resistance, which could largely degrade the electrochemical performance of the device (Du and Pan 2006).
- *Flexible plastic substrate supported*: Plastic substrates are used to prepare bendable, stretchable, and transparent paper-like flexible electrodes and supercapacitors that can be applied on transparent displays or touch screen displays (Yu et al. 2010; Shi et al. 2013). In instances where the metallic foil substrates are opaque and non-stretchable, the plastic substrate supported electrodes can easily elongate and integrate into our wearables. For e.g., graphene films can easily be prepared

on a PET (polyethylene terephthalate) substrate. When used as supercapacitor electrodes, these films can deliver a gravimetric capacitance of 135 F g^{-1} (Yu et al. 2010). MnO_2 nanosheets (active material) can be very easily deposited on an indium tin oxide (ITO) coated PET substrate through screen printing (Shi et al. 2013). Such an electrode can deliver a large specific capacitance of 774 F g^{-1} and can operate for more than 10,000 cycles of charge and discharge.

- *Paper substrate supported*: Papers made using cellulose fibers are also a popular choice of flexible substrates for 2D flexible supercapacitors. Compared to the metal and plastic substrates, paper substrates are highly porous, light weight, low cost and easily processable (Zhong et al. 2013; Hu et al. 2010). The high porosity in paper substrates helps in the deposition of electrochemically active material and facile movements of ions during the charge–discharge process. These paper substrates can be directly coated with graphene oxide by a simple dipping and drying method (Liu et al. 2014). Later, graphene oxide (GO) can be reduced to obtain rGO coated paper, which can be used to deposit more electrochemically active material like PANI. A sample fabricated electrode PANI/rGO/paper can deliver a high gravimetric capacitance of 464 F g^{-1} . Likewise, CNTs or PPy or graphene can be deposited on paper supported substrates (Yao et al. 2013).

Three dimensional substrate. Many fiber-like and paper-like supercapacitors display outstanding gravimetric capacitance, energy density and power density. They are well suited when they are used in devices like microelectronics. However, they are hard to use in applications requiring high-energy output within a short duration of time (Jost et al. 2011; Stoller and Ruoff 2010; Chmiola et al. 2010). The reason is their limited size/volume. Though individual fibers can be weaved into a larger area supercapacitor there are several issues in weaving large area devices without bearing a high cost and other complexities (Meng et al. 2013; Kou et al. 2014). Similarly, for a paper-like 2D supercapacitors, they need to be very thin in order to be flexible. This means that there will be low material mass loading per unit area of the device. Hence, the areal energy density is compromised.

To make high energy density electrodes, a slightly thick, porous substrate can be chosen where active material can be deposited up to some thickness. For these flexible porous electrodes (including flexible textile electrodes, aerogel, and sponge electrodes), the body materials are usually porous, thick, and decently flexible. In general, the thickness of the reported body material usually exceeds $100 \mu\text{m}$. Some of these porous electrodes are discussed below.

Textile-based 3D porous electrodes: There are several textiles like cotton cloth, carbon fabric, polyester microfiber twill, etc., that can be used as a porous 3D substrate to fabricate flexible supercapacitor electrodes (Jost et al. 2014). Using active materials like SWCNTs that can be easily adhered to cotton fibers in textile, such that there would not be any delamination can help fabricate 3D electrodes out of these textiles. Based on the reported literature, such a device can deliver almost 0.48 F cm^{-2} areal capacitance with good electrical conductivity and can sustain a strain of 120% without any degradation in the performance (Hu et al. 2010). Similarly, carbon fibers-based fabrics can also be used as a 3D porous substrate which serves as a current collector.

An all-carbon textile-based flexible electrode can be fabricated by growing CNTs directly onto a carbon fabric (Hsu et al. 2012). In the reported work, this electrode could deliver a high gravimetric capacitance of 225 F g^{-1} in $0.5 \text{ M Na}_2\text{SO}_4$ neutral aqueous electrolyte. An assembled symmetric supercapacitor using these electrodes in the solid-state delivered 210 F g^{-1} gravimetric capacitance and an energy density of 27.8 Wh kg^{-1} with a decent cyclability. Metal oxides and hydroxides are generally superior in capacitance compared with pure carbon-based materials. MnO_2 nano particles can be easily coated onto flexible carbon fiber cloths by an anodic electrodeposition process (Yang et al. 2014). The morphology of this deposition process can be easily controlled by manipulating technological parameters like voltage, concentration, etc. Worm-like MnO_2 nanowires coated on carbon fiber cloth delivered a gravimetric capacitance as high as 334.7 F g^{-1} (calculated based only on MnO_2 weight).

Sponge-like 3D porous electrodes. These are commonly termed sponge-like monoliths, which include polymeric sponges, carbon aerogels, carbon-coated sponges, nickel foams, and some other 3D carbon frame works. Polymeric sponges are insulating materials which can only provide a framework for depositing current collector or active material. Researchers have shown that depositing SWCNTs throughout the porous structure of a polymeric substrate can be utilized as a conducting bed current collector for depositing better pseudocapacitive materials (Chen et al. 2011; Chen et al. 2012). These polymeric substrates, with their porous framework, provide better adhesion for any material compared to paper-like or fiber-like thin substrates. SWCNT can guarantee good electrical conductivity upon which MnO_2 can be deposited to offer its high pseudocapitance. The reported sponge/SWCNT/ MnO_2 composite electrode delivered a high energy density of 38 Wh kg^{-1} in 1 M LiClO_4 electrolyte solution. Since polymeric sponge-based substrates are insulating and do not offer anything beyond providing a framework, nickel foam offers a better solution as they are conducting and can also function as a current collector. CNT and graphene nanosheets can be very easily deposited on nickel foams through CVD and electrodeposition, respectively (Chang et al. 2013; Cao et al. 2011). Researchers have shown coating graphene nanosheets onto the nickel foam followed by growth of Ni_3S_2 nanorods/ $\text{Ni}(\text{OH})_2$ nanosheets on the coated graphene Nickel foam (Zhou et al. 2013). Such a composite electrode can impart an ultra-high areal capacitance of 4.7 F cm^{-2} . However, it should be noted that even though these nickel foams are flexible, it is still important to investigate how many bending cycles they can sustain without any delamination of the material or breaking of the substrate by itself.

4 Supercapacitor Assembly Configurations

The assembly of the flexible supercapacitors employed for wearable electronics consists of various configurations depending on the substrate type of the current

collector employed. In the case of 1-D substrates used such as wire, fiber and yarn-based supercapacitors, the device can be assembled via designs like parallel, twisted, coiled and coaxial configurations (Varma et al. 2018). The sandwich-type configuration is very common in the case of planar substrates (Kumar et al. 2019; Kumar et al. 2020). Apart from these, the electrodes can be directly screen printed or laser printed onto substrates in various patterns depending on the final applications. In all assembly configurations, the easy integration of these flexible supercapacitors without compromising wearer comfort and safety is a vital factor to keep in mind. One of the key factors to be considered during the assembly is the charge balance of the electrodes under consideration. This can be done based on an individual electrode's performance, including its active charge storing mass or area, overall capacitance, and the potential window (Kumar et al. 2020). This charge balance is vital in getting a higher cycle life and energy storage from the assembled device.

Parallel configuration. One of the assembly configurations followed for the 1 D substrate-based supercapacitor is the parallel assembly wherein two electrodes are placed side by side separated by gel electrolyte or a separator soaked in electrolyte (Fu et al. 2012; Cao et al. 2013; Guo et al. 2016). Followed by this, the whole assembly can either be inserted into a heat shrinkable plastic tubing or packed using a wrapping film. One such example is PVA–LiCl coated nitrogen/oxygen-rich carbon fiber obtained through combined wet spinning and KOH activation assembled in a parallel structure. The fiber-shaped supercapacitor, which was sealed using a cling film, delivered an energy density of 6.8 mWh cm^{-3} (Qin et al. 2017). In a parallel assembly configuration, an asymmetric configuration is a smart approach to follow for obtaining high voltage and high energy density (Kumar et al. 2021). One such approach to fabricate cable-type supercapacitor was developed using wire-shaped current collectors made of copper and stainless steel with $\beta\text{-Ni(OH)}_2$ and activated carbon (AC) as active electrodes (Senthilkumar and Selvan 2014). The individual wire-shaped electrodes were developed by making an active material slurry with polymer binders and brush coating them on the current collectors. The wire-shaped electrodes were then dip-coated in PVA–KOH gel electrolyte, which would provide them ions and act as a separator. This is followed by parallel insertion of the electrodes into a rubber tube with gel electrolyte infused into it. This cable-based supercapacitor delivered a working voltage of 1.4 V with a maximum energy density of $10.7 \mu\text{Wh cm}^{-1}$ at a power density of $169 \mu\text{Wh cm}^{-1}$. Cotton threads can also be used as a substrate for easy integration of the fiber supercapacitors into clothing (Liu et al. 2013). The cotton threads can be made conductive by dipping them into conductive ink made of single-walled CNTs (SWCNTs). The energy storage of this fiber supercapacitor was provided by electrochemically depositing MnO_2 followed by polypyrrole (PPy) on the SWCNT/cotton thread. The PPy deposited on MnO_2 has dual functionality of charge collection and storage and collecting electrons. The symmetric fiber supercapacitor was assembled by wrapping a cotton thread over one of the fiber electrodes, which would then act as a separator. The whole symmetric assembly was then inserted into a silicone pipe with 0.5 M Na_2SO_4 electrolyte added as the electrolyte. This cotton thread-based fiber supercapacitor delivered an areal

energy density of $33 \mu\text{Wh cm}^{-2}$ at a power density of 0.67 mW cm^{-2} with decent cycling behavior of 96% capacitance retention after 3000 cycles.

With the growing demand for wearable electronics, an increase in electronic waste (e-waste) accumulation is a major concern to be resolved. Utilizing e-waste and recycling the supercapacitors and batteries for developing new next-gen energy storage devices has a huge economic and environmental impact. An eco-friendly approach to employing Cu fibers from waste cable wires as a current collector to develop a wearable fiber-based hybrid supercapacitor was successfully developed (Nagaraju et al. 2018). Here, a Cu wire used to grow CuO nanowire arrays (NWAs) followed by CNT wrapping was done to develop high surface area, conductive and nanostructured substrate. A wet chemical approach followed by post-annealing treatment was made to further grow NiO nanosheets (NSs) on the CNTs@CuO NWAs. These NiO NSs@CNTs@CuO NWAs on Cu fiber electrode acts as the cathode. It is assembled into an asymmetric supercapacitor with AC@carbon fiber (CF) anode in a parallel configuration with PVA–KOH electrolyte. The assembled device delivered a voltage of 1.55 V with a capacitance of 29.09 mF cm^{-1} (93.42 F g^{-1}). This fiber-based hybrid supercapacitor in a normal state had decent cycling stability with 83.6% retention after 2000 cycles and 94.5% retention after 200 bending cycles. The practicality of this fiber device was displayed by weaving it into a shirt and powering an LED and electronic display. The parallel assembly configuration to fabricate fiber supercapacitor is easy for assembling and scaling purposes. But the device has limited interfacial contact between the electrolyte and electrode material, which severely impacts the energy density. This leads to other innovative assembly configurations with enhanced storage performance.

Twisted configuration. The next assembly configuration which is better than parallel assembly is the twisted configuration. The twisted configuration involves intertwining or twisting two fiber electrodes with a separator in between them (Li et al. 2017; Zhang et al. 2017; Noh et al. 2017; Lu et al. 2019). The twisted assembly has an improved interfacial area compared to parallel assembly, thus increasing the electrochemical performance and energy density. Two-ply yarn supercapacitors fabricated by twisting two strands of fibers acting as anode and cathode is a very common fiber supercapacitor for wearable electronics. A two-ply yarn supercapacitor was fabricated using twisted CNT fibers with ordered PANI nanowire (CNT/PANI yarn) (Wang et al. 2013). The CNT acts as both current collector and charge storing material. The PANI nanowires stores charges via faradaic reaction, thus providing higher electrochemical performance. The PVA–H₂SO₄ gel electrolyte coated on the electrode surface acts as both electrolyte and separator. The final fiber supercapacitor can be assembled by twisting similar CNT/PANI yarn to fabricate two-ply yarn supercapacitor. The thickness of the gel electrolyte in fiber supercapacitors has to be optimized to avoid short circuits caused by thinner film or weaving issues caused by a very thick film. This two-ply yarn supercapacitor delivered an aerial capacitance of 38 mF cm^{-2} at a current density of 0.01 mA cm^{-2} , which was 6 times higher than a pure CNT yarn-based supercapacitor with 2.3 mF cm^{-2} . The twisted configuration also provides excellent flexibility for the supercapacitor with 100% capacitance retention even after 150 bending cycles. Another twisted assembly configuration involving

SWCNT fiber was followed to develop a solid-state asymmetric fiber supercapacitor (Li et al. 2017). The V_2O_5 –SWCNT hybrid fiber electrode was used as a cathode here. The synthesis process of this hybrid fiber is done via the wet spinning method (Fig. 3a). A homogeneous suspension was prepared for wet spinning the fibers by stirring together V_2O_5 and SWCNT suspension and is injected into a coagulation bath with $CaCl_2$ ethanol–water solution. The twisted hybrid fibers configuration made of V_2O_5 /SWCNT and RGO/SWCNT with PVA– H_3PO_4 gel electrolyte (Fig. 3a) has shown a volumetric energy density of 1.95 mWh cm^{-3} at a volumetric power density of 7.5 mW cm^{-3} .

As the CNT yarns are commonly used as the current collector cum energy-storing material in fiber supercapacitors, their conductivity and strength are vital parameters for developing efficient wearable electronics. Electron irradiation and ion beam irradiation helps in engineering and strengthening CNTs (Krasheninnikov and Banhart 2007). For instance, CNT yarns subjected to gamma irradiation have improved the elastic modulus and tensile strength of CNTs (Miao et al. 2011). In another work gamma-irradiated CNT yarn deposited with PEDOT/PSS was employed to fabricate

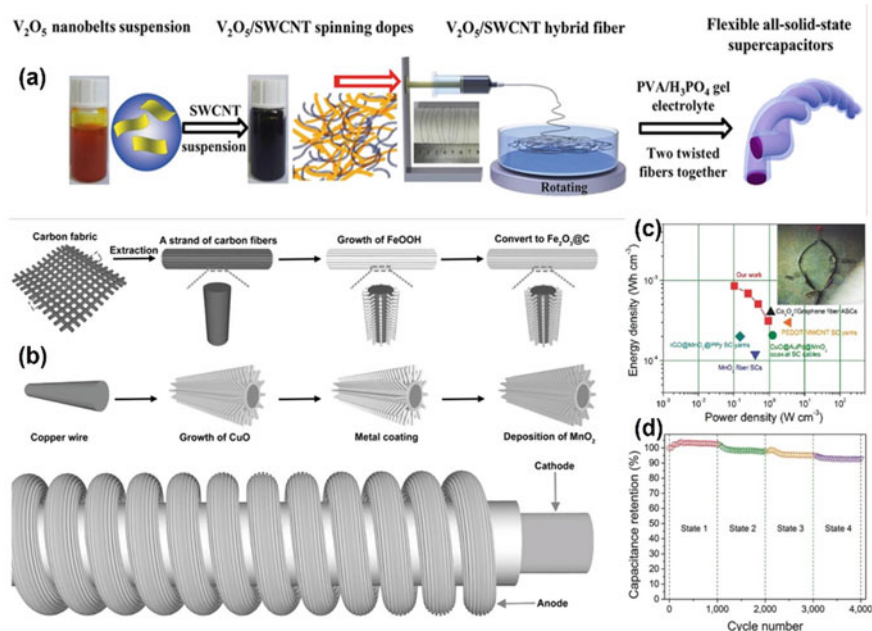


Fig. 3 a Schematic preparation representation of the all-solid-state flexible fiber supercapacitors based on V_2O_5 –SWCNT hybrid fiber electrodes. Reprinted with permission from (Li et al. 2017) copyright 2017 Elsevier. b Schematics illustration shows the synthesis process of anode, cathode, and fabrication of coil type assembly of fiber supercapacitor. c Ragone plots of the device showing energy and power density of coil type fiber supercapacitor. The inset shows a LED powered by a fiber supercapacitor. d Cycle stability tested at different bending states up to 4000 cycles. (Reprinted with permission from (Yu et al. 2015), copyright (2015) © John Wiley and Sons)

a two-ply yarn supercapacitor (Su and Miao 2014). Gamma irradiation is shown to improve the electrochemical performance, mechanical and electrical properties of the CNT yarn-based supercapacitor (Miao et al. 2011; Skakalova et al. 2003). The gamma irradiated CNT (IR-CNT) yarn has shown a 34% increase in breaking strength (773 MPa) and a 52% increase in electrical conductivity (5494 S m^{-1}). Also, the IR-CNT yarn exhibited an improved storage behavior with 2 times increased capacitance (18.5 F g^{-1} at a current density of 0.1 A g^{-1}) compared to pure CNT yarn. The irradiation improves all the essential properties of the wearable yarn supercapacitor. It does not affect the flexibility of the yarns (98.8% capacitance retention after 200 bending cycles), thus making it easy to weave into the fabric.

An asymmetric configuration was also followed for two-ply yarn-based supercapacitors with CNT/MnO₂ yarn as the cathode and CNT yarn as the anode (Su and Miao 2014). The asymmetric yarn supercapacitor delivered a voltage of 2 V, with an energy density of 42 Wh kg^{-1} at a power density of 483.7 W kg^{-1} . This device displayed decent cycle stability of 98% capacitance retention after 500 cycles under normal conditions and 99.5% capacitance retention after 200 bending cycles. This demonstrates that this two-ply yarn supercapacitor can be used for powering wearable electronics by weaving or knitting them into fabrics without negatively influencing its electrochemical performance. Multi-ply yarn supercapacitor is another assembly, which can be employed to fabricate wearable supercapacitor. A multi-ply yarn fiber supercapacitor fabricated by combining metal or alloy with yarn has shown an increase in the current density of the supercapacitor. As the conductivity of CNT yarn is always an issue to be worried about, twisting them with a conductive metal filament can solve the issue of electron transport. Among different metal or metal alloy filaments chosen for the study, Cu and Pt–Cu showed the best properties (Zhang et al. 2015).

A conventional multi-ply yarn-based supercapacitor can be constructed by twisting the metal/alloy and CNT yarn with a PVA–H₃PO₄ gel electrolyte coating with another multi-yarn electrode. The multi-ply yarn supercapacitor exhibited a capacitance close to 150 F g^{-1} due to the CuO formation via Cu filament oxidation leading to two active materials (CuO and CNT) contributing to the charge storage. A multi-ply yarn supercapacitor has shown a decent bending strength with ~98% capacitance retention even after 1000 cycles. This makes it an ideal candidate for powering wearable electronics. Again, with a twisted assembly configuration, 100% electrode and electrolyte interfacial area utilization is not guaranteed. This will impact the electrochemical performance during normal and bending conditions.

Coil type wrapping configuration. A coil-type fiber used in supercapacitor assembly sustains more mechanical strain than a typical twisted fiber configuration. In coil type assembly, one of the electrode fibers is coiled or spiraled around the other straight fiber with an electrolyte-soaked separator or a gel electrolyte in between (Yu et al. 2015; Dong et al. 2014). A coil-type assembly can be used to develop a flexible supercapacitor. For example, in a recent report, Nickel wire is used as the current collector for both inner and wrapping electrodes (Wu et al. 2015). The active material used here is ZnCo₂O₄ nanorods synthesized via hydrothermal route. The individual wire electrodes were coated with PVA/KOH electrolyte, which acts

as an electrolyte and a separator. This coil-type supercapacitor exhibited a specific capacitance of 10.9 F g^{-1} with an energy density of 76 mWh kg^{-1} and a power density of 19 W kg^{-1} . Using coil-type architecture, a dual-function fiber asymmetric supercapacitor was developed with energy storage and transport characteristics (Yu et al. 2015). The synthesis procedure of the electrodes and the coil type assembly fabrication procedure of the fiber supercapacitor are shown in Fig. 3b. The inner cathode made of copper wire was made capacitive by growing copper oxide nanowires on their surface, followed by electrochemical deposition of MnO_2 . The anode was made of carbon fiber deposited with hydrothermally grown core-shell structured iron oxide/carbon ($\text{Fe}_2\text{O}_3/\text{C}$) nanorods. The coil-type assembly was done by wrapping the anode around the cathode wire with a thin ion porous separator and LiCl/PVA gel electrolyte in between them. This asymmetric fiber supercapacitor delivered an energy density of $0.85 \text{ mW h cm}^{-3}$ (Fig. 3c) with a very high rate capability of 95.4% capacitance retention. An excellent bending cycle stability with 93.0% capacitance retention after 4000 cycles (Fig. 3d) and energy transmission ability was demonstrated. This proves that this coil type supercapacitor has a huge potential in wearable electronic applications.

Hybrid lithium-ion supercapacitors can also be developed in the form of cables following a coil-type configuration. Flexible carbon nanotubes macro film (CMF) can be used as a current collector film to deposit active materials for fabricating cable-type supercapacitors (Yuan et al. 2020). The anode can be made of lithium titanate ($\text{Li}_4\text{Ti}_5\text{O}_{12}$) and the cathode can be activated carbon. These active materials can be attached to the CMF surface. In a typical preparation, the electrodes coupled on the surface of carbon nanotubes fiber provided a high mass loading of 13.6 mg cm^{-2} for the cathode and 8.84 mg cm^{-2} for the anode. The cable supercapacitor delivered a volumetric energy density of 14.1 mWh cm^{-3} . The rapid electron and ion transport offered by the anchoring of electrodes on the current collector substrate gives good electrochemical performance for the cable supercapacitor. Also, the practicality of the cable supercapacitor was demonstrated via testing them at various mechanical conditions like bending, knots, weaving and series or parallel connections. The carbon nanotube fibers can be used to directly connect with electronic devices, thereby preventing any current loss.

Coaxial configuration. All the assembly configurations which are discussed earlier have a lower interfacial contact area between the electrode and electrolyte component. This would significantly impact the charge storage and would lead to lower capacitance and energy density of the supercapacitor. Also, electrodes can easily peel off from the current collector when they undergo mechanical deformation during the application. This led to another smart design of wearable supercapacitors, viz. coaxial assembly. In a coaxial assembly, one of the electrodes forms the inner core of the supercapacitor and another electrode acts as a sheath surrounding it separated by gel electrolyte (Jha et al. 2020; Wang et al. 2014; Cao et al. 2020; Yuan et al. 2020). A coaxial fiber supercapacitor developed with CNT fibers as the core electrode and CNT sheet as the sheath electrode separated by $\text{PVA-H}_3\text{PO}_4$ gel electrolyte has shown a capacitance of 59 F g^{-1} (Chen et al. 2013). A twisted assembly supercapacitor developed with the same active material cum current collector has

shown only 1/12th of the capacitance. This study shows that the enhancement in the contact area of the electrodes with the electrolyte certainly increases the energy stored in the supercapacitor. Another instance where a coaxial fiber supercapacitor with a hollow PPy sleeve as the shell electrode was developed via electrodeposition and etching methods (Li et al. 2018). The assembled coaxial fiber supercapacitor with Au coated PTFE with PPy as the core electrode and PVA–H₃PO₄ as gel electrolyte exhibited a volume capacitance of 2.44 F cm⁻³. Compared to a twisted assembly configuration, coaxial assembly showed ~6 times higher capacitance. The simulation work performed using ANSYS has shown that the better electrochemical performance delivered by the coaxial assembly is due to higher interfacial area between electrodes, uniform potential distribution and close contact between anode and cathode.

The core of the coaxial assembly can also be developed using carbon fibers as they are lightweight, highly flexible, and electrically conductive, in addition, to being an excellent current collector. In one approach, a carbon fiber deposited with MnO₂/PPy via electrochemical deposition acted as the coaxial assembly core. It is surrounded by a dip-coated CNT layer as a shell electrode (Shen et al. 2017). The coaxial assembly was separated by 1 μm thick PVA–H₃PO₄ electrolyte. This fiber supercapacitor delivered an energy density of 2.7 mWh cm⁻³ at a power density of 13 W cm⁻³. Using carbon-fiber core electrode and CNT paper, asymmetric configuration-based coaxial fibers can be developed to achieve higher voltage. One such approach where Fe₂O₃ deposited on carbon fiber acting as an anode and MnO₂/CNT paper as the cathode has delivered a high voltage of 2.2 V in an aqueous electrolyte (Patil et al. 2018). Achieving high voltage using aqueous electrolytes has huge practical applications as they are economical, safe and deliver high energy density. This fiber supercapacitor delivered a volumetric energy density of 0.43 mWh cm⁻³ at a power density of 0.02 W cm⁻³.

A dual-function supercapacitor that can store energy and successfully transmit electricity is important for many applications (Yu and Thomas 2014). A copper wire transformed into CuO nanowhiskers via thermal annealing was used as a current collector and to enhance the surface area of the electrode. The sheath of the supercapacitor was formed with a copper foil, which was also transformed into CuO nanowhiskers following a similar procedure. The electrodes were made conductive and highly capacitive by depositing AuPd and MnO₂ nanoparticles. The coaxial assembly was done to fabricate a cable supercapacitor using PVA–KOH gel electrolyte and a porous separator in between the electrodes (Fig. 4a). The coaxial cable supercapacitor exhibited excellent mechanical stability retaining ~93% capacitance even after 100 bending cycles at an extreme bending angle of 180° (Fig. 4b), along with a stable performance of 99% capacitance retention after 5000 cycles in the normal state (Fig. 4c). The dual-function coaxial cable supercapacitor is a novel idea that saves additional space required for energy storage devices in circuit boards, portable electronics, and electric vehicles. The dual functionality has been demonstrated via I–V plots and CV curves. It has been observed that neither energy storage nor electricity transmission is affected during the operation due to the presence of others.

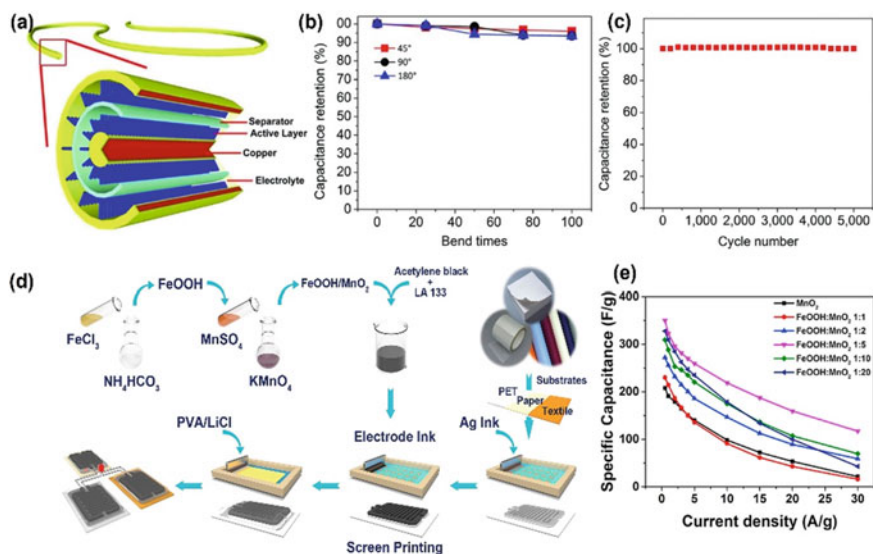


Fig. 4 **a** A cross-section schematic diagram of coaxial cable supercapacitor. **b** Bending the device up to 100 times at different bending angles shows excellent bendability. **c** Cycle performance of the device at a scan rate of 100 mV s^{-1} for 5,000 cycles. Reprinted with permission from (Yu and Thomas 2014) copyright 2014 John Wiley and Sons. **d** Schematic illustration of the synthesis procedures of amorphous FeOOH/MnO₂ composites and fabrication processes of all-printed supercapacitor devices. **e** Rate capability plot various FeOOH/MnO₂ composites. (Reprinted with permission from (Lu et al. 2017), copyright (2017) © Elsevier)

Screen printed supercapacitors. Until now, the above-discussed assembly configurations based on wires, fibers, or cable-type supercapacitors have to be weaved or incorporated into the fabric to be employed as a wearable energy storage device. The screen-printing approach is another efficient way that can be followed to develop lightweight, nontoxic, and nonflammable energy storage devices. Screen printing involves coating electrodes in the form of a conductive ink pushed using a squeegee through a screen mask onto the patterned current collector substrate. Usually, a fabric is employed. Both wearable supercapacitors and batteries with high power and energy density can be developed via screen printing techniques (Cho et al. 2015; Guo et al. 2016; Lehtimaki et al. 2017; Wang et al. 2019). Ink-jet printing (Singh et al. 2010) and dip-coating (Shi et al. 2014) are other approaches followed to develop large-area electrodes. As these screen-printed fabric supercapacitors are mostly focused on large-area fabrication, mass loading of the active material per unit area has to be a crucial factor in maximizing energy storage. The right measurement unit to be used in fabric or textile supercapacitors must be areal capacitance (mF or F cm^{-2}), as the fabric covers the human body, which has an average surface area of $\sim 1.5 \text{ m}^2$. Though high mass loading will increase the areal capacitance in fabric supercapacitor, this can impact the gravimetric capacitance if the active material is not conductive and porous enough to allow rapid electron and ion transport (Hu et al. 2009; Liu

et al. 2012). Screen printing of porous activated carbon derived from coconut shells (YP17) was conducted on various fabrics like cotton lawn, polyester microfiber, cotton twill, double knit with silver, and nylon neoprene (Jost et al. 2011). The active material slurry was developed by mixing activated carbon with 5 wt% Liquitex. A symmetric configuration was followed by assembling two fabrics on top of each other with a liquid electrolyte and PTFE separator. The whole assembly setup was enclosed in a polypropylene bag to secure the electrodes and electrolyte in place. The electrochemical performance of the cotton lawn, a hydrophilic natural staple fiber, polyester microfiber, and a high wicking fiber were better than other fabrics employed in screen printing. The cycling test demonstrated excellent stability with only 8% loss in capacitance in cotton lawn fabric even after 10,000 cycles.

Another approach involved replacing the inactive cotton and polyester backbone with highly conductive knitted and weaved carbon fibers of the supercapacitor to develop a fabric supercapacitor (Jost et al. 2013). Here, silicotungstic acid solid polymer was employed as the electrolyte. The advantage of solid electrolyte over liquid is avoiding electrolyte leaking during practical applications. The capacitive materials were inserted into the carbon fiber fabric via intarsia knitting with desired patterns within the woven textile. 3D printing machines were used here for knitting the CF electrodes into green wool to demonstrate the practicality. The machines used here for knitting were like 3D printers. Thus, they function as fast prototyping machines for mass scalability. Knitted devices showed a higher areal capacitance of 0.51 F cm^{-2} compared with 0.19 F cm^{-2} for the woven device. In another work, amorphous iron oxide hydroxide/ MnO_2 ($\text{FeOOH}/\text{MnO}_2$) composite electrodes synthesized via low-temperature wet chemical method were screen printed on various flexible substrates such as PET, paper, and textile to develop an all printed solid-state flexible supercapacitor device (Fig. 4d) (Lu et al. 2017). Here, amorphous electrode materials were favored over the crystalline materials as the slight structural disorder offered by the amorphous material facilitates a rapid ion diffusion. This ion diffusion enables irregular surfaces providing high surface area and suitable pore size distribution (Liu et al. 2016; Li et al. 2013). The fabricated all-solid-state device exhibited a large specific capacitance of 350.2 F g^{-1} at a current density of 0.5 A g^{-1} . The solid-state device also maintains a good rate capability of 159.5 F g^{-1} even at a high current density of 20 A g^{-1} (Fig. 4e). Exceptional cycling stability of 95.6% capacitance retention after 10,000 cycles shows the potential application of this screen-printed supercapacitor for the wearable electronics industry.

Micro-supercapacitors configuration. The flexible and wearable electronics, including sensors, implantable medical devices, electronic skins, and foldable displays, can be powered using one of the flexible supercapacitor assembly configurations discussed above. Another convenient way of powering them would be using a miniaturized power source, which can be easily integrated into the in-plane architecture of the electronic devices, thus saving space. The microsupercapacitors (MSCs) or microbatteries are such in-plane design power sources, which have been of great interest lately. MSCs consist of several interdigitated electrodes separated by a small gap, which enables a shorter ionic diffusion path, higher utilization of their surface

area and higher rate capability (Qi et al. 2017). The flexible substrates, which are typically used in these flexible MSCs, are made of plastic, elastomers, paper, or textile-based materials. Considering that the MSCs have a preset electrode pattern design, direct material growth or deposition techniques on the current collector substrate like electrodeposition or spray coating is the ideal way to fabricate a strong adhesive electrode precisely. PET, one of the most common substrates used in developing flexible MSCs is suitable for different electrode deposition techniques. An RGO based flexible MSCs developed on PET substrate via combined electrophoretic deposition and photolithography method has shown a high volumetric capacitance of 359 F cm^{-3} and volumetric energy density of 31.9 mWh cm^{-3} (Niu et al. 2013). The spray coating is a highly reproducible fabrication technique for developing large-area uniform electrodes. A flexible asymmetric MSC was developed via the spray-coating method using a patterned mask on a flexible nylon membrane (Shi et al. 2017). The asymmetric MSC developed with exfoliated graphene as the anode and MnO_2 as the cathode has shown good mechanical strength with no material delamination losing only 6% of capacitance even at a high bend state. Talking about the large-area fabrication of flexible MSCs, a combined methodology of photolithography and spray coating was followed to develop 100 MSC devices on a flexible PET substrate (Jiang et al. 2019). The MSC developed with MXene as active material with 100 nm thickness and $10 \mu\text{m}$ interspacing between the electrodes delivered a high volumetric capacitance of 30 F cm^{-3} and a rate capability of 300 V s^{-1} .

Vacuum filtration is another technique to deposit electrode materials on flexible MSC substrates. This technique aids in developing stacked dense film, which is well suitable for electrolyte ion permeation leading to high energy density MSCs. A hybrid film developed using phosphorene nanosheets and exfoliated graphene nanosheets through mask-assisted vacuum filtration technique acted as binder-free electrodes (Xiao et al. 2017). The fabrication process of the MSC involves the synthesis of graphene and phosphorene ink; followed by interdigitated mask-assisted vacuum filtration and transfer of hybrid electrode film to PET substrate; drop-casting of electrolyte and device packaging as shown in Fig. 5a. This approach can be followed to develop MSCs in series connection which has good flexibility and stability required for powering wearable electronics, as shown in Fig. 5b–c. The MSC developed using these hybrid films delivered a volumetric capacitance of 37.5 F cm^{-3} at a scan rate of 5 mV s^{-1} (Fig. 5d) and an energy density of 11.6 mWh cm^{-3} (Fig. 5e). The vacuum filtration technique offers an efficient approach for depositing active films for EDLCs and pseudocapacitors. This approach would provide a faster electron transport as well as higher capacitance via a synergetic EDLC and pseudocapacitive charge storage mechanism. An MSC developed using such a hybrid film via alternate exfoliated graphene film and PANI–graphene film delivered an areal capacitance of 210 mF cm^{-2} and volumetric capacitance of 436 F cm^{-3} at a scan rate of 10 mV s^{-1} (Qin et al. 2019). The vacuum-assisted technique was also followed to develop an asymmetric MSCs using vanadium nitride as the anode and MnO_2 as the cathode to obtain a voltage of 2 V. This flexible MSC showed excellent capacitance retention of 98% when subjected to mechanical bending at 180° . Etching methods such as laser etching and plasma etching have also been found to be effective in fabricating

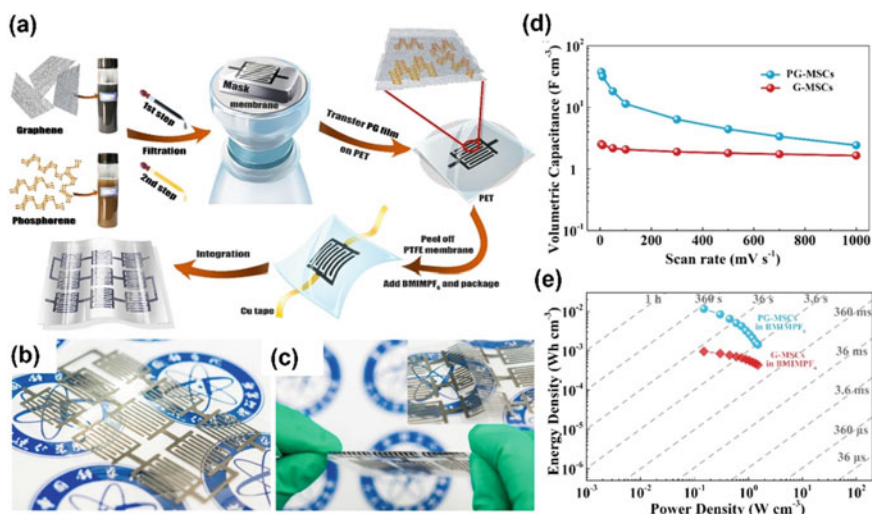


Fig. 5 a Mask-assisted vacuum filtration technique for fabrication of microsupercapacitor (MSC). Fabrication process involves the synthesis of active material ink; followed by interdigitated mask assisted vacuum filtration and transfer of hybrid electrode film to PET substrate; drop-casting electrolyte and device packaging. **b** 9 MSCs integrated in series connection. **c** Flexibility and stability demonstration of MSCs under folding conditions. **d** Volumetric capacitance of MSC at various scan rates. **e** Ragone plot of MSC. (Reprinted with permission from (Xiao et al. 2017), copyright (2017) © American Chemical Society)

flexible MSCs (Liang et al. 2018). A laser reduced graphene (LSG) developed via standard lightscribe DVD optical drive was used to develop a flexible MSC, which exhibited a power density of 200 W cm^{-3} (El-Kady and Kaner 2013). The laser scribing technique was also followed to develop an asymmetric flexible MSC using LSG–MnO₂ as cathode and LSG as the anode to deliver a voltage of 2 V in Na₂SO₄ electrolyte (El-Kady et al. 2015). This MSC exhibited an excellent rate capability of 96% even at a higher scan rate of 10 V s^{-1} and delivered a volumetric energy density of 42 mWh cm^{-3} .

Inkjet printing is followed to develop high-resolution interdigitated electrodes for flexible MSCs. A solid-state MSC was fabricated on A4 paper via inkjet printing of cellulose nanofibril nanoporous mats (Choi et al. 2016). The electrodes were made conductive using interwelded silver nanowire network. The final device is fabricated with activated carbon/CNT as the active material with ionic liquid/UV cured triacrylate polymer-based solid-state electrolyte. This MSC has shown excellent structural integrity with no capacitance loss even after 1000 bending cycles. Adding stretchability to the flexible MSCs and bendability and foldability will make them a potential power source for wearable electronics. A stretchable MSC was developed using a suspended wavy structure of graphene microribbons (Qi et al. 2015). These microribbons have a wrinkled structure which upon stretching releases strain via shape-changing ability. The stretchable MSCs have retained 92% capacitance after

5000 stretching cycles, which is highly beneficial for practical applications. Another efficient approach was followed to develop stretchable MSCs. The issues to address are electrode rigidity and interface instability between the substrate, electrode, and electrolyte (Lv et al. 2018). A composite of CNT and MnO₂ nanowires sandwiched using nanocellulose fibers was performed to overcome these issues. The strong van der Waals forces among CNTs increased the fracture strains of MnO₂ nanowires by tenfold. A honeycomb-like structure supercapacitor retained 98% capacitance even after 10,000 stretch and release cycles under reversible tensile strain of 400%.

5 Applications

Recent development in the fitness and fashion regime of youngsters has led to the development of flexible and wearable electronic gadgets, such as health monitors, on-body sensors, electronic skin, and portable displays. A recent report on wearable electronics market analysis by Grand view research states that the global market size for wearable electronics is increasing with an average annual growth of 13.8% and have predicted a similar growth till 2028 (Wearable Technology Market 2021). The report also mentions that the wearable electronics industry was valued USD 40.65 billion in 2020 (Wearable Technology Market 2021). Due to their fast charging, high power density, and reasonable energy density, supercapacitors have become a strong alternative to batteries for wearable electronic applications. Integration of supercapacitors with the electrical transmission makes them more efficient due to reduced energy losses. Furthermore, these integrated devices minimize the electrical device's weight and size, making them more acceptable for wearable electronics. To enable a more viable integration of supercapacitor with electronic equipment, a coax cables with dual functionality of energy storage and electrical transmission was developed (Yu and Thomas 2014). The coax cable showed excellent mechanical stability for 0–180° bending angles and 99% retention of charge after 5000 cycles at 100 mV s⁻¹.

As a part of maintaining fitness, wearable devices enable to continuously monitor critical human bodily signatures and communicating this information to medical specialists. Medical experts utilize this information to set baselines for individuals and intervene when abnormalities in these vital signals occur. Some of these gadgets and powered textiles are designed to measure critical bodily signatures such as blood glucose, vocal cord movements, blood pressure, pulse rate, body temperature, pulse oxygen levels, and respiration rate (Choi et al. 2016; Zhang et al. 2021). Some examples of the voltage output signal for bodily signatures are shown in Fig. 6 (Choi et al. 2016; Zhang et al. 2021). These wearable electronics are available as small-size fitness monitors and medical equipment for constant monitoring.

These devices have good prospects in commercial applications if the energy storage functions of supercapacitors can be integrated into medical equipment. Invasive equipment, such as sensing devices for electroencephalography or electromyography, along with chargeable prosthetic devices, can be included in wearable medical

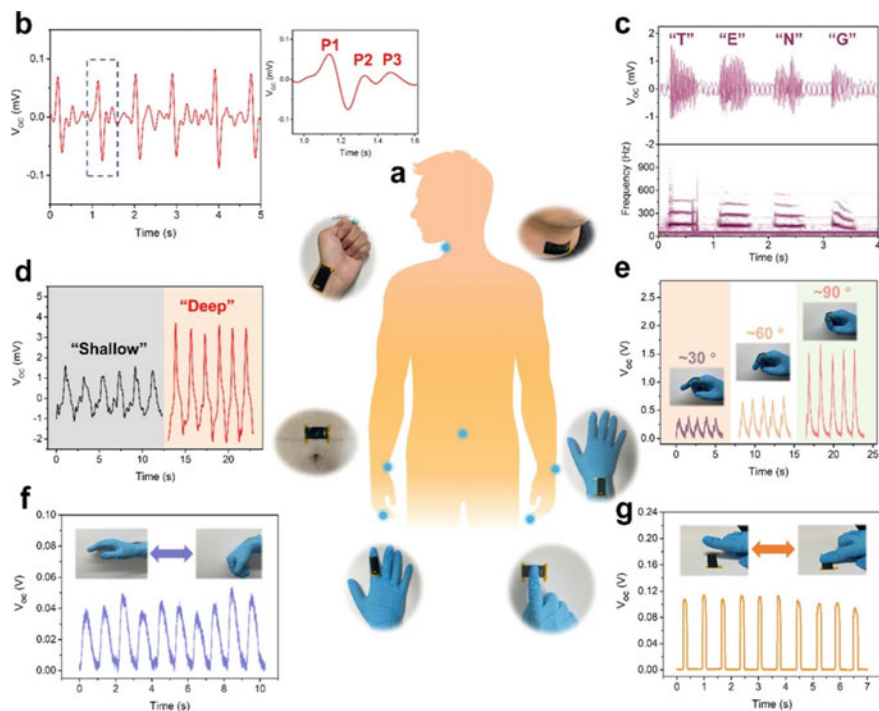


Fig. 6 A schematic depiction of several physiological signal outputs from wearables devices: **a** Signal detection nodes at human body marked in blue dot **b** Voltage output signal of an artery pulse **c** Voltage output signal corresponding to “TENG” pronunciation depicting monitoring of vocal cord vibrations **d** Voltage output signal from abdominal respiration monitoring **e–g** Voltage output signal for finger bending, wrist bending, and finger tapping. (Reprinted with permission from (Zhang et al. 2021), copyright (2021) © American Chemical Society)

devices (Choi et al. 2016; Zhang et al. 2021). Integration of supercapacitors into cardiac pacemakers can achieve the dual functionality of a self-charging power source for cardiac pacing and as an energy source for electrocardio signal detection. This makes them commercially appealing for products based solely on pulse current stimulus (Zhao et al. 2017) Medical catheters with the ability to move freely and precisely in surgery are another practical application (Lu et al. 2018a, b). Supercapacitor integrated actuators in catheters provide multiple functionalities of energy storage, precise control till millimeter scale and a multiple degrees of motion. The catheters devices can achieve as high as 11.5 kJ m^{-3} energy density (Lu et al. 2018) and exhibit excellent deformation abilities even with a low voltage of 1.0 V (Lu et al. 2018a).

The application of supercapacitor integrated devices in the medical field is mostly based on the sensors detecting variations in the normal functions. These sensors with charging capabilities can be used to read precise braille, allowing blind persons to improve their abilities. As illustrated in Fig. 7, a smart glove is designed to identify

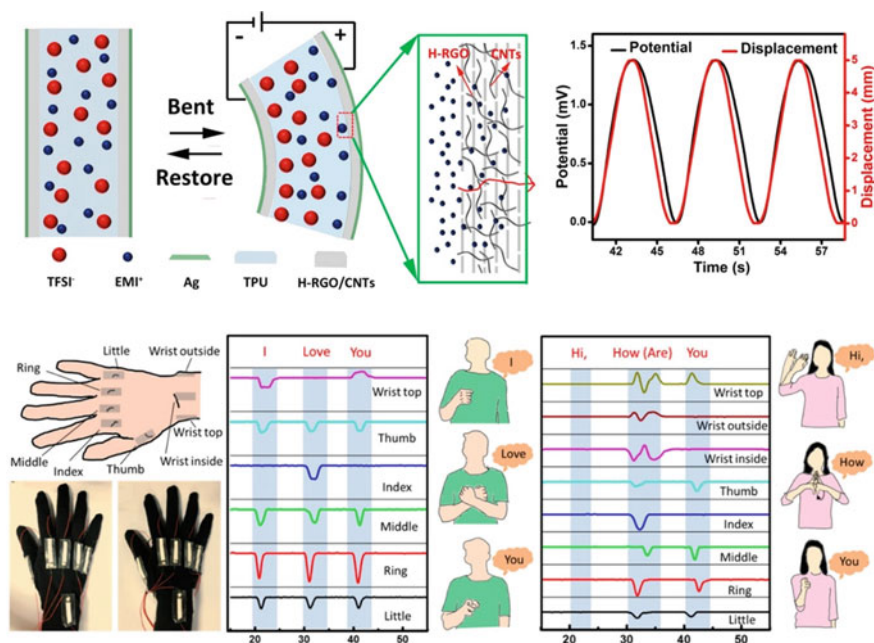


Fig. 7 Illustration of ionic sensing mechanism, charge–discharge cycle, smart gloves fabricated with ionic sensors, and a demonstration of braille communication. (Reprinted with permission from (Zhao et al. 2017), copyright (2017) © American Chemical Society)

human sign language. The glove functions due to highly sensitive supercapacitor integrated sensors (Zhao et al. 2017; Ming et al. 2018). These smart gloves can also be controlled through software on a computer. Supercapacitors integrated sensors work on the principle of ions migration between electrodes as a result of induced mechanical stresses and strains. The cations and anions migrate at different speeds and arrive in variable quantities at the anode and cathode, owing to the difference in their sizes. This ultimately results in uneven charge distribution in the electrodes. The sensor creates an output signal due to the imbalance in the charge distribution. The applied strain or stress direction is detected through the positive or negative sign of sensing potential. The sensors in the smart glove prepared by the plasma etching treatment method exhibit very high sensitivity and generate 200 mV signal even under a small bending strain of 1.6% (Zhao et al. 2017; Fu et al. 2018).

Wearable solid-state supercapacitors can also be combined with commercially available solar cells on a flexible substrate, such as textile and composite fabrics (Li et al. 2016). Chao et al. (Li et al. 2016) prepared a smart ribbon, with dual characteristics of energy harvesting and energy storage, by integrating perovskite solar cells with symmetrical supercapacitors on a copper (Cu) ribbon. The smart ribbon demonstrated a good energy density of 1.82 mWh cm^{-3} and power density 36.19 mW cm^{-3} at 1 mA cm^{-2} current density. The supercapacitors in the smart ribbon under solar light were able to hold a power density of 243 mW cm^{-3} and

an energy density of 1.15 mWh cm^{-3} . A smart fabric with high energy density and power density can be fabricated by combining the smart ribbons in parallel or series connections. The stored energy in supercapacitors, harvested through the integrated solar cell, can be used to detect strain in the arterial pulse (Yun et al. 2018). Furthermore, the addition of nanogenerative properties to supercapacitors allows them to self-charge while in operation, even removing the requirement for an external power source (Zhao et al. 2016). These self-charging supercapacitors typically harness energy using typical thermoelectric mechanisms. Supercapacitors can also be utilized as a wearable small and compact display when combined with electrochromic features. Electrochromic properties can be controlled by monitoring the charge transfer process by supercapacitors (Yang et al. 2016). For example, an electrochromic supercapacitor based on V_2O_5 demonstrated a capacitance as high as 155 F g^{-1} (Wei et al. 2012). Additionally, the color of the supercapacitor changed from grayish screen to yellow after applying a 3.2 V potential.

Apart from the health and medical industry, supercapacitors have great application potential in a wide range of electronics, including devices connected through the Internet of Things, wireless communication devices, indoor location tracking and physical activity recognition devices (Trung and Lee 2016; Son et al. 2014; Pu et al. 2016; He et al. 2017; Dubal et al. 2018). The supercapacitors have been woven into a shirt and are coupled in series to demonstrate their ability to power an LED and an electronic display. Owing to the recent developments in smart fabrics, a transition has begun in fabrics to ultra-smart fabrics by integrating sensing as well as actuation functionalities. As can be seen in several examples in Fig. 8 (Gao et al. 2018), textiles are upgraded from merely protecting the body to being used as energy storage devices. The woven cotton shirt is flexible enough to fit the shape of the body. The same method can be used to create smart lab coats that can withstand large bending deformations, as it only showed 5% decay in capacitance at different bending angles from 0 to 180° . A very high capacitance of 350.9 mF cm^{-2} was achieved at a current density of 1 mA cm^{-2} for the embedded supercapacitors. The assembled device exhibited strong potential for commercial applications due to its superior capabilities in terms of a high energy density of $109.6 \text{ } \mu\text{Wh cm}^{-2}$ at a power density of $749.5 \text{ } \mu\text{W cm}^{-2}$ and good cyclic performance of 90.5% after 3000 cycles. The working potential can be increased by connecting many supercapacitors in series to power devices that demand high energy density, such as digital watches, headphones, small motor fans, and pocket calculators (Fig. 8e–f) (Gao et al. 2018). Supercapacitors are also embedded into the artificial leather, in a similar way as in the textile (Huang et al. 2018). The pattern diversity of the artificial leather supercapacitor is also found to be excellent. Various patterns can be developed on artificial leather by simply peeling off from the patterned substrate. A supercapacitor sleeve showing fluorescence effect is developed using parallel and series assemblies of supercapacitors with an individual gravimetric capacitance of 105 F g^{-1} and powers light-emitting diodes. Polypyrrole was used as the electrode material to make it safer for daily usage.

Wireless systems have become an indispensable requirement in designing any modern electronic gadget, both user-friendly and commercial. Modern wireless systems are self-sufficient and generally have multifunction abilities, such as energy

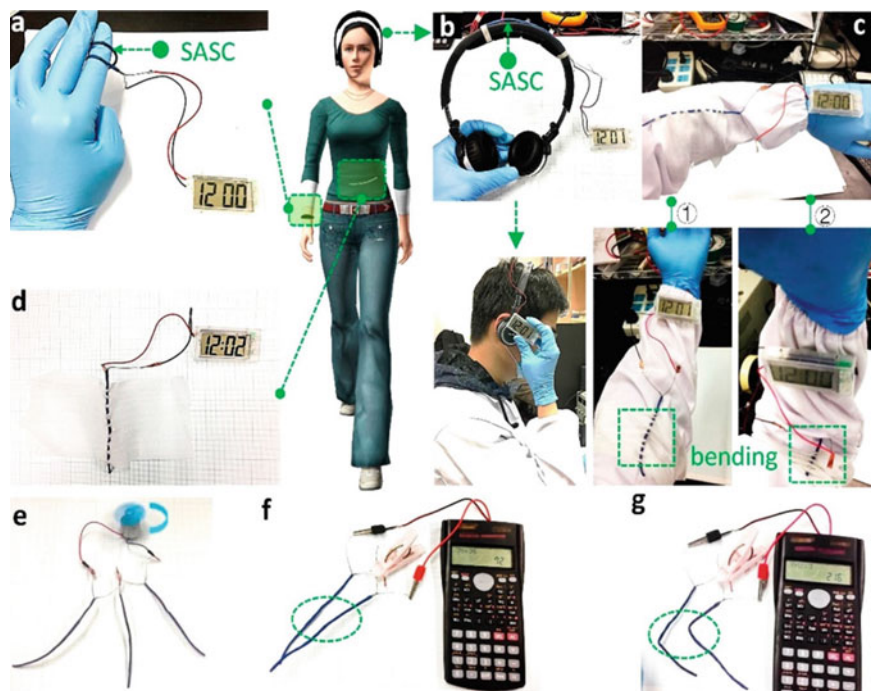


Fig. 8 Supercapacitor application in wearable electronic devices. **a** The curved supercapacitor device powers a digital watch. **b** Integration of device in a headphone. **c–d** A lab cloth with woven supercapacitor device to power various electronic gadgets under the common bending movement of hand ① (straight), ② (bending). **e, f,** and **g** illustrations of integrated supercapacitor device powering a motor fan and a pocket calculator. (Reprinted with permission from (Gao et al. 2018) Copyright (2018) © American Chemical Society)

harvesting, energy storage and sensing. In terms of new design approaches, substantial efforts are being made to develop dependable wireless systems using supercapacitors. Wireless charging of supercapacitor integrated devices by various wireless methods, such as an RFID tag (Niu et al. 2019), Bluetooth (Dong et al. 2017), inductive coupling method (Herbert et al. 2019) and NFC (Jeong et al. 2017; Kang et al. 2016), have been published recently.

Kim et al. developed a wireless system, which includes an RF power receiver, an array of supercapacitors, and strain and UV/NO₂ sensors (Kim et al. 2016). With wireless rechargeable MSCs, the system can track bio-signatures such as pulse rate, saturated oxygen levels, movement, and voice, as well as the UV radiation and NO₂ gas levels. A body area sensor network (bodynet) is fabricated with a wirelessly coupled stretchable sensor tag and a flexible RFID-enabled reader (Niu et al. 2019). The sensor and RFID-enabled reader are affixed to the skin and fabric, respectively. Response from the sensors at various body parts can be communicated to a smartphone through Bluetooth, proving enhanced commercial capabilities of supercapacitors in the tracking of bodily signatures in a true wireless manner. An array of nine

MSCs exhibited 4.7 F cm^{-3} at a current density of 0.23 A cm^{-3} was sufficient to perform the sensing and data communication.

Integrating supercapacitors with wearable materials can help astronauts, soldiers, and first responders in saving space and weight considerably. Bioinspired and bio-functional fabrics with permanent features such as self-healing capability, high flexibility, and self-repair are in demand in high-impact areas such as aerospace and military (Choi et al. 2016; Khan et al. 2016). Wearable supercapacitors also show promising potential applications in the military and aerospace in the form of backup power hold-up for emergency handheld radios and helmet torches (Dubal et al. 2018). The application in these sectors is mainly attributed to its unique characteristics of high-power delivery, ability to withstand low temperatures and charge maintenance for many cycles.

Self-healing supercapacitors fabricated by integrating electrodes into self-healing polymers can restore their performance after being damaged via recovery of the polymer network (Keum et al. 2020). The recreation property for self-healing polymers comes from either the recreation of polymer network by adding monomers or through the recreation of intermolecular bonds. Self-healing polymers based on recreation mechanisms, called intrinsic self-healing polymers, are in practical applications. Ionic gel (Cao et al. 2019; Lei et al. 2017) PU (Son et al. 2018; Wang et al. 2020), and modified PDMS (Tang et al. 2019) are some examples of intrinsic self-healing polymers. AgNWs and 1D CNTs are reported as electrode materials for self-healing supercapacitor integrated devices (Kang et al. 2019). Wearable self-healing devices, such as sensors and electronic skin, have been developed extensively in the past decade (Lei et al. 2017; Wang et al. 2019; Tee et al. 2012). Addition of shape memory property in supercapacitor devices enhance their property to withstand large deformations without permanent deformation and ultimately increase the device's lifespan. Shape memory supercapacitor devices are fabricated by integrating electrode materials in either shape memory alloys (SMAs) or shape memory polymers (SMPs) (Keum et al. 2020). Supercapacitor devices based on nickel–titanium SMAs have shown a capacitance as high as 198.2 F g^{-1} at a current density of 1 A g^{-1} . A capacitance retention of 99.1% after 1400 bending cycles and 85% capacitance retention after 15 shape memory cycles was reported for the same (Huang et al. 2016). Supercapacitors integrated into SMPs use PVA or PU as common templates to deposit electrode materials (Khosrozadeh et al. 2018; Tai et al. 2012; Zhong et al. 2015). Supercapacitors with shape memory properties could be woven into regular fabrics to regulate the fabric's overall shape (Keum et al. 2020).

Supercapacitors with bioresorbable materials such as cellulose, pectin, starch, etc., are the need of the hour to allow for a flexible application in implantable electronics (Keum et al. 2020; Gross and Kalra 2002). Biodegradable supercapacitors devices can help to reduce pollution and e-waste in the environment. The exploration of new biodegradable supercapacitor materials will help the community in keeping the environment clean as the usage of supercapacitors has increased considerably due

to the surge in demand for wearable electronics gadgets, and it requires dedicated research and efforts from all scientific communities.

6 Summary and Outlook

Owing to the limitations of fossil fuels and a societal surge towards a clean environment, the world is evolving towards renewable energy. This has led to an increase in demand for supercapacitors in the last decade. Supercapacitors in wearable electronics hold many advantages compared to conventional capacitors and batteries due to their small sizes, flexible substrates, and fast charging. Flexible supercapacitors are already being used to produce smart medical devices, biosensors, smart fabrics, and electronic devices. Integration of self-healing and shape-memory substrates in electrode materials has further enhanced their practical application in critical areas such as defense and aero industries. Although a lot of research in the last decade has focused on increasing the capacitance, charging rate, and life span, efforts on the usage of biocompatible materials in supercapacitors are still needed. Usage of bio-compatible materials will greatly enhance their capabilities in the application of prosthetic implants such as robotic hands, pacemakers, and electronic skin. The use of bio-degradable materials in supercapacitors will also make them environmentally friendly to help in combating the climate crisis.

To power flexible electronics, it becomes imperative to develop flexible energy storage sources that could be easily integrated into flexible electronics. This integration should be done carefully if the flexible electronics fall into the category of wearables. Wearable clothes and gadgets can be powered by wearable supercapacitors that can be developed using different categories of flexible substrates. These flexible substrates can be of 1D, 2D, or 3D type. 1D flexible substrates are referred to the fiber-type substrates that are long wire-shaped and have diameters ranging from micro to millimeters. These may include popularly plastic fiber, metallic fiber, and carbon fiber substrates. Next comes the 2D substrates, which resemble paper-type thin foil-type structures. These are divided into categories of free-standing (where active material itself forms the fiber network) or flexible substrate supported (flexible metal foil/plastic/paper supported). 3D flexible substrates are a porous network of materials that are a bit thick but can offer higher energy and charge storage. These may include textile-based or metal-based. On these flexible substrates, various active materials like (1) carbon-based graphene, CNTs, etc. (2) Metal oxide/hydride/hydroxide and nitride-based material, and (3) Conducting polymers coated to impart high charge storage capabilities and turning them into a flexible and durable power source.

Assembling the flexible supercapacitor using these materials is an important step as it determines how the energy storage device is integrated into the wearer's daily life. There are several assembly configurations followed depending on the substrate type used. Configurations like parallel, twisted, coiled and coaxial assembly of the fiber,

yarn, or wire-shaped electrodes are most common when it comes to developing flexible supercapacitors for powering wearable electronics. The parallel assembly configurations involve placing two electrodes side by side separated by gel electrolyte or a separator soaked in electrolyte. The twisted configuration involves intertwining or twisting two fiber electrodes with a separator in between them. In coil type assembly, one of the electrode fibers is coiled or spiraled around the other straight fiber with an electrolyte-soaked separator or a gel electrolyte in between. In a coaxial assembly, one of the electrodes forms the inner core of the supercapacitor and another electrode acts as a sheath surrounding it separated by gel electrolyte. Among all the assembly configurations, the coaxial type of assembly is one of the best approaches as they provide maximum interfacial contact between the electrode and electrolyte used. This is essential to attain the highest capacitance and energy density from the supercapacitor. Apart from these assemblies, sandwich-type configuration is also followed for fabricating flexible supercapacitors made of 2D or 3D substrates such as paper, cloth, or interconnected fiber mats. The microsupercapacitors that are gaining a lot of attention lately are in-plane power sources that provide easy integration into modern electronics. In all the assembly configurations, charge balancing is a key parameter to be considered. This can be done based on an individual electrode's performance, including its active charge storing mass or area, overall capacitance, and the potential window. This charge balance is vital in getting a higher cycle life and energy storage from the assembled device. The drawback of poor energy density in supercapacitors can be rectified by following asymmetric configuration employing two different materials as electrodes. This would help in overcoming the thermodynamic breakdown potential of water. The electrolyte is another key factor to consider as it conducts the ions between the electrode materials. The safest option for flexible supercapacitors is using aqueous-based electrolytes as it would not catch fire and are inexpensive to fabricate. The aqueous electrolytes have to be made into a gel as this would be flexible, avoid potential leaking issues and act as a separator. Finally, once assembled, all the components have to be packed well to prevent electrolyte evaporation and other environmental disturbances. The mechanical strength and flexibility are some of the key characteristics which need to be evaluated for many cycles as these wearable energy storage devices undergo a lot of deformation in everyday usage.

References

- Bae J, Song MK, Park YJ, Kim JM, Liu M, Wang ZL (2011) Fiber supercapacitors made of nanowire-fiber hybrid structures for wearable/flexible energy storage. *Angew Chem Int Ed* 50(7):1683–1687
- Barisci JN, Wallace GG, Baughman RH (2000) Electrochemical studies of single-wall carbon nanotubes in aqueous solutions. *J Electroanal Chem* 488(2):92–98
- Bonaccorso F, Colombo L, Yu G, Stoller M, Tozzini V, Ferrari AC, et al (2015) Graphene, related two-dimensional crystals, and hybrid systems for energy conversion and storage. *Science* 347(6217)

- Cao Z, Wei BB (2013) A perspective: carbon nanotube macro-films for energy storage. *Energy Environ Sci* 6(11):3183–3201
- Cao X, Shi Y, Shi W, Lu G, Huang X, Yan Q et al (2011) Preparation of novel 3D graphene networks for supercapacitor applications. *Small* 7(22):3163–3168
- Cao YC, Zhu M, Li PX, Zhang RJ, Li XM, Gong QM et al (2013) Boosting supercapacitor performance of carbon fibres using electrochemically reduced graphene oxide additives. *Phys Chem Chem Phys* 15(45):19550–19556
- Cao Y, Tan YJ, Li S, Lee WW, Guo HC, Cai YQ et al (2019) Self-healing electronic skins for aquatic environments. *Nat Electron* 2(2):75–82
- Cao XY, Liu Y, Zhong YX, Cui L, Zhang AT, Razal JM et al (2020) Flexible coaxial fiber-shaped asymmetric supercapacitors based on manganese, nickel co-substituted cobalt carbonate hydroxides. *J Mater Chem A* 8(4):1837–1848
- Chang YH, Lin CT, Chen TY, Hsu CL, Lee YH, Zhang W et al (2013) Highly efficient electrocatalytic hydrogen production by MoS_x grown on graphene-protected 3D Ni foams. *Adv Mater* 25(5):756–760
- Chen T, Dai L (2014) Flexible supercapacitors based on carbon nanomaterials. *J Mater Chem A* 2(28):10756–10775
- Chen W, Rakhi R, Hu L, Xie X, Cui Y, Alshareef HN (2011) High-performance nanostructured supercapacitors on a sponge. *Nano Lett* 11(12):5165–5172
- Chen W, Rakhi R, Alshareef HN (2012) High energy density supercapacitors using macroporous kitchen sponges. *J Mater Chem* 22(29):14394–14402
- Chen XL, Qiu LB, Ren J, Guan GZ, Lin HJ, Zhang ZT et al (2013) Novel electric double-layer capacitor with a coaxial fiber structure. *Adv Mater* 25(44):6436–6441
- Cherusseri J, Sambath Kumar K, Pandey D, Barrios E, Thomas J (2019) Vertically aligned graphene-carbon fiber hybrid electrodes with superlong cycling stability for flexible supercapacitors. *Small* 15(44):1902606
- Chmiola J, Largeot C, Taberna P-L, Simon P, Gogotsi Y (2010) Monolithic carbide-derived carbon films for micro-supercapacitors. *Science* 328(5977):480–483
- Cho S, Kim M, Jang J (2015) Screen-printable and flexible RuO₂ nanoparticle-decorated PEDOT:PSS/graphene nanocomposite with enhanced electrical and electrochemical performances for high-capacity supercapacitor. *ACS Appl Mater Interfaces* 7(19):10213–10227
- Choi C, Lee JA, Choi AY, Kim YT, Lepró X, Lima MD et al (2014) Flexible supercapacitor made of carbon nanotube yarn with internal pores. *Adv Mater* 26(13):2059–2065
- Choi KH, Yoo J, Lee CK, Lee SY (2016) All-inkjet-printed, solid-state flexible supercapacitors on paper. *Energy Environ Sci* 9(9):2812–2821
- Choi S, Lee H, Ghaffari R, Hyeon T, Kim DH (2016) Recent advances in flexible and stretchable bio-electronic devices integrated with nanomaterials. *Adv Mater* 28(22):4203–4218
- Choi C, Sim HJ, Spinks GM, Lepró X, Baughman RH, Kim SJ (2016) Elastomeric and dynamic MnO₂/CNT core-shell structure coiled yarn supercapacitor. *Adv Energy Mater* 6(5):1502119
- Conway B, Pell W (2003) Double-layer and pseudocapacitance types of electrochemical capacitors and their applications to the development of hybrid devices. *J Solid State Electrochem* 7(9):637–644
- Dong XL, Guo ZY, Song YF, Hou MY, Wang JQ, Wang YG et al (2014) Flexible and wire-shaped micro-supercapacitor based on Ni(OH)₂-nanowire and ordered mesoporous carbon electrodes. *Adv Funct Mater* 24(22):3405–3412
- Dong K, Wang YC, Deng JN, Dai YJ, Zhang SL, Zou HY et al (2017) A highly stretchable and washable all-yarn-based self-charging knitting power textile composed of fiber triboelectric nanogenerators and supercapacitors. *ACS Nano* 11(9):9490–9499
- Du C, Pan N (2006) Supercapacitors using carbon nanotubes films by electrophoretic deposition. *J Power Sources* 160(2):1487–1494
- Dubal DP, Chodankar NR, Kim DH, Gomez-Romero P (2018) Towards flexible solid-state supercapacitors for smart and wearable electronics. *Chem Soc Rev* 47(6):2065–2129

- El-Kady MF, Ihns M, Li MP, Hwang JY, Mousavi MF, Chaney L et al (2015) Engineering three-dimensional hybrid supercapacitors and microsupercapacitors for high-performance integrated energy storage. *Proc Natl Acad Sci USA* 112(14):4233–4238
- El-Kady MF, Kaner RB (2013) Scalable fabrication of high-power graphene micro-supercapacitors for flexible and on-chip energy storage. *Nat Commun* 4
- Forouzandeh P, Kumaravel V, Pillai SC (2020) Electrode materials for supercapacitors: a review of recent advances. *Catalysts* 10(9):969
- Frackowiak E, Jurewicz K, Delpoux S, Béguin F (2001) Nanotubular materials for supercapacitors. *J Power Sources* 97:822–825
- Fu Y, Cai X, Wu H, Lv Z, Hou S, Peng M et al (2012) Fiber supercapacitors utilizing pen ink for flexible/wearable energy storage. *Adv Mater* 24(42):5713–5718
- Fu RP, Yang Y, Lu C, Ming Y, Zhao XX, Hu YM et al (2018) Large-scale fabrication of high-performance ionic polymer metal composite flexible sensors by in situ plasma etching and magnetron sputtering. *ACS Omega* 3(8):9146–9154
- Gao LB, Song J, Surjadi JU, Cao K, Han Y, Sun D et al (2018) Graphene-bridged multifunctional flexible fiber supercapacitor with high energy density. *ACS Appl Mater Interfaces* 10(34):28597–28607
- Geetha S, Rao CR, Vijayan M, Trivedi D (2006) Biosensing and drug delivery by polypyrrole. *Anal Chim Acta* 568(1–2):119–125
- Gross RA, Kalra B (2002) Biodegradable polymers for the environment. *Science* 297(5582):803–807
- Guo YB, Li KR, Hou CY, Li YG, Zhang QH, Wang HZ (2016) Fluoroalkylsilane-modified textile-based personal energy management device for multifunctional wearable applications. *ACS Appl Mater Interfaces* 8(7):4676–4683
- Guo K, Ma Y, Li HQ, Zhai TY (2016) Flexible wire-shaped supercapacitors in parallel double helix configuration with stable electrochemical properties under static/dynamic bending. *Small* 12(8):1024–1033
- He HX, Fu YM, Zhao TM, Gao XC, Xing LL, Zhang Y et al (2017) All-solid-state flexible self-charging power cell basing on piezo-electrolyte for harvesting/storing body-motion energy and powering wearable electronics. *Nano Energy* 39:590–600
- Herbert R, Mishra S, Lim HR, Yoo H, Yeo WH (2019) Fully printed, wireless, stretchable implantable biosystem toward batteryless, real-time monitoring of cerebral aneurysm hemodynamics. *Adv Sci* 6(18)
- Hsu Y-K, Chen Y-C, Lin Y-G, Chen L-C, Chen K-H (2012) High-cell-voltage supercapacitor of carbon nanotube/carbon cloth operating in neutral aqueous solution. *J Mater Chem* 22(8):3383–3387
- Hu LB, Choi JW, Yang Y, Jeong S, La Mantia F, Cui LF et al (2009) Highly conductive paper for energy-storage devices. *Proc Natl Acad Sci USA* 106(51):21490–21494
- Hu W, Peng C, Luo W, Lv M, Li X, Li D et al (2010) Graphene-based antibacterial paper. *ACS Nano* 4(7):4317–4323
- Hu L, Wu H, Cui Y (2010) Printed energy storage devices by integration of electrodes and separators into single sheets of paper. *Appl Phys Lett* 96(18):183502
- Hu L, Pasta M, La Mantia F, Cui L, Jeong S, Deshazer HD et al (2010) Stretchable, porous, and conductive energy textiles. *Nano Lett* 10(2):708–714
- Huang Y, Zhong M, Huang Y, Zhu M, Pei Z, Wang Z et al (2015) A self-healable and highly stretchable supercapacitor based on a dual crosslinked polyelectrolyte. *Nat Commun* 6(1):1–8
- Huang Y, Hu H, Huang Y, Zhu M, Meng W, Liu C et al (2015) From industrially weavable and knittable highly conductive yarns to large wearable energy storage textiles. *ACS Nano* 9(5):4766–4775
- Huang Y, Tao J, Meng W, Zhu M, Huang Y, Fu Y et al (2015) Super-high rate stretchable polypyrrole-based supercapacitors with excellent cycling stability. *Nano Energy* 11:518–525
- Huang Y, Zhu M, Huang Y, Pei Z, Li H, Wang Z et al (2016) Multifunctional energy storage and conversion devices. *Adv Mater* 28(38):8344–8364

- Huang Q, Wang D, Zheng Z (2016) Textile-based electrochemical energy storage devices. *Adv Energy Mater* 6(22):1600783
- Huang Y, Zhu MS, Pei ZX, Xue Q, Huang Y, Zhi CY (2016) A shape memory supercapacitor and its application in smart energy storage textiles. *J Mater Chem A* 4(4):1290–1297
- Huang Y, Tang ZJ, Liu ZX, Wei J, Hu H, Zhi CY (2018) Toward enhancing wearability and fashion of wearable supercapacitor with modified polyurethane artificial leather electrolyte. *Nano-Micro Lett* 10(3)
- Hughes M, Spinks GM (2005) Multiwalled carbon nanotube actuators. *Adv Mater* 17(4):443–446
- Javed MS, Han X, Hu C, Zhou M, Huang Z, Tang X et al (2016) Tracking pseudocapacitive contribution to superior energy storage of MnS nanoparticles grown on carbon textile. *ACS Appl Mater Interfaces* 8(37):24621–24628
- Jeong YR, Kim J, Xie ZQ, Xue YG, Won SM, Lee G, et al (2017) A skin-attachable, stretchable integrated system based on liquid GaInSn for wireless human motion monitoring with multi-site sensing capabilities. *NPG Asia Mater* 9
- Jha MK, Ball R, Seelaboyina R, Subramaniam C (2020) All solid-state coaxial supercapacitor with ultrahigh scan rate operability of 250,000 mV/s by thermal engineering of the electrode-electrolyte interface. *ACS Appl Energy Mater* 3(4):3454–3464
- Jiang Q, Kurra N, Maleski K, Lei YJ, Liang HF, Zhang YZ, et al (2019) On-chip MXene microsupercapacitors for AC-line filtering applications. *Adv Energy Mater* 9(26)
- Jost K, Perez CR, McDonough JK, Presser V, Heon M, Dion G et al (2011) Carbon coated textiles for flexible energy storage. *Energy Environ Sci* 4(12):5060–5067
- Jost K, Stenger D, Perez CR, McDonough JK, Lian K, Gogotsi Y et al (2013) Knitted and screen printed carbon-fiber supercapacitors for applications in wearable electronics. *Energy Environ Sci* 6(9):2698–2705
- Jost K, Dion G, Gogotsi Y (2014) Textile energy storage in perspective. *J Mater Chem A* 2(28):10776–10787
- Jost K, Durkin DP, Haverhals LM, Brown EK, Langenstein M, De Long HC et al (2015) Natural fiber welded electrode yarns for knittable textile supercapacitors. *Adv Energy Mater* 5(4):1401286
- Kang J, Tok JBH, Bao ZA (2019) Self-healing soft electronics. *Nat Electron* 2(4):144–150
- Kang SK, Murphy RKJ, Hwang SW, Lee SM, Harburg DV, Krueger NA, et al (2016) Bioresorbable silicon electronic sensors for the brain. *Nature* 530(7588):71–+
- Keum K, Kim JW, Hong SY, Son JG, Lee SS, Ha JS (2020) Flexible/stretchable supercapacitors with novel functionality for wearable electronics. *Adv Mater* 32(51)
- Khan Y, Ostfeld AE, Lochner CM, Pierre A, Arias AC (2016) Monitoring of vital signs with flexible and wearable medical devices. *Adv Mater* 28(22):4373–4395
- Khosrozadeh A, Darabi MA, Xing M, Wang Q (2016) Flexible electrode design: fabrication of freestanding polyaniline-based composite films for high-performance supercapacitors. *ACS Appl Mater Interfaces* 8(18):11379–11389
- Khosrozadeh A, Singh G, Wang Q, Luo GX, Xing M (2018) Supercapacitor with extraordinary cycling stability and high rate from nano-architected polyaniline/graphene on Janus nanofibrous film with shape memory. *J Mater Chem A* 6(42):21064–21077
- Kim BC, Hong JY, Wallace GG, Park HS (2015) Recent progress in flexible electrochemical capacitors: electrode materials, device configuration, and functions. *Adv Energy Mater* 5(22):1500959
- Kim D, Kim D, Lee H, Jeong YR, Lee SJ, Yang G et al (2016) Body-attachable and stretchable multisensors integrated with wirelessly rechargeable energy storage devices. *Adv Mater* 28(4):748–756
- Kou L, Huang T, Zheng B, Han Y, Zhao X, Gopalsamy K et al (2014) Coaxial wet-spun yarn supercapacitors for high-energy density and safe wearable electronics. *Nat Commun* 5(1):1–10
- Krasheninnikov AV, Banhart F (2007) Engineering of nanostructured carbon materials with electron or ion beams. *Nat Mater* 6(10):723–733
- Kumar KS, Choudhary N, Jung Y, Thomas J (2018) Recent advances in two-dimensional nanomaterials for supercapacitor electrode applications. *ACS Energy Lett* 3(2):482–495

- Kumar KS, Cherusseri J, Thomas J (2019) Two-dimensional Mn_3O_4 nanowalls grown on carbon fibers as electrodes for flexible supercapacitors. *ACS Omega* 4(2):4472–4480
- Kumar KS, Pandey D, Thomas J (2021) High voltage asymmetric supercapacitors developed by engineering electrode work functions. *ACS Energy Lett* 6(10):3590–3599
- Kumar KS, Choudhary N, Pandey D, Hurtado L, Chung HS, Tetard L, et al (2020) High-performance flexible asymmetric supercapacitor based on rGO anode and $WO_3/WS(2)$ core/shell nanowire cathode. *Nanotechnology* 31(43)
- Le VT, Kim H, Ghosh A, Kim J, Chang J, Vu QA et al (2013) Coaxial fiber supercapacitor using all-carbon material electrodes. *ACS Nano* 7(7):5940–5947
- Lee S-Y, Choi K-H, Choi W-S, Kwon YH, Jung H-R, Shin H-C et al (2013) Progress in flexible energy storage and conversion systems, with a focus on cable-type lithium-ion batteries. *Energy Environ Sci* 6(8):2414–2423
- Lee JA, Shin MK, Kim SH, Cho HU, Spinks GM, Wallace GG et al (2013) Ultrafast charge and discharge bistructured yarn supercapacitors for textiles and microdevices. *Nat Commun* 4(1):1–8
- Lehtimäki S, Railanmaa A, Keskinen J, Kujala M, Tuukkanen S, Lupo D (2017) Performance, stability and operation voltage optimization of screen-printed aqueous supercapacitors. *Sci Rep* 7
- Lei Z, Lu L, Zhao X (2012) The electrocapacitive properties of graphene oxide reduced by urea. *Energy Environ Sci* 5(4):6391–6399
- Lei ZY, Wang QK, Sun ST, Zhu WC, Wu PY (2017) A bioinspired mineral hydrogel as a self-healable, mechanically adaptable ionic skin for highly sensitive pressure sensing. *Adv Mater* 29(22)
- Li Y, Sheng K, Yuan W, Shi G (2013) A high-performance flexible fibre-shaped electrochemical capacitor based on electrochemically reduced graphene oxide. *Chem Commun* 49(3):291–293
- Li N, Yang G, Sun Y, Song H, Cui H, Yang G et al (2015) Free-standing and transparent graphene membrane of polyhedron box-shaped basic building units directly grown using a NaCl template for flexible transparent and stretchable solid-state supercapacitors. *Nano Lett* 15(5):3195–3203
- Li C, Islam MM, Moore J, Sleppy J, Morrison C, Konstantinov K et al (2016) Wearable energy-smart ribbons for synchronous energy harvest and storage. *Nat Commun* 7(1):1–10
- Li H, He J, Cao X, Kang LP, He XX, Xu H et al (2017) All solid-state V_2O_5 -based flexible hybrid fiber supercapacitors. *J Power Sources* 371:18–25
- Li HB, Yu MH, Wang FX, Liu P, Liang Y, Xiao J, et al (2013) Amorphous nickel hydroxide nanospheres with ultrahigh capacitance and energy density as electrochemical pseudocapacitor materials. *Nat Commun* 4
- Li C, Islam MM, Moore J, Sleppy J, Morrison C, Konstantinov K, et al (2016) Wearable energy-smart ribbons for synchronous energy harvest and storage. *Nat Commun* 7
- Li L, Lou Z, Chen D, Han W, Shen GZ (2018) Hollow polypyrrole sleeve based coaxial fiber supercapacitors for wearable integrated photosensing system. *Adv Mater Technol (US)* 3(8)
- Liang HF, Ming FW, Alshareef HN (2018) Applications of plasma in energy conversion and storage materials. *Adv Energy Mater* 8(29)
- Liao Q, Li N, Jin S, Yang G, Wang C (2015) All-solid-state symmetric supercapacitor based on Co_3O_4 nanoparticles on vertically aligned graphene. *ACS Nano* 9(5):5310–5317
- Liu WW, Yan XB, Lang JW, Peng C, Xue QJ (2012) Flexible and conductive nanocomposite electrode based on graphene sheets and cotton cloth for supercapacitor. *J Mater Chem* 22(33):17245–17253
- Liu NS, Ma WZ, Tao JY, Zhang XH, Su J, Li LY et al (2013) Cable-type supercapacitors of three-dimensional cotton thread based multi-grade nanostructures for wearable energy storage. *Adv Mater* 25(35):4925–4931
- Liu T, Finn L, Yu M, Wang H, Zhai T, Lu X et al (2014) Polyaniline and polypyrrole pseudocapacitor electrodes with excellent cycling stability. *Nano Lett* 14(5):2522–2527
- Liu L, Niu Z, Zhang L, Zhou W, Chen X, Xie S (2014) Nanostructured graphene composite papers for highly flexible and foldable supercapacitors. *Adv Mater* 26(28):4855–4862

- Liu L, Yu Y, Yan C, Li K, Zheng Z (2015) Wearable energy-dense and power-dense supercapacitor yarns enabled by scalable graphene-metallic textile composite electrodes. *Nat Commun* 6(1):1–9
- Liu W, Liu N, Shi Y, Chen Y, Yang C, Tao J et al (2015) A wire-shaped flexible asymmetric supercapacitor based on carbon fiber coated with a metal oxide and a polymer. *J Mater Chem A* 3(25):13461–13467
- Liu Z, Xu J, Chen D, Shen G (2015) Flexible electronics based on inorganic nanowires. *Chem Soc Rev* 44(1):161–192
- Liu G, Jin W, Xu N (2015) Graphene-based membranes. *Chem Soc Rev* 44(15):5016–5030
- Liu JQ, Zheng MB, Shi XQ, Zeng HB, Xia H (2016) Amorphous FeOOH quantum dots assembled mesoporous film anchored on graphene nanosheets with superior electrochemical performance for supercapacitors. *Adv Funct Mater* 26(6):919–930
- Lu X, Yu M, Wang G, Tong Y, Li Y (2014) Flexible solid-state supercapacitors: design, fabrication and applications. *Energy Environ Sci* 7(7):2160–2181
- Lu Q, Liu L, Yang SL, Liu J, Tian QY, Yao WJ et al (2017) Facile synthesis of amorphous FeOOH/MnO₂ composites as screen-printed electrode materials for all-printed solid-state flexible supercapacitors. *J Power Sources* 361:31–38
- Lu C, Zhao L, Hu YM, Chen W (2018a) A molecular-regulation strategy towards low-voltage driven, multi degree of freedom IPMC catheters. *Chem Commun* 54(63):8733–8736
- Lu C, Yang Y, Wang J, Fu RP, Zhao XX, Zhao L, et al (2018b) High-performance graphdiyne-based electrochemical actuators. *Nat Commun* 9
- Lu Z, Raad R, Safaei F, Xi JT, Liu ZF, Foroughi J (2019) Carbon nanotube based fiber supercapacitor as wearable energy storage. *Front Mater* 6
- Lv T, Yao Y, Li N, Chen T (2016) Highly stretchable supercapacitors based on aligned carbon nanotube/molybdenum disulfide composites. *Angew Chem Int Ed* 55(32):9191–9195
- Lv ZS, Luo YF, Tang YX, Wei JQ, Zhu ZQ, Zhou XR, et al (2018) Editable supercapacitors with customizable stretchability based on mechanically strengthened ultralong MnO₂ nanowire composite. *Adv Mater* 30(2)
- Mastragostino M, Arbizzani C, Soavi F (2002) Conducting polymers as electrode materials in supercapacitors. *Solid State Ionics* 148(3–4):493–498
- Meng C, Liu C, Fan S (2009) Flexible carbon nanotube/polyaniline paper-like films and their enhanced electrochemical properties. *Electrochem Commun* 11(1):186–189
- Meng Y, Zhao Y, Hu C, Cheng H, Hu Y, Zhang Z et al (2013) All-graphene core-sheath microfibers for all-solid-state, stretchable fibriform supercapacitors and wearable electronic textiles. *Adv Mater* 25(16):2326–2331
- Miao MH, Hawkins SC, Cai JY, Gengenbach TR, Knott R, Huynh CP (2011) Effect of gamma-irradiation on the mechanical properties of carbon nanotube yarns. *Carbon* 49(14):4940–4947
- Ming Y, Yang Y, Fu RP, Lu C, Zhao L, Hu YM, et al (2018) IPMC sensor integrated smart glove for pulse diagnosis, braille recognition, and human-computer interaction. *Adv Mater Technol* (US) 3(12)
- Nagaraju G, Sekhar SC, Yu JS (2018) Utilizing waste cable wires for high-performance fiber-based hybrid supercapacitors: an effective approach to electronic-waste management. *Adv Energy Mater* 8(7)
- Niu Z, Zhou W, Chen J, Feng G, Li H, Ma W et al (2011) Compact-designed supercapacitors using free-standing single-walled carbon nanotube films. *Energy Environ Sci* 4(4):1440–1446
- Niu ZQ, Zhang L, Liu L, Zhu BW, Dong HB, Chen XD (2013) All-solid-state flexible ultrathin micro-supercapacitors based on graphene. *Adv Mater* 25(29):4035–4042
- Niu SM, Matsuhisa N, Beker L, Li JX, Wang SH, Wang JC et al (2019) A wireless body area sensor network based on stretchable passive tags. *Nat Electron* 2(8):361–368
- Noh J, Yoon CM, Kim YK, Jang J (2017) High performance asymmetric supercapacitor twisted from carbon fiber/MnO₂ and carbon fiber/MoO₃. *Carbon* 116:470–478
- Park S, Vosguerichian M, Bao Z (2013) A review of fabrication and applications of carbon nanotube film-based flexible electronics. *Nanoscale* 5(5):1727–1752

- Patil B, Ahn S, Yu S, Song H, Jeong Y, Kim JH et al (2018) Electrochemical performance of a coaxial fiber-shaped asymmetric supercapacitor based on nanostructured MnO₂/CNT-web paper and Fe₂O₃/carbon fiber electrodes. *Carbon* 134:366–375
- Peng X, Peng L, Wu C, Xie Y (2014) Two dimensional nanomaterials for flexible supercapacitors. *Chem Soc Rev* 43(10):3303–3323
- Pu X, Li LX, Liu MM, Jiang CY, Du CH, Zhao ZF, et al (2016) Wearable self-charging power textile based on flexible yarn supercapacitors and fabric nanogenerators. *Adv Mater* 28(1):98–+
- Qi DP, Liu ZY, Liu Y, Leow WR, Zhu BW, Yang H et al (2015) Suspended wavy graphene microribbons for highly stretchable microsupercapacitors. *Adv Mater* 27(37):5559–5566
- Qi DP, Liu ZY, Liu Y, Jiang Y, Leow WR, Pal M, et al (2017) Highly stretchable, compliant, polymeric microelectrode arrays for in vivo electrophysiological interfacing. *Adv Mater* 29(40)
- Qian J, Jin H, Chen B, Lin M, Lu W, Tang WM et al (2015) Aqueous manganese dioxide ink for paper-based capacitive energy storage devices. *Angew Chem Int Ed* 54(23):6800–6803
- Qin TF, Peng SL, Hao JX, Wen YX, Wang ZL, Wang XF, et al (2017) Flexible and wearable all-solid-state supercapacitors with ultrahigh energy density based on a carbon fiber fabric electrode. *Adv Energy Mater* 7(20)
- Qin JQ, Das P, Zheng SH, Wu ZS (2019) A perspective on two-dimensional materials for planar micro-supercapacitors. *Appl Mater* 7(9)
- Sambath Kumar K, Cherusseri J, Thomas J (2019) Two-dimensional Mn₃O₄ nanowalls grown on carbon fibers as electrodes for flexible supercapacitors. *ACS Omega* 4(2):4472–4480
- Senthilkumar ST, Selvan RK (2014) Fabrication and performance studies of a cable-type flexible asymmetric supercapacitor. *Phys Chem Chem Phys* 16(29):15692–15698
- Shao M, Li Z, Zhang R, Ning F, Wei M, Evans DG et al (2015) Hierarchical conducting polymer@clay core-shell arrays for flexible all-solid-state supercapacitor devices. *Small* 11(29):3530–3538
- Shao Y, El-Kady MF, Wang LJ, Zhang Q, Li Y, Wang H et al (2015) Graphene-based materials for flexible supercapacitors. *Chem Soc Rev* 44(11):3639–3665
- Shen CW, Xie YX, Sanghadasa M, Tang Y, Lu LS, Lin L (2017) Ultrathin coaxial fiber supercapacitors achieving high energy and power densities. *ACS Appl Mater Interfaces* 9(45):39391–39398
- Shi S, Xu C, Yang C, Chen Y, Liu J, Kang F (2013) Flexible asymmetric supercapacitors based on ultrathin two-dimensional nanosheets with outstanding electrochemical performance and aesthetic property. *Sci Rep* 3(1):1–8
- Shi CL, Zhao Q, Li H, Liao ZM, Yu DP (2014) Low cost and flexible mesh-based supercapacitors for promising large-area flexible/wearable energy storage. *Nano Energy* 6:82–91
- Shi XY, Wu ZS, Qin JQ, Zheng SH, Wang S, Zhou F, et al (2017) Graphene-based linear tandem micro-supercapacitors with metal-free current collectors and high-voltage output. *Adv Mater* 29(44)
- Singh M, Haverinen HM, Dhagat P, Jabbour GE (2010) Inkjet printing-process and its applications. *Adv Mater* 22(6):673–685
- Skakalova V, Hulman M, Fedorko P, Lukac P, Roth S (2003) Effect of gamma-irradiation on single-wall carbon nanotube paper. *AIP Conf Proc* 685:143–147
- Son D, Lee J, Qiao S, Ghaffari R, Kim J, Lee JE et al (2014) Multifunctional wearable devices for diagnosis and therapy of movement disorders. *Nat Nanotechnol* 9(5):397–404
- Son D, Kang J, Vardoulis O, Kim Y, Matsuhisa N, Oh JY, et al (2018) An integrated self-healable electronic skin system fabricated via dynamic reconstruction of a nanostructured conducting network. *Nat Nanotechnol* 13(11):1057–+
- Song Y, Liu TY, Xu XX, Feng DY, Li Y, Liu XX (2015) Pushing the cycling stability limit of polypyrrole for supercapacitors. *Adv Funct Mater* 25(29):4626–4632
- Stoller MD, Ruoff RS (2010) Best practice methods for determining an electrode material's performance for ultracapacitors. *Energy Environ Sci* 3(9):1294–1301
- Su FH, Miao MH (2014) Flexible, high performance two-ply yarn supercapacitors based on irradiated carbon nanotube yarn and PEDOT/PSS. *Electrochim Acta* 127:433–438

- Su F, Lv X, Miao M (2015) High-performance two-ply yarn supercapacitors based on carbon nanotube yarns dotted with Co_3O_4 and NiO nanoparticles. *Small* 11(7):854–861
- Su FH, Miao MH (2014) Asymmetric carbon nanotube- MnO_2 two-ply yarn supercapacitors for wearable electronics. *Nanotechnology* 25(13)
- Sumboja A, Foo CY, Wang X, Lee PS (2013) Large areal mass, flexible and free-standing reduced graphene oxide/manganese dioxide paper for asymmetric supercapacitor device. *Adv Mater* 25(20):2809–2815
- Tai ZX, Yan XB, Xue QJ (2012) Shape-alterable and -recoverable graphene/polyurethane bi-layered composite film for supercapacitor electrode. *J Power Sources* 213:350–357
- Tan YB, Lee J-M (2013) Graphene for supercapacitor applications. *J Mater Chem A* 1(47):14814–14843
- Tang J, Yuan P, Cai C, Fu Y, Ma X (2016) Combining nature-inspired, graphene-wrapped flexible electrodes with nanocomposite polymer electrolyte for asymmetric capacitive energy storage. *Adv Energy Mater* 6(19):1600813
- Tang M, Zheng P, Wang KQ, Qin YJ, Jiang YZ, Cheng YR et al (2019) Autonomous self-healing, self-adhesive, highly conductive composites based on a silver-filled polyborosiloxane/polydimethylsiloxane double-network elastomer. *J Mater Chem A* 7(48):27278–27288
- Tee BCK, Wang C, Allen R, Bao ZN (2012) An electrically and mechanically self-healing composite with pressure- and flexion-sensitive properties for electronic skin applications. *Nat Nanotechnol* 7(12):825–832
- Toupin M, Brousse T, Bélanger D (2004) Charge storage mechanism of MnO_2 electrode used in aqueous electrochemical capacitor. *Chem Mater* 16(16):3184–3190
- Tran NQ, Kang BK, Woo MH, Yoon DH (2016) Enrichment of pyrrolic nitrogen by hole defects in nitrogen and sulfur co-doped graphene hydrogel for flexible supercapacitors. *ChemSusChem* 9(16):2261–2268
- Trung TQ, Lee NE (2016) Flexible and stretchable physical sensor integrated platforms for wearable human-activity monitoring and personal healthcare. *Adv Mater* 28(22):4338–4372
- Varma SJ, Kumar KS, Seal S, Rajaraman S, Thomas J (2018) Fiber-type solar cells, nanogenerators, batteries, and supercapacitors for wearable applications. *Adv Sci* 5(9)
- Venkateshlu S, Cherusseri J, Karnan M, Kumar KS, Kollu P, Sathish M et al (2020) New method for the synthesis of 2D vanadium nitride (MXene) and its application as a supercapacitor electrode. *ACS Omega* 5(29):17983–17992
- Vlad A, Singh N, Galande C, Ajayan PM (2015) Design considerations for unconventional electrochemical energy storage architectures. *Adv Energy Mater* 5(19):1402115
- Wan C, Jiao Y, Li J (2017) Flexible, highly conductive, and free-standing reduced graphene oxide/polypyrrole/cellulose hybrid papers for supercapacitor electrodes. *J Mater Chem A* 5(8):3819–3831
- Wang K, Meng QH, Zhang YJ, Wei ZX, Miao MH (2013) High-performance two-ply yarn supercapacitors based on carbon nanotubes and polyaniline nanowire arrays. *Adv Mater* 25(10):1494–1498
- Wang X, Liu B, Liu R, Wang Q, Hou X, Chen D et al (2014) Fiber-based flexible all-solid-state asymmetric supercapacitors for integrated photodetecting system. *Angew Chem* 126(7):1880–1884
- Wang QF, Wang XF, Xu J, Ouyang X, Hou XJ, Chen D et al (2014) Flexible coaxial-type fiber supercapacitor based on NiCo_2O_4 nanosheets electrodes. *Nano Energy* 8:44–51
- Wang L, Feng X, Ren L, Piao Q, Zhong J, Wang Y et al (2015) Flexible solid-state supercapacitor based on a metal–organic framework interwoven by electrochemically-deposited PANI. *J Am Chem Soc* 137(15):4920–4923
- Wang W, Liu W, Zeng Y, Han Y, Yu M, Lu X et al (2015) A novel exfoliation strategy to significantly boost the energy storage capability of commercial carbon cloth. *Adv Mater* 27(23):3572–3578

- Wang L, Yang H, Liu X, Zeng R, Li M, Huang Y et al (2017) Constructing hierarchical tectorum-like α -Fe₂O₃/PPy nanoarrays on carbon cloth for solid-state asymmetric supercapacitors. *Angew Chem Int Ed* 56(4):1105–1110
- Wang Q, Ling SJ, Liang XP, Wang HM, Lu HJ, Zhang YY (2019) Self-healable multifunctional electronic tattoos based on silk and graphene. *Adv Funct Mater* 29(16)
- Wang YF, Shi-Yi, Bian SW (2019) Flexible textile-based electrode materials for supercapacitors. *Mater Today Proc* 16:1448–1455
- Wang D, Xu JH, Chen JY, Hu P, Wang Y, Jiang W, et al (2020) Transparent, mechanically strong, extremely tough, self-recoverable, healable supramolecular elastomers facily fabricated via dynamic hard domains design for multifunctional applications. *Adv Funct Mater* 30(3)
- Wearable Technology Market Size, Share & Trends Analysis Report By Product (Wrist-Wear, Eye-Wear & Head-Wear, Foot-Wear, Neck-Wear, Body-wear), By Application, By Region, And Segment Forecasts, 2021–2028. Grand View Research; 2021 October, 2021. Contract No. 978-1-68038-165-8
- Wee B-H, Wu T-F, Hong J-D (2017) Facile and scalable synthesis method for high-quality few-layer graphene through solution-based exfoliation of graphite. *ACS Appl Mater Interfaces* 9(5):4548–4557
- Wei D, Scherer MRJ, Bower C, Andrew P, Ryhanen T, Steiner U (2012) A nanostructured electrochromic supercapacitor. *Nano Lett* 12(4):1857–1862
- Wu H, Lou Z, Yang H, Shen GZ (2015) A flexible spiral-type supercapacitor based on ZnCo₂O₄ nanorod electrodes. *Nanoscale* 7(5):1921–1926
- Xiao H, Wu ZS, Chen L, Zhou F, Zheng SH, Ren WC et al (2017) One-step device fabrication of phosphorene and graphene interdigital micro-supercapacitors with high energy density. *ACS Nano* 11(7):7284–7292
- Yan X, Tai Z, Chen J, Xue Q (2011) Fabrication of carbon nanofiber–polyaniline composite flexible paper for supercapacitor. *Nanoscale* 3(1):212–216
- Yang P, Li Y, Lin Z, Ding Y, Yue S, Wong CP et al (2014) Worm-like amorphous MnO₂ nanowires grown on textiles for high-performance flexible supercapacitors. *J Mater Chem A* 2(3):595–599
- Yang PH, Sun P, Mai WJ (2016) Electrochromic energy storage devices. *Mater Today* 19(7):394–402
- Yao B, Yuan L, Xiao X, Zhang J, Qi Y, Zhou J et al (2013) based solid-state supercapacitors with pencil-drawing graphite/polyaniline networks hybrid electrodes. *Nano Energy* 2(6):1071–1078
- Yoo JJ, Balakrishnan K, Huang J, Meunier V, Sumpter BG, Srivastava A et al (2011) Ultrathin planar graphene supercapacitors. *Nano Lett* 11(4):1423–1427
- Yu ZA, Thomas J (2014) Energy storing electrical cables: integrating energy storage and electrical conduction. *Adv Mater* 26(25):4279–4285
- Yu A, Roes I, Davies A, Chen Z (2010) Ultrathin, transparent, and flexible graphene films for supercapacitor application. *Appl Phys Lett* 96(25):253105
- Yu D, Zhai S, Jiang W, Goh K, Wei L, Chen X et al (2015) Transforming pristine carbon fiber tows into high performance solid-state fiber supercapacitors. *Adv Mater* 27(33):4895–4901
- Yu D, Qian Q, Wei L, Jiang W, Goh K, Wei J et al (2015) Emergence of fiber supercapacitors. *Chem Soc Rev* 44(3):647–662
- Yu ZA, Moore J, Calderon J, Zhai L, Thomas J (2015) Coil-type asymmetric supercapacitor electrical cables. *Small* 11(39):5289–5295
- Yu N, Yin H, Zhang W, Liu Y, Tang Z, Zhu MQ (2016) High-performance fiber-shaped all-solid-state asymmetric supercapacitors based on ultrathin MnO₂ nanosheet/carbon fiber cathodes for wearable electronics. *Adv Energy Mater* 6(2):1501458
- Yuan W, Zou S, Liu XB, Liu KX, Lv C, Xie P et al (2020) Scalable cable-type lithium-ion supercapacitors with high loading mass and promotional volumetric energy density. *ACS Sustain Chem Eng* 8(45):16869–16877
- Yuan H, Wang G, Zhao YX, Liu Y, Wu Y, Zhang YG (2020) A stretchable, asymmetric, coaxial fiber-shaped supercapacitor for wearable electronics. *Nano Res* 13(6):1686–1692

- Yun J, Song C, Lee H, Park H, Jeong YR, Kim JW et al (2018) Stretchable array of high-performance micro-supercapacitors charged with solar cells for wireless powering of an integrated strain sensor. *Nano Energy* 49:644–654
- Zarin H, Sy S, Fu J, Jiang G, Kang K, Jun Y-S et al (2016) Molecular functionalization of graphene oxide for next-generation wearable electronics. *ACS Appl Mater Interfaces* 8(38):25428–25437
- Zeng Y, Han Y, Zhao Y, Zeng Y, Yu M, Liu Y et al (2015) Advanced Ti-doped Fe₂O₃@PEDOT core/shell anode for high-energy asymmetric Supercapacitors. *Adv Energy Mater* 5(12):1402176
- Zhai S, Jiang W, Wei L, Karahan HE, Yuan Y, Ng AK et al (2015) All-carbon solid-state yarn supercapacitors from activated carbon and carbon fibers for smart textiles. *Mater Horiz* 2(6):598–605
- Zhang LL, Zhao X (2009) Carbon-based materials as supercapacitor electrodes. *Chem Soc Rev* 38(9):2520–2531
- Zhang LL, Zhao X, Stoller MD, Zhu Y, Ji H, Murali S et al (2012) Highly conductive and porous activated reduced graphene oxide films for high-power supercapacitors. *Nano Lett* 12(4):1806–1812
- Zhang DH, Wu YL, Li T, Huang Y, Zhang AQ, Miao MH (2015) High performance carbon nanotube yarn supercapacitors with a surface-oxidized copper current collector. *ACS Appl Mater Interfaces* 7(46):25835–25842
- Zhang Y-Z, Wang Y, Cheng T, Lai W-Y, Pang H, Huang W (2015) Flexible supercapacitors based on paper substrates: a new paradigm for low-cost energy storage. *Chem Soc Rev* 44(15):5181–5199
- Zhang CJ, Higgins TM, Park S-H, O'Brien SE, Long D, Coleman JN et al (2016) Highly flexible and transparent solid-state supercapacitors based on RuO₂/PEDOT: PSS conductive ultrathin films. *Nano Energy* 28:495–505
- Zhang YZ, Cheng T, Wang Y, Lai WY, Pang H, Huang W (2016) A simple approach to boost capacitance: flexible supercapacitors based on manganese oxides@MOFs via chemically induced in situ self-transformation. *Adv Mater* 28(26):5242–5248
- Zhang M, Liu YH, Hu ML, Wei HL, Gao YH (2017) Spiral wire-type stretchable all-solid-state supercapacitors based on MnO₂/graphene/Ni wires. *Electrochim Acta* 256:44–51
- Zhang WY, Liu Q, Chao SY, Liu RP, Cui X, Sun Y et al (2021) Ultrathin stretchable triboelectric nanogenerators improved by postcharging electrode material. *ACS Appl Mater Interfaces* 13(36):42966–42976
- Zhao X, Chu BT, Ballesteros B, Wang W, Johnston C, Sykes JM et al (2009) Spray deposition of steam treated and functionalized single-walled and multi-walled carbon nanotube films for supercapacitors. *Nanotechnology* 20(6):065605
- Zhao D, Wang H, Khan ZU, Chen JC, Gabrielsson R, Jonsson MP et al (2016) Ionic thermoelectric supercapacitors. *Energy Environ Sci* 9(4):1450–1457
- Zhao JJ, Han S, Yang Y, Fu RP, Ming Y, Lu C et al (2017) Passive and space-discriminative ionic sensors based on durable nanocomposite electrodes toward sign language recognition. *ACS Nano* 11(9):8590–8599
- Zhong Q, Zhong J, Hu B, Hu Q, Zhou J, Wang ZL (2013) A paper-based nanogenerator as a power source and active sensor. *Energy Environ Sci* 6(6):1779–1784
- Zhong J, Meng J, Yang ZY, Poulin P, Koratkar N (2015) Shape memory fiber supercapacitors. *Nano Energy* 17:330–338
- Zhou W, Cao X, Zeng Z, Shi W, Zhu Y, Yan Q et al (2013) One-step synthesis of Ni₃S₂ nanorod@Ni(OH)₂ nanosheet core-shell nanostructures on a three-dimensional graphene network for high-performance supercapacitors. *Energy Environ Sci* 6(7):2216–2221